Synthesis and applications of novel fluorescent and colorimetric coumarin-based sensors towards analyte sensing in aqueous systems

By

Aidan Leigh Battison

Submitted in fulfilment of the requirements for the Doctoral degree in the faculty of Science to be awarded at the Nelson Mandela University

April 2022

Supervisor: Dr. N. Mama

Declaration

In accordance with Rule G5.6.3, I, Aidan Leigh Battison (student number: 212256254), hereby declare that the dissertation for the Doctoral degree in the faculty of Science is my own work and that it has not previously been submitted for assessment or completion of any postgraduate qualification to another University or for another qualification.

Signed: 

Printed name: Aidan Leigh Battison

Date: 10-01-2022

NELSON MANDELA UNIVERSITY

PERMISSION TO SUBMIT FINAL COPIES

OF TREATISE/DISSERTATION/THESIS TO THE EXAMINATION OFFICE

Please type or complete in black ink

FACULTY: Science

SCHOOL/DEPARTMENT: Chemistry

I, (surname and initials of supervisor) Mama, N

and (surname and initials of co-supervisor) _____

the supervisor and co-supervisor respectively for (surname and initials of

candidate) Battison, A.L

(student number) 212256254 a candidate for the (full description of qualification)

Doctor of Philosophy (Chemistry)

with a treatise/dissertation/thesis entitled (full title of treatise/dissertation/thesis):

Synthesis and applications of novel fluorescent and colorimetric coumarin-based sensors towards analyte sensing in aqueous systems

It is hereby certified that the proposed amendments to the treatise/dissertation/thesis have been effected and that **permission is granted to the candidate to submit** the final copies of his/her treatise/dissertation/thesis to the examination office.

_____ 14/03/2022

SUPERVISOR **DATE**

And

_____ _____

CO-SUPERVISOR **DATE**

"Protect me from knowing what I don't need to know. Protect me from even knowing that there are things to know that I don't know. Protect me from knowing that I decided not to know about the things that I decided not to know about. Amen"

-*Douglas Adams, The Hitchhiker's guide to the Galaxy.*

Abstract

The continuous growth of mankind has not been considerate to the environment. The release of millions of tonnes of toxic heavy metal cations and anionic species through industrial, mining, agricultural, and electronic dumping has led to disease and, in many instances, death. This is usually suffered by low-income informal populations residing in third world countries. Moreover, many unnecessary deaths of children are becoming more prevalent because of consumption and contact with contaminated water, agricultural, and animal sources. Bioaccumulation of these toxic species in fish, plants, and animals, inevitably make their way back to the unaware general population. As growth by mining, agriculture, and electronics are indeed vital aspects of human development, the negative side effects of these activities usually continue unregulated. Therefore, as these processes are set to continue until more stringent regulatory processes are put into legislature; low-cost, sensitive, selective organic-based sensors are a step in the right direction towards highlighting the need for environmental restoration and remediation; whilst also aiming to preventing unnecessary disease and death in the process.

Herein, coumarin derived small-molecule fluorescent and colorimetric sensors for the quantitative and qualitative assessment of cationic and anionic species in aqueous and organic media are described.

Ten fluorescent sensors supporting 1,4-disubstituted triazolyl moieties were synthesized according to Cu(I)-catalyzed azide-alkyne cycloaddition "click" reactions. These sensors were screened for their cationic and anionic affinities in a variety of solvent systems. Majority of the sensors responded well towards Fe^{3+}, characterized by a strong fluorescent quenching response with a good degree of sensitivity and selectivity. Selected sensors were further investigated for their affinities towards anionic species; however, they did not display the same degree of selectivity or sensitivity towards these chosen anions.

Titration studies of selected sensors with Fe^{3+} were able to be used towards determining the modes of fluorescent quenching; the photophysical mechanisms by which quenching occurs; stoichiometric binding ratios, association constants, and the number of coordination sites present between the sensors and Fe^{3+}. Reversibility studies of the sensor-metal complex was investigated with EDTA. Partial reversibility was achieved for the chosen sensors with Fe^{3+}. Hydrogen potential studies further described the application of these sensors over a good pH range. The binding site between the sensors and Fe^{3+} was investigated by NMR studies and

supported by molecular modelling analysis. Complexation was shown to involve the triazole N-atoms as the main contributors towards complexation and supported/stabilized by neighbouring electron-donor groups and solvent molecules.

Four colorimetric sensors supporting imine and azo functionalities were synthesized according to well-known organic methods. Initial absorbance screening studies of these sensors in a variety of solvent systems highlighted an imine and azo sensor as the most favourable candidates towards further sensing studies. These sensors were screened for their cationic and anionic affinities in a variety of solvent systems, however, anionic screening studies displayed little affinity towards any of the selected anions. The coumarin-imine sensor displayed excellent affinity towards Hg^{2+} in water, characterized by changes in the intensity of the absorbance peak associated with the imine functionality; whilst the coumarin-azo derivative also displayed excellent affinity towards Hg^{2+} in acetonitrile, characterized by a strong bathochromic shift in wavelength and visible colour change from yellow to red. The electronic mechanisms by which complexation occurred was determined to arise via a dual ICT-ESIPT-ESICT and ICT process for the imine and azo sensors respectively. Competition studies of both sensors in their chosen solvents displayed excellent selectivity towards Hg^{2+}. Titration studies confirmed excellent sensitivity of both sensors towards Hg^{2+}, with titration data allowing for further determination of the stoichiometric binding ratio, and association constants. Hydrogen potential studies further described the application of these sensors over a wide pH range. Reversibility studies of the sensor-metal complex in EDTA displayed the complete reversibility of the azo-sensor with Hg^{2+}. Thus, this complete reversibility allowed for the additional construction of a molecular mimicking device and molecular keypad lock. Furthermore, both sensors displayed extended applications towards Hg^{2+} determination in real-world water samples; with further applications of the azo sensor extending towards on-site assay methods. The complexation site of each sensor was proposed by NMR and FT-IR analysis and supported by molecular modelling studies. Complexation between the imine and Hg^{2+} was shown to occur between the imine-nitrogen and neighbouring phenol group; whilst complexation with the azo sensor occurred between the coumarin- and neighbouring ester-carbonyl functionalities. Both complexation scenarios were shown to occur in a pseudo-6-membered ring conformation, highlighting the stability of the sensor-metal complexes.

Lastly, a single Cu(I)-catalyzed "click" derived polymeric sensor was attempted via two different synthetic routes, however, both synthetic strategies failed.

Acknowledgements

- To God almighty, the universe, and the powers that be. I cannot fully describe the depth of gratitude I feel towards your input in this process. Thank you.
- To my beloved parents. This thesis is an extension of the passion, drive, and tenacity you have taught me throughout my life. Your continuous encouragement for me to do and be the best that I can constitutes the very foundation upon which this thesis is based. This is for you. I love you.
- My most delicious Niall. So many parts of this thesis are chronologically linked to pinnacle moments in our lives and relationship. I look at this thesis with nothing but good memories of the support and love you have shown me during this process. Thank you, my most special. I love you.
- To Dr Neliswa Mama, umama wam. How could words truly encapsulate the feelings I have for you? We have shared ten years together, learning, failing, crying, combating, but ultimately succeeding. Thank you for giving me a stable platform to become the researcher I always aspired to be. The journey has been so much sweeter with you as my guide. Enkosi.
- To Mr Stiaan Schoeman. You have truly gone beyond the call of friendship and invested so much time and energy into computational calculations and wrapping our brains around certain concepts and results! You never complained, and always accepted a challenge and opportunity to assist me with a smile. There are very few people as genuine as you. Thank you, my friend.
- To Dr Lize Greyling. You have had my back this entire process. Thank you for your support and for always being in my corner. I will always look at 11:15 am with love in my heart. Thank you, my best.

On a professional note:

- Thank you to Nelson Mandela University for giving me the opportunity, facilities, and funding needed to turn this dream into a reality.

- Thank you to the National Research Foundation (NRF) and Council for Scientific and Industrial Research (CSIR) for your support shown towards this thesis and my livelihood.
- To Mr Eric Bashman and Mr Henk Schalekamp for their unwavering technical and chemical assistance.
- To Dr Eric Hosten for single-crystal X-ray studies.
- To the Nelson Mandela Chemistry department for the opportunity to conduct this doctoral study.
- To all my friends and peers, you have made this experience so worthwhile. Who knew flash-freezing fruit and lobbing them off the third-floor balcony could be so much fun?

.

Selected Abbreviations

UV-Vis:	ultraviolet visible
CuAAC:	copper(I)-catalyzed azide alkyne cycloaddition
THF:	tetrahydrofuran
DMF:	dimethylformamide
DCM:	dichloromethane
DMSO:	dimethylsulfoxide
FRET:	Förster resonance energy transfer/fluorescence resonance energy transfer
ICT:	Intramolecular charge transfer
FT-IR:	Fourier-transform infra-red
HOMO:	highest occupied molecular orbital
LUMO:	lowest occupied molecular orbital
NMR:	nuclear magnetic resonance
PMDETA:	N,N,N',N'',N''-pentamethyldiethylenetriamine
TLC:	thin layer chromatography
GPC:	gel permeation chromatography
RAFT:	reversible addition fragmentation chain transfer

General Table of Contents

Published work

Arkivoc

The Free Internet Journal for Organic Chemistry

Paper

Archive for Organic Chemistry

Arkivoc 2020, part v, 0-0
to be inserted by editorial office

Synthesis and application of a fluorescent "turn-off" triazolyl-coumarin-based fluorescent chemosensor for the sensing of Fe^{3+} ions in aqueous solutions

Neliswa Mama* and Aidan Battison

Department of Chemistry, Nelson Mandela University, P.O Box 77000, Port Elizabeth, 6031, South Africa
Email: neliswa.mama@mandela.ac.za

Received 06-30-2020 **Accepted** 09-16-2020 **Published online** 09-19-2020

Abstract

Two coumarin derivatives containing triazole moieties have been synthesized using "click chemistry" protocol and investigated as chemosensors for the detection of metal ions. These compounds displayed a strong preference for Fe^{3+} ions with complexation resulting in fluorescent quenching. The detection limit of the preferred chemosensor was determined to be 1.4 μM. The preferred triazole-coumarin compound showed greater selectivity towards Fe^{3+} in the presence of competing metal cations. Binding stoichiometry between this triazole-coumarin and Fe^{3+} was shown to occur in a 1:1 ratio between the chemosensor and metal cation. The binding site of Fe^{3+} to the triazole-coumarin was determined using ^{1}H NMR, ^{13}C NMR and molecular modeling studies.

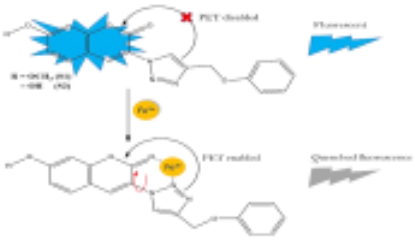

Keywords: Coumarin, triazole, click chemistry, fluorescence, chemosensor, static quenching, molecular modeling

DOI: https://doi.org/10.24820/ark.5550190.p011.283 **Page 1** **AUTHOR(S)**

In the process of publishing

A coumarin-azo derived colorimetric chemosensor for Hg^{2+} detection in organic and aqueous media and its extended real-world applications

Aidan Battison[1], Stiaan Schoeman[2], Neliswa Mama[3*]

Department of Chemistry, Nelson Mandela University, P.O Box 77000, Port Elizabeth, 6031, South Africa
Email: neliswa.mama@mandela.ac.za

Abstract

Pollution caused by the release of toxic heavy metals into the environment by industrial and farming processes has been regarded as a major problem worldwide. This has attracted a great deal of attention into restoration and remediation. Mercury is classified as a toxic heavy metal which has posed significant challenges to public and environmental health. To date, conventional methods for mercury detection rely on expensive, destructive, complex, and highly specialized methods. Evidently, there is a need to develop systems capable of easily identifying and quantifying mercury within the environment. In this way, organic-based colorimetric chemosensors are gaining increasing popularity due to their high sensitivity, selectivity, cost-effectiveness, ease of design, naked-eye, and on-site detection ability. The formation of coumarin-azo derivative **AD1** was carried out by a conventional diazotization reaction with coumarin-amine **1c** and *N,N*-dimethylaniline. Sensor **AD1** displayed remarkable visual colour change upon mercury addition with appreciable selectivity and sensitivity. The detection limit was calculated as 0.24 μM. Additionally, the reversible nature of **AD1** allowed for the construction of an IMPLICATION type logic gate and Molecular Keypad Lock. Chemosensor **AD1** displayed further sensing applications in real-world water samples and towards on-site assay methods. Herein, we describe a coumarin-derived chemosensor bearing an azo (N=N) functionality for the colorimetric and quantitative determination of Hg^{2+} in organic and aqueous media.

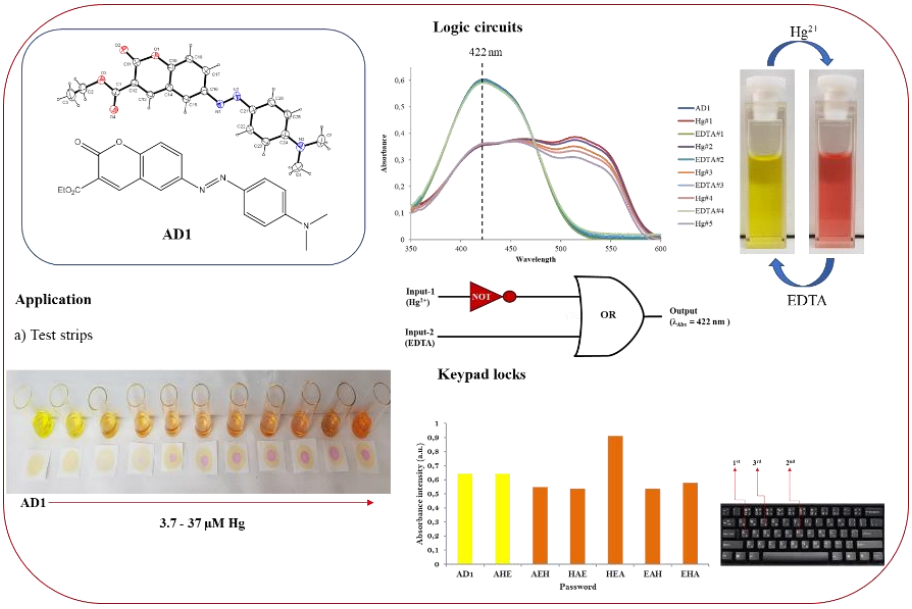

Keywords: Mercury, coumarin, azo-dye, colorimetric sensing, reversible.

Chapter 1

Table of Contents

List of Figures

List of Tables

List of Schemes

1. Introduction

1.1 Definition of molecular sensors

"A chemosensor is molecule of abiotic origin that signals the presence of matter or energy", as defined by one of the founders of molecular sensing, A.W. Czarnick.[1] Fluorescent sensors were defined as "compounds incorporating a binding site, fluorophore, and a mechanism for communication between the two sites". However, if the fluorescent sensor participates in an irreversible chemical reaction with a specific analyte, then it is generally referred to as a fluorescent chemodosimeter.[2] In the last few decades, both the terms fluorescent sensors and fluorescent chemodosimeters have been used interchangeably and fluorescent probes are now more commonly referred to by either name. From this point forward, a more generalized description of chemical sensors will be outlined. A molecular sensor is a chemical structure (both organic or inorganic complexes) that are used for sensing of an analyte to produce a detectable change or a signal.[3] This signal is produced by the disruption of the electronic environment between the receptor unit and fluorophore (reporter) brought about by interactions with analytes.[4] These signals or changes in the electronic environment result in either spectral (^{1}H NMR, electronic, optical and fluorescent) or redox behavioural changes of the system.[5,6] Among the various types of chromogenic sensors that have been developed, those based on analyte-induced fluorescence have advantages over other methods owing to its sensitivity, selectivity, ability to detect the desired analyte in trace quantities, easy operation methods and instantaneous response.[7,8] Traditional methods of analyte sensing including spectrophotometry, atomic absorption spectrometry, stripping voltammetry, potentiometry, X-ray fluorescence spectrometry and inductively coupled plasma atomic emission spectrometry have been used for the detection of various analytes.[9,10] However, these methods are associated with many drawbacks including labour-intensive procedures, high cost of equipment, complex processes, and the need for highly qualified personnel.[11] A great number of sensors that are developed for various analytes, such as heavy metal ions, are based on the conventional fluorescence emission technique by quenching (turn off) of the fluorescence intensity.[12] Fluorescence quenching can occur via different molecular interactions such as molecular rearrangements, energy transfer, ground-state complex

formations and collisional quenching. Furthermore, the polarity of the different solvent media and type of the quencher can influence the quenching process.[13]

Analyte detection by a fluorescent and/or colorimetric sensor is usually achieved through one or more common photophysical mechanisms, including Chelation Induced Enhanced/Quenched Fluorescence (CHEF/CHQF), Intramolecular Charge Transfer (ICT), Photoinduced Electron Transfer (PET), Aggregation Induced Emission (AIE), Förster/Fluorescence Resonance Energy Transfer (FRET), C=N isomerization, and Excited-State Intramolecular Proton Transfer (ESIPT), with the number of approaches still expanding. These mechanisms have been extensively outlined in the literature.[14–16] These mechanisms will be discussed where relevant in **Chapters 2-5**.

Several types of fluorescent probes have bridging units between the fluorophore and binding unit known as spacers. If the receptor is attached directly to the fluorophore it is referred to as an integrated probe. It is important to note that not all sensors require a spacer unit to effectively sense a target analyte, however, the receptor and active units are imperative to overall function. A diagram depicting the generalized structure and function of a fluorescent probe is shown in **Figure 1**.

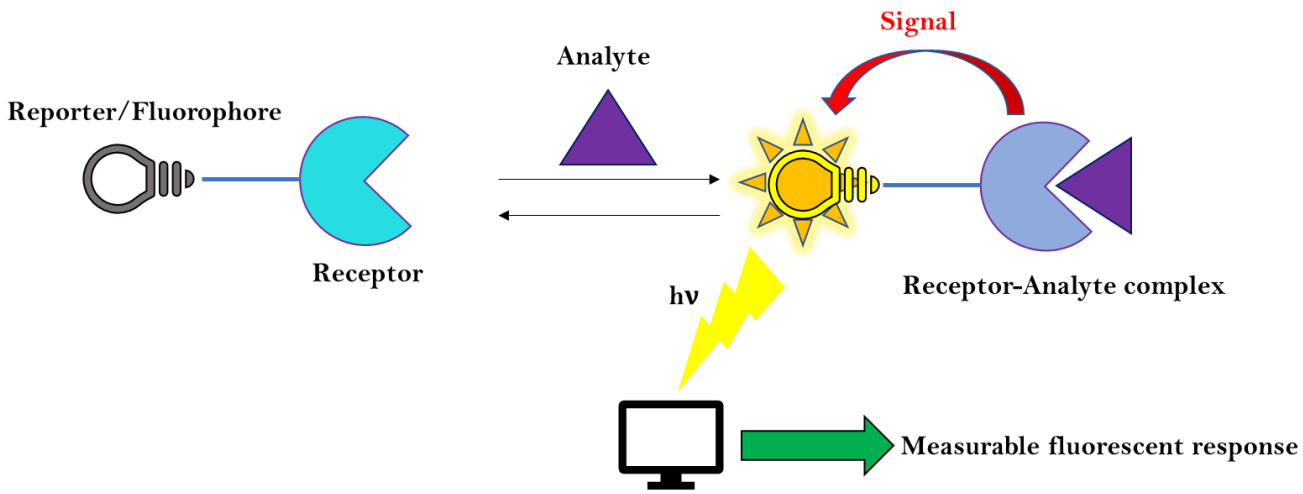

Figure 1: Simplified representation of an observable spectral response upon analyte binding to a fluorescent probe.

The receptor unit controls the binding of the target analyte with high selectivity and efficiency. Recognition is produced *via* the formation of weak interactions such as reversible covalent and non-covalent interactions between the receptor and the target analyte. These types of interactions includes noncovalent interactions such as hydrogen bonding, co-ordinate bonds, hydrophobic forces, π-π interactions, CH-π, cation-π, charge-transfer (CT) van der Waals forces and electrostatic effects.[17–19] It is the transducer or signalling unit which converts the binding event into a measurable physical response. These sensors must be designed in a manner that measuring this change and converting it to useful information is achievable. Therefore, an ideal fluorescent/colorimetric sensor must meet two basic requirements. Firstly, the receptor must have the strongest affinity with the relevant target analyte (binding-selectivity). Secondly, based on good binding-selectivity, the produced signal should not be susceptible to environmental interference. This includes interferences such as photobleaching, sensor molecule concentration, the environment around the sensor molecule (pH, polarity, temperature etc), and stability under illumination (signal-selectivity).[20]

1.2 A brief history of molecular sensors

Whilst the term "chemosensor" was only coined in the 1980's, the first reported use of a chemical sensor was by Friedrich Goppelsröder in 1868.[21] He developed a method that was used to determine the presence of Al^{3+} ions via the formation of fluorescent morin chelates. This subsequently led to the development of various other fluorescent sensors for the determination of metal ions, introducing the era of analytical chemistry as it is known today.

During the late 1970's and 1980's, there was an explosive growth in the development of fluorescent chemical sensors by the forefathers of modern day sensing; , Sousa[22], Bousa-Laurent[23], de Silva[24], Tsien[25] and Czarnik.[26] Sensors focusing on crown and aza-crown ethers (or other ligands) linked to fluorophores were able to recognize metal ions in a selective manner through changes in the emission signals. Methylene bridges were incorporated between the ligands and fluorophores and the fluorescence was monitored by the presence or absence of photoinduced electron-transfer (PET) quenching process involving lone-pair electrons on amine-nitrogen or ether-oxygen atom(s). Typically, fluorescent enhancement upon binding of the metal ion was produced due to the blocking of PET, this was referred to as chelation-enhanced fluorescence.

As a result, in its early stages, the development of sensors was benefitted greatly by advances made in host–guest, macrocyclic, and supramolecular chemistry.[27] Since then, fluorescent sensors have been extensively developed for numerous analytes. Fluorescent sensors for biologically and/or environmentally important cations, anions, small neutral molecules as well as biomacromolecules (such as proteins and DNA) have been developed. This has been coupled with the rapid advancement in microscopic imaging technologies.[28,29]

1.3 Human activities, heavy metals, and the need for sensors

It is no surprise that mankind's insatiable appetite for growth and profit has negatively impacted his own health and the well-being of the environment he occupies. Humanity releases millions of tonnes of toxic compounds into the environment each day. Environmental contamination due to waste disposal mismanagement is an ongoing global issue. Open dumping and open burning are the main forms of waste treatment and disposal systems which are prominent in low-income countries.[30] In Africa alone, the World Health Organization (WHO) has estimated that 33% of disease is attributable to environmental risk factors with hazardous waste being included amongst the first three main factors. The domestic and hazardous waste management is of particular concern.[31] In most African cities, less than 20% of urban waste is disposed of in landfills. The remaining waste tends to end up in illegal dumping sites.

With the development of the electronic industry, vast quantities of electronic wastes also referred to as "e-wastes" are released into the environment at the rate of 20–50 million tons per year.[32] E-wastes are chemically and physically distinct from other municipal or industrial wastes. Their chemical compositions vary depending on the age and type of the discarded items, mostly composed of a mixture of heavy metals attached to, covered with, or mixed with various types of plastics and ceramics.[33]

Wealthy countries will either landfill or export their e-waste to developing countries instead of recycling locally due to lack of facilities, high labour cost and strong environmental regulations.[34] Consequently, some developing countries in Asia and Africa are becoming popular destinations for the illegal export of e-waste due to cheap labour and inadequate governmental regulations.[35] In these developing countries, workers often perform informal /backyard recycling, utilizing techniques that involve cutting, acid bathing, heating/smelting

and open burning where adequate protective gear is not worn and they are exposed to these harmful chemicals and elements. The workers that are performing these dangerous tasks are predominantly women and children.[36] In addition, e-wastes are illegally recycled in these developing countries to recover economically valuable resources such as gold, silica, plastic, iron, and aluminium from electronic parts and base materials.[37] Therefore, the inadequate legislation combined with the economic value of the recovered materials is encouraging an emerging market of illegal recycling of discarded e-waste products by informal recyclers in developing countries.

The most concerning and detrimental effects of the illegal dumping and processing of e-wastes are the heavy/toxic metals which are release into the air, soil, and eventually into the water systems.[38] Some of the harmful metals resulting from this waste include Pb, As, Be, Cr, Co, In, Th, Sb, Hg, Ag, Ni and Cd, but valuable platinum group metals and Cu have also been identified.[39] Heavy metals have high toxicity, mobility, and non-biodegradability and have found to be persistent in soils leading to a serious problems in the ecosystem; causing risks to human health through bioaccumulation in plants and animals or bioconcentration in the food-chain.[40,41] These heavy metals can easily find their way into water systems. For example, heavy metals present in soil can be washed away by rainfall and end up in various types of water bodies in the environment; they can contaminate groundwater through leaching, especially under acidic conditions.[42]

Inhabitants of rural areas rely heavily upon surface water and groundwater for irrigation, drinking, and watering of livestock. Ecological risk assessments of heavy metals in and around the vicinity of e-waste dumping sites is greatly warranted. In humans, the accumulation of metals and metalloids can cause physical damage: copper can cause liver damage; lead can cause behavioural and learning disabilities in children[35]; mercury can cause severe and irreversible neurological disorders[43]; and cadmium can increase the risk of lung cancer and kidney damage, to name a few.[44]

The harmful effects of some of the most common heavy metals towards human health and the associated acceptable limits in drinking water are shown in **Table 1**. The acceptable limits of these various metals in drinking water has been extracted from "Current Drinking Water Standards", U.S.E.P.A. Office of Water and the World Health Organization (WHO) drinking water standards.[45]

Table 1: Effects of common heavy metals on human health and acceptable limits in drinking water.

Heavy Metal	Effect on human health/physiology	Acceptable limit in drinking water (mg/L)
Mercury	• Acute mercury poisoning and long-term neurological effects that arise from chronic exposure to mercury vapour.[46] • Targets the brain, causing difficulty in locomotion, reduced vision, tact, general weakness, tremors, loss of consciousness, and ultimately death. Methylmercury (MeHg) can also cause mental retardation in children whose mothers were pre-exposed.[47] • Problems with digestive system, nervous system, immune systems and cause lungs, kidneys, skin and eye disorders.[48]	**0.002-0.01**
Cadmium	• Cadmium is broadly toxic and can cause damage to the kidneys, liver, testes, cardiovascular, and endocrine systems. It has been classified as a known human carcinogen by the International Agency for Research on Cancer since 1993. It has been reported that exposure to Cd affects the skeletal system, potentially increasing the risk of osteoporosis and bone fractures.[49]	**0.003-0.005**

Lead	• Lead toxicity is a particularly insidious hazard with the potential of causing irreversible health effects. These effects include damage to the nervous, renal, cardiovascular, hematopoietic, reproductive, and endocrine systems.[50]	**0.01-0.015**
Chromium	• High dosage can promote the restraint of erythrocyte glutathione reductase, which affects the ability to diminish methaemoglobin to haemoglobin. The results from various studies show that chromate can lead to DNA dysfunction in many ways and can prompt the arrangement of DNA adducts, can cause chromosomal variations, modifications in replication, and interpretation of DNA.[51]	**0.02-0.1**
Silver	• Research findings indicate that nano-silver exposure via one of several routes (e.g. oral, intravenous) can lead to genotoxicity and DNA damage, inflammatory response in the liver and kidneys, and can cause adverse functional effects in the lungs, heart, intestines, and spleen.[52]	**0.1**
Arsenic	• Associated with bladder and lung cancers, reproductive outcomes, declined cognitive performances, kidney injury, carotid intima-media thickness, and various pulmonary defects in children. Other childhood effects such as low birth weight, low gestational age, anaemia, increased apoptosis, and decreased cognitive function have been reported.[53]	**0.005-0.01**

In a recent South African case study conducted by Elumalai and co-workers [54] titled "Human Exposure Risk Assessment Due to Heavy Metals in Groundwater", aimed to determine the heavy metal contamination in water and assess the impact of human activities on groundwater in and around two major South African towns, namely Empangeni and Richards Bay. The order of dominance of heavy metals in the drinking water sources was found to be silicon > manganese > silver > lithium > iron > lead > aluminium > copper > nickel > boron > zinc > cobalt > cadmium, whilst chromium, titanium and zirconium were below the detection limits in water. Contamination due to aluminium, lead and nickel was prevalent in both areas whilst boron, cadmium, iron, and manganese all exceeded the acceptable limits at a few of the locations. The HPI (Heavy metal Pollution Index) varied from 17 to 330 indicating high contamination in the two zones within the study areas. Examination of the sources of these heavy metals in the groundwater found that cobalt, manganese, nickel, zinc, and boron were indicative of industrial activities. Lithium, iron, and silver in the groundwater was related to mining operations and associated processes. Application of fertilizers were shown to be the likely contributors to the presence of cadmium and copper in the groundwater. Multiple sources including geogenic industries and seawater intrusion have contributed to lead, silver, and boron contaminations. The study concluded that the major pollution zones identified were the industrial sites near the coastal regions and the landfill sites near the central region of the study area.

This study serves to indicate how various human and industrial activities have greatly affected the quality of the surrounding soil and water supplies, and inevitably the health and well-being of the environment and the humans who inhabit it. The heavy metal contamination by these various sources is mostly due to the poor implementation of industrial waste regulations and illegal dumping of hazardous waste in and around rural/impoverished residential areas. Therefore, there is a great need and demand for the specific and sensitive identification of harmful species within the scope of human health and environmental restoration and remediation.

The predominant methods that have been applied for these sensing purposes include flame atomic absorption spectroscopy, inductively coupled plasma optical emission spectroscopy, stripping voltammetry, X-ray fluorescence spectrometry, and inductively coupled plasma mass spectrometry. However, most of these methods are costly, time consuming (especially during sample preparation), complex, and often require skilled personnel. This can make the option of real-time evaluations problematic. To overcome the drawbacks of conventional sensing methods, efficient and low-cost optical sensors that can detect and calculate metal

ions in real-time with very little effort, expertise, and time-consuming procedures is needed now more than ever before. Fluorescent and colorimetric sensors have become the preferred method of analyte detection due to their high sensitivity and selectivity and low detection limits of cations and anions. Fluorescent sensors have shown to be advantageous for the purpose of intercellular analyte detection.[55,56]

Some recent fluorescent small-molecule coumarin based sensors for the detection of mercury[57,58], cadmium[59] and lead[60] are shown in **Figure 2**. The experimental detection limits of these sensors are also given. It is evident that these small-molecule fluorescent sensors display the desired sensitivity required for an effective sensor. An extensive review by Rasheed et.al and Kim et.al highlight colorimetric and fluorescent sensors for these three heavy metal cations.[61,62] Rasheed and co-workers further highlight the adverse health effects of these three metals and the modes by which these toxic cations are released into the environment.

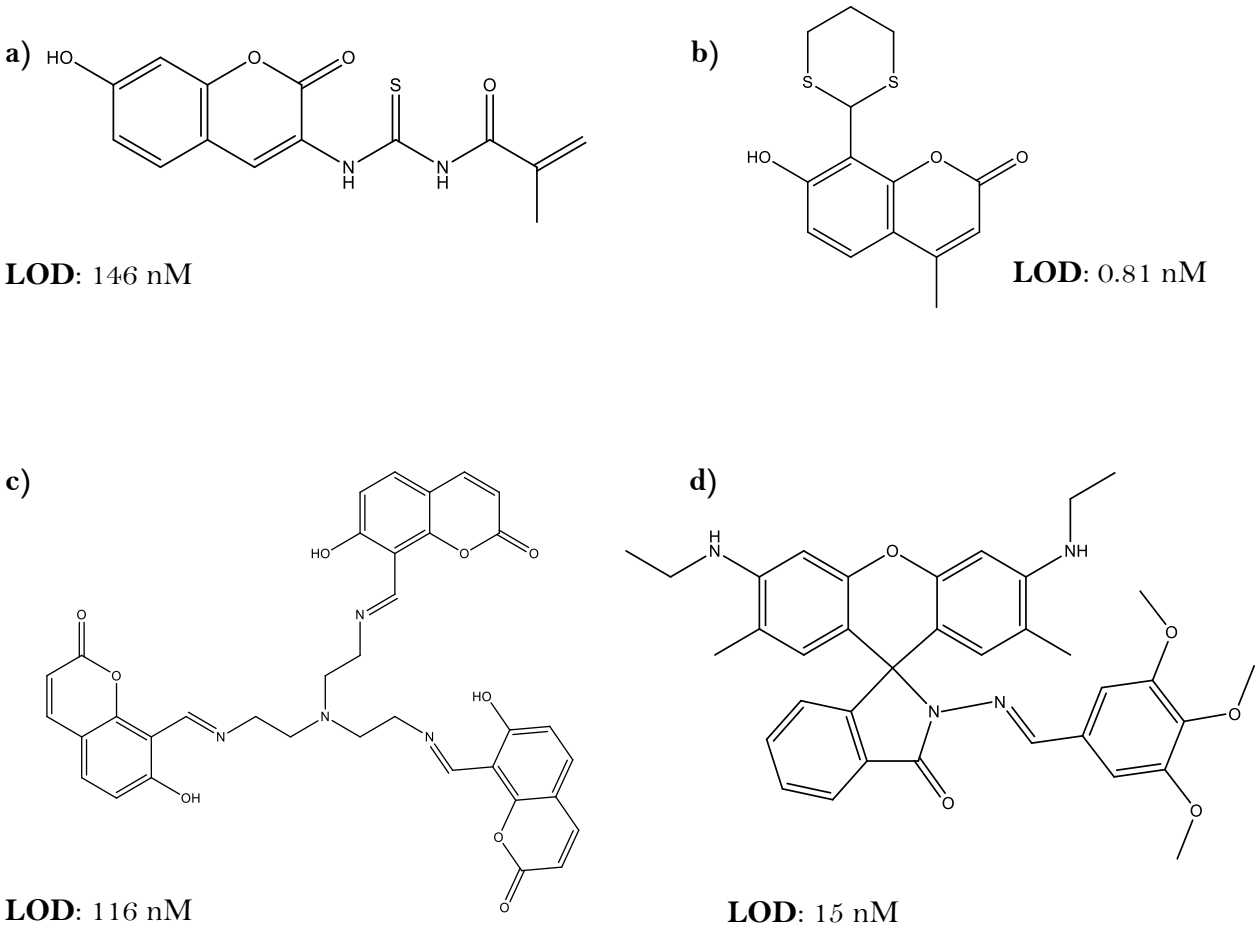

Figure 2: Small-molecule fluorescent sensors for mercury (**a** & **b**), cadmium (**c**) and lead (**d**). **LOD-** Limit of Detection.

1.4 Optical sensors and sensor design

Among the various types of sensors for analyte detection, optical sensors based on fluorescent or colorimetric signal transduction exhibit superior properties with respect to the simplicity of system operations and non-destructive analyte detection with high sensitivity and selectivity.[63] The photophysical performances of optical sensors rely on rational design of molecular fluorophore or chromophore structures. The most important factors needing to be considered during the design of optical sensors include stability against photobleaching; photoluminescence quantum yield; and visible-light absorption, as well as the structural flexibility for the accommodation of side groups that can bind analytes with sufficient affinity and selectivity.[64] As previously stated, this specific binding is driven by relatively weak interactions namely hydrogen bonding, metal coordination, van der Waals forces, electrostatic forces, or other noncovalent interactions.

1.4.1 Fluorescent and colorimetric sensors

Simply stated, fluorescent sensors are molecules that characterize sensing events via changes to their emission spectra, whilst colorimetric sensors signal events through the changes in visible colour. Fluorescent sensors have shown to be advantageous tools due to their high selectivity, excellent sensitivity, manoeuvrability, low cost of synthesis, low detection limits, ease of quantification, as well as rapid in-situ and real-time monitoring.[65–67] Recently, colorimetric sensors have also received a great deal of attention due to their "naked eye" signal detection, fast response time, sensitivity, simplistic operating procedure and are suitable for on-site assay and analysis.[68–70] Although there are many examples of colorimetric and fluorescent based sensors in the literature, an excerpt of some of the most recent examples are shown in **Table 2**.[69,71–73]

Table 2: Structures and properties of recent optical sensors.

Sensor structure	Type of optical sensor	Sensing response	Responsive analyte	Sensing Detection limit (uM)
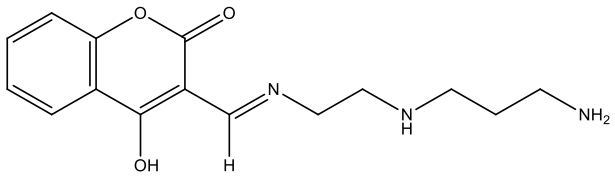	Colorimetric	Clear to yellow solution	Co^{2+}	7.09
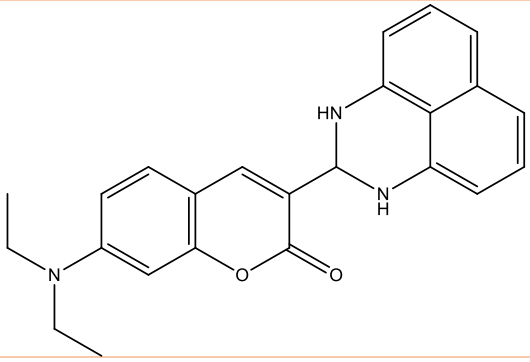	Fluorescent	Fluoresc. Enhancement "turn-on"	Hg^{2+}	1.08
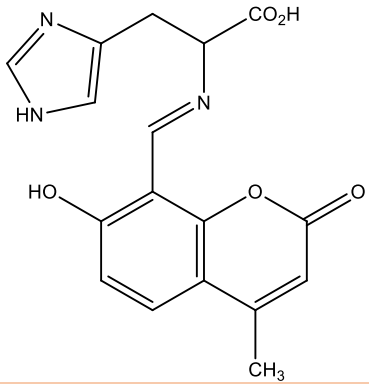	Fluorescent	Fluoresc. Quenching "turn-off"	Fe^{3+}	0.0873
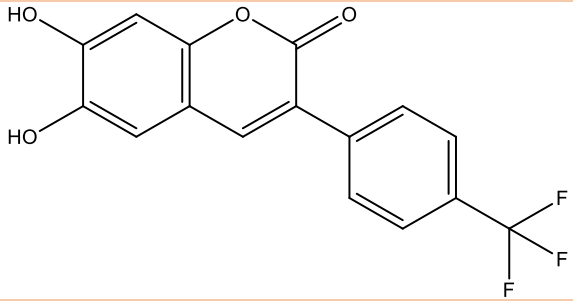	Fluorescent	"turn-off"	Cu^{2+}	0.0245

Owing to the advantageous properties that both fluorescent and colorimetric sensors offer individually, recent literature has witnessed the explosion of dual recognition sensors for analyte detection. Dual fluorescence and colorimetric sensors are increasingly popular due to their great sensitivities, selectivity, mutual calibration, rapid response time, simple operation, and significantly low costs.[74,75] In essence, they combine the best of both worlds. Due to the advantages of versatile optical properties and ligand functionalities, organic dual-channel based sensors have prompted researchers to develop new sensors as tools for heavy metal ion determination and an all-around tool in chemistry, cell imaging, and biochemistry.[76] A 2019 study conducted by Gu and colleagues have developed a thiocoumarin-based probe for the dual fluorescent and colorimetric detection of Hg^{2+} and F^- ions in organic and aqueous media over a wide pH range.[77] Upon the addition of Hg^{2+} and F^- the sensor was subjected to desulfurization and desilylation respectively. Addition of Hg^{2+} increased the fluorescence intensity and sharp colour change from light yellow to dark purple occurred. Interaction with F^- ions also lead to fluorescent enhancement and caused a visible colour to change from light yellow to light brown (**Figure 3**).

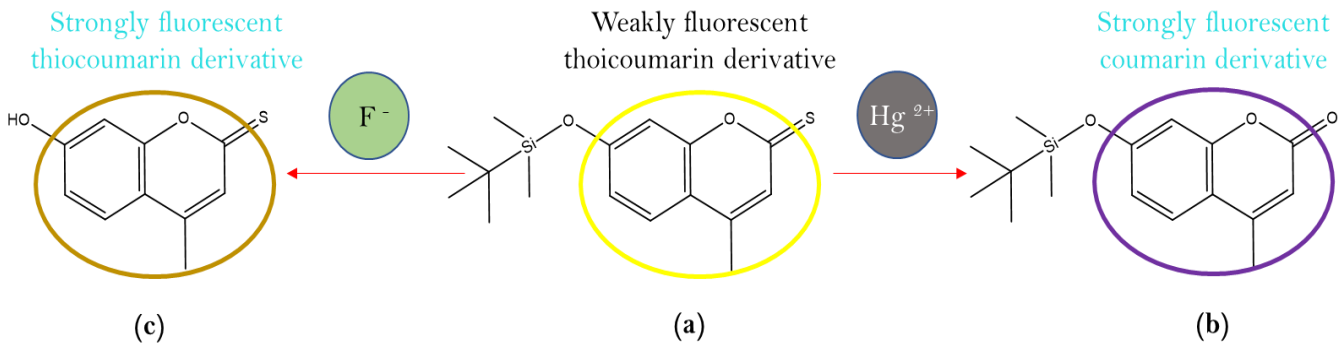

Figure 3: Fluorescent and colour changes to thiocoumarin derivative (**a**). The quantum yields (Φ) of (**b**) and (**c**) were reported as 0.19 and 0.12, respectively.

In addition, for sensing of cations and anions in aqueous and organic media, dual-optical sensors have been applied in the field of cellular imaging. A recent study by Fu and co-workers exhibit two coumarin derived fluorescent-colorimetric sensors (CHP and CHS) for the dual determination of Zn^{2+} and phosphate ions in living cells.[78] Upon the addition of zinc to either coumarin-based sensor, a pronounced fluorescent enhancement accompanied by visible colour changes in natural and UV light was observed. The fluorescent mechanism that occurred through the binding processes was determined to be Photoinduced Electronic

Transfer (PET). Cell imaging experiments further determined the applicability of both coumarin-derived probes towards Zn^{2+} and phosphate anion sensing within in vitro cells. **Figure 4** exhibits the proposed binding and sensing mechanisms of CHP and CHS with Zn^{2+} and phosphate anions respectively. The detection limits of CHP and CHS toward Zn^{2+} were determined as 0.103 and 0.187 μM respectively.

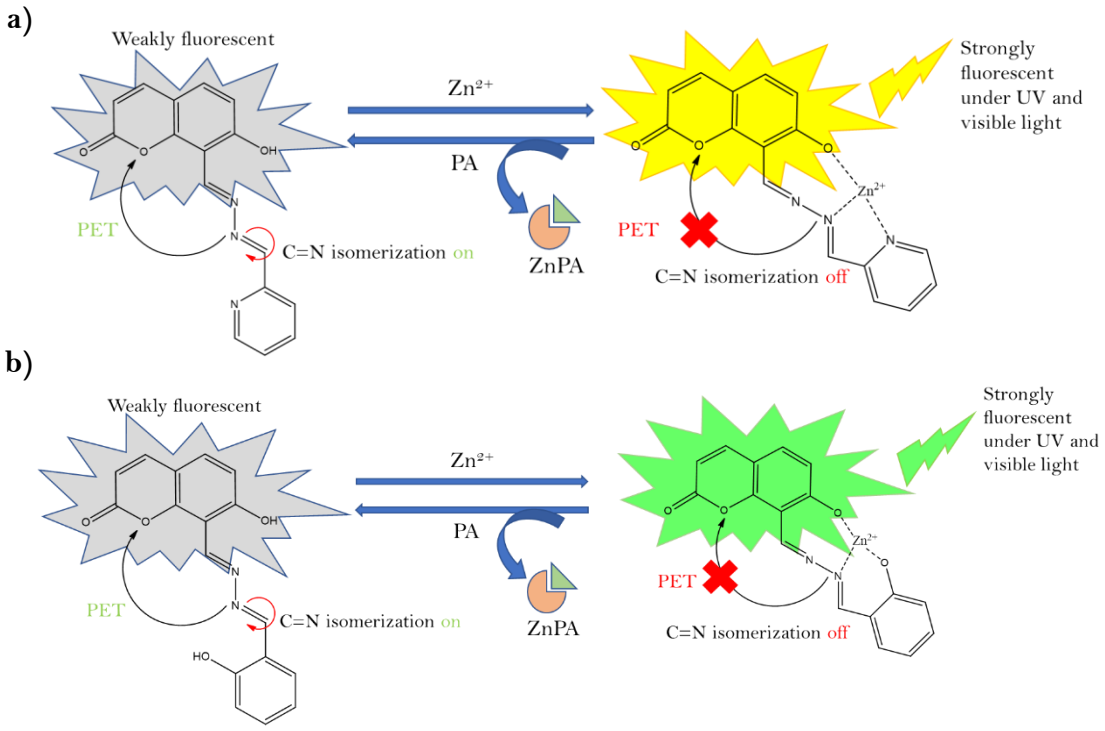

Figure 4: a) proposed binding and sensing mechanism of Zn^{2+} and Phosphate (PA) with coumarin-based sensor CHP and b) proposed binding and sensing mechanism of Zn^{2+} and Phosphate (PA) with coumarin-based sensor CHS.

In addition to these sensors, several other novel coumarin-based sensors for dual fluorescent-colorimetric sensing for metals and/or anions have been recently employed.[79–82] It is apparent that the coumarin functionality plays an important role towards sensing strategies.

1.5 Coumarin and its contribution towards sensor design

1.5.1 A brief history

Coumarin and its derivatives belong to a large family of compounds containing the 2*H*-chromen-2-one motif. Coumarin is a naturally occurring compound found in a wide variety of plants; but found in higher concentrations in the tonka bean (*Dipteryx oderata*) which was first isolated over 200 years ago in 1820 by A. Vogel.[83] Thereafter, W. H. Perkin described the first chemical synthesis by heating acetic acid with the sodium salt of salicylaldehyde, initiating the work leading to the named 'Perkin reaction'.[84] Since then, other methods for the synthesis of coumarin and its derivatives have been described including Pechmann condensation, Knoevenagel condensation, and Wittig condensation, which have been extensively described in literature. These various synthetic procedures have been well-outlined in a recent publication by Sakinah and Jumal.[85] The structure and universally accepted atomic labelling of the coumarin motif is sown in **Figure 5**.

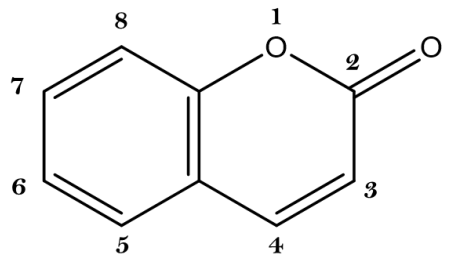

Figure 5: Chemical structure and atomic labelling of coumarin.

1.5.2 Applications of coumarin and the era of facile sensor design

It is well-known that coumarin serves many advantageous biological and pharmacological properties. A simple Google search into these applications of coumarin will return hundreds of articles stating the many health benefits and biological applications of this versatile molecule. This is as a result of its low toxicity.[86] However, at high doses they are reported to be hepatotoxic.[87] Applications including anti-inflammatory, antiproliferative, antibacterial, antifungal, anticoagulant, antioxidant, antineurodegenerative, antiviral (including anti-HIV

activities), photosensitization, and cholinesterase (ChE) and monoamine oxidase (MAO) inhibitory properties have been extensively reported.[88] Moreover, coumarins exhibited significant anticancer activity through diverse mechanisms of action, including inhibition of carbonic anhydrase, inhibition of microtubule polymerization, inhibition of tumour angiogenesis, and regulating the reactive oxygen species, among others.[89–91]

Besides, the coumarin motif has been widely adopted in the design of small-molecule fluorescent and colorimetric sensors for cationic and anionic detection strategies owing to its excellent solubility, large Stokes shifts, high fluorescent quantum yields, comparatively high molar absorption, good light stability, tunable emission wavelengths, reduced toxicity, excellent functionality and addressing to their microenvironments.[92–94] Furthermore, fluorescent and colorimetric small-molecule coumarin based sensors have the added advantages of low cost, high sensitivity and selectivity, non-destructive analytical techniques, "naked-eye" on-site visualization, and experimental convenience, thus setting them apart from conventional laboratory evaluation methods.[95] The fluorescence emission properties of the coumarin motif are due to the push-pull effect through attaining planar rigid structures of charge separated excited geometries and the conformational restrictions which can significantly increase the fluorescence quantum yields[96]; with push-pull chromophore systems containing strong electron acceptor and donor moieties connected by a π-conjugated spacer.[97] An insightful, in-depth, and extensive review of coumarin based small-molecule fluorescent sensors for the recognition of cationic and anionic species, among others, has been outlined by Cao and co-workers.[98] Additionally, a more recent review by Sun and co-workers have compiled a substantial review on the synthesis and application of coumarin-based fluorescent probes.[99]

Sensor design is based on the appropriate choice of the ion chelating group as well as the fluorophore/chromophore moiety. The sensor of choice should be able to fulfil a series of requirements including a large extinction coefficient (high absorbance), significant fluorescence Stokes-shift (to avoid the overlap of excitation and emission peaks), a large fluorescence quantum yield, an excitation and/or shift in the emission wavelength upon coordination of the probe with its target analyte and an excitation wavelength above 400 nm to minimise "background" fluorescence.[100]

Coumarin is a favourable candidate as a fluorophore as well as an analyte chelating site in fluorescent/colorimetric probes and dyes. This is due to its excellent biocompatibility and appreciable photophysical properties such as its high molar absorptivity, high quantum yield, high photostability and large Stokes-shifts, variable size, hydrophobicity, chelation abilities and easy scaffold modification.[101] The spectral properties (both visible/colour and fluorescent) of coumarin can be modified by introducing an electron donating group at position -7- or an electron withdrawing group at position -3-.[102,103] As a result, this compound has found wide applications for fluorescent and colorimetric sensors in the field of molecular recognition, pharmaceuticals, molecular imaging, bioorganic chemistry, analytical chemistry, materials chemistry, laser dyes, fluorescent whiteners, as well as in environmental and medical sciences.[104–106]

With respect to environmental protection, heavy metal ion pollution has become increasingly problematic in recent years. It has become pertinent to be able to detect the concentration and content of heavy metal ions in the environment effectively and rapidly. Therefore, the development fluorescent and colorimetric probes for the detection of environmental pollution has great research value.[107–109] **Figure 6** illustrates some coumarin-based sensors and their specific application within their field of use.

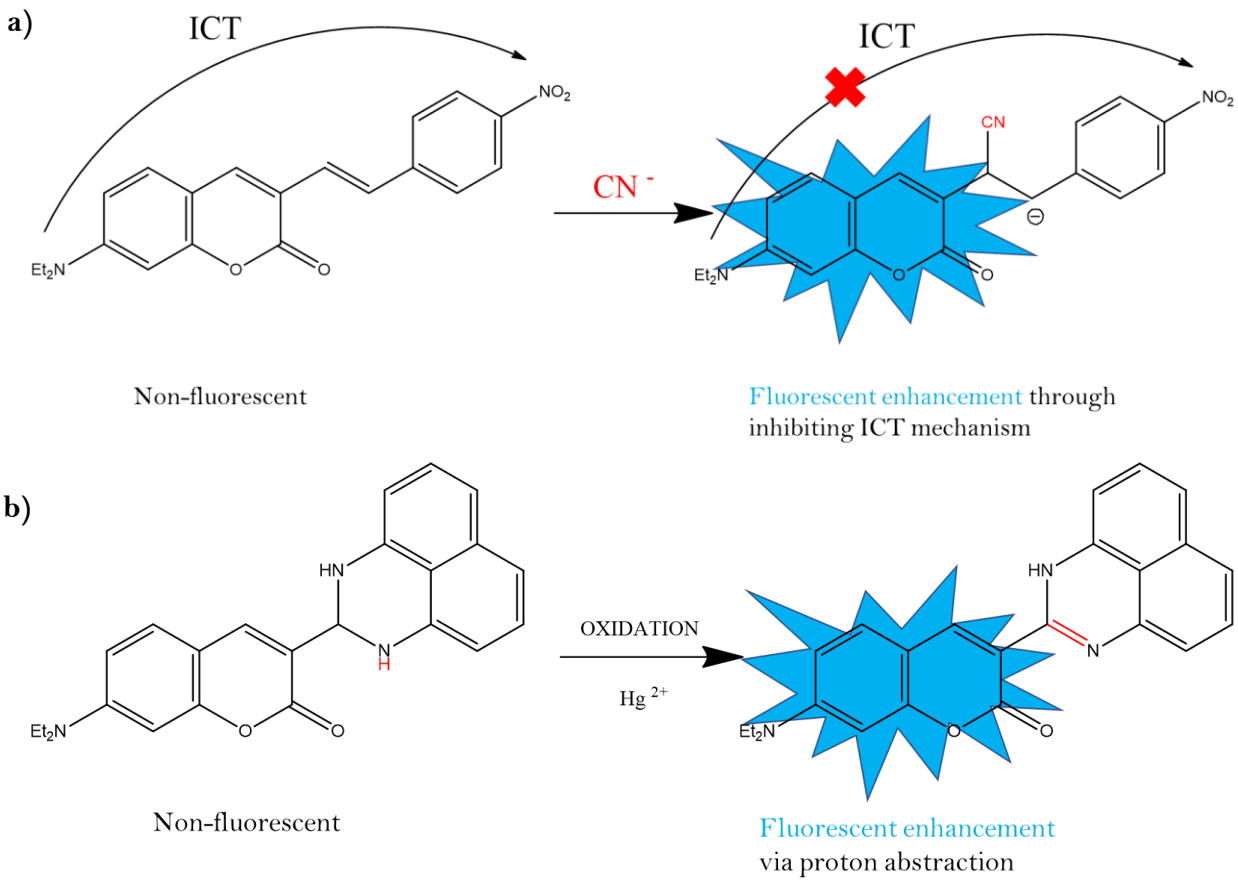

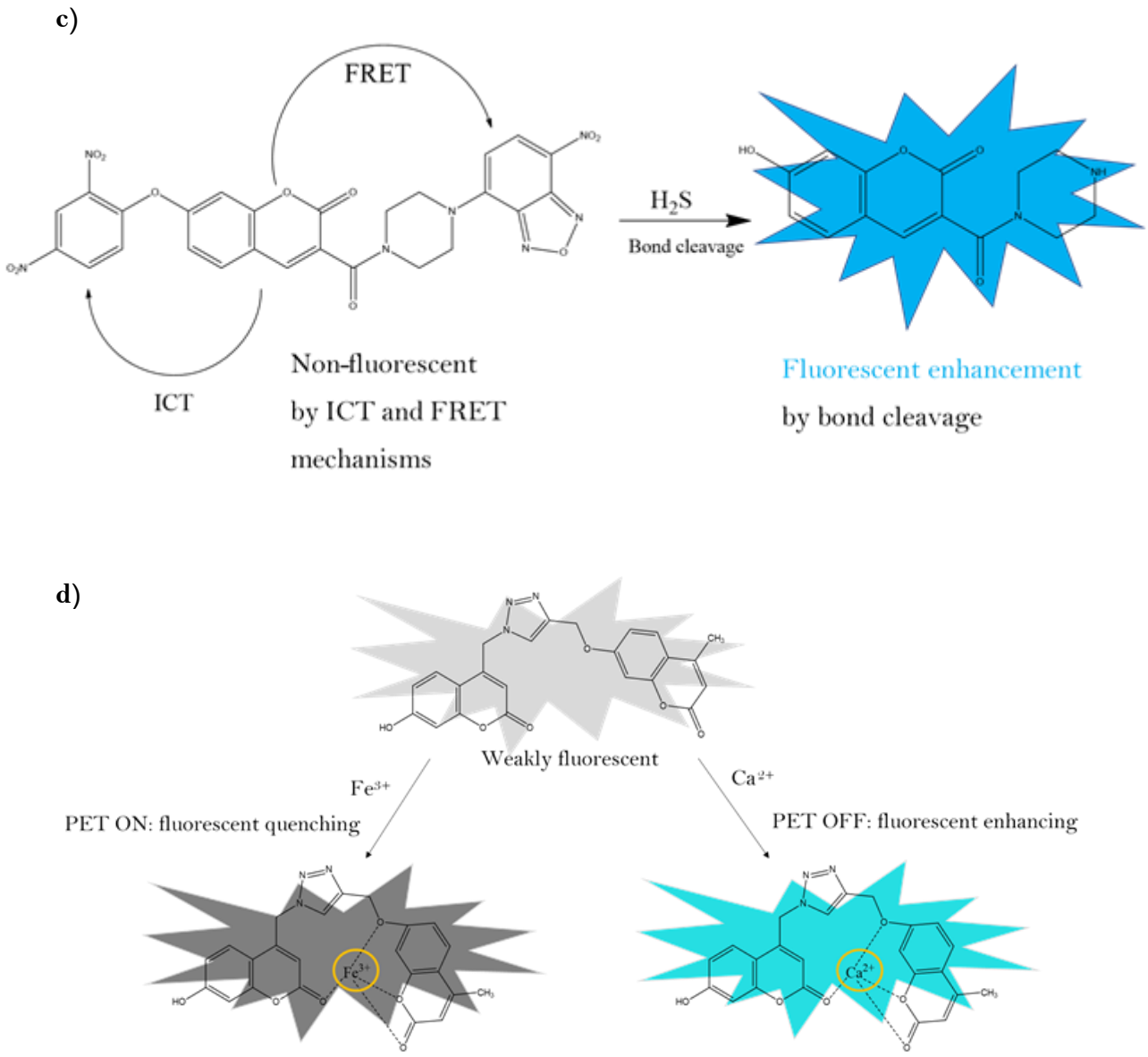

Figure 6: Coumarin-based sensors for applications towards a) cyanide anions in aqueous systems[110], b) for Hg^{2+} cations in Bio-imaging[71], c) Bio-imaging of H_2S in living cells[111], d) dual sensing of Fe^{3+} and Ca^{2+}.[5]

Coumarin based small-molecule sensors bearing 1,2,3-triazole, azomethine/imine, and azo functionalities are herein reported, thus, related synthesis, photophysical properties, coordination scenarios, and relevant examples from literature will be briefly outlined.

1.6 1,2,3-Triazole

The 1,2,3-triazole heterocycle has been reported since the end of the 19th century.[112] Fully substituted triazole complexes have found use in chemical, biological, and pharmaceuticals, with their uses being widely applied in medicine and materials science.[113,114] The synthesis of substituted 1,2,3-triazole moieties can be traced back to the 1960's whereby Huisgen developed a simple and useful approach to synthesize 1,4- and 1,5-disubstituted 1,2,3-triazole mixtures *via* the 1,3-dipolar cycloaddition of terminal azides and alkynes.[115] However, it wasn't until the early 2000's whereby Sharpless' group introduced the concept of Cu(I)-catalyzed "click" chemistry of azides and alkynes (CuAAC) leading to the efficient and regioselective formation of 1,4-disubstituted 1,2,3-triazoles.[116] The "click" reaction protocol describes chemistry that is tailored to efficiently generate novel compounds by linking small units together under "green" conditions.[117] This has proven to be a facile and powerful concept which has permitted the assembly of novel molecular frameworks. In general, click-chemistry describes a class of chemical transformations with a variety of attractive features including excellent functional group tolerance, strong selectivity and performance under ambient experimental conditions.[118] Indeed, the most popular reaction representing the "click" chemistry concept is the Cu(I)-catalyzed alkyne–azide (CuAAC) cycloaddition with the exclusive regioselective formation of 1,4-disubstituted 1,2,3-triazoles. Moreover, Ru-catalyzed azide-alkyne (RuAAC) reactions was later disclosed to regioselectively form 1,5-disubstituted 1,2,3-triazoles. The conventional Huisgen and more modern metal-catalyzed "click" reaction protocols to form 1,4- and 1,5-disubstituted 1,2,3-triazole derivatives have been outlined in recent literature.[119] The typical representation of metal-catalyzed and uncatalyzed 1,3-dipolar cycloaddition reactions is shown in **Scheme 1**, whilst the proposed mechanism for CuAAC 1,3-dipolar cycloaddition as described by Fokin and co-workers is shown in **Scheme 2**.[120]

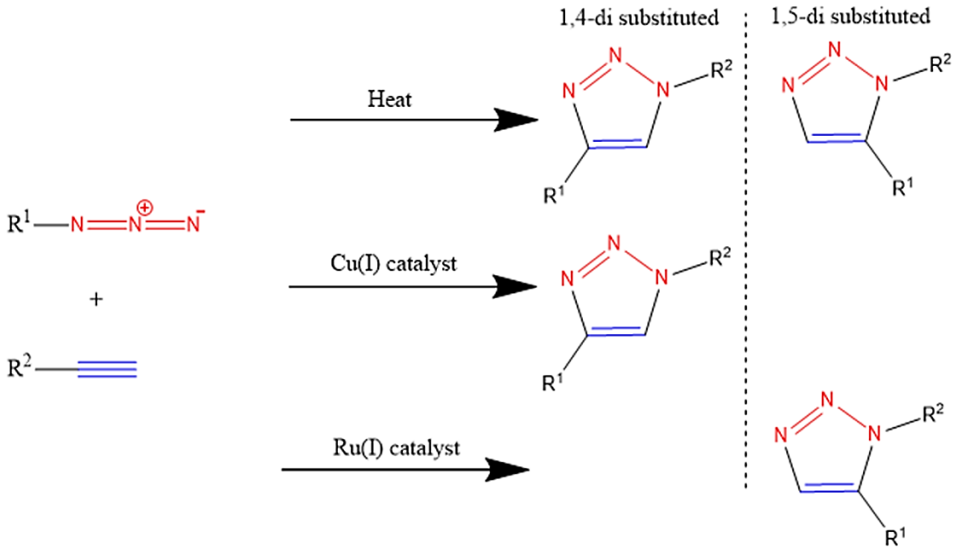

Scheme 1: Heat and metal-catalyzed formation of 1,4- and 1,5-disubstituted 1,2,3-triazole heterocycles.

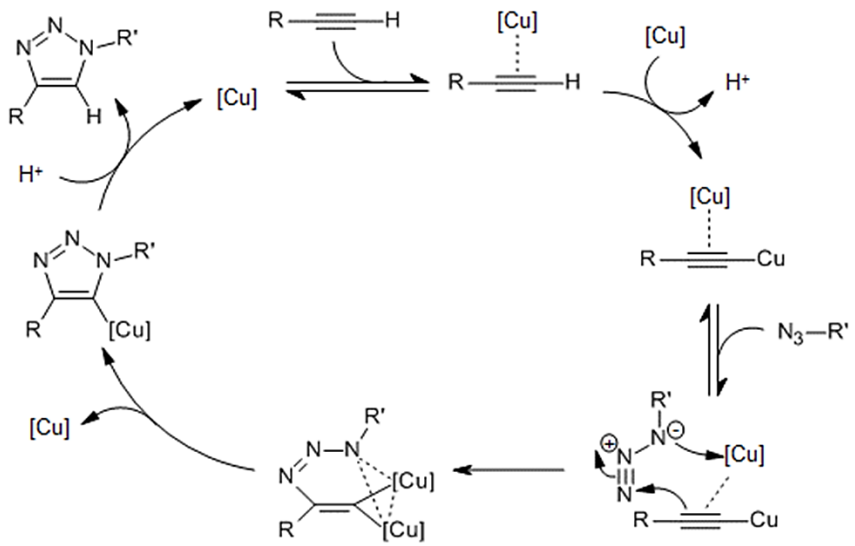

Scheme 2: The initial mechanism of CuAAC proposed by Fokin and co-workers.

In addition to the synthetic simplicity, high-yield methods, and modular nature of the click-reaction, the resulting triazoles can perform a variety of important roles towards sensing strategies. They have been reported to contribute to the binding of a target analyte, act as a linker between the binding site and the reporter, and/or contribute to the reporter usually as part of a conjugated fluorophore.[121] Additionally, reports indicate the incorporation of 1,2,3-triazole moieties at either the -3- or -7- position of the coumarin scaffold has shown to increase the quantum yield and fluorescent emission of the resulting sensors.[122] Owing to these favourable sensing and photophysical properties, this heterocyclic chemistry now appears as a new area with potential applications towards metal and anionic sensing strategies.

1.6.1 The role of 1,4-disubstituted 1,2,3-triazole heterocycles towards metal and anion sensing strategies

Triazole-based sensors have attracted great attention due to their remarkable sensing characteristics and ability to form non-bonding interactions with both anions and cations alike. This is owing to their ease of synthesis and abilities to exhibit various noncovalent interactions such as hydrogen bonding, π-π stacking and C-H-π interactions with guest molecules.[123] 1,2,3-Triazoles exhibit a high dipole moment which permits hydrogen bonding with guest entities. The proton of triazole ring further displays weak hydrogen bond donating capability with anions. Hence, sensors incorporating this heterocycle have been widely accepted and studied for environmental and biological sensing systems due to their high sensitivity, selectivity, specificity, and cost-effectiveness.[124,125]

1,2,3-Triazoles support several donor sites which have been used towards metal coordination. Generally, there are three modes by which triazole heterocycles have been reported to coordinate with transition metals. The first mode is through nitrogen coordination of neutral simple triazoles and chelating triazoles. DFT calculations have shown that the triazole-N3 is a more effective donor compared to the N2 site.[126] Therefore, the triazole can coordinate to a metal through the N3 nitrogen atom, either as a monodentate ligand (Type A) or as part of a bi- or poly-dentate chelator (Type B), when there are other donor sites nearby.[127] When the additional donor site is adjacent to the N1 atom, coordination through N2 is possible to form a bi- or polydentate chelator (Type C).[128] Thus, for the metal chelators, five- or six-membered cycles are usually formed (**Figure 7**).

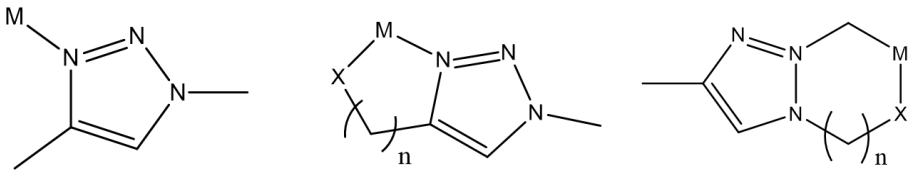

Type A Type B Type C

M = Metal cation
X = O, N, S, P, C etc

Figure 7: Coordination modes of 1,4-disubstituted 1,2,3-triazole to metal cations.

From recent literature, anions capable of interacting through N–H and C–H hydrogen bonding have been the fundamental sensing strategy compared to other noncovalent interactions.[129] Heteroaromatic 1,2,3-triazole rings with the more polar C–H group have been used for anionic sensing strategies, as the ring exhibits greatly enhanced polarization of the C–H bond in the system due to the three nitrogen atoms.[130] In this sense, the more polarized form of the C–H bond can be useful for the sensing of anions via hydrogen bonding.[131] Two examples of fluorescent coumarin-triazole based sensors for Pb^{2+} and F^- are shown in **Figure 8**.[132,133] Other coumarin-triazole based sensors for cationic and anionic recognition strategies have been reported.[134–136]

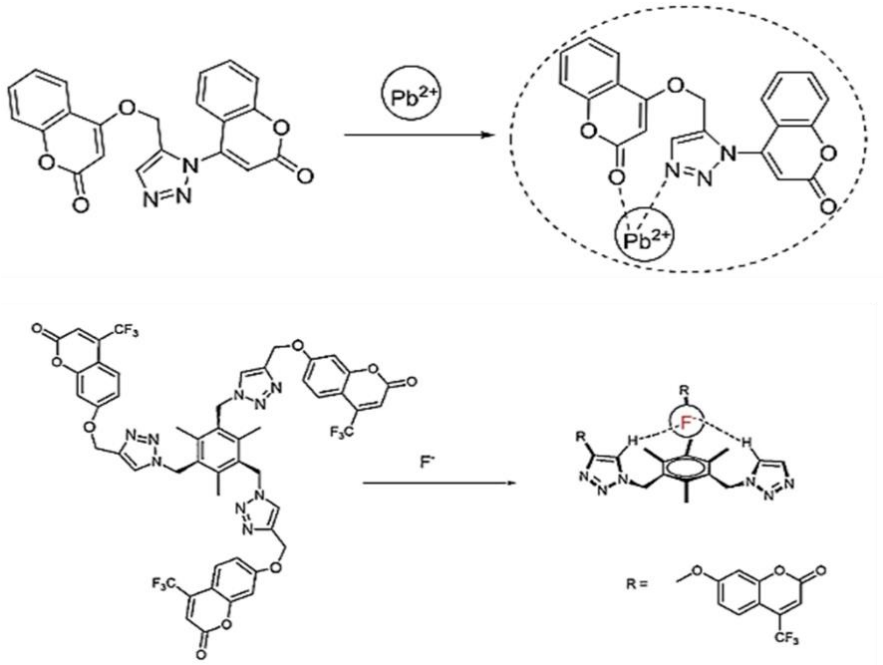

Figure 8: Coumarin-triazole based fluorescent sensors for Pb^{2+} and F^- recognition and determination.

1.7 Schiff bases and azo dyes

The term Schiff base (SB) is derived from the name of Hugo Schiff who synthesized the first so-called Schiff base in 1864.[137] Azomethines, imines, and anils fall under the description of Schiff bases. SB's containing the imine group (R–CH=N–R') are typically synthesized by condensation reactions of an active carbonyl compound (aldehydes/ketones) with a primary amine.[138] They are promising candidates towards a variety of applications related to biological activities, such as antiapoptotic, antituberculosis, antineoplastic, antimalarial, anticancer, antifungal, antibacterial, anti-inflammatory and antiviral activities, catalytic activities, electroluminescent properties, fluorescence properties, nonlinear optical (NLO) properties, applications in electrochemical sensing, and organic photovoltaic materials.[139–142]

1.7.1 The role of Schiff base ligands towards cationic and anionic sensing strategies

Owing to the ease of preparation and tunability of their stereo-electronic structures, most SBs are attractive ligands for sensing purposes, as they readily form stable complexes with most heavy and transition metal cations with high selectivity and sensitivity.[143] Additionally, they are able to coordinate with various metal ions in different oxidation states, therefore they are among the most important ligands used in current coordination chemistry; as well as in fluorescent and colorimetric sensors.[144,145] SBs are an important type of colorimetric sensor as their interaction with cations, anions, and toxic pollutants can be rapidly detected by naked-eye colour changes, without the use of expensive equipment and at a relatively low-cost.[146] Furthermore, they boast simple synthetic methods, rapid detection, and high sensitivity towards the interacting analyte.[147] When the metal ion coordinates to the sensor, significant colorimetric and spectroscopic changes can occur. These spectroscopic changes may present themselves by certain mechanisms including metal-ligand charge transfer (MLCT), ligand-metal charge transfer (LMCT), PET, and ICT.[148] It is well known that for colorimetric sensors, the shifts observed in the UV-Vis spectra are affected by the respective increase or decrease in electron density on the chromophore moiety. Furthermore, the colour changes are more prominent when the interacting species includes electrostatic charges (cation-anion) than for neutral molecules.[149]

Specifically, the imine nitrogen is basic and exhibits π-receptive properties.[144,150] Coordination is achieved via the imine nitrogen, and supported by neighbouring groups attached to the SB.[151] It is known that these ligands form σ-bonds by donating a lone pair to the metal cation from the nitrogen and forming a π-bond by abstracting electrons from the metal centre to the C=N π* molecular orbital. Deprotonation of a hydroxyl group (or other hydrogen-bonded functionalities) can assist in metal coordination. Generally, the functionality closest to the imine group is an OH moiety.[152]

Schiff bases can exist as bi-, tri-, tetra-, or polydentate ligands.[153–157] They can form stable five or six-membered chelate complexes with a wide range of metal cations. Monodentate SBs are not reported to form stable complexes. Bidentate or tridentate ligands can coordinate with many different metal ions through both imine and OH/SH groups.[158]

A coumarin moiety with hydroxy and imine groups possess nitrogen and oxygen atoms able to coordinate with metal ions.[159] The excellent optical and physical properties of coumarin coupled with the selective, sensitive, and easily detectable metal coordination abilities of the imine, make coumarin-imine based fluorescent and colorimetric sensors a promising tool towards metal sensing strategies. Examples of fluorescent and colorimetric coumarin-imine-metal coordination complexes are shown in **Figure 9**[160,161], with other examples reported.[159,162–170]

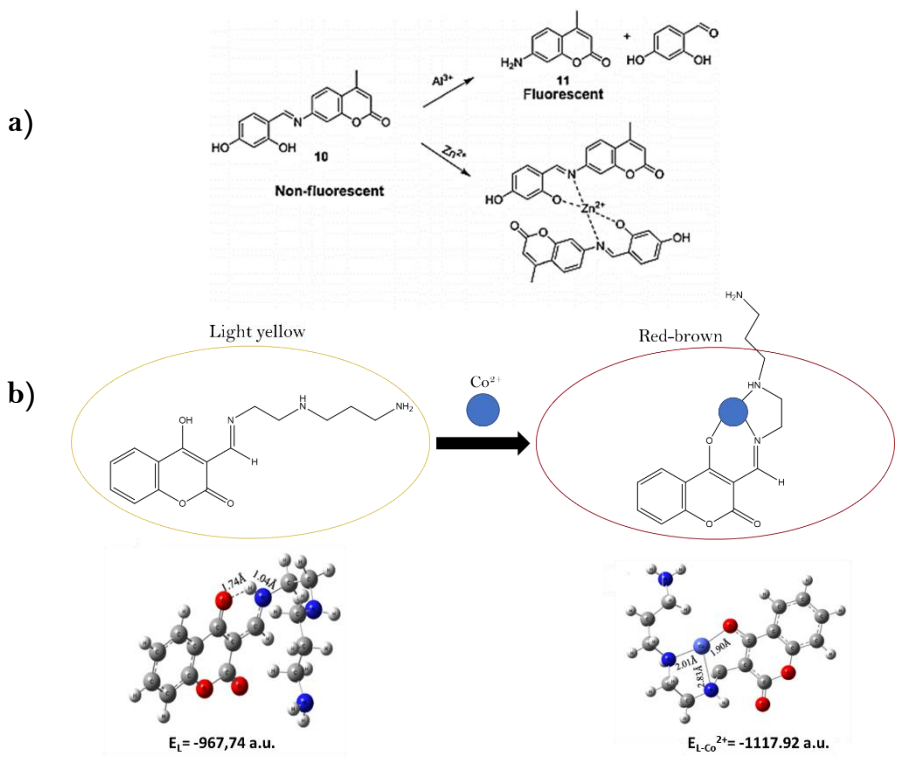

Figure 9: a) Fluorescent and b) colorimetric coumarin-imine based sensors for various cation sensing strategies.

Sensors bearing the imine functionality as well as OH/NH binding sites have been used for the fluorescent and colorimetric detection of anions through hydrogen bonding and/or deprotonation.[171] For instance, F^- ion detection by Schiff bases conventionally deals with adjustments of optical properties via interactions with acidic hydrogen atom(s) bearing portion(s) of a C=N bonded molecule. Deprotonation of active hydrogen atom(s) by fluoride, or the formation of hydrogen bond with fluoride ion, changes the electron-delocalization resulting in changes to the optical properties from the parent Schiff base. Therefore, any incremental change in the charge delocalization or charge-transfer can trigger a notable change in the absorption or emission spectra of a sensor.[172]

Azo dyes are a class of chemical compounds bearing an -N=N- functionality, joining two symmetrical and/or asymmetrical identical or non-azo alkyl or aryl radicals.[173] Historically, they have been used for the dying of textiles and fabrics. These coloured compounds were initially derived from vegetable extracts and animal products, but it wasn't until the mid-1870's whereby Caro and Witt conducted the first diazotization and azo coupling reaction in modern industry.[174] The majority of azo dyes are synthesized by diazotization of an aromatic primary amine, followed by coupling with one or more electron-rich nucleophiles such as amino and hydroxyl functionalities.[175] Other methods for the synthesis of azo-compounds include reduction of nitroaromatic derivatives in alkaline medium, reduction of nitroso compounds by $LiAlH_4$, oxidation of primary amines by potassium permanganate or lead tetraacetate, condensation of hydrazines and quinones, and the condensation of primary amines with nitroso derivatives.[176,177]

1.7.2 The role of azo dyes towards metal ion sensing

More recently, most azo compounds have found widespread commercial use in dyes, pigments, optical information storage devices, heat transfer printing, textiles, switching technology, photo-refractive polymer industry, pharmaceuticals, non-linear optics, dye-sensitized solar cells, photoswitching devices and metal sensing strategies due to structural adaptability that offers multiple proficient coordination sites.[178–182] They exhibit favourable characteristics such as excellent absorption and emission properties, good molar absorption coefficient, solvatochromism, and can undergo photochemical and thermal isomerization.[183]

It is well known that the introduction of an azo-chromophore to the sensor's design increases the total chromogenic capability.[184] Therefore, azo dyes containing aromatic conjugated heterocyclic moieties serve to increase and alter the chromophoric strength and resulting colour of the sensor respectively. These molecules containing extended conjugation and greater number of electron releasing substituents on the diazo group can enhance the electron density of the molecule which in turn results in more intense optical absorption and related optical properties.[185]

For this reason, azo dyes and related compounds have become increasingly important colorimetric-based sensors for the visible "naked-eye" detection of cationic species. Metal chelated azo dyes are more light stable, allow for easier control of the wavelength by selection of the appropriate substituent groups, and have good thermal stability.[186] Furthermore, complexes of transition metals with azo ligands have interesting physical, chemical, photophysical, photochemical, catalytic and material properties.[187] The metal-complexes can coordinate via the nitrogen atom(s) of azo group or through other donor functionalities on the sensor, sometimes supported by water and/or solvent molecules. The number of donor atoms in the ligand further enhances the coordination sites providing more options towards complexation. The electronic delocalization is enhanced after coordination to a metal cation. Generally, azo dyes possess different numbers of possible donor atoms, and depending upon the donor atoms, the ligand behaves as either monodentate, bidentate or tridentate in nature.[188]

Coumarin-based azo compounds bearing this N=N functionality form a segment of ligands with donor atoms (N and O) capable of coordinating with various metal ions which can be used for the fabrication of colorimetric probes.[188] The incorporation of the azo-functionality to the coumarin heterocycle is responsible for the colour production in the visible region forming the coumarin-azo chromophore.[173,189]

Although colorimetric based azo dyes for metal sensing strategies have been recently reported [190–192], very few sensors incorporate the coumarin moiety into their design. A coumarin-based azo dye for Cu^{2+} and Mn^{2+} detection has been recently described, however, the function and binding activity has only been computationally/theoretically investigated.[193] Most coumarin-based azo dyes have been reported for pharmaceutical and biological activities[194,195], as well as for optical materials and devices. [196] Therefore, novel coumarin-azo colorimetric sensors for cationic and anionic sensing and recognition strategies are a promising field of research going forward.

2. Aim of the study

Fluorescent molecular sensors containing both the triazole and coumarin moieties form the basis of this project. These novel compounds with complexation capabilities will be used for the detection of cationic and anionic species in aqueous and organic media. The interactions between the sensor and the analyte can be observed and measured from their changes in absorption and emission properties. The role of the assisting groups from the coumarin scaffold towards selectivity and sensitivity will be investigated.

Hence, the aims of the study were to synthesize and characterized fluorescent triazolyl functionalized coumarin based sensors using Cu(I)-catalyzed 1,3-dipolar cycloaddition reactions of azide and alkyne groups. The structures of these sensors were designed such that they possess various substituents (units) that could potentially contribute towards complexation with an analyte.

The photophysical properties of these novel compounds were investigated and compared in different solvent systems. Their sensing potential for metal ions and anions were investigated using absorption and emission studies, whilst the complexation site was investigated by NMR spectral analysis and were further confirmed by molecular modelling studies.

In addition, coumarin based Schiff bases and an azo dye were synthesised in multiple steps from the starting aldehydes and amines. Their sensing potentials were investigated by absorbance analysis, with the different sites of complexation suggested by FT-IR, and NMR spectral analysis. The complexation site of these sensors with their chosen analytes were confirmed by molecular modelling studies. Application of these novel compounds as colorimetric sensors were investigated in water and organic solvents. Additionally, the azo dye was observed to function further as a molecular mimicking device and keypad lock owing to its reversible nature.

Finally, real-life application of these developed sensors for the detection of selected metal ions was tested using environmental water samples from a local river system near industrial and residential areas.

3. References

(1) Czarnick, A. W. Fluorescent Chemosensors for Ion and Molecule Recognition. *Am. Chem. Soc. Washington, D.C* **1993**. https://pubs.acs.org/doi/pdf/10.1021/bk-1993-0538.fw001

(2) Kwon, N.; Hu, Y.; Yoon, J. Fluorescent Chemosensors for Various Analytes Including Reactive Oxygen Species, Biothiol, Metal Ions, and Toxic Gases. *ACS Omega* **2018**, *3* (10), 13731–13751. https://doi.org/10.1021/acsomega.8b01717.

(3) Wu, D.; Sedgwick, A. C.; Gunnlaugsson, T.; Akkaya, E. U.; Yoon, J.; James, T. D. Fluorescent Chemosensors: The Past, Present and Future. *Chem. Soc. Rev.* **2017**, *46* (23), 7105–7123. https://doi.org/10.1039/c7cs00240h.

(4) Wang, W.; Wu, J.; Liu, Q.; Gao, Y.; Liu, H.; Zhao, B. A Highly Selective Coumarin-Based Chemosensor for the Sequential Detection of Fe^{3+} and Pyrophosphate and Its Application in Living Cell Imaging. *Tetrahedron Lett.* **2018**. https://doi.org/10.1016/j.tetlet.2018.04.007.

(5) Puthiyedath, T.; Bahulayan, D. A Click Derived Triazole-Coumarin Derivative as Fluorescence on-off PET Based Sensor for $Ca^{2+}$and Fe^{3+} Ions. *Sensors Actuators, B Chem.* **2018**, *272*, 110–117. https://doi.org/10.1016/j.snb.2018.05.126.

(6) H. Sharma, N. Kaur, A. Singh, A. Kuwar, *J. Mater. Chem. C* **2016**, 5154–5194. https://doi.org/10.1039/C6TC00605A

(7) Wu J, Kwon B, Liu W, Anslyn EV, Wang P, K. J. Chromogenic/Fluorogenic Ensemble Chemosensing Systems. *Chem. Rev.* **2015**, *115* (15), 7893–7943. https://doi.org/10.1021/cr500553d

(8) Min Hee Lee, Jong Seung Kim, and J. L. S. Small Molecule-Based Ratiometric Fluorescence Probes for Cations, Anions, and Biomolecule. *Chem. Soc. Rev.* **2015**, *44* (13), 4185–4191. https://doi.org/10.1039/C4CS00280F

(9) Bansod. B, Kumar. T, Thakur. R, Rana. S, S. I. A Review on Various Electrochemical Techniques for Heavy Metal Ions Detection with Different Sensing Platforms. *Biosense. Bioelectron* **2017**, *94*. https://doi.org/10.1016/j.bios.2017.03.031

(10) T. Gong, J. Liu, X. Liu, J. Liu, J. Xiang, Y. W. A Copper-Catalyzed Sulfonylative C–H

Bond Functionalization from Sulfur Dioxide and Aryldiazonium Tetrafluoroborates. *Org. Chem. Front.* **2018**, *5*, 366–370. https://doi.org/10.1039/C7QO00866J

(11) Arulraj, A. D.; Devasenathipathy, R.; Chen, S. M.; Vasantha, V. S.; Wang, S. F. Highly Selective and Sensitive Fluorescent Chemosensor for Femtomolar Detection of Silver Ion in Aqueous Medium. *Sens. Bio-Sensing Res.* **2015**, *6*, 19–24. https://doi.org/10.1016/j.sbsr.2015.10.004.

(12) M. Li, H.Y. Lu, R.L. Liu, J.D. Chen, C. F. C. Turn-On Fluorescent Sensor for Selective Detection of Zn^{2+}, Cd^{2+}, and Hg^{2+} in Water. *J. Org. Chem.* **2012**, *77* (7), 3670–3673. https://doi.org/10.1021/jo3002744

(13) Koppal, V. V.; Melavanki, R.; Kusanur, R.; Patil, N. R. Analysis of Fluorescence Quenching of Coumarin Derivative under Steady State and Transient State Methods. *J. Fluoresc.* **2021**, 393–400. https://doi.org/10.1007/s10895-020-02663-3.

(14) Fukuhara, G. Analytical Supramolecular Chemistry: Colorimetric and Fluorimetric Chemosensors. *J. Photochem. Photobiol. C Photochem. Rev.* **2020**, *42*, 100340. https://doi.org/10.1016/j.jphotochemrev.2020.100340.

(15) Gupta, A.; Kumar, N. A Review of Mechanisms for Fluorescent "Turn-on" Probes to Detect Al^{3+} Ions. *RSC Adv.* **2016**, *6* (108), 106413–106434. https://doi.org/10.1039/c6ra23682k.

(16) Wu, J.; Liu, W.; Ge, J.; Zhang, H.; Wang, P. New Sensing Mechanisms for Design of Fluorescent Chemosensors Emerging in Recent Years. *Chem. Soc. Rev.* **2011**, *40* (7), 3483–3495. https://doi.org/10.1039/c0cs00224k.

(17) Chen, W.; Tian, X.; He, W.; Li, J.; Feng, Y.; Pan, G. Emerging Functional Materials Based on Chemically Designed Molecular Recognition. *BMC Mater.* **2020**, *2* (1), 1–22. https://doi.org/10.1186/s42833-019-0007-1.

(18) Lehn, J. M. Supramolecular Chemistry-Scope and Perspectives Molecules, Supermolecules, and Molecular Devices (Nobel Lecture). *Angew. Chem. Int. Ed. Engl* **1988**, *27*, 89–112. https://doi.org/10.1002/anie.198800891

(19) F. Huang, E. V. A. Introduction: Supramolecular Chemistry. *Chem. Rev.* **2015**, *115*, 6999–7000. https://doi.org/10.1021/acs.chemrev.5b00352

(20) Xu, Z.; Yoon, J.; Spring, D. R. Fluorescent Chemosensors for Zn^{2+}. *Chem. Soc. Rev.*

2010, *39* (6), 1996–2006. https://doi.org/10.1039/b916287a.

(21) Goppelsröder, F. Ueber Eine Fluorescirende Substanz Aus Dem Kubaholze (Fortsetzung) Und Über Fluorescenzanalyse. *J. Prakt. Chem* **1868**, *104*, 10–27.

(22) Sousa, L. R.; Larson, J. M. Crown Ether Model Systems for the Study of Photoexcited State Response to Geometrically Oriented Perturbers. The Effect of Alkali Metal Ions on Emission from Naphthalene Derivatives. *J. Am. Chem. Soc.* **1977**, *99*, 307–310. https://doi.org/10.1021/ja00443a084

(23) Konopelski, J. P.; Kotzyba-Hibert, F.; Lehn, J.-M.; Desvergne, J.P.; Fagès, F.; Castellan, A.; Bouas-Laurent, H. Synthesis, Cation Binding, and Photophysical Properties of Macrobicyclic Anthraceno Cryptands. *J. Chem. Soc., Chem. Commun.* **1985**, 433–436. http://dx.doi.org/10.1021/acsomega.8b01717

(24) de Silva, A.P, de Silva, S. . Fluorescent Signalling Crown Ethers; "Switching on" of Fluorescence by Alkali Metal Ion Recognition and Binding in Situ. *J. Chem. Soc., Chem. Commun.* **1986**, 1709–1710. https://doi.org/10.1039/C39860001709

(25) Grynkiewicz, G.; Poenie, M.; Tsien, R. Y. A New Generation of Ca^{2+} Indicators with Greatly Improved Fluorescence Properties. *J. Biol. Chem.* **1985**, *260* (6), 3440–3450. https://doi.org/3838314.

(26) Huston, M. E.; Haider, K. W.; Czarnik, A. W. Chelation Enhanced Fluorescence in 9,10-Bis[[(2-(Dimethylamino)Ethyl)Methylamino]Methyl]Anthracene. *J. Am. Chem. Soc.* **1988**, *110*, 4460–4462. https://doi.org/10.1021/ja00221a083

(27) Li, J.; Yim, D.; Jang, W.-D.; Yoon, J. Recent Progress in the Design and Applications of Fluorescence Probes Containing Crown Ethers. *Chem. Soc. Rev.* **2017**, *46*, 2437–2458. https://doi.org/10.1039/C6CS00619A

(28) Kim, H. M.; Cho, B. R. Small-Molecule Two-Photon Probes for Bioimaging Applications. *Chem. Rev.* **2015**, *115*, 5014–5055. https://doi.org/10.1021/cr5004425

(29) Schmidt, R.; Wurm, C. A.; Jakobs, S.; Engelhardt, J.; Egner, A.; Hell, S. W. Spherical Nanosized Focal Spot Unravels the Interior of Cells. *Nat. Methods* **2008**, *5*, 539–544. DOI: 10.1038/nmeth.1214 PMID: 18488034

(30) Ferronato, N.; Torretta, V. Waste Mismanagement in Developing Countries: A Review of Global Issues. *Int. J. Environ. Res. Public Health* **2019**, *16* (6).

https://doi.org/10.3390/ijerph16061060.

(31) Nweke OC, S. W. I. Modern Environmental Health Hazards: A Public Health Issue of Increasing Significance in Africa. *Env Heal. Persp.* **2009**, *117*, 863–870. DOI: 10.1289/ehp.0800126

(32) Gao, Y.; Ge, L.; Shi, S.; Sun, Y.; Liu, M.; Wang, B.; Shang, Y.; Wu, J.; Tian, J. Global Trends and Future Prospects of E-Waste Research: A Bibliometric Analysis. *Environ. Sci. Pollut. Res.* **2019**, *26* (17), 17809–17820. https://doi.org/10.1007/s11356-019-05071-8.

(33) Jiang, B.; Adebayo, A.; Jia, J.; Xing, Y.; Deng, S.; Guo, L.; Liang, Y.; Zhang, D. Impacts of Heavy Metals and Soil Properties at a Nigerian E-Waste Site on Soil Microbial Community. *J. Hazard. Mater.* **2019**, *362*, 187–195. https://doi.org/10.1016/j.jhazmat.2018.08.060.

(34) Robinson, B. E-Waste: An Assessment of Global Production and Environmental Impacts. *Sci. Total Environ.* **2009**, *408*, 183–191. https://doi.org/10.1016/j.scitotenv.2009.09.044

(35) Soetrisno, F. N.; Delgado-Saborit, J. M. Chronic Exposure to Heavy Metals from Informal E-Waste Recycling Plants and Children's Attention, Executive Function and Academic Performance. *Sci. Total Environ.* **2020**, *717*, 137099. https://doi.org/10.1016/j.scitotenv.2020.137099.

(36) Perkins. DN, Drisse. BMN, Nxele. T, S. P. E-Waste: A Global Hazard. *Ann Glob Heal.* **2014**, *80*, 286–295. DOI: 10.1016/j.aogh.2014.10.001

(37) Awasthi, A.K., Zeng, X.L., Li, J. H. Environmental Pollution of Electronic Waste Recycling in India: A Critical Review. *Environ. Pollut.* **2016**, *211*, 259–270. DOI: 10.1016/j.envpol.2015.11.027

(38) Ouabo, R. E.; Ogundiran, M. B.; Sangodoyin, A. Y.; Babalola, B. A. Ecological Risk and Human Health Implications of Heavy Metals Contamination of Surface Soil in E-Waste Recycling Sites in Douala, Cameroun. *J. Heal. Pollut.* **2019**, *9* (21). https://doi.org/10.5696/2156-9614-9.21.190310.

(39) Frazzoli. C, Orisakwe. OE, D. R. Mantovani A. Diagnostic Health Risk Assessment of Electronic Waste on the General Population in Developing Countries' Scenarios. *Environ. Impact. Assess. Rev.* **2010**, *30*, 388–399.

http://dx.doi.org/10.1016/j.eiar.2009.12.004

(40) Singh, U.K.; Kumar, B. Pathways of Heavy Metals Contamination and Associated Human Health Risk in Ajay River Basin, India. *Chemosphere* **2017**, *173*, 183–199. https://doi.org/10.1016/j.chemosphere.2017.01.103

(41) Huang, L.; Rad, S.; Xu, L.; Gui, L.; Song, X.; Li, Y.; Wu, Z.; Chen, Z. Risk Assessment in Huixian Wetland , South China. *Water* **2020**, *12* (431), 1–14. https://doi.org/10.3390/w12020431

(42) Yi, L.; Gao, B.; Liu, H.; Zhang, Y.; Du, C.; Li, Y. Characteristics and Assessment of Toxic Metal Contamination in Surface Water and Sediments near a Uranium Mining Area. *Int. J. Environ. Res. Public Health* **2020**, *17* (2). https://doi.org/10.3390/ijerph17020548.

(43) Ran, E.; Wang, M.; Yi, Y.; Feng, M.; Liu, Y. Mercury Poisoning Complicated by Acquired Neuromyotonia Syndrome. *Medicine (Baltimore).* **2021**, *100* (32), e26910. https://doi.org/10.1097/md.0000000000026910.

(44) Liu, Y.; Ma, R. Human Health Risk Assessment of Heavy Metals in Groundwater in the Luan River Catchment within the North China Plain. *Geofluids* **2020**, *2020.* https://doi.org/10.1155/2020/8391793.

(45) Cobbina, S. J.; Duwiejuah, A. B.; Quansah, R.; Obiri, S.; Bakobie, N. Comparative Assessment of Heavy Metals in Drinking Water Sources in Two Small-Scale Mining Communities in Northern Ghana. *Int. J. Environ. Res. Public Health* **2015**, *12* (9), 10620–10634. https://doi.org/10.3390/ijerph120910620.

(46) O, Gyamfi.; P, Sorenson.; G, Darko.; E, Ansah.; J, Bak. Human Health Risk Assessment of Exposure to Indoor Mercury Vapour in a Ghanaian Artisanal Small-Scale Gold Mining Community. *Chemosphere* **2020**, *241*, 1–8. https://doi.org/10.1016/j.chemosphere.2019.125014

(47) Costa, F.; Coelho, J. P.; Baptista, J.; Martinho, F.; Pereira, M. E.; Pardal, M. A. Mercury Accumulation in Fish Species along the Portuguese Coast: Are There Potential Risks to Human Health? *Mar. Pollut. Bull.* **2020**, *150,* 110740. https://doi.org/10.1016/j.marpolbul.2019.110740.

(48) Shahid, N., Khalid, S., Bibi, I., Bundschuh, J., Niazi, N., Dumat, C. A Critical Review of Mercury Speciation, Bioavailability, Toxicity and Detoxification in Soil-Plant

Environment: Ecotoxicology and Health Risk Assessment. *Sci. Total. Environ.* **2020**, *711*, 1–22. https://doi.org/10.1016/j.scitotenv.2019.134749

(49) Buha, A.; Jugdaohsingh, R.; Matovic, V.; Bulat, Z.; Antonijevic, B.; Kerns, J. G.; Goodship, A.; Hart, A.; Powell, J. J. Bone Mineral Health Is Sensitively Related to Environmental Cadmium Exposure- Experimental and Human Data. *Environ. Res.* **2019**, *176*, 108539. https://doi.org/10.1016/j.envres.2019.108539.

(50) Paul, V.; Gupta, P. A Comprehensive Review of Environmental Exposure of Toxicity of Lead. *J. Pharmacogn. Phytochem.* **2018**, *7* (4), 1991–1995.

(51) Shah, M. T. Determination of Heavy Metals in Drinking Water and Their Adverse Effects on Human Health. A Review. *Pure Appl. Biol.* **2020**, *9* (1), 96–104. https://doi.org/10.19045/bspab.2020.90012.

(52) Rezvani, E.; Rafferty, A.; McGuinness, C.; Kennedy, J. Adverse Effects of Nanosilver on Human Health and the Environment. *Acta Biomater.* **2019**, *94*, 145–159. https://doi.org/10.1016/j.actbio.2019.05.042.

(53) Khan, K., Chakraborty, R., Bundschuh, J., Bhattacharya, P., Parvez, F. Health Effects of Arsenic Exposure in Latin America: An Overview of the Past Eight Years of Research. *Sci. Total Environ.* **2020**, *710*, 1–17. https://doi.org/10.1016/j.scitotenv.2019.136071

(54) Elumalai, V.; Brindha, K.; Lakshmanan, E. Human Exposure Risk Assessment Due to Heavy Metals in Groundwater by Pollution Index and Multivariate Statistical Methods: A Case Study from South Africa. *Water (Switzerland)* **2017**, *9* (4). https://doi.org/10.3390/w9040234.

(55) Wang, P.; An, Y.; Wu, J. Highly Sensitive Turn-on Detection of Mercury(II) in Aqueous Solutions and Live Cells with a Chemosensor Based on Tyrosine. *Spectrochim. Acta - Part A Mol. Biomol. Spectrosc.* **2020**, *230*, 118004. https://doi.org/10.1016/j.saa.2019.118004.

(56) He, W.; Liu, R.; Liao, Y.; Ding, G.; Li, J.; Liu, W.; Wu, L.; Feng, H.; Shi, Z.; He, M. A New 1,2,3-Triazole and Its Rhodamine B Derivatives as a Fluorescence Probe for Mercury Ions. *Anal. Biochem.* **2020**, *598*, 113690. https://doi.org/10.1016/j.ab.2020.113690.

(57) Ke, X.; Fan, Y.; Zhou, J.; Huang, Z. A Novel Coumarin-Derived Dithioacetal

Chemosensor for Trace Detection of Hg^{2+} in Real Water Samples. *J. Chem. Res.* **2020**, *44* (3–4), 142–147. https://doi.org/10.1177/1747519819890561.

(58) Pan, Z.; Xu, Z.; Chen, J.; Hu, L.; Li, H.; Zhang, X.; Gao, X.; Wang, M.; Zhang, J. Coumarin Thiourea-Based Fluorescent Turn-on Hg^{2+} Probe That Can Be Utilized in a Broad PH Range 1–11. *J. Fluoresc.* **2020**. https://doi.org/10.1007/s10895-020-02517-y.

(59) Zehra, S.; Khan, R. A.; Alsalme, A.; Tabassum, S. Coumarin Derived "Turn on" Fluorescent Sensor for Selective Detection of Cadmium (II) Ion: Spectroscopic Studies and Validation of Sensing Mechanism by DFT Calculations. *J. Fluoresc.* **2019**, *29* (4), 1029–1037. https://doi.org/10.1007/s10895-019-02416-x.

(60) Sunnapu, O.; Kotla, N. G.; Maddiboyina, B.; Singaravadivel, S.; Sivaraman, G. A Rhodamine Based "Turn-on" Fluorescent Probe for Pb(II) and Live Cell Imaging. *RSC Adv.* **2015**, *6* (1), 656–660. https://doi.org/10.1039/c5ra20482h.

(61) Rasheed, T.; Bilal, M.; Nabeel, F.; Iqbal, H. M. N.; Li, C.; Zhou, Y. Fluorescent Sensor Based Models for the Detection of Environmentally-Related Toxic Heavy Metals. *Sci. Total Environ.* **2018**, *615*, 476–485. https://doi.org/10.1016/j.scitotenv.2017.09.126.

(62) Kim, H. N.; Ren, W. X.; Kim, J. S.; Yoon, J. Fluorescent and Colorimetric Sensors for Detection of Lead, Cadmium, and Mercury Ions. *Chem. Soc. Rev.* **2012**, *41* (8), 3210–3244. https://doi.org/10.1039/c1cs15245a.

(63) Wang, H.; Ji, X.F.; Li, Z.T.; Huang, F. H. Fluorescent Supramolecular Polymeric Materials. *Adv. Mater.* **2017**, *29*. https://doi.org/10.1002/adma.201606117

(64) Chen, S.; Xue, Z.; Gao, N.; Yang, X.; Zang, L. Perylene Diimide-Based Fluorescent and Colorimetric Sensors for Environmental Detection. *Sensors (Switzerland)* **2020**, *20* (3), 1–28. https://doi.org/10.3390/s20030917.

(65) Junjie Wang, Tao Wei, Feng Ma, T. L.; Qingfen Niu. A Novel Fluorescent and Colorimetric Dual-Channel Sensor for the Fast, Reversible and Simultaneous Detection of Fe^{3+} and Cu^{2+} Based on Terthiophene Derivative with High Sensitivity and Selectivity. *J. Photochem. Photobiol. A* **2019**, *383*, 1–9. http://dx.doi.org/10.1016/j.jphotochem.2019.111982

(66) Y.X. Chang, J.X. Fu, K. Yao, B. Li, K.X. Xu, X. B. P. Novel Fluorescent Probes for Sequential Detection of Cu^{2+} and Citrate Anionand Application in Living Cell Imaging.

Dye. Pigment. **2019**, *161*, 331–340. https://doi.org/10.1016/j.dyepig.2018.09.080

(67) P. Wang, K. Yao, J.X. Fu, Y.X. Chang, B. Li, K. X. X. Novel Fluorescent Probes for Relay Detection Copper/Citrate Ion and Application in Cell Imaging. *Spectrochim. Acta A* **2019**, *211*, 9–17. https://doi.org/10.1016/j.saa.2018.11.038

(68) Cui, W. R.; Zhang, C. R.; Jiang, W.; Liang, R. P.; Wen, S. H.; Peng, D.; Qiu, J. D. Covalent Organic Framework Nanosheet-Based Ultrasensitive and Selective Colorimetric Sensor for Trace Hg^{2+} Detection. *ACS Sustain. Chem. Eng.* **2019**, *7* (10), 9408–9415. https://doi.org/10.1021/acssuschemeng.9b00613.

(69) Vashishta, D.; Kaura, K.; Jukariaa, R.; Vashishtb, A.; Sharmac, S.; Mehta, S. K. Colorimetric Chemosensor Based on Coumarin Skeleton for Selective Naked Eye Detection of Cobalt (II) Ion in near Aqueous Medium. *Sensors Actuators B Chem.* **2019**, *280*, 219–226. https://doi.org/10.1016/j.snb.2018.10.020

(70) Soufeena, P. P.; Nibila, T. A.; Aravindakshan, K. K. Coumarin Based Yellow Emissive AIEE Active Probe: A Colorimetric Sensor for Cu^{2+} and Fluorescent Sensor for Picric Acid. *Spectrochim. Acta - Part A Mol. Biomol. Spectrosc.* **2019**, *223*, 117201. https://doi.org/10.1016/j.saa.2019.117201.

(71) Chen, C. G.; Vijay, N.; Thirumalaivasan, N.; Velmathi, S.; Wu, S. P. Coumarin-Based Hg^{2+} Fluorescent Probe: Fluorescence Turn-on Detection for Hg^{2+} Bioimaging in Living Cells and Zebrafish. *Spectrochim. Acta - Part A Mol. Biomol. Spectrosc.* **2019**, *219*, 135–140. https://doi.org/10.1016/j.saa.2019.04.048.

(72) Wang, W.; Wu, J.; Liu, Q.; Gao, Y.; Liu, H.; Zhao, B. A Highly Selective Coumarin-Based Chemosensor for the Sequential Detection of Fe^{3+} and Pyrophosphate and Its Application in Living Cell Imaging. *Tetrahedron Lett.* **2018**, *59* (19), 1860–1865. https://doi.org/10.1016/j.tetlet.2018.04.007.

(73) Arslan, F. N.; Geyik, G. A.; Koran, K.; Ozen, F.; Aydin, D.; Elmas, Ş. N. K.; Gorgulu, A. O.; Yilmaz, I. Fluorescence "Turn On–Off" Sensing of Copper (II) Ions Utilizing Coumarin–Based Chemosensor: Experimental Study, Theoretical Calculation, Mineral and Drinking Water Analysis. *J. Fluoresc.* **2020**, *30* (2), 317–327. https://doi.org/10.1007/s10895-020-02503-4.

(74) Kim, M., Jo, T., Yang, M., Han, J., Lim, M., Kim, C. A Fluorescent and Colorimetric Schiff Base Chemosensor for the Detection of Zn^{2+} and Cu^{2+}: Application in Live Cell

Imaging and Colorimetric Test Kit. *Spectrochim. Acta Part A Mol. Biomol. Spectrosc.* **2019**, *211*, 34–43. https://doi.org/10.1016/j.saa.2018.11.058

(75) Q. Xia, S. Feng, D. Liu, G. F. A Highly Selective and Sensitive Colorimetric and Near-Infrared Fluorescent Turn-on Probe for Rapid Detection of Palladium in Drugs and Living Cells. *Sens. Actuators B-Chem.* **2018**, *258*, 98–104. https://doi.org/10.1016/j.snb.2017.11.099

(76) Zhang, X.; Wang, Y.; Yuan, H.; Guo, X.; Dai, B.; Jia, X. An Acid-Fluorescence and Alkali-Colorimetric Dual Channels Sensor for Hg^{2+} Selective Detection by Different Coordination Manners in Aqueous Media. *J. Photochem. Photobiol. A Chem.* **2019**, *373*, 12–19. https://doi.org/10.1016/j.jphotochem.2018.12.009.

(77) Gu, L., Zheng, T., Xu, Z., Song, Y., Li, H., Xia, S., Shen, L. A Novel Bifunctional Fluorescent and Colorimetric Probe for Detection of Mercury and Fluoride Ions. *Spectrochim. Acta Part A Mol. Biomol. Spectrosc.* **2019**, *207*, 88–95. https://doi.org/10.1016/j.saa.2018.08.060

(78) Fu, J.; Yao, K.; Li, B.; Mei, H.; Chang, Y.; Xu, K. Coumarin-Based Colorimetric-Fluorescent Sensors for the Sequential Detection of Zn^{2+} Ion and Phosphate Anions and Applications in Cell Imaging. *Spectrochim. Acta - Part A Mol. Biomol. Spectrosc.* **2020**, *228*, 117790. https://doi.org/10.1016/j.saa.2019.117790.

(79) Yin, Z. Y.; Hu, J. H.; Gui, K.; Fu, Q. Q.; Yao, Y.; Zhou, F. L.; Ma, L. L.; Zhang, Z. P. AIE Based Colorimetric and "Turn-on" Fluorescence Schiff Base Sensor for Detecting Fe^{3+} in an Aqueous Media and Its Application. *J. Photochem. Photobiol. A Chem.* **2020**, *396*, 112542. https://doi.org/10.1016/j.jphotochem.2020.112542.

(80) Lv, H.; Yuan, G.; Zhang, G.; Ren, Z.; He, H.; Sun, Q.; Zhang, X.; Wang, S. A Novel Benzopyran-Based Colorimetric and near-Infrared Fluorescent Sensor for Hg^{2+} and Its Imaging in Living Cell and Zebrafish. *Dye. Pigment.* **2020**, *172*, 107658. https://doi.org/10.1016/j.dyepig.2019.107658.

(81) Chen, H.; Yang, P.; Li, Y.; Zhang, L.; Ding, F.; He, X.; Shen, J. Insight into Triphenylamine and Coumarin Serving as Copper (II) Sensors with "OFF" Strategy and for Bio-Imaging in Living Cells. *Spectrochim. Acta - Part A Mol. Biomol. Spectrosc.* **2020**, *224*, 117384. https://doi.org/10.1016/j.saa.2019.117384.

(82) Zhang, Q.; Ma, R.; Li, Z.; Liu, Z. A Multi-Responsive Crown Ether-Based

Colorimetric/Fluorescent Chemosensor for Highly Selective Detection of Al^{3+}, Cu^{2+} and Mg^{2+}. *Spectrochim. Acta - Part A Mol. Biomol. Spectrosc.* **2020**, *228*, 117857. https://doi.org/10.1016/j.saa.2019.117857.

(83) Vogel, A. Darstellung von Benzoesäure Aus Der Tonka-Bohne Und Aus Den Meliloten - Oder Steinklee - Blumen. *Ann. Phys.* **1820**, *64* (2), 161–166. https://doi.org/10.1002/andp.18200640205.

(84) Perkin, W. Coumarin By W. H. PERKIN, F.R.S. IT. *J. Chem. Soc.* **1868**, *21*, 53–63. https://doi.org/10.1039/JS8773100388

(85) Jumal, J.; Norhanis Sakinah. Synthesis, Characterization, and Applications of Coumarin Derivatives: A Short Review. *Malaysian J. Sci. Heal. Technol.* **2021**, *7* (1), 62–68. https://doi.org/10.33102/mjosht.v7i1.145.

(86) Stefanachi, A.; Leonetti, F.; Pisani, L.; Catto, M.; Carotti, A. *Coumarin: A Natural, Privileged and Versatile Scaffold for Bioactive Compounds*; 2018; Vol. 23. https://doi.org/10.3390/molecules23020250.

(87) Lončar, M.; Jakovljević, M.; Šubarić, D.; Pavlić, M.; Služek, V. B.; Cindrić, I.; Molnar, M. *Coumarins in Food and Methods of Their Determination*; 2020; Vol. 9. https://doi.org/10.3390/foods9050645.

(88) Garg, S. S.; Gupta, J.; Sharma, S.; Sahu, D. D. An Insight into the Therapeutic Applications of Coumarin Compounds and Their Mechanisms of Action. *Eur. J. Pharm. Sci.* **2020**, *152*, 105424. https://doi.org/10.1016/j.ejps.2020.105424.

(89) Carneiro, A.; Matos, M. J.; Uriarte, E.; Santana, L. Trending Topics on Coumarin and Its Derivatives in 2020. *Molecules* **2021**, *26* (2), 1–15. https://doi.org/10.3390/molecules26020501.

(90) Becerra, D.; Portilla, J. 2-Oxo-2 H -Chromen-7-Yl 4-Chlorobenzoate. **2021**, 2–7. https://doi.org/10.3390/M1279

(91) Xu, Z.; Chen, Q.; Zhang, Y.; Liang, C. Coumarin-Based Derivatives with Potential Anti-HIV Activity. *Fitoterapia* **2021**, *150*, 104863. https://doi.org/10.1016/j.fitote.2021.104863.

(92) Lu, W.; Chen, J.; Shi, J.; Li, Z.; Xu, L.; Jiang, W.; Yang, S.; Gao, B. An Acylhydrazone Coumarin as Chemosensor for the Detection of Ni^{2+} with Excellent Sensitivity and

Low LOD: Synthesis, DFT Calculations and Application in Real Water and Living Cells. *Inorganica Chim. Acta* **2021**, *516*, 2–9. https://doi.org/10.1016/j.ica.2020.120144.

(93) Arooj, M.; Zahra, M.; Islam, M.; Ahmed, N.; Waseem, A.; Shafiq, Z. Coumarin Based Thiosemicarbazones as Effective Chemosensors for Fluoride Ion Detection. *Spectrochim. Acta - Part A Mol. Biomol. Spectrosc.* **2021**, *261*, 120011. https://doi.org/10.1016/j.saa.2021.120011.

(94) Mohd Yusof Chan, N. N.; Idris, A.; Zainal Abidin, Z. H.; Tajuddin, H. A.; Abdullah, Z. White Light Employing Luminescent Engineered Large (Mega) Stokes Shift Molecules: A Review. *RSC Adv.* **2021**, *11* (22), 13409–13445. https://doi.org/10.1039/d1ra00129a.

(95) Huang, L.; Sheng, W.; Wang, L.; Meng, X.; Duan, H.; Chi, L. A Novel Coumarin-Based Colorimetric and Fluorescent Probe for Detecting Increasing Concentrations of Hg^{2+}in Vitroandin Vivo. *RSC Adv.* **2021**, *11* (38), 23597–23606. https://doi.org/10.1039/d1ra01408k.

(96) Muthusamy, S.; Rajalakshmi, K.; Zhu, D.; Zhu, W.; Wang, S.; Lee, K. B.; Xu, H.; Zhao, L. Dual Detection of Mercury (II) and Lead (II) Ions Using a Facile Coumarin-Based Fluorescent Probe via Excited State Intramolecular Proton Transfer and Photo-Induced Electron Transfer Processes. *Sensors Actuators B Chem.* **2021**, *346*, 130534. https://doi.org/10.1016/j.snb.2021.130534.

(97) Khalid, M.; Khan, M. U.; Shafiq, I.; Hussain, R.; Ali, A.; Imran, M.; Braga, A. A. C.; Fayyaz ur Rehman, M.; Akram, M. S. Structural Modulation of π-Conjugated Linkers in D–π–A Dyes Based on Triphenylamine Dicyanovinylene Framework to Explore the NLO Properties. *R. Soc. Open Sci.* **2021**, *8* (8), 210570. https://doi.org/10.1098/rsos.210570.

(98) Cao, D.; Liu, Z.; Verwilst, P.; Koo, S.; Jangjili, P.; Kim, J. S.; Lin, W. Coumarin-Based Small-Molecule Fluorescent Chemosensors. *Chem. Rev.* **2019**, *119* (18), 10403–10519. https://doi.org/10.1021/acs.chemrev.9b00145.

(99) Sun, X. Y.; Liu, T.; Sun, J.; Wang, X. J. Synthesis and Application of Coumarin Fluorescence Probes. *RSC Adv.* **2020**, *10* (18), 10826–10847. https://doi.org/10.1039/c9ra10290f.

(100) Rovira, A.; Pujals, M.; Gandioso, A.; López-Corrales, M.; Bosch, M.; Marchán, V. Modulating Photostability and Mitochondria Selectivity in Far-Red/NIR Emitting Coumarin Fluorophores through Replacement of Pyridinium by Pyrimidinium. *J. Org. Chem.* **2020**, *85* (9), 6086–6097. https://doi.org/10.1021/acs.joc.0c00570.

(101) Li, S.; Cao, D.; Meng, X.; Hu, Z.; Li, Z.; Yuan, C.; Zhou, T.; Han, X.; Ma, W. A Novel Fluorescent Chemosensor Based on Coumarin and Quinolinyl-Benzothiazole for Sequential Recognition of Cu^{2+} and PPi and Its Applicability in Live Cell Imaging. *Spectrochim. Acta - Part A Mol. Biomol. Spectrosc.* **2020**, *230*, 118022. https://doi.org/10.1016/j.saa.2019.118022.

(102) Tan, D.; Akdag, A. Synthesis of New Flexible Coumarin Dimers for Sodium and Potassium Differentiation. *J. Fluoresc.* **2020**, *30* (1), 27–34. https://doi.org/10.1007/s10895-020-02492-4.

(103) He, H.-Z.; Li, K.; Yu, K.-K.; Lu, P.-L.; Feng, M.-L.; Chen, S.-Y.; Yu, X.-Q. Additive- and Column-Free Synthesis of Rigid Bis-Coumarins as Fluorescent Dyes for G-Quadruplex Sensing via Disaggregation-Induced Emission . *Chem. Commun.* **2020**, 6870–6873. https://doi.org/10.1039/d0cc01437k.

(104) Jung, Y.; Jung, J.; Huh, Y.; Kim, D. Benzo[g]Coumarin-Based Fluorescent Probes for Bioimaging Applications. *J. Anal. Methods Chem.* **2018**, https://doi.org/10.1155/2018/5249765.

(105) Beninatto, R.; Barbera, C.; De Lucchi, O.; Borsato, G.; Serena, E.; Guarise, C.; Pavan, M.; Luni, C.; Martewicz, S.; Galesso, D.; Elvassore, N. Photocrosslinked Hydrogels from Coumarin Derivatives of Hyaluronic Acid for Tissue Engineering Applications. *Mater. Sci. Eng. C* **2019**, *96*, 625–634. https://doi.org/10.1016/j.msec.2018.11.052.

(106) Bettoschi, A.; Ceglie, A.; Lopez, F.; Meli, V.; Murgia, S.; Tamburro, M.; Caltagirone, C.; Cuomo, F. On the Role of a Coumarin Derivative for Sensing Applications: Nucleotide Identification Using a Micellar System. *J. Colloid Interface Sci.* **2016**, *477*, 8–15. https://doi.org/10.1016/j.jcis.2016.05.034.

(107) Gan, Y.; Liang, T.; Hu, Q.; Zhong, L.; Wang, X.; Wan, H.; Wang, P. In-Situ Detection of Cadmium with Aptamer Functionalized Gold Nanoparticles Based on Smartphone-Based Colorimetric System. *Talanta* **2020**, *208*, 120231. https://doi.org/10.1016/j.talanta.2019.120231.

(108) Kim, H.; Jang, G.; Yoon, Y. Specific Heavy Metal/Metalloid Sensors: Current State and Perspectives. *Appl. Microbiol. Biotechnol.* **2020**, *104* (3), 907–914. https://doi.org/10.1007/s00253-019-10261-y.

(109) Park, S. H.; Kwon, N.; Lee, J. H.; Yoon, J.; Shin, I. Synthetic Ratiometric Fluorescent Probes for Detection of Ions. *Chem. Soc. Rev.* **2020**, *49* (1), 143–179. https://doi.org/10.1039/c9cs00243j.

(110) Sun, X.; Wang, Y.; Zhang, X.; Zhang, S.; Zhang, Z. A New Coumarin Based Chromo-Fluorogenic Probe for Selective Recognition of Cyanide Ions in an Aqueous Medium. *RSC Adv.* **2015**, *5* (117), 96905–96910. https://doi.org/10.1039/c5ra14500g.

(111) Zhang, C.; Wei, L.; Wei, C.; Zhang, J.; Wang, R.; Xi, Z.; Yi, L. A FRET-ICT Dual-Quenching Fluorescent Probe with Large off-on Response for H_2S: Synthesis, Spectra and Bioimaging. *Chem. Commun.* **2015**, *51* (35), 7505–7508. https://doi.org/10.1039/c5cc01184a.

(112) Purnell, L. G.; Estes, E. D.; Hodgson, D. J. Interaction of Metal Ions with 8-Azapurines. II. Synthesis and Structure of Bis(8-Azahypoxanthinato)Tetraaquocadmium(II). *J. Am. Chem. Soc.* **1976**, *98* (3), 740–743. https://doi.org/10.1021/ja00419a016.

(113) Li, P. Z.; Wang, X. J.; Zhao, Y. Click Chemistry as a Versatile Reaction for Construction and Modification of Metal-Organic Frameworks. *Coord. Chem. Rev.* **2019**, *380*, 484–518. https://doi.org/10.1016/j.ccr.2018.11.006.

(114) Cai, H.; Shukla, S.; Wang, C.; Masarapu, H.; Steinmetz, N. F. Heterologous Prime-Boost Enhances the Antitumor Immune Response Elicited by Plant-Virus-Based Cancer Vaccine. *J. Am. Chem. Soc.* **2019**, *141* (16), 6509–6518. https://doi.org/10.1021/jacs.9b01523.

(115) Huisgen, R. 1,3-Dipolar Cycloadditions Past and Future. *Angew. Chem. Int. Ed. Engl* **1963**, *2* (10), 565–632. https://doi.org/10.1002/anie.196305651

(116) Rostovtsev, V. V.; Green, L. G.; Fokin, V. V.; Sharpless, K. B. A Stepwise Huisgen Cycloaddition Process: Copper(I)-Catalyzed Regioselective "Ligation" of Azides and Terminal Alkynes - Rostovtsev - 2002 - Angewandte Chemie - Wiley Online Library. *Angew. Chemie.*, **2002**, (14), 2708–2711. https://doi.org/10.1002/1521-3773(20020715)41:14%3C2596::aid-anie2596%3E3.0.co;2-4

(117) Saiyasombat, W.; Kiatisevi, S. Bis-BODIPY Linked-Triazole Based on Catechol Core for Selective Dual Detection of $Ag^{+}$and Hg^{2+}. *RSC Adv.* **2021**, *11* (6), 3703–3712. https://doi.org/10.1039/d0ra09686e.

(118) Morozova, M. A.; Yusubov, M. S.; Kratochvil, B.; Eigner, V.; Bondarev, A. A.; Yoshimura, A.; Saito, A.; Zhdankin, V. V.; Trusova, M. E.; Postnikov, P. S. Regioselective Zn(OAc)2-Catalyzed Azide-Alkyne Cycloaddition in Water: The Green Click-Chemistry. *Org. Chem. Front.* **2017**, *4* (6), 978–985. https://doi.org/10.1039/c6qo00787b.

(119) Kalra, P.; Kaur, R.; Singh, G.; Singh, H.; Singh, G.; Pawan; Kaur, G.; Singh, J. Metals as "Click" Catalysts for Alkyne-Azide Cycloaddition Reactions: An Overview. *J. Organomet. Chem.* **2021**, *944*, 121846. https://doi.org/10.1016/j.jorganchem.2021.121846.

(120) Hein, J. E.; Fokin, V. V. Copper-Catalyzed Azide-Alkyne Cycloaddition (CuAAC) and beyond: New Reactivity of Copper(i) Acetylides. *Chem. Soc. Rev.* **2010**, *39* (4), 1302–1315. https://doi.org/10.1039/b904091a.

(121) Lau, Y. H.; Rutledge, P. J.; Watkinson, M.; Todd, M. H. Chemical Sensors That Incorporate Click-Derived Triazoles. *Chem. Soc. Rev.* **2011**, *40* (5), 2848–2866. https://doi.org/10.1039/c0cs00143k.

(122) Key, J. A.; Koh, S.; Timerghazin, Q. K.; Brown, A.; Cairo, C. W. Photophysical Characterization of Triazole-Substituted Coumarin Fluorophores. *Dye. Pigment.* **2009**, *82* (2), 196–203. https://doi.org/10.1016/j.dyepig.2009.01.001.

(123) Rani, P.; Lal, K.; Aruna; Shrivastava, R.; Ghule, V. D. Synthesis and Characterization of 1,2,3-Triazoles-Linked Urea Hybrid Sensor for Selective Sensing of Fluoride Ion. *J. Mol. Struct.* **2020**, *1203*, 127437. https://doi.org/10.1016/j.molstruc.2019.127437.

(124) Ali, I.; Imkan; Ikram, F.; Ahmad, F.; Nisar, J.; Shah, M. R.; Ali, S.; ullah, S.; Althagafi, I. I.; Ateeq, M. Sensing Applications of Triazole Conjugated Silver Nanoparticles. *J. Mol. Struct.* **2021**, *1226*, 129306. https://doi.org/10.1016/j.molstruc.2020.129306.

(125) Ozukanar, O.; Gunduz, H.; Unlu, C.; Kumbaraci, V. A Novel Anthracene Functionalized Dibenzoxanthene Fluorophore for Copper (II) Sensing. *Opt. Mater. (Amst).* **2021**, *119*, 111370. https://doi.org/10.1016/j.optmat.2021.111370.

(126) Struthers, H.; Mindt, T. L.; Schibli, R. Metal Chelating Systems Synthesized Using the

Copper(I) Catalyzed Azide-Alkyne Cycloaddition. *Dalt. Trans.* **2010**, *39* (3), 675–696. https://doi.org/10.1039/b912608b.

(127) Heidari, L.; Ghassemzadeh, M.; Fenske, D.; Fuhr, O.; Mohsenzadeh, F.; Bon, V. 3D Coordination Polymers Constructed from D10 Metal Ions, Flexible 1,2,4-Triazole Derivatives and Aromatic Tetracarboxylates: Syntheses, Structures, Thermal and Luminescent Properties. *J. Solid State Chem.* **2021**, *296*, https://doi.org/10.1016/j.jssc.2021.122011.

(128) Urankar, D.; Pinter, B.; Pevec, A.; De Proft, F.; Turel, I.; Košmrlj, J. Click-Triazole N2 Coordination to Transition-Metal Ions Is Assisted by a Pendant Pyridine Substituent. *Inorg. Chem.* **2010**, *49* (11), 4820–4829. https://doi.org/10.1021/ic902354e.

(129) Eytel, L. M.; Fargher, H. A.; Haley, M. M.; Johnson, D. W. The Road to Aryl CH···anion Binding Was Paved with Good Intentions: Fundamental Studies, Host Design, and Historical Perspectives in CH Hydrogen Bonding. *Chem. Commun.* **2019**, *55* (36), 5195–5206. https://doi.org/10.1039/c9cc01460h.

(130) Pasini, D. The Click Reaction as an Efficient Tool for the Construction of Macrocyclic Structures. *Molecules* **2013**, *18* (8), 9512–9530. https://doi.org/10.3390/molecules18089512.

(131) Ramachandran, M.; Syed, A.; Marraiki, N.; Anandan, S. The Aqueous Dependent Sensing of Hydrazine and Phosphate Anions Using a Bis-Heteroleptic Ru(Ii) Complex with a Phthalimide–Anchored Pyridine-Triazole Ligand . *Analyst* **2021**, 1430–1443. https://doi.org/10.1039/d0an02299c.

(132) Shaily; Kumar, A.; Parveen, I.; Ahmed, N. Highly Selective and Sensitive Coumarin–Triazole-Based Fluorometric 'Turn-off' Sensor for Detection of Pb^{2+} Ions. *Luminescence* **2018**, *33* (4), 713–721. https://doi.org/10.1002/bio.3468.

(133) Jain, A.; Jain, Y.; Gupta, R.; Agarwal, M. Trifluoromethyl Group Containing C3 Symmetric Coumarin-Triazole Based Fluorometric Tripodal Receptors for Selective Fluoride Ion Recognition: A Theoretical and Experimental Approach. *J. Fluor. Chem.* **2018**, *212*, 153–160. https://doi.org/10.1016/j.jfluchem.2018.06.005.

(134) Joshi, S.; Kumari, S.; Bhattacharjee, R.; Sarmah, A.; Sakhuja, R.; Pant, D. D. Experimental and Theoretical Study: Determination of Dipole Moment of Synthesized Coumarin-Triazole Derivatives and Application as Turn off Fluorescence Sensor: High

Sensitivity for Iron(III) Ions. *Sensors Actuators, B Chem.* **2015**, *220*, 1266–1278. https://doi.org/10.1016/j.snb.2015.07.053.

(135) Park, J. E.; Anand, T.; Bharadwaj, V.; Sahoo, S. K.; Choi, H. J. A Novel Fluorescent Triazole Trindane-Coumarin Receptor for the Selective Detection of Nitroaromatics. *J. Photochem. Photobiol. A Chem.* **2019**, *383*, 111990. https://doi.org/10.1016/j.jphotochem.2019.111990.

(136) Ngororabanga, J. M. V.; Tshentu, Z. R.; Mama, N. A New Highly Selective Colorimetric and Fluorometric Coumarin-Based Chemosensor for Hg^{2+}. *J. Fluoresc.* **2020**. https://doi.org/10.1007/s10895-020-02542-x.

(137) Schiff, H. Mittheilungen Aus Dem Universitätslaboratorium in Pisa: Eine Neue Reihe Organischer Basen. *Justus Liebigs Ann. Chem.* **1864**, *131* (1), 118–119. https://doi.org/10.1002/jlac.18641310113.

(138) Sumrra, S. H.; Zafar, W.; Asghar, M. L.; Mushtaq, F.; Raza, M. A.; Nazar, M. F.; Nadeem, M. A.; Imran, M.; Mumtaz, S. Computational Investigation of Molecular Structures, Spectroscopic Properties, Cholinesterase Inhibition and Antibacterial Activities of Triazole Schiff Bases Endowed Metal Chelates. *J. Mol. Struct.* **2021**, *1238*, 130382. https://doi.org/10.1016/j.molstruc.2021.130382.

(139) Bernadette Amali, I.; Kesavan, M. P.; Vijayakumar, V.; Indra Gandhi, N.; Rajesh, J.; Rajagopal, G. Structural Analysis, Antimicrobial and Cytotoxic Studies on New Metal(II) Complexes Containing N 2 O 2 Donor Schiff Base Ligand. *J. Mol. Struct.* **2019**, *1183*, 342–350. https://doi.org/10.1016/j.molstruc.2019.02.005.

(140) Adams, J. B.; Pretorius, L.; Snow, G. C. Deterioration in the Water Quality of an Urbanised Estuary with Recommendations for Improvement. *Water SA* **2019**, *45* (1), 86–96. https://doi.org/10.4314/wsa.v45i1.10.

(141) Iacopetta, D.; Ceramella, J.; Catalano, A.; Saturnino, C.; Bonomo, M. G.; Franchini, C.; Sinicropi, M. S. Schiff Bases: Interesting Scaffolds with Promising Antitumoral Properties. *Appl. Sci.* **2021**, *11* (4), 1–20. https://doi.org/10.3390/app11041877.

(142) M. Ibrahim, F.; M. Abdalhadi, S. Performance of Schiff Bases Metal Complexes and Their Ligand in Biological Activity: A Review. *Al-Nahrain J. Sci.* **2021**, *24* (1), 1–10. https://doi.org/10.22401/anjs.24.1.01.

(143) Kaya, İ.; Daban, S.; Şenol, D. Synthesis and Characterization of Schiff Base, Co(II) and

Cu(II) Metal Complexes and Poly(Phenoxy-Imine)s Containing Pyridine Unit. *Inorganica Chim. Acta* **2021**, *515*. https://doi.org/10.1016/j.ica.2020.120040.

(144) Rafiee Samani, Z.; Mehranpour, A. Synthesis of New Allylidene Amino Phenol-Containing Schiff Bases and Metal Complex Formation Using Trimethinium Salts. *RSC Adv.* **2021**, *11* (35), 21695–21701. https://doi.org/10.1039/d1ra04214a.

(145) Khan, S.; Chen, X.; Almahri, A.; Allehyani, E. S.; Alhumaydhi, F. A.; Ibrahim, M. M.; Ali, S. Recent Developments in Fluorescent and Colorimetric Chemosensors Based on Schiff Bases for Metallic Cations Detection: A Review. *J. Environ. Chem. Eng.* **2021**, 106381. https://doi.org/10.1016/j.jece.2021.106381.

(146) Hosseinjani-Pirdehi, H.; Mahmoodi, N. O.; Pasandideh Nadamani, M.; Taheri, A. Novel Synthesized Azo-Benzylidene-Thiourea as Dual Naked-Eye Chemosensor for Selective Detection of Hg^{2+} and CN^- Ions. *J. Photochem. Photobiol. A Chem.* **2020**, *391*, 112365. https://doi.org/10.1016/j.jphotochem.2020.112365.

(147) Slassi, S.; Aarjane, M.; Amine, A. A Novel Imidazole-Derived Schiff Base as Selective and Sensitive Colorimetric Chemosensor for Fluorescent Detection of Cu^{2+} in Methanol with Mixed Aqueous Medium. *Appl. Organomet. Chem.* **2021**, No. May, 1–11. https://doi.org/10.1002/aoc.6408.

(148) Makki, S. Q.; Alhussein, N. M. A.; Tizkam, H. H.; Balakit, A. A. Highly Sensitive and Selective Colorimetric Sensor for Iron (II) Ion Detection Based on 4-Amino-Antipyrine Derivative. *AIP Conf. Proc.* **2020**, *2290*. https://doi.org/10.1063/5.0027459.

(149) Sánchez-Portillo, P.; Hernández-Sirio, A.; Godoy-Alcántar, C.; Lacroix, P. G.; Agarwal, V.; Santillán, R.; Barba, V. Colorimetric Metal Ion (II) Sensors Based on Imine Boronic Esters Functionalized with Pyridine. *Dye. Pigment.* **2021**, *186*. https://doi.org/10.1016/j.dyepig.2020.108991.

(150) Athanas, A. B.; Kalaiyar, S. Proton Coupled Electron Transport of PH Sensitive Coumarin Based Ruthenium(II) Complex: A Functional Mimic of Photosystem II. *J. Photochem. Photobiol.* **2021**, *8*, 100057. https://doi.org/10.1016/j.jpap.2021.100057.

(151) Salihović, M.; Pazalja, M.; Špirtović Halilović, S.; Veljović, E.; Mahmutović-Dizdarević, I.; Roca, S.; Novaković, I.; Trifunović, S. Synthesis, Characterization, Antimicrobial Activity and DFT Study of Some Novel Schiff Bases. *J. Mol. Struct.* **2021**, *1241*. https://doi.org/10.1016/j.molstruc.2021.130670.

(152) Naureen, B.; Miana, G. A.; Shahid, K.; Asghar, M.; Tanveer, S.; Sarwar, A. Iron (III) and Zinc (II) Monodentate Schiff Base Metal Complexes: Synthesis, Characterisation and Biological Activities. *J. Mol. Struct.* **2021**, *1231*, 129946. https://doi.org/10.1016/j.molstruc.2021.129946.

(153) Nozha, S. G.; Morgan, S. M.; Ahmed, S. E. A.; El-Mogazy, M. A.; Diab, M. A.; El-Sonbati, A. Z.; Abou-Dobara, M. I. Polymer Complexes. LXXIV. Synthesis, Characterization and Antimicrobial Activity Studies of Polymer Complexes of Some Transition Metals with Bis-Bidentate Schiff Base. *J. Mol. Struct.* **2021**, *1227*, 129525. https://doi.org/10.1016/j.molstruc.2020.129525.

(154) Kargar, H.; Aghaei-Meybodi, F.; Behjatmanesh-Ardakani, R.; Elahifard, M. R.; Torabi, V.; Fallah-Mehrjardi, M.; Tahir, M. N.; Ashfaq, M.; Munawar, K. S. Synthesis, Crystal Structure, Theoretical Calculation, Spectroscopic and Antibacterial Activity Studies of Copper(II) Complexes Bearing Bidentate Schiff Base Ligands Derived from 4-Aminoantipyrine: Influence of Substitutions on Antibacterial Activity. *J. Mol. Struct.* **2021**, *1230*, 129908. https://doi.org/10.1016/j.molstruc.2021.129908.

(155) Reshma, R.; Selwin Joseyphus, R.; Arish, D.; Reshmi Jaya, R. J.; Johnson, J. Tridentate Imidazole-Based Schiff Base Metal Complexes: Molecular Docking, Structural and Biological Studies. *J. Biomol. Struct. Dyn.* **2021**, (0), 1–13. https://doi.org/10.1080/07391102.2021.1914171.

(156) Nguyen, Q. T.; Pham Thi, P. N.; Nguyen, V. T. Synthesis, Characterization, and in Vitro Cytotoxicity of Unsymmetrical Tetradentate Schiff Base Cu(II) and Fe(III) Complexes. *Bioinorg. Chem. Appl.* **2021**, *2021*. https://doi.org/10.1155/2021/6696344.

(157) Subin Kumar, K.; Aravindakshan, K. K. Synthesis, Cytotoxic, Anticancer and Antimicrobial Activities of Some Metal Complexes of a Novel Tetradentate Schiff Base Ligand, (E)-3-((2-((E)-(1-(2-Hydroxyphenyl)Ethylidene)Amino)Ethyl)Imino)-N-Phenylbutanamide. *Results Chem.* **2021**, *3* (April), 100129. https://doi.org/10.1016/j.rechem.2021.100129.

(158) Ebosie, N. P.; Ogwuegbu, M. O. C.; Onyedika, G. O.; Onwumere, F. C. *Biological and Analytical Applications of Schiff Base Metal Complexes Derived from Salicylidene-4-Aminoantipyrine and Its Derivatives: A Review*; Springer Berlin Heidelberg, 2021. https://doi.org/10.1007/s13738-021-02265-1.

(159) Arvas, B.; Ucar, B.; Acar, T.; Arvas, M. B.; Sahin, Y.; Aydogan, F.; Yolacan, C. A New

Coumarin Based Schiff Base Fluorescence Probe for Zinc Ion. *Tetrahedron* **2021**, *88*, 132127. https://doi.org/10.1016/j.tet.2021.132127.

(160) Qin, J. C.; Fan, L.; Wang, B. D.; Yang, Z. Y.; Li, T. R. The Design of a Simple Fluorescent Chemosensor for Al^{3+}/Zn^{2+}via Two Different Approaches. *Anal. Methods* **2015**, *7* (2), 716–722. https://doi.org/10.1039/c4ay02351j.

(161) Vashisht, D.; Kaur, K.; Jukaria, R.; Vashisht, A.; Sharma, S.; Mehta, S. K. Colorimetric Chemosensor Based on Coumarin Skeleton for Selective Naked Eye Detection of Cobalt (II) Ion in near Aqueous Medium. *Sensors Actuators, B Chem.* **2019**, *280*, 219–226. https://doi.org/10.1016/j.snb.2018.10.020.

(162) Mathivanan, M.; Tharmalingam, B.; Devaraj, T.; Murugan, A.; Lin, C. H.; Jothi, M.; Murugesapandian, B. A New7-Diethylamino-4-Hydroxycoumarin Based Reversible Colorimetric/Fluorometric Probe for Sequential Detection of Al^{3+}/PPi and Its Potential Use in Biodetection and Bioimaging Applications. *New J. Chem.* **2021**, *45* (13), 6067–6079. https://doi.org/10.1039/d0nj05718e.

(163) Wang, Z. G.; Ding, X. J.; Huang, Y. Y.; Yan, X. J.; Ding, B.; Li, Q. Z.; Xie, C. Z.; Xu, J. Y. The Development of Coumarin Schiff Base System Applied as Highly Selective Fluorescent/Colorimetric Probes for Cu2+ and Tumor Biomarker Glutathione Detection. *Dye. Pigment.* **2020**, *175*, 108156. https://doi.org/10.1016/j.dyepig.2019.108156.

(164) Asha, M. S.; Sangamesha, M. A.; Pinto, O.; Sandra, T. O.; Shaji, R. P. Synthesis and Characterization of Hetero Cyclic Imine and Its Metal Complexes for Anticorrosion Application. *Mater. Today Proc.* **2021**, *46*, 2436–2444. https://doi.org/10.1016/j.matpr.2021.01.356.

(165) Vaseghi, S.; Yousefi, M.; Shokrzadeh, M.; Hossaini, Z.; Hosseini-khah, Z.; Emami, S. Synthesis, Computational Study and Cytotoxicity of 4-Hydroxycoumarin-Derived Imines/Enamines. *Mol. Divers.* **2021**, *25* (2), 1011–1024. https://doi.org/10.1007/s11030-020-10086-2.

(166) Fang, Y.; Dehaen, W. Small-Molecule-Based Fluorescent Probes for f-Block Metal Ions: A New Frontier in Chemosensors. *Coord. Chem. Rev.* **2021**, *427*, 213524. https://doi.org/10.1016/j.ccr.2020.213524.

(167) Gao, L. L.; Wang, B. B.; Chen, X.; Wang, Y.; Wu, W. N.; Zhao, X. L.; Yan, L. L.; Fan,

Y. C.; Xu, Z. H. Hydrazone Derivative Bearing Coumarin for the Relay Detection of Cu^{2+} and H_2S in an Almost Neat Aqueous Solution and Bioimaging in Lysosomes. *Spectrochim. Acta - Part A Mol. Biomol. Spectrosc.* **2021**, *255*, 119693. https://doi.org/10.1016/j.saa.2021.119693.

(168) Duan, Y. W.; Tang, H. Y.; Guo, Y.; Song, Z. K.; Peng, M. J.; Yan, Y. The Synthesis and Study of the Fluorescent Probe for Sensing Cu^{2+} Based on a Novel Coumarin Schiff-Base. *Chinese Chem. Lett.* **2014**, *25* (7), 1082–1086. https://doi.org/10.1016/j.cclet.2014.05.001.

(169) Wang, L.; Ye, D.; Cao, D. A Novel Coumarin Schiff-Base as a Ni(II) Ion Colorimetric Sensor. *Spectrochim. Acta - Part A Mol. Biomol. Spectrosc.* **2012**, *90*, 40–44. https://doi.org/10.1016/j.saa.2012.01.017.

(170) Bhorge, Y. R.; Chou, T. L.; Chen, Y. Z.; Yen, Y. P. New Coumarin-Based Dual Chromogenic Probe: Naked Eye Detection of Copper and Silver Ions. *Sensors Actuators, B Chem.* **2015**, *220*, 1139–1144. https://doi.org/10.1016/j.snb.2015.06.059.

(171) Nandhini, C.; Kumar, P. S.; Poongodi, K.; Shanmugapriya, R.; Elango, K. P. Development of Simple Imine Based Probe for Selective Fluorescent Cyanide Sensing with Red-Emission in Solid and Solution Phases. *J. Mol. Liq.* **2021**, *327*, 114833. https://doi.org/10.1016/j.molliq.2020.114833.

(172) Jali, B. R.; Baruah, J. B. Recent Progress in Schiff Bases in Detections of Fluoride Ions. *Dye. Pigment.* **2021**, *194*, 109575. https://doi.org/10.1016/j.dyepig.2021.109575.

(173) Benkhaya, S.; M'rabet, S.; El Harfi, A. Classifications, Properties, Recent Synthesis and Applications of Azo Dyes. *Heliyon* **2020**, *6* (1). https://doi.org/10.1016/j.heliyon.2020.e03271.

(174) Bafana, A.; Devi, S. S.; Chakrabarti, T. Azo Dyes: Past, Present and the Future. *Environ. Rev.* **2011**, *19* (1), 350–370. https://doi.org/10.1139/a11-018.

(175) Muhiebes, R. M. Synthesis of New Heterocyclic Containing Azo Group from 2-N-Chloro Acetamido Creatinine and Studying Their Biological Activity. **2021**, *3*, 401–405. DOI: 10.22034/ecc.2021.281946.1170

(176) Shukla, C. A.; Kute, M. S.; Kulkarni, A. A. Towards Sustainable Continuous Production of Azo Dyes: Possibilities and Techno-Economic Analysis. *Green Chem.* **2021**, *23* (17), 6614–6624. https://doi.org/10.1039/d1gc01133b.

(177) Zhao, R.; Tan, C.; Xie, Y.; Gao, C.; Liu, H.; Jiang, Y. One Step Synthesis of Azo Compounds from Nitroaromatics and Anilines. *Tetrahedron Lett.* **2011**, *52* (29), 3805–3809. https://doi.org/10.1016/j.tetlet.2011.05.054.

(178) Hamidian, K.; Rahimi, R.; Hosseini-Kharat, M. Bisazo Dye Compounds Based on Aliphatic and Aromatic Diamine Linking Groups: Thermal Behavior, Chemical Stability, Electrochemical Study, Interaction with AgNPs and in Vitro Anti-Pathogen Activity. *Inorg. Chem. Commun.* **2021**, *128*, 108559. https://doi.org/10.1016/j.inoche.2021.108559.

(179) Said, B.; Souad M', R.; Ahmed, E. H. A Review on Classifications, Recent Synthesis and Applications of Textile Dyes. *Inorg. Chem. Commun.* **2020**, *3* (March), 107891. http://dx.doi.org/10.1016/j.inoche.2020.107891

(180) Mohammed, G. I.; El-Ghamry, H. A.; Saber, A. L. Rapid, Sensitive, and Selective Copper (II) Determination Using Sensitive Chromogenic Azo Dye Based on Sulfonamide. *Spectrochim. Acta - Part A Mol. Biomol. Spectrosc.* **2021**, *247* (Ii), 119103. https://doi.org/10.1016/j.saa.2020.119103.

(181) Singh, G.; Satija, P.; Singh, A.; Diksha; Pawan; Suman; Sushma; Mohit; Soni, S. Azo Dye Featuring Triazole Appended Organosilicon Multifunctionalized Sensor: Paradigm for Detection of Cu^{+2} and Fe^{+2} Ions. *Mater. Chem. Phys.* **2020**, *249* (January), 123005. https://doi.org/10.1016/j.matchemphys.2020.123005.

(182) Kudelko, A.; Olesiejuk, M.; Luczynski, M.; Swiatkowski, M.; Sieranski, T.; Kruszynski, R. 1,3,4-Thiadiazole-Containing Azo Dyes: Synthesis, Spectroscopic Properties and Molecular Structure. *Molecules* **2020**, *25* (12). https://doi.org/10.3390/molecules25122822.

(183) Manjunatha B, Yadav D. Bodke, Sandeep kumar Jain R, Lohith T. N, Sridhar M. A,. Novel Isoxazolone Based Azo Dyes: Synthesis, Characterization, Computational, Solvatochromic UV-Vis Absorption and Biological Studies. *J. Mol. Struct.* **2021**, *1244*, 130933. https://doi.org/10.1016/j.molstruc.2021.130933.

(184) Dhaka, G.; Jindal, G.; Kaur, R.; Rana, S.; Gupta, A.; Kaur, N. Multianalyte Azo Dye as an On-Site Assay Kit for Colorimetric Detection of Hg^{2+} ions and Electrochemical Sensing of Zn^{2+} Ions. *Spectrochim. Acta - Part A Mol. Biomol. Spectrosc.* **2020**, *229*, 117869. https://doi.org/10.1016/j.saa.2019.117869.

(185) Ngaini, Z.; Mortadza, N. A. Synthesis of Halogenated Azo-Aspirin Analogues from Natural Product Derivatives as the Potential Antibacterial Agents. *Nat. Prod. Res.* **2019**, *33* (24), 3507–3514. https://doi.org/10.1080/14786419.2018.1486310.

(186) Abdallah, S. M. Metal Complexes of Azo Compounds Derived from 4-Acetamidophenol and Substituted Aniline. *Arab. J. Chem.* **2012**, *5* (2), 251–256. https://doi.org/10.1016/j.arabjc.2010.08.019.

(187) El-Wakiel, N. A.; Rizk, H. F.; Ibrahim, S. A. Synthesis and Characterization of Metal Complexes of Azo Dye Based on 5-Nitro-8-Hydroxyquinoline and Their Applications in Dyeing Polyester Fabrics. *Appl. Organomet. Chem.* **2017**, *31* (10), 1–10. https://doi.org/10.1002/aoc.3723.

(188) Alothman, A. A.; Albaqami, M. D.; Alshgari, R. A. Synthesis, Spectral Characterization, Quantum Chemical Calculations, Thermal Studies and Biological Screening of Nitrogen and Oxygen Donor Atoms Containing Azo-Dye Cu(II), Ni(II) and Co(II) Complexes. *J. Mol. Struct.* **2021**, *1223*, 128984. https://doi.org/10.1016/j.molstruc.2020.128984.

(189) Nagaraja, O.; Bodke, Y. D.; Pushpavathi, I.; Ravi Kumar, S. Synthesis, Characterization and Biological Investigations of Potentially Bioactive Heterocyclic Compounds Containing 4-Hydroxy Coumarin. *Heliyon* **2020**, *6* (6), e04245. https://doi.org/10.1016/j.heliyon.2020.e04245.

(190) Kshtriya, V.; Koshti, B.; Gour, N. A New Azo Dye Based Sensor for Selective and Sensitive Detection of Cu(II), Sn(II), and Al(III) Ions. **2021**. https://doi.org/10.26434/chemrxiv.13708249.v1.

(191) Fukushima, Y.; Aikawa, S. Colorimetric Detection of Cu^{2+} Using of a Mixture of Ponceau 6R and a Cationic Polyelectrolyte in Aqueous Solution. *J. Incl. Phenom. Macrocycl. Chem.* **2021**, *100* (1–2), 143–148. https://doi.org/10.1007/s10847-021-01064-8.

(192) Aysha, T. S.; Mohamed, M. B. I.; El-Sedik, M. S.; Youssef, Y. A. Multi-Functional Colorimetric Chemosensor for Naked Eye Recognition of Cu^{2+}, Zn^{2+} and Co^{2+} Using New Hybrid Azo-Pyrazole/Pyrrolinone Ester Hydrazone Dye. *Dye. Pigment.* **2021**, *196*, 109795. https://doi.org/10.1016/j.dyepig.2021.109795.

(193) Sezgin, B.; Dede, B.; Tilki, T. Structural, Theoretical and Enzyme-like Activities of

Novel Cu(II) and Mn(II) Complexes with Coumarin Based Bidentate Ligand. *Inorganica Chim. Acta* **2021**, *524*. https://doi.org/10.1016/j.ica.2021.120430.

(194) Manjunatha B, Yadav D. Bodke, Nagaraja O, Lohith T. N, Nagaraju G, Sridhar MA,. Coumarin-Benzothiazole Based Azo Dyes: Synthesis, Characterization, Computational, Photophysical and Biological Studies. *J. Mol. Struct.* **2021**, *1246*, 131170. https://doi.org/10.1016/j.molstruc.2021.131170.

(195) Naseem, H. A.; Aziz, T.; Shah, H. ur R.; Ahmad, K.; Parveen, S.; Ashfaq, M. Rational Synthesis and Characterization of Medicinal Phenyl Diazenyl-3-Hydroxy-1h-Inden-1-One Azo Derivatives and Their Metal Complexes. *J. Mol. Struct.* **2021**, *1227*, 129574. https://doi.org/10.1016/j.molstruc.2020.129574.

(196) Özarslan, A.; Çakmaz, D.; Erol, F.; Şenöz, H.; Seferoğlu, N.; Barsella, A.; Seferoğlu, Z. Synthesis and Investigation of Photophysical, NLO and Thermal Properties of D-π-A-π-D Dyes. *J. Mol. Struct.* **2021**, *1229*. https://doi.org/10.1016/j.molstruc.2020.129583.

Chapter 2

Table of Contents

List of Figures

List of Tables

List of Schemes

Chapter 2:
Application of 7-functionalized 3-triazolyl coumarin-derived sensors towards ionic sensing strategies

Summary

Two coumarin-triazolyl derived fluorescent sensors containing supporting methoxy and hydroxyl functionalities at position -7- have been synthesized, characterized, and investigated for their potential as cationic and anionic sensors in aqueous and organic solutions. These compounds displayed a strong preference for Fe^{3+} ions with complexation resulting in fluorescent quenching. The 7-methoxy derivative displayed advanced selectivity towards Fe^{3+} in the presence of competing metal cations. The detection limit of the preferred sensor was determined to be 1.4 μM. Binding stoichiometry between this triazole-coumarin derivative and Fe^{3+} was conducted by means of Job's plot analysis and was shown to occur in a 1:1 ratio. The binding site of Fe^{3+} to the coumarin-triazole derivative was determined using ^{1}H NMR, ^{13}C NMR and Molecular Modelling studies. Complexation was shown to involve the coumarin-carbonyl and triazole moiety. Hydrogen potential studies of the emissive effects of Fe^{3+} towards **A1** in different pH solutions indicated usability over an acceptable pH range. Reversibility studies with EDTA displayed that Fe^{3+} complexation was not reversible. This derivative was further tested towards anionic analyte sensing studies. Anionic screening studies were conducted in a variety of solvents, yet an aqueous solution displayed the most reasonable preference of the same chosen sensor towards CN^{-}. Although the selectivity of the chosen sensor towards CN^{-} was poor, making it unfavourable for real-world sensing purposes, the spectroscopic and complexation studies were conducted to investigate the characteristics of anionic sensing. The detection limit was calculated to be 6.7 μM. Binding stoichiometry between the sensor and CN^{-} was shown to occur in a 1:1 ratio. The binding sites of CN^{-} towards the coumarin-triazole sensor was determined using ^{1}H NMR titration analysis, herniarin titration, and molecular modelling studies and was shown to involve the triazolyl and neighbouring phenyl ring protons. Reversibility studies utilizing TFA, TCA (trifluoro- and trichloro- acetic acid) and perchloric acid indicated that CN^{-} complexation was only partially reversible in the presence of TFA. The quenching of **A1** with Fe^{3+} and CN^{-} was shown to occur via a PET "on-off" mechanism by Molecular Orbital Energy calculations.

2.1 Results and Discussion

2.1.1 Synthesis and characterization of 7-functionalized coumarin-triazolyl sensors A1, A2 and A3

The synthesis of the three prospective coumarin-triazolyl derivatives **A1-3** was performed as outlined in **Scheme 1**. Initially, 7-hydroxy coumarin-derivative containing an azide functionality (**1a**) was prepared according to literature procedure[1], and modified by well-known organic reactions to produce methoxy- and ester-azide derivatives **1b** and **1c**. The final step to produce the triazole functionality was achieved via Cu(I)-catalyzed 1,3-dipolar cycloaddition "click" reaction between azide and alkyne (**2**) functionalities in THF to afford coumarin-triazolyl derivatives **A1** and **A2** in yields of 80 and 65 % respectively. It was discovered that prospective ester-coumarin-triazole derivative **A3** no longer supported an ester functionality at position -7-. It was determined that the ester group had hydrolysed to its original hydroxy functionality during the "click" reaction protocol. This will be discussed later.

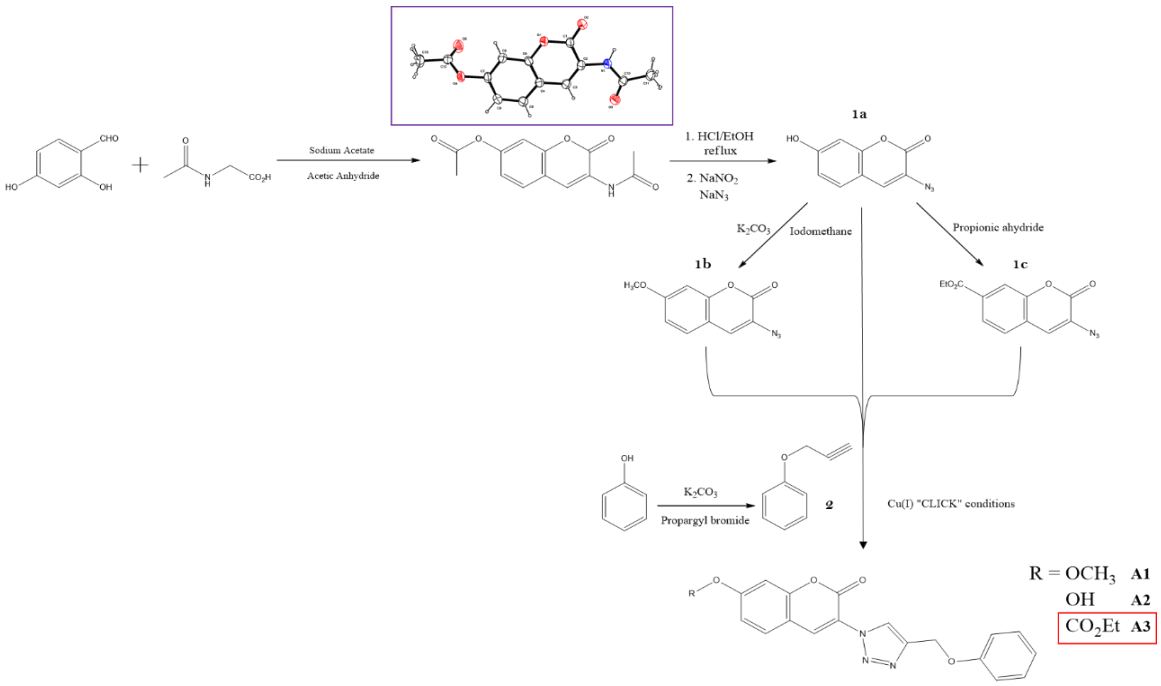

Scheme 1: Synthetic route of coumarin-triazolyl derivatives **A1**, **A2** and **A3**. "click" reaction conditions: $CuSO_4.5H_2O$, NaAsc and PMDETA. Inset: single crystal X-Ray structure of 7-ester-3-amide coumarin intermediate. Inset: Proposed structure of attempted 7-ester coumarin-triazole derivative **A3**.

The ^{1}H NMR analysis of coumarin-azide derivatives **1a**, **1b**, and **1c** are shown in **Figures 1-3**. Compounds **1b** and **1c** were synthesized by modification of **1a** by etherification and esterification reactions (for ^{13}C NMR analysis of **1b** and **1c** see **Figures 1** and **2** in **Appendix A**). The ^{1}H NMR and ^{13}C NMR spectra of phenol-alkyne derivative **2** are shown in **Figures 4** and **5** (for the FT-IR spectra of alkyne-derivative **2** please see **Figure 3** in **Appendix A**).

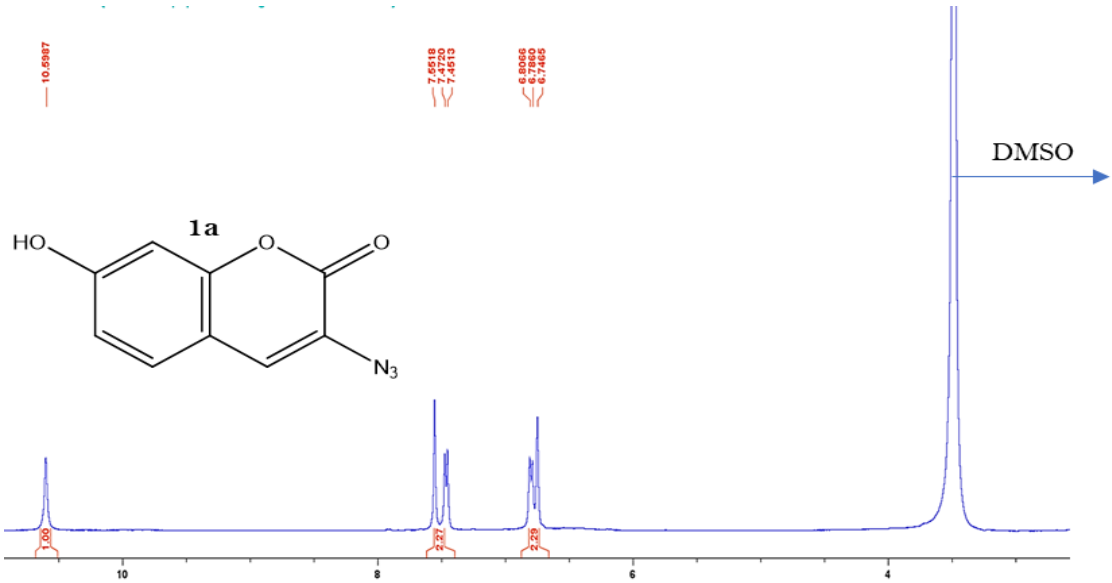

Figure 1: ^{1}H NMR of hydroxy coumarin-azide derivative **1a** in d_6-DMSO.

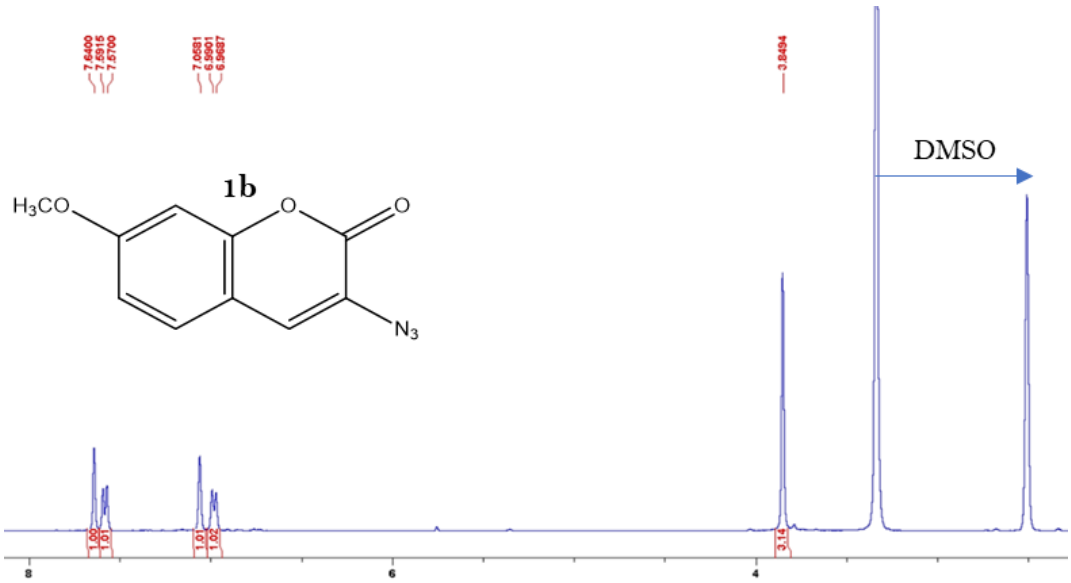

Figure 2: ^{1}H NMR of methoxy coumarin-azide derivative **1b** in d_6-DMSO.

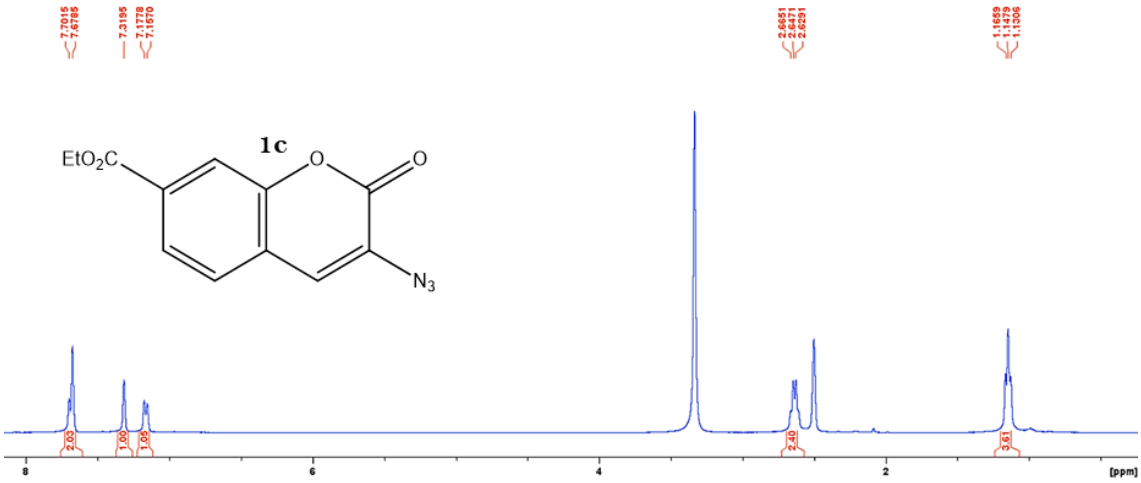

Figure 3: ^{1}H NMR of ester coumarin-azide derivative **1c** in d_6-DMSO.

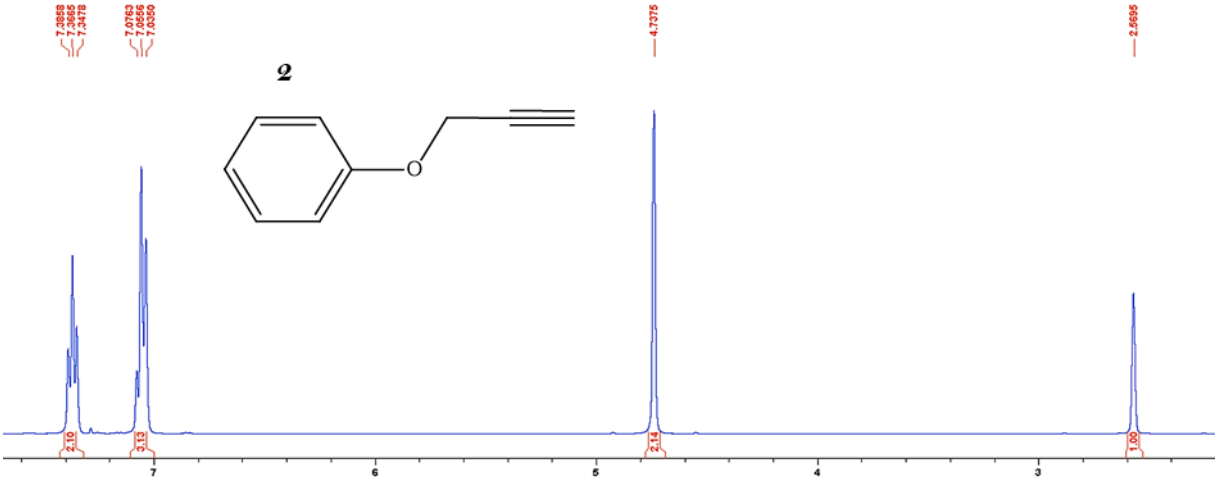

Figure 4: ^{1}H NMR spectra of phenol-alkyne derivative **2** in $CDCl_3$.

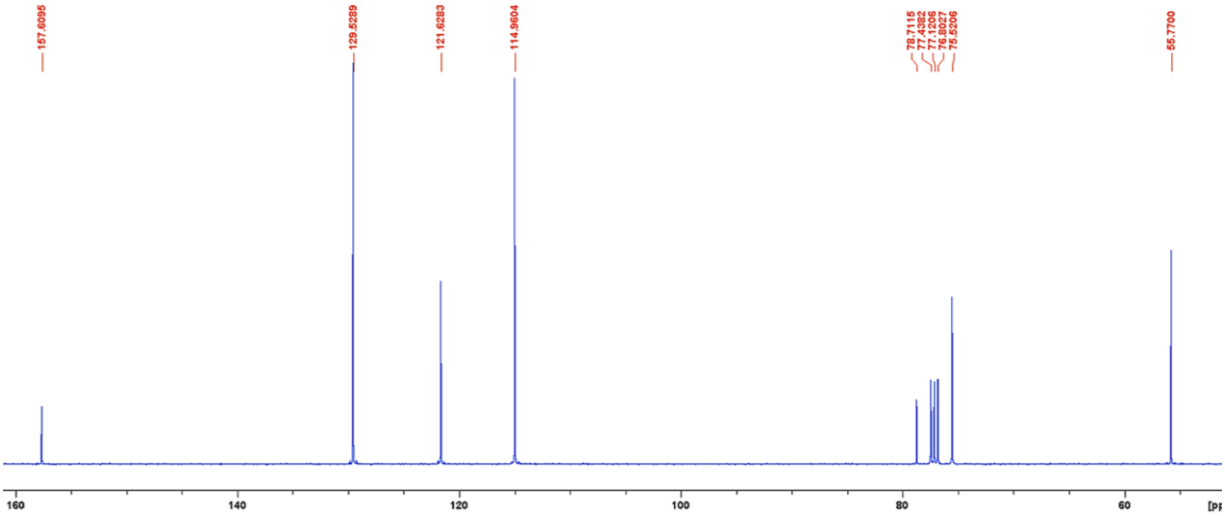

Figure 5: ^{13}C NMR spectra of phenol-alkyne derivative **2** in $CDCl_3$.

The formation of the triazole functionality via the "click" synthetic procedure had no effect on the methoxy nor the hydroxy functionalities at position -7- on the coumarin molecule (For ^{1}H NMR and ^{13}C NMR analysis of coumarin-triazole derivatives **A1** and **A2** see **Figures 4-7** in **Appendix A**). However, the ester group from the ester-azide derivative **1c** disappeared during the attempted formation of **A3** as seen in the ^{1}H NMR spectra (**Figure 6**). The conditions under which the triazole forming cycloaddition reaction occurs appeared to cause the cleavage of the ester group to the original hydroxy functionality (**A2**). This cleavage was verified by FT-IR spectral overlay whereby the spectra of **A2** and **A3** are in close agreement (for the FT-IR spectral overlay of **A2** and **A3** see **Figure 8** in **Appendix A**). It has been reported that an ester functionality may react with amines to form amide groups via the process of aminolysis. In an article published by Alessandro Mandoli, the author explains how the aminolysis of the ester group with *N,N*-dimethylethylenediamine under "click" reaction conditions afforded the formation of different chelating groups.[2] In this study, *N,N,N′,N″,N″*-Pentamethyldiethylenetriamine (PMDETA) was employed as the transporting ligand. This amine, together with ester-azide derivative **1c**, was postulated to undergo an aminolysis reaction to form the original hydroxy functionality, thereby resulting in the same structure as hydroxy coumarin-triazole derivative **A2**.

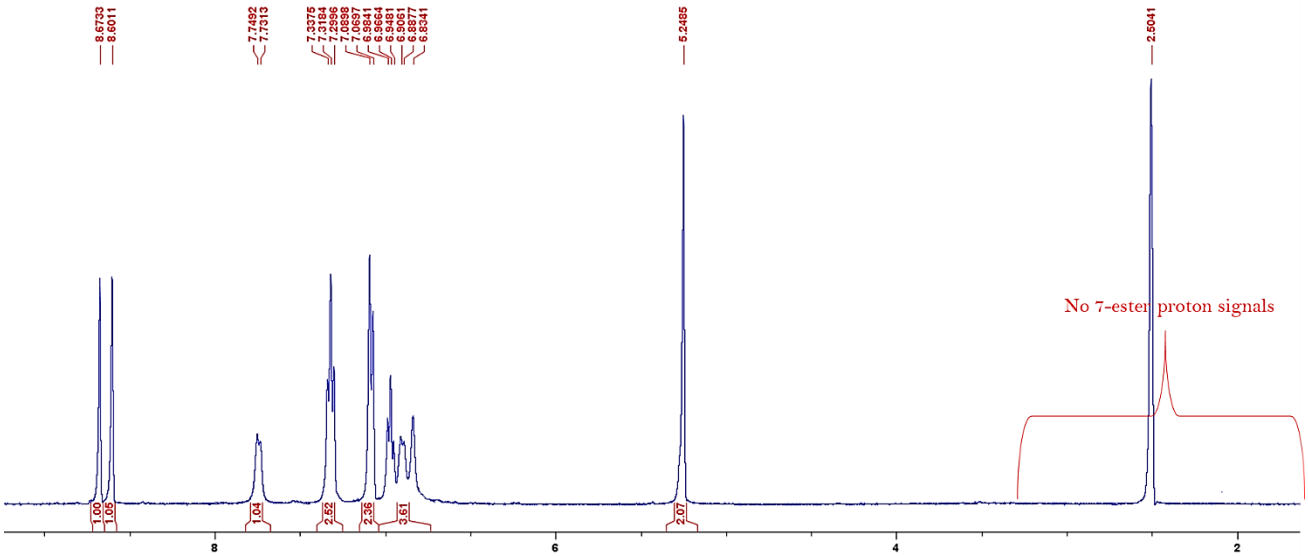

Figure 6: ^{1}H NMR spectra of attempted synthesis of coumarin-triazole derivative **A3** in d_6-DMSO.

The single crystal XRD of both **A1** and **A2** confirms the reported structures which shows the presence of the coumarin ring system with the triazole functionality situated at position -3-. The nitrogen atoms of the triazole ring are orientated away from the coumarin carbonyl in both **A1** and **A2** whilst the carbon double-bond of the triazole ring is situated closest to the coumarin-carbonyl functionality (**Figure 7**). Crystals were produced by dissolving both **A1** and **A2** in minimal amounts of solvent and left to slowly evaporate.

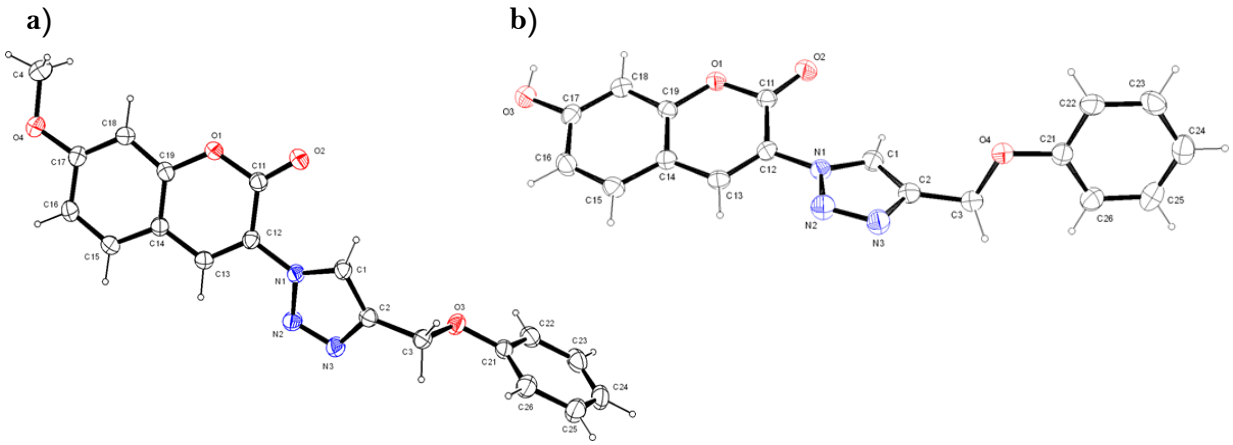

Figure 7: Single crystal XRD analysis of a) **A1** and b) **A2**.

The success of the azide-alkyne cycloaddition reaction was further supported by the disappearance of the azide signal in the coumarin-triazole product as seen from the FT-IR spectra (**Figure 8**). The infrared spectroscopy is significant in the characterization efforts of triazole compounds. The signals at 1570-1550 cm^{-1} are due to N=N vibrations, and signals in the region of 1600-1411 cm^{-1} are due to C-N vibrations.[3,4]

a) Ether-azide derivative **1a**.

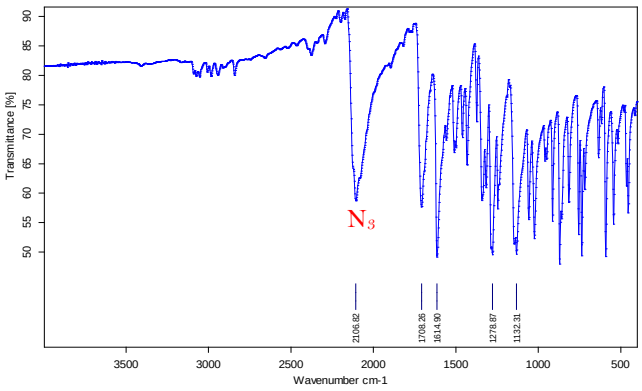

b) Ether-triazole derivative **A1**.

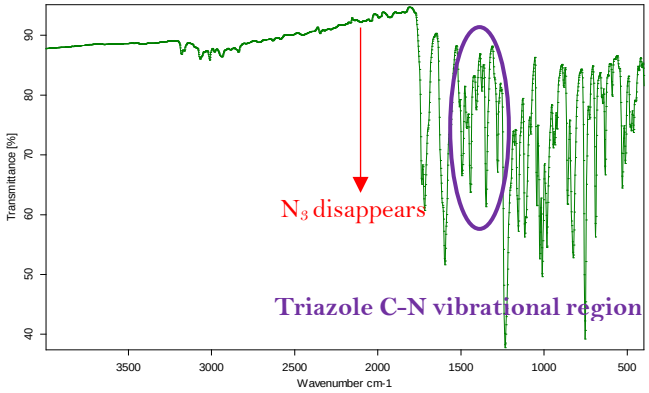

c) Hydroxy-azide derivative **1b**.

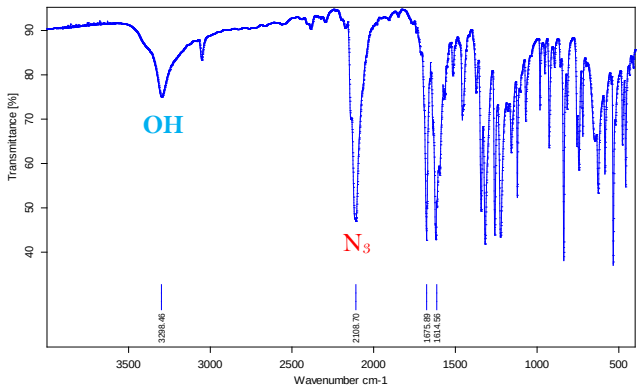

d) Hydroxy-triazole derivative **A2**.

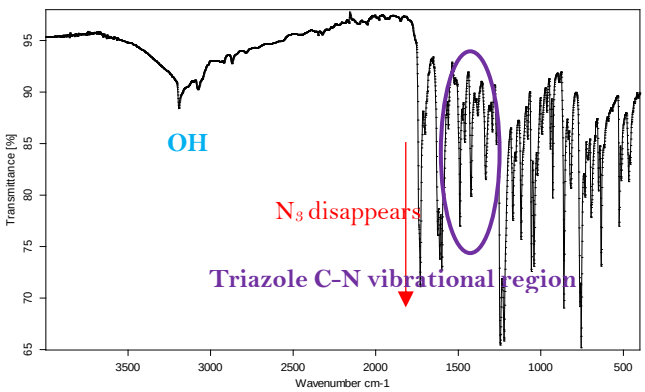

Figure 8: FT-IR spectra of coumarin-azide and corresponding coumarin-triazole derivatives.

2.1.2 Absorption and emission studies of triazolyl-coumarin derivatives A1 & A2

The absorbance and emission behaviors of coumarin-triazolyl derivatives **A1** and **A2** were investigated in acetonitrile and water respectively. Acetonitrile and water were chosen for the studies due to their environmentally favourable characteristics. The excitation wavelength for both compounds was determined by UV-Vis analysis. The sensors displayed the same excitation wavelength of 340 nm with the absorption intensity of **A1** being appreciably greater than that of **A2**. The emission properties of both sensors were further investigated at the same excitation wavelength of 340 nm (**Figure 9**). Again, **A1** displayed stronger emission properties at 420 nm than that of **A2**, which showed to emit at a longer wavelength of 480 nm. This contrast in the emission wavelength could arise as a result of the different functionalities situated at position -7- on the coumarin molecule.

It is well documented that electron donating groups at position -7- in combination with electron withdrawing groups at position -3- induce a push-pull effect which concentrates electron density into the conjugated π-system of the coumarin moiety, thereby enhancing the emissive output (**Figure 10**). This method has been widely used to improve the fluorescence efficiency and intensity of coumarin compounds.[5,6] This difference between the emissive intensities of **A1** and **A2** may be rationalized when the theoretical calculated electron density around the methoxyl and hydroxyl functionalities, coumarin carbonyl, and triazole moiety are considered. **Figure 11** displays the calculated electron density around the 7-substituted functionalities, within the coumarin π-conjugated system, and surrounding the triazole ring. It is evident from the larger area of electron deficiency surrounding the three methoxy hydrogen atoms, and greater area of increased electron density surrounding the triazole

moiety of **A1**, that electron density has been drawn into the conjugated system via the push-pull electronic effect. It is known that the triazole moiety may enhance fluorescence when attached to a suitable fluorophore at the pre-described -3- substituted site. The increased electron density surrounding the triazole moiety of **A1** may facilitate the greater initial fluorescent intensity observed. In this way, the emission intensity of **A1** is notably greater than that of **A2**.

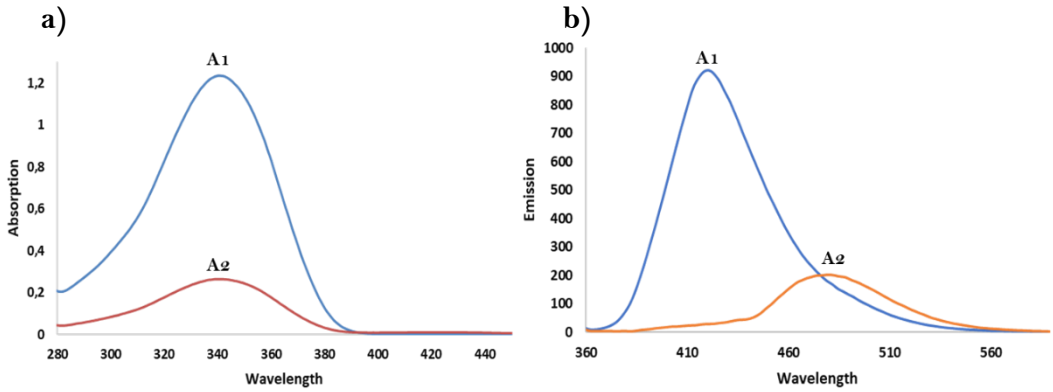

Figure 9: a) Absorbance and b) Emission of coumarin-triazole derivatives **A1** and **A2**.

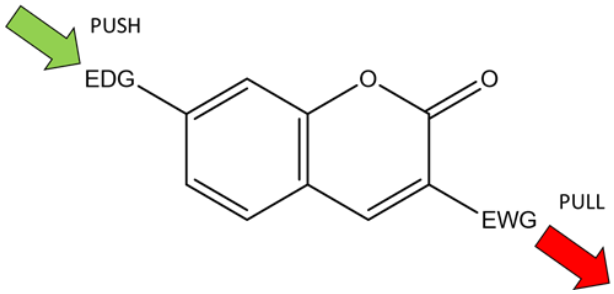

Figure 10: Push-pull effect of substituted coumarin scaffolds.

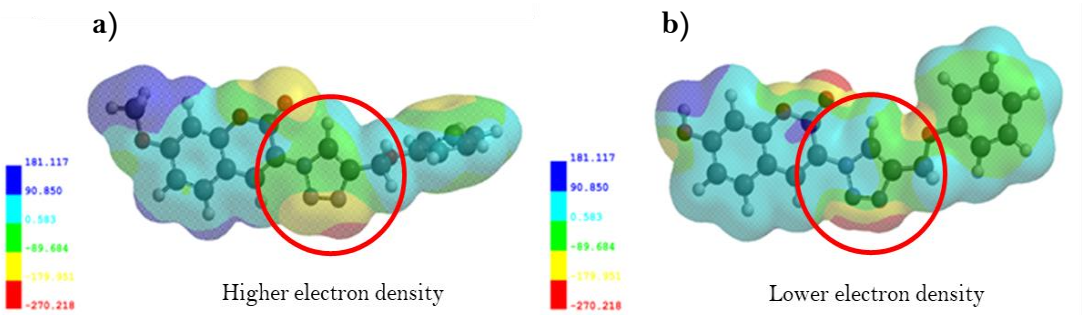

Figure 11: Calculated electronic densities of a) **A1** and b) **A2** at MMFF calculation level.

Cationic sensing studies

2.1.3 The sensing responses of sensors A1 and A2 towards various metal ions

The application of compounds **A1** and **A2** were studied for their potential as metal sensors using fluorescence spectral analysis at room temperature. A range of metal cations were investigated. These cationic solutions were prepared in deionized water from their nitrate salts. Stock solutions of **A1** and **A2** were prepared in acetonitrile. The experiments were conducted by adding aliquots of the selected metal ions (Fe^{2+}, Fe^{3+}, Cd^{2+}, Pb^{2+}, Ag^{+}, Na^{+}, K^{+}, Ca^{2+}, Cr^{3+}, Al^{3+}, Ba^{2+}, Cu^{2+}, Co^{2+}, Hg^{2+}, $Zn^{2+}$and Ni^{2+}) to solutions containing compounds **A1** and **A2** in water as the medium. Water was chosen as the sensing medium as aqueous sensing is environmentally friendly and greatly preferred.

The strongest quenching responses of both compounds were observed for Fe^{3+} compared to other cations. This indicates a stronger interaction between compounds **A1** and **A2** with Fe^{3+} (**Figure 12**). Selectivity studies of both compounds towards Fe^{3+}, in the presence of competing metal cations, was conducted in water. Notably, **A1** displayed excellent selectivity towards Fe^{3+} in the presence of other competing metal cations (**Figure 13**). Furthermore, when all competing metal cations were present in solution, **A1** continued to display excellent selectivity towards Fe^{3+}. This same selectivity trend towards Fe^{3+} was not observed for **A2** with all other competing metals (**Figure 14**). For this reason, including the enhanced absorption and emission properties of **A1**, it was chosen for further investigations as a potential sensor for quantitative and qualitative sensing of Fe^{3+} ions in aqueous media. The observed quenching response upon Fe^{3+} addition can be ascribed to the photo-induced electron transfer (PET) from the sensor to the d-orbitals of the Fe^{3+} cation. The electron deficiency of half-filled d-orbitals increases the electrostatic attraction of the binding site to form stable coordination with Fe^{3+} ions, leading to more quenching of the fluorescence and better selectivity. This proposed PET quenching mechanism was verified by UV-Vis titration studies.

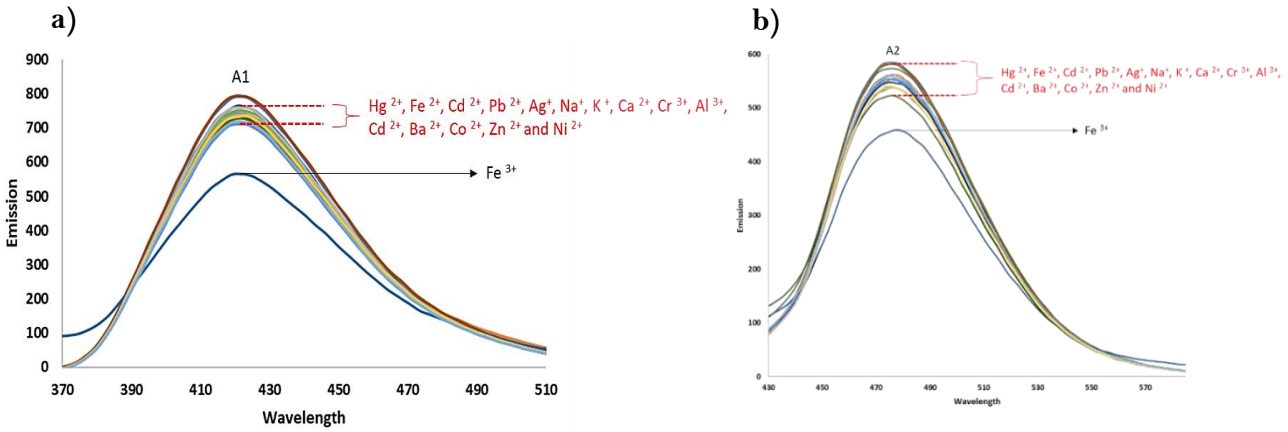

Figure 12: Fluorescent responses of a) **A1** and b) **A2** with selected metal cations in water. Excitation: 340 nm. Screening studies were conducted in triplicate.

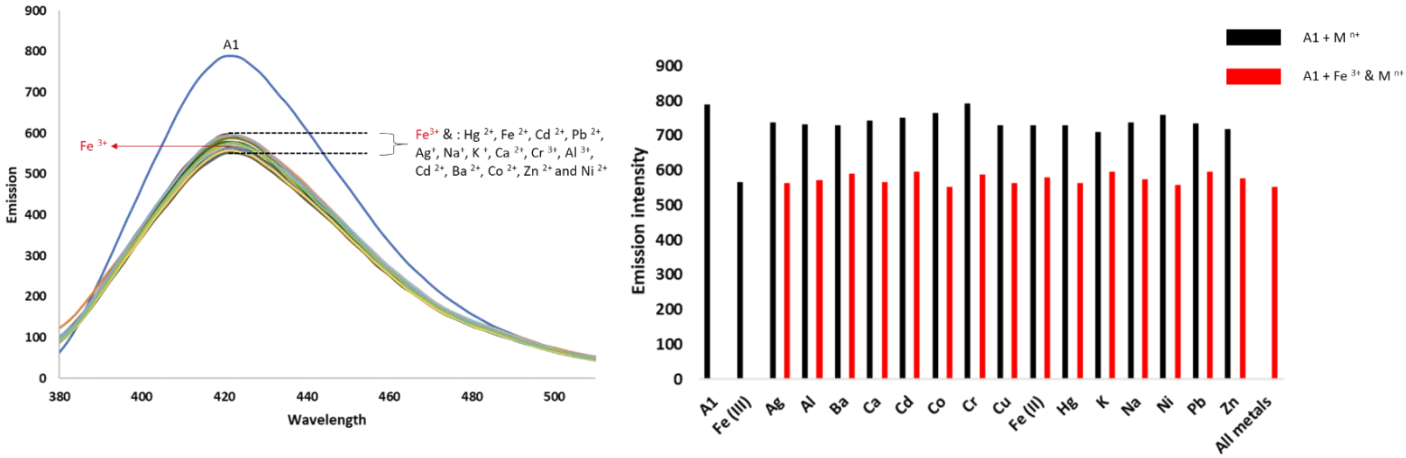

Figure 13: Selectivity of **A1** towards Fe^{3+} with competing metal cations in water. Competition studies were performed in triplicate. Excitation: 340 nm.

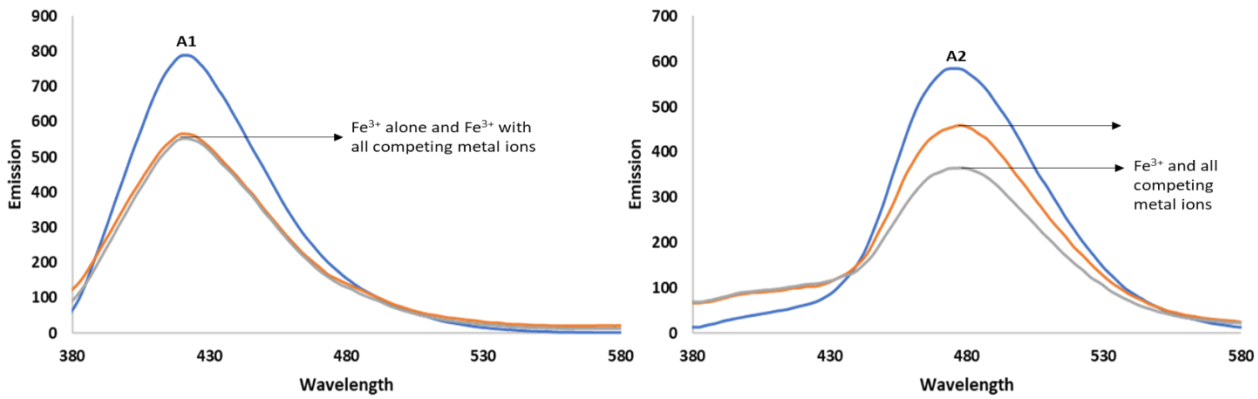

Figure 14: Competition of a) **A1** and b) **A2** towards Fe^{3+} in the presence of all other competing metal cations in aqueous solution. Excitation of 340 nm.

2.1.4 Emission titration studies of A1 with Fe^{3+} in water and acetonitrile

To gain greater insight into the fluorescent properties of **A1** in the presence of Fe^{3+}, the fluorescence response was investigated with Fe^{3+} in both water and acetonitrile. From this investigation, it is evident how the solvent system used can affect the outcome of the emission response, including other properties such as detection limit and binding/association constants *inter alia*. **Figure 15** illustrates the variations in the fluorescent intensities of **A1** upon continuous addition of Fe^{3+} aliquots in water and acetonitrile. The titration experiment of **A1** with Fe^{3+} in acetonitrile yielded three new shoulder peaks at longer wavelengths of 445, 487 and 531 nm. The titration of **A1** with Fe^{3+} in water evolved one small new shoulder peak at 487nm at higher concentrations of Fe^{3+}. The shifts in peak maxima and minima of **A1** with Fe^{3+} in water and acetonitrile were calculated to be 1 and 8 nm respectively. To ensure that the quenching response of **A1** towards Fe^{3+} is dependent on successive analyte addition, and that progressive self-quenching from single analyte addition does not occur, time-delay studies of **A1** with one aliquot of Fe^{3+} were conducted. Results show that between the initial quenching response of **A1** with a single aliquot of Fe^{3+}, and after the 20th scan (1-minute intervals), no additional fluorescent quenching was observed. This supports the rapid, and strong sensing response of **A1** towards Fe^{3+}. Hence, it can be concluded that the quenching response is dependent on analyte addition which is vital for titration analysis (**Figure 16**).

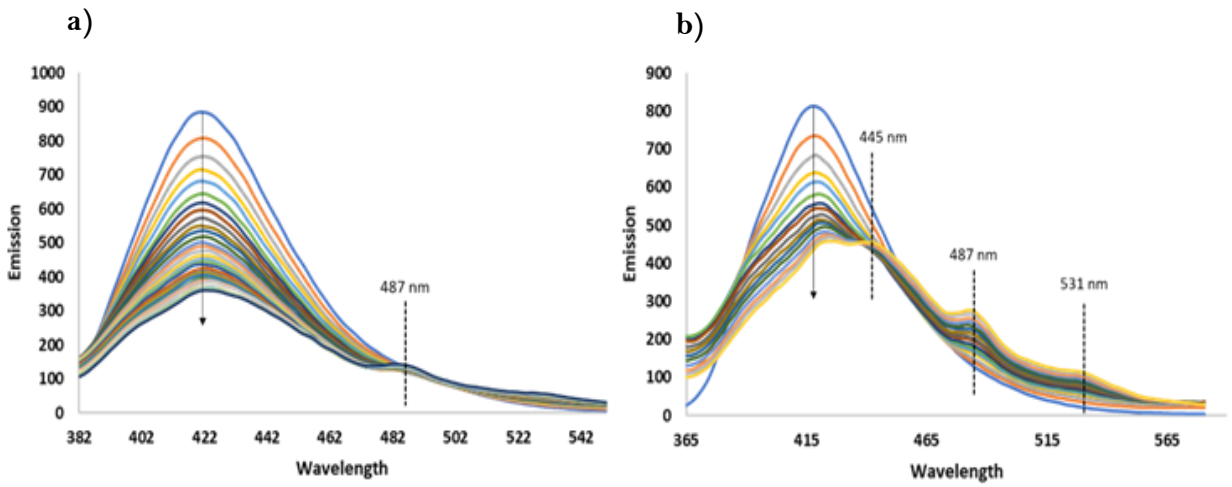

Figure 15: Changes in the fluorescence spectrum of **A1** in **a)** water and **b)** acetonitrile upon addition of Fe^{3+} ions. Excitation: 340nm. Titration conducted in triplicate.

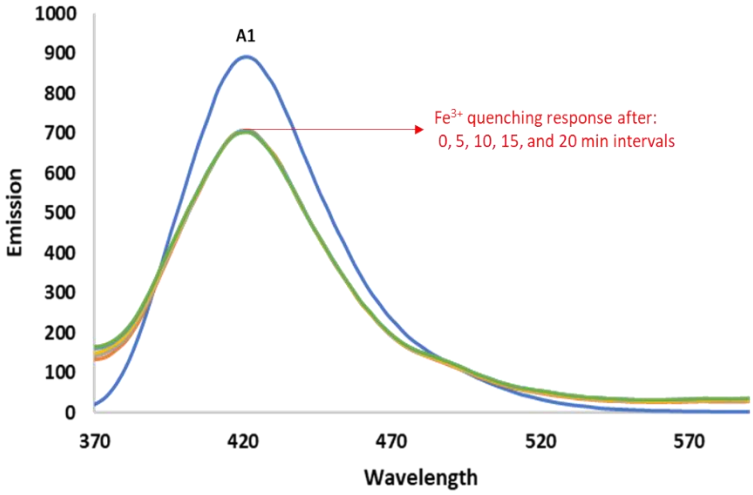

Figure 16: Time delay studies of **A1** with a single aliquot of Fe^{3+}. Excitation of 340 nm.

When the polarity of the solvents is taken into consideration, the observations of the new shoulder peaks upon Fe^{3+} titration may be explained. It is known that the fluorescent emission spectra of many fluorophores are sensitive to the polarity of their surrounding environment. Water has a greater polarity than acetonitrile and will therefore have a different effect on cation binding and stability. This may be attributed to the difference in the dipole moments in the ground state and the excited state. If electrically neutral molecules have a larger dipole moment in the excited state than in the ground state, the excited state becomes more stabilized with increasing solvent polarity.[7] The excited states of the compounds are mainly affected by the polarity, refractive index as well as dielectric constants of solvents and also, by the solvation effect of solvents towards compounds.[8] The differences observed between acetonitrile and water could be attributed to factors such as hydrogen bonding. Possible intermolecular hydrogen bonding interactions between water molecules and coumarin carbonyl inhibit the formation of intramolecular hydrogen bonds which can alter the dipole moments of the ground and excited states. This plausible larger dipole moment in the excited state is stabilized in water. Compared to water, acetonitrile is less polar and may not have as great an ability to stabilize this excited state complex. Possible intramolecular hydrogen bonding may result in the formation of new excited state complexes or vibrational energy levels with increasing Fe^{3+} amounts, resulting in the formation of the three new shoulder peaks at longer wavelengths. The appearance of these new shoulder peaks in acetonitrile gives further justification towards the use of water as the medium of choice for further studies.

Closer consideration of the titration of **A1** in water shows a clear iso-emissive point at 387 nm between the titration amounts of 4-19 μM additions of Fe^{3+}. At higher concentrations of Fe^{3+} the titration no longer displays this phenomenon (**Figure 17**).

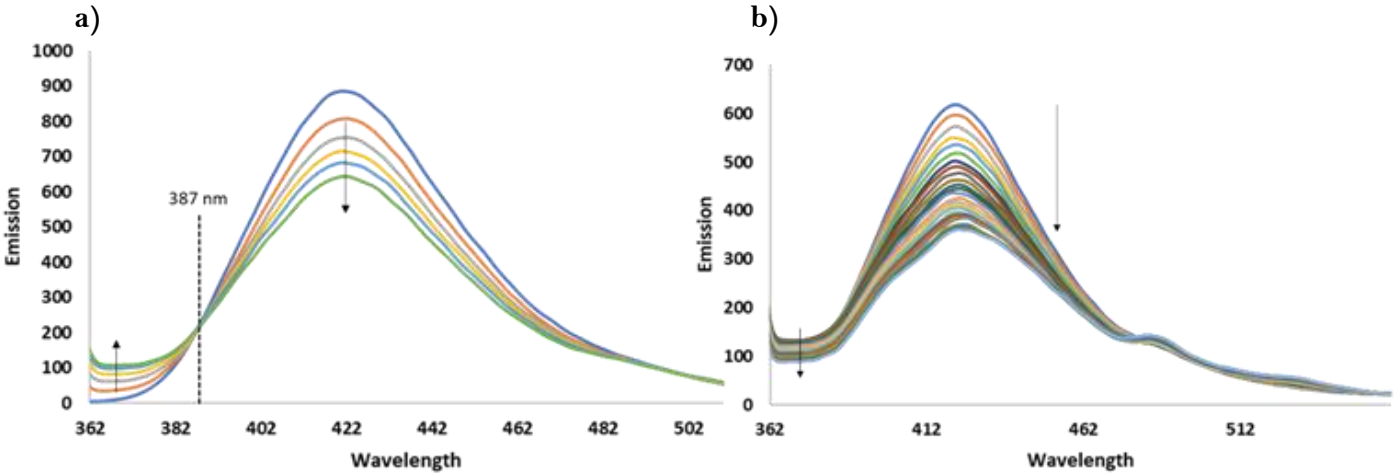

Figure 17: a) titration of **A1** with 4-19 μM additions of Fe^{3+}. A clear iso-emissive point is observed at 387 nm; b) titration of **A1** with 23 to 106 μM Fe^{3+}, the iso-emissive point is no longer visible.

The appearance of iso-emissive points in a fluorescent spectrum may be attributed to several reasons. This includes ground state binding between **A1** and Fe^{3+} in solution[9], the presence of two absorbing and emitting species in the system[10], two or more emitting species in the excited state[11], and neutral and ionic forms of the complexes existing in equilibrium in the photo-excited state[12]. Whilst ground state binding between **A1** and Fe^{3+} and greater than one emitting species could be a plausible explanations, studies conducted by dos Santos and co-workers describe how complexation induced twisting reduces the effect of the PET quenching by 'blocking' the pathway of the electron transfer, thus leading to the appearance of the iso-emissive point.[13] Interestingly, a minor yet similar conformational change was observed between the X-ray crystallographic structures of **A1** alone and the **A1**-Fe^{3+} complex (**Figure 18**). Although the complex of **A1** with Fe^{3+} did not crystallize, it did appear to change the crystal system from triclinic to monoclinic and induced this same twisting of the molecule as described by dos Santos et al. This initial twisting of the molecule at lower concentrations of Fe^{3+}, complexation of **A1** and Fe^{3+} in the ground state, and two emitting species at lower concentrations, could explain the appearance of the iso-emissive point.

This plausible "twisting" was further verified by computational analysis whereby the triazole ring twists upon metal complexation thereby situating the triazole N-atoms *syn* to the coumarin carbonyl functionality.

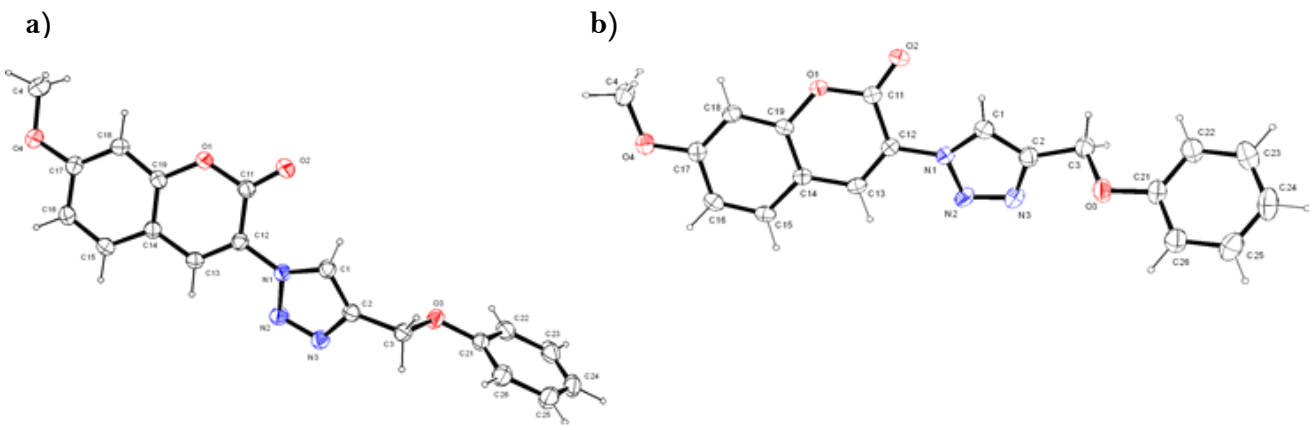

Figure 18: Singe-crystal X-Ray diffraction (XRD) of **A1** a) before complexation; b) after complexation with Fe^{3+} at lower concentrations.

2.1.5 UV/Vis titration of A1 with Fe^{3+}

The UV-Vis titration of **A1** with Fe^{3+} was conducted in acetonitrile. The titration of **A1** with Fe^{3+} in acetonitrile is shown in **Figure 19**. Evidently, titration led to increased absorption upon Fe^{3+} additions. No visible hypsochromic (blue) or bathochromic (red) shift in wavelength was noted, indicating that CHQF (Chelating Quenched Fluorescence) via PET (Photoinduced Electron Transfer) was the most likely mechanisms of fluorescent quenching and not that of ICT (Intramolecular Charge Transfer) which is generally associated with spectral shift upon analyte addition.[14] CHQF is the quenching of fluorescence upon metal binding or coordination and can occur via PET, ICT, ISC or isomerization.[15] The notable "opposite effect" of increasing amounts of Fe^{3+} on the absorption and emission spectra has also been reported for a dual coumarin-triazole based PET type sensor reported by Puthiyedath and Bahulayan for Fe^{3+} and Ca^{2+}.[16] The titration of Fe^{3+} with the dual coumarin-triazole sensor displayed fluorescent quenching with an opposite increase in absorption (**Figure 19**). Furthermore, the titration displayed a total enhancement of the spectral curve over the entirety of the wavelength range and not only in the range of the main absorption peak.

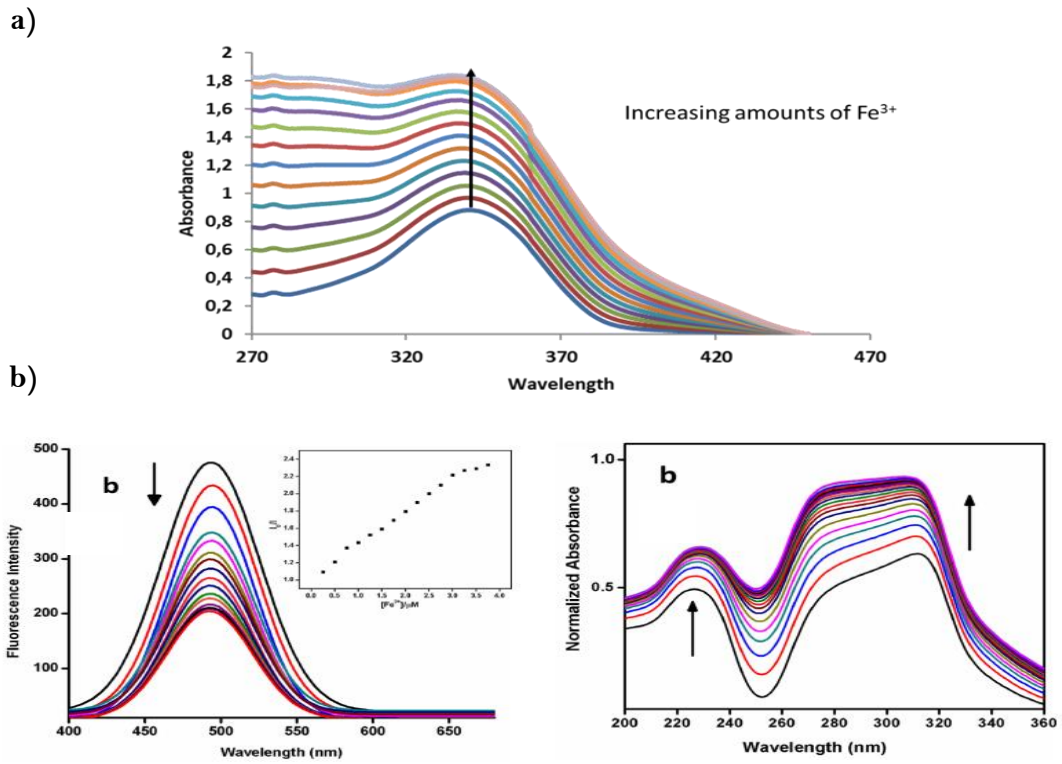

Figure 19: a) UV-Vis titration of **A1** with Fe^{3+} in acetonitrile; b) Comparative emission and absorption spectra of dual coumarin-triazole sensor titrated with Fe^{3+}.

2.1.6 PET fluorescent mechanism and changes upon Fe^{3+} complexation

The highest occupied (HOMO) and lowest unoccupied (LUMO) molecular orbital diagrams for the optimized structure of sensor **A1** was calculated by Molecular Orbital Energy calculations. The HOMO is shown to be situated on the substituted triazole ether-phenyl derivative. The LUMO is situated around the triazole moiety and coumarin fluorophore. Upon excitation (hν) photo electronic transfer (PET) occurs from the HOMO to LUMO orbital(s). This excitation promotes an electron from the HOMO to the LUMO of the fluorophore, forming the excited state species. The excited electron falls to the original orbital, emitting radiation as fluorescence. This results in the "turn-on" fluorescent response of the system. At this stage, the HOMO of the excited state fluorophore is higher in energy than that of the resulting **A1**-Fe^{3+} complex. Upon analyte complexation, the electron transfer is disrupted, preventing the necessary electronic transition, resulting in the "turn-off" state, and quenching the emission intensity. In terms of molecular orbitals, upon analyte complexation the HOMO of the excited state fluorophore is lower in energy than the HOMO of the sensor-analyte complex. As a results, an electron transfers from the HOMO of the

bound receptor to the HOMO of the excited fluorophore and energy is released via a non-radiative relaxation pathway. **Figure 20** shows the calculated HOMO and LUMO of **A1**, the molecular orbital energy diagram of sensor **A1** and **A1**-Fe^{3+} complexation[17], and the proposed PET "on-off" quenching mechanism of **A1**-Fe^{3+} complexation.

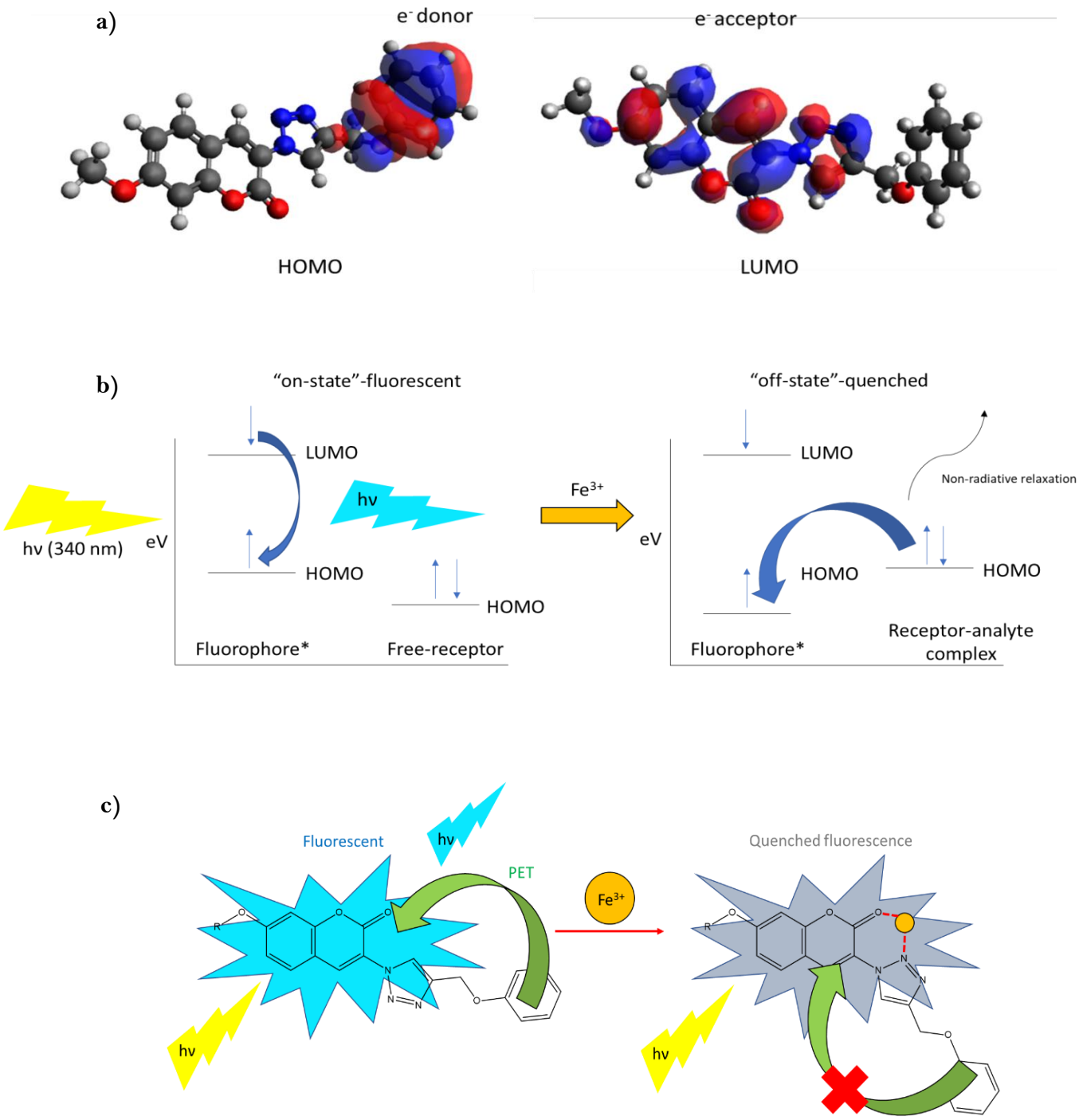

Figure 20: a) Calculated HOMO (-6.088 eV) and LUMO (-2.610 eV) of **A1** in the absence of Fe^{3+} b) molecular orbital energy diagram of the electronic transitions for the PET "on-off"

fluorescent mechanism upon Fe^{3+} complexation, and c) diagrammatic representation of the PET "on-off" quenching mechanism upon **A1**-Fe^{3+} complex formation.

2.1.7 Determination of fluorescence quenching process, association constant and detection limit.

To understand the quenching process of **A1** by Fe^{3+} in both water and acetonitrile, the observed decrease in fluorescence was followed using the linear Stern-Volmer equation (**1**)

$$\frac{F_0}{F} = 1 + K_{SV}[Q] \qquad (1)$$

where F is the fluorescence intensity in the presence of the quencher, F_0 is the intensity in the absence of the quencher, [Q] is the quencher concentration, and K_{SV} is the Stern–Volmer quenching constant. **Figure 21** shows the results for the plot of the titration of **A1** with Fe^{3+} in water following the Stern-Volmer equation. The constant K_{SV} is a general term that may refer to either dynamic or static quenching processes. Although the value for the regression line indicates correlation over the entire concentration range, the slight sigmoidal shape to the curve may indicate that different modes of quenching could be occurring. The detection limit in water and acetonitrile was calculated to be 3.6 & 5 μM respectively, whilst the value for the Stern-Volmer constant (K_{SV}) was 1.32 x 10^4 M^{-1} and 1.28 x 10^4 M^{-1} respectively.

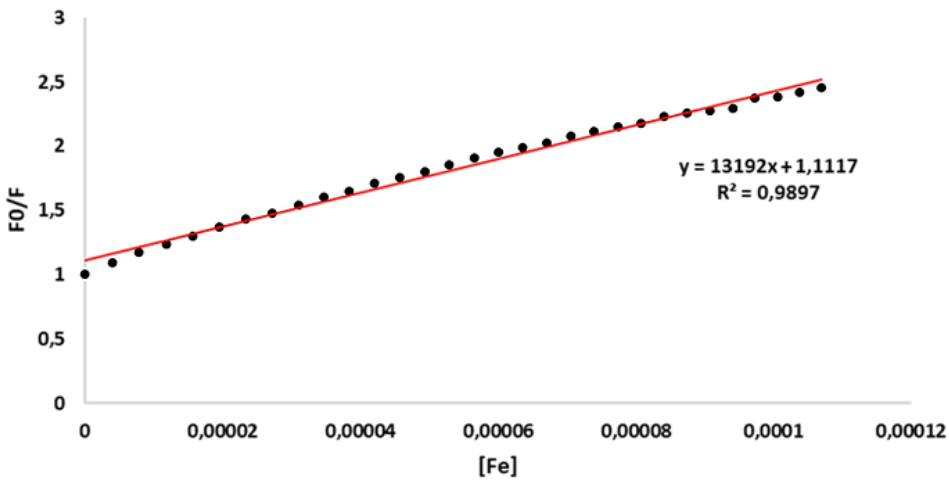

Figure 21: Plot of **A1** and Fe^{3+} in water following the linear Stern Volmer equation.

2.1.7.1 Benesi-Hildebrand calculations for A1 with Fe^{3+}

The Benesi-Hildebrand (BH) method for evaluation of the association constant and binding ratio was used for the titration of **A1** with increasing amounts of Fe^{3+} in water and acetonitrile. The plot of $1/F_0$-F vs $1/[Fe^{3+}]$ resulted in a positive slope with a good regression coefficient of R^2= 0.9962 and 0.9993 in water and acetonitrile respectively (**Figure 22**). The association coefficient, K_a, was calculated from the ratio of the intercept to the slope of the graph.[18] The values for the association constants and theoretical binding ratios for **A1** in water and acetonitrile are shown in **Table 1**. Based on the observed straight line of the plot, it could be concluded that the binding between the sensor and metal occurs in a 1:1 ratio.[19] This binding stoichiometry was later verified by Jobs Plot analysis.

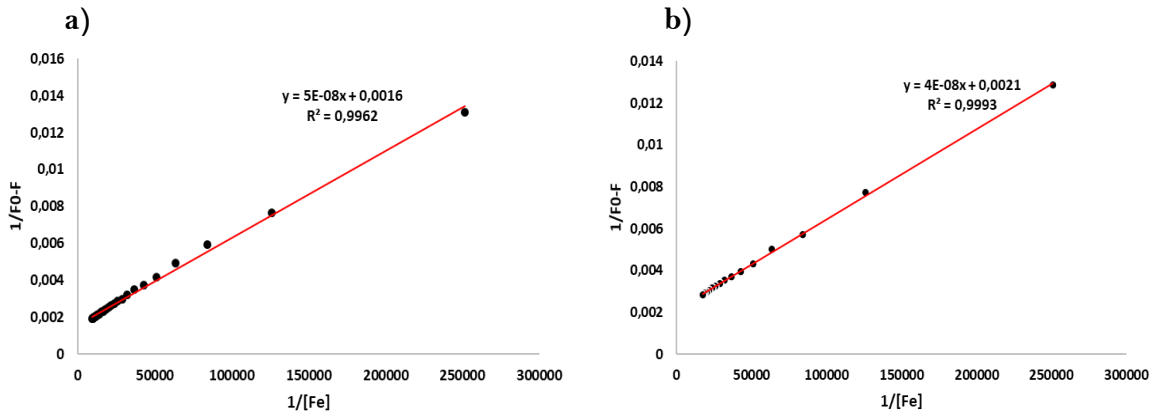

Figure 22: Benesi-Hildebrand plot of **A1** with Fe^{3+} in (**a**) water and (**b**) acetonitrile.

Table 1: Association constants and binding stoichiometry of **A1** with Fe^{3+} in water and acetonitrile.

A1	K_a values ($x10^4$) M^{-1}	R^2 value	Suggested binding stoichiometry
Water	3.3	0.9962	1:1
Acetonitrile	4.9	0.9993	1:1

The association/binding coefficient gives an indication of the strength of the sensor-analyte bond. Evidently, **A1** displayed a larger association constant in acetonitrile than in water. This appreciable value for K_a in both water and acetonitrile could explain the selectivity of **A1** towards Fe^{3+} in the presence of all other competing metal cations. In addition, the reported value of K_a is appreciable and thus indicates a strong complexation between **A1** and Fe^{3+} which may contribute to the CHQF (chelation quenched fluorescent) effect in addition to the PET mechanism.[20] The strength of this sensor-metal bond could clarify why **A1**-Fe^{3+} binding was not reversible in the presence of EDTA. This will be discussed later together with computational data.

2.1.7.2 Explanation of quenching process by Perrin sphere of action model

The linear Stern-Volmer equation for dynamic/collisional quenching is applicable if the experimental results show linear variation over the entire concentration range. The slight deviance from linearity (sigmoidal shape) in **Figure 21** suggested that the quenching mechanism may not be purely collisional/dynamic or static, and thus may be attributed either to the ground state complex formation, a combined collisional and static quenching system or to the Perrin and modified sphere of action static quenching models.[21]

For a combined collisional and static quenching model, a plot of $\left[\frac{F_0}{F} - 1\right]\frac{1}{[Q]}$ vs [Q] should yield a straight line. The experimental data did not fit the equation as shown by a poor regression coefficient. This indicates that the quenching behaviour cannot be explained by the combined dynamic and static quenching mechanism alone.

The slight upward curvature of the plot at lower concentrations indicates that some static quenching may be taking place, or something that is called "the quenching sphere of action" (SOA), indicating that the analyte is capable of quenching the system within a specific radius of the receptor motif.[22] The downward curvature at the higher quencher concentrations can be interpreted as two populations. One population of fluorophores is accessible to quenchers and the other being inaccessible to the quenchers.[23] For quenching within rigid solutions, Perrin introduced the concept of an "active sphere"; a volume of interaction around a quencher molecule such that a fluorophore excited within this volume is instantaneously quenched.[24] The values for K_p (Perrin constant), Perrin radius (Å) and detection limits (μM)

were determined over the linear quencher-concentration range of 4 – 20 μM of 0.001 M Fe^{3+} solution. The calculated values are shown in **Table 2**.

Table 2: Values for constants and detection limits by the Perrin and Sphere of Action methods. The detection limit calculated from the linear Stern-Volmer method is also included for comparison.

A1	Kp ($x10^4$ M^{-1})	LOD Linear Stern Volmer μM	LOD Perrin method μM	Perrin Radius (Å)
Water	1.42	3.64	1.41	4.62
Acetonitrile	1.47	5.05	2.63	4.67

Evidently, the value for the detection limit from the Perrin sphere of action method is more than half of that determined by the linear Stern-Volmer method. This shows the importance of determining the correct mode of quenching as it can have a drastic effect on the reported outcome. In addition, the size of **A1** from the methoxy derivative to the end of the phenyl functionality was determined by computational analysis (Spartan '10 V1.10.). The length of the molecule was calculated to be 18.037 Å. The diameter of the quenching sphere (9.2 Å) resides within this calculated distance.

2.1.8 Quantum Yield studies

The fluorescence quantum yield (ϕ) of **A1** was evaluated using anthracene as a standard fluorophore with a known ϕ_S = 0.27 in ethanol. **A1**, in acetonitrile as the solvent, and the standard were excited using the same excitation wavelength (340 nm) and their absorbance were tuned to *ca.* 0.05 nm at this excitation wavelength. The integrated areas under the emission spectra were obtained using fl. Winlab software and the fluorescence quantum yields (ϕ) were calculated in accordance with the equation **(2)** below:

$$\frac{\phi_X}{\phi_S} = \left[\frac{A_X}{A_S}\right]\left[\frac{Abs_S}{Abs_X}\right]\left[\frac{\eta_X}{\eta_S}\right]^2 \qquad (2)$$

Where ϕ_X and ϕ_S are the respective fluorescence quantum yield of the samples and standard, A_X and A_S are the integrated areas under the emission spectra of the samples and standard, Abs_X and Abs_S are the optical densities at the excitation wavelength of both samples and standards whilst η_X and η_S are the respective refractive indices of the solvents used for the sample and standard. The quantum yield (ϕ) of **A1** was determined to be 0.71. This value indicates a high proportion/number of excited state species that can emit after excitation.

2.1.9 Reversibility studies of A1 for sensing Fe^{3+}

The reversibility of **A1** was investigated using the hexadentate chelating ligand ethylenediaminetetraacetic acid (EDTA). A quenched solution of **A1** with Fe^{3+} was titrated with a 0.01 M solution of EDTA. After the addition of up to 100 ul of the EDTA solution, no drastic enhancement in the emission spectra of the complex was observed, suggesting a stronger interaction between **A1** and Fe^{3+} than that of Fe^{3+} and EDTA (**Figure 23**). This stronger interaction between **A1** and Fe^{3+} was later verified by computational analysis.

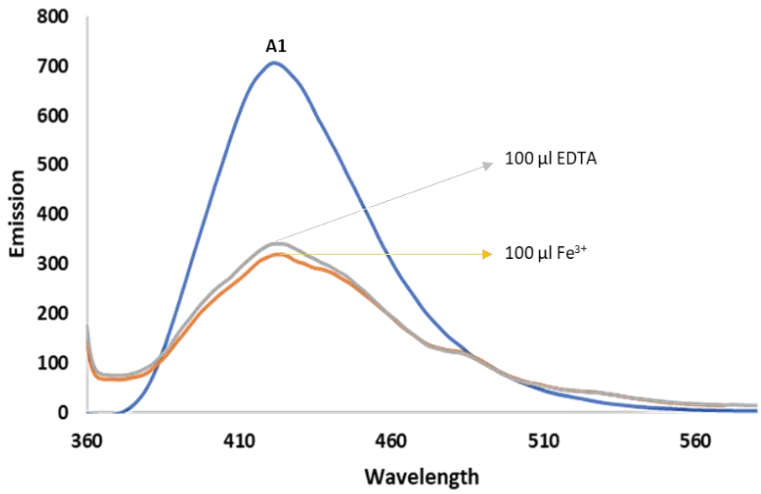

Figure 23: Titration of quenched **A1**-Fe^{3+} system after the titration of up to 100 µL aliquot of 0.01 M solution EDTA.

2.1.10 Determination of the binding stoichiometry using Job plots analysis

Stock solutions of equal concentrations (0.01 M) of **A1** and Fe^{3+} were prepared. The molar fraction of **A1** and Fe^{3+} was varied whilst keeping the total concentration constant for each run. The emission spectra for increasing and decreasing amounts of Fe^{3+} were recorded in both acetonitrile and water. Jobs plots were constructed by plotting the maximum emission vs molar fraction of Fe^{3+} (**Figure 24**). These plots indicated that both the acetonitrile and water experiments facilitated a 1:1 sensor-metal binding ratio

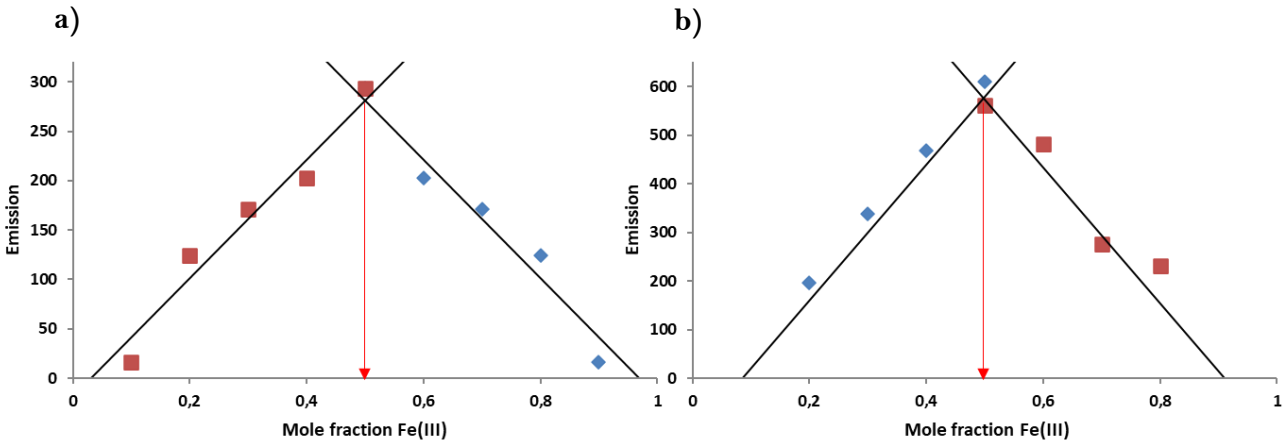

Figure 24: Job's plot of **A1** and Fe^{3+} in a) water and b) acetonitrile. Excitation of 340 nm.

2.1.11 pH studies

To analyze the effect of varying pH on sensing capabilities, titration studies in different pH solutions were conducted. Different arrays of store-bought solutions with pH values of 10, 5, and 4 were utilized for the study. Addition of **A1** and Fe^{3+} into deionized water was compared to that of **A1** and Fe^{3+} in a buffered solution. The pH range of the solutions were chosen as they reflect the range of common wastewater from industrial processes and acid mine drainage.[25–27] Results show that the sensing response upon Fe^{3+} additions is constant in acidic and alkaline solutions. (**Figure 25**).

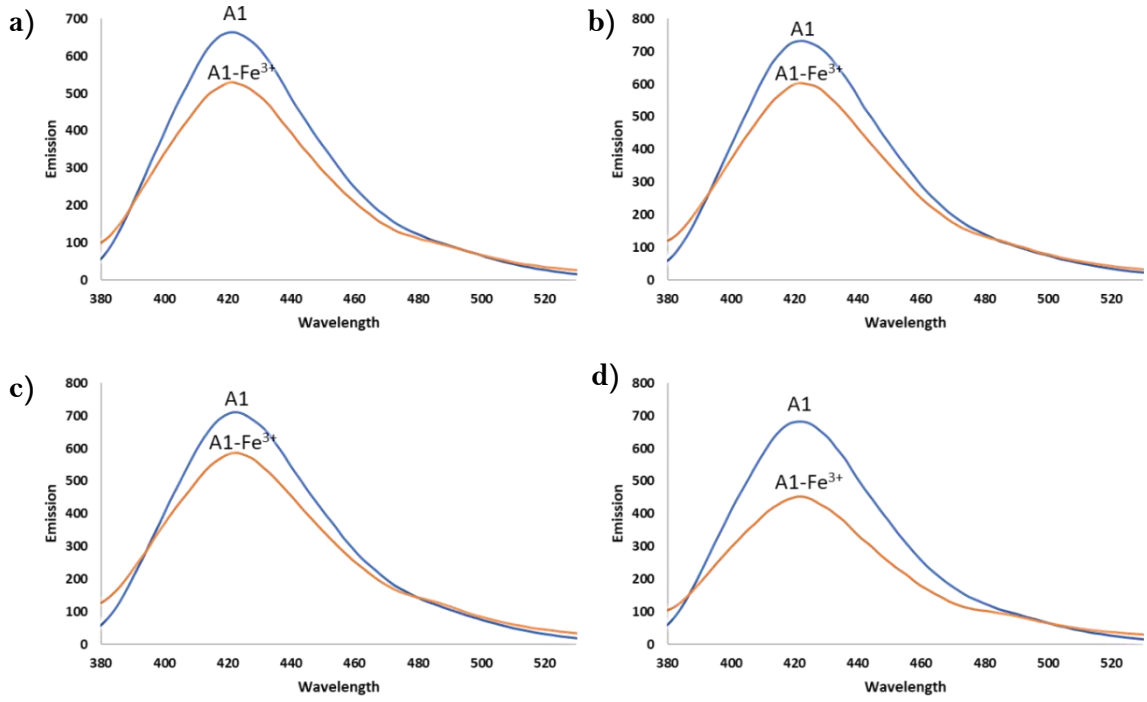

Figure 25: Effect of pH on emission properties of **A1** with Fe^{3+} in a) the original pH of the solution (pH 6.89), b) pH 4, c) pH 5, and d) pH 10.

2.1.12 Proposed binding site between A1 and Fe^{3+}

Literature has reported the ability of the N2 nitrogen atom of the triazole ring to coordinate with metal ions to form stable complexes when neighboring assisting groups are available.[28–30] Triazole moieties have become popular for metal analyte sensing as a result of their ability to interact with metal cations *via* the nitrogen atoms on the ring.[31,32] It is proposed that the interaction between the sensor **A1** and Fe^{3+} involves the coumarin carbonyl and triazole nitrogen in a stable pseudo six-membered ring as shown in **Figure 26**. The complexation affinity was attributed to the N2 nitrogen lone electron pair donation from the triazole ring to the metal ion, assisted by a lone pair of electrons from the coumarin-carbonyl group.

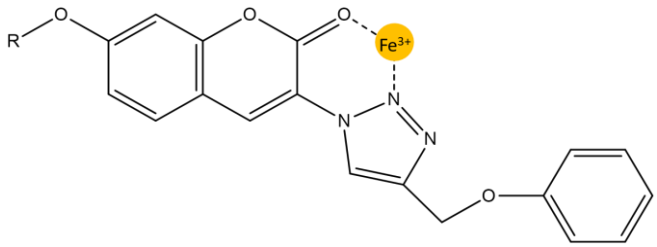

Figure 26: Proposed stable six-membered ring formation between **A1** with a Fe^{3+} ion.

In addition to the triazole and coumarin-carbonyl moiety, complexation may also occur via different functional groups attached to the coumarin scaffold, in this case, the ether group at position -7- may also contribute to analyte binding. To identify whether the oxygen atom of the ether group is involved in complexation, 7-methoxycoumarin (Herniarin) **H1** was synthesized and titrated with a Fe^{3+} solution and the emission response observed (for the synthetic pathway of Herniarin see **Scheme 1** in **Appendix A**). The titration of Herniarin with Fe^{3+} in water resulted in a quenching response which decreased as more iron was introduced (**Figure 27**). As previously shown, the binding stoichiometry of **A1** towards Fe^{3+} occurred in a 1:1 ratio. Therefore, two possible binding scenarios are applicable. Binding was postulated to occur either via the oxygen atom of the ether group, or via the combined nitrogen/carbonyl binding scenario. However, both are unable to occur simultaneously as seen from the 1:1 binding ratio (for the ^{1}H NMR of Herniarin **H1** see **Figure 9** in **Appendix A**).

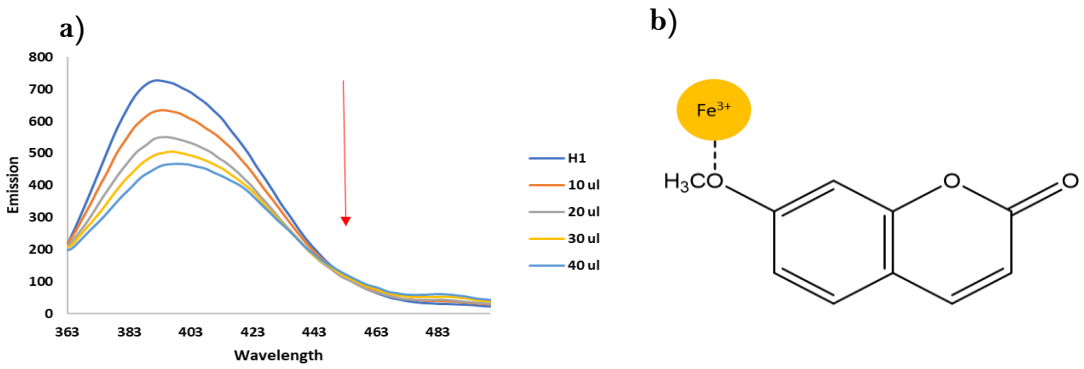

Figure 27: a) The quenching response of **H1** towards Fe^{3+} titration, and b) the possible binding scenario of **H1** towards Fe^{3+} cations via the lone electron pair on the oxygen atom.

The proposed binding site of **A1** towards Fe^{3+} was investigated by ^{1}H NMR and ^{13}C NMR spectral analysis. Initial titrations of **A1** with aliquots of $Fe(NO_3)_3$ displayed no shift in the proton signals. Additionally, the peaks became less resolved as more Fe^{3+} was added (**Figure 28**). This indicated that the complexation of **A1** with Fe^{3+} did not occur via hydrogen bonding. This was later confirmed by computational studies of theoretical hydrogen bonding

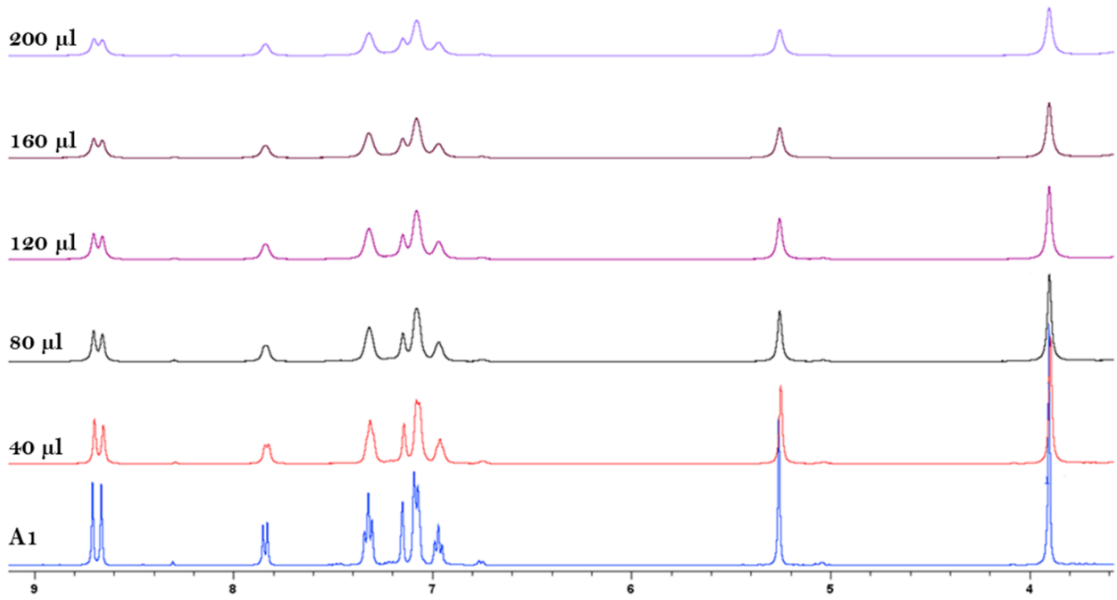

Figure 28: ^{1}H NMR titration of **A1** with $Fe(NO_3)_3$ in d_6-DMSO.

In addition to ^{1}H NMR studies, ^{13}C NMR analysis was used to investigate the possible involvement of the triazole carbon double bond in metal complexation. It is known that alkene and alkyne ligands can be involved in binding modes via σ- and π-electrons in organometallic complexes.[33] Furthermore, it has been reported that the C-5 atom in the triazole ring can be involved in metal coordination.[34] The carbon spectrum of **A1** was compared to that of **A1** with 200 µl of Fe^{3+}. Notably, two peaks displayed pronounced shifts. These peaks were identified as the two double-bonded carbon atoms of the triazole ring. A single carbon signal has shown to have shifted upfield, whilst the other has shifted downfield. During this possible complexation, triazole-carbon labeled **A** has become more nucleophilic, resulting in an upfield shift, whilst carbon **B** has become slightly electrophilic, leading to a shift downfield. This electron-density shift from **B** towards **A** may facilitate an interaction with the Fe^{3+} ion. In addition, the coumarin carbonyl **C** displayed no noticeable shift in the spectrum of the sensor-metal complex. It is therefore proposed that the lone pair of electrons from the oxygen atom could be taking part in the complexation rather than π-electrons from the carbon-oxygen double bond, forming a stable pseudo-6-membered ring between the C=O lone pair, Fe^{3+}, and triazole-carbon **A** (**Figure 29**).

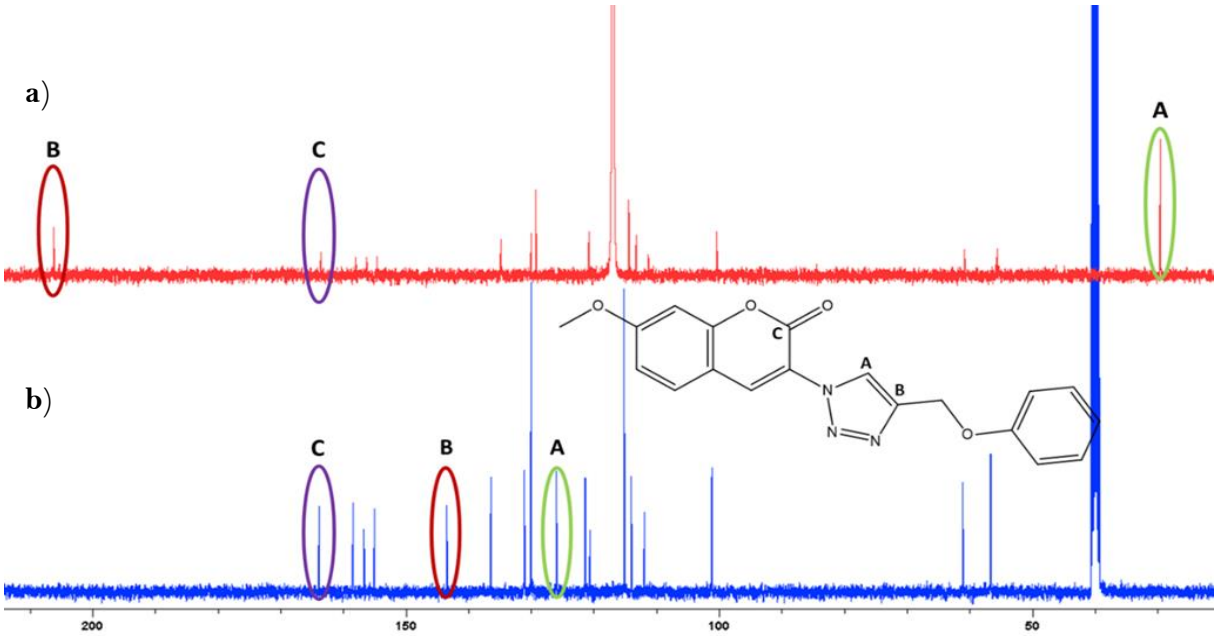

Figure 29: ^{13}C NMR spectra of a) **A1**-Fe^{3+} complex and b) **A1**. Inset structure: Possible positioning of the triazole functionality relative to the coumarin carbonyl to facilitate Fe^{3+} coordination. Spectra recorded in d_6-DMSO.

From the postulated N2 triazole and coumarin-carbonyl lone-pair involvement in metal coordination, the possible involvement of the ether oxygen at position -7-, and the observed triazole carbon shift in **Figure 29**, three possible coordination conformations (**a-c**) are proposed (**Figure 30**).

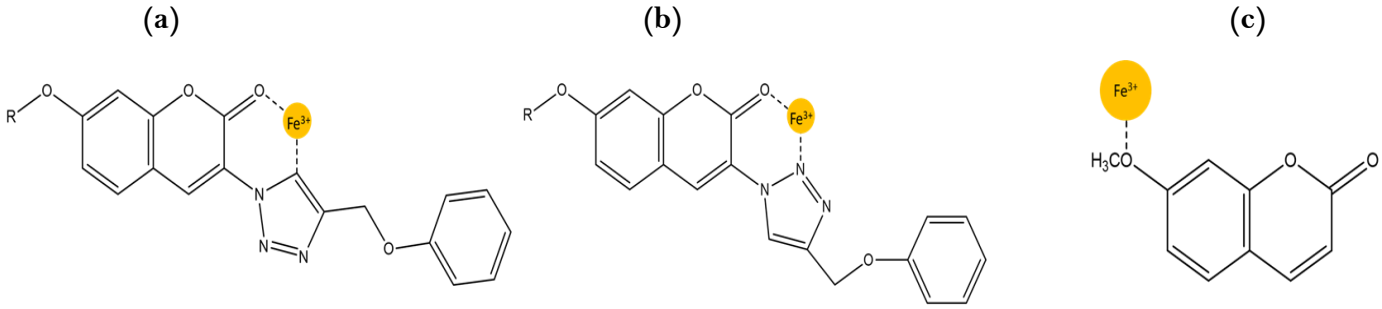

Figure 30: Three possible binding scenarios of **A1** with Fe^{3+}.

2.1.13 Computational analysis

2.1.13.1 Comparison of most stable conformation of A1 to XRD results

Molecular modelling studies were used to determine the lowest energy conformer of **A1** at the density-functional theory (DFT) level. This conformation was compared to that of the single crystal XRD data. Results from these computational calculations are in close agreement with the observed crystal structures (**Figure 31**). The calculated energy of **A1** in this specific conformation was -3145754.12 kJ/mol, indicating the appreciable stability of **A1**. Although the calculated and observed conformations are not completely identical, the differences can be reconciled when the medium and interactions between other molecules are considered. These differences could arise as the calculations are carried out on one compound (in vacuum) whereas the crystal structure determination takes multiple factors into consideration, such as multiple compounds close to each other (proximity), solvents present (medium), forces and the interactions between them, and their packing arrangement.

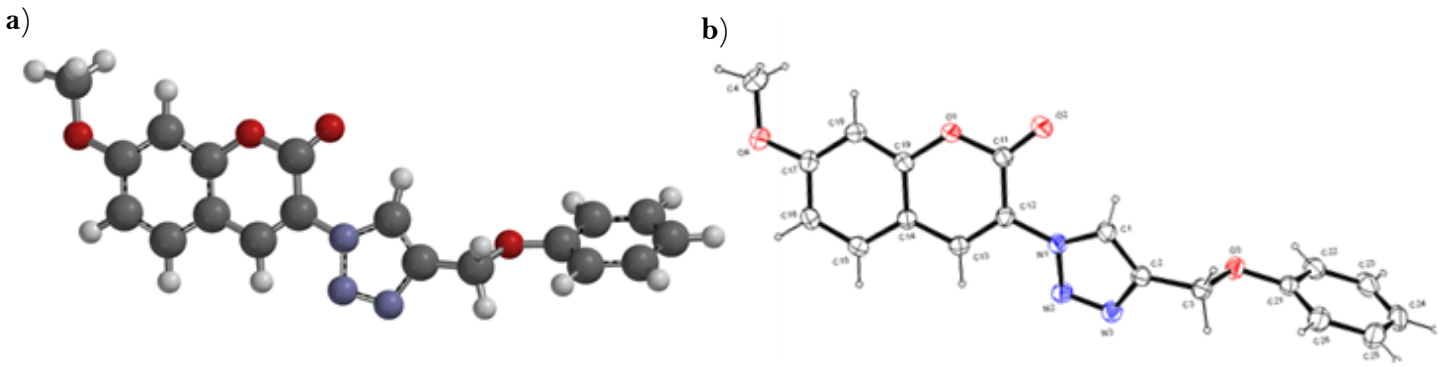

Figure 31: a) computationally calculated most stable conformation, and b) experimental XRD results of **A1**.

2.1.13.2 Reconciliation of binding site of A1 with Fe^{3+}

Once the most stable conformer of **A1** was established, it was then used to study the binding site during complexation with Fe^{3+}. Calculations conducted at Molecular Mechanics level (MMFF) displayed a proposed twisting of the triazole nitrogen atoms towards the coumarin carbonyl to facilitate the postulated pseudo-6-membered ring between the N2 triazole

nitrogen and the lone pair of electrons on the coumarin carbonyl oxygen (**Figure 32**). This agrees with what has been reported previously with respect to the binding properties of the triazole nitrogen atoms towards metal complexation in the presence of nearby assisting groups. Using their combination of σ-donor (nitrogen lone-pair electrons) and π-receptor properties, these N-heterocycles have been considered as very useful ligands towards Fe^{3+} complexation. Furthermore, when the triazole functionality is present on the coumarin scaffold, complexation involving the ring nitrogen is more preferred than the lone pair oxygen binding from the ether group at position -7-.[35] Notably the phenyl ring has twisted towards the Fe^{3+} cation, however, hydrogen bond calculations showed that no hydrogen bonding was taking place. This agrees with the ^{1}H NMR titration analysis. Additionally, this indicates the unlikelihood of the complexation scenario between the 7-methoxy functionality with the Fe^{3+} cation as seen in the Herniarin titrations. This quenching effect may arise because of the NO_3^- counterion.

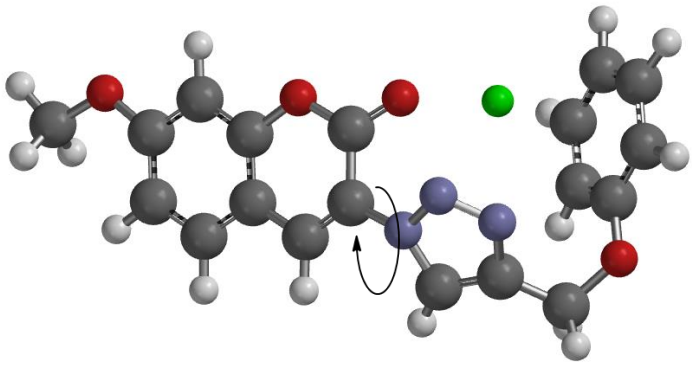

Figure 32: Computational conformation of the most energetically preferred **A1**-Fe^{3+} binding scenario. The green sphere represents the calculated position of the Fe^{3+} cation.

In addition to computational analysis, titration data of **A1** with a concentrated Fe^{3+} solution was able to verify the number of binding sites present between the sensor and metal cation. According to equation (**3**), a plot of $Log[F_0-F/F]$ vs $Log[Q]$ should yield a straight line with the gradient equal to n, where n is the number of binding sites present.[36] A straight line occurs when the predominant mode of quenching occurs via a static process. This agrees with the mode of quenching determined by titration analysis. The regression coefficient indicated an appreciable correlation with the number of binding sites shown to equal to 1 (**Figure 33**). This agrees with what has been shown computationally and what has been postulated whereby the N2 triazole nitrogen is the main contributor of binding electrons towards Fe^{3+}

complexation and may be partially assisted by the lone electron pair of the coumarin carbonyl functionality.

$$Log\left[\frac{F_0 - F}{F}\right] = LogK + nLog[Q] \quad (3)$$

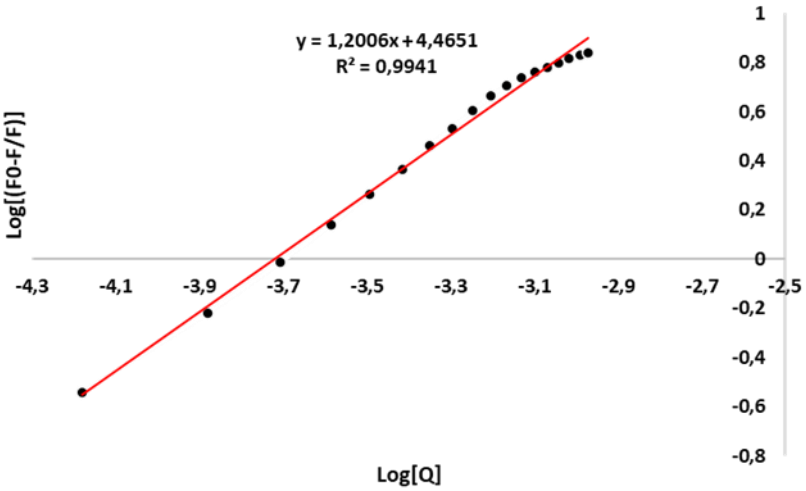

Figure 33: Double logarithmic plot of the fluorescence quenching response of **A1** towards Fe^{3+}.

Although the computed binding between **A1** and Fe^{3+} provides promising observations, it does not explain the shift observed from the triazole carbon atoms as seen in the ^{13}C NMR spectrum. As stated previously, the carbon double bond of the triazole ring can take part in binding due to its electron density. The nitrate counterion from $Fe(NO_3)_3$ was computed with the most stable conformer of **A1** in water as the medium. The calculated structure of the sensor and anion displayed similar twisting of the triazole ring nitrogen atoms towards the coumarin carbonyl (**Figure 32**), and the placement of the nitrate anion in the region of the coumarin triazole carbon double bond (**Figure 34**). Hydrogen bond calculations indicated no hydrogen bonding between the nitrate and **A1** were present. Therefore, it is proposed that the water molecules, together with the carbon double bond of the triazole moiety, could form a stable complex with the nitrate counterion resulting in the observable shifts in the ^{13}C NMR spectrum. The strong interaction of **A1** with Fe^{3+} could cause the carbon double bond π-

electrons to become more readily available for bonding due to the shift in electron density from the triazole ring towards Fe^{3+}.

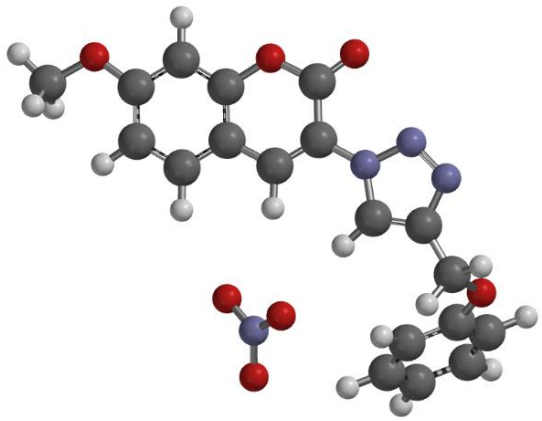

Figure 34: Computed conformation of **A1** in the presence of nitrate counterions. Computation conducted in water as a medium.

2.1.13.3 Verification of selectivity trends of A1 with Fe^{3+}

The most energetically stable conformer of **A1** was used to reconcile the selectivity trend observed. As stated, **A1** was selective towards Fe^{3+} despite the presence of other competing metal ions. The proposed site of metal binding in the cavity between the triazole nitrogen and coumarin-carbonyl was used for these calculations. Water was used as the medium in which the energies were calculated. The energy of the **A1**-Fe^{3+} complex at this proposed position was found to be -846.22 kJ/mol, an acceptably low, and energetically-stable-binding scenario. In addition, the calculated energies of **A1**-Hg^{2+} and **A1**-Cu^{2+} were considerably higher than that of **A1**-Fe^{3+}, thereby, reconciling the selectivity observed between **A1** and Fe^{3+} in the presence of competing metal cations. The complex energies between **A1** and the three tested metal cations is shown in **Table 3**.

Table 3: Calculated complex energies between **A1** and three competing metal ions.

Metal Cation	Fe^{3+}	Cu^{2+}	Hg^{2+}
Calculated complex energy (kJ/mol)	-846.22	-372.47	48.55

2.1.13.4 Computation of reversibility studies of A1 - Fe^{3+} with EDTA

The trends observed in the reversibility studies between **A1**-Fe^{3+} and the hexadentate ligand ethylenediaminetetraacetic acid (EDTA) were computed. Titration analysis of EDTA with **A1**-Fe^{3+} showed that Fe^{3+} was not fully released following continuous EDTA additions. Calculation of complex energies between EDTA-Fe^{3+} and **A1**-Fe^{3+} were performed. **Table 4** shows the energies of the ligand and ligand-metal complexes calculated using molecular mechanics (MMFF).

Table 4: Energy calculations of EDTA, **A1**-Fe^{3+}, and the EDTA-Fe^{3+} complex.

Ligand / Ligand-Metal complex	Complex energy (kJ/mol)
EDTA	467.81
EDTA-Fe^{3+}	-350.85
A1-Fe^{3+}	-846.22

The calculated energy of the **A1**-Fe^{3+} complex is considerably lower than that of the EDTA-Fe^{3+} binding scenario. This lower energy complex could prevent the abstraction of the metal ion from the binding sites on **A1** by EDTA. Henceforth, it is evident why Fe^{3+} was not fully reversible in the presence of increasing amounts of EDTA.

Anionic sensing studies

2.1.14 Screening studies

Owing to the selectivity and sensitivity displayed by **A1** towards Fe^{3+} cations, this sensor was tested for its affinity and sensitivity towards a variety of different anions. These anions included CN^-, SCN^-, SO_4^{2-}, NO_3^-, CH_3COO^-, I^-, Br^-, Cl^-, F^- and PF_6^-. The anions were all prepared in water from their ammonium salts. The sensing properties of **A1** was tested in a variety of different organic solvents and mixtures, namely ethanol, water, acetonitrile, and a 50/50 water-acetonitrile mixture. The screening studies were conducted by adding 20 µl aliquots of a 0.1 M anion solution to sensor **A1** and monitoring the changes in the fluorescent emission. The effect that each anion had towards the fluorescent emission of **A1** in differing solvent/solvent mixtures are shown in **Figure 35**.

a)

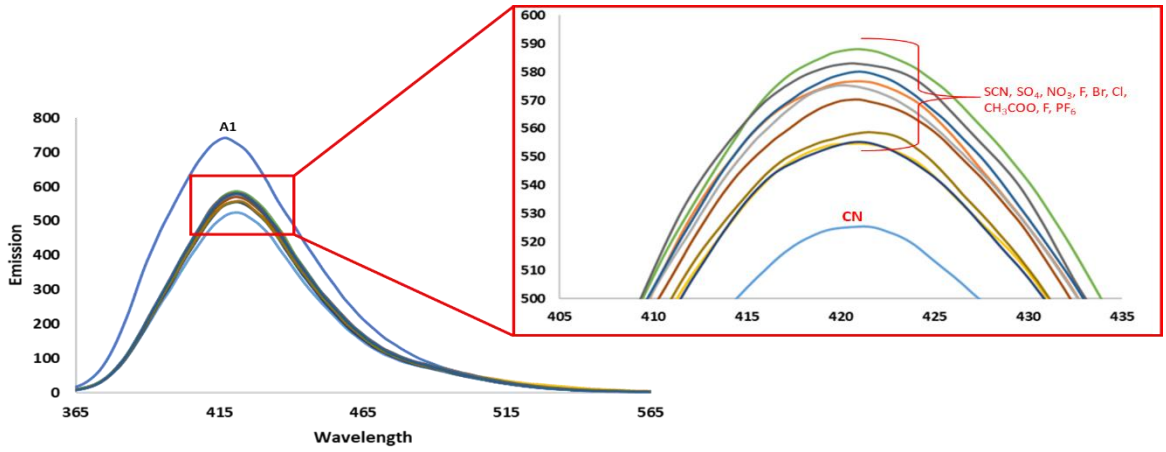

b)

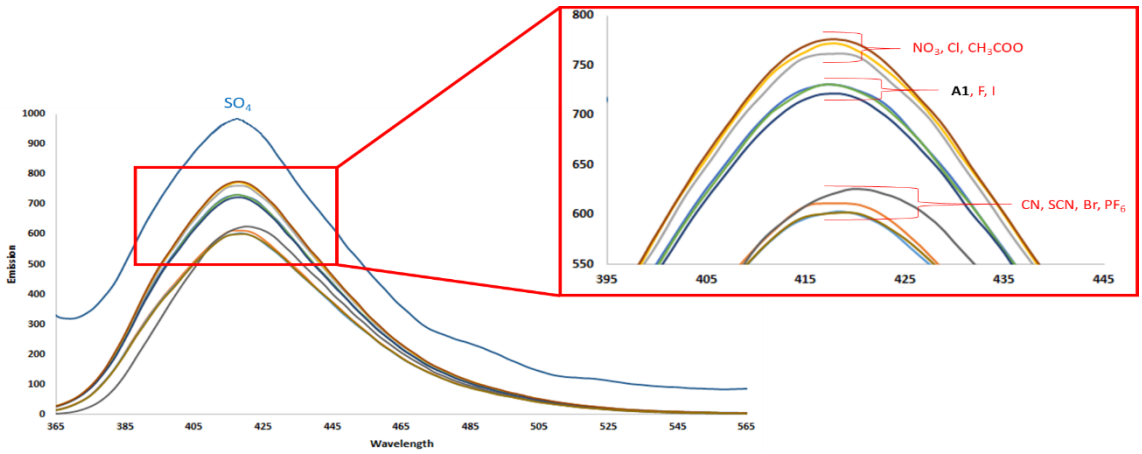

c)

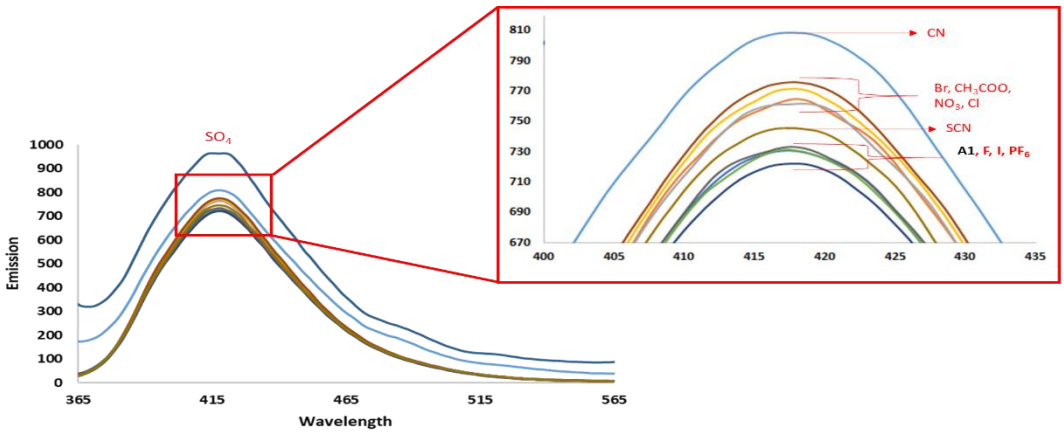

d)

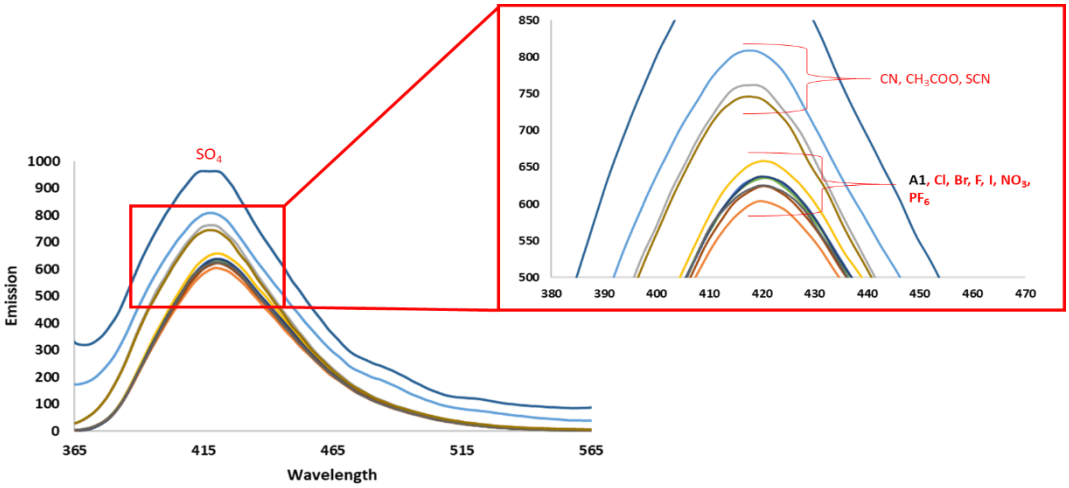

Figure 35: Screening studies of **A1** towards selected anions in a) water, b) ethanol, c) acetonitrile and d) 50/50 water-acetonitrile. Excitation of 340 nm.

When compared to the previous metal sensing studies, it is evident that **A1** does not display the same degree of affinity towards anions as it showed towards cations. No single anion caused a noticeable or sizeable effect on the fluorescent emission of **A1** in either of the four solvent mediums/mixture. Although it appears that the anion SO_4^{2-} caused the greatest emission response by fluorescent enhancement in ethanol, acetonitrile and 50/50 water-acetonitrile, it in truth caused a solid to precipitate from solution leading to this observed fluorescent enhancement. This is not a favourable trait for fluorescent studies and was therefore omitted from further investigations. The solid precipitates were not further analysed.

2.1.15 Selectivity studies of A1 towards cyanide in water and acetonitrile

The effect of cyanide in both water and acetonitrile displayed the greatest quenching and enhancing responses respectively. The responses of **A1** towards the anions in ethanol and water/acetonitrile were too alike to allow for accurate selectivity determination. Owing to this, water and acetonitrile were chosen for further studies as cyanide was observed to stand partially alone compared to the other anions, although not significantly. **Figure 36** shows the selectivity studies of **A1** towards CN^- in both water and acetonitrile. Evidently, **A1** does not display the same level of selectivity towards CN^- as towards Fe^{3+} in both solvent systems. Although the selectivity of **A1** towards cyanide makes it an unfavorable candidate for anionic sensing, it was still investigated for its fluorescent, absorbance, NMR, and computational characteristics to further understand the chemistry of the system.

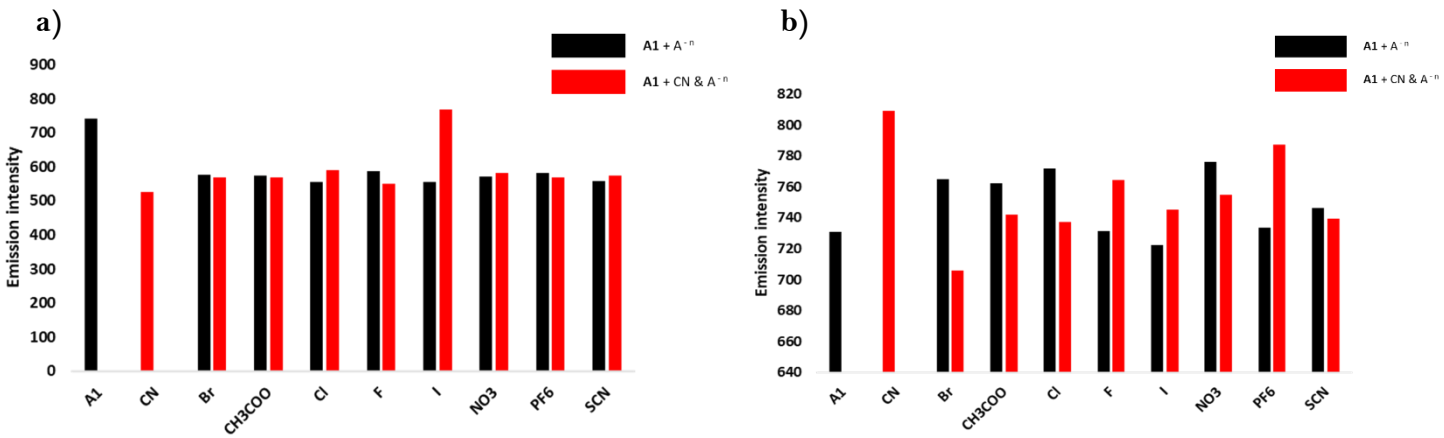

Figure 36: Selectivity of **A1** towards CN^- in the presence of competing metal cations in a) water and b) acetonitrile. Excitation 340 nm.

2.1.16 Titration studies of A1 with CN^- in water

The selectivity of **A1** towards cyanide in the presence of competing anions in both water and acetonitrile is substantially inferior to that of **A1** with Fe^{3+} amongst competing metal cations. Although the selectivity of the sensor towards anions is poor, **A1** was titrated with CN^- in water to determine whether it could be used as a cyanide-specific sensor in real-world applications. Water was chosen as the medium for titration studies as cyanide contaminants have been identified in various water sources.[37,38]

Although the sensitivity of **A1** towards CN^- was poor, the titration data was analyzed to determine other properties such as the quenching mechanism, binding stoichiometry, complexation energies, reversibility, and the detection limit (μM). The titration of **A1** with CN^- in water is shown in **Figure 37**. Visibly, the increasing addition of CN^- to **A1** did not cause a red or blue shift in peak maxima. This suggests that a PET and not an ICT fluorescent mechanism is most likely to be involved duringcomplexation.[39]

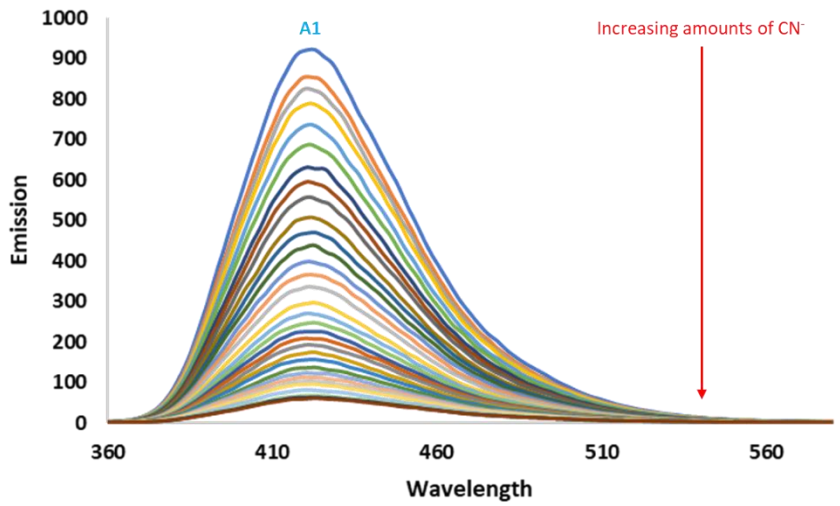

Figure 37: Titration of **A1** with equal aliquots of CN^- in water. Excitation of 340 nm.

2.1.17 Determination of the quenching mode of A1 towards CN^-

It is pertinent to recognize that the observation of a linear Stem-Volmer plot does not distinguish between static or dynamic types of fluorescent quenching. These processes need to be evaluated separately. The quenching mechanisms are usually determined by their differing dependence on temperature, viscosity, and lifetime measurements. Static quenching constant decreases with increasing temperature, while dynamic quenching constant increases with increasing temperature.[40,41] A graphical representation of the effect of temperature on both dynamic and static quenching is shown in **Figure 38**. Higher temperatures result in faster diffusion and hence larger extents of dynamic quenching and will result in the dissociation of weakly bound complexes, and hence smaller extents of static quenching.

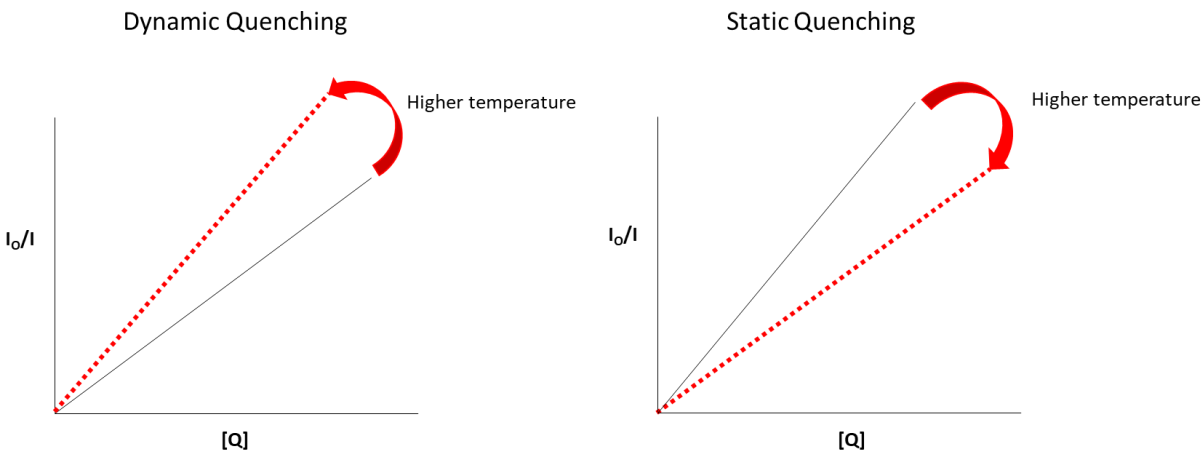

Figure 38: The effect of temperature on Dynamic vs Static fluorescent quenching.

The fitting of the titration data with the linear Stern-Volmer equation is shown in **Figure 39**. Evidently, the plot of F_0/F vs [CN] displays a positive deviation from linearity with an appreciable regression coefficient. Positive deviations from linearity in Stern-Volmer plots suggest that : (**1**) the quenching process could simultaneously follow two mechanisms, namely combined dynamic and static quenching processes or (**2**) quenching relates to static processes either through the formation of non-fluorescent complexes between the fluorophore and quencher in the ground state (ground-state complexes) or to the presence of a quenching sphere that diminishes the fraction of fluorescing molecules.[42–45]

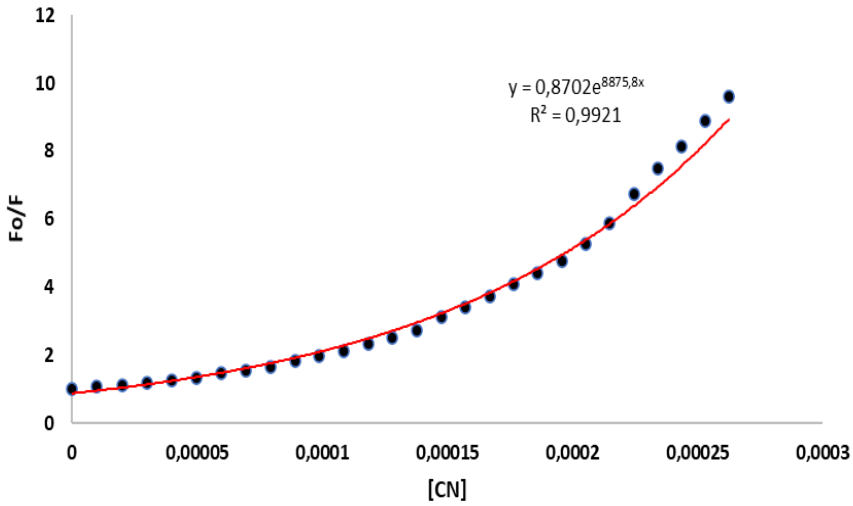

Figure 39: Plot of titration data fitted to the linear Stern-Volmer equation.

An exponential equation was used to best fit the data points. From this, results such as the detection limit (LOD) and Stern-Volmer quenching constant (K_{SV}) were investigated and determined to be 35 μM and 3.01 x10^4 M^{-1}, respectively. The results from this curve cannot be used to explain the system fully due to the positive deviation seen, therefore, a plot for combined dynamic and static quenching model was implemented.

In the case of quenching via simultaneous dynamic and static quenching or static quenching through the formation of a ground state complex[21,45] , a plot of $\left[\frac{F_0}{F} - 1\right]\frac{1}{[Q]}$ vs [Q] should yield a straight line with the slope equal to values associated with the Stern-Volmer and ground state complex constants K_{SV} and K_g. However, the experimental data did not fit the formula as shown by a poor regression coefficient (see **Appendix A Figure 10**). This indicates that the quenching behaviour cannot be explained by the combined dynamic and static quenching mechanism or through the formation of a ground-state complex alone. Therefore, the static contribution of the quenching process was investigated by the Perrin and Sphere of Action models.

The Perrin-model is valid for energy transfer between donor–acceptor components unable to change spatial position with respect to each other on the time scale of the quenching process.[46] Furthermore, it describes the static quenching between randomly distributed fluorophores and quenchers that are located in a certain proximity. In this model, one assumes that there is instantaneous quenching of an excited donor by quencher molecule, if the quencher is located inside a sphere of volume (Vq) around the fluorophore and there is no quenching when the quencher is outside of this quenching sphere.

The dynamic contribution is measured in terms of fluorescent lifetimes according to the equation $\tau_o/\tau = 1 + K_D[Q]$. A plot of τ_o/τ vs [Q] should yield a straight line with the value of the gradient equal to K_D. The larger the value of K_D the greater the contribution of dynamic/collisional modes towards fluorescent quenching.[47]

Dynamic quenching is controlled by diffusion processes. Fluorescent lifetimes are usually determined by Time-correlated single-photon counting (TCSPC). Calculations of fluorescent lifetimes were not able to be determined and as a result the dynamic contribution towards quenching was unable to be determined.

According to the simplified Perrin equation (*3*) a plot of $\ln(F_o/F)$ vs [CN] should yield a straight line with the Perrin quenching constant K_p equal to the gradient of the slope. Generally, the higher the value of the quenching constant (K_p, K_{sv}) the more sensitive the system and the lower the concentration of quencher is needed to quench fluorescence.[48,49]

$$\ln\left(\frac{F_O}{F}\right) = K_p[Q] \qquad (3)$$

The fitting of the titration data towards the Perrin quenching model displayed appreciable linearity over the entire concentration range of the quenching analyte (**Figure 40**).

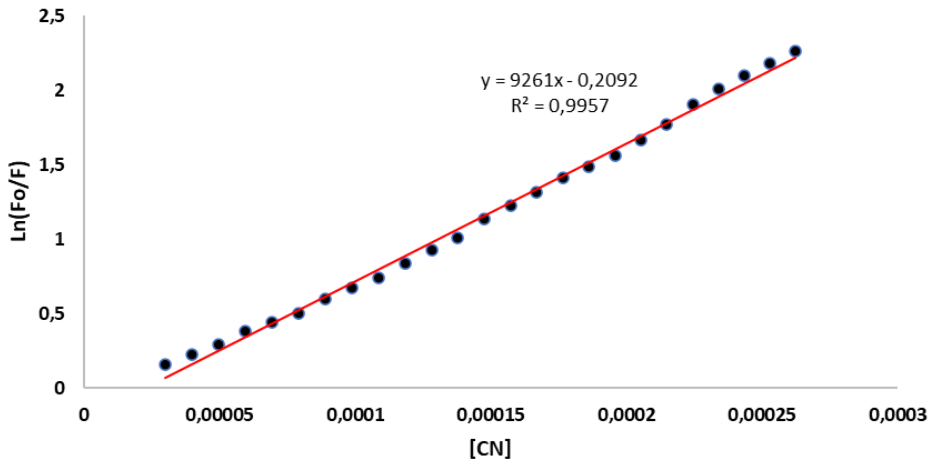

Figure 40: Plot of quenching titration data according to the Perrin equation.

A comparison of the detection limits and values for the Perrin constant (K_p) of **A1** in the presence of Fe^{3+} and CN^- in water is shown in **Table 5**.

Table 5: Comparison of detection limits and quenching constants of **A1** with Fe^{3+} and CN^- following the Perrin quenching model.

Quenching of **A1** by:	Detection limit µM	K_p (x 10^n M^{-1})
Fe^{3+}	1.4	1.42 (n=4)
CN^-	6.7	9.26 (n=3)

Evidently, the value of K_p in the **A1**-Fe^{3+} complex was greater than the **A1**-CN^- complex. As mentioned previously, the higher the value of the quenching constant, the greater the sensitivity of the system. This is observed as the values of the detection limits differ by approximately 5-fold between these two quenching systems. According to the World Health Organization (WHO) the acceptable level of cyanide species in drinking water is estimated to be 1.9 μM.[50,51] The sensing capabilities of **A1** towards CN^- does not make it a suitable sensor for real-world cyanide-sensing applications in aqueous media.

The value of K_p can be used to determine the radius of the quenching zone V_q from equation (**4**).

$$Kp = V_q \times N_A$$
$$V_q = \frac{4}{3}\Pi R^3 \qquad (4)$$

The radius (R) of the quenching sphere was determined to be 154 nm, a sphere of which would fit comfortably around **A1** with length equal to 18.037 Å. Hypothetically, if the length of the molecule is taken as the diameter of a potential sphere, the corresponding radius is equal to 9.02 Å. The volume around **A1** of which is calculated as 3.07×10^{-27} cm^3 whilst the quenching sphere according to the titration of **A1** with CN^- is calculated as 1.54×10^{-23} L. The quenching sphere is therefore large enough to envelop the entirety of **A1**.

The positive deviation from linearity in the Stern-Volmer plots could also arise due to the "sphere of action" static quenching model. This model was first described by Frank and Waliwow in the early 1930's.[52] It explains the existence of a sphere of active volume around a fluorophore (V_q) and quenching occurs when the analyte is near the fluorescent molecule at the moment of its excitation but does not result in the formation of a ground-state complex. To quench the fluorescence, the analyte must be within this active volume.[53] The probability of the quencher to be found in the sphere of action depends on the volume of the sphere (V_q) and on the quencher concentration. A representation of this quenching process is illustrated in **Figure 41**.

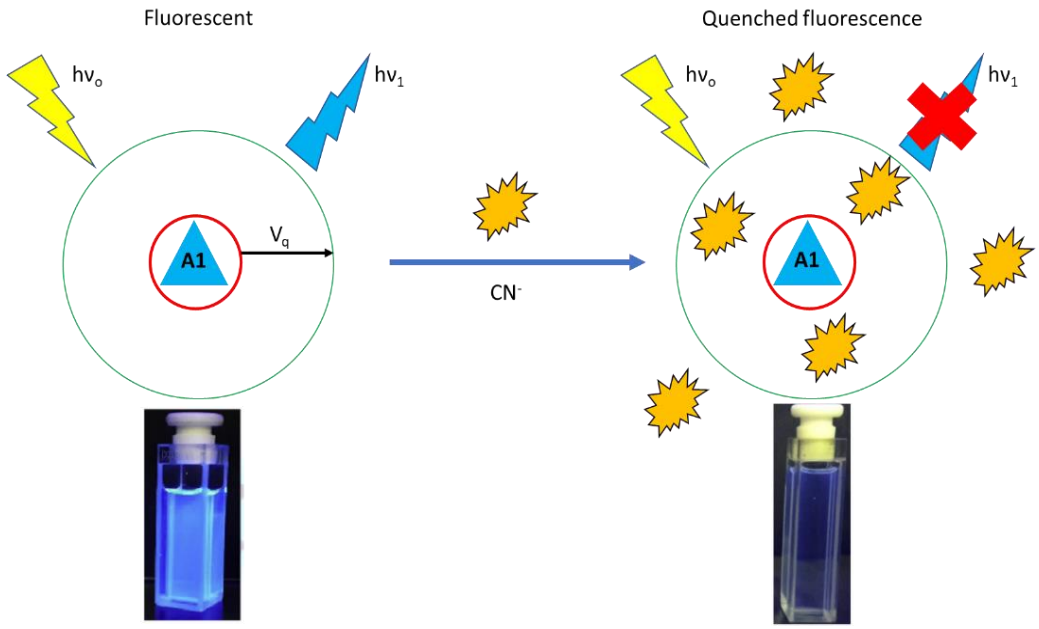

Figure 41: Fluorescent quenching of **A1** by the "sphere of action" static quenching model in the absence and presence of the analyte in the quenching sphere. The green circle represents the active sphere within which quenching by the analyte occurs.

The equation for the sphere of action quenching formula is shown in equations (**4** and **5**).[46]

$$\left(1-\frac{F}{Fo}\right)\frac{1}{[Q]} = K_{SV}\frac{F}{Fo} + (1-W)\frac{1}{[Q]} \qquad (4)$$

$$W = e^{-V[Q]} \qquad ln\frac{1}{W} = V[Q] \qquad (5)$$

A plot of $(1-F/F_0)/[Q]$ vs F/F_0 should yield a straight line with gradient equal to K_{sv}. The fitting of the titration data towards this formula displayed linearity only at the higher concentrations of the CN quencher. This suggests that the sphere of action model does not play the predominant quenching role in this system. It may, however, play a smaller role in analyte quenching at higher concentrations where the ratio of quenchers to available fluorophores is greater. **Figure 42** shows the plot of **A1** quenching by CN^- according to this model.

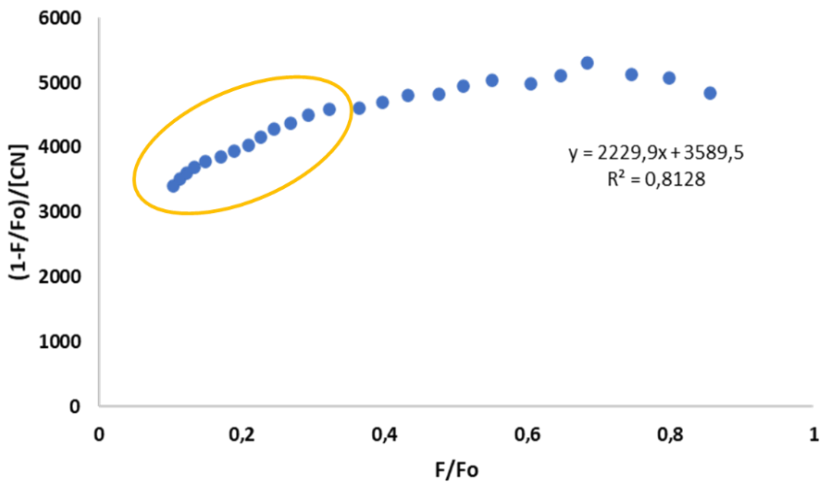

Figure 42: Plot of titration of CN with **A1** in water according to the sphere of action static quenching model. The orange circle denotes the region of linear correlation at higher quencher concentrations.

Notably, the fitting of the data displayed a poor regression coefficient over the entire data range ($R^2 = 0.8128$). The Perrin model for static quenching displayed linearity over the entire data range ($R^2 = 0.9957$) and thus can be suggested as the main contributor towards the static quenching process. Values for K_{SV}, V, V_q and W were calculated from where the graph displayed linearity at higher concentrations of cyanide. This plot is shown in **Figure 43**.

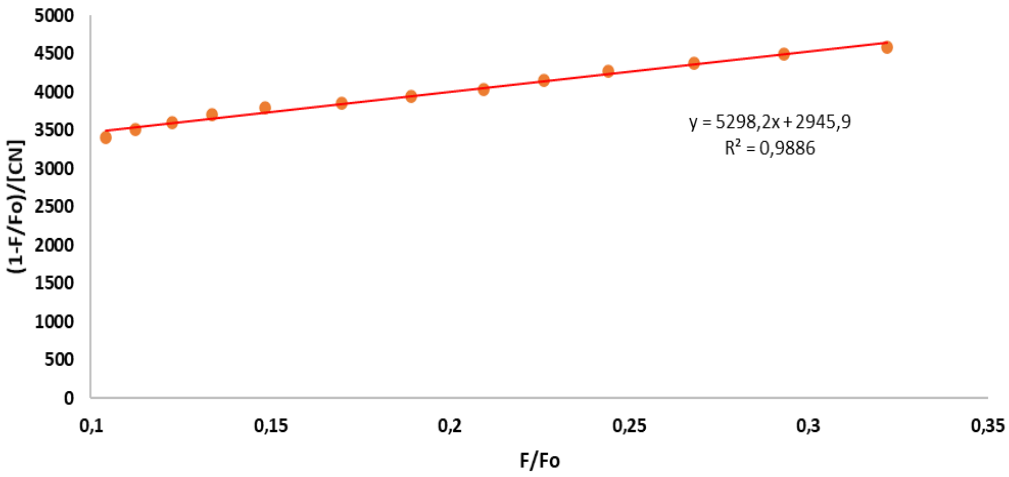

Figure 43: Linear correlation of data at higher concentrations of quencher species according to the SOA quenching model.

The value for K_{SV} is obtained directly from the slope and is shown to be 5.3×10^3 M^{-1}. This is still lower than that of the Perrin constant K_p of 9.3×10^3 M^{-1}. The value of the Stern-Volmer constant is still comparable with the value of K_p, therefore it could still play a role in

fluorescent quenching. The regression coefficient shows a better fit of linear data at higher quencher concentrations.

The values of constant (V), fluorophore fraction (W), active sphere volume (V_q) and radius (r) were calculated from this data. Should the quenching sphere of action play some role in the fluorescent quenching of **A1** by CN^-, a plot of ln(1/W) vs [Q] should yield a straight line with slope equal to constant (V). The values of W were determined from the intercept at each quencher concentration [Q] according to equation (4). The plot of ln(1/W) vs [Q] is shown in **Figure 44**.

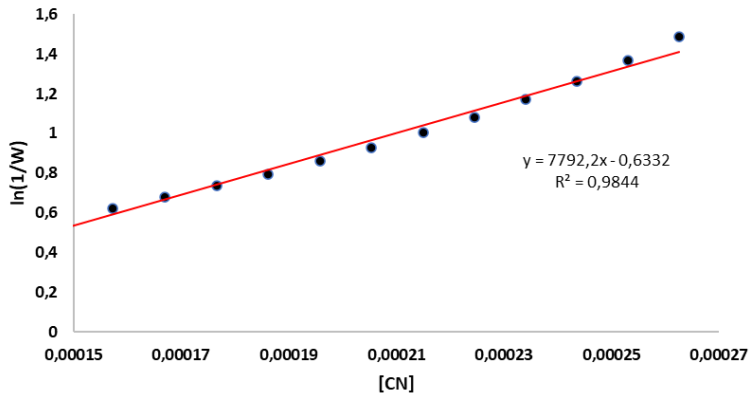

Figure 44: Linear relationship of ln(1/W) vs [CN].

The graph displayed an acceptable regression over the entire data range. This further suggests that the sphere of action quenching process could be occurring at these larger quencher concentrations. Since this expected linearity holds, the value of the quenching constant (V) can be determined from the slope of the graph. This was found to be 7.8 x 10^3 M^{-1}. The value of V_q and quenching radius r was calculated to be 8.8 x 10^{-24} L and 128 nm, respectively. The smaller volume of the quenching sphere by the SOA model suggests why it may have only come into effect at higher quencher concentration where the proximity of quenching analytes to the quenching sphere is closer and therefore more favourable.

The combined values for all calculated data following the three different quenching mechanisms are shown in **Table 6**.

Table 6: Combined results of tested fluorescent quenching mechanisms of **A1** towards CN^-.

Quenching Mechanism	R^2 value over concentration range	Quenching constant K_{SV}, K_P (M^{-1})	Detection Limit (μM)	V_q (L)	radius (nm)	V (M^{-1})
Linear Stern-Volmer	0,9921 (entire conc. range	3.01×10^4	35	-	-	-
Perrin	0,9957 (entire range)	9.3×10^3	6.7	1.5×10^{-23}	154	-
Sphere of Action	0,9886 (only at higher conc. Range)	5.3×10^3	N/A	8.8×10^{-24}	128	7.8×10^3

Plainly, the results confirm that the Perrin static quenching model contributes most of the static component in the proposed combined dynamic and static quenching mechanism as seen by the positive deviation in the linear Stern-Volmer plot. The value of K_p is larger than the value of both K_{SV} and V from the sphere of action quenching mechanism. The magnitude of the quenching constant directly correlates to its contribution towards the mechanism of fluorescent quenching.

In addition, the Perrin model displayed linear fit across the entire quencher concentration range whilst the sphere of action model only displayed this linearity at higher concentrations of analyte. However, the contribution of the SOA model was verified by the plot of ln(1/W) vs [Q] at higher concentrations of cyanide. The linear fit with an appreciable regression coefficient of $R^2 = 0.9844$ confirms the contribution of the sphere of action quenching model at higher concentrations of quencher to the static component of this combined Stern-Vomer system. It is understandable that higher quencher concentrations may promote the relevancy of the SOA model as a greater number of quenchers will be surrounding **A1**, and thus the probability of analytes present in this calculated sphere increases.

The Perrin static quenching mechanism was shown to be the preferred mode of quenching observed between **A1** and Fe^{3+} in water. A comparison of the value of K_p and the detection limit of **A1** with Fe^{3+} and CN^- is tabulated below (**Table 7**).

Table 7: Comparison of Perrin quenching data of **A1** with both Fe^{3+} and CN^-.

Perrin quenching of A1 with:	**K_P (x 10 ^{n} M^{-1})**	**LOD (µM)**
Fe^{3+}	1.4 x10 n=4	1.4
CN^-	9.3 x10 n=3	6.7

The value of the Perrin quenching constant of the **A1**-Fe^{3+} complex is ten times greater than that of **A1**-CN^-. As previously stated, the value of the quenching constant is directly related to the sensitivity of the system and the lower the concentration of quencher is needed to quench fluorescence. The detection limit of **A1** towards Fe^{3+} is nearly five times lower than that of **A1** towards CN^-. This validates the differences observed in the detection limits.

2.1.18 The Benesi-Hildebrand calculations of A1 with CN^-

The Benesi-Hildebrand method was applied to the titration data of **A1** with CN^-. Fitting of the data to the equation (shown previously), a linear correlation was observed (R^2=0.9961). This linearity suggests a 1:1 sensor-ligand binding ratio which was later confirmed by Jobs Plot analysis. The value of the binding/association constant indicates the strength of the sensor-ligand bond. The value of the association constant (K_a) of the complex was calculated to be 1.4 x10^3 M^{-1}. The same constant reported between **A1** and Fe^3 was 3.3 x 10^4 M^{-1}. This compares well with the differences seen between the values of the quenching constant K_P. **Figure 45** shows the Benesi-Hildebrand plot of **A1** with CN^-.

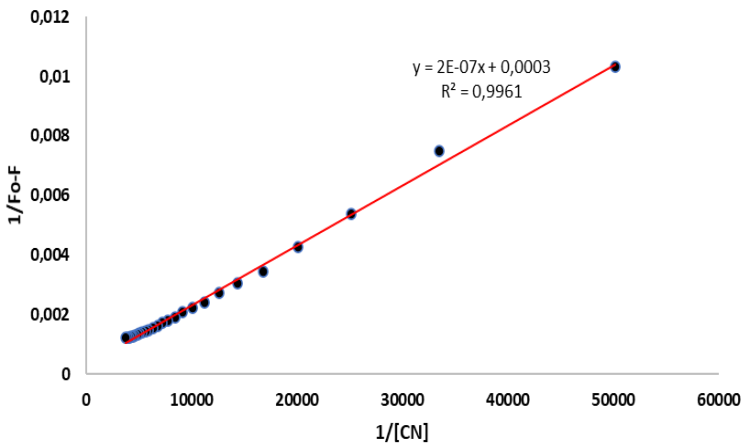

Figure 45: Benesi-Hildebrand plot of **A1** with CN^-.

2.1.19 Reversibility studies of A1 with cyanide

Fully quenched **A1-CN** systems were tested for their reversibility in the presence of anionic-reversing agents perchloric, trichloroacetic and trifluoroacetic acid. The efficacy of the acid may promote the cyanide to abstract a proton and evolve from solution as hydrogen cyanide gas. The results of the three reversibility studies as titrated with aliquots of a 0.1 M solution of differing acids is shown in **Figure 46**.

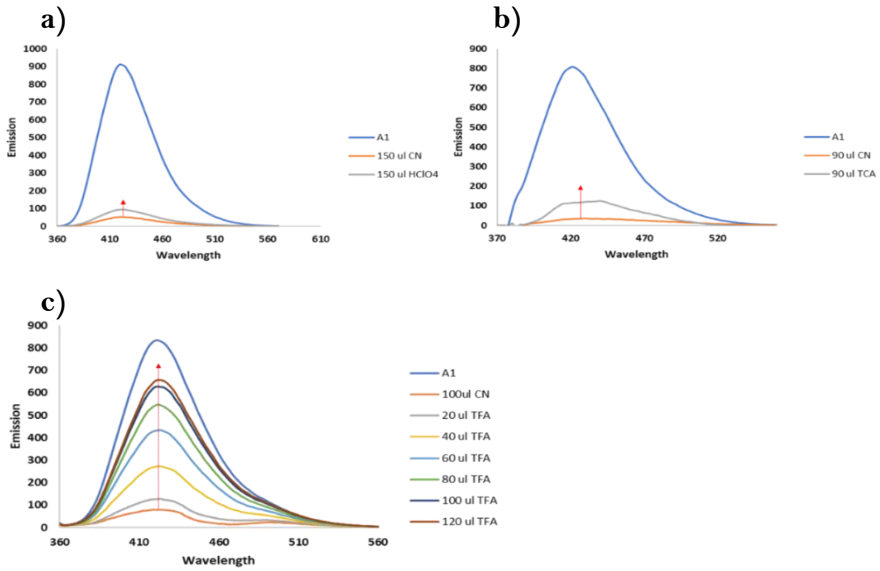

Figure 46: Reversibility studies of **A1** towards CN^- complexation in the presence of increasing amounts of a) perchloric acid, b) trichloroacetic acid, and c) trifluoroacetic acid. Excitation of 340nm.

Visibly, the only acid that induced fluorescent enhancement upon addition was TFA. The strength of the acid was able to dissociate the cyanide from the binding site(s) of **A1** and evolve from the system as hydrogen cyanide. The system was calculated to be 79% reversible in the presence of increasing amounts of TFA. Interestingly, the reversibility of the **A1**-Fe^{3+} complex with EDTA was poor when compared to the cyanide complex. When the values of the association constants (K_a) are reconsidered, conclusions can be made. The value of the association constant for the Fe^{3+} complex was greater than that of the CN^- complex. This indicated that **A1** "held tighter" to Fe^{3+} than with CN^-, thus preventing it from being fully abstracted by EDTA.

2.1.20 Job's plot analysis

The Job's plot relationship between quencher mole fraction and emissive output was plotted for ascending and descending amounts of CN^- whilst keeping the total molar concentration constant. Results show a 1:1 binding ration between **A1** and CN^-. This confirms what was suggested by the linearity of the Benesi-Hildebrand plot. The Jobs plot of **A1** with CN^- is shown in **Figure 47**.

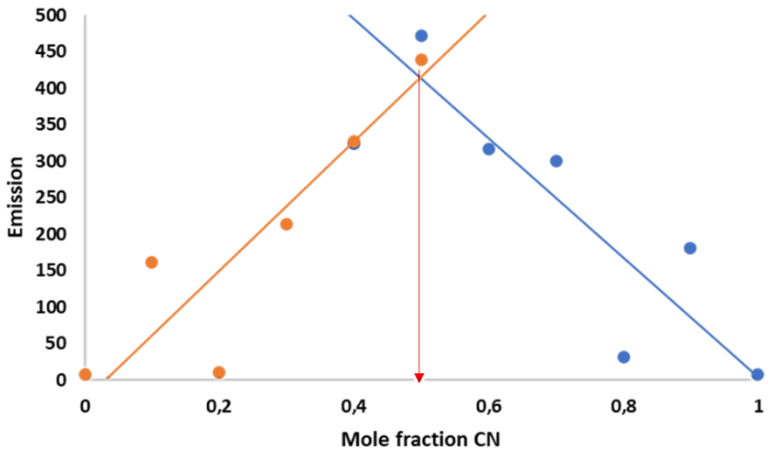

Figure 47: Job's Plot of **A1** with CN^- in water.

2.1.21 UV/Vis titration data of A1 with CN^-

The UV-Vis titration of **A1** with CN^- in acetonitrile is shown in **Figure 48**. Visibly, the titration yielded the formation of what appears to be two isosbestic points at 313 and 368 nm. The formation of these isosbestic points may suggest the fluorescent quenching mechanism that **A1** follows is that of an ICT, FRET or PET process. Isosbestic points could also be indicative of conversion of one species to another species via a chemical equilibrium or that complexation between **A1** and CN^- is occurring.[54,55]

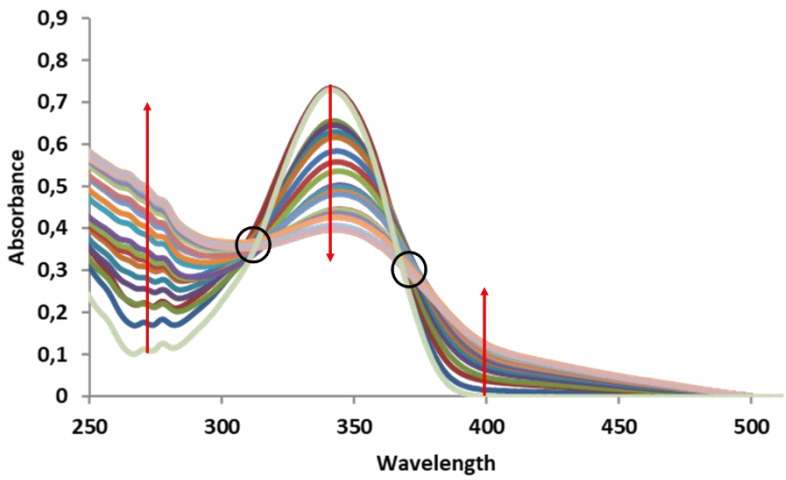

Figure 48: UV-Vis spectra of **A1**-CN^- titration in acetonitrile. Black circles indicate isosbestic points

The appearance of two isosbestic points in absorbance spectra could indicate two chemical equilibriums, notably the formation of the **A1**-CN^- complex and that of free **A1** and CN^- ions in solution.[56] Upon analyte addition there is no shift in wavelength between peak maxima. A shift in absorbance peak maxima indicates the occurrence of a charge transfer process.[57] In addition, the structure of the sensor **A1** does not favour an ICT fluorescent mechanism. Structural characteristics of ICT type quenching systems require a fluorophore-spacer-receptor framework.[58] The fluorophore of **A1** is linked directly into the triazole unit without the presence of a spacer, therefore the appearance of these isosbestic points does not infer an ICT quenching mechanism.

The involvement of FRET as the main fluorescent quenching mechanism was investigated by structural evaluation using the definition of FRET sensors and by spectral overlap studies. FRET (Fluorescent Resonance Energy Transfer) involves energy transfer between a pair of fluorophores that act as energy donors and acceptors, respectively. This is a distance-dependent interaction between the electronic excited states of two different fluorophores in which electrons are transferred from a donor moiety to an acceptor moiety without photoemission. The efficiency of this process is determined by the degree of spectral overlap and the distance between the acceptor and donor fluorophores.[59,60] Good spectral overlap between the absorption and emission bands indicate effective FRET.[61] **Figure 49** shows the normalized emission and absorbance spectra of **A1** in the absence of CN^-.

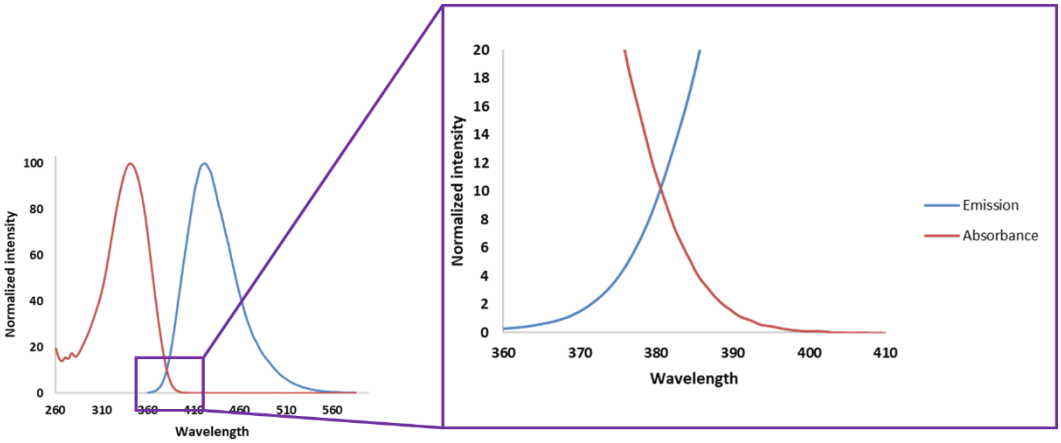

Figure 49: Normalized absorbance (red) and emission (blue) of free **A1** in water. Expanded area shows the area of spectral overlap.

A very small region of spectral overlap is identified; therefore, the efficiency of the FRET process is unlikely. In addition, the structure of **A1** does not support the likelihood of this process. As stated previously, FRET mechanisms occur when two fluorophores are connected via spacer groups or covalent bonding. The only fluorophore present in sensor **A1** is the coumarin molecule. The triazole moiety at position -3- is known to enhance fluorescence but on its own it does not fluoresce. Therefore, it can be postulated that the appearance of the isosbestic points at 313 and 368 nm is due to two chemical equilibria taking place simultaneously in solution. The fluorescent quenching mechanism takes place via a PET turn-off mechanism, not unlike that between **A1** and Fe^{3+}. The value of K_a in the **A1**-CN^- complex was calculated as 1.4×10^3 M^{-1}. This suggests that the quenching of CN^- to **A1** is unlikely to occur by CHQF, unlike that of **A1** with Fe^{3+}. This interaction may occur through weaker covalent interactions like hydrogen bonding.

2.1.22 Investigation of the binding site of A1 with CN^-

Triazole based sensors are popular in analyte sensing due to their ability to form bonds with both cations and anions alike,[62] and can exhibit versatile coordination modes upon complexation.[63] Hydrogen bonding has become a key asset in anion recognition. Anionic sensing is possible by their ability to interact with N-H and C-H hydrogen bearing groups. Hydrogen bonding sensing strategies show greater prevalence than other non-covalent interactions.[64,65] Hydrogen bonding between sensor and analyte in 1,2,3-triazoles is as a result of the high dipole moment which permits them to form hydrogen bonds with the guest entity. The proton of triazole ring shows weak hydrogen bond donating ability with anions.[66]

To determine whether the presence of the 1,2,3-triazole functionality contributes towards complexation, titration of CN^- with a stock Herniarin solution (**H1**) was investigated. **Figure 50** displays this titration study. Clearly, negligible fluorescent quenching occurs in the absence of the triazole moiety, therefore, this heterocyclic ring structure is essential for the sensing of **A1** towards CN^-.

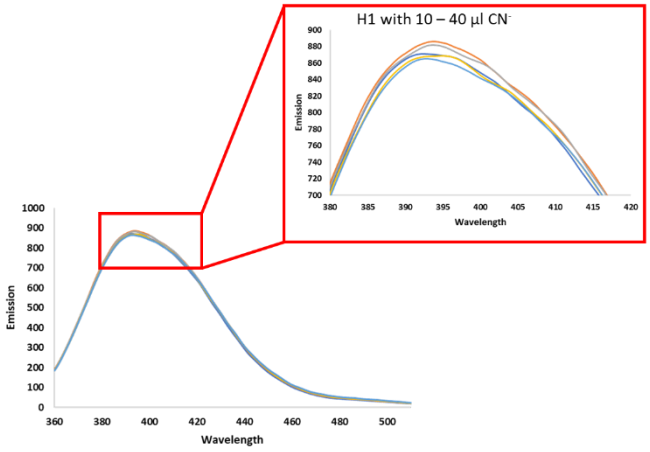

Figure 50: Herniarin titration with equal aliquots of a 0.01M solution CN^-. Excitation of 340nm.

^{1}H NMR titration studies were conducted to evaluate the proposed hydrogen-bonding between the proton on the triazole ring and the CN^- anion. A 1M solution of KCN dissolved in water was used for the titration experiment. The analysis was run with water suppression to negate the proton signals associated with water. Additionally, it was previously determined that K^+ had no sizeable effect on the fluorescent emission of **A1**, therefore, it would not

interfere in any NMR analysis. The titration of **A1** with aliquots of KCN is shown in **Figure 51**.

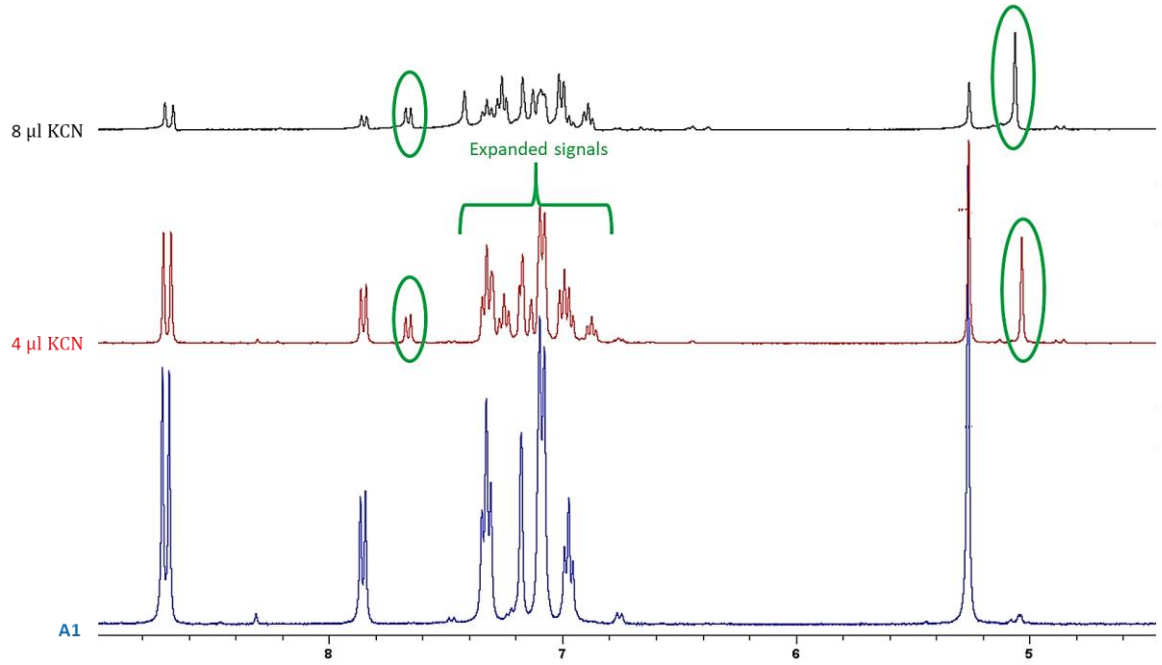

Figure 51: ^{1}H NMR titration of **A1** with aliquots of a KCN (aq) solution in d_6-DMSO.

The ^{1}H NMR titration results show noticeable shifts of two signals. The signals observed were a singlet and a doublet. Furthermore, the addition of KCN has "expanded" the signal region between 6.8 and 7.2 ppm. These signals correspond to the protons present on the coumarin fluorophore, triazole, and neighbouring phenyl group attached to the 1,2,3-triazole functionality. The protons on the coumarin fluorophore are too distant to take part in effective coordination, therefore, these two proton signals must arise from the triazole- and phenyl-proton interactions with CN^-. The singlet is postulated to derive from the triazole ring hydrogen, whilst the doublet is thought to arise from a proton on the phenyl substituent. The triazole proton was unable to be identified before KCN addition due to the signal overlap in the region of 7-8 ppm. Evidently, the shift of the postulated triazole proton is substantially greater than that of the phenyl proton. This substantial shift indicates that the proton of 1,2,3-triazole has a greater contribution towards anionic hydrogen bonding.

The substantial upfield shift of the triazole proton indicates the good shielding nature of the electronic interaction, whilst the downfield shift of the phenyl doublet indicates the deshielding nature of this interaction. These interactions can be explained when the binding interaction of **A1** with CN^- is investigated.

The cyanide anion is referred to as an ambident nucleophile or anion. This implies that the total negative anionic charge resides over both the carbon and nitrogen atoms through resonance.[67] The electronegative nature of the nitrogen atoms result in an electron shift through the triple bond forming a partial negative charge on the nitrogen atom. The carbon atom will therefore hold a corresponding partial positive charge. The electron donating capability of the nitrogen will contribute towards the shielding of the triazole proton signal, whilst the doublet associated with the phenyl hydrogen is deshielded due to the electron withdrawing effect of the partial positive charge created on the cyanide carbon atom. However, the extent to which these signals are shielded or deshielded is not equal. Evidently, the triazole proton is more extensively shielded than that of the deshielded phenyl proton signal. This suggests that during this binding scenario, the total negative charge of the CN anion shifts in favour of the nitrogen atom and is the predominant contributor towards triazole-hydrogen bonding. The interaction of the cyanide carbon and hydrogen of the phenyl ring serves to stabilize the complex but is not the predominant contributor towards complexation. The total valency of this stabilized complex will be 0 and no longer -1. The proposed binding scenario of **A1** with cyanide is shown in **Figure 52**.

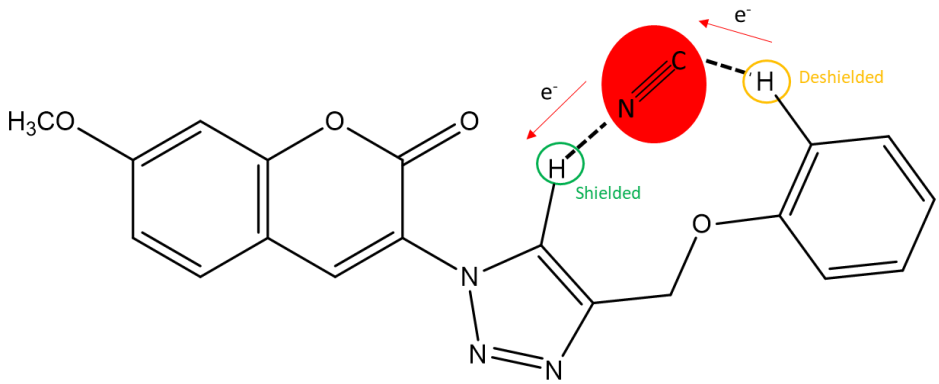

Figure 52: Proposed binding scenario of **A1** with cyanide according to the ^{1}H NMR titration data. Electron density resides predominantly on the nitrogen atom of cyanide species.

Additionally, a visible colour change upon CN^- titration with **A1** in d_6-DMSO was observed (**Figure 53**).

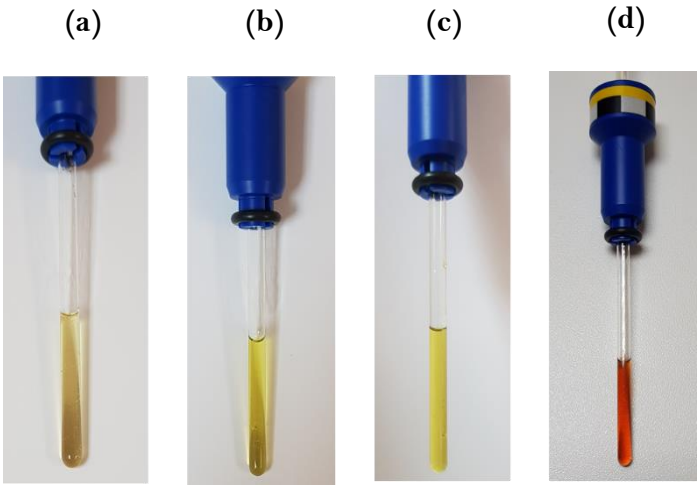

Figure 53: Changes in colour upon KCN addtion to **A1** in d_6-DMSO after a) no analyte, b) 4 µl, c) 8 µl, and d) 8 µl CN^- left for 24 hrs.

The number of binding sites as seen from **Figures 51** & **52** was confirmed using the double logarithm plot of Log[(F$_o$-F)/F] vs Log[CN]. This equation applies only towards systems that undergo static modes of quenching upon analyte addition. The value of the slope gives an indication of the number of binding sites (n).[68,69] This data was fitted by use of the titration results of **A1** with CN^- in water. The double logarithm plot of the static quenching is shown in **Figure 54**.

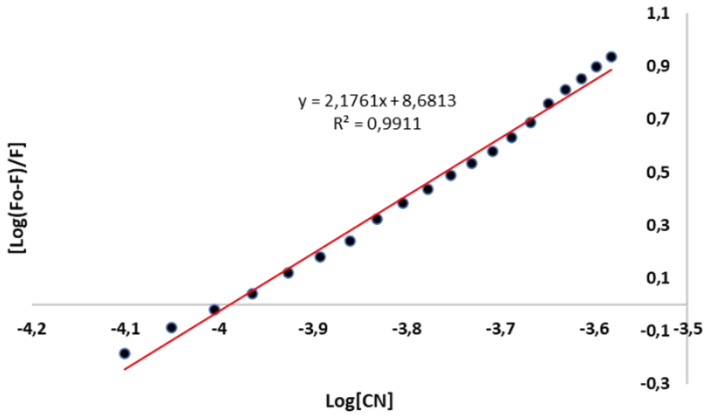

Figure 54: Double logarithm plot of **A1** with CN^- in water. Excitation of 340nm.

The value of the number of binding sites is shown to equal to 2 (n=2). This confirms what was observed in the ^{1}H NMR titration of **A1** with KCN. As previously mentioned, the value of the association constant (K_a) as determined by the Benesi-Hildebrand plot was ten times lower than that of **A1** with Fe^{3+}. This supports the involvement of hydrogen bonding as the main type of coordination method as weaker bonds are to be expected.

Molecular modelling studies of the binding scenario of **A1** towards CN^- was investigated, although to a lesser degree to that of **A1** with Fe^{3+}. Calculations of most energetically preferred conformation was calculated to determine the lowest energy conformer of **A1** with cyanide at the density-functional theory level. Notably, the most energetically preferred conformer agrees well with the postulated binding site scenario from the ^1H NMR titration analysis. The most preferred conformer indicates the involvement of the triazole proton with the nitrogen atom of cyanide, whilst the phenyl proton is calculated to interact with the cyanide carbon atom. In addition, hydrogen bond calculations indicated that hydrogen bonding should theoretically occur. This agrees well with what has already been shown (**Figure 55**).

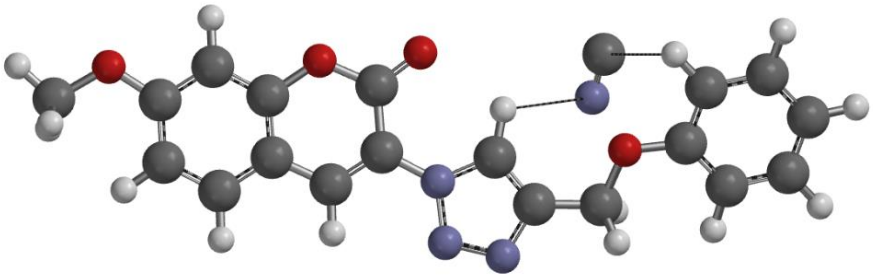

Figure 55: Most energetically preferred conformer of **A1** and cyanide according to density-functional theory level (DFT B3LYP/6-31G).

2.2 Conclusion

Herein, two novel coumarin-triazole based sensors for the purpose of cation and anion recognition in aqueous and organic solvent systems are reported. These sensors differ by their functionalities attached at the -7- position on the coumarin fluorophore. The sensor exhibiting the greatest fluorescent response upon cation addition was methoxy-derived sensor **A1** with Fe^{3+}. In addition, this sensor displayed greater selectivity towards Fe^{3+} in the presence of competing metal cations than that of the hydroxy derivative **A2**. The calculated quantum yield of **A1**, with anthracene as reference, was determined to be 0.71. With respect to anionic sensing studies, **A1** did not display the same degree of selectivity towards CN^- as it did towards Fe^{3+}. However, **A1** was titrated with cyanide to determine its possible sensing capabilities as a cyanide-specific sensor.

Results show that both Fe^{3+} and CN^- produced quenching responses upon analyte addition. The main modes of fluorescent quenching were shown to occur by static processes, namely, the Perrin and Sphere of Action quenching models. The lack of observable shift upon analyte titration for both **A1**-Fe^{3+} and CN^- complexes in both emission and absorbance studies indicate the mechanism of quenching occurs via a PET-off type quenching process. The PET quenching process of **A1** with Fe^{3+} further occurs via CHQF. This was not noted in the **A1**-CN^- complexation due to the observable weaker hydrogen bonding. The detection limits of **A1** towards Fe^{3+} and CN^- were determined to be 1,4 and 6,7 μM respectively. Binding was found to occur in a 1:1 ration with complexation occurring predominantly via the triazole nitrogen atom in the **A1**-Fe^{3+} complex, and the triazole proton in the **A1**-CN^- complex. In addition, the sensing of **A1** with Fe^{3+} was determined to be possible in a variety of differing pH solutions.

2.3 Experimental

2.3.1 Measurements

All starting materials and solvents were purchased from Sigma Aldrich or Merck and used as received without further purification unless stated. ^{1}H NMR and ^{13}C NMR spectra were recorded on a Bruker Advance DPX 400 (400 MHz) spectrometer. The NMR samples were prepared in deuterated solvents ($CDCl_3$ and DMSO-d_6). The samples were run at room temperature. Coupling constants (*J*) are given in Hz, whilst chemical shifts are expressed in parts per million (ppm) using TMS as internal reference. Infrared FT-IR spectra were recorded on a Bruker TENSOR 27 FT-IR spectrometer. Column chromatography was performed using silica gel (particle size 0.040-0.063 mm) while thin layer chromatography (TLC) analyses was performed on pre-coated silica gel 60 F254 aluminium sheets (0.063-0.2 mm/70 - 230 mesh); compounds were detected by observation under UV light and/or exposure to iodine vapour. The emission spectra were recorded at room temperature using a Perkin Elmer LS 45 fluorescence spectrophotometer and a 1 cm quartz cell. UV-Vis absorbance studies were recorded on a Shimadzu UV-3100 spectrophotometer with a 1 cm glass cell. Single crystal X-ray diffraction analyses were performed at 200 K using a Bruker Kappa Apex II diffractometer with monochromated Mo Kα radiation (λ = 0.71073 Å). APEX2 software was used for data collection and SAINT for cell refinement and data reduction.[70] Data was corrected for absorption effects using the numerical method implemented in SADABS.[71] The structures were solved using SHELXT–2018/2 using a dual-space algorithm and refined by least-squares procedures using SHELXL-2018/3 with SHELXLE as a graphical interface.[71,72] Stock solutions of the sensors were prepared by dissolving the samples in acetonitrile and diluting them to the desired concentrations. Computational analysis was utilized as a means of verification between theoretical and experimental results. Calculations of the most energetically preferred conformation (DFT B3LYP/6-31G), sensor-metal bond energies and EDTA-metal bond energies (Molecular Mechanics MMFF) were conducted to verify the trends observed. Computations were conducted using Spartan '10 V1.10 software. Molecular Orbital Energy calculations including HOMO and LUMO computations were calculated using Gaussian software (basis set: aug-cc-pVDZ).

2.3.2 Materials

Stock solutions of triazolyl-coumarin derivatives **A1** and **A2** were prepared by dissolving the respective samples in 25 mL of acetonitrile to afford a final stock concentration of 0.001 M. Deionized water was used to prepare solutions of metal ions to the concentration of 0.01 M which were diluted further to their desired concentrations. All metal ion solutions were prepared from their nitrate salts, apart from Fe^{2+} which was prepared from its corresponding sulfate. Anionic solutions were prepared in water from their ammonium salts to the desired concentration and diluted as required. The emission and absorbance titration experiments were performed in 3 mL quartz and glass cuvettes respectively using diluted solutions of compounds **A1** and **A2**. Spectroscopic measurements were performed after each aliquot of selected cationic and anionic solutions.

Synthesis of 3-azidocoumarin derivative 1

3-Azidocoumarin derivatives **1a-c** were synthesized according to literature procedures.[1]

Synthesis of 1-(prop-2-ynyloxy)benzene 2

A solution of phenol (5g, 53 mmol) and K_2CO_3 (14.7g, 106 mmol) in dry acetone (50 mL) was refluxed under nitrogen atmosphere for 4 hours to afford sodium alkoxide ions *in situ*. The reaction mixture was cooled to room temperature and propargyl bromide (6.32g, 53 mmol) was added dropwise. The resulting mixture was left to stir at room temperature for 24 hours. The solvent was removed under reduced pressure and the residue dissolved in water and extracted with ethyl acetate (3 x 40 ml). The extracts were combined and dried over anhydrous Na_2SO_4. Ethyl acetate was removed under reduced pressure. The crude product was purified by column chromatography using hexane: ethyl acetate (80:20) as eluent to afford the pure product as a light-yellow oil (4.23 g, 60%). ^{1}H NMR: ($CDCl_3$, 400MHz) δ_H: 2.56 (s, 1H), 4.73 (s, 2H), 7.05 (m, 3H), 7.36 (t, 2H, *J* 7.6). ^{13}C NMR ($CDCl_3$, 100.6 MHz) δ_C: (75.52, C-1), (78.71, C-2), (55.77, C-3), (157.60, C-4), (114.96, C-5), (129.52, C-6), (121.62, C-7). IR ν_{max} (cm^{-1}): 3290 (alkyne C-H), 2116 (alkyne C≡C), 1212 (C-O-C).

Synthesis of triazolyl coumarin sensors A1 & A2

A mixture of coumarin-azide derivatives **1a-c** (0.3g, 148 mmol (OH); 0.3g, 138 mmol (OCH_3); 0.3 g, 99 mmol (CO_2Et)), 1-(prop-2-ynyloxy)benzene **2** (0.3g, 227 mmol), $CuSO_4.5H_2O$ (0.01g, 0.05 mmol), sodium ascorbate (0.02g, 0.10 mmol) and N,N,N′,N″,N″-pentamethyldiethylenetriamine (PMDETA) (0.02g, 0.10 mmol) in THF (20 mL) was stirred at room temperature for 48 hrs. The solvent was evaporated under vacuum and the residue dissolved in ethyl acetate (30 mL), washed with water (3x30ml) and dried over anhydrous Na_2SO_4. The organic layer was evaporated under vacuum and crude product purified by recrystallization from DCM (5 mL) and petroleum ether (40 mL) to yield coumarin-triazolyl derivatives **A1** (0.297 g, 62%) and **A2** (0.119 g, 24%). Compound **A1:** ^{1}H NMR: (CD_3CN, 400MHz) δ_H: 3.94 (s,3H), 5.26 (s, 2H), 7.04 (m, 5H), 7.35 (t, 2H, *J* 7.3), 7.72 (d, 1H, *J* 8.5), 8.49 (s, 1H), 8.55 (s,1H). ^{13}C NMR (DMSO-d_6, 100.6 MHz) δ_C: 56.67, 61.11, 101.19, 111.94, 114.02, 115.17, 120.65, 121.39, 125.97, 130.00, 131.10, 136.46, 143.47, 155.03, 156.69, 158.45, 163.91. Compound **A2**: ^{1}H NMR: (DMSO-d_6, 400MHz) δ_H: 5.25 (s, 2H), 6.94 (m, 5H), 7.08 (d, 2H, *J* 7.8), 7.32 (t, 2H, *J* 7.32), 7.75 (d, 1H, *J* 8.2), 8.61 (s, 1H), 8.68 (s, 1H), 10.91 (s, 1H). ^{13}C NMR (DMSO-d_6, 100.6 MHz) δ_C: 61.12, 102.64, 110.79, 114.77, 115.16, 119.75, 121.38, 125.99, 130.00, 131.45, 136.98, 143.41, 155.15, 156.80, 158.45, 162.96.

2.4 References

(1) Sivakumar, K.; Xie, F.; Cash, B. M.; Long, S.; Barnhill, H. N.; Wang, Q. A Fluorogenic 1 , 3-Dipolar Cycloaddition Reaction of 3-Azidocoumarins And. *Org. Lett.* **2010**, *6* (24), 4603–4606. https://doi.org/10.1021/ol047955x.

(2) Mandoli, A. *Recent Advances in Recoverable Systems for the Copper-Catalyzed Azide-Alkyne Cycloaddition Reaction (CuAAC)*; 2016; Vol. 21. https://doi.org/10.3390/molecules21091174.

(3) Shneine, J. K.; Alaraji, Y. H. Chemistry of 1, 2, 4-Triazole: A Review Article. *Int. J. Sci. Res.* **2016**, *5* (3), 1411–1423. https://doi.org/10.21275/v5i3.nov161902.

(4) Al-radadi, N. S.; Zayed, E. M.; Mohamed, G. G.; Abd, H. A.; Salam, E. Synthesis, Spectroscopic Characterization, Molecular Docking, and Evaluation of Antibacterial Potential of Transition Metal Complexes Obtained Using Triazole Chelating Ligand. *J. Chem* **2020**, *2020*, 1–12.

(5) Zhang, J.; Pang, Z.; Dong, C. Synthesis and Spectral Studies of Coumarin Derivatives as Fluorescent Probes. **2020**, *59* (July), 895–903.

(6) Bhalekar, S. B.; Bhagwat, A. A.; Sekar, N. Orange-Red Fluorescent (Partially Rigidified) Donor-π-(Rigidified)-Acceptor System – Computational Studies. *J. Fluoresc.* **2020**, *30* (3), 565–579. https://doi.org/10.1007/s10895-020-02506-1.

(7) Sato, K.; Sato, R.; Iso, Y.; Isobe, T. Surface Modification Strategy for Fluorescence Solvatochromism of Carbon Dots Prepared from: P -Phenylenediamine. *Chem. Commun.* **2020**, *56* (14), 2174–2177. https://doi.org/10.1039/c9cc09333h.

(8) Yadav, S. B.; Sonvane, S. S.; Sekar, N. Novel Blue-Green Emitting NLOphoric Triphenylamine-Imidazole Based Donor-π-Acceptor Compound: Solvatochromism, DFT, TD-DFT and Non-Linear Optical Studies. *Spectrochim. Acta - Part A Mol. Biomol. Spectrosc.* **2020**, *224*, 117421. https://doi.org/10.1016/j.saa.2019.117421.

(9) Ray, A.; Bhattacharya, S. Study of Alloyed Quantum Dots-Porphyrazine Interaction in Solution. *J. Mol. Liq.* **2020**, *299*, 112168. https://doi.org/10.1016/j.molliq.2019.112168.

(10) Ramamurthy, K.; Ponnusamy, K.; Chellappan, S. Excitation-Resolved Area-

Normalized Emission Spectroscopy: A Rapid and Simple Steady-State Technique for the Analysis of Heterogeneous Fluorescence. *RSC Adv.* **2019**, *10* (2), 998–1006. https://doi.org/10.1039/c9ra10154c.

(11) Basu, N.; Mandal, D. Time-Dependent Emission Stokes Shift in Au, Ag and Au/Ag Fluorescent Nanoclusters: Evidence of Multiple Emissive States. *Photochem. Photobiol. Sci.* **2019**, *18* (7), 1782–1792. https://doi.org/10.1039/c8pp00540k.

(12) Ray, A.; Sengupta, S.; Chattopadhyay, N. Concurrent Ground and Excited State Proton Transfer of (E)-2-((Napthalen-2-Ylimino)-Methyl)Phenol: Modulation in Micellar Media. *J. Photochem. Photobiol. A Chem.* **2019**, *371*, 433–443. https://doi.org/10.1016/j.jphotochem.2018.11.026.

(13) dos Santos, C. M. G.; McCabe, T.; Gunnlaugsson, T. Selective Fluorescent Sensing of Chloride. *Tetrahedron Lett.* **2007**, *48* (18), 3135–3139. https://doi.org/10.1016/j.tetlet.2007.03.061.

(14) Park, S. H.; Kwon, N.; Lee, J. H.; Yoon, J.; Shin, I. Synthetic Ratiometric Fluorescent Probes for Detection of Ions. *Chem. Soc. Rev.* **2020**, *49* (1), 143–179. https://doi.org/10.1039/c9cs00243j.

(15) Zhang, Z.; Wang, C.; Zhang, Z.; Luo, Y.; Sun, S.; Zhang, G. Cd(II) Enhanced Fluorescence and Zn(II) Quenched Fluorescence with Phenylenevinylene Terpyridine: A Theoretical Investigation. *Spectrochim. Acta - Part A Mol. Biomol. Spectrosc.* **2019**, *209* , 40–48. https://doi.org/10.1016/j.saa.2018.10.022.

(16) Puthiyedath, T.; Bahulayan, D. A Click Derived Triazole-Coumarin Derivative as Fluorescence on-off PET Based Sensor for $Ca^{2+}$and Fe^{3+} Ions. *Sensors Actuators, B Chem.* **2018**, *272*, 110–117. https://doi.org/10.1016/j.snb.2018.05.126.

(17) Kowser, Z.; Rayhan, U.; Akther, T.; Redshaw, C.; Yamato, T. A Brief Review on Novel Pyrene Based Fluorometric and Colorimetric Chemosensors for the Detection of Cu^{2+} . *Mater. Chem. Front.* **2021**, 2173–2200. https://doi.org/10.1039/d0qm01008a.

(18) Fateh, F.; Yildirim, A.; Bhatti, A. A.; Yilmaz, M. A New Benzothiazin-Functionalized Calix[4]Arene-Based Fluorescent Chemosensor for the Selective Detection of Co^{2+} Ion. *J. Fluoresc.* **2021**, 1075–1083. https://doi.org/10.1007/s10895-021-02745-w.

(19) Goswami, S.; Aich, K.; Das, A. K.; Manna, A.; Das, S. A Naphthalimide-Quinoline Based Probe for Selective, Fluorescence Ratiometric Sensing of Trivalent Ions. *RSC Adv.*

2013, *3* (7), 2412–2416. https://doi.org/10.1039/c2ra22624c.

(20) Maity, D.; Kumar Mandal, S.; Guha, B.; Roy, P. A Salicylaldehyde Based Dual Chemosensor for Zinc and Arsenate Ion Detection: Biological Application. *Inorganica Chim. Acta* **2021**, *519*, 120258. https://doi.org/10.1016/j.ica.2021.120258.

(21) Thipperudrappa, J.; Hanagodimath, S. M. Fluorescence Quenching of 1,4-Bis [2-(2-Methylphenyl)Ethenyl] -Benzene By Aniline in Benzene-Acetonitrile Mixtures. *Int. J. Life Sci. Pharma Res.* **2013**, *3* (1), 77–87.

(22) Diana E. Schlamadinger, Dina I. Kats, and J. E. K. Quenching of TryptophanFluorescence in Unfolded Cytochrome c: A Biophysics Experiment for Physical Chemistry Students. *J. Chem. Educ.* **2010**, *87* (9), 961–964.

(23) Panda, M.; Chandel, T. I.; Kamil, M.; Khan, R. H. Fluorescence Quenching of Chloroquine by Cu^{2+} in Micelles. *J. Mol. Liq.* **2020**, *306*, 112763. https://doi.org/10.1016/j.molliq.2020.112763.

(24) Perrin, F. C. R. No Title. *Acad. Sci. Paris* **1924**, *178*, 1978.

(25) Chen, H.; Xiao, T.; Ning, Z.; Li, Q.; Xiao, E.; Liu, Y.; Xiao, Q.; Lan, X.; Ma, L.; Lu, F. In-Situ Remediation of Acid Mine Drainage from Abandoned Coal Mine by Filed Pilot-Scale Passive Treatment System: Performance and Response of Microbial Communities to Low PH and Elevated Fe. *Bioresour. Technol.* **2020**, *317*, 123985. https://doi.org/10.1016/j.biortech.2020.123985.

(26) Vélez-Pérez, L. S.; Ramirez-Nava, J.; Hernández-Flores, G.; Talavera-Mendoza, O.; Escamilla-Alvarado, C.; Poggi-Varaldo, H. M.; Solorza-Feria, O.; López-Díaz, J. A. Industrial Acid Mine Drainage and Municipal Wastewater Co-Treatment by Dual-Chamber Microbial Fuel Cells. *Int. J. Hydrogen Energy* **2020**, *45* (26), 13757–13766. https://doi.org/10.1016/j.ijhydene.2019.12.037.

(27) Sun, R.; Zhang, L.; Wang, X.; Ou, C.; Lin, N.; Xu, S.; Qiu, Y. Y.; Jiang, F. Elemental Sulfur-Driven Sulfidogenic Process under Highly Acidic Conditions for Sulfate-Rich Acid Mine Drainage Treatment: Performance and Microbial Community Analysis. *Water Res.* **2020**, *185*, 116230. https://doi.org/10.1016/j.watres.2020.116230.

(28) Sumrra, S. H.; Sahrish, I.; Raza, M. A.; Ahmad, Z.; Zafar, M. N.; Chohan, Z. H.; Khalid, M.; Ahmed, S. Efficient Synthesis, Characterization, and in Vitro Bactericidal Studies of Unsymmetrically Substituted Triazole-Derived Schiff Base Ligand and Its

Transition Metal Complexes. *Monatshefte fur Chemie* **2020**, *151* (4), 549–557. https://doi.org/10.1007/s00706-020-02571-z.

(29) Schlagintweit, J. F.; Dyckhoff, F.; Nguyen, L.; Jakob, C. H. G.; Reich, R. M.; Kühn, F. E. Mixed Tetradentate NHC/1,2,3-Triazole Iron Complexes Bearing Cis Labile Coordination Sites as Highly Active Catalysts in Lewis and Brønsted Acid Mediated Olefin Epoxidation. *J. Catal.* **2020**, *383*, 144–152. https://doi.org/10.1016/j.jcat.2020.01.011.

(30) Snyder, E. M.; Chowdhury, M. S. I.; Morrow, J. R. Co(II) and Fe(II) Triazole-Appended 4,10-Diaza-15-Crown-5-Ether Macrocyclic Complexes for CEST MRI Applications. *Inorganica Chim. Acta* **2020**, *509*, 119649. https://doi.org/10.1016/j.ica.2020.119649.

(31) Saiyasombat, W.; Kiatisevi, S. Bis-BODIPY Linked-Triazole Based on Catechol Core for Selective Dual Detection of $Ag^{+}$and Hg^{2+}. *RSC Adv.* **2021**, *11* (6), 3703–3712. https://doi.org/10.1039/d0ra09686e.

(32) Singh, G.; Satija, P.; Singh, A.; Pawan; Mohit; Kaur, J. D.; Devi, A.; Saini, A.; Singh, J. Bis-Triazole with Indole Pendant Organosilicon Framework: Probe for Recognition of Pb^{2+} Ions. *J. Mol. Struct.* **2021**, *1231*, 1–7. https://doi.org/10.1016/j.molstruc.2021.129963.

(33) Mulks, F. F.; Hashmi, A. S. K.; Faraji, S. Sesquicarbene Complexes: Bonding at the Interface between M-C Single Bonds and M=C Double Bonds. *Organometallics* **2020**, *39* (10), 1814–1823. https://doi.org/10.1021/acs.organomet.0c00102.

(34) Radhakrishna, L.; Kunchur, H. S.; Namdeo, P. K.; Butcher, R. J.; Balakrishna, M. S. New 1,2,3-Triazole Based Bis- And Trisphosphine Ligands: Synthesis, Transition Metal Chemistry and Catalytic Studies. *Dalt. Trans.* **2020**, *49* (11), 3434–3449. https://doi.org/10.1039/c9dt04302k.

(35) Huang, D.; Zhao, P.; Astruc, D. Catalysis by 1,2,3-Triazole- and Related Transition-Metal Complexes. *Coord. Chem. Rev.* **2014**, *272*, 145–165. https://doi.org/10.1016/j.ccr.2014.04.006.

(36) Ngororabanga, J. M. V.; Tshentu, Z. R.; Mama, N. A New Highly Selective Colorimetric and Fluorometric Coumarin-Based Chemosensor for Hg^{2+}. *J. Fluoresc.* **2020**, No. Lc. https://doi.org/10.1007/s10895-020-02542-x.

(37) Alvillo-Rivera, A.; Garrido-Hoyos, S.; Buitrón, G.; Thangarasu-Sarasvathi, P.; Rosano-

Ortega, G. Biological Treatment for the Degradation of Cyanide: A Review. *J. Mater. Res. Technol.* **2021**, *12*, 1418–1433. https://doi.org/10.1016/j.jmrt.2021.03.030.

(38) Jaszczak, E.; Polkowska, Ż.; Narkowicz, S.; Namieśnik, J. Cyanides in the Environment—Analysis—Problems and Challenges. *Environ. Sci. Pollut. Res.* **2017**, *24* (19), 15929–15948. https://doi.org/10.1007/s11356-017-9081-7.

(39) Fu, J.; Yao, K.; Li, B.; Mei, H.; Chang, Y.; Xu, K. Coumarin-Based Colorimetric-Fluorescent Sensors for the Sequential Detection of Zn2+ Ion and Phosphate Anions and Applications in Cell Imaging. *Spectrochim. Acta - Part A Mol. Biomol. Spectrosc.* **2020**, *228*, 117790. https://doi.org/10.1016/j.saa.2019.117790.

(40) Mohammadi, M.; Shareghi, B.; Farhadian, S.; Saboury, A. A. The Effect of Sorbitol on the Structure and Activity of Carboxypeptidase A: Insights from a Spectroscopic and Computational Approach. *J. Mol. Liq.* **2021**, *330*, 115710. https://doi.org/10.1016/j.molliq.2021.115710.

(41) Gehlen, M. H. The Centenary of the Stern-Volmer Equation of Fluorescence Quenching: From the Single Line Plot to the SV Quenching Map. *J. Photochem. Photobiol. C Photochem. Rev.* **2020**, *42*, 100338. https://doi.org/10.1016/j.jphotochemrev.2019.100338.

(42) Deepa, H. R.; Thipperudrappa, J.; Kumar, H. M. S. Effect of Temperature on Fluorescence Quenching and Emission Characteristics of Laser Dyes. *J. Phys. Conf. Ser.* **2020**, *1473* (1). https://doi.org/10.1088/1742-6596/1473/1/012046.

(43) Koppal, V. V.; Melavanki, R.; Kusanur, R.; Patil, N. R. Analysis of Fluorescence Quenching of Coumarin Derivative under Steady State and Transient State Methods. *J. Fluoresc.* **2021**, *393*–400. https://doi.org/10.1007/s10895-020-02663-3.

(44) Santoshakumar, R. M.; Malatesh, P. S.; Nirupama, M. J.; Ashok, S. H. Fluorescence Quenching of Anthracene by Aniline in Two Solvents: S-V Plot Analysis. *AIP Conf. Proc.* **2020**, *2244*. https://doi.org/10.1063/5.0010245.

(45) Krishnan, S.; Suneesh, C. V. Fluorene – Triazine Conjugated Porous Organic Polymer Framework for Superamplified Sensing of Nitroaromatic Explosives. *J. Photochem. Photobiol. A Chem.* **2019**, *371*, 414–422. https://doi.org/10.1016/j.jphotochem.2018.11.044.

(46) El-Daly, S. A.; Salem, I. A.; Hussein, M. A.; Asiri, A. M. Fluorescence Quenching N,N-

Bis(2,6-Dimethylphenyl)-3,4:9,10-Perylenetetracarboxylic Diimide (BDPD) Laser Dye by Colloidal Silver Nanoparticles. *J. Fluoresc.* **2015**, *25* (2), 379–385. https://doi.org/10.1007/s10895-015-1523-3.

(47) Sheldrick, G.M. Photobiological Sciences Online. *Choice Rev. Online* **2013**, *51* (04), 51-2070-51–2070. https://dx.doi.org/10.5860/choice.51-2070

(48) Airinei, A.; Tigoianu, R. I.; Rusu, E.; Dorohoi, D. O. Fluorescence Quenching of Anthracene by Nitroaromatic Compounds. *Dig. J. Nanomater. Biostructures.* **2011**, *6* (3), 1265–1272.

(49) Vaughns, C. Stern-Volmer Quenching of Conjugated Polymers : A Study of Fluorophore Concentration. Georgia Institute of Technology, School of Chemistry and Biochemistry. **2007**, 1-22.

(50) Sun, C.; Gradzielski, M. Fluorescence Sensing of Cyanide Anions Based On. **2021**, 27–30. https://doi.org/10.1039/d0an01954b.

(51) Wan, H.; Xu, Q.; Gu, P.; Li, H.; Chen, D.; Li, N.; He, J.; Lu, J. AIE-Based Fluorescent Sensors for Low Concentration Toxic Ion Detection in Water. *J. Hazard. Mater.* **2021**, *403*, 123656. https://doi.org/10.1016/j.jhazmat.2020.123656.

(52) Frank, J. M.; Vavilov, S. I. Z.. *Physik* **1931**, *69*, 100.

(53) Rasteniene, A.; Gruskiene, R.; Sereikaite, J. Interaction of Ectoine and Hydroxyectoine with Protein : Fluorescence Study. *Chem. Pap.* **2021**, https://doi.org/10.1007/s11696-021-01527-9.

(54) Punithakumari, G.; Velmathi, S. Triple Action Sensing Behaviour of a Single Receptor for the Detection of Multiple Analytes via Different Approaches. *J. Fluoresc.* **2021**. https://doi.org/10.1007/s10895-021-02700-9.

(55) Hemdan, S. S.; Jebaly, A. M.; Ali, F. Importance of Isosbestic Point in Spectroscopy : A Review Abstract. **2019**. (62).1-22. https://www.researchgate.net/publication/348394084.

(56) Mudi, N.; Hazra, P.; Shyamal, M.; Maity, S.; Giri, P. K.; Samanta, S. S.; Mandal, D.; Misra, A. Designed Synthesis of Fluorescence 'Turn-on' Dual Sensor for Selective Detection of Al^{3+} and Zn^{2+} in Water. *J. Fluoresc.* **2021**, 315–325. https://doi.org/10.1007/s10895-020-02664-2.

(57) Long, L.; Zhou, L.; Wang, L.; Meng, S.; Gong, A.; Du, F.; Zhang, C. A Coumarin-Based Fluorescent Probe for Biological Thiols and Its Application for Living Cell Imaging. *Org. Biomol. Chem.* **2013**, *11* (47), 8214–8220. https://doi.org/10.1039/c3ob41741g.

(58) Zerafa, N.; Cini, M.; Magri, D. C. Molecular Engineering of 1,3,5-Triaryl-2-Pyrazoline Fluorescent Logic Systems Responsive to Acidity and Oxidisability and Attachment to Polymer Beads. *Mol. Syst. Des. Eng.* **2021**, *6* (1), 93–99. https://doi.org/10.1039/d0me00136h.

(59) Zhu, Q.; Li, L.; Mu, L.; Zeng, X.; Redshaw, C.; Wei, G. A Ratiometric Al3+ Ion Probe Based on the Coumarin-Quinoline FRET System. *J. Photochem. Photobiol. A Chem.* **2016**, *328*, 217–224. https://doi.org/10.1016/j.jphotochem.2016.06.006.

(60) Lee, M. H; Kim, J. S; Sessler, J. L. Small Molecule-Based Ratiometric Fluorescence Probes for Cations, Anions, and Biomolecule. *Chem. Soc. Rev.* **2015**, *44* (13), 4185–4191. DOI: 10.1039/c4cs00280f

(61) Chernikova, E. Y.; Grachev, A. I.; Peregudov, A. S.; Fedorova, O. A.; Fedorov, Y. V. Reversible ON-OFF Switching of FRET Effect in the Functionalized CB[6]-Guest Complex via Photoisomerization. *Dye. Pigment.* **2021**, *189*, 109194. https://doi.org/10.1016/j.dyepig.2021.109194.

(62) Ali, I.; Imkan; Ikram, F.; Ahmad, F.; Nisar, J.; Shah, M. R.; Ali, S.; ullah, S.; Althagafi, I. I.; Ateeq, M. Sensing Applications of Triazole Conjugated Silver Nanoparticles. *J. Mol. Struct.* **2021**, *1226*, 129306. https://doi.org/10.1016/j.molstruc.2020.129306.

(63) Amiri, S.; Ghassemzadeh, M.; Neumüller, B.; Mohsenzadeh, F. A New Silver(I) Coordination Polymer Containing Bitopic 1,2,4-Triazole Derivative: Synthesis, Structural Investigation, and Thermal Behavior. *Polyhedron* **2021**, *197*, 115039. https://doi.org/10.1016/j.poly.2021.115039.

(64) Eytel, L. M.; Fargher, H. A.; Haley, M. M.; Johnson, D. W. The Road to Aryl CH···anion Binding Was Paved with Good Intentions: Fundamental Studies, Host Design, and Historical Perspectives in CH Hydrogen Bonding. *Chem. Commun.* **2019**, *55* (36), 5195–5206. https://doi.org/10.1039/c9cc01460h.

(65) Ramachandran, M.; Syed, A.; Marraiki, N.; Anandan, S. The Aqueous Dependent Sensing of Hydrazine and Phosphate Anions Using a Bis-Heteroleptic Ru(Ii) Complex with a Phthalimide–Anchored Pyridine-Triazole Ligand . *Analyst* **2021**, 1430–1443.

https://doi.org/10.1039/d0an02299c.

(66) Rani, P.; Lal, K.; Aruna; Shrivastava, R.; Ghule, V. D. Synthesis and Characterization of 1,2,3-Triazoles-Linked Urea Hybrid Sensor for Selective Sensing of Fluoride Ion. *J. Mol. Struct.* **2020**, *1203*, 127437. https://doi.org/10.1016/j.molstruc.2019.127437.

(67) Perry, W. D.; Vogel, G. C.; Bishop, M. B. Revisited. *J. Chem. Edu.* **1992**, *69*, 222–224.

(68) Ren, S.; Giusti, M. M. Monitoring the Interaction between Thermally Induced Whey Protein and Anthocyanin by Fluorescence Quenching Spectroscopy. *Foods* **2021**, *10* (2), 310. https://doi.org/10.3390/foods10020310.

(69) Gan, Y.; Bai, N.; Li, X.; Gao, S.; Wang, R. A Study of the Binding between Radicicol and Four Proteins by Means of Spectroscopy and Molecular Docking. *J. Chem. Res.* **2021**. https://doi.org/10.1177/1747519821993068.

(70) Bruker. No Title. **2007**, *APEX2, SAI* (Bruker AXS Inc., Madison, Wisconsin, USA.).

(71) Sheldrick, G. M. *Acta Cryst.* **2015**, *A71*, 3–8.

(72) C. B. Hübschle, G. M. Sheldrick., B. D. No Title. *J. Appl. Cryst.* **2011**, *44*, 1281–1284.

APPENDIX A

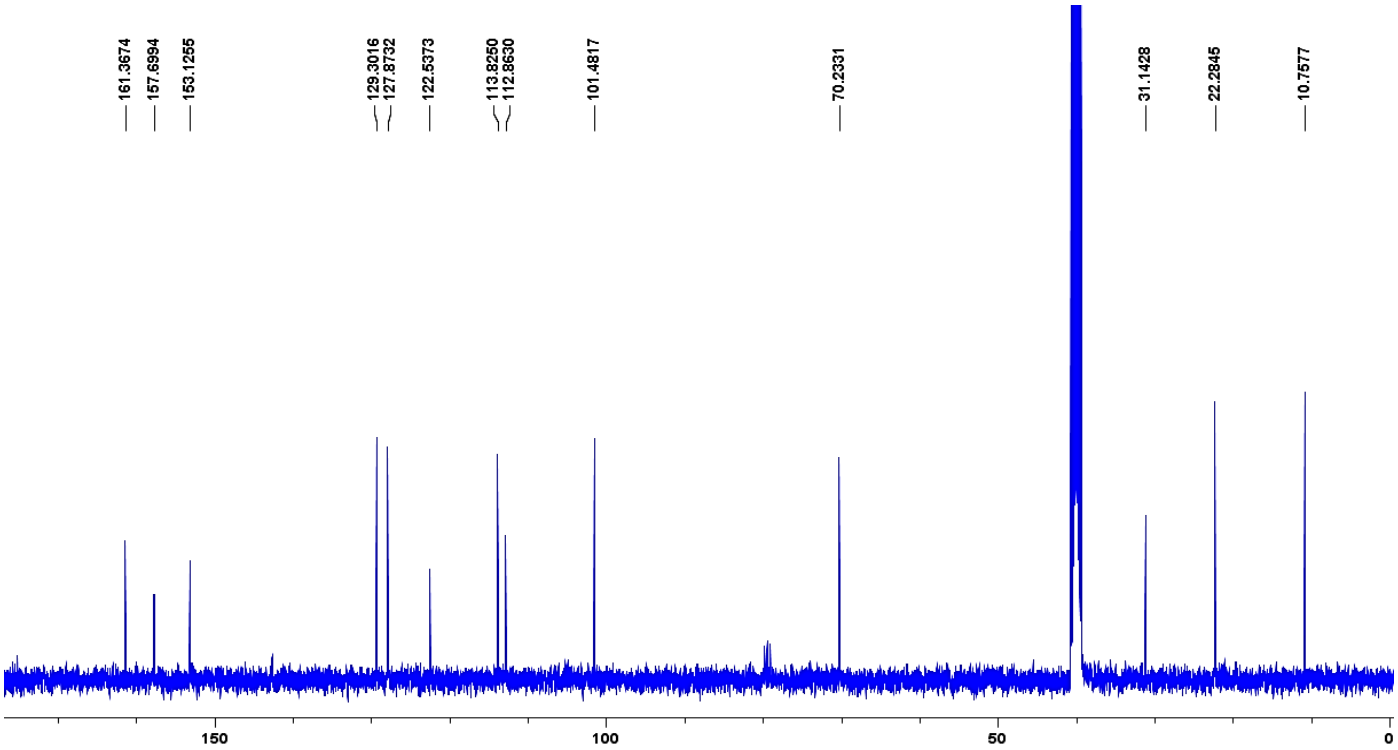

Figure 1: ^{13}C NMR of ether-azide derivative **1b** in d_6-DMSO.

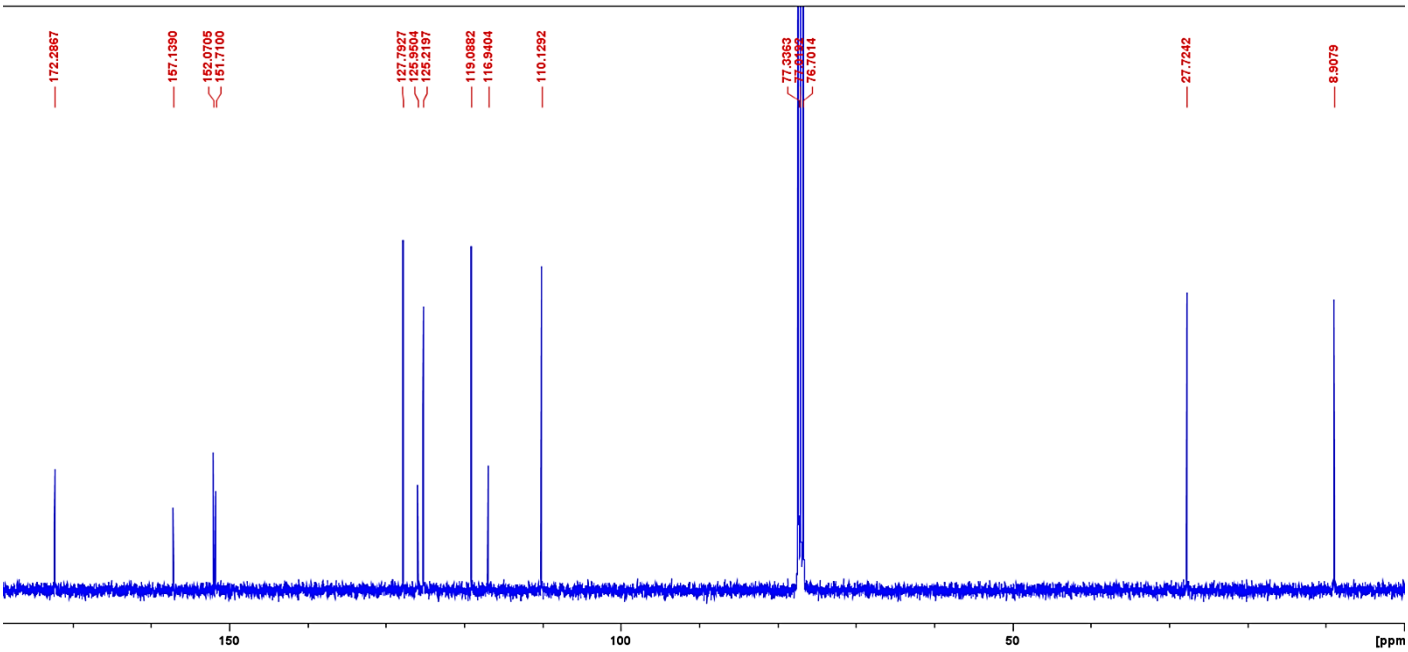

Figure 2: ^{13}C NMR of ester-azide derivative **1c** in d_6-DMSO.

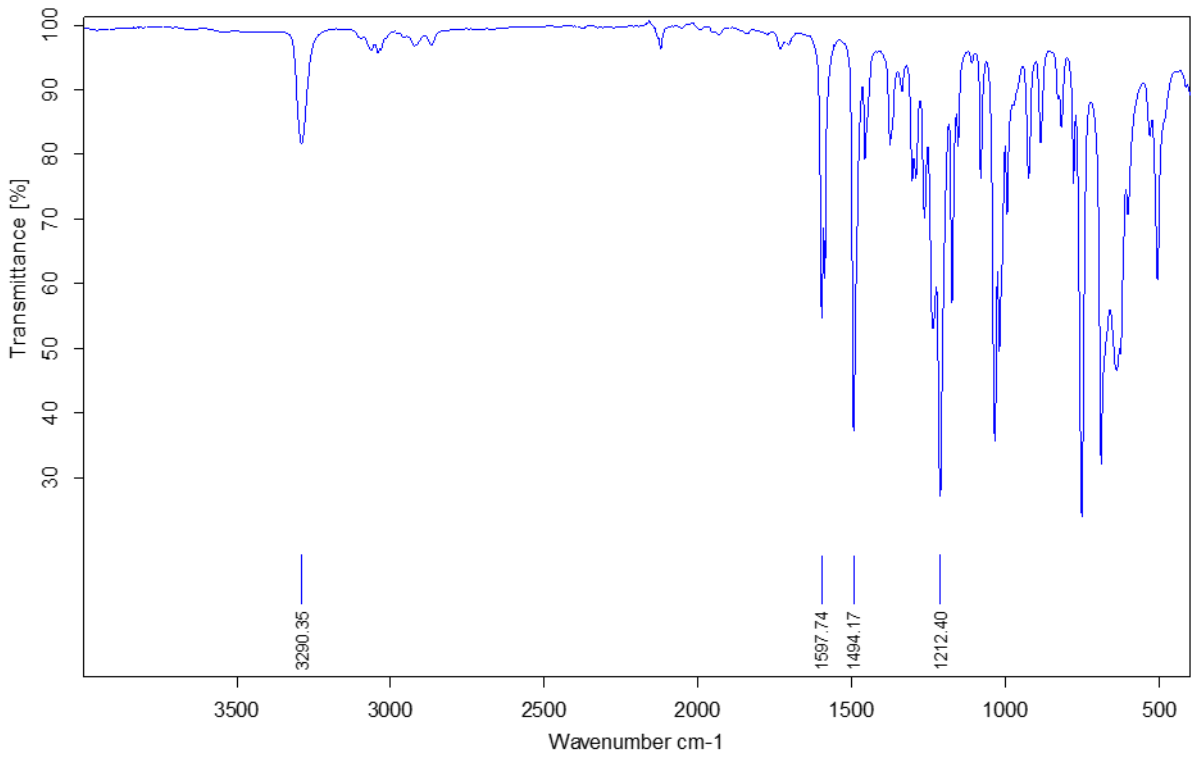

Figure 3: FT-IR spectra of phenol-alkyne derivative **2**.

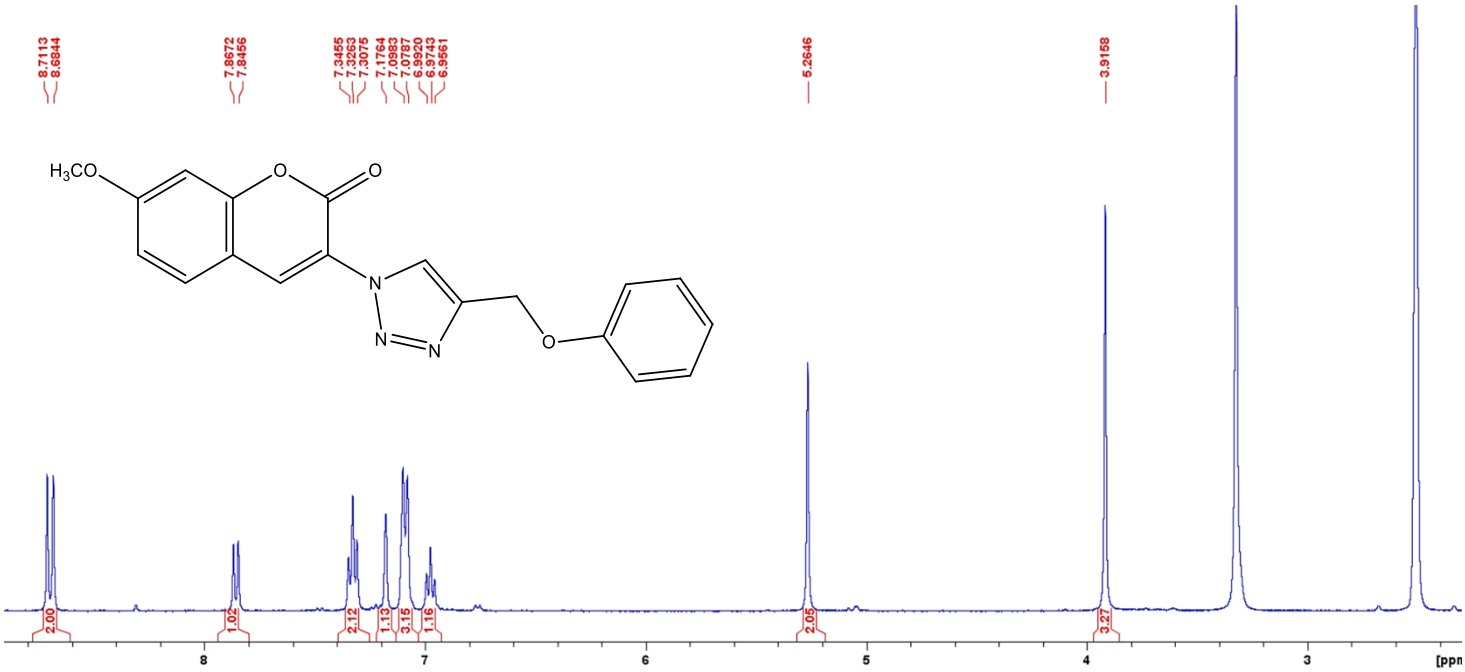

Figure 4: ^{1}H NMR of coumarin-triazole derivative **A1** in d_6-DMSO.

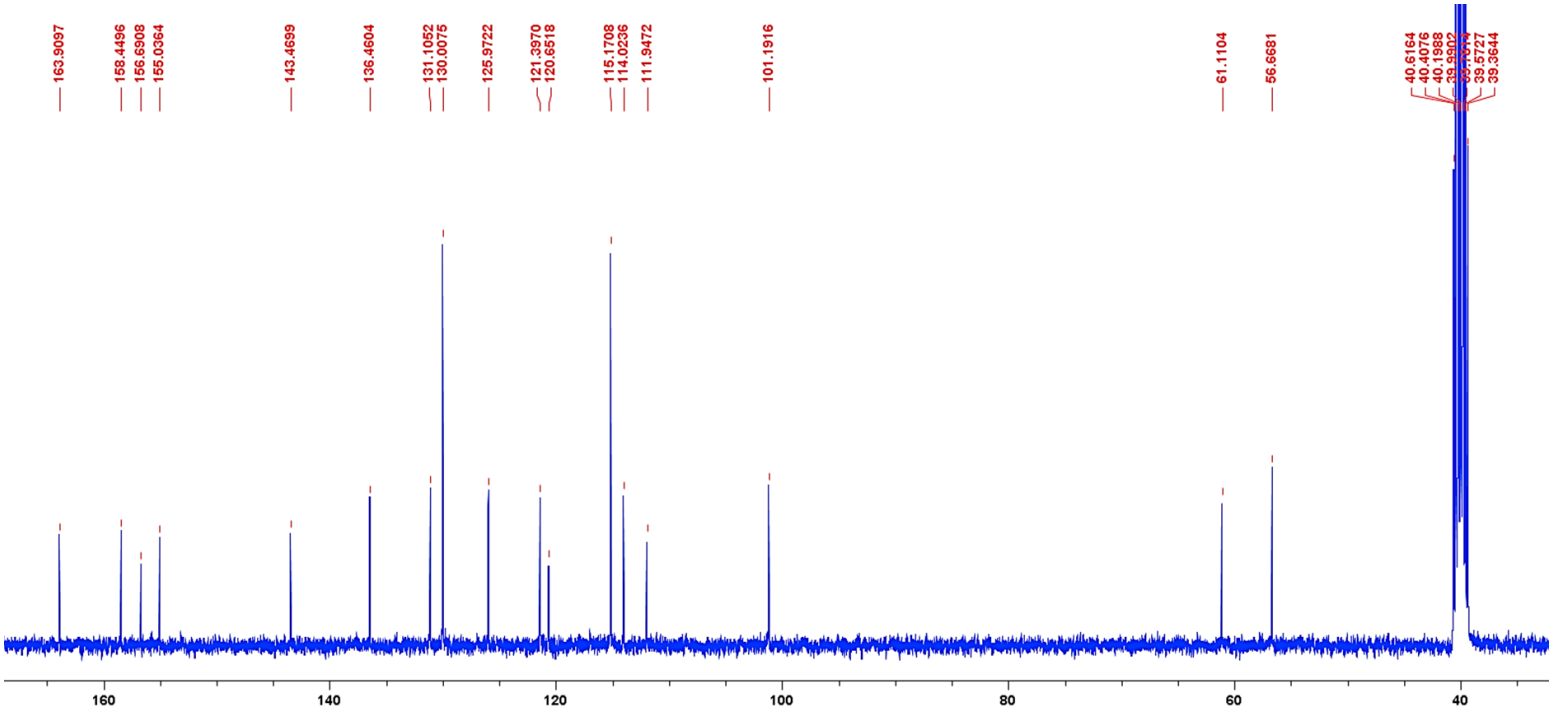

Figure 5: ^{13}C NMR of coumarin-triazole derivative **A1** in d_6-DMSO.

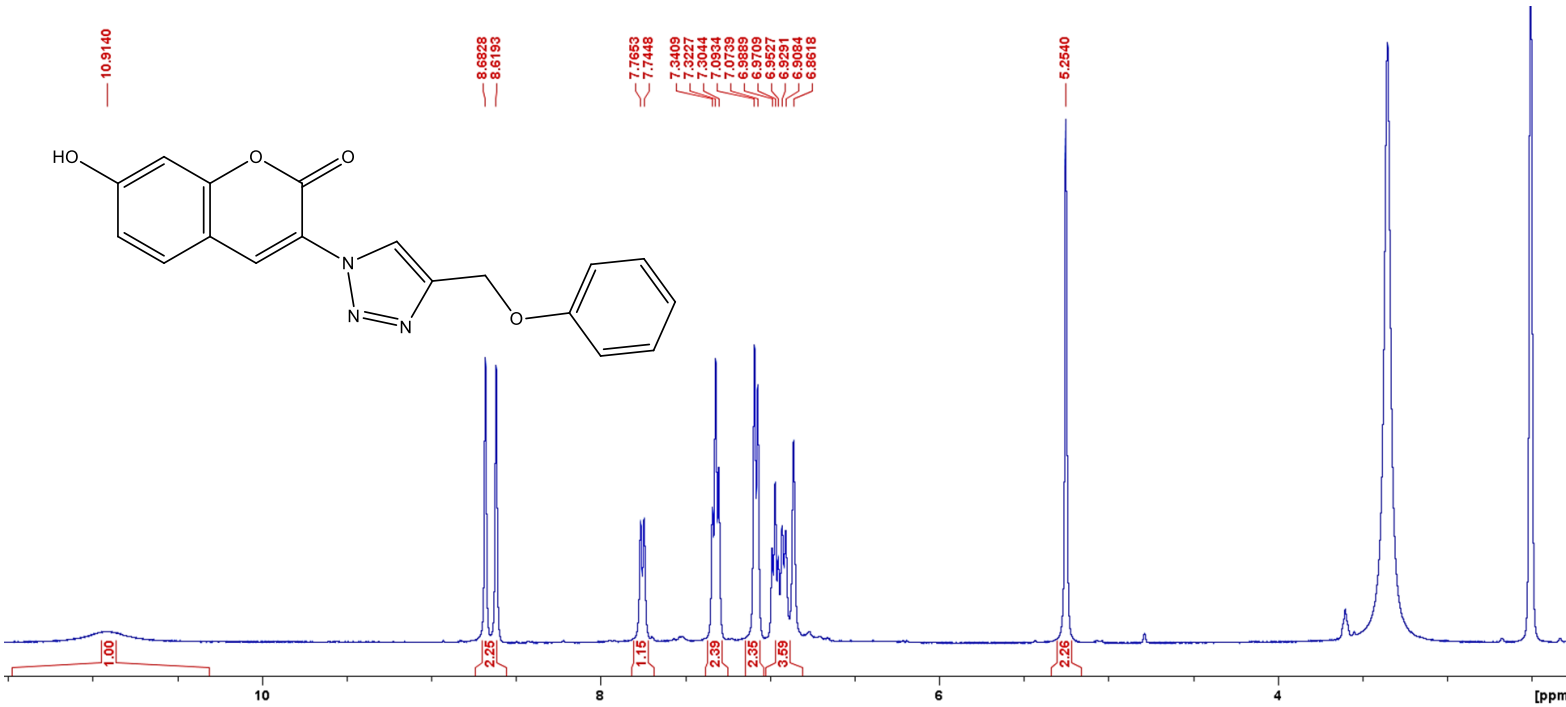

Figure 6: ^{1}H NMR of coumarin-triazole derivative **A2** in d_6-DMSO.

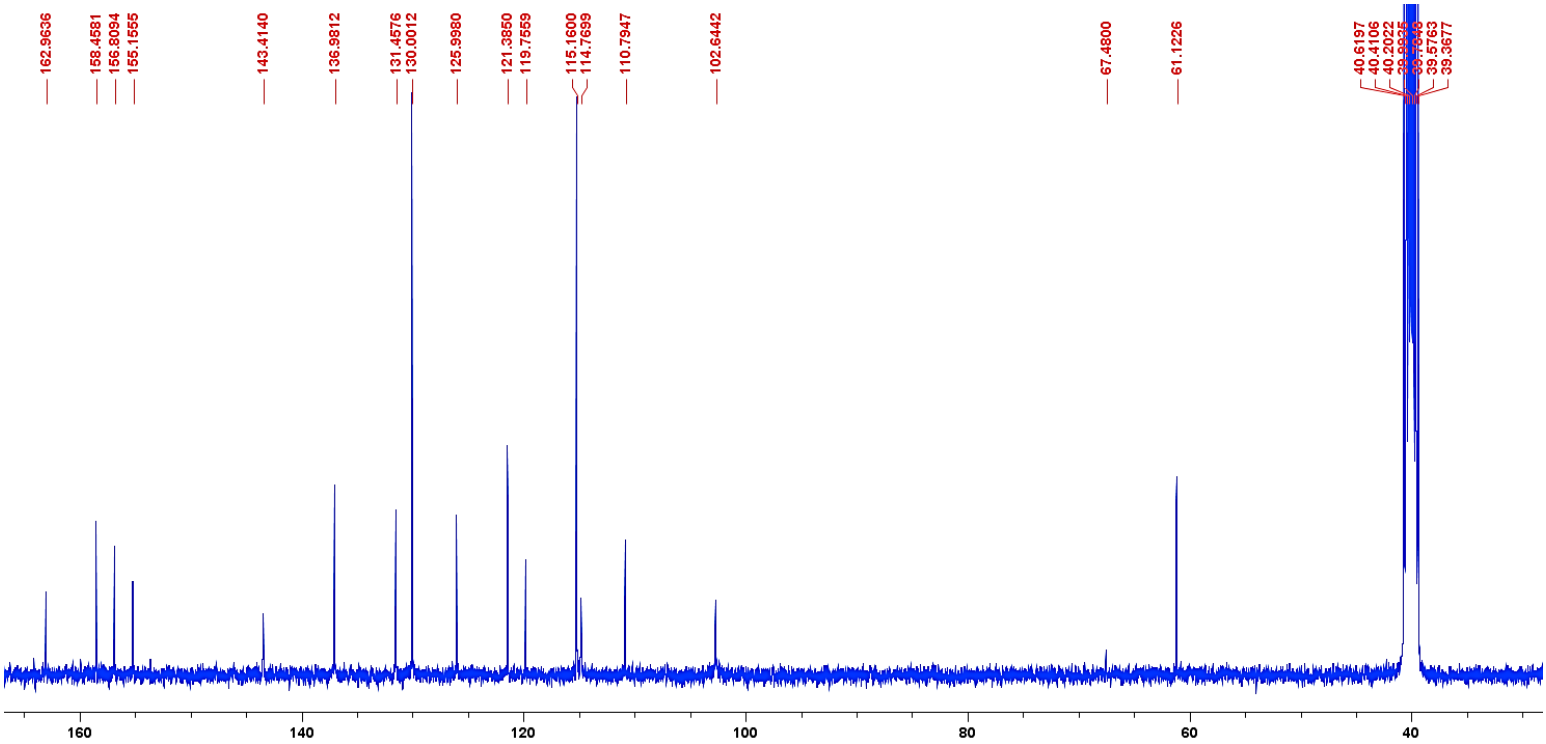

Figure 7: ^{13}C NMR spectra of coumarin-triazole derivative **A2** in d_6-DMSO.

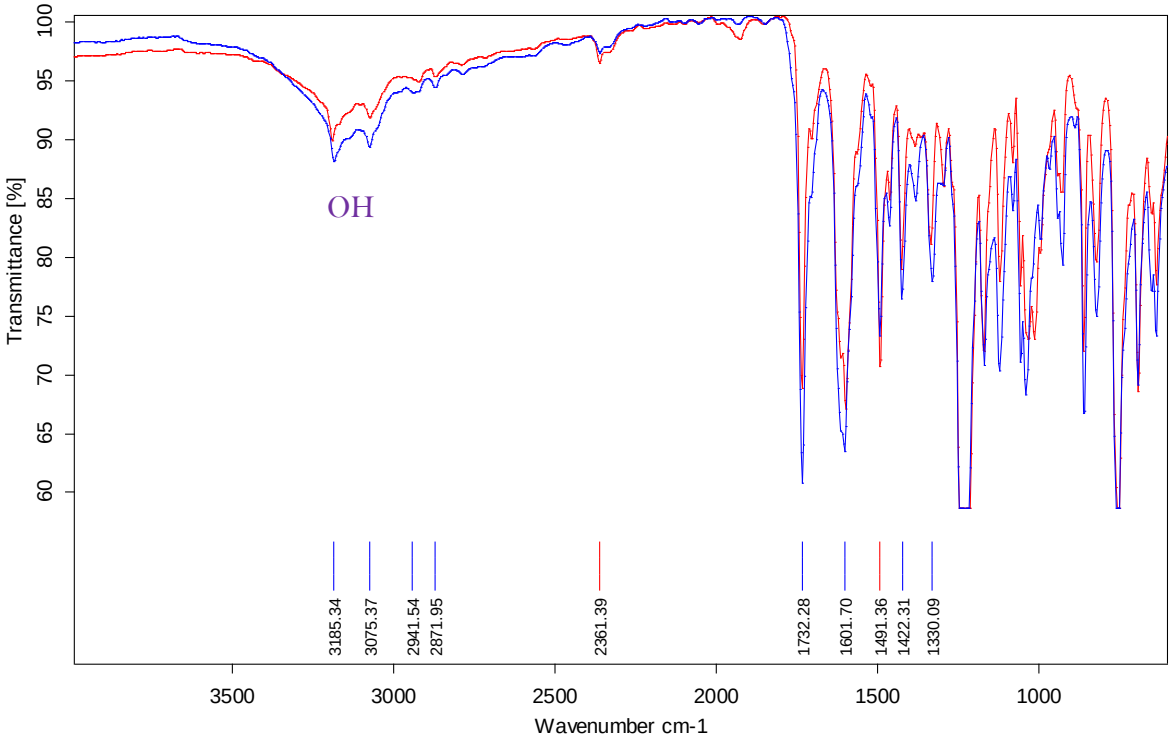

Figure 8: FT-IR spectral overlay of coumarin-triazole derivatives **A2** (red) and **A3** (blue).

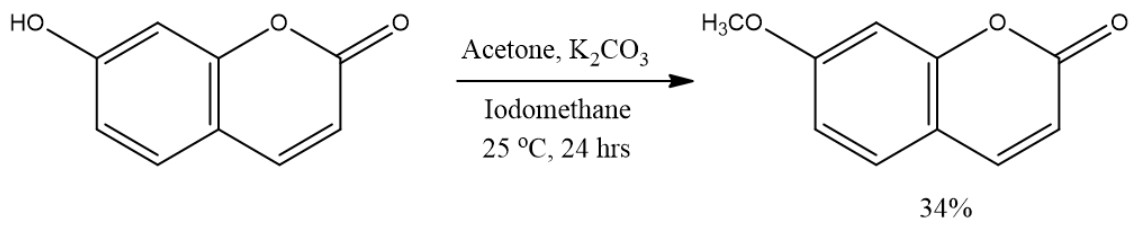

Scheme 1: General synthetic pathway to produce Herniarin **H1** from umbelliferone.

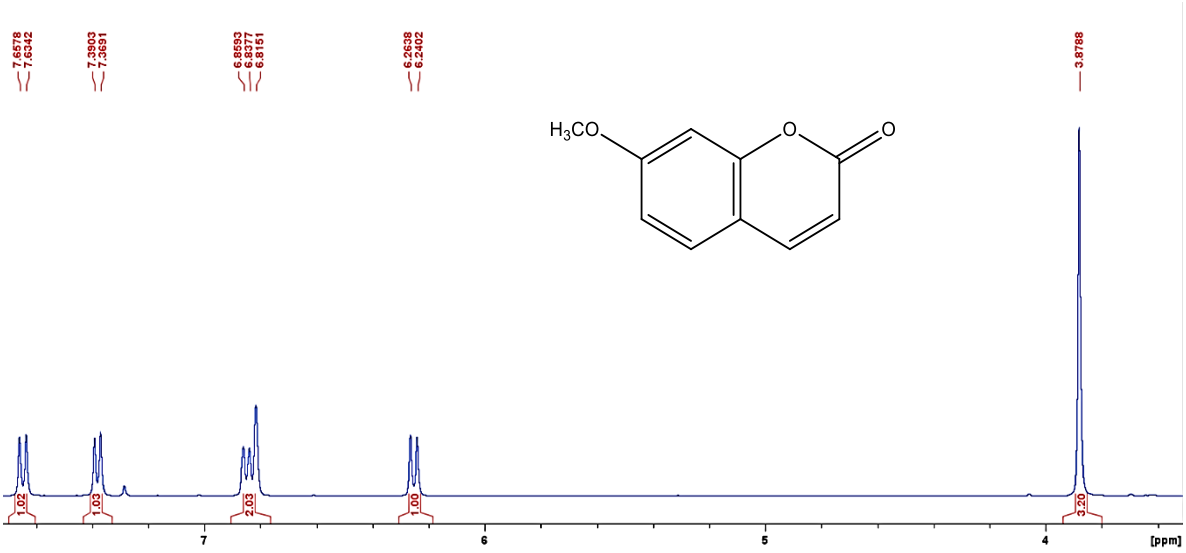

Figure 9: ^{1}H NMR of Herniarin **H1** in $CDCl_3$.

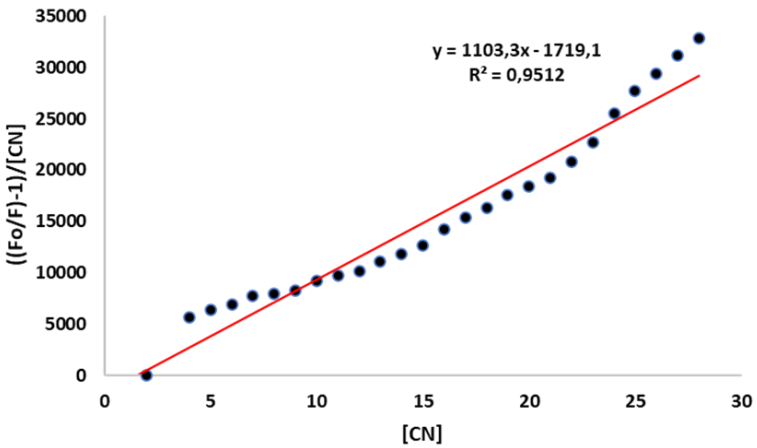

Figure 10: Plot for the titration of **A1** with CN^- in water as fitted by the combined dynamic and static quenching model.

Chapter 3

Table of Contents

List of Figures

List of Tables

List of Schemes

Chapter 3:
Application of 7-triazolyl coumarin-derived sensors towards ionic sensing strategies

Summary

Four 3-ester-7-triazolyl substituted coumarin derivatives were synthesized, characterized, and assessed for their abilities as fluorescent sensors for cationic and anionic analytes in organic and aqueous media. All compounds displayed a strong preference towards Fe^{3+} in their chosen solutions. Sensors **B1** and **B3** displayed the strongest preference towards Fe^{3+}, characterized by a fluorescent quenching response, in their respective solvents. Sensor **B3** was chosen for further analysis as it displayed better selectivity towards Fe^{3+} than **B1**. Additionally, **B3** was able to function as a potential sensor in more environmentally favourable solvents than that of **B1**. The detection limit and association constant were determined to be 2.7 μM and 4.6 x 10^3 M^{-1} respectively from titration experiments, with fluorescent quenching occurring via a combined Perrin-SOA (Sphere of action) static quenching model with quenching occurring via a CHQF PET "on-off" quenching mechanism. Job's plot analyses determined binding to occur in a 1:1 ratio, which was supported by Benesi-Hildebrand studies. Reversibility studies of **B3**-Fe^{3+} complexation with EDTA indicated a total reversibility of 21%. Hydrogen potential studies of **B3** with Fe^{3+} indicated usability over an appreciable pH range. ^{1}H NMR, ^{13}C NMR, and Molecular Modelling studies were used to determine the most preferred binding scenario between **B3** and Fe^{3+} with complexation occurring primarily through the triazole N=N bond and supported by hydrogen bonding of coumarin-carbonyl lone electron pair with surrounding water and/or solvent molecules. Anionic screening studies of **B3** show a sizeable enhancing response towards F^-. Titration experiments of **B3** with F^- was shown to occur via a PET "off-on" fluorescent enhancing mechanism, through the abstraction of the triazole C-2 proton and evolution of HF gas.

3.1 Results and discussion

3.1.1 Synthesis and characterization of coumarin-triazolyl derivatives B1-4

The synthesis of 7-triazolyl-coumarin derivatives **B1-4** were prepared according to the reaction as outlined in **Scheme 1**. Initially, four different aniline derivatives were converted to their corresponding azides (**1a-d**) by azidonation reactions.[1,2] These azides were reacted with 7-substituted coumarin-alkyne derivative **2** via 1,3-Cu(I)-catalyzed azide-alkyne cycloaddition to afford coumarin-triazole derivatives **B1-4**. Coumarin-alkyne derivative **2** was synthesized according to literature procedure as shown in **Scheme 1**.[3]

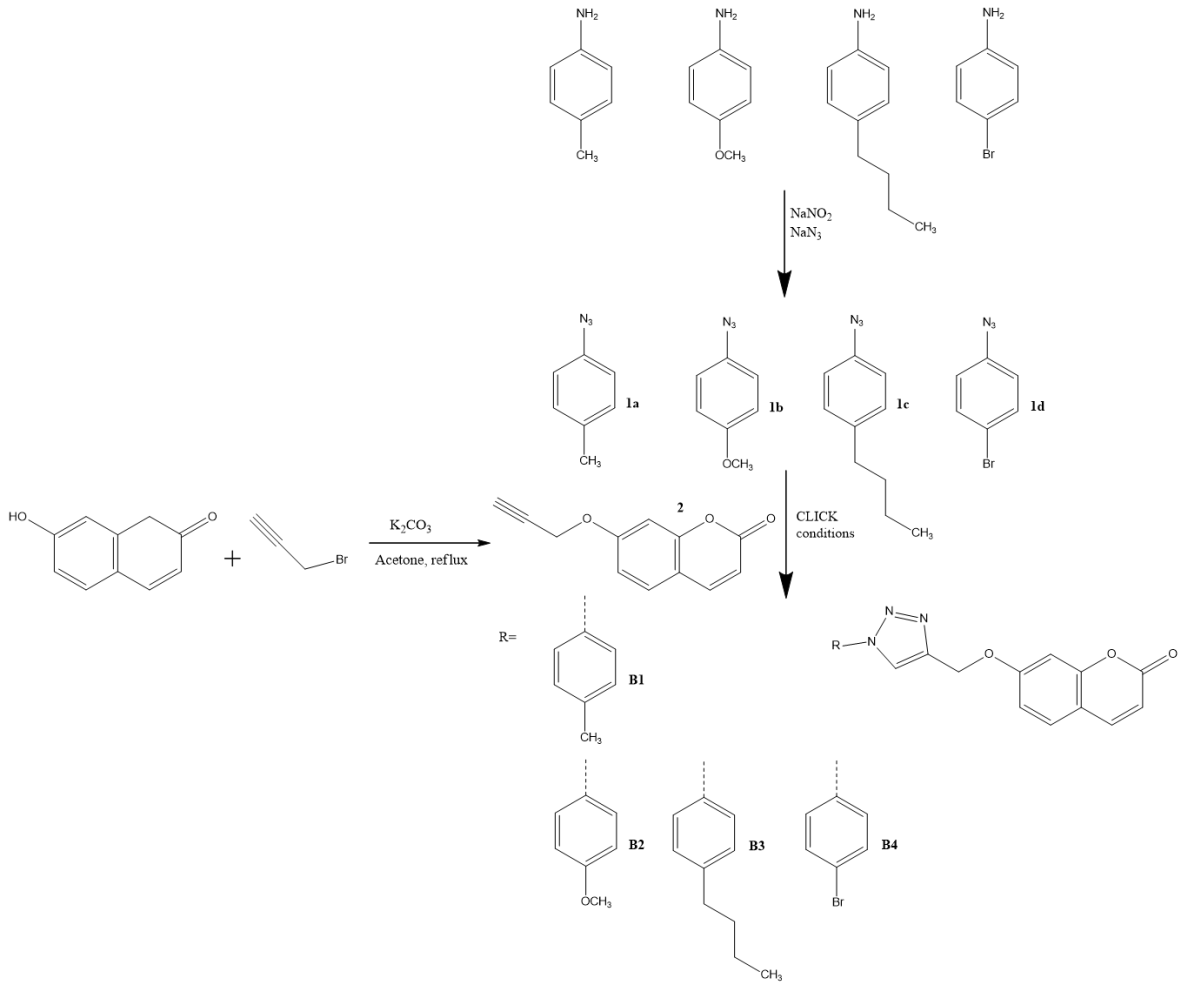

Scheme 1: Synthetic route towards 7-triazolyl coumarin sensors **B1-4**. "Click" reaction conditions: THF, NaAsc, PMDETA, $CuSO_4.5H_2O$.

The conversion of the four aniline derivatives containing methyl, butyl, bromo and methoxy functionalities were monitored by FT-IR analysis. The appearance of the sharp, strong peaks in the region of 2000 cm^{-1} confirmed the conversion of the amine to the azide group (**Figure 1**).

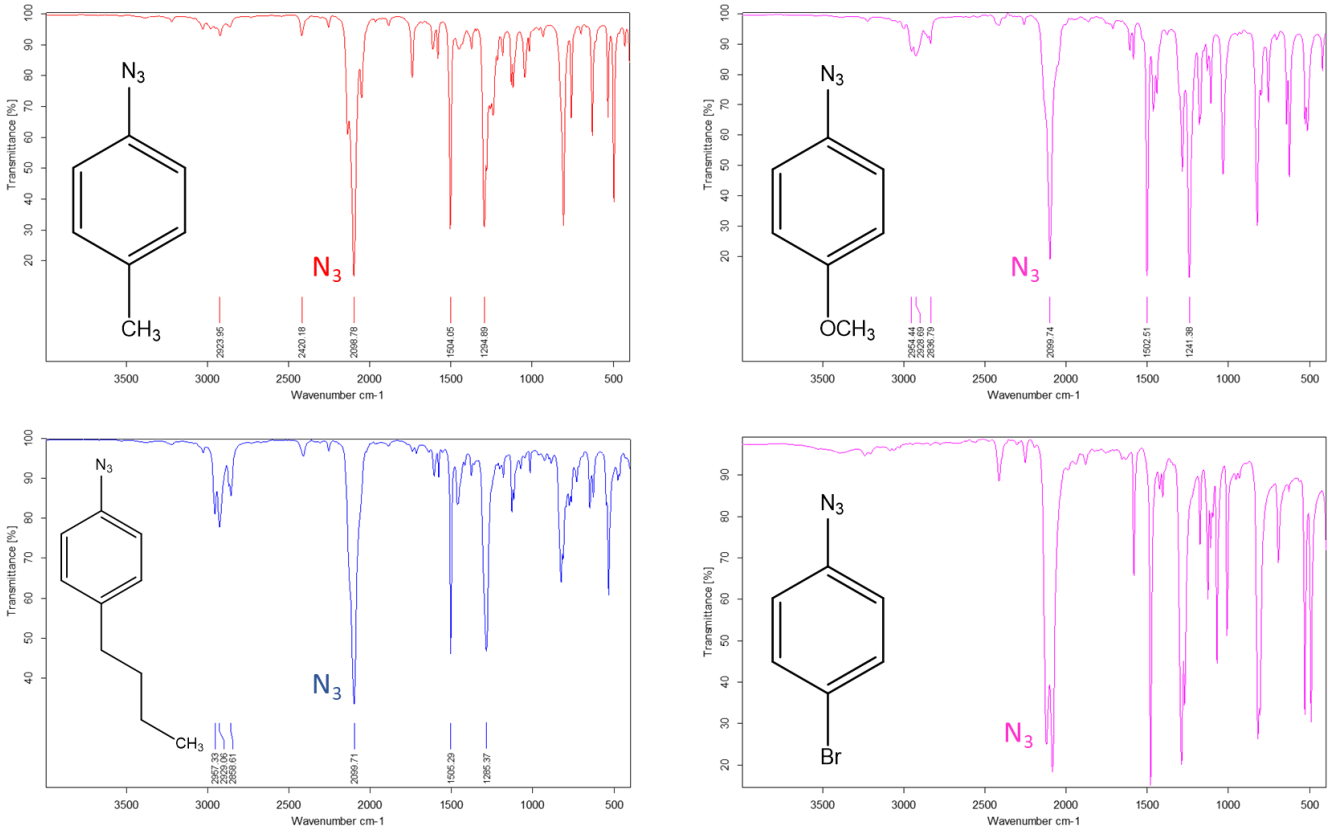

Figure 1: FT-IR spectra of methyl-, methoxy-, butyl-, and bromo- azide derivatives **1a-d**.

Single-crystal X-Ray studies and ^{1}H NMR spectral analysis were used to confirm the formation of the coumarin-alkyne derivative **2** (**Figure 2**). In the ^{1}H NMR spectra, the singlet associated with the alkyne proton appears at 2.6 ppm whilst the singlet associated with the two CH_2 (labelled -f-) was observed at 4.7 ppm. For the ^{13}C NMR spectra of propinyloxy coumarin derivative **2** see **Appendix B Figure 1**.

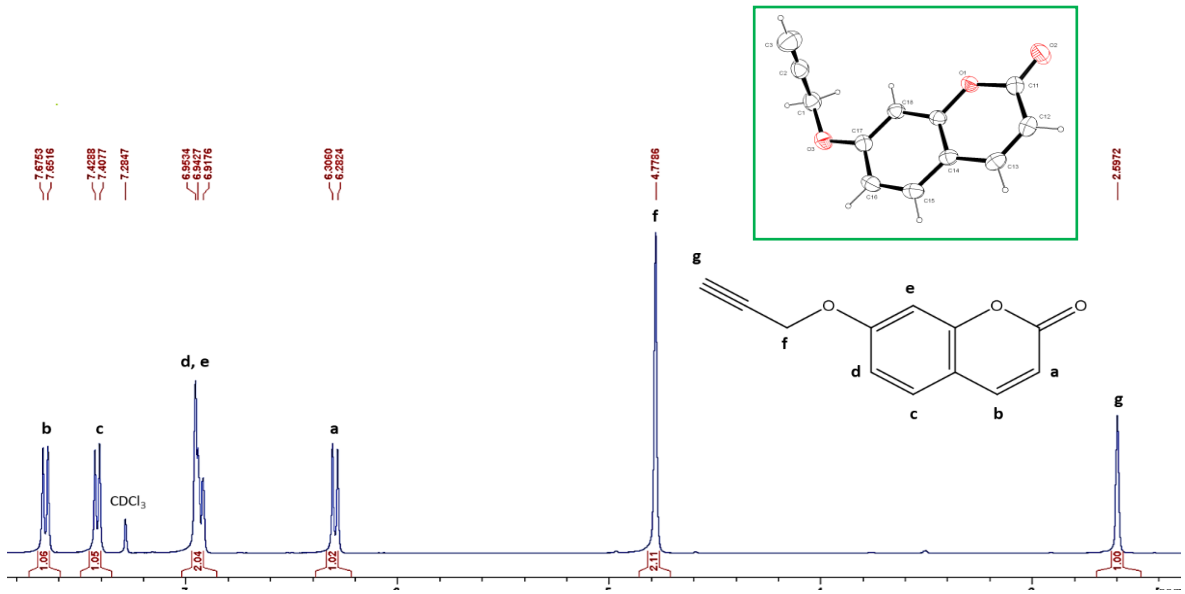

Figure 2: ^{1}H NMR spectra of propinyloxy coumarin derivative **2** in $CDCl_3$. Inset: single-crystal XRD structure of derivative **2**.

The success of the Cu(I)-catalyzed "click" reaction was evaluated by ^{1}H NMR, ^{13}C NMR, FT-IR, and single crystal XRD analysis. Evidently, the disappearance of the peak associated with the azide functionality indicated the successful conversion to the triazole moiety. The triazole moiety (N=N and C=C) functionalities appear between 1386-1136 cm^{-1} in the FT-IR spectrum and may be partially overlapped[4] (for the FT-IR spectra of coumarin triazole sensors **B1-4** see **Figures 2-5** in **Appendix B**). The ^{1}H NMR spectra of coumarin-triazole compounds **B1-4** is shown in **Figures 3-6**.

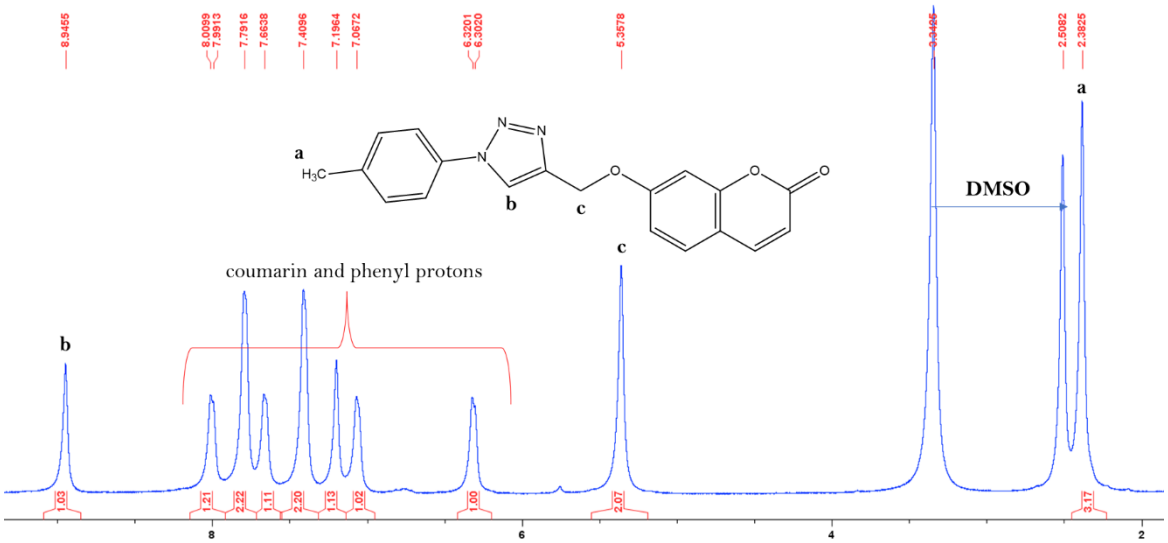

Figure 3: ^{1}H NMR of sensor **B1** in d_6-DMSO.

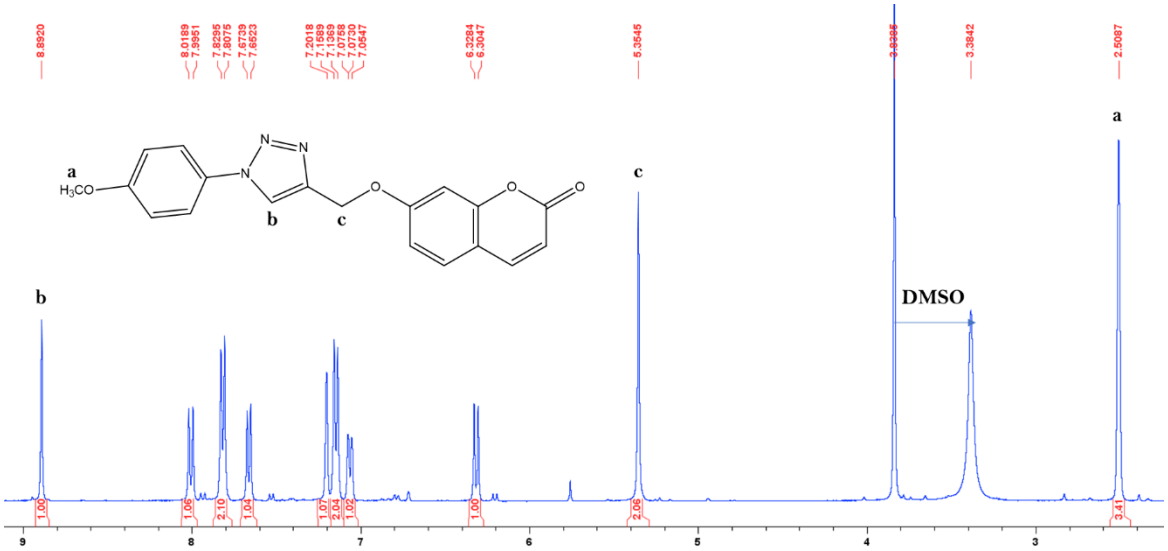

Figure 4: ^{1}H NMR of sensor **B2** in d_6-DMSO.

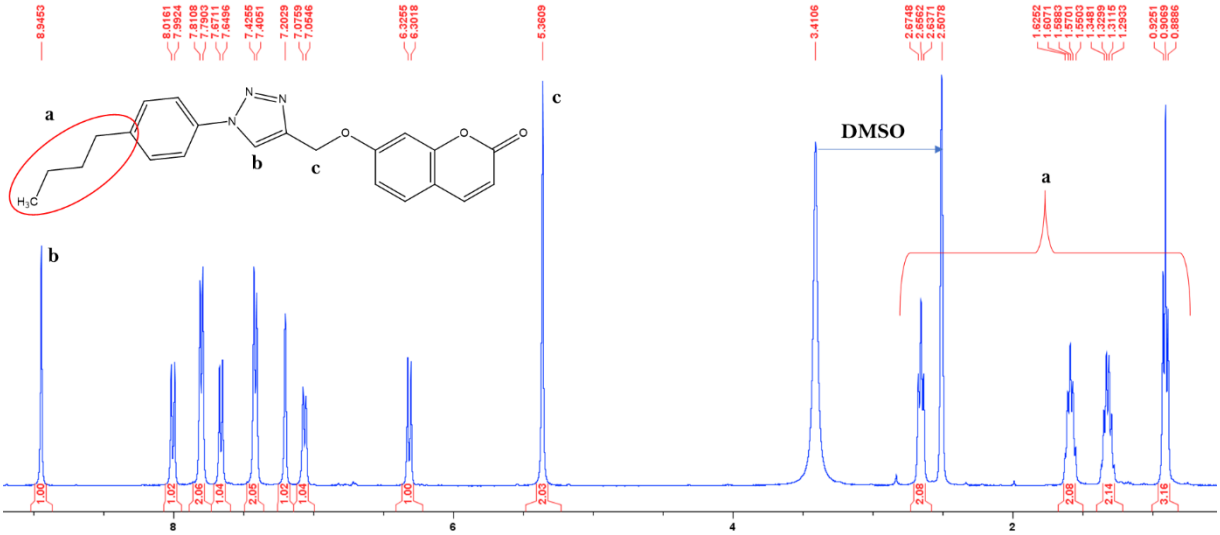

Figure 5: ^{1}H NMR of sensor **B3** in d_6-DMSO.

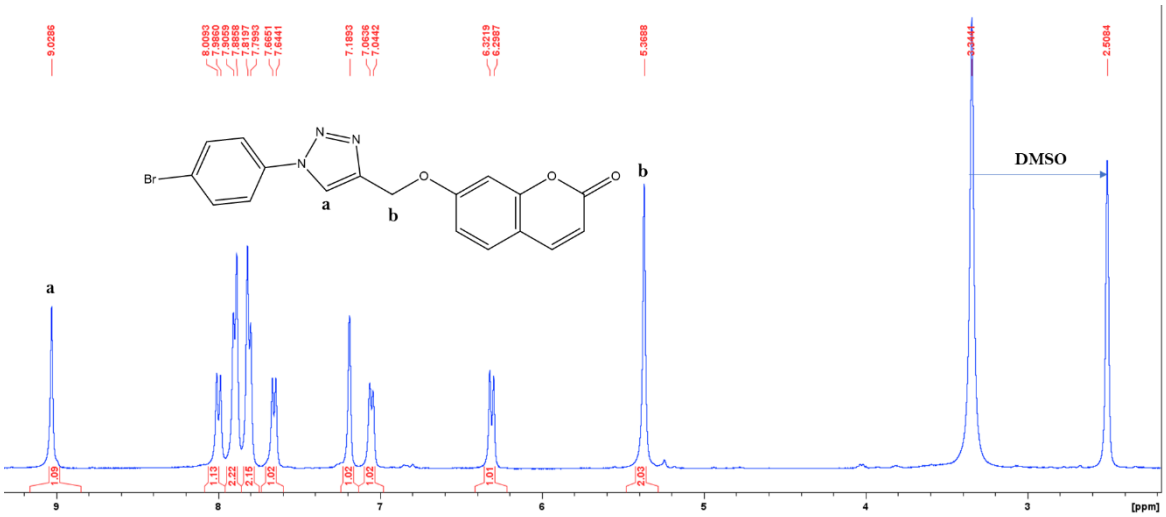

Figure 6: ^{1}H NMR of sensor **B4** in d_6-DMSO.

The obtained spectra showed all expected peak splitting patterns and integration values for the verification of successful conversion. In addition to the ^{1}H and ^{13}C NMR analysis, single-crystal XRD structures of all four 7-substituted triazolyl-coumarin derivatives were obtained, thus confirming desired product formation (**Figure 7**.) For the ^{13}C NMR spectra of sensors **B1-4**, see **Appendix B Figures 6-9**.

a)

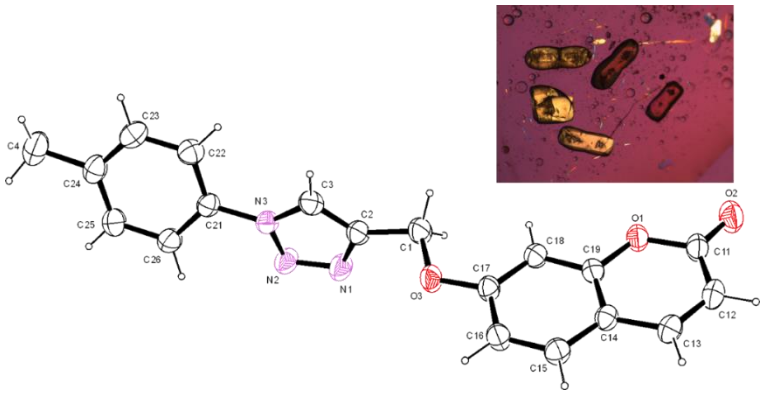

b)

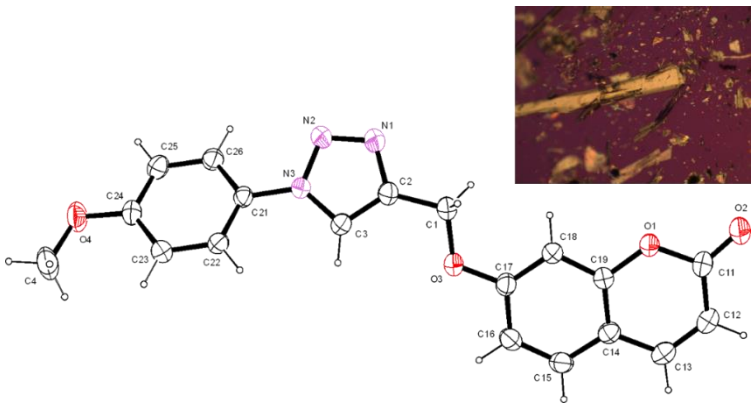

c)

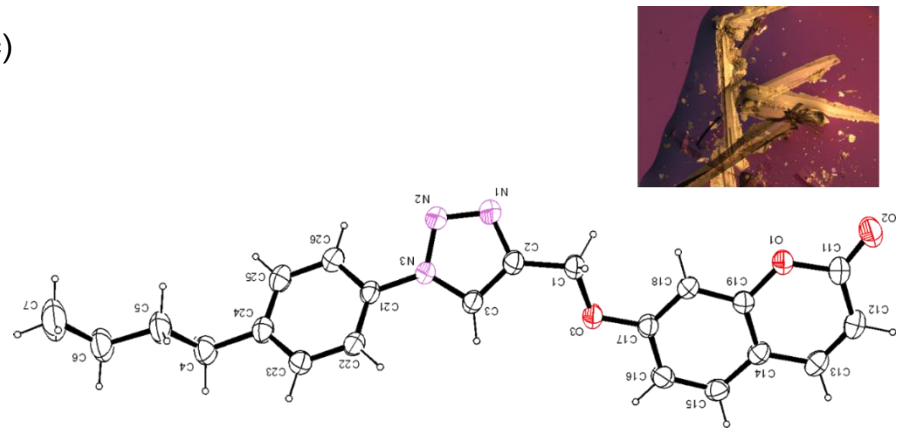

d)

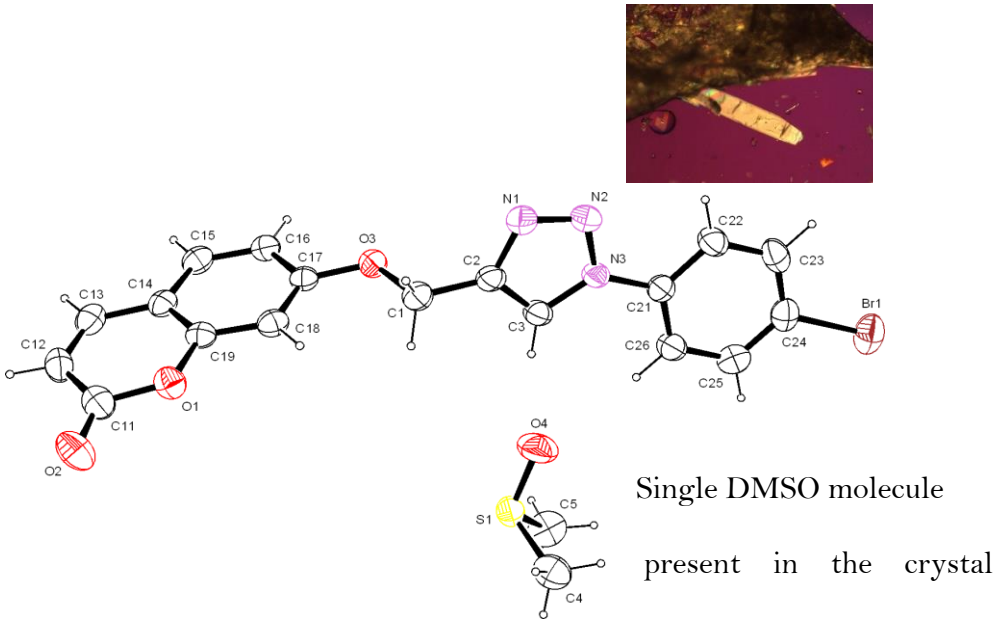

Figure 7: Single crystal XRD structures of a) **B1**, b) **B2**, c) **B3**, and d) **B4**. Inset: XRD obtained pictures of the physical crystal appearance.

Cationic sensing studies

3.1.2 The sensing responses of sensors B1-4 towards various metal ions in organic and aqueous solution

Coumarin-triazolyl sensors **B1-4** were tested for their affinity towards an array of different metal cations. These cations include Fe^{2+}, Fe^{3+}, Cd^{2+}, Pb^{2+}, Ag^{+}, Na^{+}, K^{+}, Ca^{2+}, Cr^{3+}, Al^{3+}, Ba^{2+}, Cu^{2+}, Co^{2+}, Hg^{2+}, $Zn^{2+}$and Ni^{2+}. Metal solutions were prepared in deionized water from their nitrate salts. Stock solutions of **B1-4** were prepared in both methanol and DMF. Anisidine and butyl derivatives **B2** and **B3** were soluble in methanol whilst toluidine and bromo derivatives **B1** and **B4** were soluble in DMF. Based on these reasons, sensors were dissolved to methanol and DMF to account for possible solvent interactions on photophysical properties. The sensors all displayed the same excitation wavelength of 320 nm.

Screening studies were performed by adding equal aliquots of the 0.01 M metal solution into solutions of sensors **B1- 4** in ethanol. Ethanol was chosen due to its low boiling point and low environmental impact compared to DMF or DMSO.

Figure 8 shows the screening studies of sensors **B2** and **B3** towards the different metal cations in ethanol (for the screening studies of **B1** and **B4** in ethanol, see **Appendix B Figures 10** & **11**).

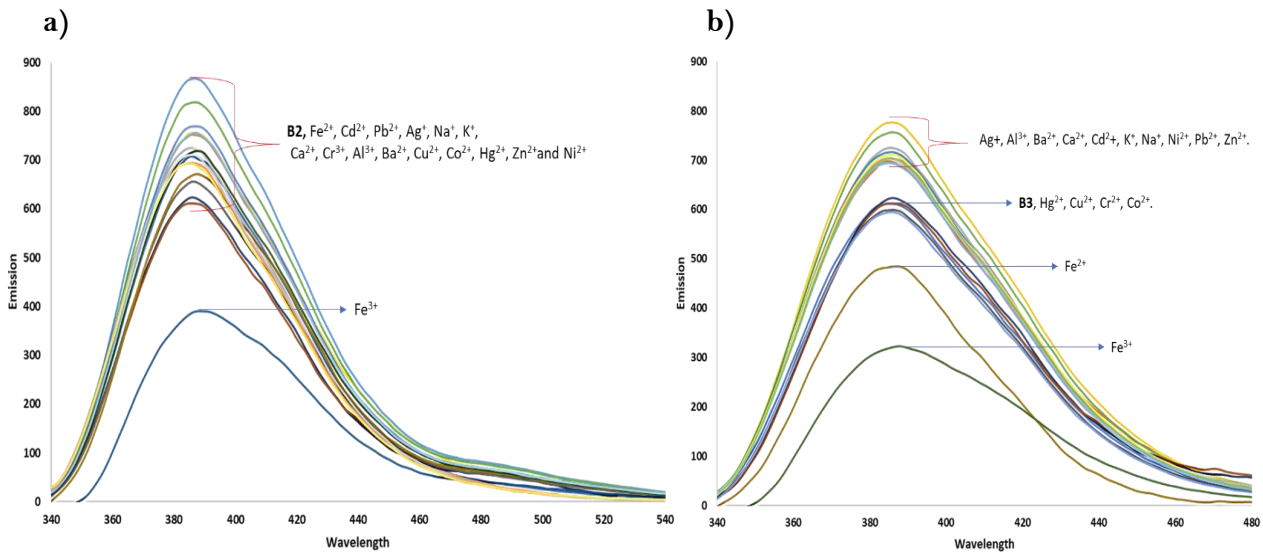

Figure 8: Screening studies of a) **B2** and b) **B3** towards selected metal cations in ethanol. Excitation: 320 nm.

Butyl derivative **B3** displayed four dispersed groupings of emission signals whilst anisidine derivative **B2** displayed only two. Nevertheless, the cation showing the greatest effect on fluorescent emission is Fe^{3+}, by a singularly large quenching emission response towards both sensors. Toluidine and bromo derivatives **B1** & **B4** also displayed the same quenching response towards Fe^{3+}. All four sensors displayed the same excitation and emission wavelengths, together with similar observations in sensing responses. It can be concluded that the methyl-, methoxy-, butyl-, and bromo- substituents attached to the phenyl ring play no significant role in metal binding.

3.1.3 Competition studies

Selectivity studies of sensors **B1-4** and Fe^{3+} in the presence of competing metal cations was conducted in ethanol. Notably, all four sensors displayed a strong affinity towards Fe^{3+} in the presence of competing metal cations. This was observed by a large fluorescent quenching response at similar/same emission intensities as seen in the response of Fe^{3+} alone. Competition studies of sensors **B1- 4** towards Fe^{3+} cations in the presence of competing metal ions are shown in **Figure 9**. All four sensors displayed appreciable selectivity towards Fe^{3+}. Sensors dissolved in like stock solvent solutions were compared. The most selective sensor in each solvent group was used for further investigation.

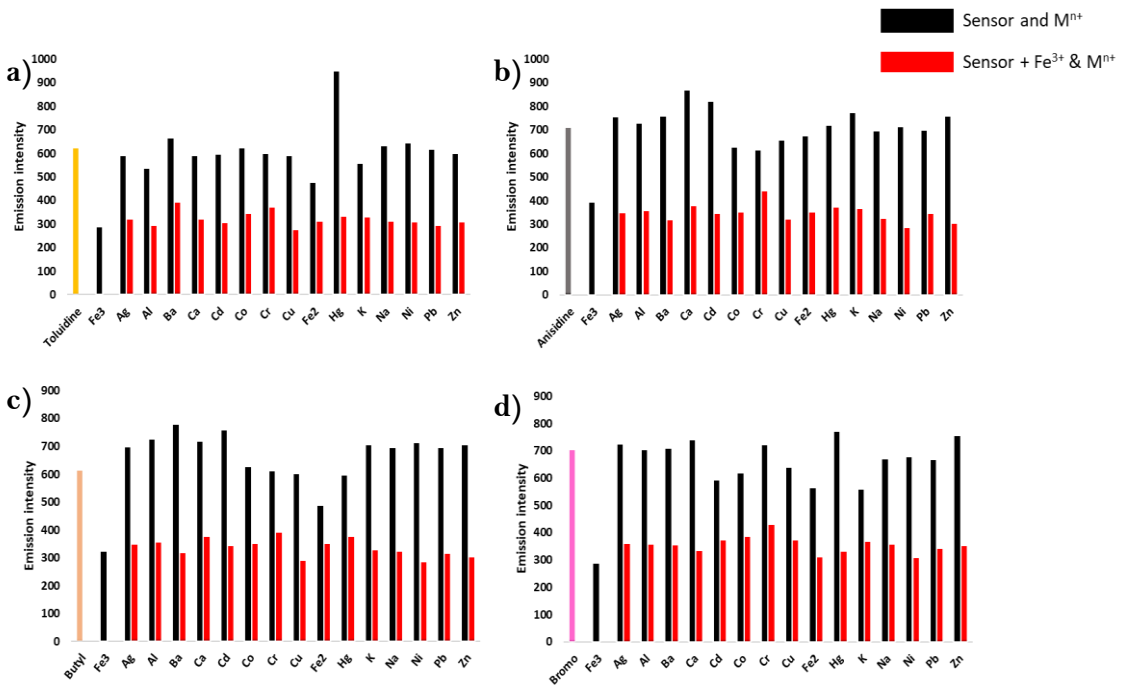

Figure 9: Competition studies of a) **B1**, b) **B2**, c) **B3**, and d) **B4** towards Fe^{3+} in the presence of competing metal cations. Studies conducted in ethanol at an excitation of 320 nm.

The overall selectivity of each sensor was determined by means of averages. The average of the values of the sensor with Fe^{3+} & M^{n+} were calculated and compared to that of the sensor with Fe^{3+} alone. The sensor displaying the lowest difference between these two values would exhibit greater overall selectivity. Evidently, sensors **B1** and **B3** displayed the lowest difference in these values and were thus chosen for further studies. A comparison of these values is shown in **Table 1**.

Table 1: Comparison of sensors **B1- 4** affinities towards Fe^{3+}.

Sensors	Stock solvent	Emission intensity of sensor with Fe^{3+}	Average of all Sensor + Fe^{3+} 7 M^{n+}	Difference (Absolute value)
B1	DMF	286.4	319.2	32,8
B4		287.2	354.3	67,1
B2	Methanol	390.1	345.1	45
B3		322.7	335.9	13,2

3.1.4 Titration studies of sensors B1 and B3 with Fe^{3+} in ethanol

The emission titration studies of **B1** and **B3** with Fe^{3+} in ethanol is shown in **Figure 10**.

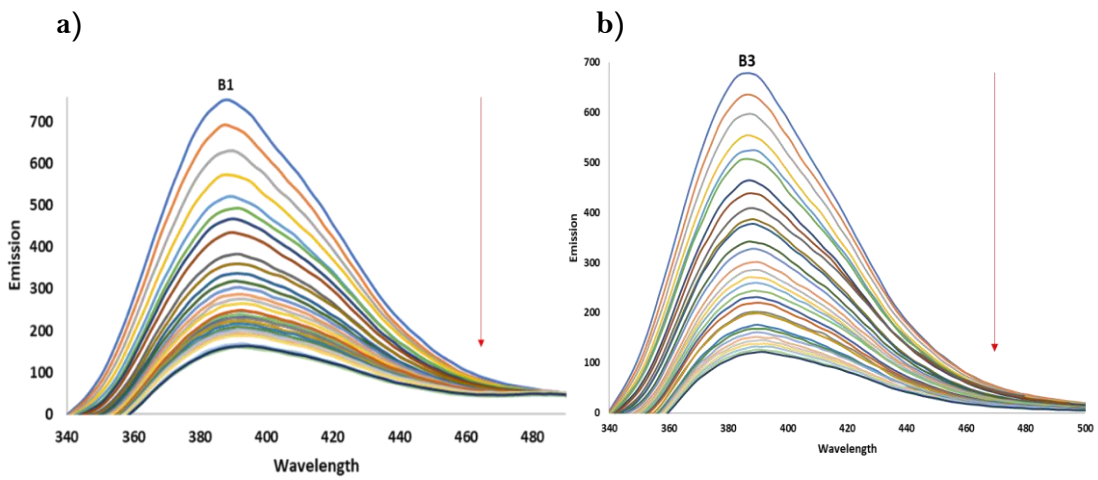

Figure 10: Titration of sensors a) **B1** and b) **B3** with Fe^{3+} in ethanol. Excitation: 320nm. Titrations completed in triplicate.

Visibly, no iso-emissive points in the titration curves are present. This could indicate that only a single fluorescent emitting species is formed during Fe^{3+} complexation/addition. The appearance of an iso-emissive point provides convincing evidence for the existence of two different emissive states and consequently assists in determining their fluorescent lifetimes.

Although this has been shown to be undoubtedly true, the converse is not always correct. It has been shown that the absence of an iso-emissive point does not necessarily indicate that there is no direct interconversion between the sensor and complex, in fact, a point can exist only if the precursor and product spectra can be addressed as nearly stationary.[5]

3.1.5 PET fluorescent quenching mechanism of B1 & B3 with Fe^{3+}

Titration experiments of **B1** and **B3** with Fe^{3+} displayed no visible hypso- nor bathochromic shift in emissive wavelength upon Fe^{3+} titration, which could indicate that an ICT-type quenching mechanism is occurring. This lack of spectral shift favours the PET "on-off" type quenching mechanism by the sensors towards Fe^{3+}. The structure of sensors **B1** and **B3** also contribute towards the PET-type of fluorescent mechanism. ICT-type fluorescent sensors are composed of electron-pushing and electron-withdrawing groups connected through a π-electron system. It exhibits the presence of a polarized structure in the ground state. The dipole moment strengthens this polarization characteristic under light excitation which in turn induces the ICT process causing a shift in wavelength.[6] Conversely, a PET-type sensor requires the presence of donor and acceptor molecule/moiety that can be fully separated as individual species in solution or connected through an aliphatic (non-conjugated) linker.[7] The structural characteristics of sensors **B1** and **B3** fulfil the requirements of a PET-type sensor. The molecular orbital diagram and corresponding energies of **B3** is shown in **Figure 11**. The HOMO of the sensor resides around the coumarin fluorophore whilst the LUMO resides over the triazole moiety and phenyl ring. Thus, similar to the description in **Chapter 2**, upon excitation, electron density is transferred from the coumarin fluorophore to the phenyl ring. This overall process produces a fluorescent response. Upon analyte complexation with the triazole moiety, the π-conjugation of the system is disrupted, and energy is dispersed via a non-radiative relaxation pathway, resulting in a quenching fluorescent response. The changes in orbital energies and electronic transitions are in a similar mode to that of **Figure 20** in **Chapter 2**. The PET "on-off" fluorescent quenching system proposed for **B1**-Fe^{3+} and **B3**-Fe^{3+} complexation is also shown in **Figure 11**.

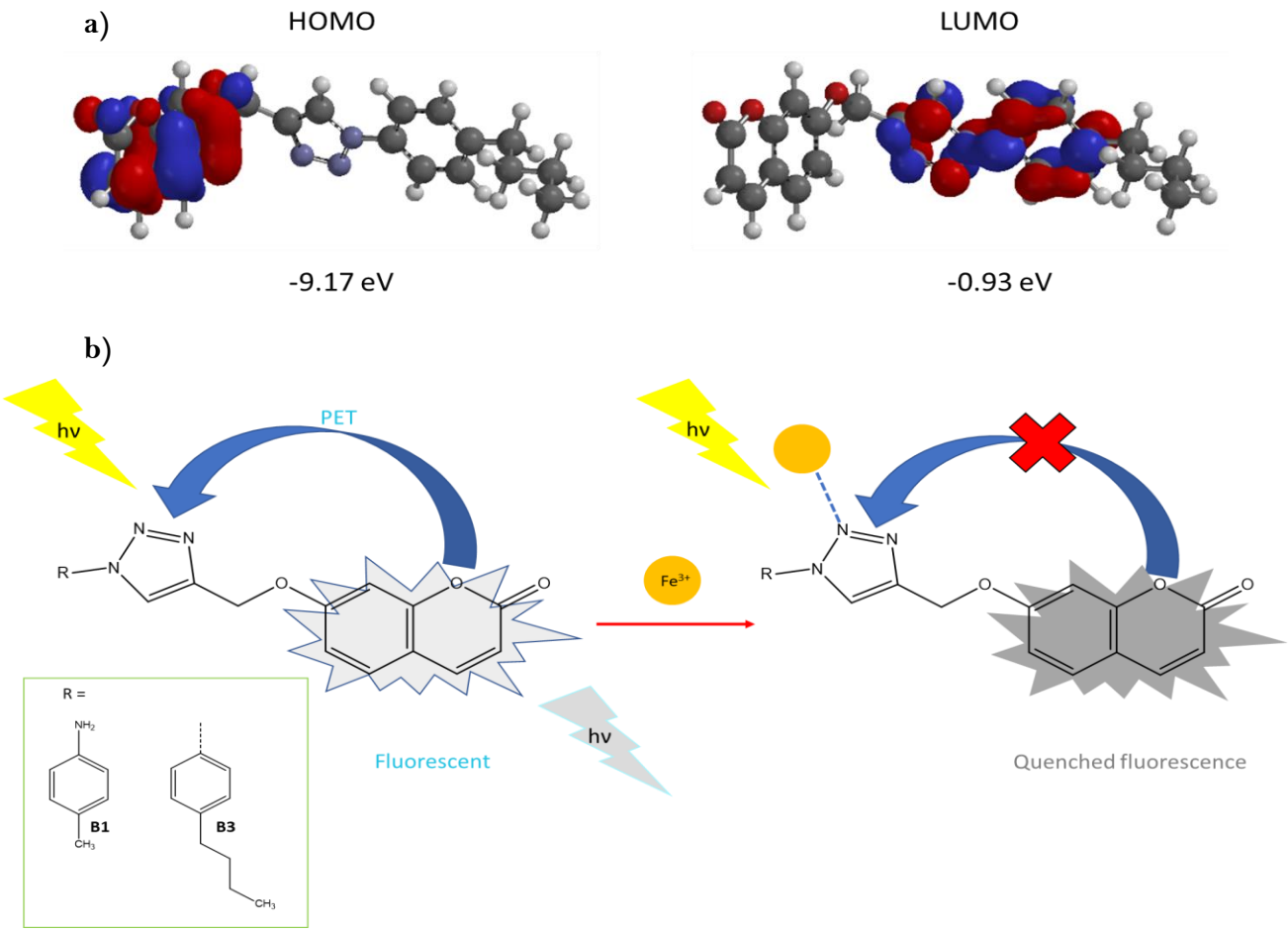

Figure 11: a) Calculated HOMO and LUMO molecular orbitals of **B3** at PM3 calculation level, b) PET "on-off" quenching mechanism of **B1** and **B3** towards Fe^{3+}.

3.1.5 UV-Vis titration of B3 with Fe^{3+} in ethanol

The UV-Vis titration of sensor **B3** with Fe^{3+} is shown in **Figure 12**. There are no visible isosbestic points in the titration analysis which could indicate the presence of more than one absorbing species. Additionally, no visible shifts in wavelength upon analyte titration is observed which would suggest the involvement of an ICT mechanism. This verifies the contribution of the PET mechanism in both the absorbance and emission studies. The association constant (K_a) will be later determined by Benesi-Hildebrand analysis. Calculations showed a large value for the association constant (K_a) between **B3** and Fe^{3+}. This infers the fluorescent quenching of **B3** by Fe^{3+} occurs via CHQF PET-type "on-off" mechanism.

The absorbance titration of the sensor with Fe^{3+} shows an opposite effect compared to the emission studies. The addition of Fe^{3+} to sensor **B3** results in an increase in the absorbance, but conversely, an emissive quenching. The same effect was observed previously in **Chapter 1** between sensor **A1** and Fe^{3+}.

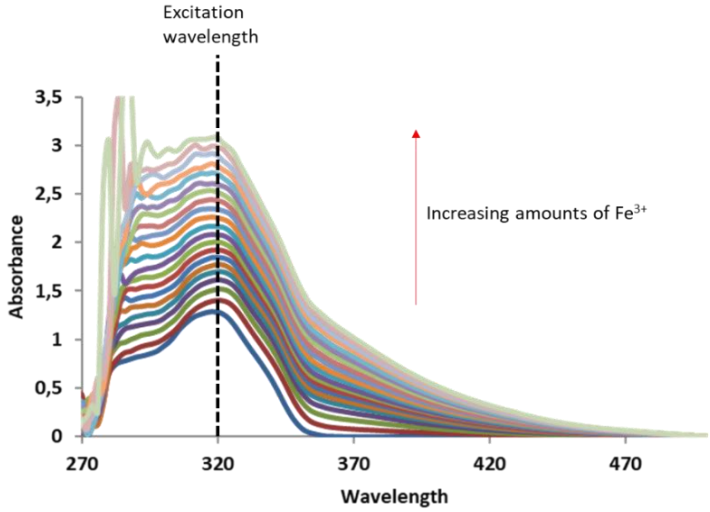

Figure 12: UV-Vis titration of **B3** with Fe^{3+} in ethanol.

The feasibility of a FRET fluorescent mechanism is unlikely when the structure of the sensor and normalized absorbance and emission spectra are considered (**Figure 13**). The area/degree of spectral overlap between the absorbance and emission spectra was minimal. As mentioned previously, FRET fluorescent mechanisms require a large degree of spectral overlap between the absorbance and emission spectra and the presence of both donor and acceptor fluorophores.[8–10]

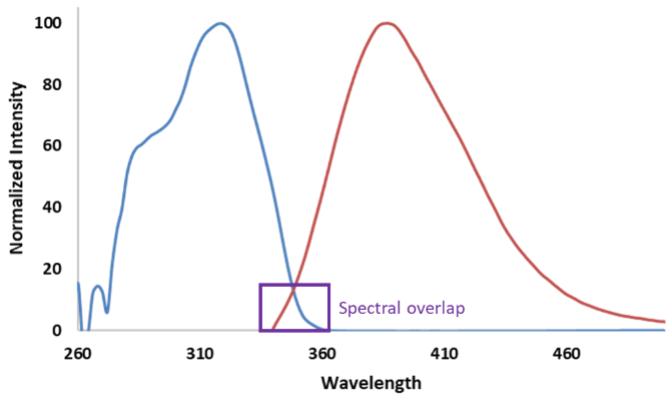

Figure 13: Normalized absorbance (blue) and emission (red) spectra of **B3** in ethanol.

3.1.6 Determination and comparison of fluorescent quenching processes, association constants, and detection limits of sensors B1 and B3 in ethanol

To determine the quenching process of sensors **B1** and **B3** by Fe^{3+}, the titration data were fitted with the linear Stern-Volmer equation (F_0/F vs $[Fe^{3+}]$) where the value of the slope is equal to quenching constant K_{SV}. Evidently, the quenching process of **B1** and **B3** with Fe^{3+} is different (**Figure 14**). Sensor **B1** displays a strong linear correlation whilst sensor **B3** shows a positive deviation from linearity. A linear SV plot suggests that either static (complex) or dynamic (collisional) quenching processes are occurring. The effect of the dynamic component can be evaluated by the effect of temperature on the value of K_{SV}. The dynamic component for this quenching process was not investigated. It was assumed that the sensor-metal complexation between the triazole moiety and Fe^{3+} was the major contributor to quenching (as described and determined in **Chapter 2**).

The positive deviation from linearity in the quenching experiments of **B3** with Fe^{3+} suggests that not only static or dynamic processes are occurring, but rather two distinct situations: the presence of a quenching sphere or that the fluorophore can be quenched by both (static and dynamic) mechanisms simultaneously with the same quencher via a ground state complex.[11,12] For a combined static and dynamic system (ground-state complex formation) the plot of $((F_0/F) - 1)/[Fe^{3+}]$ vs $[Fe^{3+}]$ should yield a straight line with a slope and intercept values equal to quenching coefficients K_{SV} and K_g. The value of the regression coefficient was $R^2 = 0.9573$ (for the plot of the combined dynamic and static plot see **Appendix B Figure 12**). However, the calculated values for K_{SV} and K_g using the least-square fit method[13,14] were imaginary. This negated the possibility of the formation of a ground-state complex between **B3** and Fe^{3+}.

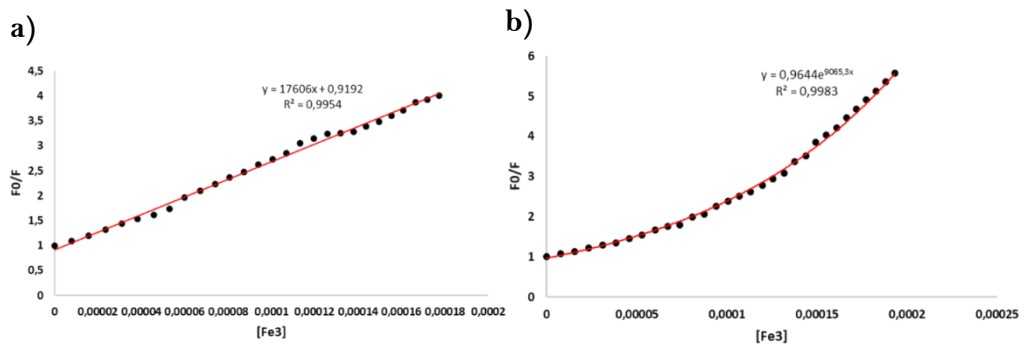

Figure 14: Plot of quenching analysis of a) **B1** and b) **B3** fitted with the linear Stern-Volmer equation.

The variance in the quenching process observed between sensors **B1** and **B3** could arise due to structural differences and/or by the solvent used for the stock solutions. The effect of the structural differences on the quenching mode was deemed unlikely. Both sensors displayed the same affinity and selectivity towards Fe^{3+} despite their structural differences. It can be concluded that the methyl- and butyl- functionalities, of **B1** and **B3** respectively, may serve only to influence the photophysical properties, such as quantum yields (discussed later) and initial fluorescent intensities (F_0), and do not contribute to analyte sensing or binding. This was later verified by ^{1}H NMR and ^{15}N NMR spectral analysis whereby both sensors are suggested to form a complex with Fe^{3+} via the triazole nitrogen (with assistance from the coumarin carbonyl) as seen previously between **A1** and Fe^{3+} in **Chapter 2**. Therefore, the effect of the stock solution could contribute to the contrasting quenching modes observed.

Literature reports that deviations from linearity can occur due to differences in molecular environments (solvent polarity) as well as chemical association prior to excitation.[15] The polarity of the solvent used can greatly affect the fluorescent emission behaviour by lowering the energy by the stabilization of the excited state of the fluorophore which presents a larger dipole moment in this state. The nature of the solvent (π-bonds, polar bonds, molecule size, dielectric constant and refractive index) has shown to dictate the mode of interaction between ligand and analytes.[16] It is known that methanol has a higher relative polarity (0,762 a.u relative to water) than DMF (0.386 a.u). The polarity of the solvent and the interaction of the stock solvent with the fluorophore and metal cation could influence the mode of fluorescent quenching observed between sensors **B1** and **B3**.

The positive deviation from linearity of **B3** with Fe^{3+} was investigated further by the Perrin and Sphere of Action static quenching models. The quenching of **B1** with Fe^{3+} was suggested to be to be purely static/dynamic in nature due to the linear relationship of the SV-plot. The poor linear regression coefficient of **B1** with Fe^{3+} by the Perrin static quenching model supported this assumption (see **Appendix B Figure 13**). The quenching plot of **B3** with Fe^{3+} according to the Perrin model is shown in **Figure 15**.

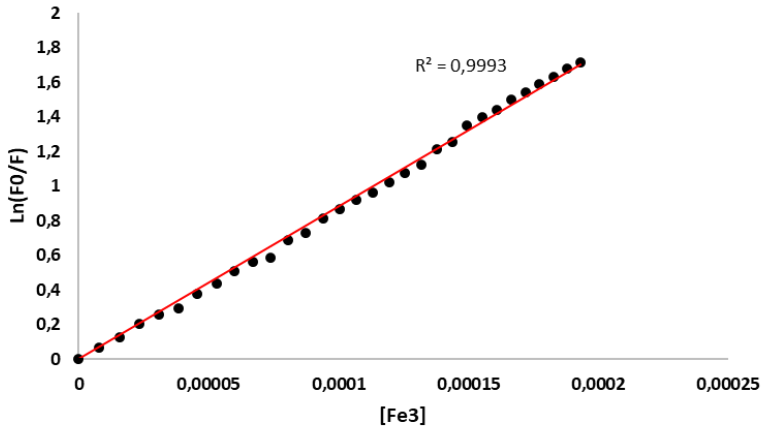

Figure 15: Fit of quenching data of **B3** by Fe^{3+} according to the Perrin static quenching model.

An excellent correlation was observed according to this model. The value for the Perrin quenching constant (K_p) was obtained from the slope of the graph (K_p = 9.1 x 10^3 M^{-1}). The respective detection limits of **B3** and **B1** by the Perrin and linear SV methods were determined to be 2.7 and 4.3 μM as calculated by: LOD = 3xσ/m. According to the United States Environmental Protection Agency (USEPA) the permissible amount of Fe^{3+} in drinking water is between 4.5 and 5.4 μM.[17,18] This indicates the applicability of these sensor towards Fe^{3+} determination.

The sphere of action (SOA) static quenching model was also investigated for its contribution towards fluorescent quenching of **B3** by Fe^{3+}. As mentioned in **Chapter 2**, the contribution of the quenching model is determined by the value of the quenching constant. The higher the value, the greater the contribution is towards the quenching model.

The plot of the titration data as fitted by the Sphere of Action static quenching model for **B3** in ethanol is shown in **Figure 16**. Linearity was only visible at higher quencher concentration (lower F/F_0 value) and not over the entire range, unlike the case of the Perrin model in **Figure 15**. The value of the regression coefficient was shown to be equal to 0.9768, a less linear correlation. The value for K_{SV} was calculated to be 4.7 x 10^3 M^{-1}, almost half the value obtained by the Perrin quenching model.

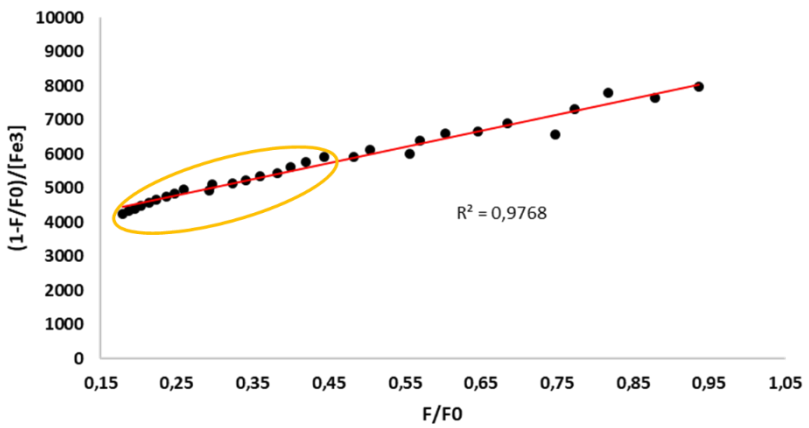

Figure 16: Plot of quenching titration data of **B3** fitted to the sphere of action static quenching model. The orange outline denotes the region of linearity used in calculations.

Although the values of the SOA quenching constant and regression coefficient were lower than that of the Perrin model, it still may play a role in fluorescent quenching. To determine this, a plot of ln(1/W) vs [Q] should yield a straight line with slope equal to constant (V). The values for W were determined from the intercept at each quencher concentration [Q] as according to Equation 4 in **Chapter 2**.

Figure 17 depicts the graph of the data fitted by ln(1/W) vs [Q]. An excellent correlation, corresponding to the region of higher quencher concentrations from the SOA plot, suggests the strong involvement of this quenching model at higher quencher concentrations. From this plot, the value of the quenching constant (V) and the radius of the proposed sphere of action can be calculated. The value of the quenching constant and sphere radius was reported as 5.0 x 10^3 M^{-1} and 126 nm respectively. Although the value of K_p was nearly double that of constant V, the amounts are still comparable. Therefore, it should be concluded that the Perrin model, together with the spere of action quenching model, constitutes the main static component in the proposed combined dynamic and static quenching model of **B3** with Fe^{3+}.

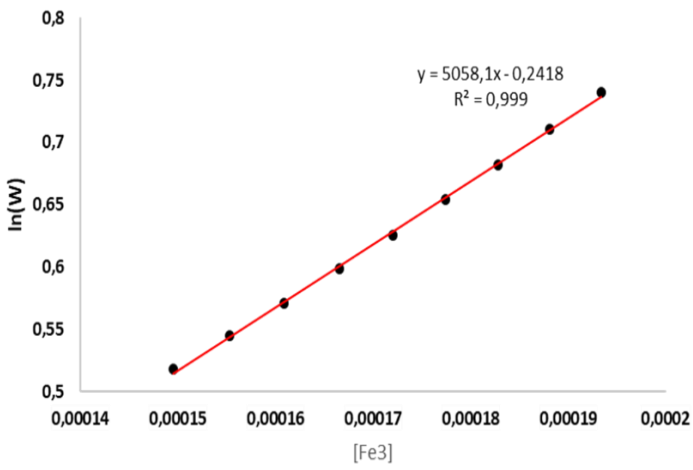

Figure 17: Plot of ln(1/W) vs [Q] of **B3** at higher [Fe^{3+}] titrations.

The value for the association constants (K_a) of both **B1** and **B3** were determined by the Benesi-Hildebrand analysis. Titration data was used to plot a graph of $1/F_0$-F vs 1/[Fe^{3+}]. The plots according to this equation for both sensors with Fe^{3+} is shown in **Figure 18**. Sensors **B1** and **B3** display a linear relationship with R^2 values of 0.9949 and 0.9994 respectively. This suggests a 1:1 sensor-ligand binding ratio which was later confirmed by Jobs-Plot analysis. The value for the association constants were calculated by the ratio of the intercept to the slope. These values are shown in **Table 2**.

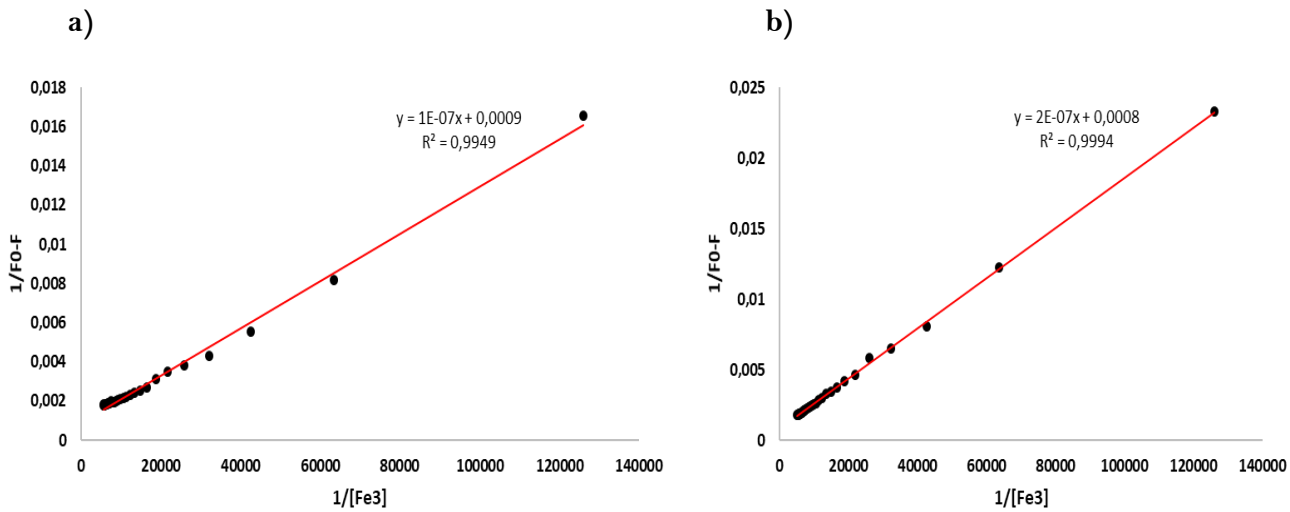

Figure 18: Benesi-Hildebrand plots of a) **B1** and b) **B3** with Fe^{3+}.

Table 2: Association constants (K_a) of sensors **B1** and **B3**.

Sensor	K_a x 10^3 M^{-1}
B1	7.4
B3	4.6

The strength of the sensor-metal bond between Fe^{3+} and **B1** is greater than that of Fe^{3+} with **B3**. The difference in association constant may be attributed to the solvent used to prepare the samples. Sensor **B1** and **B3** were prepared in DMF and methanol respectively. As mentioned previously, methanol has greater polarity than DMF. This difference in polarity may influence the binding between the sensors and Fe^{3+}. Since both experiments were conducted in ethanol, and binding is suggested to occur via the triazole ring nitrogen for both sensors, the stock solvent could be influencing the strength of this sensor-metal bond. The methanol molecules surrounding **B3** may pull greater electron density from the triazole ring system, thus making it less effective to donate to the vacant Fe^{3+} d-orbitals. This in turn will weaken the bond between the sensor and metal cation as fewer electrons will be available for bonding. Nevertheless, the values for the association constants are respectable. Reversibility studies with the hexadentate chelating ligand EDTA were conducted to determine whether binding towards Fe^{3+} was reversible.

3.1.7 Reversibility studies of B1 and B3-Fe^{3+} complexes with EDTA

The reversibility studies of **B1** and **B3** with hexadentate ligand EDTA are shown in **Figure 19**. Both sensors displayed a maximum of 27% reversibility upon EDTA addition from a quenched sensor-Fe^{3+} system. This suggests that the strength of the bond between the sensor and Fe^{3+} outweighs that of EDTA with Fe^{3+}, hence the poor reversibility.

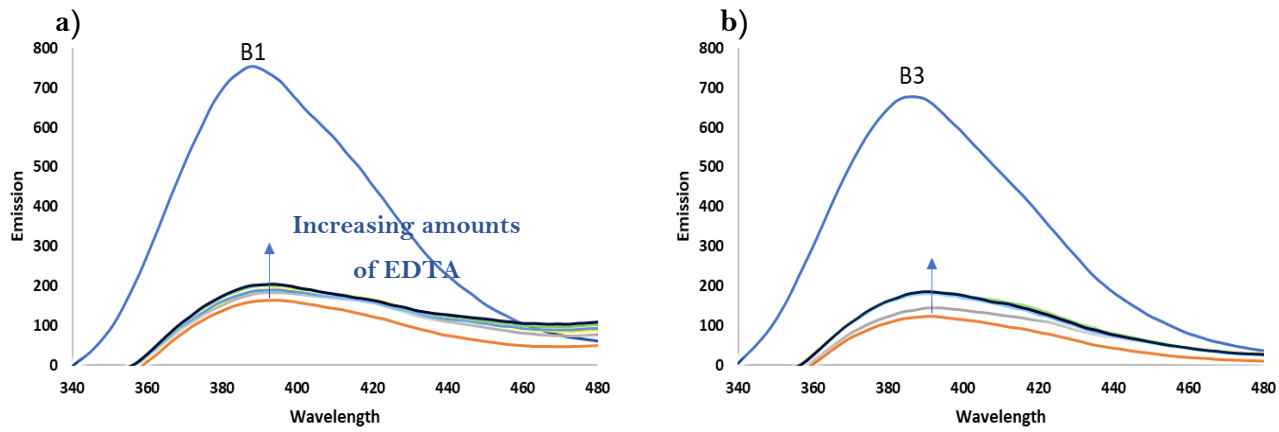

Figure 19: Reversibility studies of a) **B1** and b) **B3** with EDTA. The orange curve represents the fully quenched sensor-Fe^{3+} system. Excitation: 320nm.

3.1.8 Job's plot analysis

A Job's plot relationship between Fe^{3+} mole fraction and emissive output was plotted for increasing and decreasing amounts of Fe^{3+} whilst keeping the total molar concentration of the system constant. Results indicate that both sensors display a 1:1 binding stoichiometry with Fe^{3+} as suggested from the linearity of the Benesi-Hildebrand analysis. The binding ratio is determined where the emission intensity of the intersecting plots is greatest. The Job's plots of both **B1** and **B3** with Fe^{3+} (in DMF and methanol respectively) is shown in **Figure 20**.

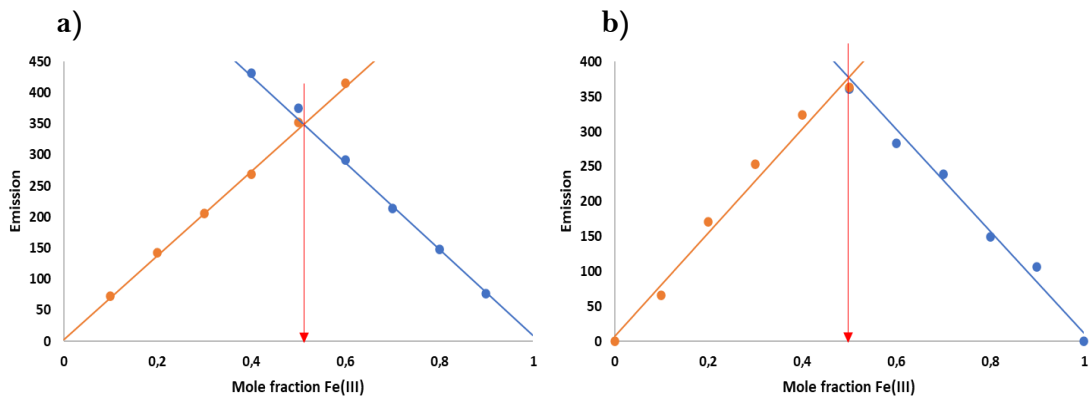

Figure 20: Jobs Plot analysis of a) **B1** and b) **B3** with Fe^{3+}. The red arrow denotes the 50/50 sensor-ligand binding ratio.

3.1.9 pH studies

To determine the effect of pH variations on sensing abilities, titration studies in different solutions were conducted. Different arrays of buffer solutions with pH of 10, 7, 5, and 4 were utilized for the study. Notably both sensors displayed quenching responses upon Fe^{3+} addition in all solutions. This indicates that the sensing of **B1** and **B3** towards Fe^{3+} is not pH dependant. This is a promising application for industrial application as mentioned in **Chapter 2**. **Figure 21** shows the quenching response of sensor **B1** with Fe^{3+} in different pH solutions (for the pH analysis of sensor **B3** with Fe^{3+} in different buffer solutions see **Appendix B Figure 14**).

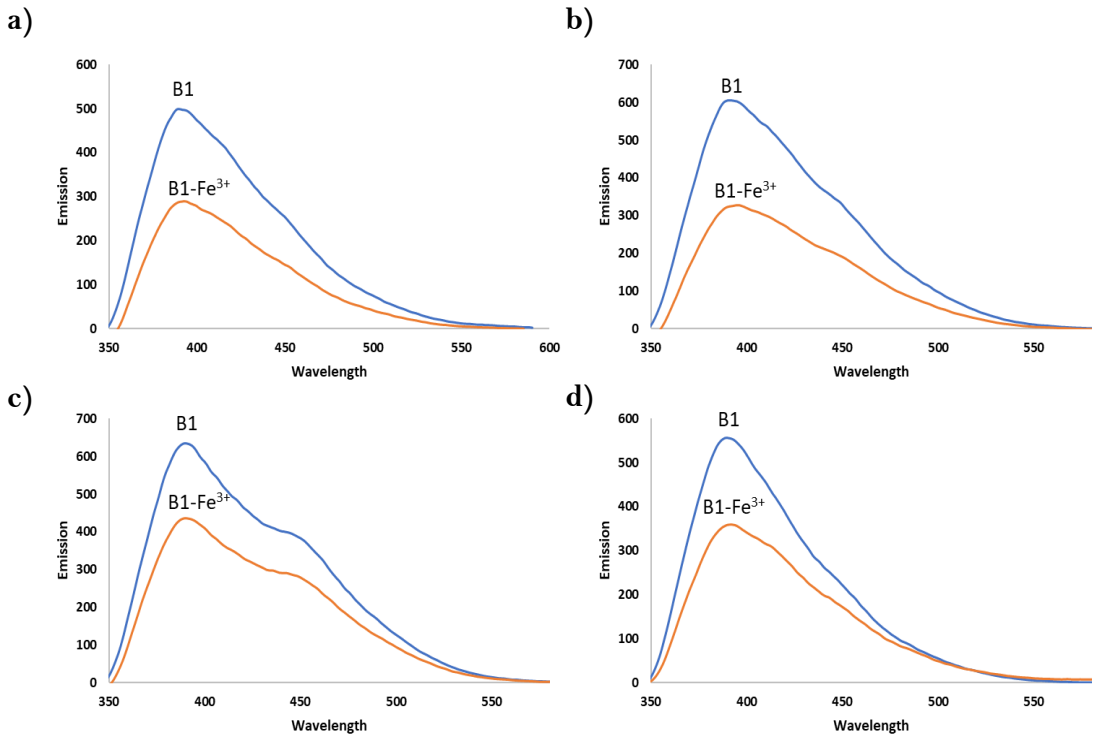

Figure 21: Effect of pH of sensor **B1** upon Fe^{3+} addition at pH: a) 4, b) 5, c) 7, and d) 10. Excitation of 320 nm.

3.1.10 Quantum yield studies

The fluorescence quantum yield (ϕ) of **B1** and **B3** were evaluated using anthracene as a standard fluorophore with a known ϕ_S of 0.27 in ethanol. The quantum yield of **B1** was evaluated in DMF whilst **B3** was evaluated in methanol. The samples and standard were excited with the same excitation wavelength (320 nm) and their absorbances were tuned to ca. 0.05 nm at this wavelength. The integrated areas under the emission spectra were obtained using fl. Winlab software and the quantum yields (ϕ) were calculated in accordance with **Equation 1** from **Chapter 2**. The value of the quantum yields for **B1** and **B3** were 0.005 and 0.044 respectively. This indicates that derivative **B3** has a greater proportion/fraction of excited state species upon excitation than that of **B1**.

3.1.11 Emission intensity (F_0)

As described in **Chapter 2**, the presence of the extended π-conjugated system with an electron donating, at position -7-, and an electron withdrawing group, at position -3-, enhances the overall emissive intensity of the fluorophore. In a similar study conducted by Ordonez-Hernandez and co-workers, the team describes how the electronic push-pull system in coumarin fluorophores play a crucial role in the overall device performance. The selection of the donor and acceptor units as well as the placement on the coumarin scaffold can either add to or detract from the extended π-conjugated system, thus altering the photophysical properties of the sensor.[19] They conclude that substituted -7- donating and -3- withdrawing coumarin-based functionalities best fit the criteria intended for extended spectral range and greater emissive intensity.[20]

Similarly, Chen and co-workers confirm this specified push-pull notion stating that the introduction of electron donating groups at position -7- and electron-withdrawing groups at position -3- or -4- on the coumarin scaffold, results in the establishment of highly fluorescent compounds ranging in wavelength bands from blue to red.[21] This statement has been further supported in other studies.[22,23] **Figure 22** illustrates the difference in the push-pull π-conjugated electronic character between coumarin sensors **A1** and **B3**. The initial fluorescent intensity of **A1** and **B3** at equimolar concentrations were vastly different. Sensor **A1** displayed extreme emissive intensity compared to **B3** and needed to be diluted further for fluorescent

studies. The possible placement of the functionalities on the coumarin fluorophore may drastically affect the emissive output observed. The oxygen and triazole functionality at position -7- of sensor **B3** would pull electron density away from the coumarin conjugated π-system, thereby inhibiting optimal electron transfer. Additionally, the electronegative characteristics of the triazole moiety extract further electron density from the coumarin fluorophore. The calculated electronic density map of **B3** is shown in **Figure 23**. The predominantly blue colour of the coumarin electron cloud relates to this electron deficiency and resulting low emissive intensity.

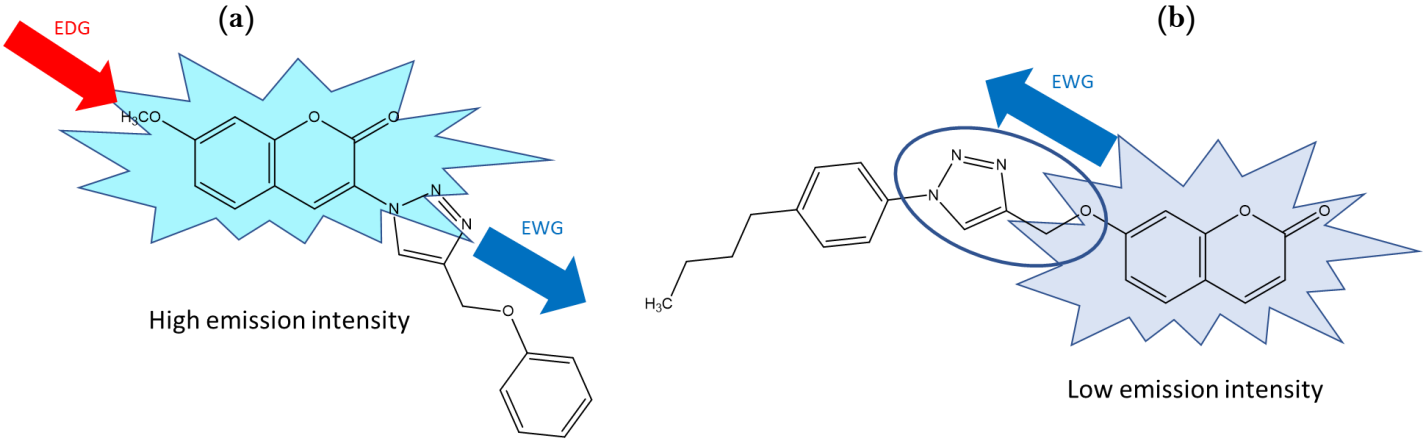

Figure 22: Electron donating and withdrawing characteristics by functionalities on a) **A1** and b) **B3**.

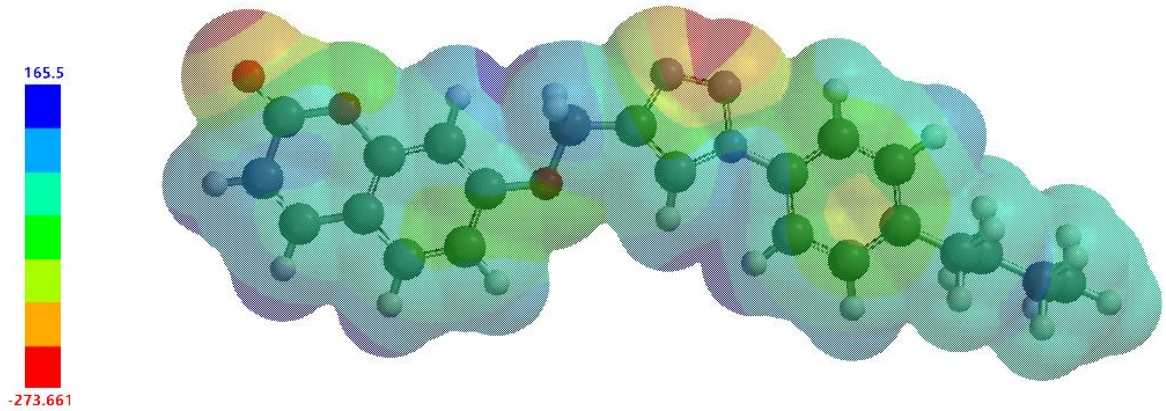

Figure 23: Calculated electron density of sensor **B3** at MMFF level.

In terms of the molecular orbital diagrams previously discussed, electronic transfer from the coumarin fluorophore (HOMO) towards the phenyl ring (LUMO) may provide reasons as to why the initial fluorescent intensity was greatly lower than that of **A1** in **Chapter 2**. In **B3**, electrons are drawn from the coumarin moiety, this consequently lowers the overall electron density and "push-pull" efficiency in the fluorophore. As a result, the intensity of the fluorescent output is subdued. As **Figure 23** shows, an area of concentrated electron density around the phenyl ring and triazole moiety, and a general electron deficiency within the coumarin scaffold. Conversely, the HOMO-LUMO arrangement of **A1** exhibited how electrons are transferred from the ether-phenyl derivative towards the coumarin fluorophore. This influx in electron density may amplify the emission intensity and alter the electronic environment by enhancing this "push-pull" character in the system, resulting in a brighter fluorophore.

3.1.12 Proposed binding site between B3 and Fe^{3+}

As previously mentioned, the triazole nitrogen atoms have been reported as contributors towards both metal- and anionic-sensor bonding scenarios. The coordination geometry of triazoles may be viewed as a combination of imidazoles and pyrazoles. Therefore, they possess the ability to act as a monodentate ligands or bridging agents between metal ions resulting in mono-, bi-, and polynuclear complexes.[24] A proposed coordination scenario between sensor **B3** and Fe^{3+} is shown in **Figure 24**. Complexation is postulated to involve the double bond N=N π-electrons.

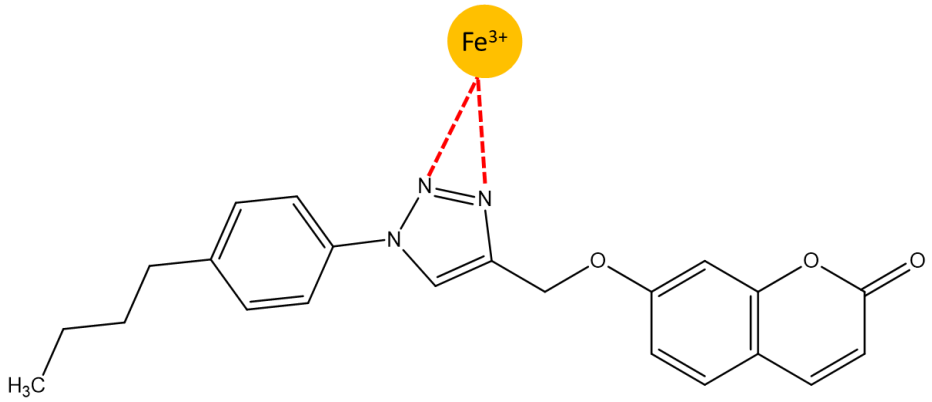

Figure 24: Proposed binding between sensor **B3** and Fe^{3+} via the triazole moiety.

^{1}H NMR, ^{13}C NMR, and ^{15}N NMR titration studies were used to validate the proposed binding scenario between **B3** and Fe^{3+}. The same binding scenario may be assumed between sensor **B1** and Fe^{3+}. The methyl functionality on the phenyl ring in **B1** would be an unlikely contributor towards coordination, therefore, the same complexation scenario can be assumed. The ^{1}H NMR titration of **B3** with aliquots of $Fe(NO_3)_3$ is shown in **Figure 25**. Evidently, the more Fe^{3+} is added, the less resolved the signals become. Computational studies predict that no hydrogen bonding is involved. This agrees with the experimental data. As sensor **B3** has shown the same affinity and selectivity towards Fe^{3+} as **A1** displayed in **Chapter 2**, it is assumed that the triazole nitrogen contributes most of the electrons towards coordination with Fe^{3+} with possible assistance from neighbouring functionalities like the coumarin-carbonyl lone electron pair.

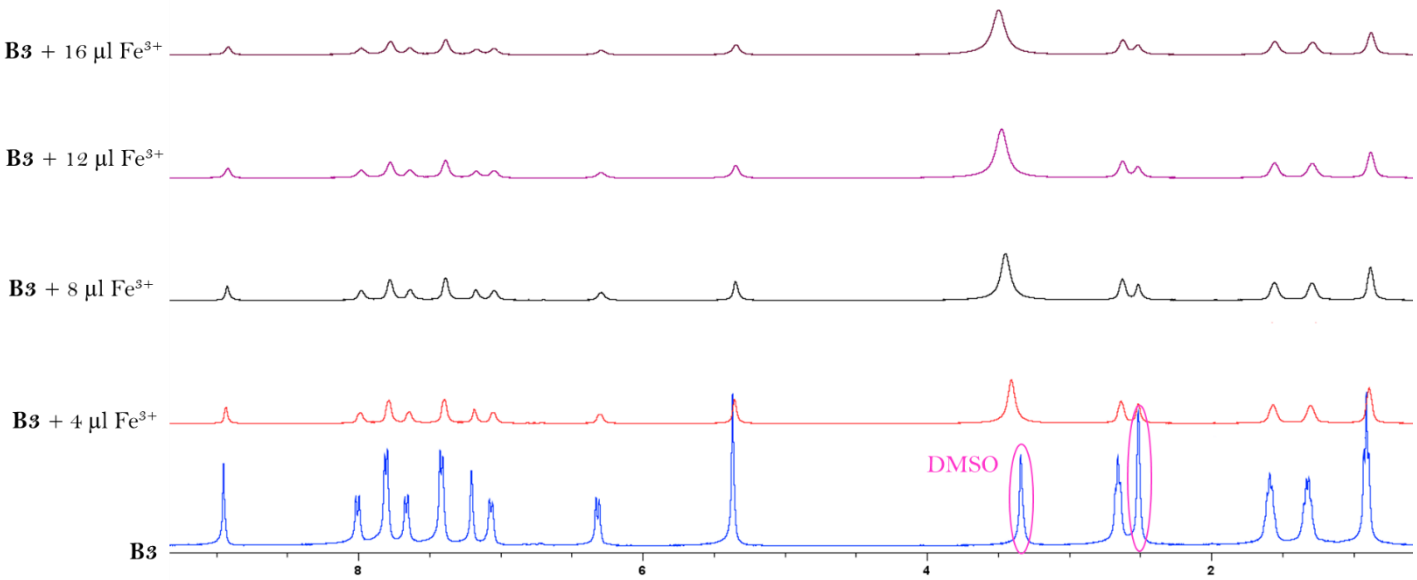

Figure 25: ^{1}H NMR titration of **B3** with Fe^{3+} in d_6-DMSO.

^{13}C NMR titration studies of **B3** with Fe^{3+} are shown in **Figure 26**. Upon Fe^{3+} addition, no shift of signals was observed. As seen in **Chapter 2**, the peak associated with the coumarin-carbonyl functionality displayed no shift in ppm value. Theoretical computations suggest that complexation could be assisted by the lone pair of electrons from the carbonyl functionality. Since no formal covalent bond is formed, minimal to no shift in ppm value would be expected. The involvement of the coumarin-carbonyl was later suggested by computational analysis.

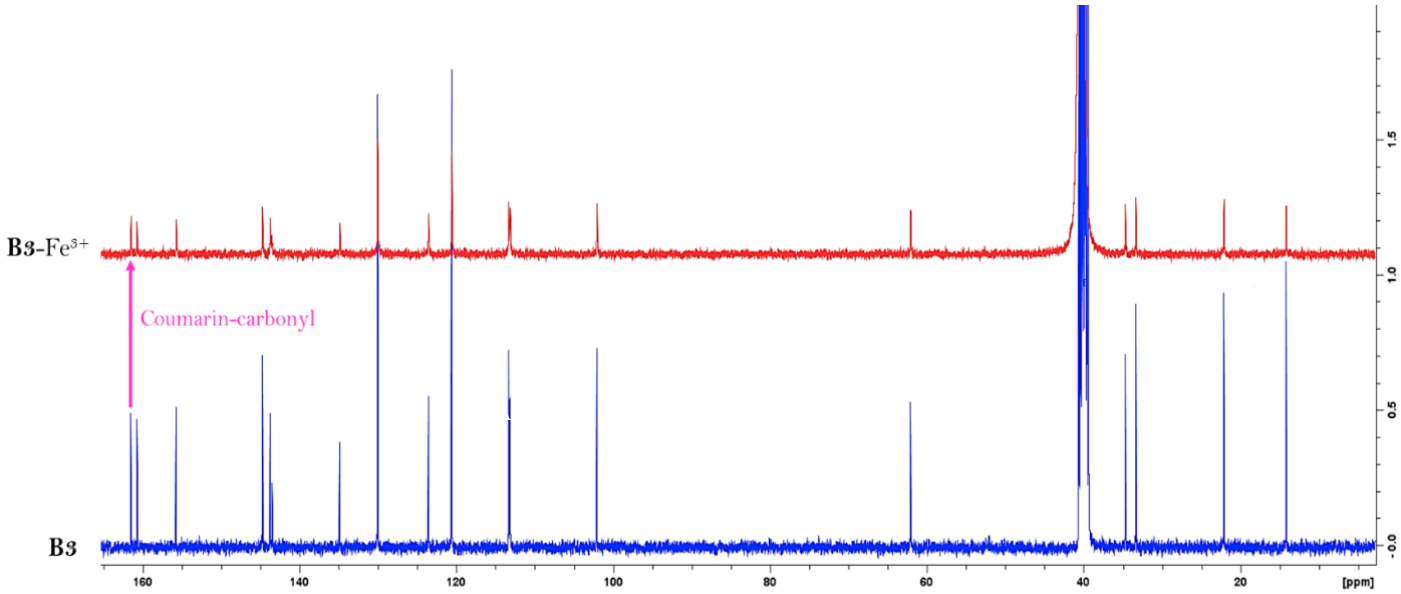

Figure 26: ^{13}C NMR overlay of **B3** with Fe^{3+} in d_6-DMSO.

The ^{15}N NMR spectral comparison of **B3** and the **B3**-Fe^{3+} complex suggested the involvement of the triazole moiety towards complexation. The ^{15}N NMR of **B3** is shown in **Figure 27**. ^{15}N NMR spectroscopy has been used as a method to assign the coordination of metals with triazole-bearing structures in solution. The nitrogen atoms in these complexes are reported to experience the most dramatic changes upon analyte coordination. Additionally, nitrogen chemical shifts are highly sensitive to structural changes, more so than ^{13}C chemical shifts.[25] Evidently, only two of the three expected peaks for the triazole moiety were observed. The low abundance and gyromagnetic ratio of ^{15}N could account for the difficulties in nitrogen signal observation. An increase in scan time could assist in amplifying the third nitrogen signal.

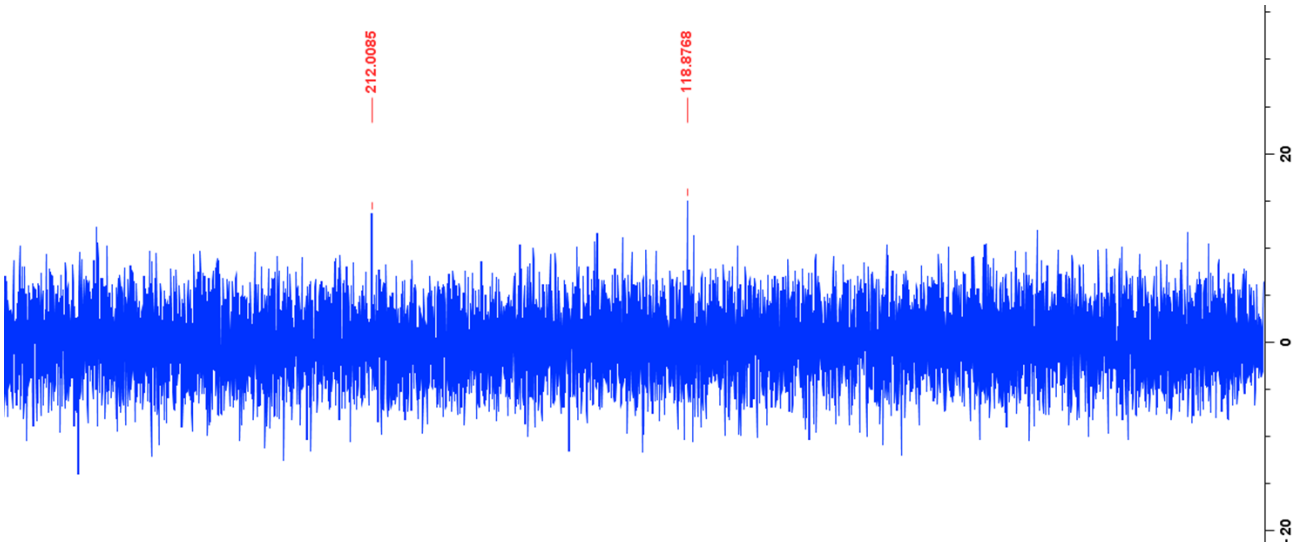

Figure 27: ^{15}N NMR of **B3** in d_6-DMSO.

Figure 28 shows the ^{15}N NMR of the **B3**-Fe^{3+} complex. The two peaks at 212 and 118 ppm are no longer visible. A single peak is observed at -1.38 ppm. This could either be the third "missing" nitrogen signal of **B3**; or it could pertain to the shift of one of the two nitrogen signals upon coordination. Literature reports the shielding characteristics of 1,2,3-triazoles occurring in the order N1>>N3>N2.[26] The appearance of the signal at -1.38 ppm could account for the N-1 triazole nitrogen atom due to the great "gap" that literature reports between N-1 and N-3. Owing to the disappearance/decreased resolution of N-3 and N-2 upon complexation, the signal for N-1 could become more pronounced. Therefore, the two signals observed in **B3** which disappeared upon Fe^{3+} addition are postulated to be double-bonded nitrogen atoms N-2 and N-3. Complexation at this site agrees well with general organometallic coordination chemistry of triazole-metal complexes previously discussed. Lastly, as the triazole moiety provides the singular source of nitrogen atoms towards complexation, the changes in the ^{15}N NMR spectra observed could have only arisen from triazole interaction in the **B3**-Fe^{3+} coordination scenario.

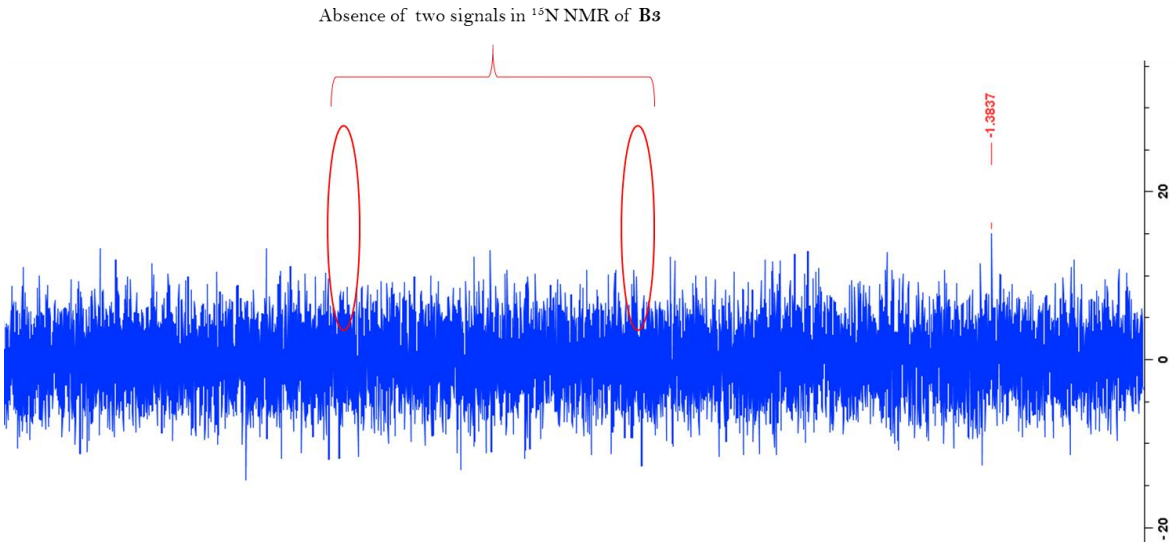

Figure 28: ^{15}N NMR of **B3**-Fe^{3+} complexation in d_6-DMSO.

3.1.13 Calculated number of binding sites between B3 and Fe^{3+}

The titration data of **B1** and **B3** with Fe^{3+} was used to verify the number of binding sites between the sensor and metal cation during complexation. The double-logarithm plot of Log[F_0-F/F] vs Log[Q] should yield a straight line with the gradient equal to n, where n is the number of binding sites between the two species. Notably, both plots show an appreciable linear correlation, thus confirming the dominance of the static quenching process. This was observed for both **B1** and **B3** from titration studies. The number of binding sites was shown to be 1.14 and 1.39 for **B1** and **B3** respectively. This further suggests that both the methyl and butyl functionalities serve only to differ the emissive intensity and do not contribute towards metal complexation. Owing to the calculated number of binding sites between **B3** and Fe^{3+} being equal to ±1.39, it is proposed that the triazole moiety may be assisted by another functionality. In **Chapter 2** it was shown how the coumarin carbonyl lone electron pair could contribute towards stabilizing coordination. This was strongly suggested by molecular modelling studies whereby the coumarin carbonyl appears to bend towards the Fe^{3+} cation to facilitate complexation. The double-logarithm plots of sensors **B1** and **B3** with Fe^{3+} is shown in **Figure 29**.

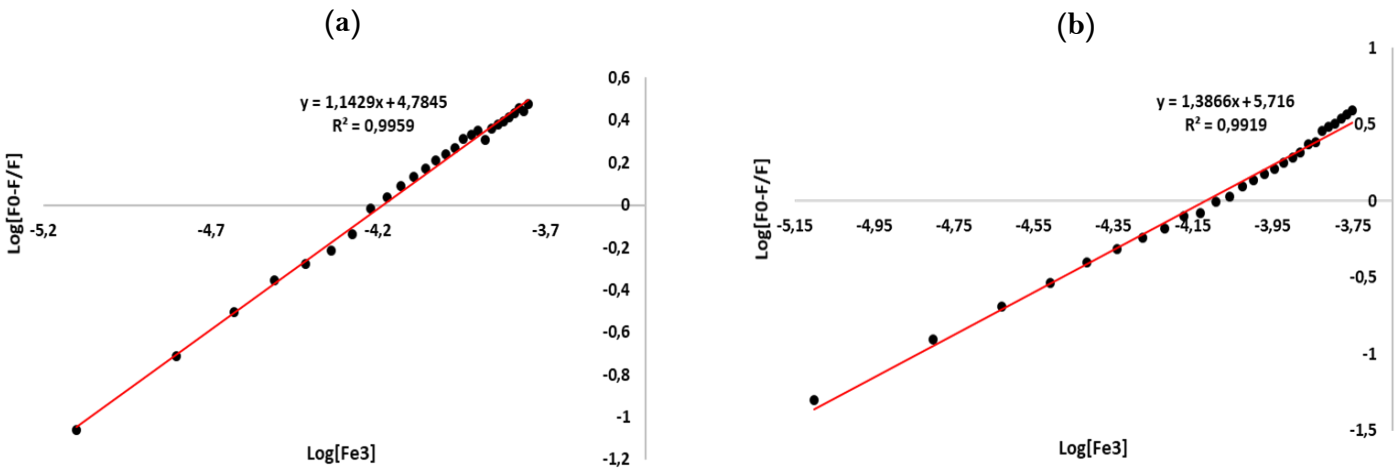

Figure 29: Double-logarithm plot of a) **B1** and b) **B3** with Fe^{3+}.

3.1.14 Computational analysis of B3

3.1.14.1 Most preferred conformer

Molecular modelling studies performed to determine the lowest energy conformer of **B3** at PM3 calculation level. This conformation was compared to that of the single crystal XRD data. Results are in close agreement with the observed crystal structure (**Figure 30**). The N-2 and N-3 triazole atoms are orientated in the same direction as the coumarin-carbonyl functionality in both the calculated and observed crystal structure of **B3**.

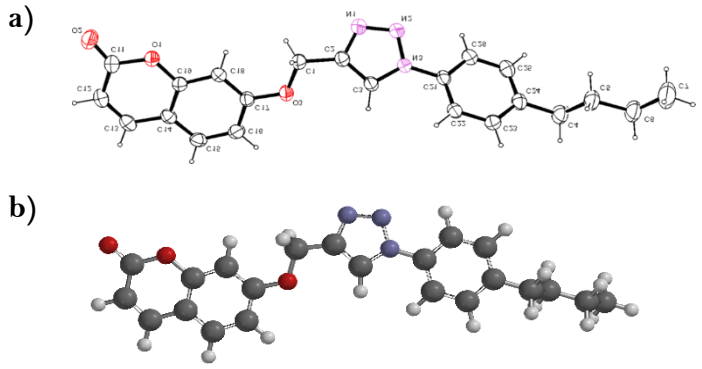

Figure 30: a) Experimental single-crystal XRD results and b) computationally calculated most stable conformation of **B3**.

3.1.14.2 Metal binding energies and selectivity trends

Once the most energetically preferred conformer of **B3** was determined, complexation with metal cations were calculated. As previously seen, **B3** displayed the strongest affinity to Fe^{2+} and Fe^{3+} which was characterized by large quenching emission responses. The calculated energies of **B3**-Fe^{2+} and **B3**-Fe^{3+} were -410 and -964 kJ/mol respectively. The complexation of **B3** with Fe^{3+} showed more than two times the energetic stability compared to that of Fe^{2+}. This could account for the appreciable selectivity **B3** showed towards Fe^{3+} and strong PET-CHQF quenching response.

3.1.14.3 Binding scenario and of B3 with Fe^{3+}

Computations of the most preferred binding site between **B3** and Fe^{3+} was calculated at the PM3 calculation level. Computations indicate the proximity of the Fe^{3+} cation to the triazole N=N and coumarin carbonyl functionalities. Complexation was calculated in the presence of water and polar solvents. Evidently, surrounding water and solvent molecules assist in the coordination and stabilization of the **B3**-Fe^{3+} complex. The energy of the complexation was calculated to be -1652.13 kJ/mol. The complexation of **B3** with Fe^{3+} is energetically more favourable than **B3** alone. This stability could explain the reason as to why the **B3**-Fe^{3+}complex was minimally reversible in the presence of EDTA. The calculated most stable conformation of the **B3**-Fe^{3+} complex is shown in **Figure 31**. Although total confirmation of the binding scenario\sites could be elucidated by single-crystal XRD analysis; organometallic compounds of these nature (coumarin derivatives) do not readily crystallize with the metal cation present.

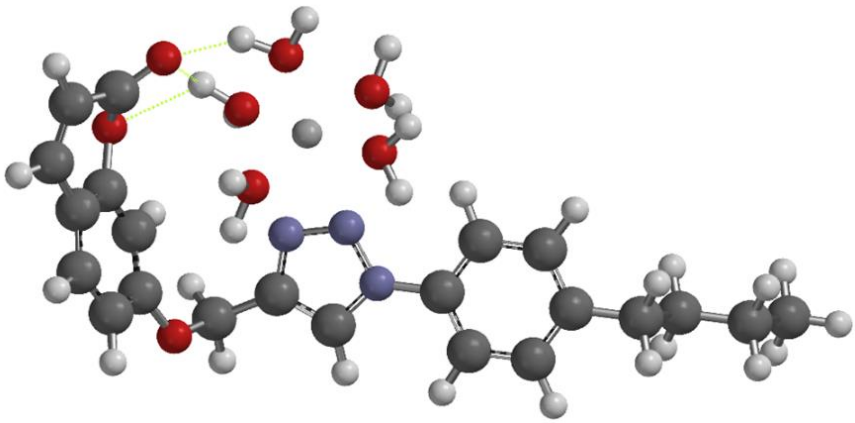

Figure 31: Calculated most preferred conformer of **B3**-Fe^{3+}complexation at PM3 calculation level.

The resulting conformer correlates well with the experimental data and literature reports. The proximity of the cation to the N=N triazole atoms and the bending of the coumarin-carbonyl functionality towards the Fe^{3+} strongly suggest their involvement towards complexation. Computations were calculated in water for this experiment. The water would be introduced together with the Fe^{3+} from the prepared stock solution. Ethanol (used in emission and absorbance studies) is a non-polar protic solvent, therefore, its disruption of the stabilizing water molecules towards Fe^{3+} would be unlikely. The hydrogen bonding between

the coumarin carbonyl with the hydrogen atoms of the water molecules stabilizes their interaction with the Fe^{3+} cation. The weak hydrogen bonding between the coumarin carbonyl and water protons elucidate why there were no visible shifts in the ^{13}C NMR studies. High electron density resides on the triazole N-2 and N-3 (N=N) atoms, which are favourable sites of complexation in organometallic complexes. Therefore, most of the electrons involved in complexation are postulated to come from the triazole moiety and are stabilized by water and hydrogen bonding with the coumarin-carbonyl functionality.

Anionic sensing studies

3.1.15 Screening studies

Sensor **B3** was chosen for the investigation for its affinity towards a variety of anions in different solvent systems. These anions included: CN^-, SCN^-, SO_4^{2-}, NO_3^-, CH_3COO^-, I^-, Br^-, Cl^-, F^- and PF_6^-. Solutions of theses anions were prepared in deionized water from their ammonium salts. The sensing properties of **B3** was tested in four different organic solvents namely acetonitrile, DMF, methanol, ethanol, and water. An excitation wavelength of 320 nm was used. Screening studies were conducted by adding 20 µl aliquots of a 0.1 M solution and monitoring the change in fluorescent intensity. The effect of each anion towards **B3** in differing solvents are shown in **Figure 32**. Screening studies conducted in water were not investigated further due to the irregularity of the emission curve of **B3** (see **Appendix B Figure 15**).

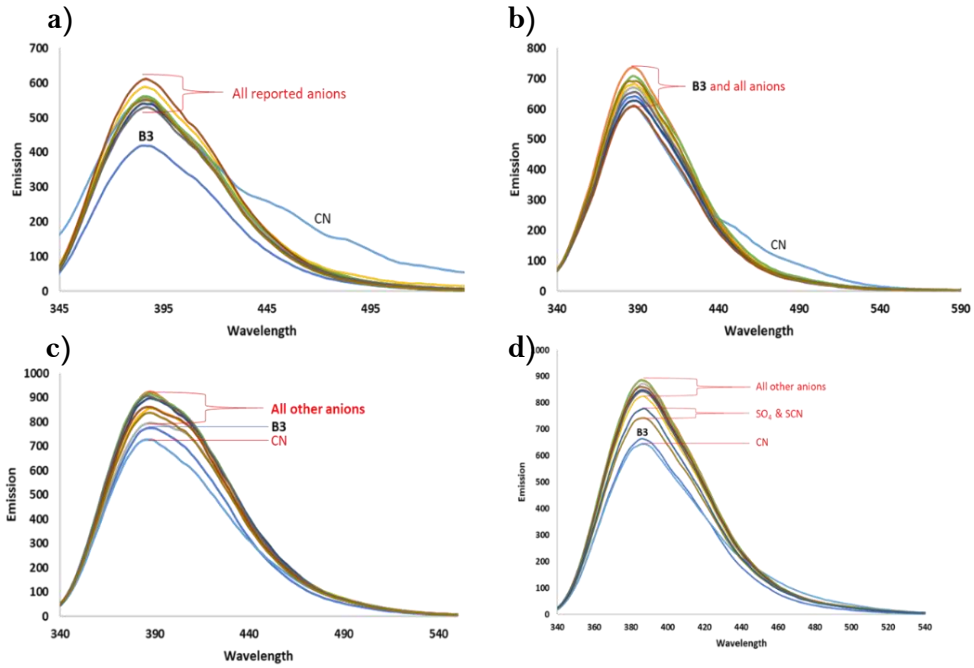

Figure 32: Screening studies of **B3** with different anions in a) acetonitrile, b) DMF, c) ethanol, and d) methanol. Excitation 320 nm.

When compared to the metal screening studies, **B3** does not display the same affinity or preference to any singular anion in all four organic solvents. No sizeable enhancement nor quenching effect for any single anion was observed. The screening studies conducted in ethanol displayed CN^- as the only anion to induce a quenching response, although minimally. Competition studies of **B3** with CN^- in ethanol was conducted to observe whether **B3** showed any affinity towards CN^- in the presence of competing anions.

3.1.16 Competition studies of B3 with CN^- in ethanol

The competition study of **B3** with CN^- in ethanol is shown in **Figure 33**. Notably, **B3** appears to show selectivity towards CN^- only in the presence of F^- and PF_6^-.

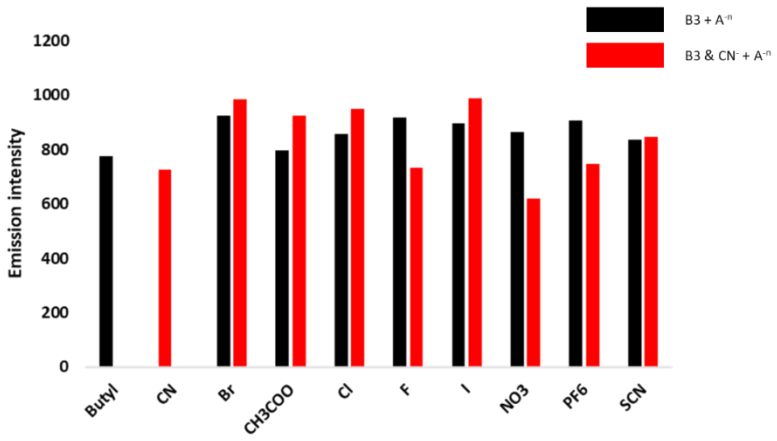

Figure 33: Selectivity of **B3** towards CN^- in the presence of competing anions in ethanol. Excitation of 320nm.

3.1.17 Titration studies of B3 with F^-

Titration studies of sensor **B3** with CN^- in ethanol were conducted despite the poor selectivity reported. Although it displayed poor selectivity, the sensitivity it could display towards CN^- could support its application towards CN^- sensing in isolated systems. Addition of a single aliquot of a 0.01 M solution CN^- showed an initial quenching response. However, upon titration, the emission intensity began increasing. Therefore, the titration of **B3** with CN^- in ethanol was no longer a viable titration option. For this reason, F^- in methanol was chosen for titration and complexation analysis as it displayed the greatest fluorescent enhancement (an emission property yet to be investigated) as well as being a detrimental anion to environmental and human health.[27–30] Additionally, the interaction of CN^- with triazole bearing complex **A1** was investigated experimentally and computationally in **Chapter 2**. Competition studies were not conducted as screening emission curves of F^- were too closely confined with other competing anions. The enhancing titrations of **B3** with F^- is illustrated in **Figure 34**. No hypso- nor bathochromic- shifts in wavelength were observed upon analyte titration. This suggests a PET-type "off-on" fluorescent system with binding suggested to occur via the acidic triazole proton.

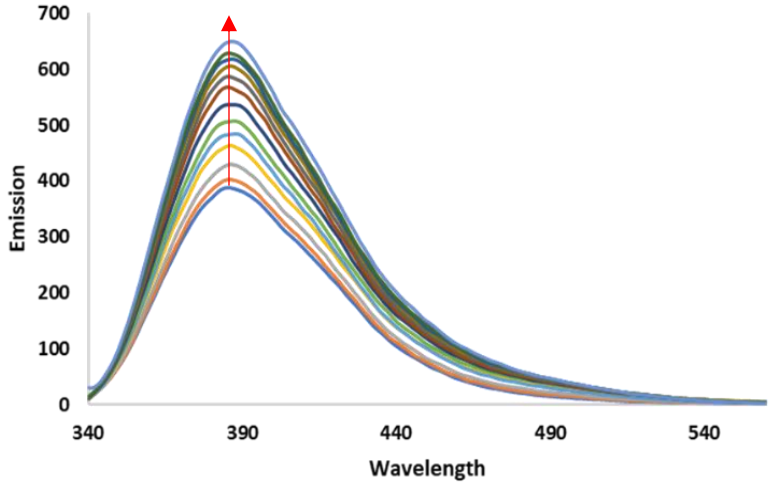

Figure 34: Titration of **B3** with F^- in methanol. Excitation of 320nm.

3.1.18 PET "off-on" fluorescent enhancing mechanism of B3-F^- interaction

Although the removal of the triazolyl proton can be suggested from the calculated bond lengths and electron density map, it cannot explain the enhancing changes in fluorescence observed upon F^- titration. The calculated HOMO and LUMO orbital arrangement of **B3** post F^- interaction is shown in **Figure 35**. Upon the abstraction of the triazole proton and evolution of HF, the HOMO of the resulting structure resides on the triazole moiety. This increased electron density amplifies its donor capabilities. The LUMO of the resulting complex resides around the coumarin fluorophore, amplifying its acceptor capabilities. Upon interaction and abstraction electron density is transferred from the triazole to the coumarin fluorophore via a PET "off-on" fluorescent mechanism, leading to an overall enhancement in fluorescence. The molecular orbital energy diagram of the PET "off-on" mechanism resulting in fluorescent enhancement is also shown in **Figure 35**.[31] The HOMO and LUMO of **B3** in the presence of F^- is shown in **Appendix B Figure 16**. The configuration of the HOMO and LUMO of the complex remains consistent with fluorescent enhancement.

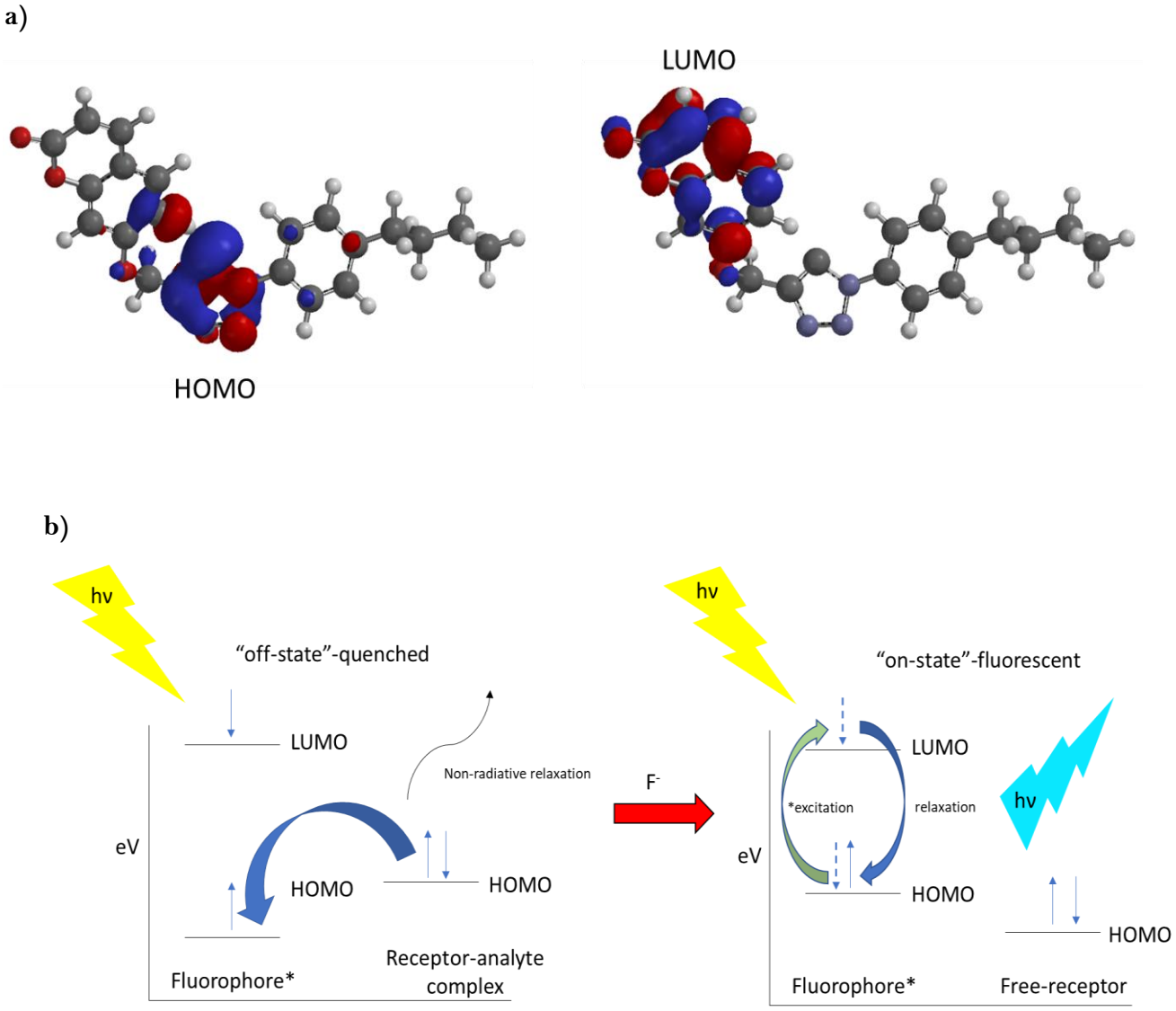

Figure 35: a) HOMO and LUMO of **B3** post-proton abstraction and HF(g) evolution, and b) molecular orbital energy diagram of electronic transitions post HF evolution leading to fluorescent enhancement.

3.1.19 Proposed binding site of B3 with F^-

Literature reports that 1,2,3-triazole supports polar C-H groups which have been used for sensing strategies. The ring is shown to have enhanced polarization of the C-H bond in this heteroaromatic system because of the three nitrogen atoms. As a result, the more polarized form of the C-H bond can be utilized for anion recognition *via* hydrogen bonding.[32] In **Chapter 2**, the binding of **A1** with NO_3^- was shown to occur via the triazole carbon double bond by ^{13}C NMR and molecular modelling studies. A similar binding scenario could be

assumed for **B3** with NO_3^-. The binding of CN^- with **A1** was shown to involve the triazole proton. The involvement of the triazole proton with F^- was postulated as a preferred complexation site due to the acidic nature of the proton and high electronegativity of F^-. The proposed interaction of F^- with **B3** is shown in **Figure 36**.

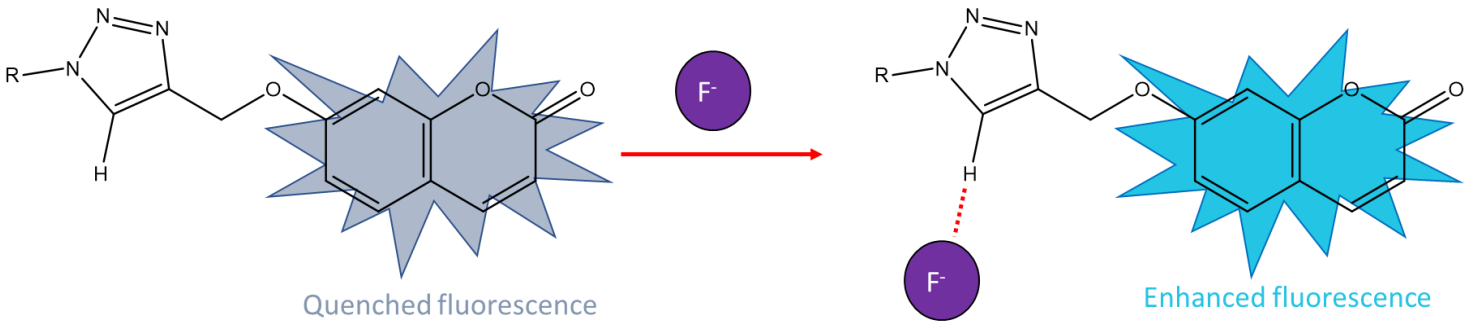

Figure 36: Proposed complexation of **B3** with F^-.

Computational analysis was able to resolve the proposed interaction between **B3** and F^-. The most energetically stable conformer was calculated and then used for coordination with F^- at PM3 computation level. The theoretical complexation of **B3** with F^- is illustrated in **Figure 37**. This structure agrees well with what is reported and proposed regarding triazole-proton interactions with anions. Evidently, an abnormally long bond exists between the triazole C-2 atom and its proton; and a comparatively shorter bond distance between the fluoride anion and the triazole proton. This could infer that the proton has been abstracted by the highly electronegative F^- anion, thus evolving HF gas into solution.

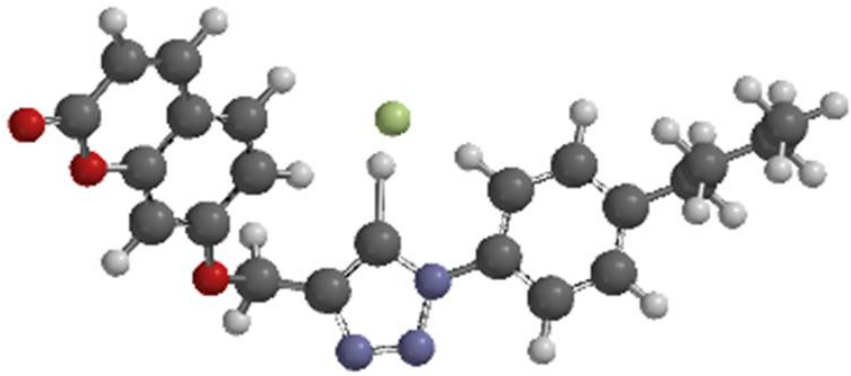

Figure 37: Calculated binding interaction of F^- with **B3**. The green sphere represents the fluoride anion.

The possible abstraction of the acidic triazole proton by F^- to form HF gas was investigated by calculating the theoretical bond lengths observed for atoms involved in the complex. **Table 3** shows the theoretical bond lengths of the complex compared to that of HF.

Table 3: Calculated bond lengths between different atoms involved in complexation.

Bond specifications	Bond length (Å)
(HF theoretical)	0.938
(F^------H)----C	1.007
(F^-----------C)	1.620
(F^------(H----C)	1.093

The calculated bond lengths for the different bonding scenarios point towards the evolution of HF gas during complexation. The bond length between F^- with the triazole proton is comparable to that of HF alone. The bond length between the F^- anion and the triazole C-2 carbon is too long to assume possible coordination. Additionally, the calculated bond length between the triazole carbon and proton is longer than that observed between the same proton and F^-. This abstraction of the singular hydrogen becomes increasingly probable when the electrostatic potential map of **B3** with F^- is considered (**Figure 38**).

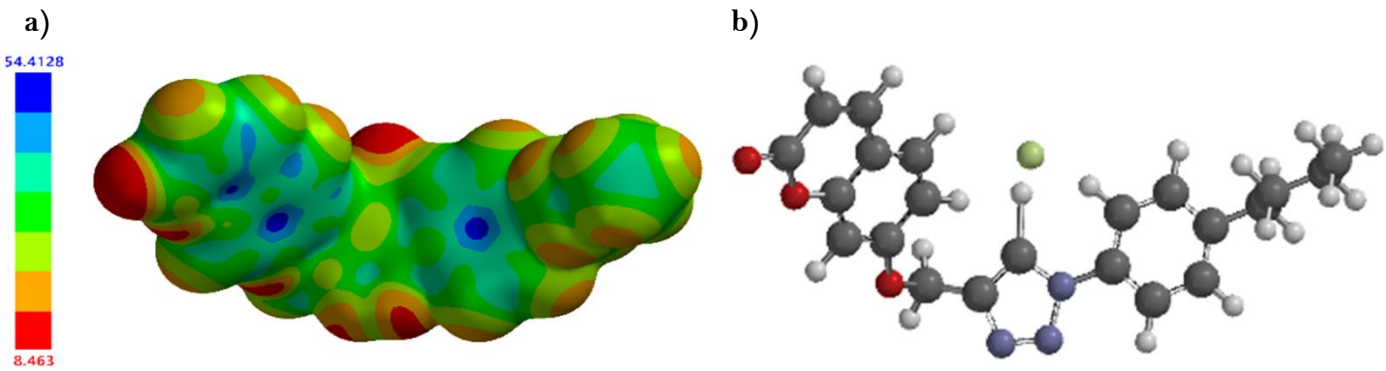

Figure 38: a) calculated electrostatic potential of **B3** with F^- and b) most stable conformation of **B3**-F^- interaction for spatial reference.

The result clearly indicates a region of high electron density surrounding the fluoride anion, conversely, a region of electron deficiency is located around the triazole C-2 carbon previously bearing the proton. The high electronegativity and ionizing capability of F^- contributes to the total abstraction of the proton, and not the formation of a covalent bond with continued connection to the triazole moiety.

3.2 Conclusion

Herein, four novel 7-functionalized coumarin-triazole derivatives for investigations towards cationic and anionic sensing strategies have been described. These sensors bear a substituted triazole moiety at the -7- position on the coumarin scaffold. Sensors **B1** and **B3** displayed the greatest affinity towards Fe^{3+}, with sensor **B3** exhibiting greater overall selectivity towards Fe^{3+} in ethanol. Both sensors were investigated for their photophysical properties and titration response towards Fe^{3+} in ethanol. Both **B1** and **B3** displayed fluorescent quenching responses upon Fe^{3+} addition via a linear Stern-Volmer and combined Perrin-SOA static quenching models respectively. Additionally, the fluorescence of both sensors was concluded to be quench via a CHQF PET "on-off" mechanism. These sensors were shown to complex to Fe^{3+} in a 1:1 stoichiometric binding ratio, with detection limits and association constants (K_a) of 4.3 μM & 7.4 x 10^3 M^{-1}, and 2.7 μM & 4.6 x 10^3 M^{-1} for **B1** and **B3** respectively. Reversibility studies indicates a 21% reversibility for both **B1**-Fe^{3+} and **B3**-Fe^{3+} in the presence of EDTA. Hydrogen potential studies showed good usability over an appreciable pH range for both sensors. Complexation was shown to involve the triazole N=N bond, supported by the coumarin-carbonyl and surrounding solvent/water molecules. Finally, quantum yield studies indicate sensor **B3** as a brighter fluorophore with a ϕ of 0.044 as compared to 0.005 of **B1**.

Screening studies of **B3** with a variety of anions did not display the same visible affinity with any of the selected analytes; with CN^- being the only ion to induce a quenching response in ethanol. Titration studies with CN^- were inconclusive, thus F^- was selected for further photophysical investigations owing to its unique fluorescent enhancing response observed from the screening studies. Fluorescent enhancement was shown to occur via the abstraction of the triazole acidic C-2 proton, with the subsequent evolution of HF gas. This fluorescent enhancement was postulated to occur via a PET "off-on" mechanism, supported by the calculated molecular orbital arrangement of the triazole-donor and coumarin-acceptor moieties.

3.3 Experimental

3.3.1 Materials

Stock solutions of coumarin-triazole derivatives **B1-4** were prepared by dissolving the respective samples in 25 mL of methanol and DMF to afford stock solution concentration of 0.001 M. Deionized water was used to prepare solutions of metal ions to the concentration of 0.01 M which were then diluted further for titration studies. All metal ion solutions were prepared using nitrate salts; apart from Fe^{2+} which was prepared from its corresponding sulphate salt. The anion stock solutions were prepared in deionized water from their ammonium salts to a concentration of 0.1 M. They were then diluted to the desired concentrations for titration studies. The emission and absorbance titration experiments were performed in 3 mL quartz and glass cuvettes respectively using solutions of compounds **B1-4**. Spectroscopic measurements were performed after each addition of an aliquot of selected metal and anion solution.

Generalized synthesis of azide-derivatives 1a-d

Azide derivatives were prepared from their respective anilines. These *para* functionalized aniline derivatives include toluidine, anisidine, butylaniline, and bromoaniline. Hydrolysis of the amine to the azide functionality was carried out by reacting the respective aniline (2g) and an HCl:EtOH mixture of 1:2 by volume. The refluxed was carried out for 2hr, after which the reaction mixture was cooled to 0°C in an ice-bath and distilled water was added to the reaction mixture. To this mixture, sodium nitrite (3 molar eq.), and sodium azide (2 molar eq.) were added carefully to the reaction vessel and left to stir at 0°C for 2 hrs. The toluidine, anisidine, and butyl derivatives were extracted from solution using 3 x 40ml of ethyl acetate and washed with equal proportions of water. The extracts were combined, dried over anhydrous sodium sulphate (Na_2SO_4), and the solvent was removed under reduced pressure. This afforded the azide derivatives **1a-c** as a liquid/oil product in yields of 82, 28 and 91 % respectively. The bromo-azide derivative **1d** was precipitated, filtered, dried, and collected as an off-white solid with a yield of 93 %. For the FT-IR spectra of azide derivatives **1a-d** see **Figure 1**. The azide functionality was observed as strong, sharp peak between 2100-2000 cm^{-1}.

Synthesis of 7-propinyloxy coumarin derivative 2

7-propinyloxy coumarin was synthesized from umbelliferone following literature procedure.[3] Umbelliferone (7-hydroxycoumarin) was refluxed in proportionate molar quantities of propargyl bromide and K_2CO_3 in acetone. The reaction mixture was separated with ethyl acetate and washed with water. The extracts were combined, washed, separated, and dried with anhydrous Na_2SO_4. The solvent was removed under reduced pressure to afford a white precipitate which was recrystallized with DCM and ether to afford the product as a white solid at a high yield (86%). ^{1}H NMR: (d_6-DMSO, 400 MHz) δ_H: 2.59(s, 1H), 4.78(s, 2H), 6.29(d, 2H, *J* 9.44), 6.92(s, 1H), 6.95(d, 1H, *J* 4.28), 7.41(d, 1H, *J* 8.44), 7.66(d, 1H, *J* 9.48). ^{13}C NMR (DMSO-d_6, 100.6 MHz) δ_C: 56.21, 102.15, 113.06, 113.19, 113.68, 128.83, 143.26, 155.65, 160.54, 160.99.

Synthesis of 7-substituted coumarin-triazole sensors B1-B4

Azide derivatives **1a-d** (0.3g) and 7-propinyloxy coumarin derivative **2** (1 eq.) were reacted in THF (20 ml) in the presence of $CuSO_4.5H_2O$ (0.01 g, 0.05 mmol), sodium ascorbate (0.02 g, 0.10 mmol), and N,N,N′,N″,N″- pentamethyldiethylenetriamine (PMDETA) (0.02 g, 0.10 mmol). The reaction mixture was stirred at room temperature for 48 hrs. The solvent was evaporated under vacuum and the residue dissolved in ethyl acetate (30 mL), washed with water (3x30ml) and dried over anhydrous Na_2cxSO4. The solvent was evaporated under vacuum and crude product purified by recrystallization from DCM (5 mL) and petroleum ether (40 mL) to give the desired triazolyl coumarin derivatives **B1-4** as solid products in yields of 72, 61, 77, and 72% respectively. Crystals were prepared by dissolving compounds **B1-3** in acetone and **B4** in d_6-DMSO and left to slowly evaporate.

Sensor **B1**: ^{1}H NMR: (d_6-DMSO, 400 MHz) δ_H: 2.38(s, 3H), 5.35(s, 2H), 6.31(d, 1H, *J* 7.2), 7.06-8.00(aromatic H's), 8.94(s, 1H, triazole proton). ^{13}C NMR (DMSO-d_6, 100.6 MHz) δ_C: 21.05, 62.11, 102.01, 113.25, 113.38, 120.57, 123.58, 130.05, 130.74, 138.98, 144.76, 160.73.

Sensor **B2**: ^{1}H NMR: (d_6-DMSO, 400 MHz) δ_H: 2.50(s, 3H), 5.35(s, 2H), 6.32(d, 1H, *J* 9.48), 7.06(d, 1H, *J* 8.44), 7.15(d, 2H, *J* 8.80), 7.20(s, 1H), 7.66(d, 1H, *J* 8.64), 7.82(d, 2H, *J* 8.80), 8.00(d, 1H, *J* 9.52), 8.89(s, 1H). ^{13}C NMR (DMSO-d_6, 100.6 MHz) δ_C: 62.13, 102.01, 113.15,

113.22, 113.37, 115.37, 122.35, 123.62, 130.02, 130.40, 143.37, 144.74, 155.78, 159.84, 160.71, 161.54.

Sensor **B3**: ^{1}H NMR: (d_6-DMSO, 400 MHz) δ_H: 0.91(t, 3H, *J* 7.2), 1.32(m, 2H), 1.59(m, 2H), 2.66(t, 2H, *J* 7.56), 5.36(s, 2H), 6.31(d, 1H, *J* 9.48), 7.06(d, 1H, *J* 8.52), 7.20(s, 1H), 7.41(d, 2H, *J* 8.16), 7.66(d, 1H, *J* 8.6), 7.80(d, 1H, *J* 8.2), 8.00(d, 1H, *J* 9.48), 8.94(s, 1H). ^{13}C NMR (DMSO-d_6, 100.6 MHz) δ_C: 14.20, 22.14, 33.39, 37.71, 62.11, 102.10, 113.16, 113.22, 113.37, 120.63, 123.57, 130.02, 130.08, 134.91, 143.50, 143.76, 144.74, 155.78, 160.71, 161.53.

Sensor **B4**: ^{1}H NMR: (d_6-DMSO, 400 MHz) δ_H: 5.37(s, 2H), 6.31(d, 1H, *J* 9.3), 7.05(d, 1H, *J* 7.8), 7.19(s, 1H), 7.65(d, 1H, *J* 8.4), 7.80(d, 2H, *J* 8.2), 7.89(d, 2H, *J* 8.0), 7.99(d, 1H, *J* 9.3), 9.02(s, 1H). ^{13}C NMR (DMSO-d_6, 100.6 MHz) δ_C: 62.03, 102.10, 113.19, 113.25, 113.36, 121.99, 122.61, 123.73, 130.04, 133.28, 123.73, 130.04, 133.28, 136.18, 143.86, 144.73, 155.77, 160.70, 161.47.

3.4 References

(1) Doganci, E. Synthesis, Characterization and Chemical Sensor Applications of Pyrene Side-Functional Polylactide Copolymers. *Polym. Int.* **2021**, *70* (2), 202–211. https://doi.org/10.1002/pi.6116.

(2) Tanimoto, H.; Kakiuchi, K. Recent Applications and Developments of Organic Azides in Total Synthesis of Natural Products. *Nat. Prod. Commun.* **2013**, *8* (7), 1021–1034. https://doi.org/10.1177/1934578x1300800730.

(3) Li, H.; Mu, Y.; Qian, S.; Lu, J.; Wan, Y.; Fu, G.; Liu, S. Synthesis of Fluorescent Dye-Doped Silica Nanoparticles for Target-Cell-Specific Delivery and Intracellular MicroRNA Imaging. *Analyst* **2015**, *140* (2), 567–573. https://doi.org/10.1039/c4an01706d.

(4) Bratanovici, B. I.; Shova, S.; Lozan, V.; Dascălu, I. A.; Ardeleanu, R.; Roman, G. 1-(4-Carboxyphenyl)-5-Methyl-1H-1,2,3-Triazole-4-Carboxylic Acid – A Versatile Ligand for the Preparation of Coordination Polymers and Mononuclear Complexes. *Polyhedron* **2021**, *200* (3), 1–11. https://doi.org/10.1016/j.poly.2021.115115.

(5) Nazarov, A. E.; Ivanov, A. I. Effect of the Transition Rate between Two Excited States on the Spectral Dynamics of Dual Fluorescence: Blurring of the Isoemissive Point. *J. Photochem. Photobiol. A Chem.* **2021**, *404* (July 2020), 112881. https://doi.org/10.1016/j.jphotochem.2020.112881.

(6) Li, M.; Yang, M.; Zhu, W. H. Advances in Fluorescent Sensors for β-Galactosidase. *Mater. Chem. Front.* **2021**, *5* (2), 763–774. https://doi.org/10.1039/d0qm00683a.

(7) Novakova, V.; Hladík, P.; Filandrová, T.; Zajícová, I.; Krepsová, V.; Miletin, M.; Lenčo, J.; Zimcik, P. Structural Factors Influencing the Intramolecular Charge Transfer and Photoinduced Electron Transfer in Tetrapyrazinoporphyrazines. *Phys. Chem. Chem. Phys.* **2014**, *16* (11), 5440–5446. https://doi.org/10.1039/c3cp54731k.

(8) Roebroek, T.; Vandenberg, W.; Zhang, J.; Dedecker, P. Photochromism. *Nat. Commun.* **2021**, 1–12. https://doi.org/10.1038/s41467-021-22043-0.

(9) Gordon, F.; Elcoroaristizabal, S.; Ryder, A. G. Modelling Förster Resonance Energy Transfer (FRET) Using Anisotropy Resolved Multi-Dimensional Emission

Spectroscopy (ARMES). *Biochim. Biophys. Acta - Gen. Subj.* **2021**, *1865* (2), 129770. https://doi.org/10.1016/j.bbagen.2020.129770.

(10) Zhu, Q.; Li, L.; Mu, L.; Zeng, X.; Redshaw, C.; Wei, G. A Ratiometric Al3+ Ion Probe Based on the Coumarin-Quinoline FRET System. *J. Photochem. Photobiol. A Chem.* **2016**, *328*, 217–224. https://doi.org/10.1016/j.jphotochem.2016.06.006.

(11) Francisco, T.; Rosa, P.; Soares, S.; Mateus, N.; Centeno, F.; F, M. De. Understanding the Molecular Interactions between a Yeast Protein Extract and Phenolic Compounds. **2021**, *143*. https://doi.org/10.1016/j.foodres.2021.110261.

(12) Shubham, K.; Anukiruthika, T.; Dutta, S.; Kashyap, A. V.; Moses, J. A.; Anandharamakrishnan, C. Iron Deficiency Anemia: A Comprehensive Review on Iron Absorption, Bioavailability and Emerging Food Fortification Approaches. *Trends Food Sci. Technol.* **2020**, *99* (August 2019), 58–75. https://doi.org/10.1016/j.tifs.2020.02.021.

(13) Santoshakumar, R. M.; Malatesh, P. S.; Nirupama, M. J.; Ashok, S. H. Fluorescence Quenching of Anthracene by Aniline in Two Solvents: S-V Plot Analysis. *AIP Conf. Proc.* **2020**, *2244*. https://doi.org/10.1063/5.0010245.

(14) Butnarasu, C.; Barbero, N.; Viscardi, G.; Visentin, S. Spectrochimica Acta Part A : Molecular and Biomolecular Spectroscopy Unveiling the Interaction between PDT Active Squaraines with CtDNA : A Spectroscopic Study. *Spectrochim. Acta Part A Mol. Biomol. Spectrosc.* **2021**, *250*, 119224. https://doi.org/10.1016/j.saa.2020.119224.

(15) Hassan, S. A. E.; Ahmed, S. A. E.; Youssef, N. F. Spectrofluorimetric Study on Fluorescence Quenching of Tyrosine and L -Tryptophan by the Aniracetam Cognition Enhancer Drug : Quenching Mechanism Using Stern – Volmer and Double-Log Plots. **2020**, 1–10. https://doi.org/10.1002/bio.3778.

(16) Stoian, M. C.; Mihalache, I.; Matache, M.; Radoi, A. Dyes and Pigments Terbium-Functionalized Silica Nanoparticles for Metal Ion Sensing by Fluorescence Quenching. *Dye. Pigment.* **2021**, *187*, 109144. https://doi.org/10.1016/j.dyepig.2021.109144.

(17) Srivastava, R. R.; Singh, V. K.; Srivastava, A. Facile Synthesis of Highly Fluorescent Water-Soluble SnS 2 QDs for Effective Detection of Fe^{3+} and Unveiling Its Fluorescence Quenching Mechanism. *Opt. Mater. (Amst).* **2020**, *109*, 110337. https://doi.org/10.1016/j.optmat.2020.110337.

(18) Murugan, A. S.; Kiruthika, M.; Noelson, E. R. A.; Yogapandi, P.; Gnana, G.; Annaraj, J. Fluorescent Sensor for In-Vivo Bio-Imaging , Precise Tracking of Fe^{3+} Ions in Zebrafish Embryos and Visual Measuring of Cu^{2+} Ions in Pico-Molar Level. *Arab. J. Chem.* **2021**, *14* (1), 102910. https://doi.org/10.1016/j.arabjc.2020.11.016.

(19) Dinastiya, E. M.; Verbitskiy, E. V.; Gadirov, R. M.; Samsonova, L. G.; Degtyarenko, K. M.; Grigoryev, D. V.; Kurtcevich, A. E.; Solodova, T. A.; Tel'minov, E. N.; Rusinov, G. L.; Chupakhin, O. N.; Charushin, V. N. Investigation of 4,6-Di(Hetero)Aryl-Substituted Pyrimidines as Emitters for Non-Doped OLED and Laser Dyes. *J. Photochem. Photobiol. A Chem.* **2021**, *408*, 113089. https://doi.org/10.1016/j.jphotochem.2020.113089.

(20) Ordóñez-Hernández, J.; Arcos-Ramos, R.; Alvarez-Venicio, V.; Basiuk, V. A.; González-Antonio, O.; Flores-Álamo, M.; García-Ortega, H.; Farfán, N.; Carreón-Castro, M. del P. NnEngineering Coumarin-BODIPY Thin-Films and Molecular Crystals: Tailoring Supramolecular Self-Assembly for Organic Electronic Applications. *J. Mol. Struct.* **2021**, 130437. https://doi.org/10.1016/j.molstruc.2021.130437.

(21) Rui Chen, Guang-Jin Shi, Jia-Jia Wang, Hai-Feng Qin, Qi Zhang, Shaojin Chen, Yonghong Wen, J.-B. G.; ⇑ K.-P. W.; Zhi-Qiang Hu. A Highly-Sensitive "turn on" Probe Based on Coumarin b-Diketone for Hydrazine Detection in PBS and Living Cells. *Spectrochim. Acta - Part A Mol. Biomol. Spectrosc.* **2021**, *12*, 1–9.

(22) Kim, J.; Oh, J. H.; Kim, D. Recent Advances in Single-Benzene-Based Fluorophores: Physicochemical Properties and Applications. *Org. Biomol. Chem.* **2021**, *19* (5), 933–946. https://doi.org/10.1039/d0ob02387f.

(23) Igor O. Akchurin, Anna I. Yakhutina, Andrei Y. Bochkov, Natalya P. Solovjova, Michael G. Medvedev, Valerii F. Traven, Novel Push-Pull Fluorescent Dyes - 7-(Diethylamino)Furo- and Thieno [3,2-c]Coumarins Derivatives: Structure, Electronic Spectra and TD-DFT Study. *J. Mol. Struct.* **2018**, *1160*, 215–221.

(24) Heidari, L.; Ghassemzadeh, M.; Fenske, D.; Fuhr, O.; Mohsenzadeh, F.; Bon, V. 3D Coordination Polymers Constructed from D10 Metal Ions, Flexible 1,2,4-Triazole Derivatives and Aromatic Tetracarboxylates: Syntheses, Structures, Thermal and Luminescent Properties. *J. Solid State Chem.* **2021**, *296*, 122011. https://doi.org/10.1016/j.jssc.2021.122011.

(25) Bolje, A.; Urankar, D.; Košmrlj, J. Synthesis and NMR Analysis of 1,4-Disubstituted 1,2,3-Triazoles Tethered to Pyridine, Pyrimidine, and Pyrazine Rings. *European J. Org. Chem.* **2014**, *2014* (36), 8167–8181. https://doi.org/10.1002/ejoc.201403100.

(26) Banert, K.; Lehmann, J.; Quast, H.; Meichsner, G.; Regnat, D.; Seiferling, B. ^{15}N NMR Spectra, Tautomerism and Diastereomerism of 4,5-Dihydro-1H-1,2,3-Triazoles. *J. Chem. Soc. Perkin Trans. 2* **2002**, *2* (1), 126–134. https://doi.org/10.1039/b107326e.

(27) Meng, X.; Yao, Y.; Ma, Y.; Zhong, N.; Alphonse, S.; Pei, J. Effect of Fluoride in Drinking Water on the Level of 5-Methylcytosine in Human and Rat Blood. *Environ. Toxicol. Pharmacol.* **2021**, *81*, 103511. https://doi.org/10.1016/j.etap.2020.103511.

(28) Liu, J.; Peng, Y.; Li, C.; Gao, Z.; Chen, S. A Characterization of Groundwater Fluoride, Influencing Factors and Risk to Human Health in the Southwest Plain of Shandong Province, North China. *Ecotoxicol. Environ. Saf.* **2021**, *207*, 111512. https://doi.org/10.1016/j.ecoenv.2020.111512.

(29) Alam, I.; Rehman, J. U.; Nazir, S.; Nazeer, A.; Akram, M.; Batool, Z.; Ullah, H.; Hameed, A.; Hussain, A.; Hussain, A.; Tahir, M. B. Health Risk Assessment in Different Age-Group Due to Nitrate, Fluoride, Nitrite and Geo-Chemical Parameters in Drinking Water in Ahmadpur East, Punjab, Pakistan. *Hum. Ecol. Risk Assess. An Int. J.* **2021**, *0* (0), 1–17. https://doi.org/10.1080/10807039.2021.1902264.

(30) Arooj, M.; Zahra, M.; Islam, M.; Ahmed, N.; Waseem, A.; Shafiq, Z. Coumarin Based Thiosemicarbazones as Effective Chemosensors for Fluoride Ion Detection. *Spectrochim. Acta - Part A Mol. Biomol. Spectrosc.* **2021**, *261*, 120011. https://doi.org/10.1016/j.saa.2021.120011.

(31) De Silva, A. P.; Moody, T. S.; Wright, G. D. Fluorescent PET (Photoinduced Electron Transfer) Sensors as Potent Analytical Tools. *Analyst* **2009**, *134* (12), 2385–2393. https://doi.org/10.1039/b912527m.

(32) Ramachandran, M.; Syed, A.; Marraiki, N.; Anandan, S. The Aqueous Dependent Sensing of Hydrazine and Phosphate Anions Using a Bis-Heteroleptic Ru(II) Complex with a Phthalimide-Anchored Pyridine-Triazole Ligand. *Analyst* **2021**, *146* (4), 1430–1443. https://doi.org/10.1039/d0an02299c.

APPENDIX B

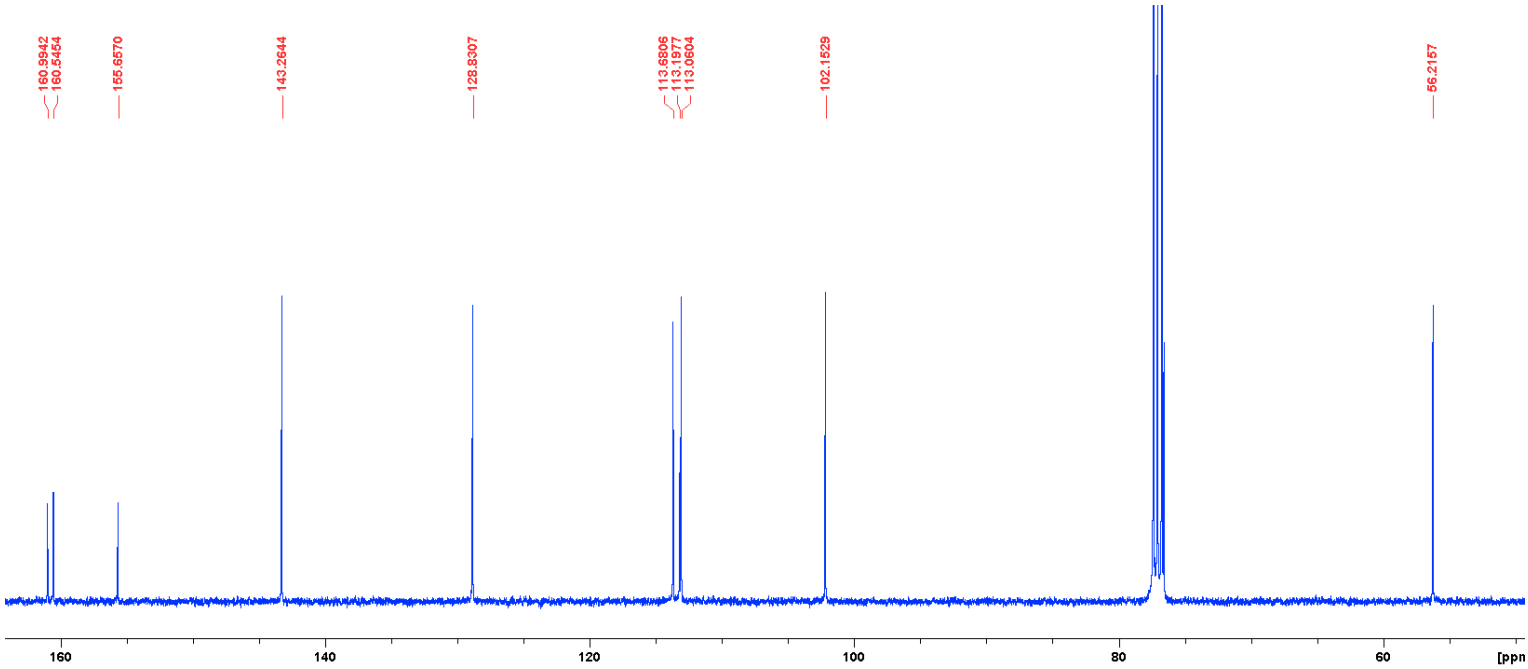

Figure 1: ^{13}C NMR of propinyloxy coumarin derivative **2** in $CDCl_3$.

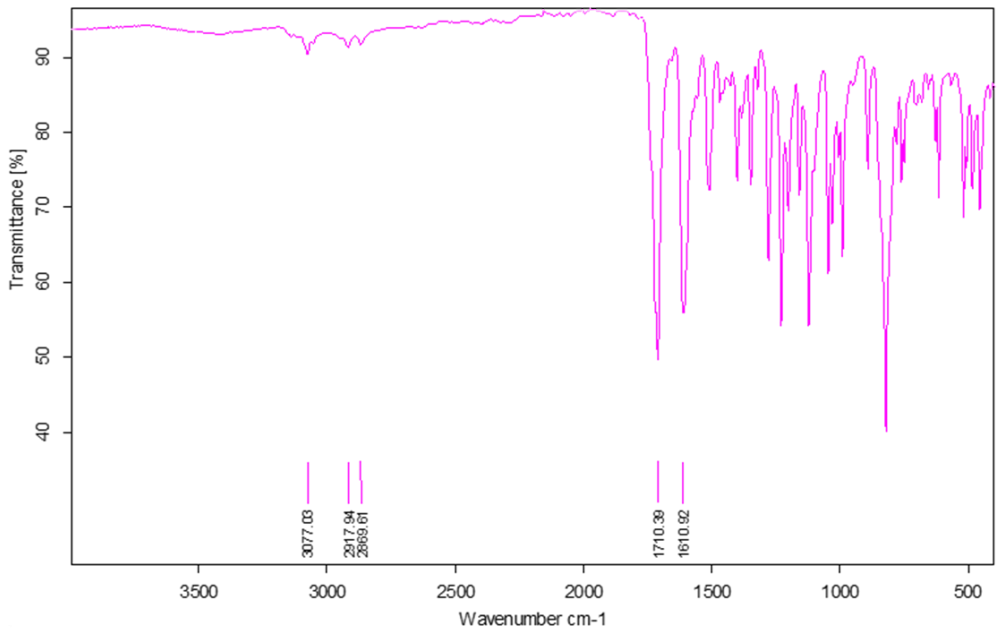

Figure 2: FT-IR spectra of coumarin-triazolyl derivative **B1**.

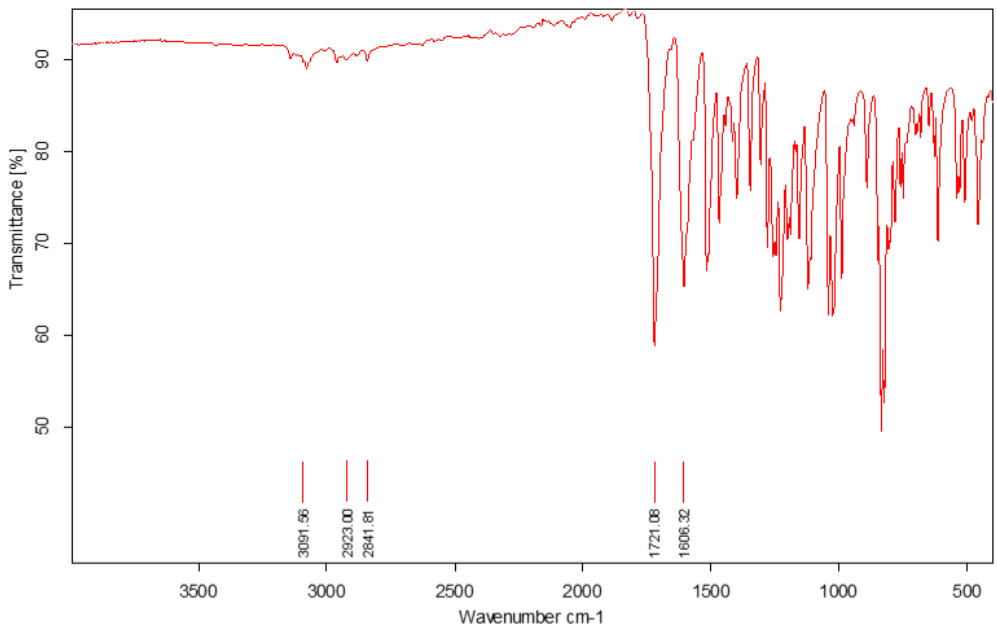

Figure 3: FT-IR spectra of coumarin-triazolyl derivative **B2**.

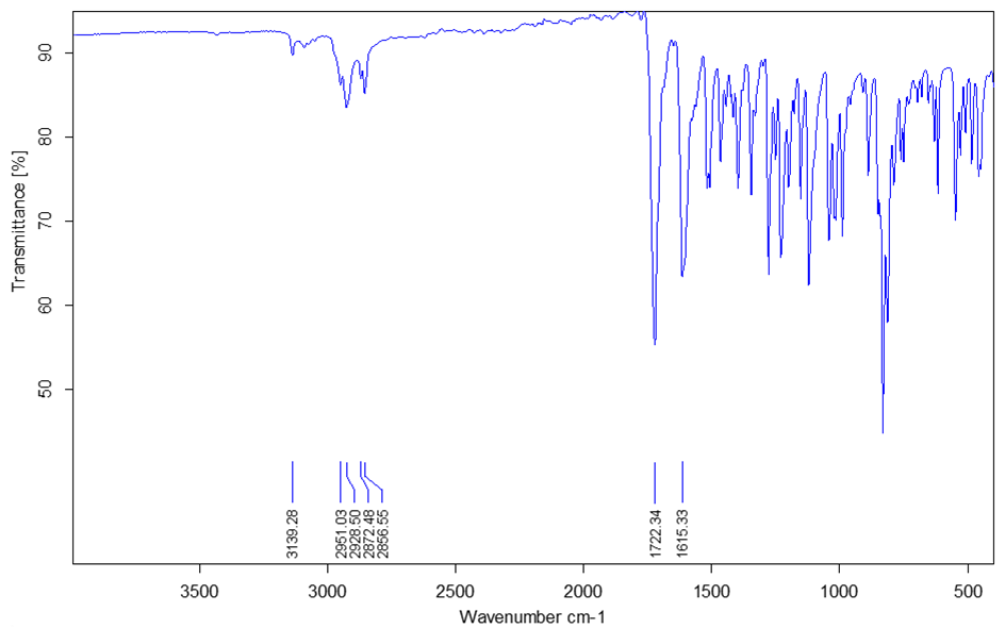

Figure 4: FT-IR spectra of coumarin-triazolyl derivative **B3**.

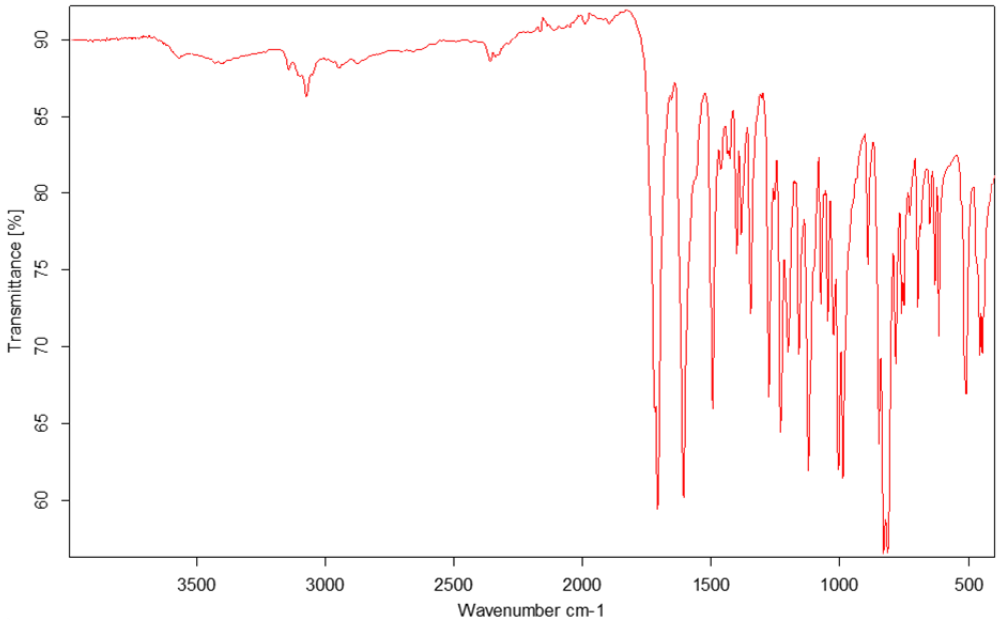

Figure 5: FT-IR of coumarin-triazolyl derivative **B4**.

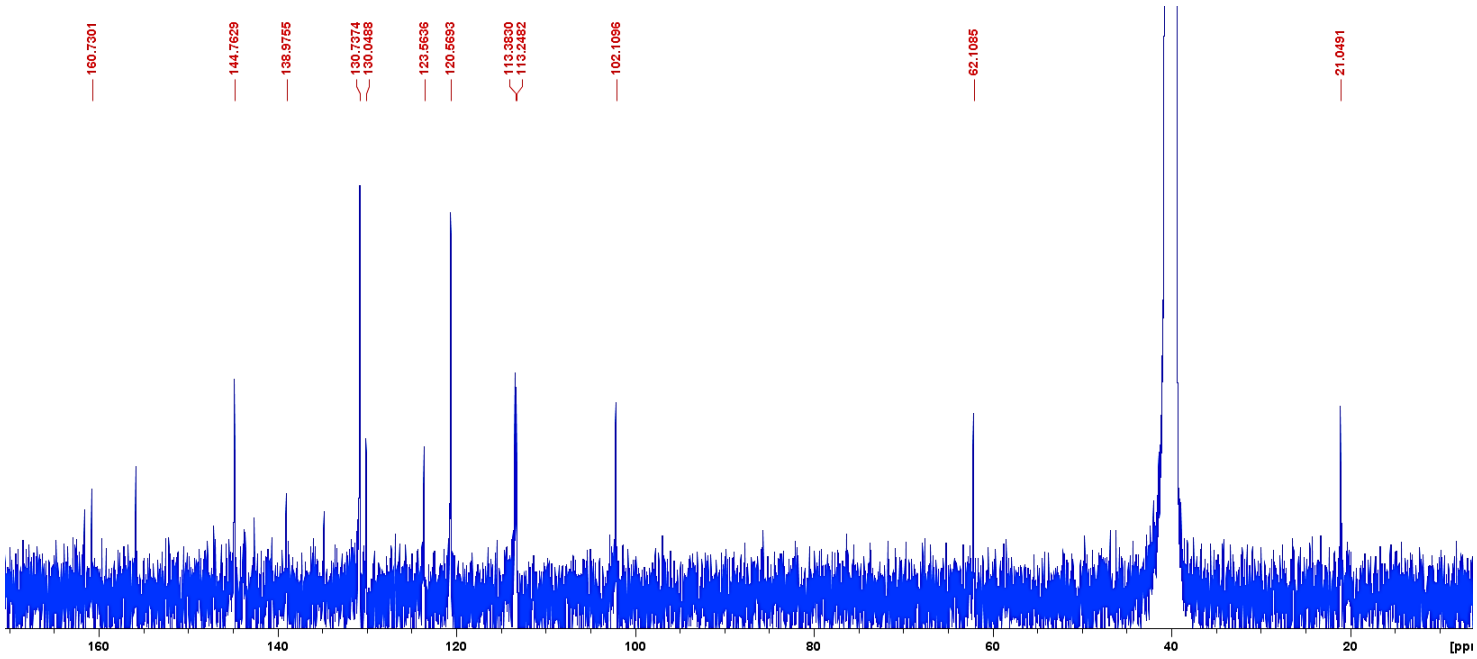

Figure 6: ^{13}C NMR spectra of sensor **B1** in d_6-DMSO.

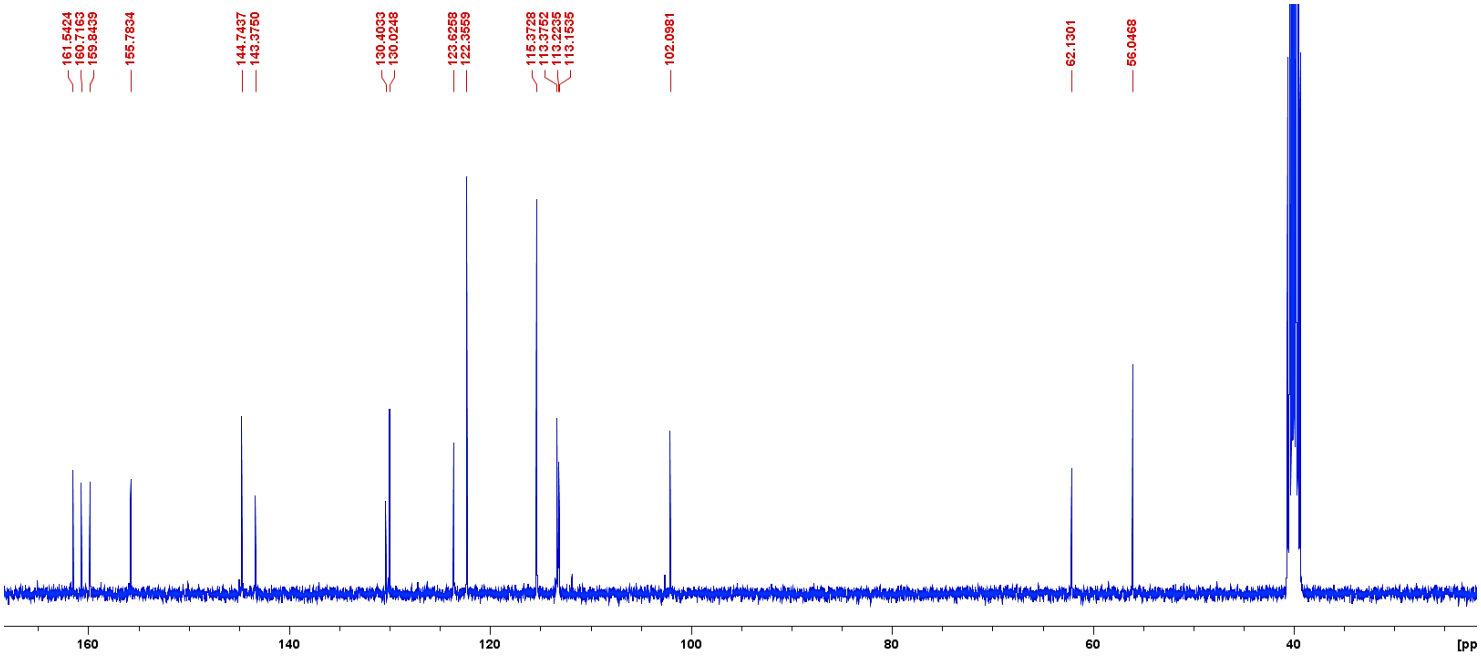

Figure 7: ^{13}C NMR spectra of sensor **B2** in d_6-DMSO.

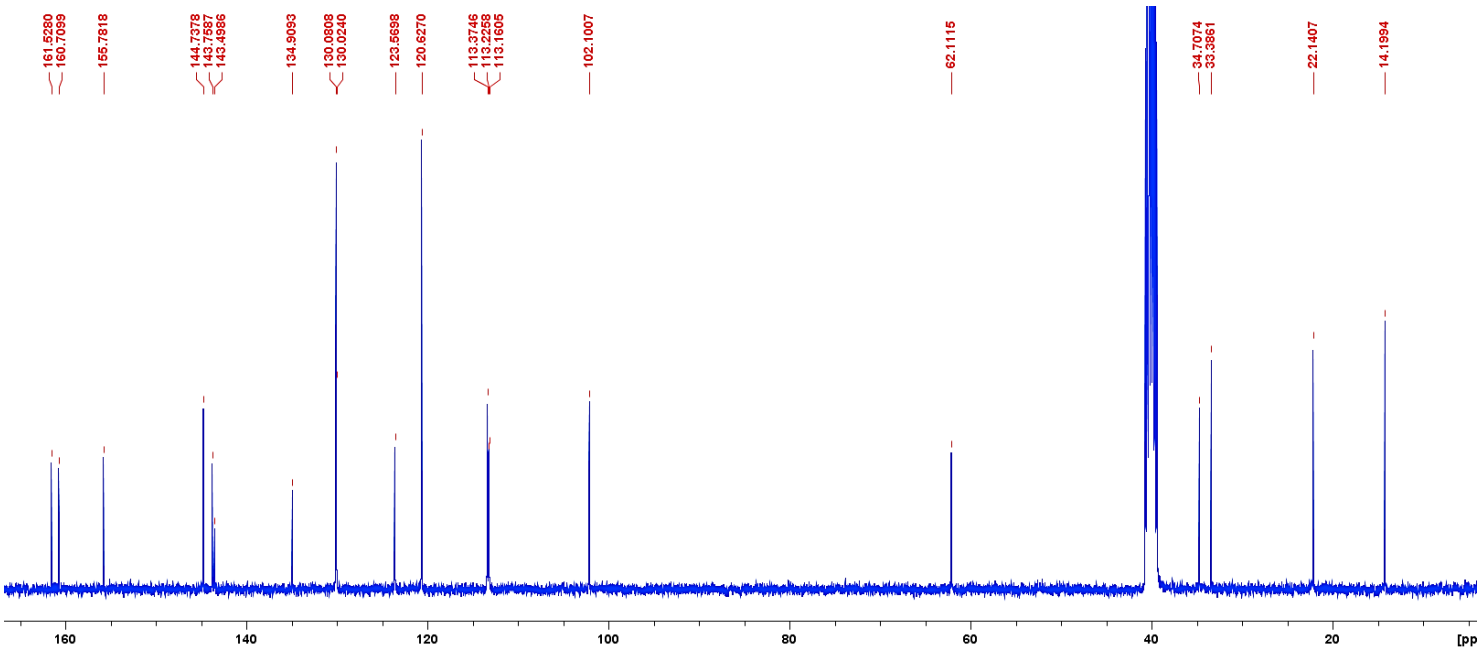

Figure 8: ^{13}C NMR spectra of sensor **B3** in d_6-DMSO.

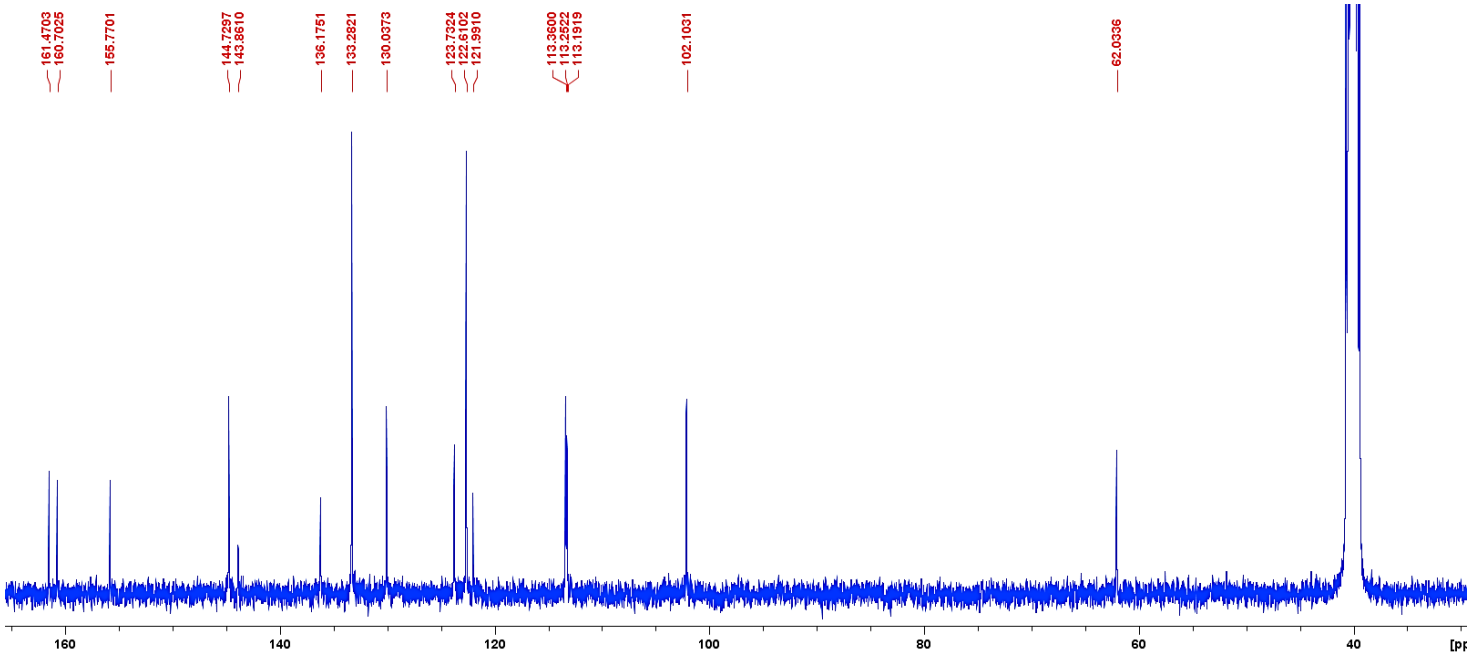

Figure 9: ^{13}C NMR spectra of sensor **B4** in d_6-DMSO.

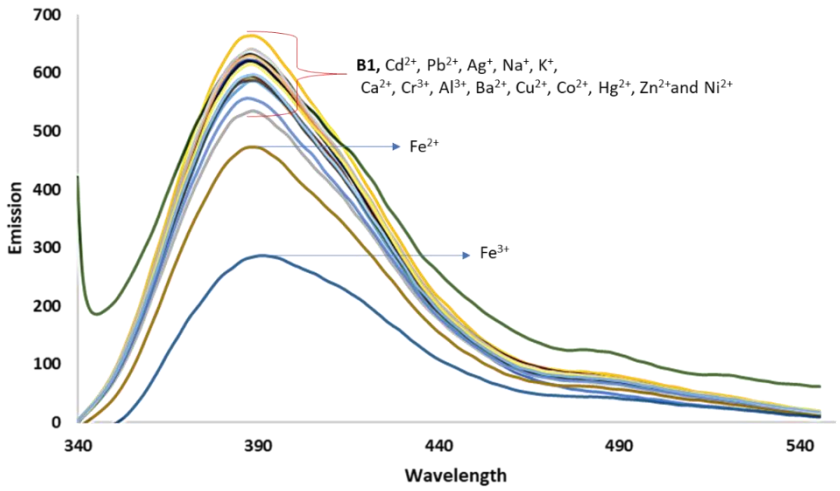

Figure 10: Screening studies of sensor **B1** in ethanol. Excitation of 320 nm.

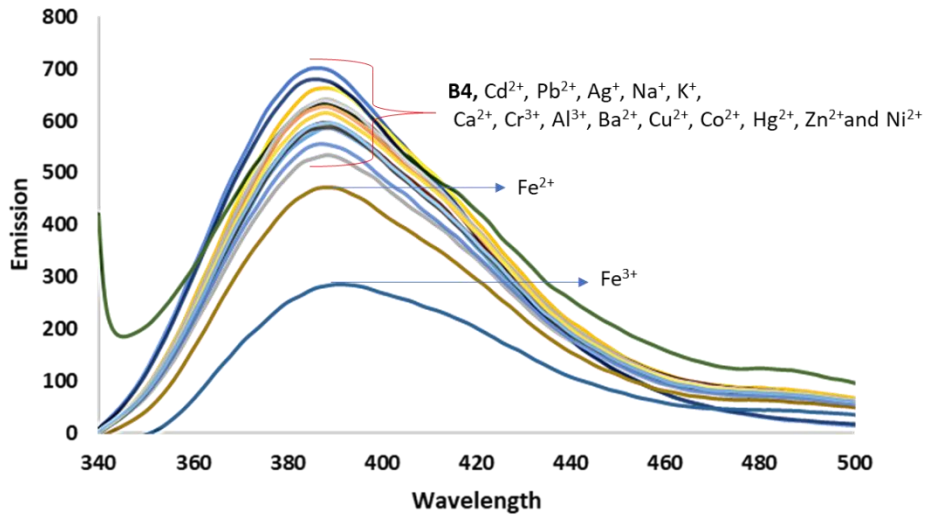

Figure 11: Screening studies of sensor **B4** in ethanol. Excitation of 320 nm.

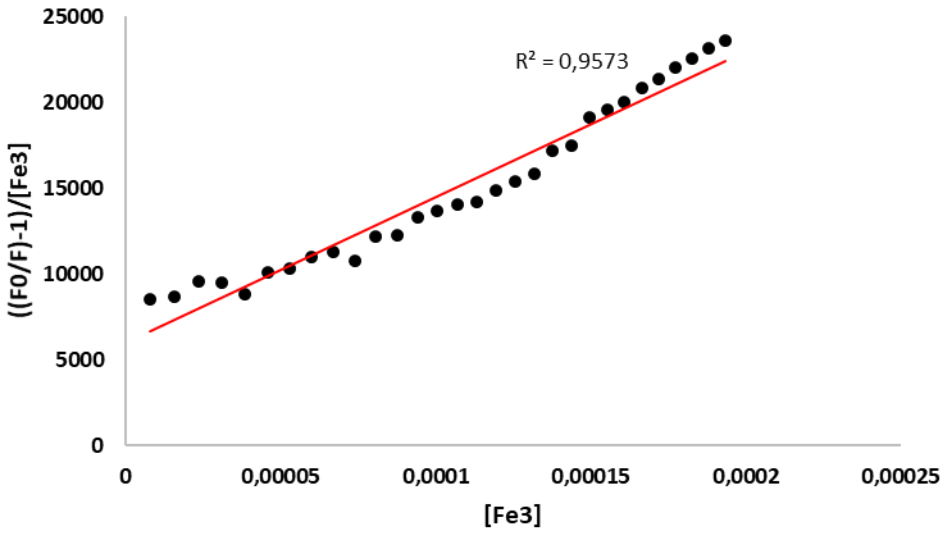

Figure 12: Plot of combined static and dynamic quenching process (ground-state complex formation) of **B3** with Fe^{3+} in ethanol. Excitation of 320 nm.

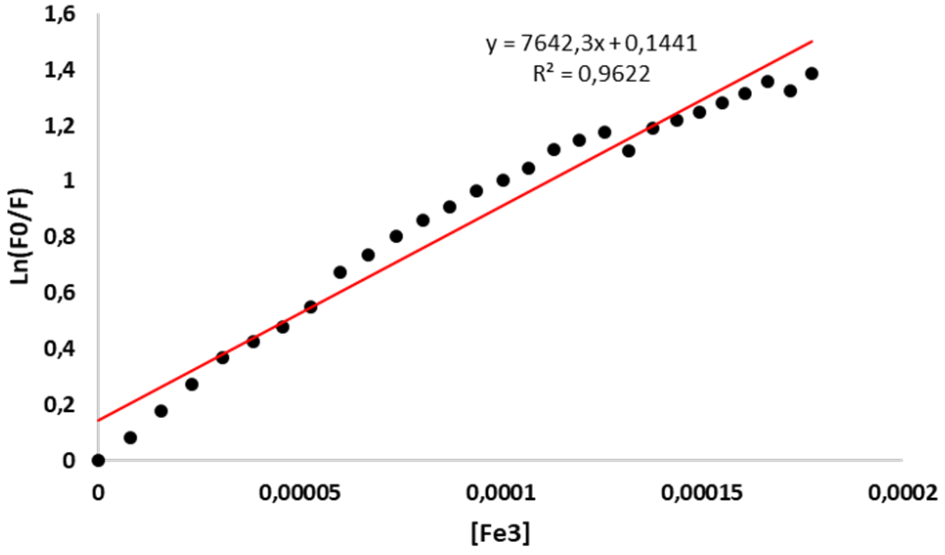

Figure 13: Fit of quenching data of **B1** by Fe^{3+} according to the Perrin static quenching model

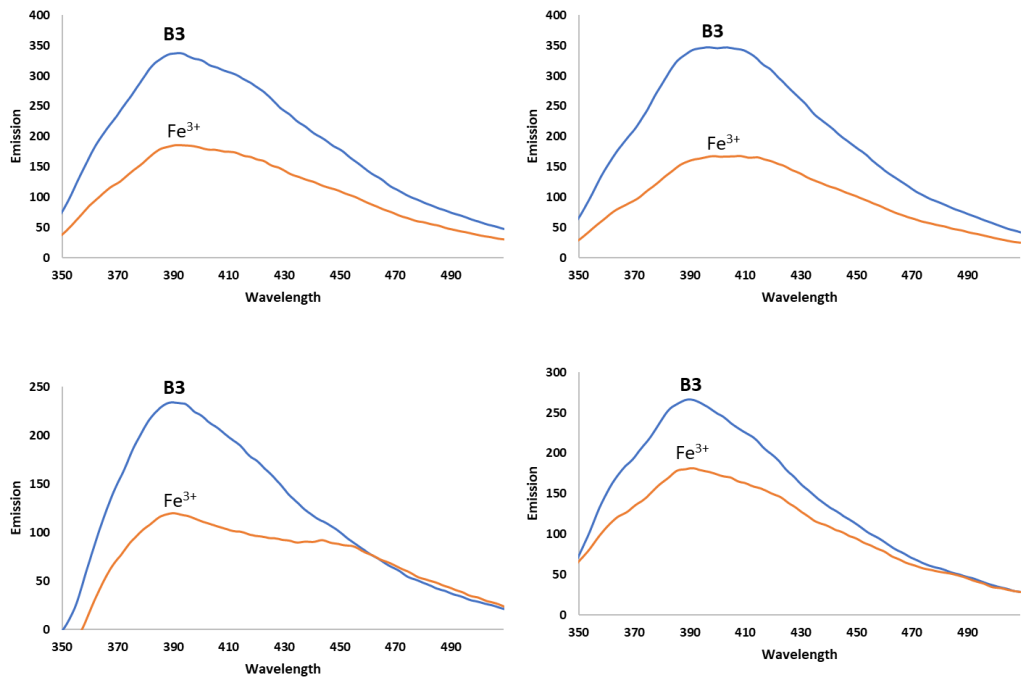

Figure 14: Effect of pH on sensor **B3** upon Fe^{3+} addition at pH: a) 4, b) 5, c) 7, and d) 10. Excitation 320 nm.

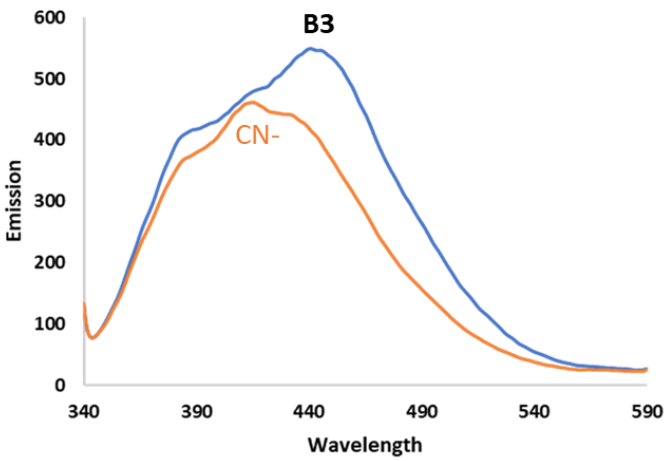

Figure 15: Screening of **B3** with CN^- in water. Excitation of 320nm.

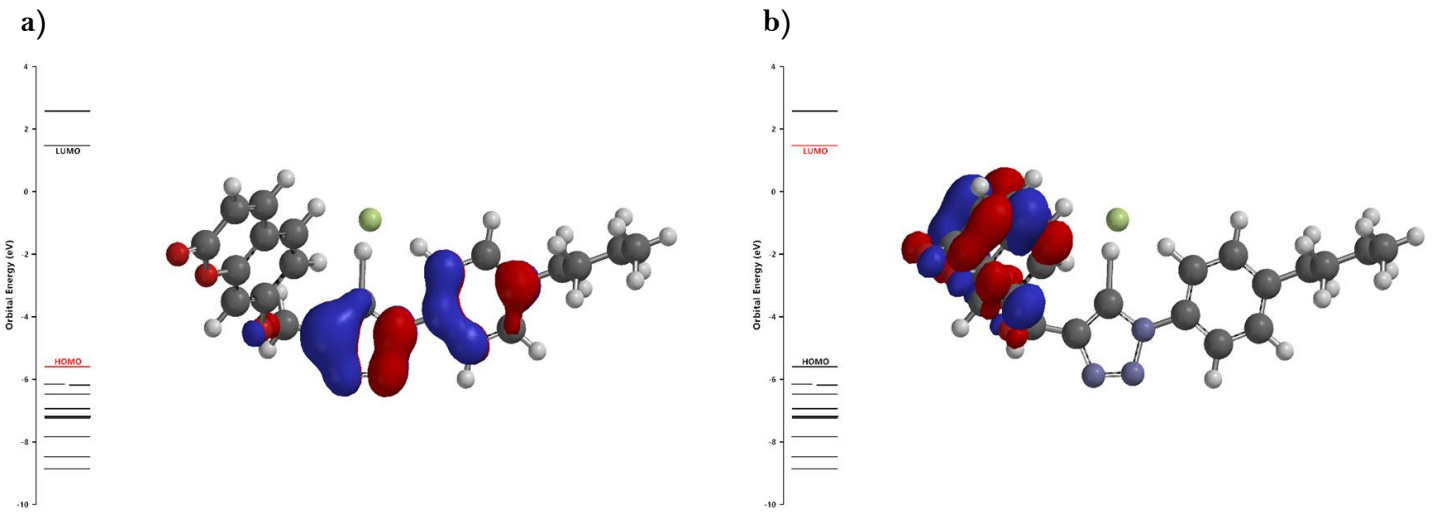

Figure 16: a) Calculated HOMO and b) LUMO of the interaction between **B3** and F^-.

Chapter 4

Table of Contents

List of Figures

List of Tables

List of Schemes

Chapter 4:
Application of 3-ester-6-triazolyl coumarin-derived sensors towards ionic sensing strategies

Summary

Four 3-ester-6-triazole coumarin derivatives have been synthesized, characterized, and tested for their affinity towards a variety of cationic and anionic species in organic and aqueous media. Coumarin derivatives **C1** and **C3** displayed the highest emission intensity in a variety of solvents including DMF, water, acetonitrile, and ethanol. These sensors displayed a high affinity towards Fe^{3+} through a sizeable fluorescent quenching response. Competition studies between both sensors with Fe^{3+} in the presence of competing metal cations were conducted. Sensor **C1** showed greater selectivity towards Fe^{3+} than **C3** in both ethanol and DMF. Additionally, **C1** displayed preference towards Fe^{3+} in the presence of all other competing metal cations. The detection limit was determined to be 1.86 and 3.66 μM in ethanol and DMF respectively. The stoichiometric binding ratio was found to be 1:1 according to the Job's plot and supported by Benesi-Hildebrand studies. The association constant (K_a) was 1.8 x 10^4 M^{-1}. The quenching was determined to occur via a PET "on-off" mechanism. The binding site of Fe^{3+} with **C1** occurs via the triazole nitrogen atom. This was confirmed with ^1H and ^{13}C NMR, and double-logarithm analysis. Hydrogen potential analysis showcased the sensors good response towards Fe^{3+} in a desired pH range. Reversibility studies with EDTA show that **C1**-Fe^{3+} complexation is 51% reversible. Sensor **C1** was tested for its anionic sensing capabilities in ethanol, water, acetonitrile, and DMF. Cyanide anions displayed a fluorescent quenching response in ethanol, acetonitrile, and DMF. Competition studies of **C1** towards CN^- in the presence of competing anions highlighted a poor selectivity of **C1** towards CN^-.

4.1 Results and Discussion

4.1.1 Synthesis and characterization of 3-ester-6-triazole coumarin derivatives

A coumarin-derived compound **1** containing an ester group at position -3- was synthesized by a Knoevenagel reaction according to literature procedure.[1] Compound **1** was then nitrated by $NaNO_3$ in conc. H_2SO_4 to yield -6- nitro -3- ester coumarin derivative **1a**. The nitrated product **1a** was reduced to the amine functionality using iron in an acetic acid/water mixture to form derivative **1b**. The amine group was first converted to diazonium salt and then subjected to an azidonation reaction to yield -6- azide -3- ester functionalized coumarin derivative **1c**. Four different alkyne derivatives were selected for Cu(I)-catalyzed azide-alkyne "click" reaction protocol with coumarin-azide derivative **1c** to form 3-ester-6-triazole coumarin derivatives **C1-4**. The generalized synthetic route for sensors **C1-4** is shown in **Scheme 1**.

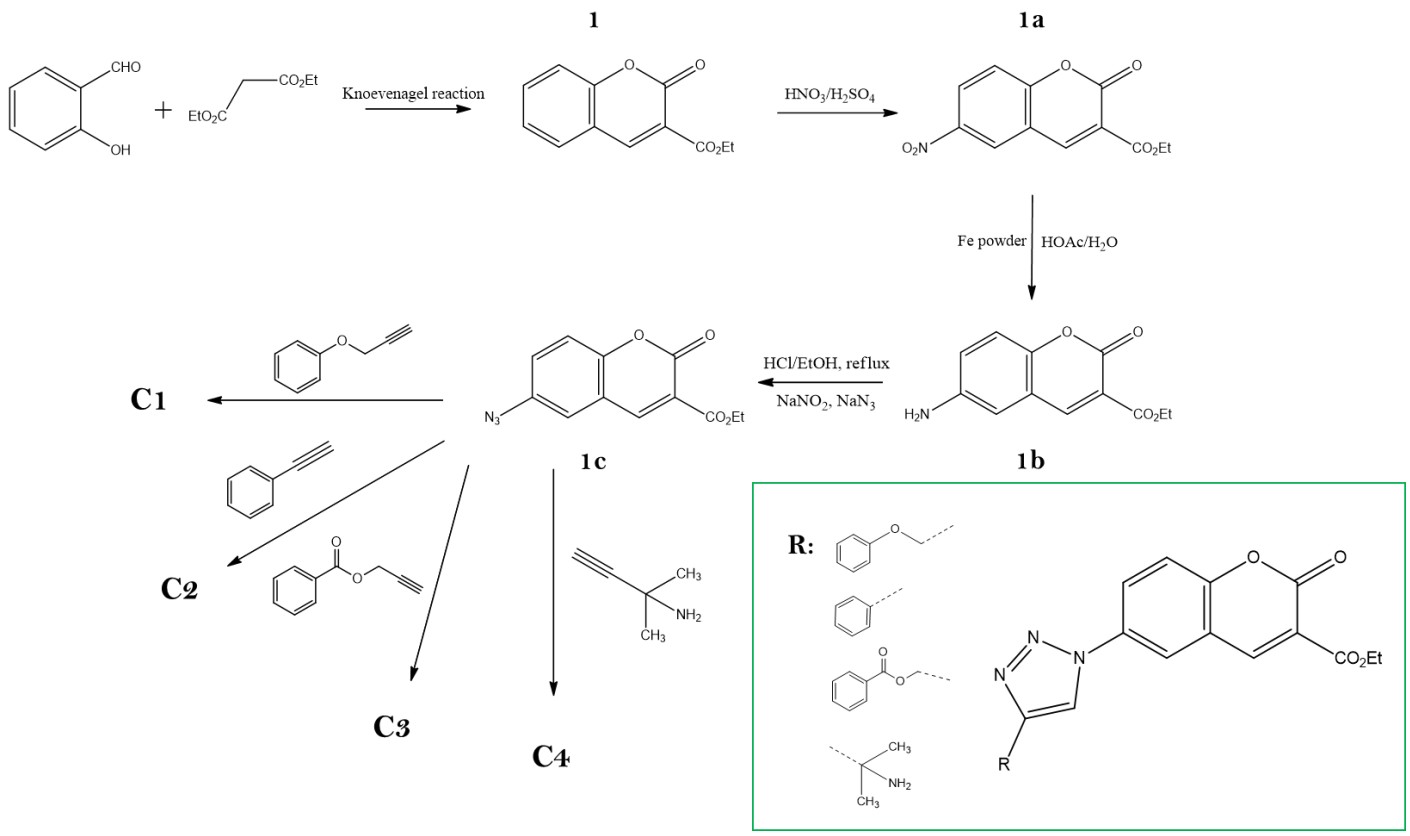

Scheme 1: Generalized synthetic pathway of 3-ester-6-triazole functionalized coumarin-based compounds **C1-4**. Green box: generalized structures of triazole derivatives **C1-4**.

Compounds **1a-c** and coumarin-triazole derivatives **C1-4** were fully characterized by NMR and FT-IR spectral analysis. For the ^{1}H NMR of compounds **1a-c** see **Figures 1-3** (for the ^{13}C NMR and FT-IR spectra of compounds **1a-c**, see **Appendix C Figures 1-6**). Additionally, the single-crystal X-Ray structures of compounds **1** and **1a** were determined (**Figure 4**). **Figures 5-8** show the ^{1}H NMR spectra of 3-ester-6-triazole coumarin derivatives **C1-4**. The ester groups at position -3- on the coumarin scaffold of derivatives **C1-4** did not undergo aminolysis with PMDETA to an original hydroxyl group as seen in the Cu(I)-catalyzed cycloaddition of 7-ester-3-azide coumarin derivative **1c** in **Chapter 2.** This is due to the fact that the ester group is attached to the coumarin moiety directly via the carbonyl carbon rather than via the ethoxy-oxygen atom. The disappearance of the azide peak from the FT-IR spectra and appearance of the characteristic triazole signals confirms the success of the Cu(I)-catalyzed "click" reaction (for the ^{13}C NMR and FT-IR spectra of compounds **C1-4** see **Appendix C Figures 7-13**).

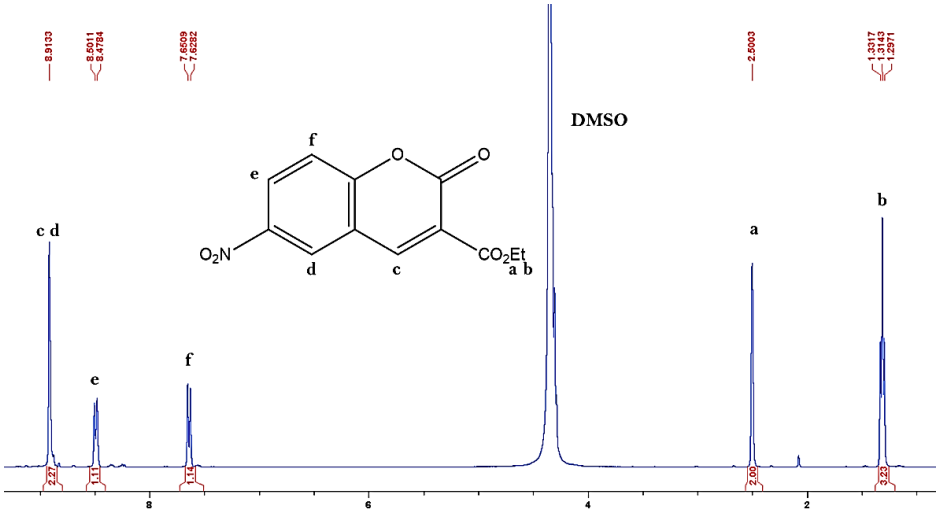

Figure 1: ^{1}H NMR spectra of 6-nitrated-3-ester coumarin derivative **1a** in d_6-DMSO.

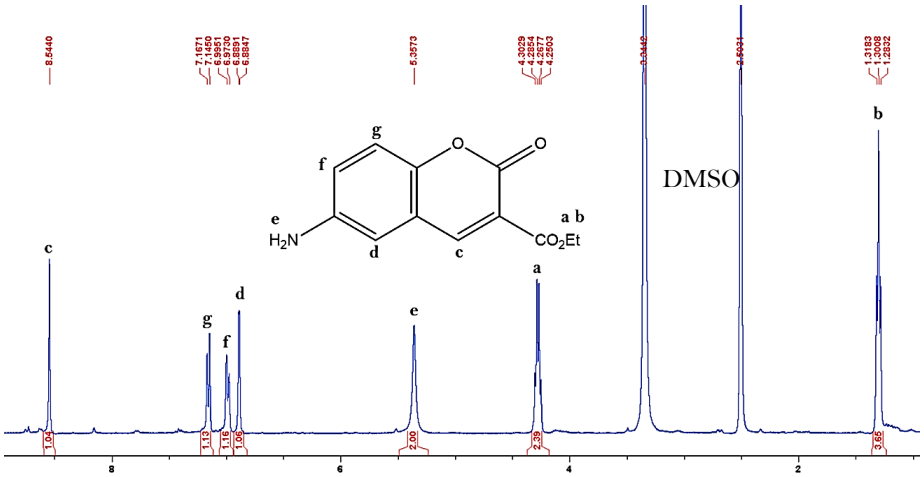

Figure 2: ^{1}H NMR spectra of 3-ester-6-amine coumarin derivative **1b** in d_6-DMSO.

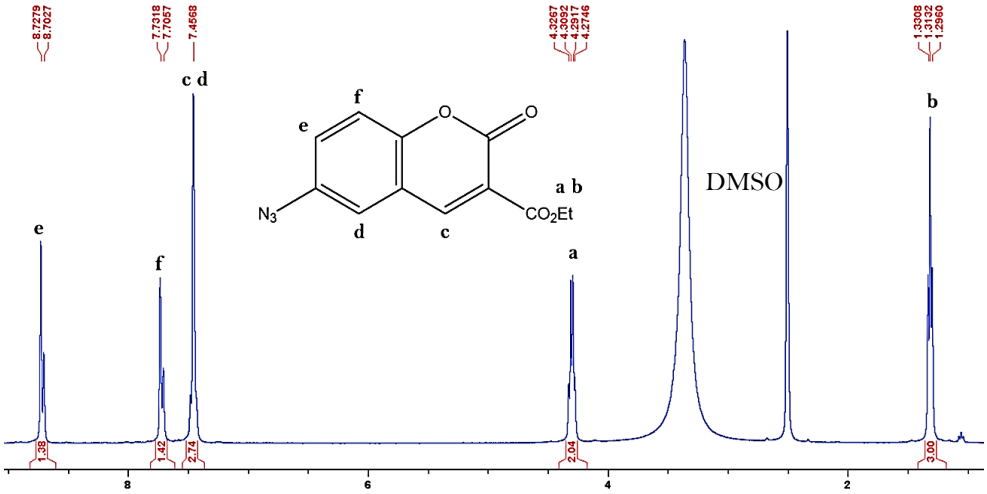

Figure 3: ^{1}H NMR of 6-azide-3-ester coumarin derivative **1c** in d_6-DMSO.

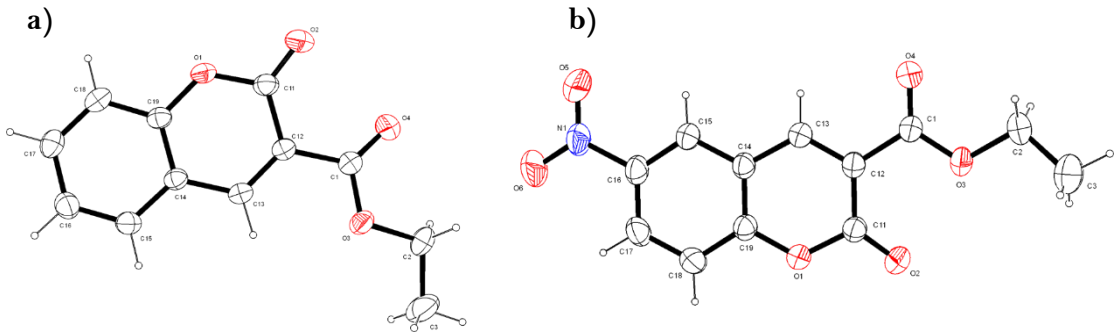

Figure 4: Single-crystal XRD structures of coumarin derivatives a) **1** and b) **1b**.

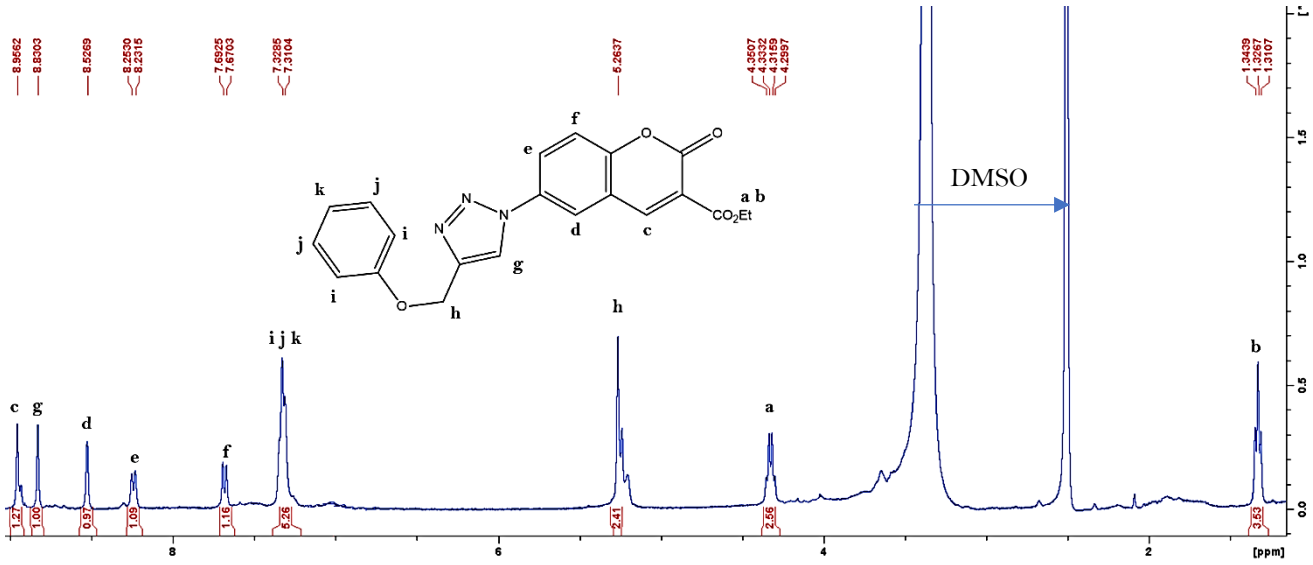

Figure 5: ^{1}H NMR spectra of 3-ester-6-triazole coumarin compound **C1** in d_6-DMSO.

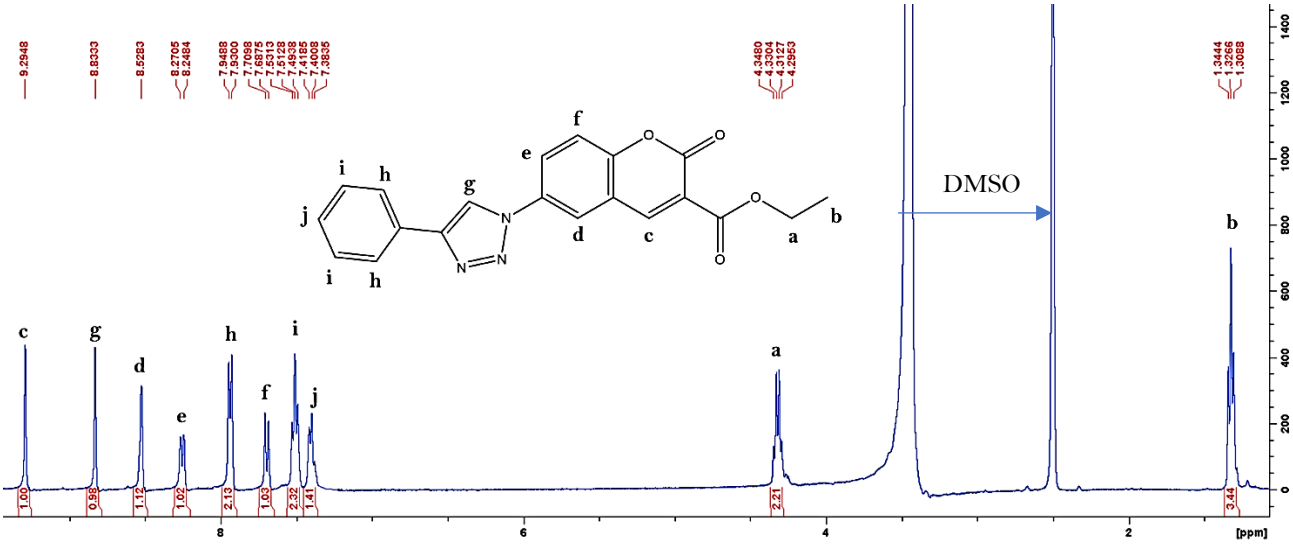

Figure 6: ^{1}H NMR spectra of 3-ester-6-triazole coumarin compound **C2** in d_6-DMSO.

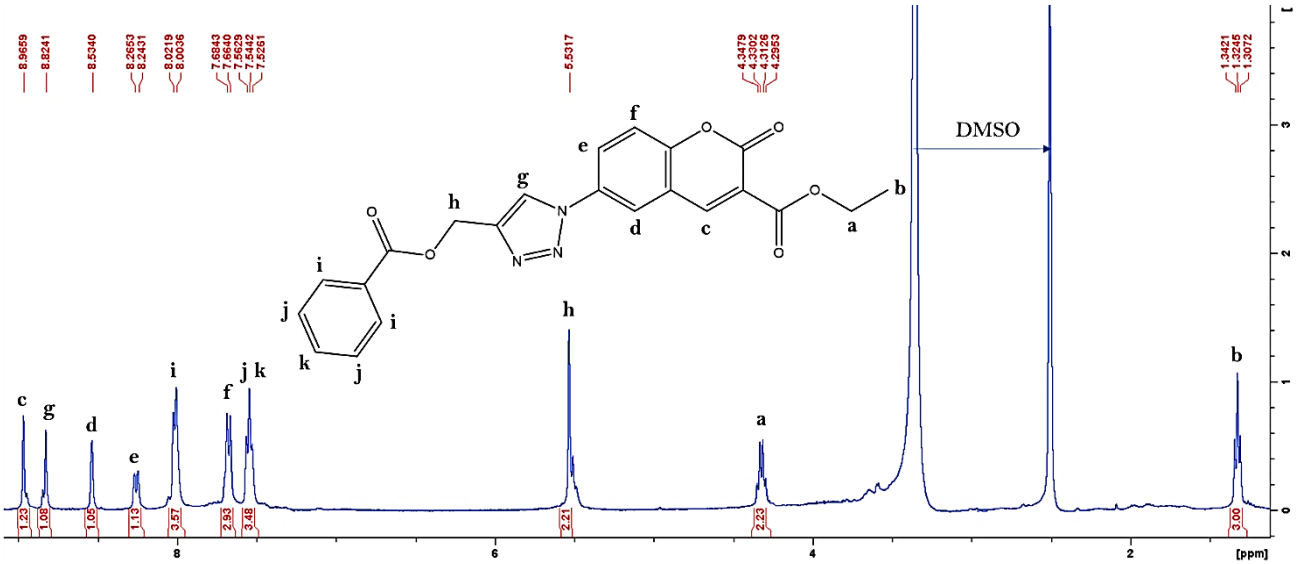

Figure 7: ^{1}H NMR spectra of 3-ester-6-triazole coumarin compound **C3** in d_6-DMSO.

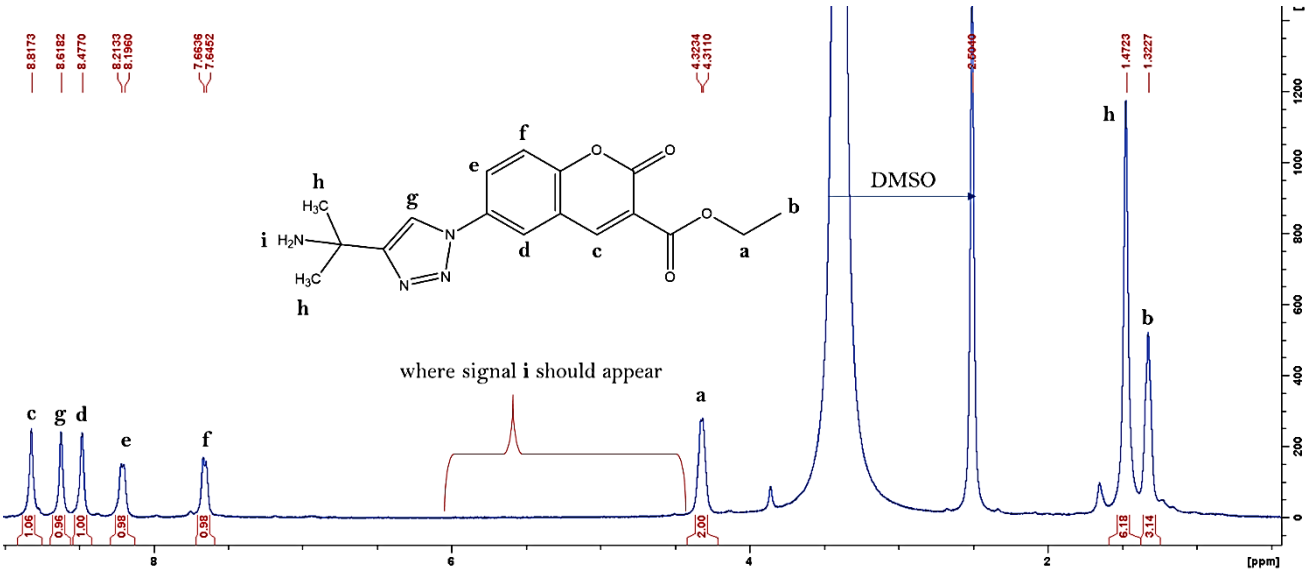

Figure 8: ^{1}H NMR spectra of 3-ester-6-triazole coumarin compound **C4** in d_6-DMSO.

According to the spectrum of coumarin-triazole derivative C4, the two protons associated with the substituted amine functionality are absent. The singlet at 1.47 ppm, integrated for six hydrogen atoms, verifies the presence of the substituted methyl-amine functionality, as well as the hydrogen signal at 8.6 ppm which is associated with the triazole moiety.

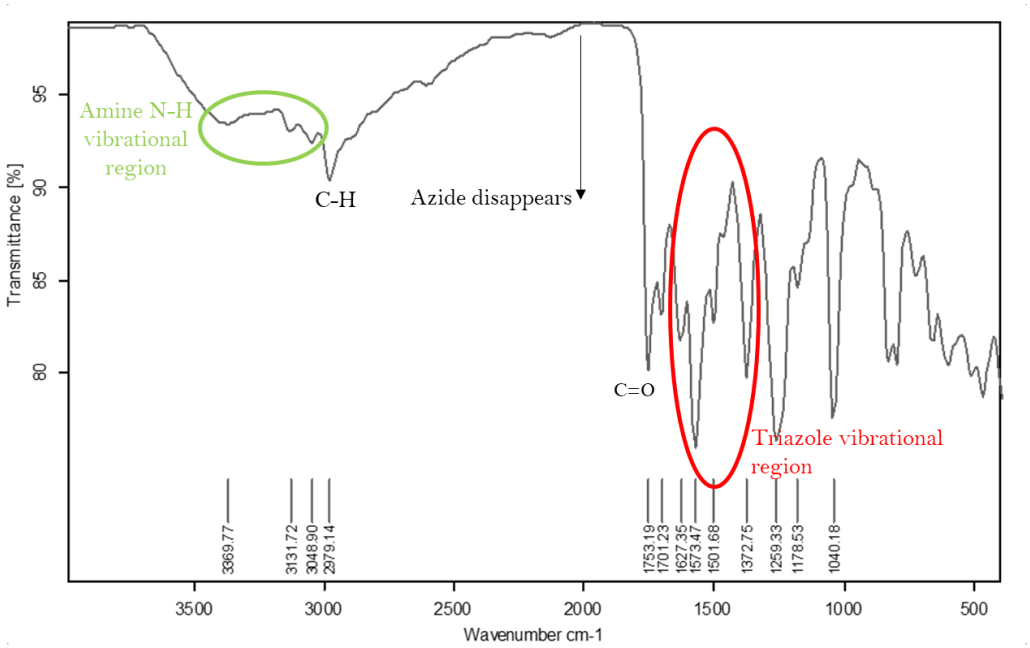

Figure 9: FT-IR spectra of coumarin-triazole derivative **C4**.

Figure 9 shows the FT-IR spectra of coumarin-triazole derivative **C4**. The amine protons in the ^{1}H NMR spectrum were not observed due to possible overlapping with DMSO peaks, however, the characteristic broad vibrational signal of the N-H bond was observed in the FT-IR spectrum. The broad signal from 3048-3369 cm^{-1} was assigned to the amine group. The success of the azide-alkyne cycloaddition was verified by the characteristic triazole vibrational signal between 1300-1650 cm^{-1} associated with N=N and C-N groups, and the disappearance of the sharp peak at 2000 cm^{-1} associated with azide functionality.

4.1.2 Absorption and emission studies of derivatives C1-4

The absorbance and emission characteristics of 3-ester-6-triazole coumarin derivatives **C1-4** were investigated in a variety of solvents including water, acetonitrile, ethanol, THF, and DMF. Stock solutions of **C1-4** were prepared in DMF to a concentration of 0.001 M. The excitation wavelengths were determined by UV-Vis analysis in different solvent media. The excitation wavelengths were found to be 340 nm for all compounds in different solvents (for the UV-Vis comparison of compounds **C1-4** in ethanol, see **Appendix C Figure 14**). **Figure 10** shows the emission response of compounds **C1-4** in acetonitrile. Derivative **C3** displayed the greatest emission intensity, followed by **C1**, **C2**, and **C4**. The two compounds exhibiting the greatest emission intensity in each solvent were selected and tested for their affinities towards a variety of metal cations in their respective solvents. **Table 1** shows the two compounds chosen for screening studies in their respective solvents based on their emission responses.

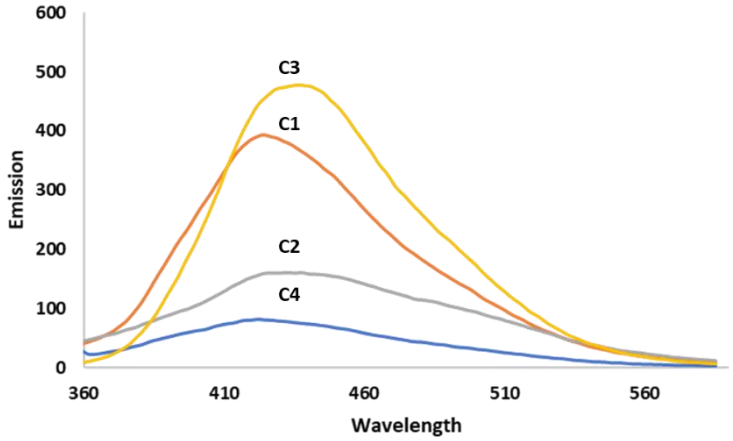

Figure 10: Fluorescent intensity comparison of sensors **C1-4** in acetonitrile. Excitation of 340 nm.

Table 1: Greatest emission response of compounds **C1-4** in different solvents at 340 nm excitation.

Solvent	Two sensors showing highest emission at 340 nm excitation
DMF	C3 & C1
THF	C2 & C1
Water	C3 & C1
Acetonitrile	C3 & C1
Ethanol	C3 & C1

Cationic Sensing Studies

4.1.3 Sensing responses of 3-ester-6-triazole coumarin derivatives C1 and C3 in different organic solvents and aqueous media

Coumarin-triazole sensors **C1** and **C3** exhibited the greatest emission properties in the tested solvents. The screening studies of **C1** were conducted by adding equal aliquots of metal solutions and monitoring the emission response. **Figure 11** shows the screening studies of coumarin-triazole derivatives **C1** and **C3** with selected metal cations in ethanol and DMF. Metal cations used for screening studies include Fe^{2+}, Fe^{3+}, Cd^{2+}, Pb^{2+}, Ag^{+}, Na^{+}, K^{+}, Ca^{2+}, Cr^{3+}, Al^{3+}, Ba^{2+}, Cu^{2+}, Co^{2+}, Hg^{2+}, Zn^{2+} and Ni^{2+}. Compounds **C1** and **C3** showed the greatest affinity towards Fe^{2+} and Fe^{3+} cations in ethanol and DMF by a comparatively large observable quenching response. Screening studies in water showed no notable enhancing or quenching response towards **C1** or **C3** (for the screening studies of **C1** and **C3** in acetonitrile see **Appendix C Figures 15**).

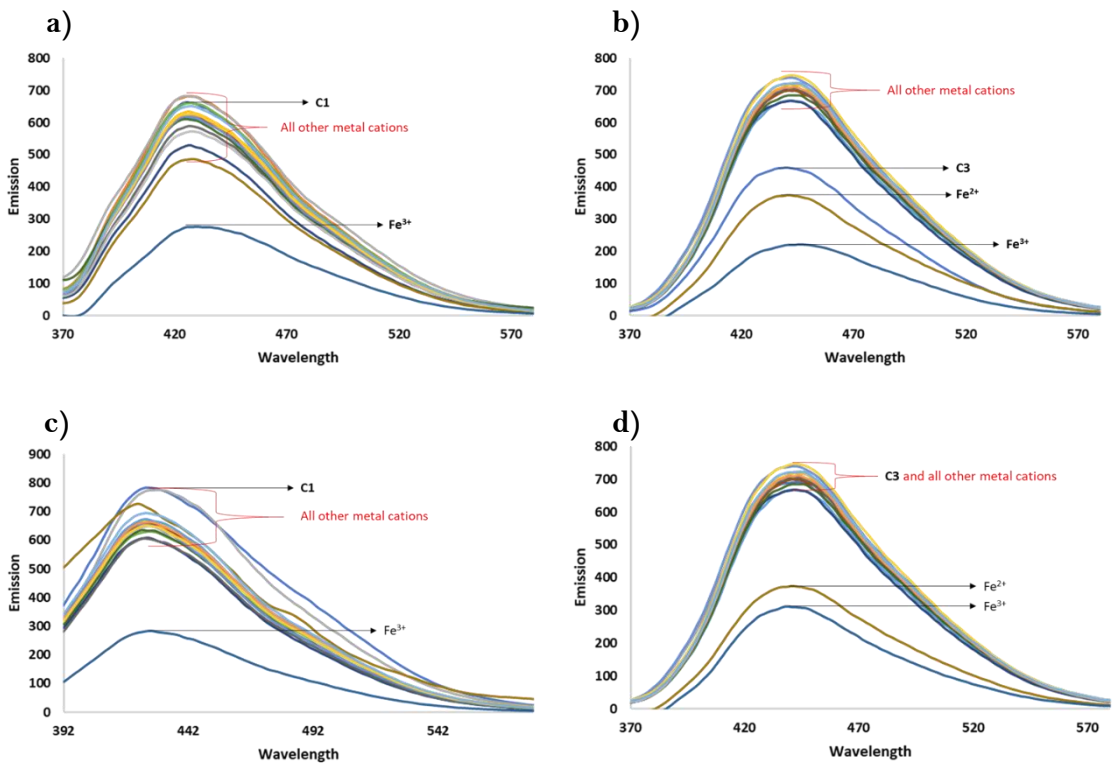

Figure 11: Metal cation screening studies of 3-ester-6-triazole coumarin derivatives **C1** and **C3** in ethanol (a & b) and DMF (c & d) respectively. Excitation of 340 nm. Emission and wavelength expressed in arbitrary units (a.u.) and nm respectively.

Screening studies show that sensors **C1** and **C3** display appreciable quenching responses towards Fe^{3+} in both ethanol and DMF. Sensor **C1** displayed a singular large quenching response to Fe^{3+} alone whilst sensor **C3** showed quenching responses to both Fe^{2+} and Fe^{3+}. This suggests that the sensing response of **C1** towards Fe^{3+} would produce greater selectivity towards Fe^{3+} than that of **C3**. Further studies in acetonitrile were omitted as it displayed similar quenching characteristics to that of ethanol.

4.1.4 Competition studies of C1 and C3 towards Fe^{3+} in ethanol and DMF

The competition studies of **C1** and **C3** towards Fe^{3+} in ethanol and DMF are shown in **Figure 12**. The selectivity of each sensor towards Fe^{3+} was determined by means of calculating the difference between the peak maxima of the sensor with Fe^{3+} alone and the average peak maxima value of the response towards Fe^{3+} with a competing cation. In both solvent systems, sensor **C1** displayed the greatest selectivity (lowest difference between these two values)

towards Fe^{3+}. Additionally, **C1** alone displayed appreciable selectivity towards Fe^{3+} in the presence of all competing cations. Therefore, it was chosen for titration studies in ethanol and DMF.

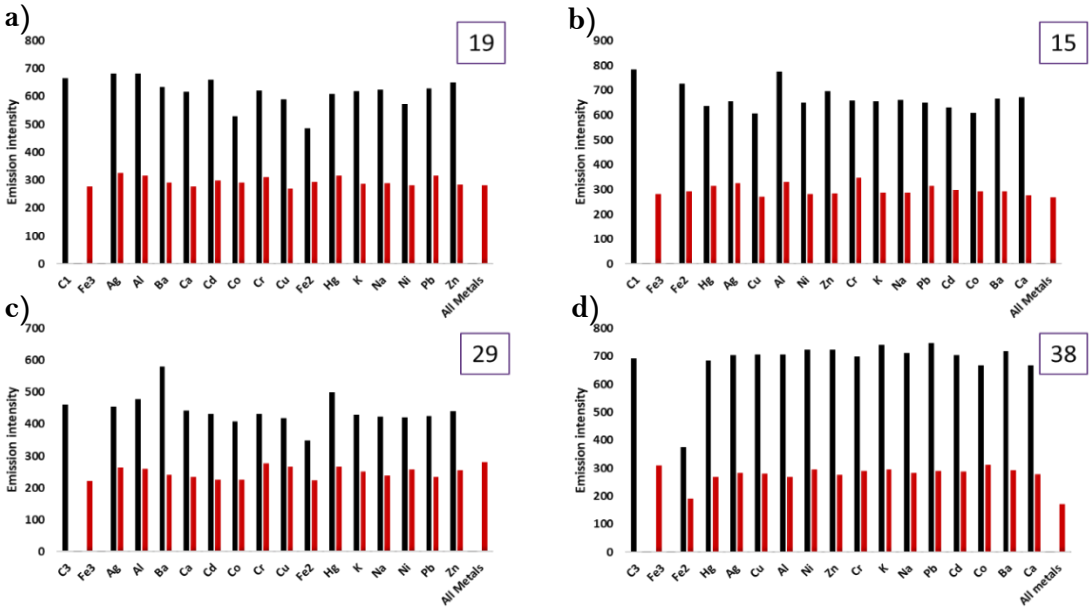

Figure 12: Competition studies of sensors **C1** and **C3** towards Fe^{3+} in the presence of competing cations in ethanol (a & c) and DMF (b & d) respectively. Excitation of 340 nm. Purple inset: difference in values between sensor with Fe^{3+} and the average of the sensor with Fe^{3+} and a competing metal cation.

4.1.5 Emission and absorption titration studies of C1 with Fe^{3+} in ethanol and DMF

Owing to the favourable selectivity that sensor **C1** displayed towards Fe^{3+}, this compound was then selected for fluorescent titration studies in ethanol and DMF. Sensor **C1** was capable of titrating with 2 µl aliquots from a 1 x 10^{-3} M Fe^{3+} solution. The titration of **C1** with Fe^{3+} in ethanol and DMF are shown in **Figure 13**. Notably, both titrations displayed no batho- nor hypsochromic shift in emission wavelength with peak maxima remaining at 425 nm. This suggests an "on-off" PET fluorescent quenching mechanism similar to that previously described in both **Chapters 2** and **3** is involved. Additionally, the titration did not result in any iso-emissive points, indicating the presence of a singular fluorescent species before and after complexation in both solvent systems.

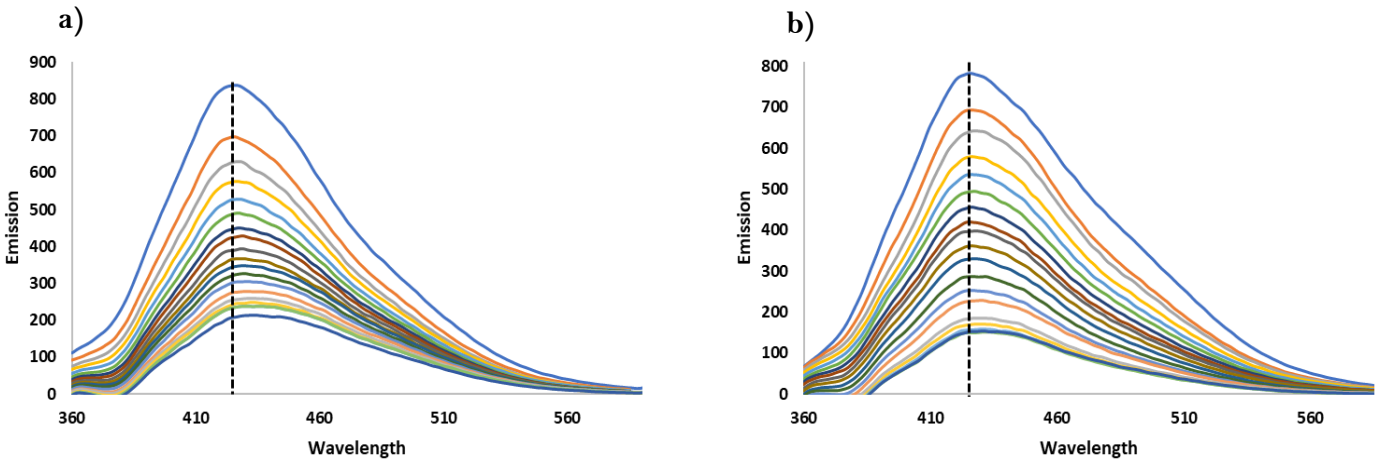

Figure 13: Emission titration studies of **C1** with Fe^{3+} in a) ethanol and b) DMF. Excitation of 340 nm. Titrations were completed in triplicate. Emission: a.u.; wavelength: nm.

The absorbance titration response of **C1** towards Fe^{3+} was investigated in ethanol (**Figure 14**). Titration of **C1**with Fe^{3+} resulted in an increase in optical density with no appearance of any isosbestic points. Additionally, no hypsochromic nor bathochromic shift in absorption wavelength was observed upon the addition of Fe^{3+}. This further supports the PET-type "on-off" quenching mechanism.

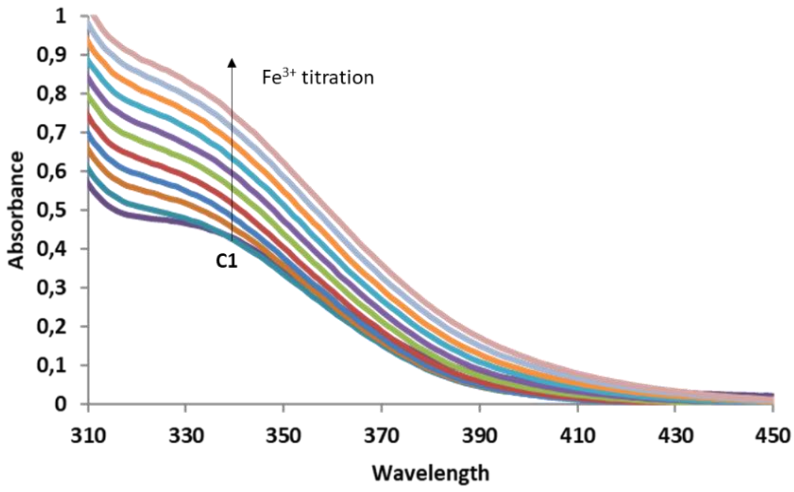

Figure 14: UV-Vis titration of sensor **C1** with Fe^{3+} in ethanol. Absorbance: a.u.; wavelength: nm.

4.1.6 PET "on-off" fluorescent quenching mechanism of C1 with Fe^{3+}

The probability of a FRET-type fluorescent quenching mechanism is unlikely based on structural and spectral characteristics of these coumarin-triazole based sensors as described in **Chapters 2** and **3**. The normalized absorbance and emission spectra of **C1**, in the absence of Fe^{3+}, showed no sizeable spectral overlap, thereby supporting the proposed PET-type "on-off" quenching mechanism. Complexation is expected to involve the triazole nitrogen atom(s) as seen in both **Chapters 2** and **3** (for the normalized absorbance and emission spectra of **C1** see **Appendix C Figure 16**). Computational analysis was utilized to determine the HOMO and LUMO of **C1**. The HOMO was computed to reside primarily around the phenyl ring and adjacent oxygen atom, whilst the LUMO of the sensor resides around the carbon atoms of the coumarin scaffold. Thus, upon excitation, electronic density is transferred from the phenyl-oxygen derivative towards the coumarin scaffold resulting in an excited state fluorophore and a measurable fluorescent response. Upon Fe^{3+} addition, complexation with the triazole moiety disrupts the extended π-conjugation of the system, with energy being emitted through a non-radiative relaxation pathway. This, in turn, results in a measurable fluorescent quenching response. The changes in orbital energies and electronic transitions are proposed to follow the same sequence as that of A1 as shown in **Figure 20 Chapter 2**. The calculated HOMO and LUMO and proposed PET "on-off" fluorescent quenching mechanism of C1 with Fe^{3+} is shown in **Figure 15**.

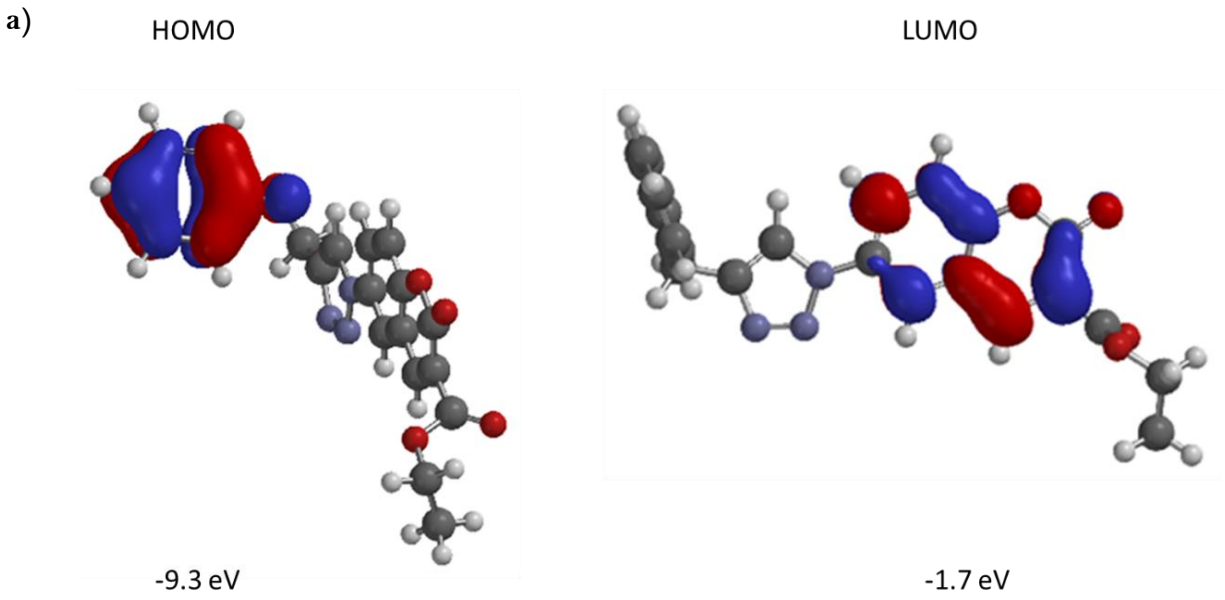

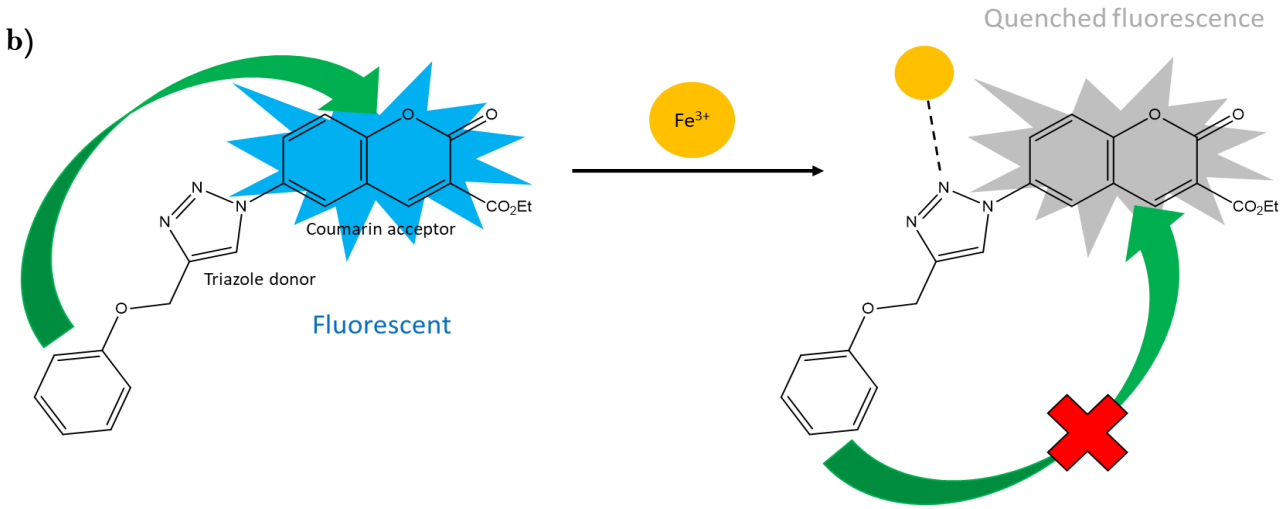

Figure 15: a) HOMO and LUMO molecular orbital diagram of **C1** and b) proposed fluorescent quenching mechanism of **C1** by addition of Fe^{3+} according to the PET-type "on-off" quenching mechanism.

4.1.7 Determination of quenching process, association constant, and detection limit of C1 with Fe^{3+}

The fluorescent quenching model was determined in accordance with the methodologies as outlined in **Chapters 2** and **3**. The titration data of **C1** with Fe^{3+} was compared in both ethanol and DMF. Titration data of **C1** with Fe^{3+} was plotted according to the linear Stern Volmer equation in both solvents (**Figure 16**). The values for the quenching constants (K_{sv}) and detection limits (LOD) were calculated at the lower concentration region of the titration curves where linearity is maintained. The values for K_{sv} were calculated to be 4.2 and 3.3 x 10^4 M^{-1} and the detection limits were found to be 2.9 and 1.5 μM for **C1** with Fe^{3+} in ethanol and DMF respectively. As previously mentioned, a linear SV plot suggests a singular static or dynamic quenching process. Deviations from linearity could infer a combined static and dynamic quenching mechanism.

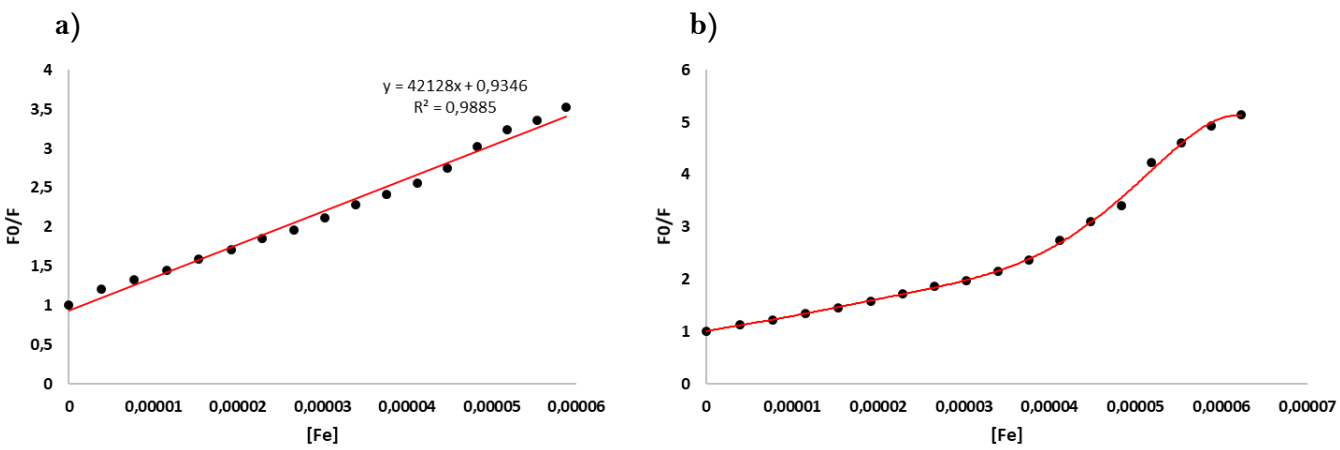

Figure 16: Titration of **C1** with Fe^{3+} according to the linear Stern-Volmer equation in a) ethanol, and b) DMF. Excitation of 340 nm.

Based on the result of the slight sigmoidal shape of the ethanol-titration (a) and the upwards curvature at higher quencher concentrations of DMF-titration (b) from the linear SV plot, it was assumed that the process may not be purely static or dynamic, as a fully linear plot would suggest. Henceforth, the titration data was fitted in accordance with the combined static and dynamic quenching model (see **Chapter 2**). The regression coefficients for **C1** in both ethanol and DMF were unfavourable, therefore, the quenching of **C1** by Fe^{3+} cannot be described by the combined static and quenching mechanism alone. This may infer that the quenching of **C1** by Fe^{3+} occurs either by a static or dynamic process (for the combined dynamic and static quenching plots of **C1** in ethanol and DMF see **Figure 17** in **Appendix C**). It is worth noting that a dynamic factor could be the main contributor towards the fluorescent quenching process observed, however, its contribution was unable to be assessed and calculated due to equipment constraints.

To determine which model has the greatest contribution towards the static quenching of **C1** with Fe^{3+}, titration data was fitted according to the Perrin and Sphere of Action (SOA) static quenching equations. The values for the quenching constants and detection limits were compared to that determined by the linear Stern Volmer plot. These values are reported in **Table 2** (for the graphs of the titration data as plotted according to the Perrin and SOA static quenching models in ethanol and DMF, see **Appendix C Figures 18** & **19**).

Table 2: Comparison of data obtained from the quenching response of **C1** to Fe^{3+} by the three stipulated quenching mechanisms.

C1	Quenching constants ($x10^4$ M^{-1})			Detection limits (μM)			R^2		
	SV	Perrin	SOA	SV	Perrin	SOA	SV	Perrin	SOA
Ethanol	4.2	2.0	2.1	2.9	1.86	NA	0.9885	0.9969	0.9952
DMF	3.3	2.7	NA	1.5	3.66	NA	0.9948	0.9848	NA

The mechanism by which **C1** is quenched by Fe^{3+} appears to be influenced by the surrounding solvent media. This similar property was shown in **Chapter 3** between derivatives **B1** and **B3** and was concluded not to be due to structural differences, but rather the effect of solvent polarity on the quenching process. Ethanol has a higher relative polarity than DMF and thus may influence the surrounding electronic environment of the coumarin-triazole derivative and/or interact with the analyte.

The primary mode of quenching between **C1** and Fe^{3+} in DMF initially appears to occur via the linear Stern Volmer quenching process. The value of the regression coefficient, detection limit, and quenching constant are more favourable than that determined by the Perrin static quenching mechanism. The SOA method resulted in poor correlation of data and was thus omitted from further studies and deemed unlikely as the main contributor towards static quenching.

The deviation from linearity in the DMF-titration may arise from restrictions in fluorophore accessibility at higher quencher concentrations where most of the sensor species are already Fe^{3+} coordinated. Owing to this deviation, the Perrin quenching mechanism was investigated as the possible main static contributor of the quenching process. The value of the regression coefficient calculated was close to that determined by the linear SV method, however, this linearity was calculated over the entire concentration range, whilst the values determined by the linear SV method were only observed at the lower quencher concentrations where

linearity was maintained. The value of the detection limit calculated from the Perrin method was not as low as that determined by the original SV plot. Additionally, the value for the quenching constant (K_{sv}) was greater than that determined by the Perrin method (K_p). It has been determined that Fe^{3+} chelates to the sensors in a static chemical bond and quenches via a chelation quenched fluorescent (CHQF) PET-type mechanism. As the values for the quenching constants, detection limits, and regression coefficients between the SV and Perrin methods are in close agreement, it was concluded that the Perrin method was the main static contributor to fluorescent quenching. The value of the detection limit of **C1** with Fe^{3+} in DMF (3.66 μM) is lower than what is deemed acceptable by the Environmental Protection Agency (4.5 – 5.4 μM) in drinking water. Although the detection limit is favourable for Fe^{3+} sensing strategies, DMF is an environmentally unfavourable solvent. For this reason, further studies of **C1** with Fe^{3+} in DMF were ceased.

The sensing of **C1** towards Fe^{3+} in ethanol is more favourable due to the solvents environmental friendliness. The plot of the titration data according to the linear SV method shows appreciable linearity, bearing a slight sigmoidal shape, over the entire concentration range. This may suggest that either a static or dynamic quenching process is occurring. As previously mentioned, the dynamic component was unable to be calculated and compared to the static component. Both the Perrin and SOA quenching mechanism were investigated for their individual contributions towards the static quenching process. The value of the regression coefficient for the Perrin and SOA method are in close agreement (R^2 = 0.9969 and 0.9952 respectively), however, the value of the detection limit calculated by the SOA method was substantially higher than that determined by the Perrin method. The plot of the titration data as fitted by the Perrin method is shown in **Figure 17**.

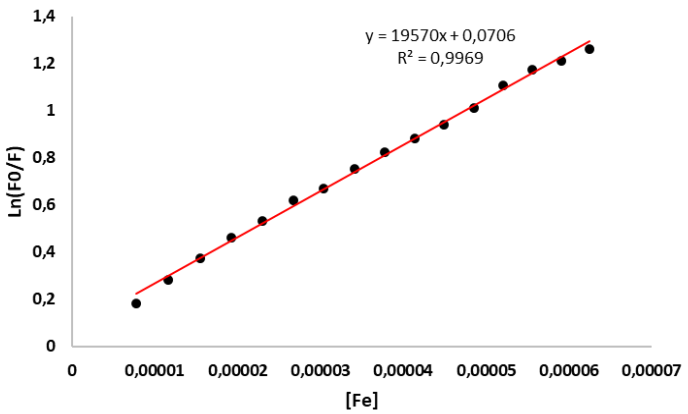

Figure 17: Titration of **C1** with Fe^{3+} in ethanol fitted by the Perrin static quenching model.

The detection limit was calculated according to the equation LOD = 3*σ/m and was found to be 1.86 μM. This is lower than what was determined from the Perrin titration analysis in DMF. This lower detection limit, coupled with the favourable environmental impact of ethanol, was then considered as the more favourable solvent for further studies.

Owing to this evaluated static quenching mechanism, the strength of the sensor-analyte bond was investigated by the Benesi-Hildebrand (BH) method. The value of the association constant (K_a) of **C1** with Fe^{3+} in ethanol was calculated according to K_a = int/slope and found to be 1.8 x 10^4 M^{-1}, an appreciably strong sensor-analyte coordination. This strong coordination value (together with the R^2 value of the double-logarithm plot discussed later) firmly suggest that the main mode of fluorescent quenching of **C1** by Fe^{3+} occurs via a static process whereby a strong coordination bond is achieved. This coordination may also influence the reversibility of **C1** towards Fe^{3+} in the presence of a reversing agent. The large value for the association constant supports the proposed CHQF-PET type quenching mechanism. Furthermore, the linearity (R^2 = 0.9979) suggests a 1:1 stoichiometric binding ratio. This was later confirmed by Job's plot analysis. The titration data as fitted to the BH equation is shown in **Figure 18** (for the BH plot of **C1** with Fe^{3+} in DMF, see **Appendix C Figure 20**).

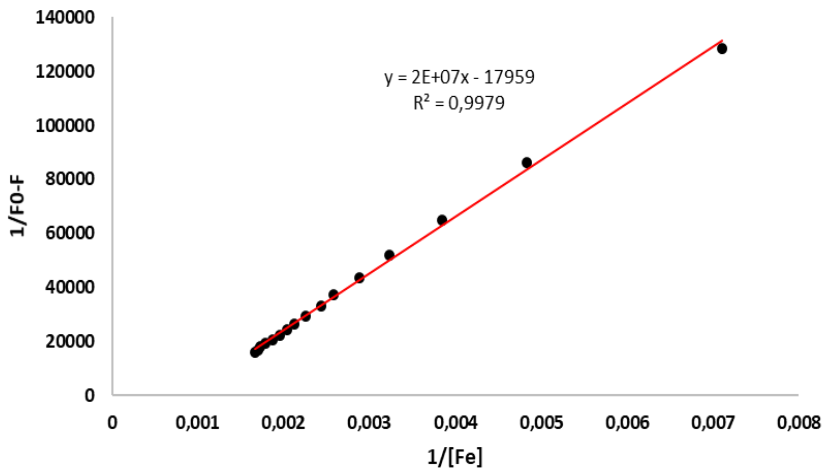

Figure 18: Benesi-Hildebrand plot of **C1** with Fe^{3+} in ethanol.

4.1.8 Reversibility of C1 towards Fe^{3+} with EDTA

The reversibility of **C1** towards Fe^{3+} was investigated through titration studies with the hexadentate chelating ligand EDTA in ethanol as shown in **Figure 19**. The sensor-analyte complex was found to be 51 % reversible. As mentioned previously, the large value calculated for the association constant may prevent full reversibility in EDTA. Sensor **C1** displayed greater percentage reversibility towards Fe^{3+} with EDTA than sensors **A1** and **B3** in **Chapters 2** and **3** respectively.

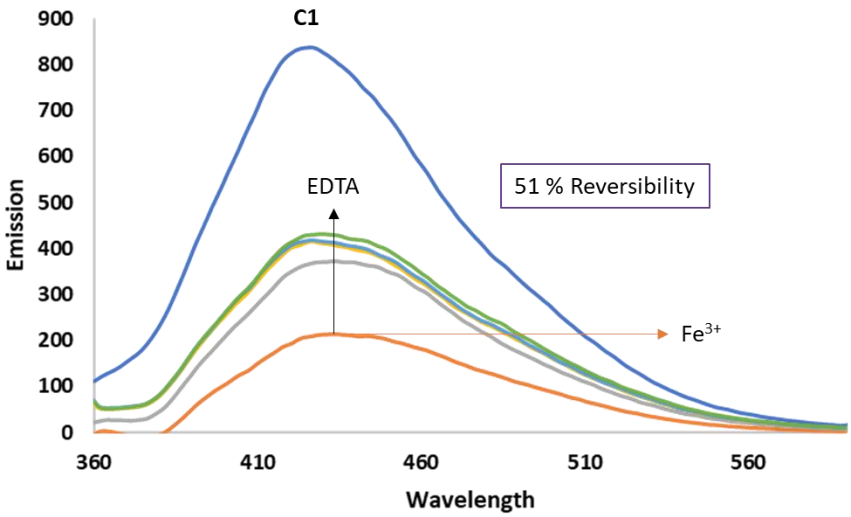

Figure 19: Reversibility of **C1** with Fe^{3+} in the presence of EDTA. Excitation of 340 nm.

4.1.9 Job's plot analysis of C1 with Fe^{3+} in ethanol

The stoichiometric binding ratio of **C1** with Fe^{3+} was investigated by Job's plot analysis in ethanol. The results are shown in **Figure 20**. The stoichiometric binding between **C1** and Fe^{3+} was shown to occur in a 1:1 ratio. These observations agree with the linearity of the Benesi-Hildebrand plot previously described. The mole fraction is obtained at the intersection of the two plots where the emission intensity is greatest.

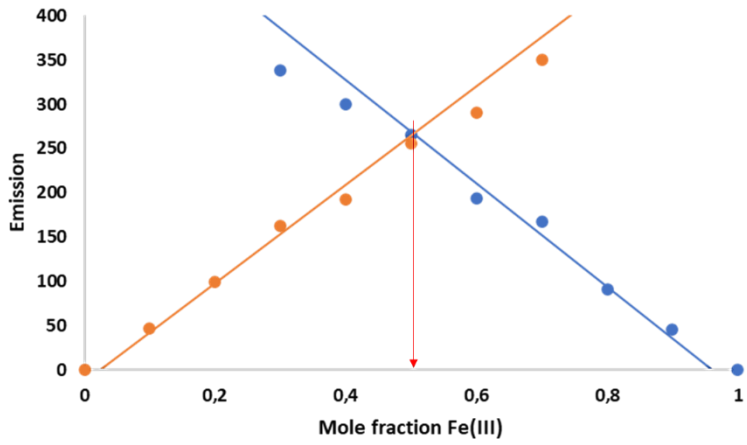

Figure 20: Job's plot analysis of **C1** with Fe^{3+} in ethanol. Excitation of 340 nm.

4.1.10 pH studies of C1 and Fe^{3+}

To determine the effect of pH variations on sensing abilities, titration studies in different pH solutions were conducted. Different arrays solutions with pH of 10, 7, 5, and 4 were utilized for the study. The emission of **C1** was monitored before and after Fe^{3+} addition at different pH values. Notably, **C1** exhibits the same quenching response towards Fe^{3+} in all solutions (**Figure 21**).

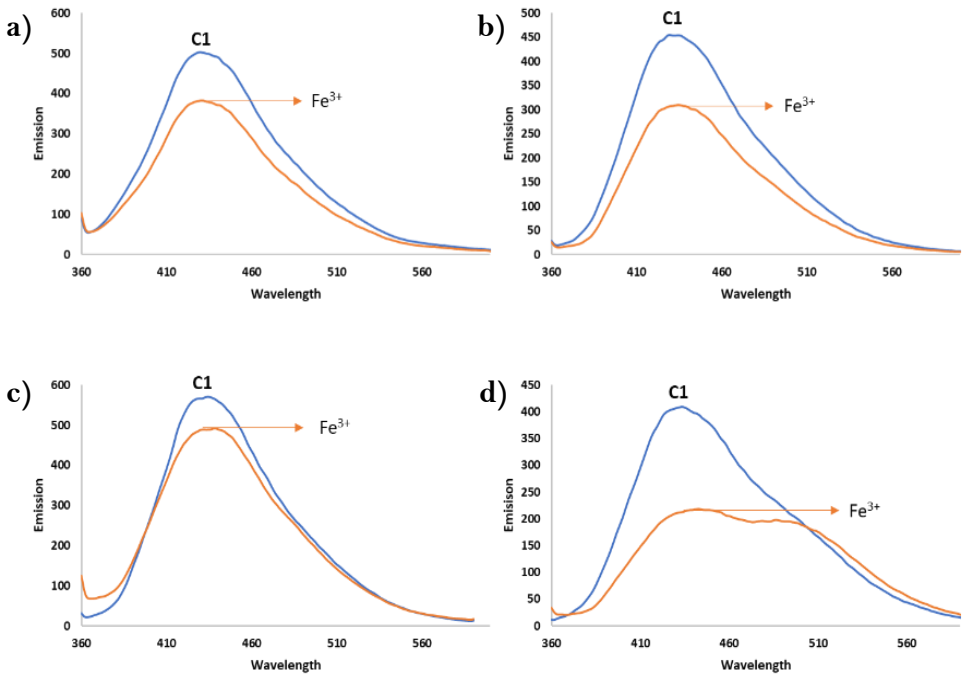

Figure 21: Effect of pH of sensor **C1** upon Fe^{3+} addition at pH: a) 4, b) 5, c) 7, and d) 10. Excitation of 340 nm.

4.1.11 Quantum yield studies

The fluorescence quantum yield (ϕ) of **C1** was evaluated using anthracene as a standard fluorophore with a known ϕ_S of 0.27 in ethanol. The sensor and standard were excited with the same excitation wavelength (340 nm) and their absorbances were tuned to ca. 0.05 nm at this wavelength. The integrated areas under the emission spectra were obtained using fl.Winlab software and the fluorescence quantum yields (ϕ) were calculated in accordance with **Equation 1** from **Chapter 2**. From these calculations, the quantum yield of sensor **C1** was calculated as 0.018 a.u.

4.1.12 Emission intensity and fluorescent output

As mentioned in **Chapter 3**, the lack of the electronic "push-pull" system between a 7-substituted electron donating group (EDG) and 3-substituted electron withdrawing group (EWG) creates an electronic deficit in the coumarin scaffold, thereby effecting the emission intensity. As the ester-carbonyl carbon is connected directly to the coumarin scaffold, it will pull electron density from the ring structure. The calculated electron density of **C1** is shown in **Figure 22**.

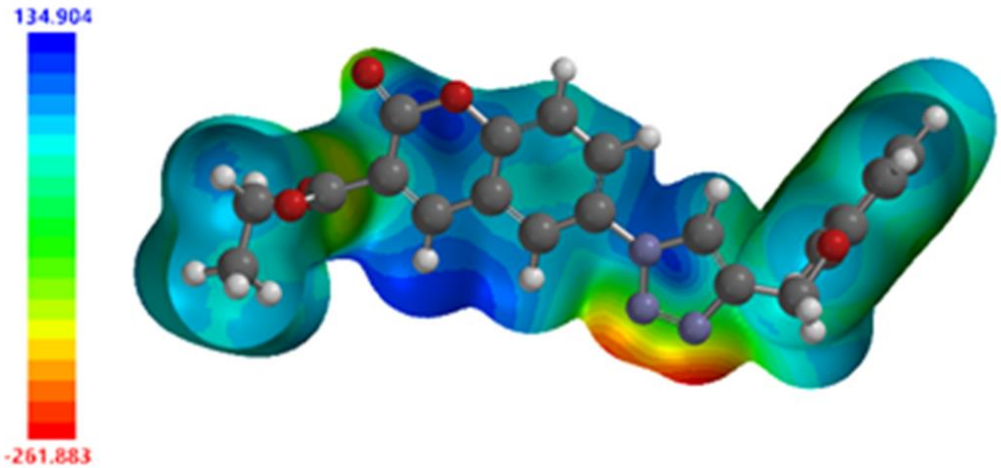

Figure 22: Electron density of sensor **C1** at PM3 calculation level.

Clearly, the coumarin fluorophore is subjected to a large electronic deficiency, illustrated by the dark blue colour surrounding the structure. Compared to **A1** in **Chapter 2**, a higher concentration and volume of **C1** was warranted to produce the same emission intensity. Visibly, the greatest electronic density resides on the N=N of the triazole moiety. Therefore, it would show the greatest potential for electron donation towards cationic coordination.

4.1.13 Proposed binding site between C1 and Fe^{3+}

The complexation abilities of both triazole-nitrogen, and carbonyl-oxygen atoms make them common candidates for many different organometallic complexes.[2–4] Sensor **C1** possesses both electron donating triazole-nitrogen and carbonyl functionalities for complexation towards Fe^{3+}. Two proposed binding scenarios between **C1** and Fe^{3+} are shown in **Figure 23**. In **Chapters 2** and **3**, it was shown how the triazole-nitrogen atom(s) functions as the prominent binding site towards Fe^{3+} complexation. This specific complexation results in a pseudo six-membered ring configuration which results in high energetic stability.

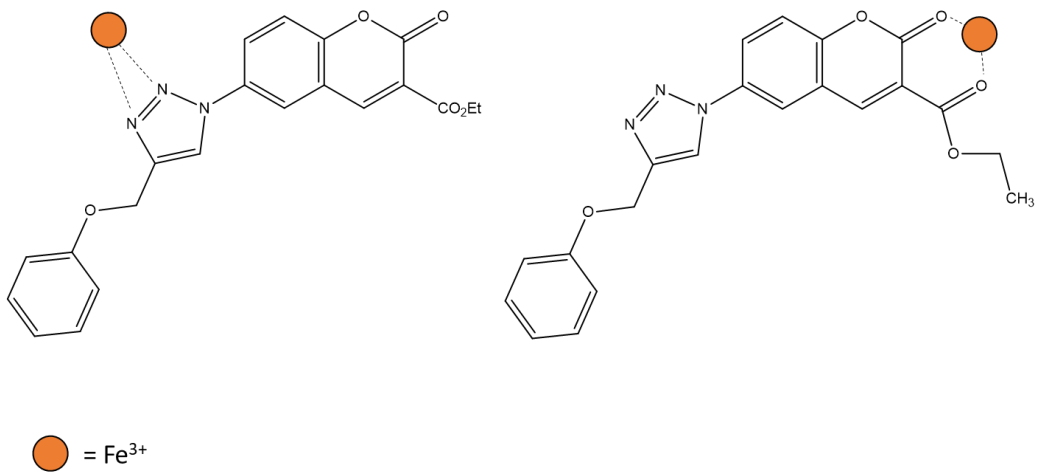

Figure 23: Proposed complexation sites between **C1** and Fe^{3+}.

The correct complexation site was evaluated by ^{1}H NMR, ^{13}C NMR, and double-logarithm plot analysis, and was finally supported by Molecular Modelling studies. The ^{1}H NMR titration of **C1** with Fe^{3+} is shown in **Figure 24**. Upon Fe^{3+} titration, the peaks become less resolved but without changes of the ppm values. This indicates that complexation does not occur via hydrogen bonding. Furthermore, computational calculations indicate that no hydrogen bonding should occur. This agrees with the observations in the ^{1}H NMR spectrum.

It could then be assumed that the main site of complexation involves the triazole nitrogen atom with possible assistance/stabilization from neighbouring groups and/or solvent molecules.

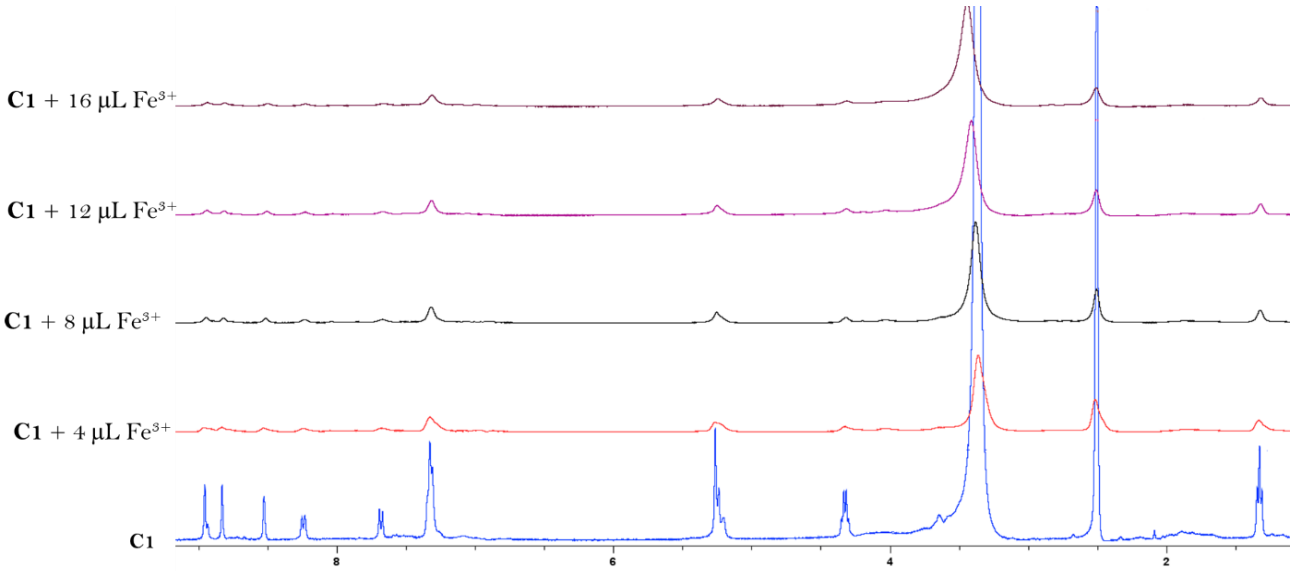

Figure 24: ^{1}H NMR titration of **C1** with Fe^{3+}.

The ^{13}C NMR of **C1** with peak assignment is shown in **Appendix C Figure 7**. The spectral overlay of **C1** and **C1**-Fe^{3+} complex after the addition of 16 µL of the Fe(III)NO_3 solution is shown in **Figure 25**. The two peaks assigned to the coumarin- and ester-carbonyl functionalities do not display any shift upon Fe^{3+} addition. In **Chapters 2** and **3**, it was described that minimal to no shift is plausible due to the contribution of the lone electron pair towards complexation and not the complete covalent bond from the C=O π-electrons. Therefore, double-logarithm and molecular modelling studies were used to verify the possible complexation site(s).

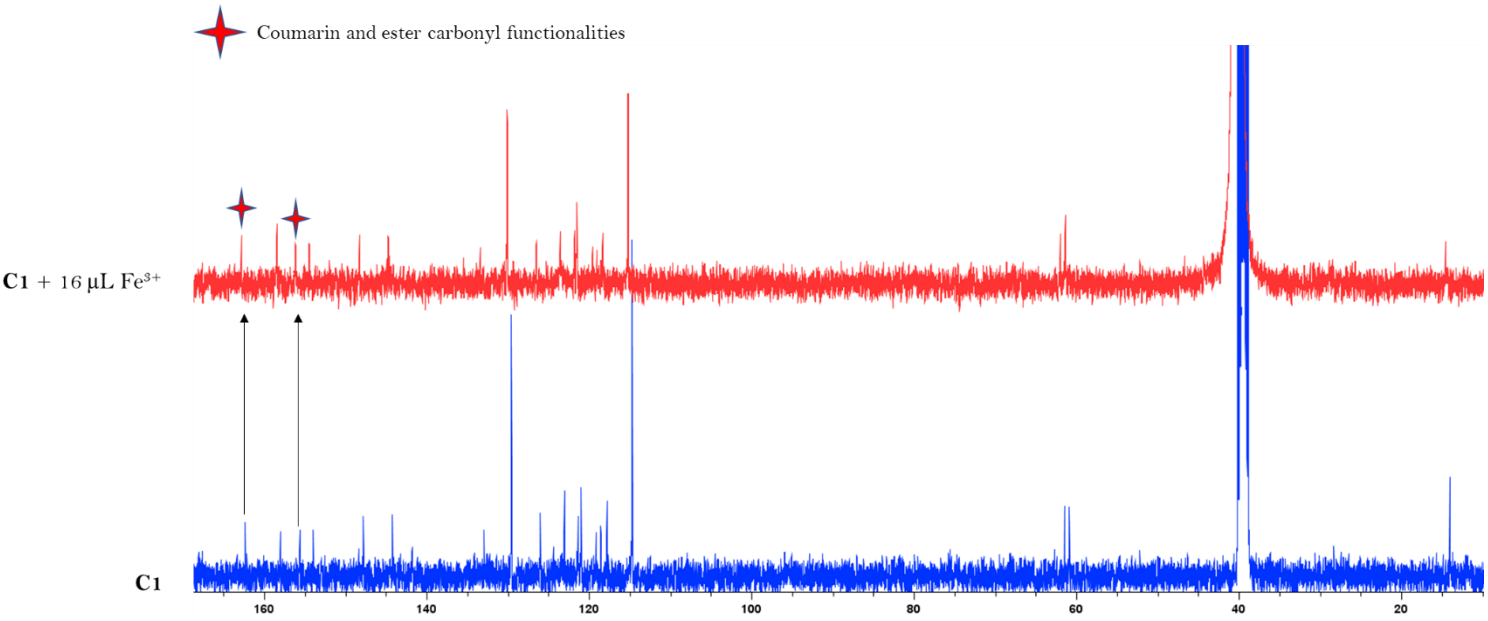

Figure 25: ^{13}C NMR overlay of **C1** and **C1** after the addition of 16 µL Fe^{3+} in d_6-DMSO.

The number of theoretical binding sites was calculated using the available titration data by means of a double-logarithm plot. The double-logarithm plot from the titration of **C1** with Fe^{3+} is shown in **Figure 26**. As mentioned in previous chapters, a straight line occurs when the predominant mode of fluorescent quenching occurs via a static process. This confirms the Perrin static quenching mechanism reported. Additionally, the value of n is equal to 1.2, indicating that the triazole-nitrogen binding is the only plausible coordination scenario. Triazole coordination is possibly assisted by solvent and water molecules.

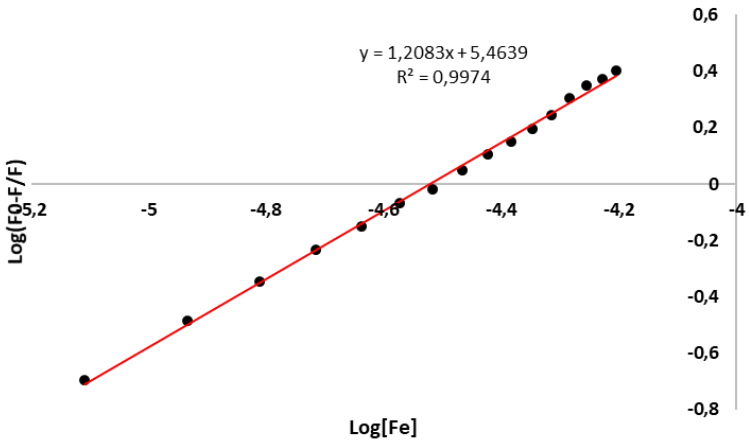

Figure 26: Double-logarithm plot of **C1** with Fe^{3+}.

Finally, molecular modelling studies confirmed the proposed interaction between sensor **C1** and Fe^{3+} via the triazole functionality. The area of higher electron density surrounding the triazole N=N bond (as seen in **Figure 22**) facilitates bonding with the Fe^{3+} cation and is further assisted by solvent and/or water molecules. This coordination scenario is supported by previous **Chapters 2** and **3**. The calculated most energetically preferred conformer of the **C1**-Fe^{3+} binding scenario is illustrated in **Figure 27**.

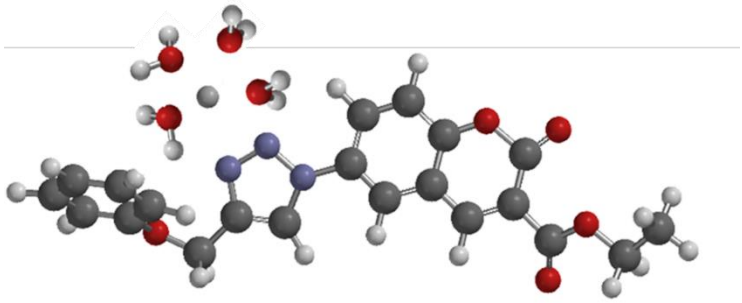

Figure 27: Computed most energetically favourable binding scenario between **C1** and Fe^{3+}.

Anionic Sensing studies

4.1.14 Screening studies

Owing to the favourable selectivity that sensor **C1** showed towards Fe^{3+}, it was investigated for its sensing potential towards a variety of anions in different solvent systems. Solutions of anions were prepared in water from their ammonium salts. The anions used for these experiments included: CN^-, SCN^-, SO_4^{2-}, NO_3^-, CH_3COO^-, I^-, Br^-, Cl^-, F^- and PF_6^-. Screening studies were conducted in four different solvents namely ethanol, water, acetonitrile, and DMF. The screening studies of **C1** towards these listed anions in different solvent systems are shown in **Figure 28**. Visibly, sensor **C1** showed a notable affinity towards CN^- in all solvent systems used, however, the effect on emission was not as strong in water. Additionally, the DMF screening studies show the occurrence of a shift in peak maxima upon CN^- addition. Additionally, a strong enhancing effect upon Cl^- addition was observed. To

determine whether **C1** could be applied towards selective and sensitive CN^- sensing strategies, competition studies with CN^- in the presence of competing anions were conducted in ethanol, acetonitrile and DMF. The competition studies of **C1** towards CN^- in the three solvent systems are shown in **Figure 29**.

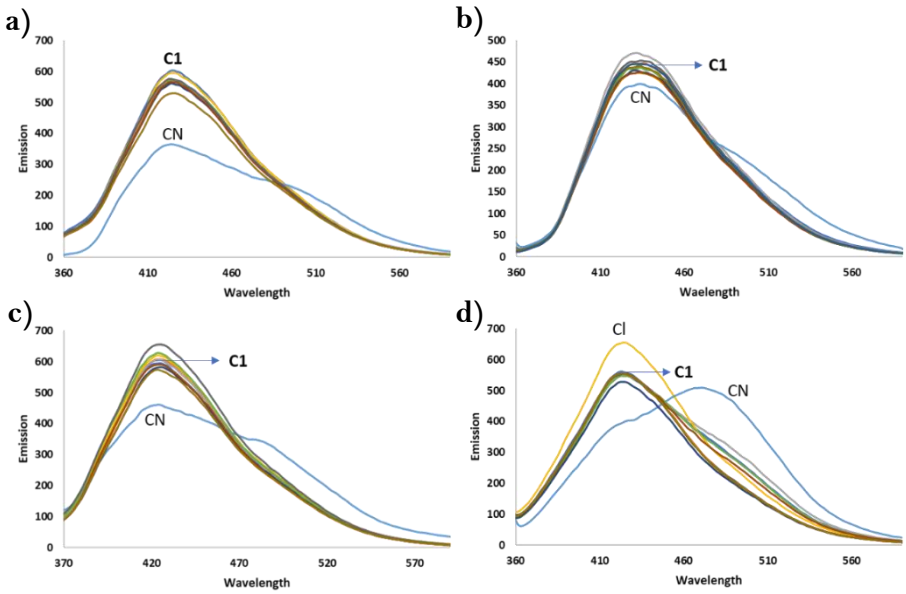

Figure 28: Screening studies of **C1** with listed anions in a) ethanol, b) water, c) acetonitrile, and d) DMF. Excitation of 340 nm.

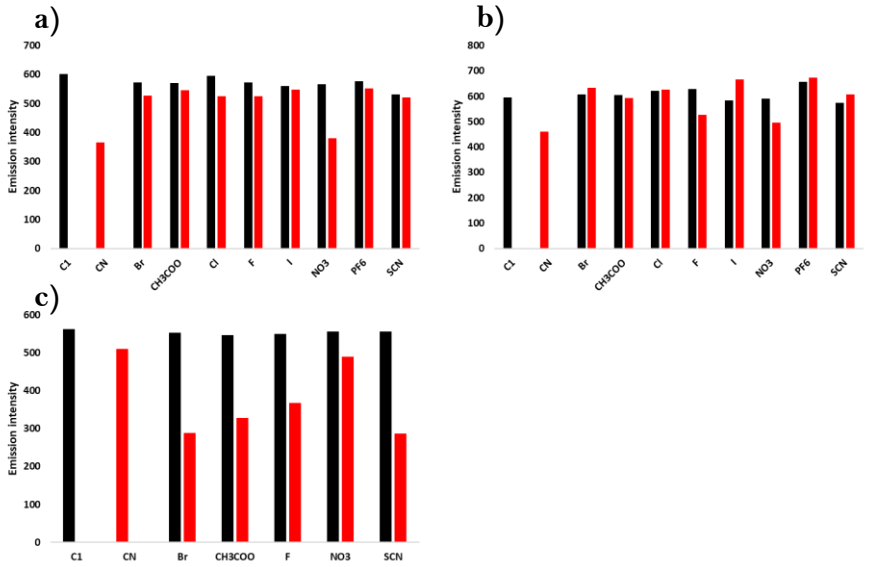

Figure 29: Competition studies of **C1** towards CN^- in the presence of competing anions in a) ethanol, b) acetonitrile, and d) DMF. PF_6^-, I^-, and Cl^- left out of DMF study (d) as CN^- had no effect on their emission intensity. Excitation of 340 nm.

It is evident that **C1** does not display any selectivity towards CN^- in the presence of competing anions. Due to these observations, further studies including both emission and absorbance titration analysis, Job's plot studies, association constant and detection limit determination, ^1H NMR and ^{13}C NMR titration experiments were not conducted. Molecular Modelling studies were used to elucidate the possible coordination scenario between **C1** and CN^-. The calculated binding site of **C1** with CN^- is shown in **Figure 30**. Computations indicate the interaction of the acidic triazole proton towards complexation, with possible assistance from a neighbouring coumarin proton. This agrees well with reported results from previous chapters and literature.

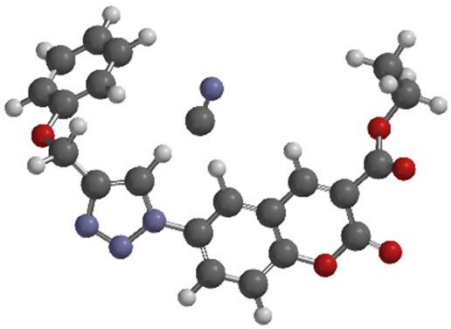

Figure 30: Most energetically preferred conformer for the interaction between **C1** and CN^-

.

4.2 Conclusion

Herein, four novel 3-ester-6-triazole coumarin derivatives were synthesized, characterized, and tested for their selectivity and sensitivity towards a variety of cations and anions in different solvent systems. These sensors differ based on the functionality attached to the triazole moiety. The greatest emission intensities were observed for derivatives **C1** and **C3**. Both sensors showed a reasonable affinity for Fe^{3+} in ethanol and DMF through a strong fluorescent quenching response. However, sensor **C1** displayed greater selectivity towards Fe^{3+} than **C3** in both ethanol and DMF. Owing to the greater selectivity **C1** displayed towards Fe^{3+}, it was selected for further titration analysis in both solvents. Titration studies of **C1** with Fe^{3+} in ethanol and DMF were further conducted. The detection limit of **C1** towards Fe^{3+} was determined to be 1.86- and 3.66 μM in ethanol and DMF respectively. The main mode of fluorescent quenching for **C1** in ethanol and DMF was determined to occur via a static mechanism, namely the Perrin static quenching model. UV-Vis titration of **C1** with Fe^{3+} resulted in no spectra shift which supported the CHQF-PET "on-off" fluorescent mechanism. The association constant was determined to be 1.8×10^4 M^{-1}. When the **C1**-Fe^{3+} complex was titrated with EDTA, up to 51% reversibility was achieved. The stoichiometric binding was shown to occur in a 1:1 ratio. The sensor displayed a good quenching response towards Fe^{3+} in a variety of buffered solutions with pH of 4,5,7, and 10. The quantum yield was determined to be 0.018. The complexation of **C1** towards Fe^{3+} was shown to coordinate via the triazole-nitrogen atom. Sensor **C1** was applied towards anionic sensing strategies in ethanol, water, acetonitrile and DMF. Screening studies show that **C1** displayed a reasonable response to CN^- in ethanol, acetonitrile, and DMF. Selectivity studies showed poor affinity towards CN^- in the presence of competing anions. Sensor **C1** was not deemed appropriate for further anionic sensing studies.

4.3 Experimental

4.3.1 Materials

Stock solutions of 3-ester-6-triazolyl coumarin derivatives **C1-4** were prepared by dissolving the respective samples in 25 mL of DMF (dimethylformamide) to a final stock concentration of 0.001 M. Deionized water was used to prepare solutions of metal ions to the concentration of 0.01 M which were diluted further to their desired concentrations. All metal ion solutions were prepared from their nitrate salts, apart from Fe^{2+} which was prepared from its corresponding sulfate. Anionic solutions were prepared in deionized water from their ammonium salts. The titration experiments were performed in 3 mL quartz and glass cuvettes, respectively. Spectroscopic measurements were performed after each aliquot of selected cationic and anionic solutions.

Synthesis of coumarin-ester derivative 1

The synthesis of coumarin-ester derivative **1** was carried out by literature procedure.[1] The success of the reaction was determined by ^{1}H NMR and singe-crystal XRD analysis (see **Figure 4**). For the ^{1}H NMR of coumarin-ester derivative **1** see **Appendix C Figure 21**. ^{1}H NMR: (DMSO-d_6, 400MHz) δ_H: 1.36(t, 3H, *J* 7.2), 4.36(q, 2H, *J* 7.12), 7.29(m, 2H), 7.60(m, 2H), 8.48(s, 1H). ^{13}C NMR (DMSO-d_6, 100.6 MHz) δ_C: 14.18, 61.89, 116.65, 117.82, 118.17, 124.86, 129.54, 134.34, 148.57, 155.06, 155.69, 162.93.

Synthesis of 6-nitro-3-ester coumarin derivative 1a

Coumarin-ester derivative **1** (1g, 4.6 mmol) was added in portions to a cold solution of $NaNO_3$ (2g, 23 mmol) in HCl (30 mL) with stirring. The mixture was stirred at 0 °C for 2 hrs, after which it was poured into ice water and the resulting precipitate filtered and dried to afford 6-

nitro-3-ester coumarin derivative **1a** as a white solid (0.98g, 82%). ^{1}H NMR: (DMSO-d_6, 400MHz) δ_H: 1.31 (t, 3H, *J* 13.8), 2.5 (s, 2H), 7.63 (d, 1H, *J* 9.1), 8.48 (d, 1H, *J* 9.1), 8.91 (s, 2H). ^{13}C NMR (DMSO-d_6, 100.6 MHz) δ_C: 13.97, 61.52, 117.71, 118.15, 119.45, 126.01, 128.51, 143.62, 147.58, 155.01, 158.01, 162.04. IR ν_{max} (cm^{-1}): 1500 (NO_2), 1687, 1773 (C=O), 3088 (C-H). Elemental Anal: expected C 55.76, H 3.45, N 5.32, O 36.47; found C 55.74, H 3.45, N 5.31, O 36.47.

Reduction of 1a to 3-ester-6-amine derivative 1b

Nitrated coumarin derivative **1a** (0.4 g, 1.52 mmol) was added to a solution of Fe-powder (0.1 g, 1.52 mmol) in HOAc/H_2O (30 mL/20 mL) and was left to stir at room temperature for 24 hrs. The resulting mixture was filtered through celite powder to remove any residual Fe-powder. The filtrate was separated with ethyl acetate (3 x 50 mL) and washed with deionized water (3 x 20 mL). The organic layers were combined, dried over anhydrous Na_2SO_4, and the solvent removed under vacuum. The solid was recrystallized by minimal DCM and ether to afford the product as an orange/brown solid (0.25 g, 71%). ^{1}H NMR: (DMSO-d_6, 400MHz) δ_H: 1.30 (t, 3H, *J* 7.02), 4.27 (q, 4H, *J* 7.02), 5.35 (s, 2H), 6.88 (s, 1H), 6.98 (d, 1H, *J* 8.84), 7.15 (d, 1H, *J* 8.84), 8.54 (s, 1H). ^{13}C NMR (DMSO-d_6, 100.6 MHz) δ_C: 14.02, 61.06, 110.97, 116.47, 117.45, 118.07, 121.51, 154.89, 146.22, 148.55, 156.49, 163.00. IR ν_{max} (cm^{-1}): 3224-3403 (N-H), 2982-3055 (C-H), 1745 (C=O), 1567 (N-H). Elemental Anal: expected C 61.8, H 4.75, N 6.01, O 27.44; found C 61.76, H 4.73, N 5.99, O 27.43.

Conversion of coumarin-amine 1b to coumarin-azide 1c

The conversion of coumarin-amine to coumarin-azide derivative **1c** was conducted according to literature procedure.[5] The reaction of **1b** (0.25 g, 1.07 mmol) under the aforementioned reaction conditions, afforded the desired product as a bright yellow solid (0.26 g, 95%). ^{1}H NMR: (DMSO-d_6, 400MHz) δ_H: 1.31 (t, 3H, *J* 6.96), 4.29 (q, 2H, *J* 7.0), 7.45 (s, 2H), 7.71 (d, 1H, *J* 10.44), 8.71 (d, 1H, *J* 10.08). ^{13}C NMR (DMSO-d_6, 100.6 MHz) δ_C: 8.91, 27.72, 110.13, 116.94, 119.09, 125.22, 125.95, 127.79, 151.71, 152.07, 157.14,

172.29. IR ν_{max} (cm^{-1}): 3000 (C-H), 2110 (N_3), 1707 (C=O). Elemental Anal: expected C 55.60, H 3.50, N 16.21, O 24.69; found C 55.59, H 3.48, N 16.19, O 24.67.

Synthesis of 3-ester-6-triazolyl coumarin derivatives C1-4

Coumarin-azide derivative **1c** (0.3 g, 1.16 mmol) was reacted under the triazole forming "click" reaction protocol from **Chapters 2** and **3** with previously outlined phenol-alkyne derivative (compound **2** in **Chapter 2**), and store-bought alkyne derivatives including phenylacetylene, propargyl benzoate, and 2-methyl-3-butyne-2-amine (1.2 molar eq.).The solvent was evaporated under vacuum and the residue dissolved in ethyl acetate (30 mL), washed with water (3x30ml) and dried over anhydrous Na_2SO_4. The organic layer was evaporated under vacuum and crude product purified by recrystallization from DCM (5 mL) and petroleum ether (40 mL) to yield solid coumarin-triazolyl derivatives **C1** (0.35 g, 78%), **C2** (0.18 g, 43%), **C3** (0.01 g, 20 %), **C4** (0.09 g, 24%).

Sensor **C1** ^{1}H NMR: (DMSO-d_6, 400MHz) δ_H: 1.32 (t, 3H, *J* 6.64), 4.32 (q, 2H, 6.92), 5.26 (s, 2H), 7.32 (s, 5H), 7.68 (d, 1H, *J* 8.88), 8.24 (d, 1H, *J* 8.60), 8.53 (s, 1H), 8.83 (s, 1H), 8.95 (s,1H). ^{13}C NMR (DMSO-d_6, 100.6 MHz) δ_C: 14.00, 60.86, 61.42, 114.68, 117.78, 118.53, 119.09, 120.98, 121.30, 123.00, 125.97, 129.54, 132.89, 144.20, 147.76, 153.94, 155.58, 157.93, 162.32. IR ν_{max} (cm^{-1}): 3047-2875 (C=C-H; C-H), 1728 (C=O), 1595-1374 (triazole), 1237-1030 (ether C-O-C). Elemental Anal: expected C 64.45, H 4.38, N 10.74, O 20.44; found C 63.91, H 4.36, N 10.56, O 20.39.

Sensor **C2** ^{1}H NMR: (DMSO-d_6, 400MHz) δ_H: 1.32 (t, 3H, *J* 7.12), 4.32 (q, 2H, *J* 7.08), 7.40 (t, 1H, *J* 7.0), 7.51 (t, 2H, *J* 7.50), 7.69 (d, 1H, *J* 8.92), 7.94 (d, 2H, *J* 7.52), 8.25 (d, 1H, *J* 8.84), 8.53 (s, 1H), 8.83 (s, 1H), 9.29 (s, 1H). ^{13}C NMR (DMSO-d_6, 100.6 MHz) δ_C: 13.98, 61.46, 117.83, 118.54, 119.09, 119.81, 121.06, 125.33, 125.81, 128.39, 129.04, 129.94, 132.96, 147.48, 147.76, 153.89, 155.61, 162.33. IR ν_{max} (cm^{-1}): 3126-2981 (C=C-H; C-H), 1755 (C=O), 1621-1371 (triazole), 1250-1026 (ether C-O-C). Elemental Anal: expected C 66.48, H 4.18, N 11.63, O 17.71; found C 66.47, H 4.11, N 11.62, O 17.70.

Sensor **C3** ^{1}H NMR: (DMSO-d_6, 400MHz) δ_H: 1.32 (t, 3H, *J* 6.98), 4.32 (q, 2H, *J* 7.08), 5.53 (s, 2H), 7.54 (t, 3H, *J* 7.36), 7.67 (d, 1H, *J* 8.12), 8.01 (d, 2H, *J* 7.32), 8.25 (d, 1H, *J* 8.88), 8.53 (s, 1H), 8.82 (s, 1H), 8.96 (s, 1H). ^{13}C NMR (DMSO-d_6, 100.6 MHz) δ_C: 13.99, 57.79, 61.41,

117.75, 118.51, 119.07, 121.32, 123.20, 125.99, 128.79, 129.28, 132.83, 133.57, 143.35, 147.74, 153.96, 155.56, 162.29, 165.42. IR ν_{max} (cm^{-1}): 3052-2976 (C=C-H, C-H), 1720 (C=O), 1620-1374 (triazole), 1259-1027 (ether C-O-C). Elemental Anal: expected C 63.01, H 4.09, N 10.02, O 22.89; found C 63.00, H 4.09, N 9.98, O 22. 85.

Sensor **C4** ^{1}H NMR: (DMSO-d_6, 400MHz) δ_H: 1.32 (s, 3H), 1.47 (s, 6H), 4.31 (d, 2H, *J* 4.96), 7.65 (d, 1H, *J* 7.36), 8.20 (d, 1H, *J* 6.92), 8.48 (s, 1H), 8.61 (s, 1H), 8.82 (s, 1H). ^{13}C NMR (DMSO-d_6, 100.6 MHz) δ_C: 13.99, 61.42, 117.74, 118.61, 118.66, 119.02, 120.78, 125.61, 133.17, 147.80, 153.66, 155.62, 162.33. Elemental Anal: expected C 59.64, H 5.30, N 16.37, O 18.69; found C 59.58, H 5.27, N 16.36, O18.65.

4.4 References

(1) Abdel-Wahab, B. F.; Mohamed, H. A.; Farhat, A. A. Ethyl Coumarin-3-Carboxylate: Synthesis and Chemical Properties. *Org. Commun.* **2014**, *7* (1), 1–27.

(2) Vielhaber, T.; Faust, K.; Topf, C. Group 6 Metal Carbonyl Complexes Supported by a Bidentate PN Ligand: Syntheses, Characterization, and Catalytic Hydrogenation Activity. *Organometallics* **2020**, *39* (24), 4535–4543. https://doi.org/10.1021/acs.organomet.0c00612.

(3) Hebenbrock, M.; González-Abradelo, D.; Hepp, A.; Meadowcroft, J.; Lefringhausen, N.; Strassert, C. A.; Müller, J. Influence of the Ancillary Ligands on the Luminescence of Platinum(II) Complexes with a Triazole-Based Tridentate C^N^N Luminophore. *Inorganica Chim. Acta* **2021**, *516* (II), 119988. https://doi.org/10.1016/j.ica.2020.119988.

(4) Amoah, C.; Obuah, C.; Ainooson, M. K.; Muller, A. Synthesis, Characterization and Fluorescent Properties of Ferrocenyl Pyrazole and Triazole Ligands and Their Palladium Complexes. *J. Organomet. Chem.* **2021**, *935*, 121664. https://doi.org/10.1016/j.jorganchem.2020.121664.

(5) Sivakumar, K.; Xie, F.; Cash, B. M.; Long, S.; Barnhill, H. N.; Wang, Q. A Fluorogenic 1 , 3-Dipolar Cycloaddition Reaction of 3-Azidocoumarins And. *Org. Lett.* **2004**, *6* (24), 4603–4606. https://doi.org/10.1021/ol047955x.

APPENDIX C

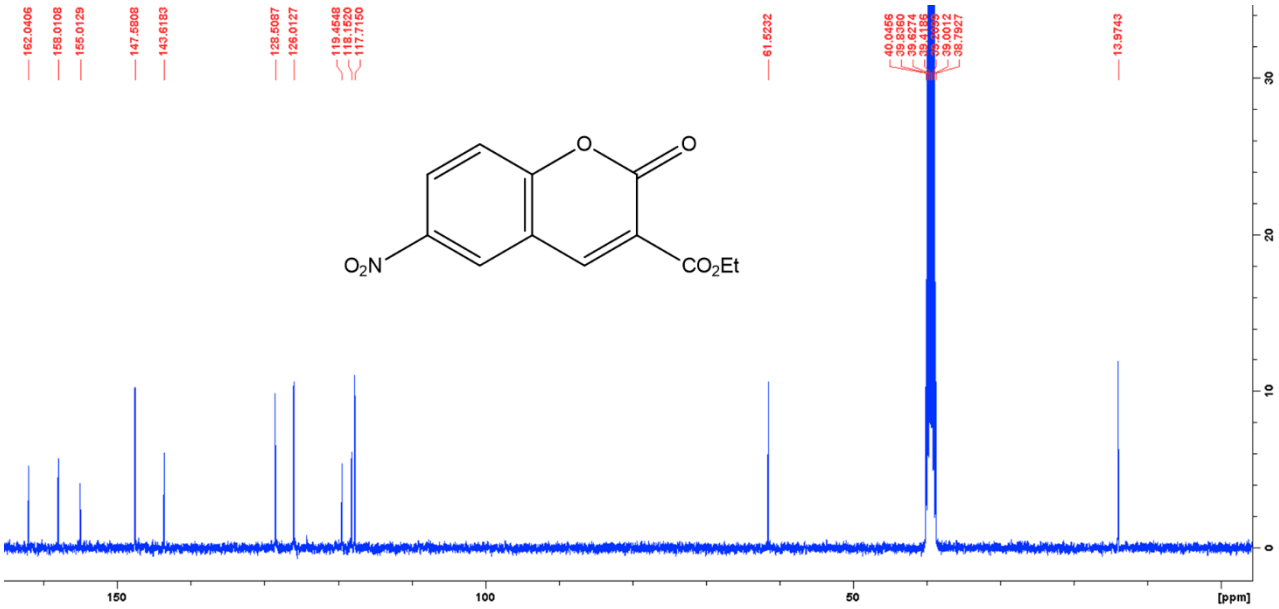

Figure 1: ^{13}C NMR spectra of 3-ester-6-nitro coumarin derivative **1a** in d_6-DMSO.

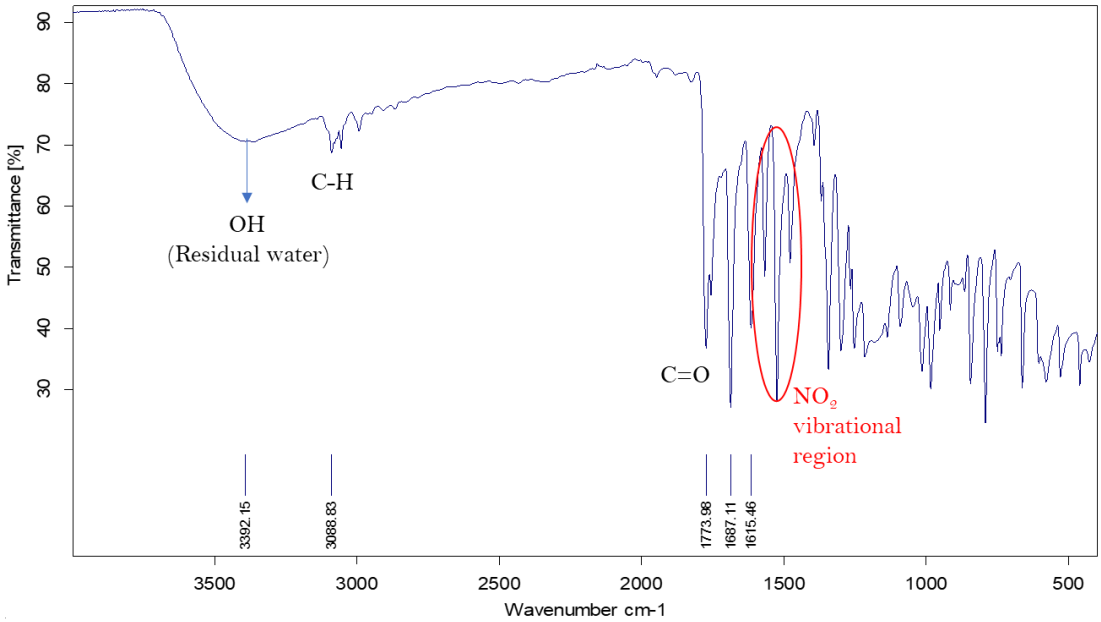

Figure 2: FT-IR spectra of coumarin derivative **1a**.

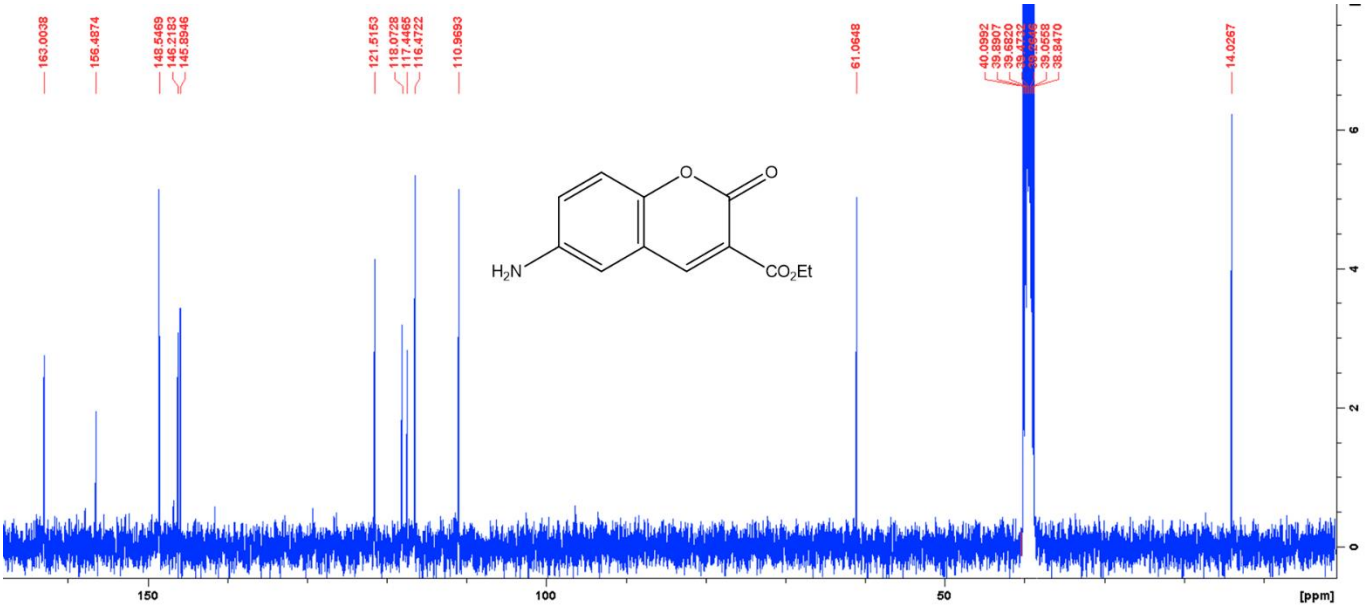

Figure 3: ^{13}C NMR spectra of 3-ester-6-amine coumarin derivative **1b** in d_6-DMSO.

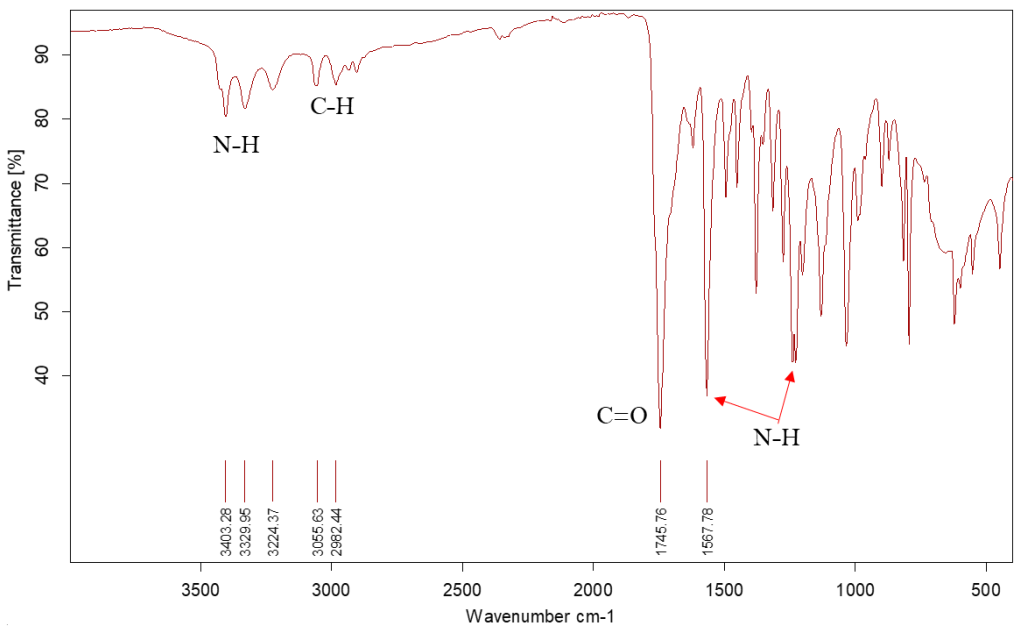

Figure 4: FT-IR spectra of derivative **1b**.

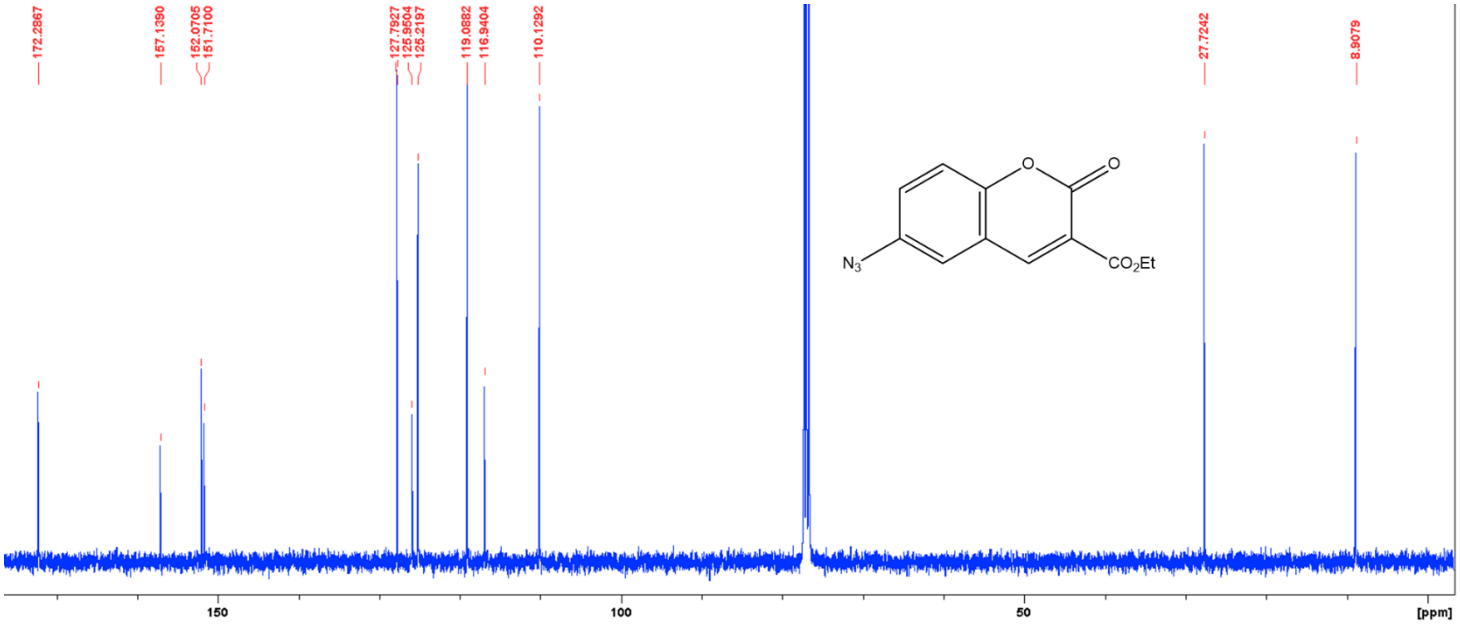

Figure 5: ^{13}C NMR spectra of 3-ester-6-azide coumarin derivative **1c** in d_6-DMSO.

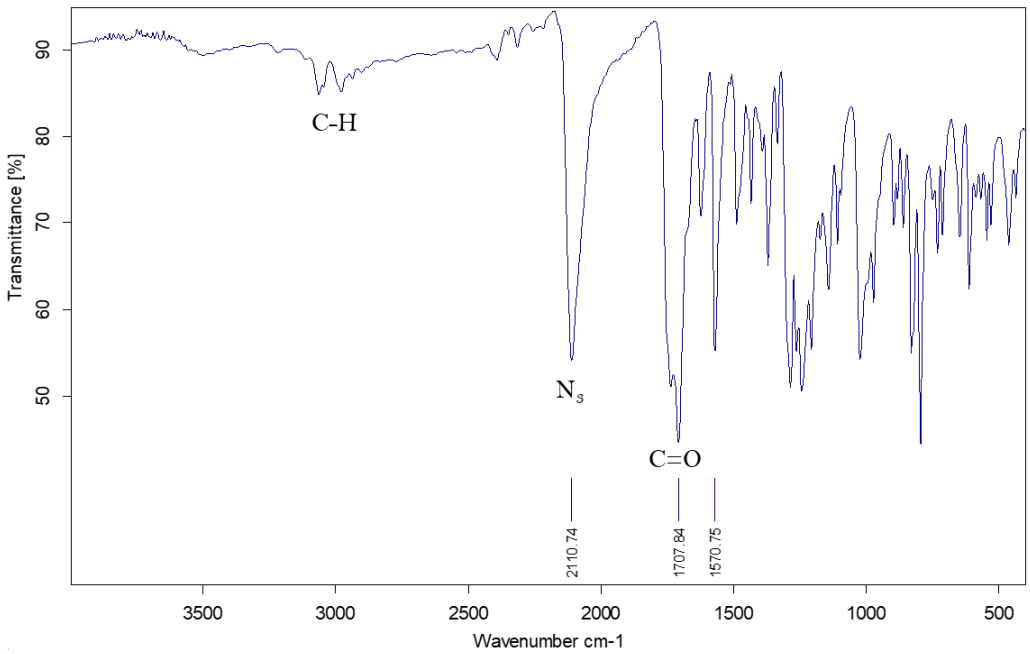

Figure 6: FT-IR spectra of coumarin derivative **1c**.

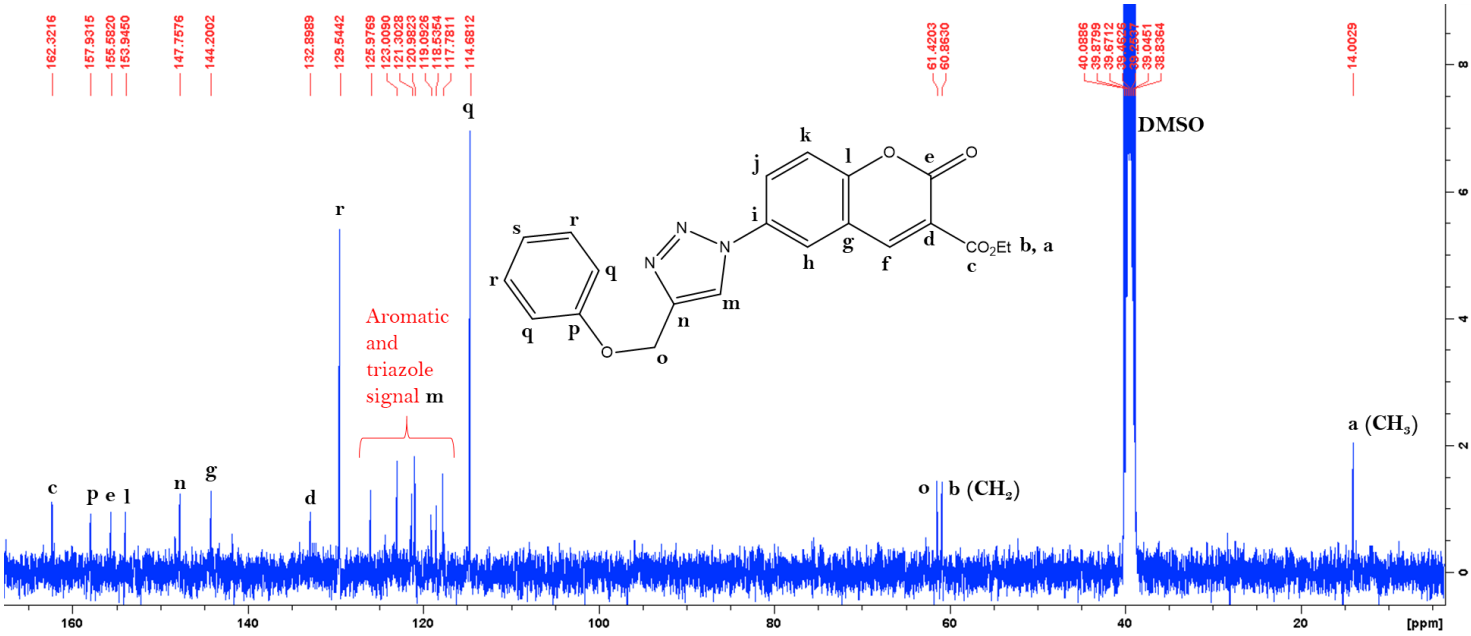

Figure 7: ^{13}C NMR spectra coumarin-triazole derivative **C1** in d_6-DMSO.

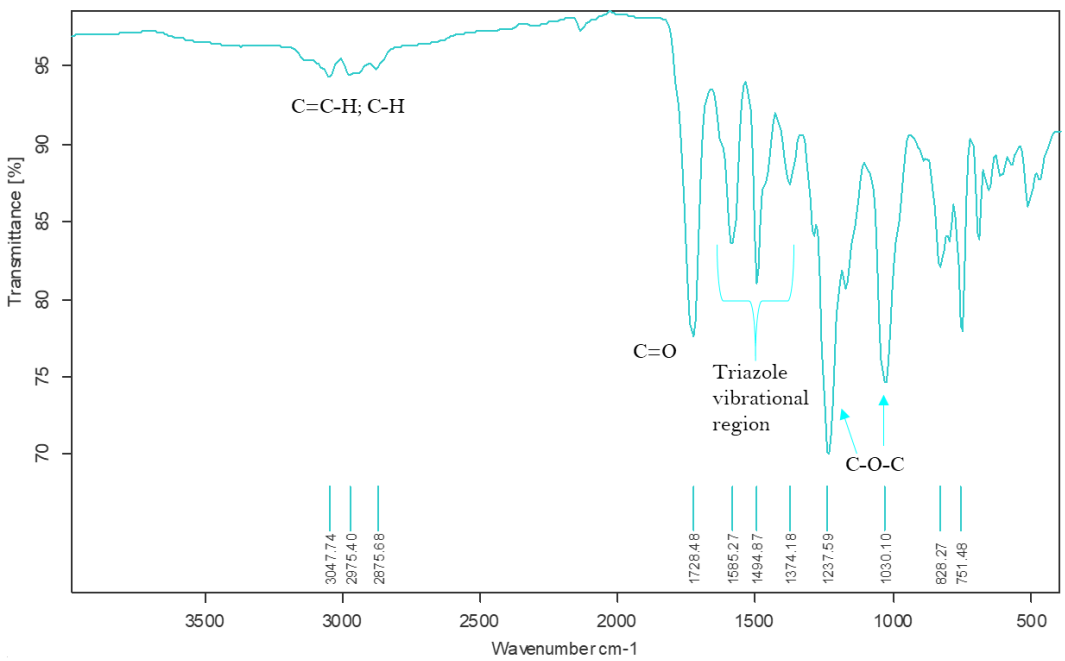

Figure 8: FT-IR spectra of **C1**.

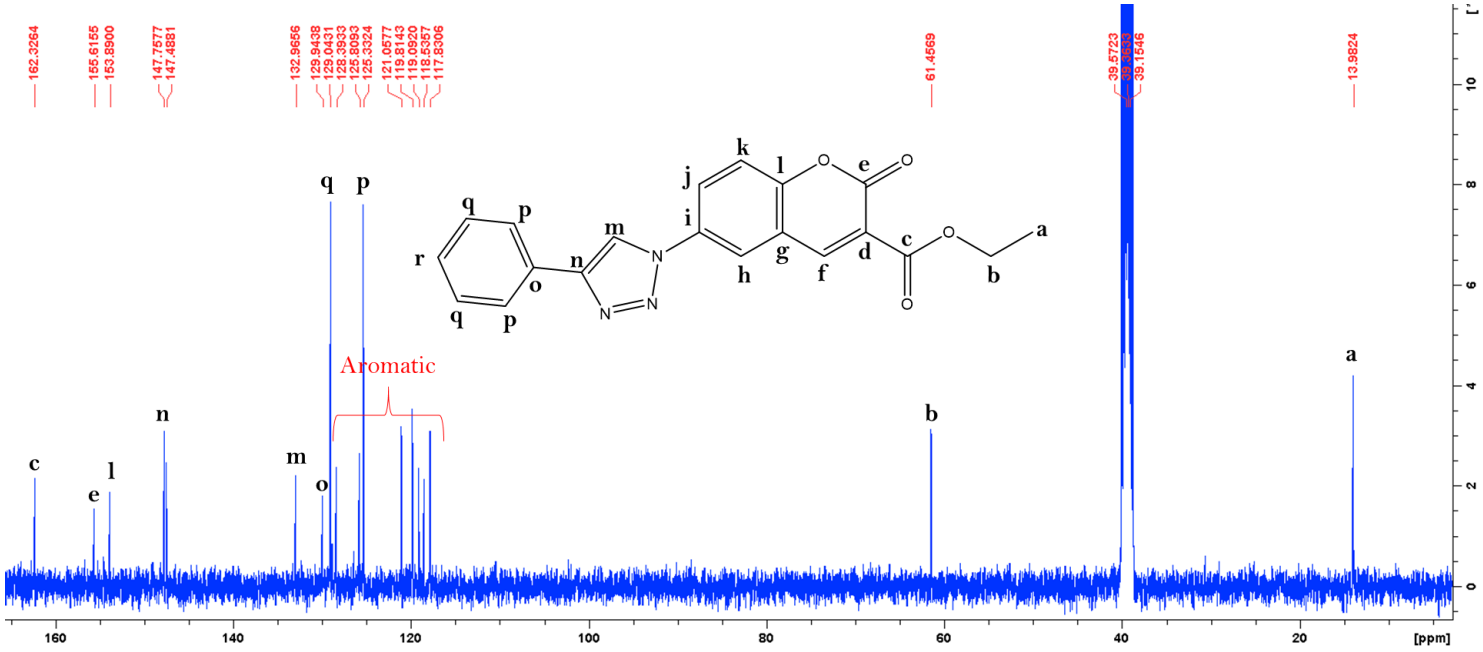

Figure 9: ^{13}C NMR spectra of coumarin-triazole derivative **C2** in d_6-DMSO.

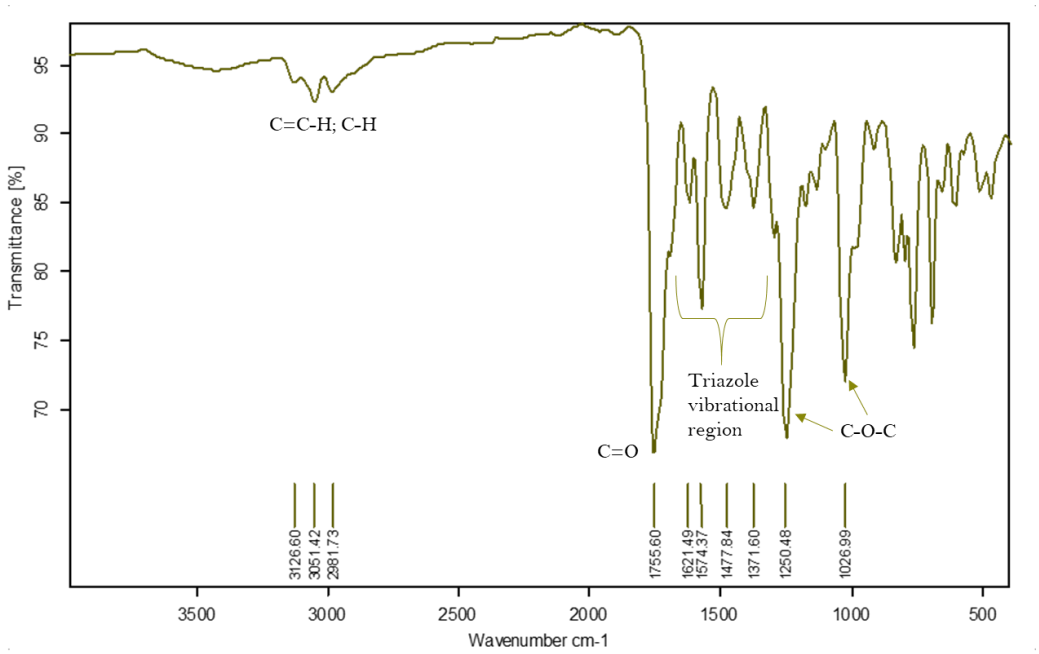

Figure 10: FT-IR spectra of **C2**.

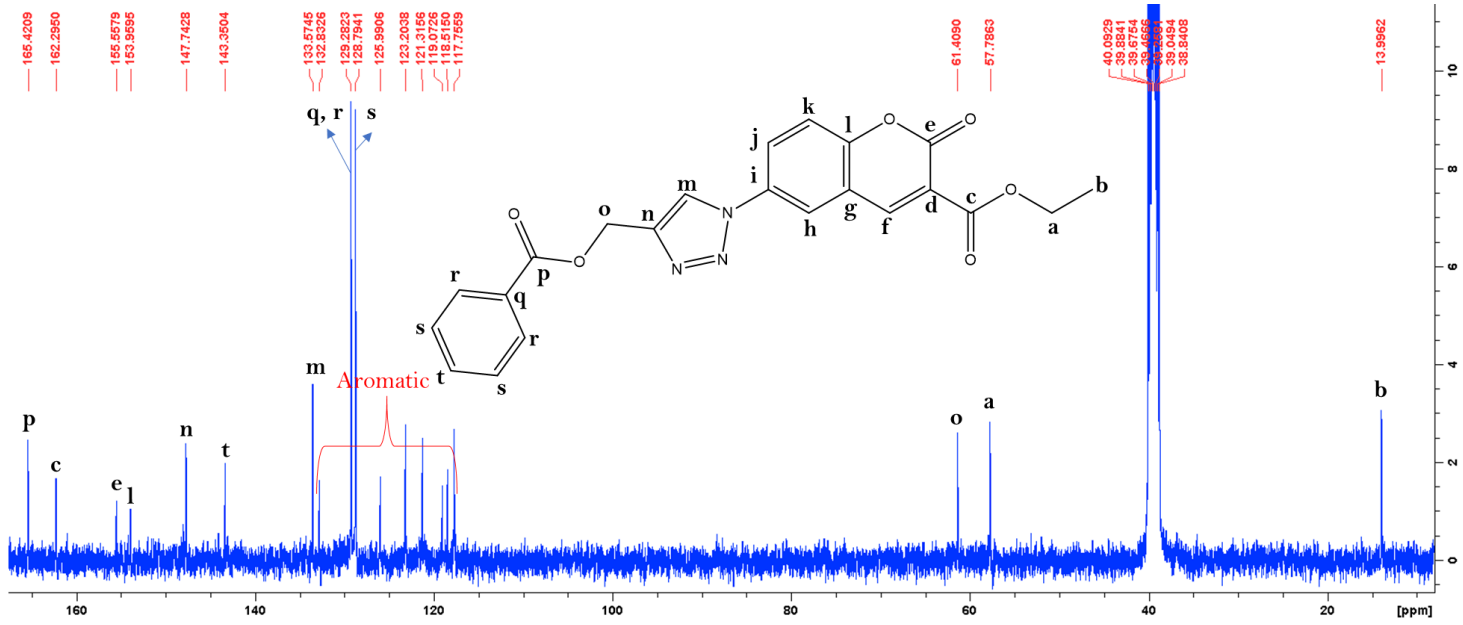

Figure 11: ^{13}C NMR spectra of coumarin-triazoe derivative **C3** in d_6-DMSO.

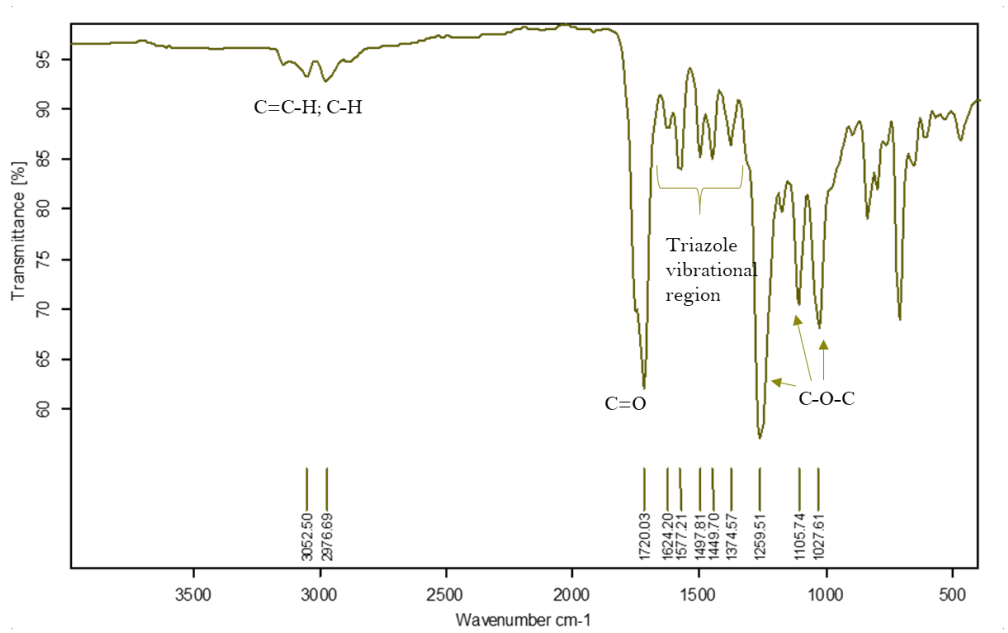

Figure 12: FT-IR spectra of **C3**.

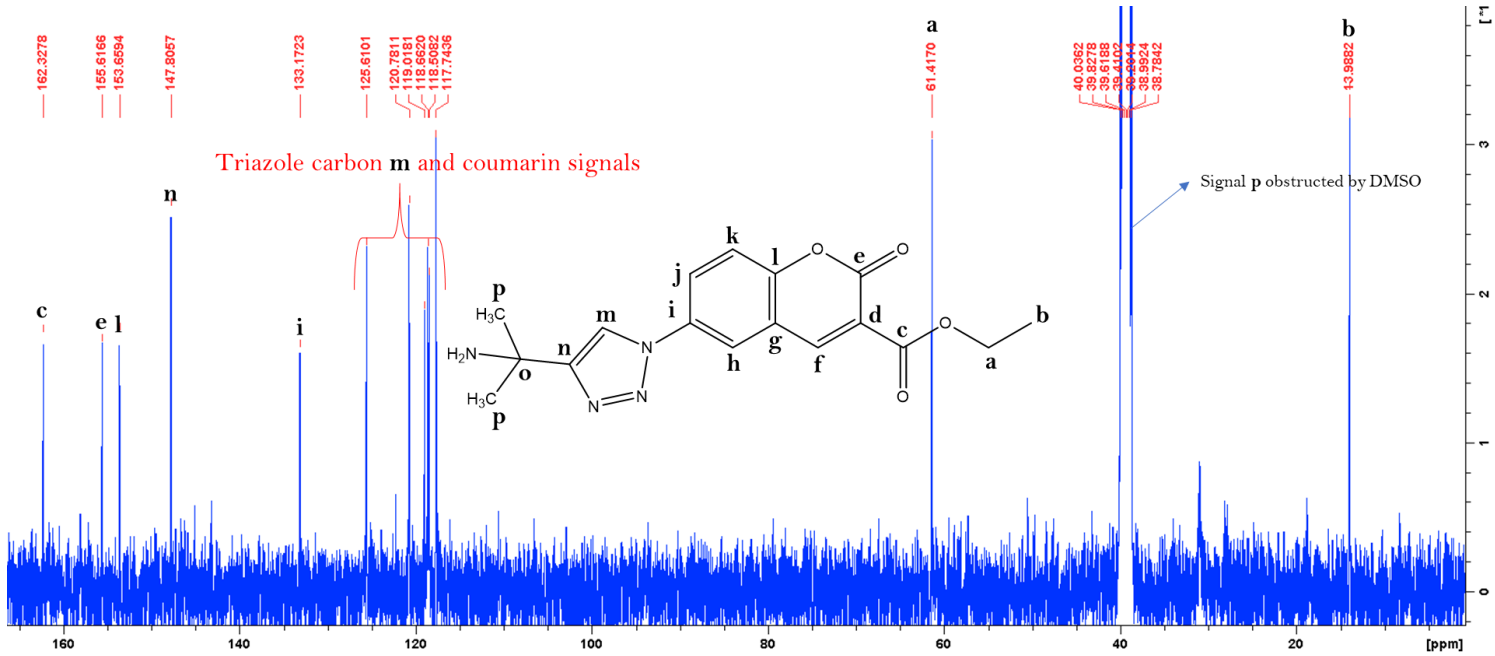

Figure 13: ^{13}C NMR spectra of coumarin-triazole derivative **C4**.

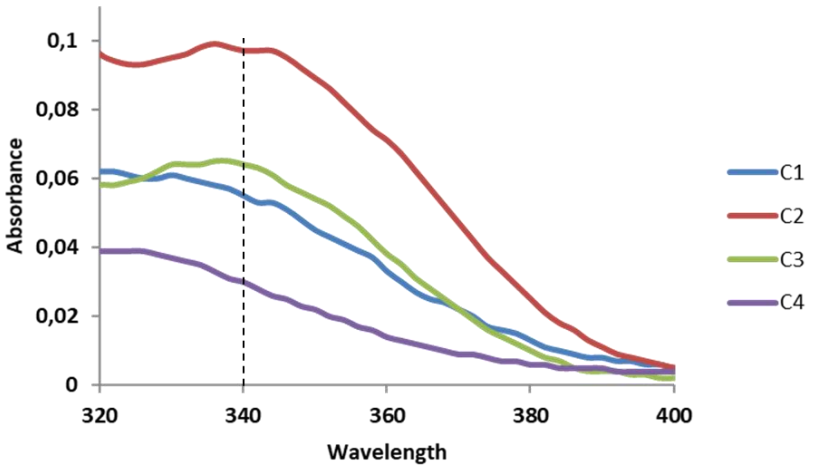

Figure 14: UV-Vis absorbance comparison of compounds **C1-4** in ethanol.

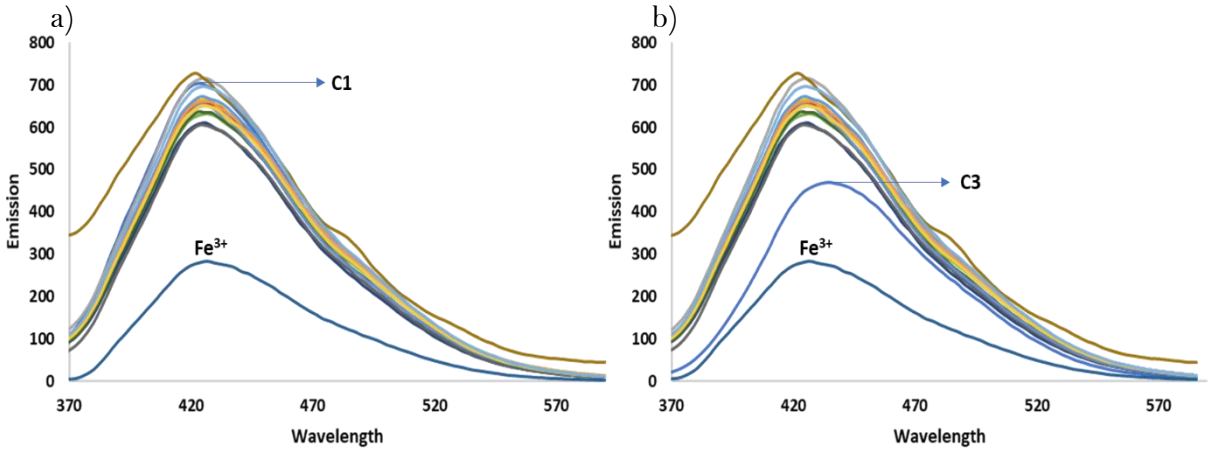

Figure 15: Metal cation screening studies of a) **C1** and b) **C3** in acetonitrile. Excitation of 340 nm.

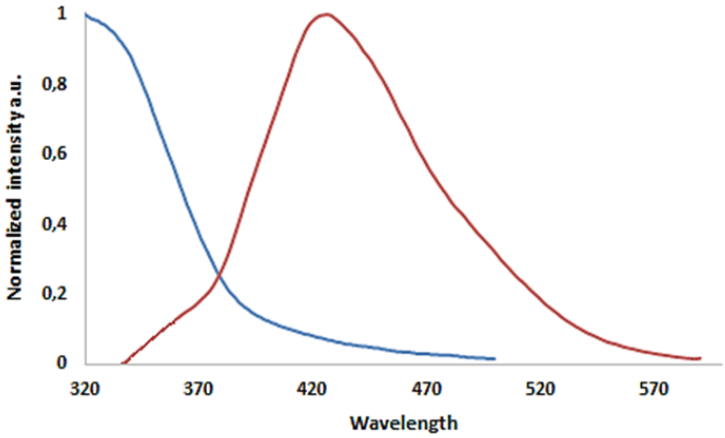

Figure 16: Normalized absorbance (blue) and emission (red) of sensor **C1** in the absence of Fe^{3+}.

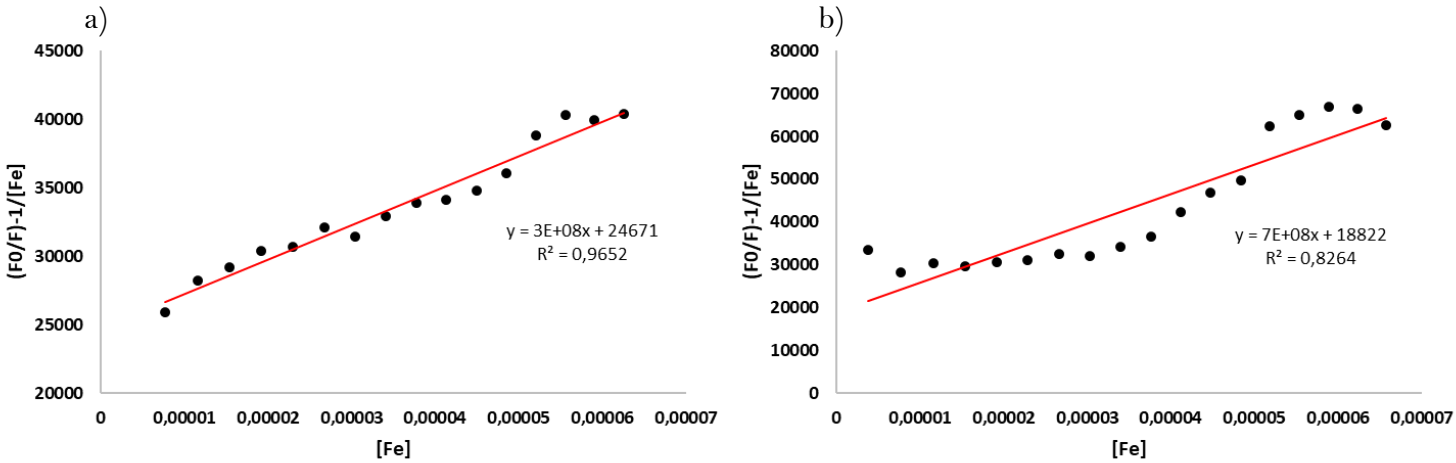

Figure 17: Titration data of **C1** with Fe^{3+} plotted using the equation for the combined dynamic and static quenching mechanism in a) ethanol and b) DMF.

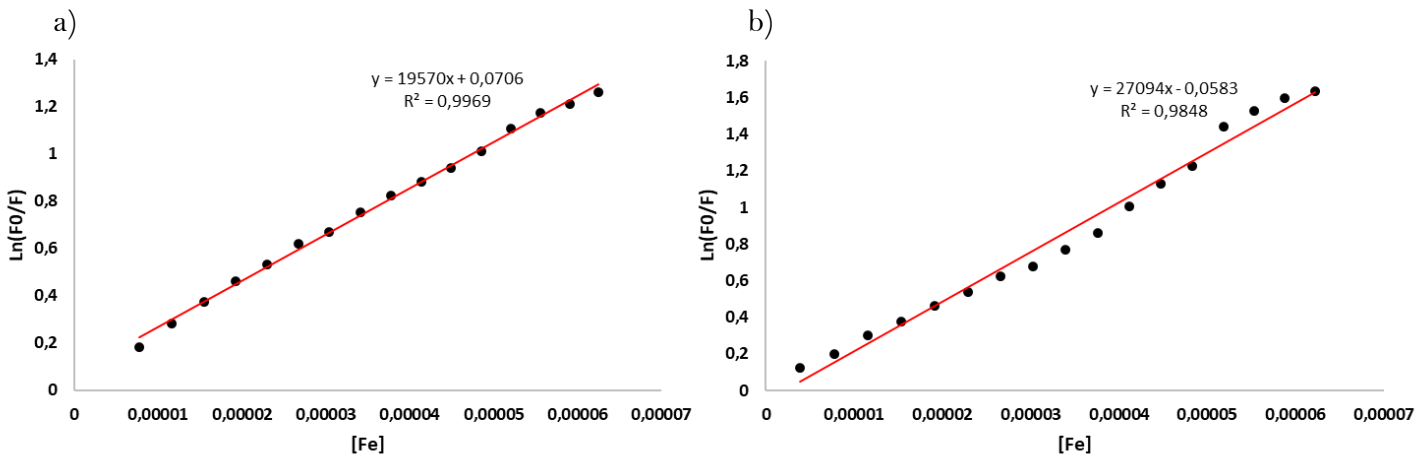

Figure 18: Titration of **C1** with Fe^{3+} fitted according to the Perrin static quenching equation in a) ethanol and b) DMF.

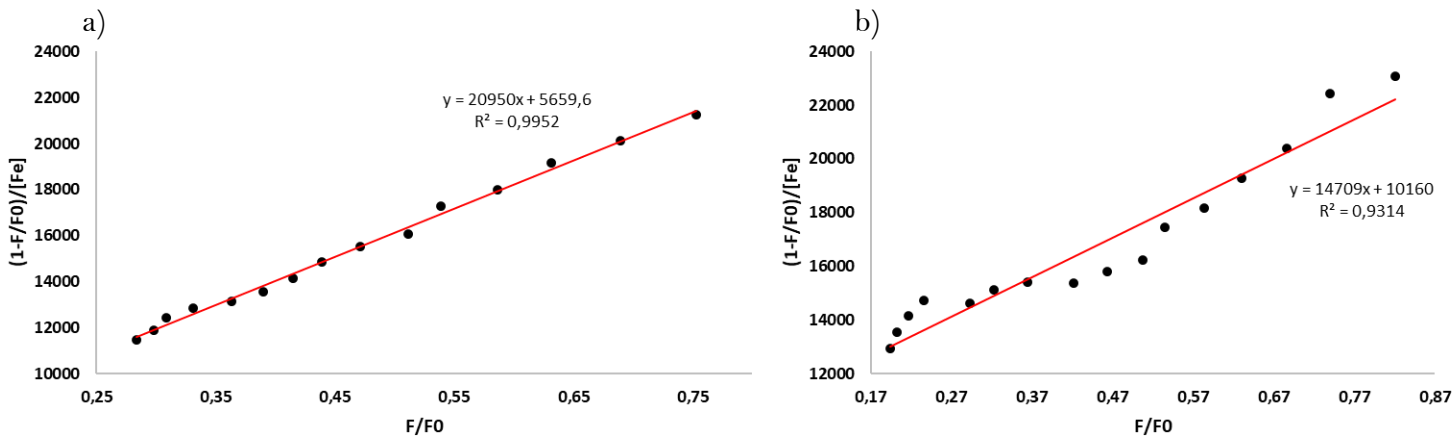

Figure 19: Titration of **C1** with Fe^{3+} fitted according to the Sphere of Action static quenching equation in a) ethanol and b) DMF.

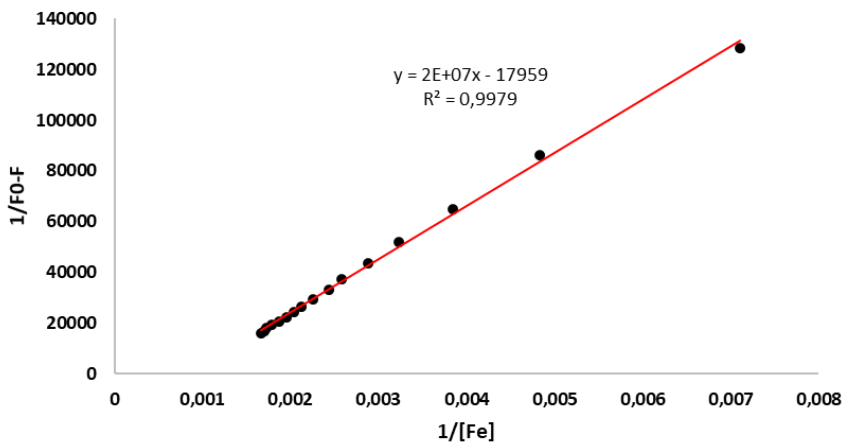

Figure 20: Benesi-Hildebrand plot of **C1** with Fe^{3+} in ethanol.

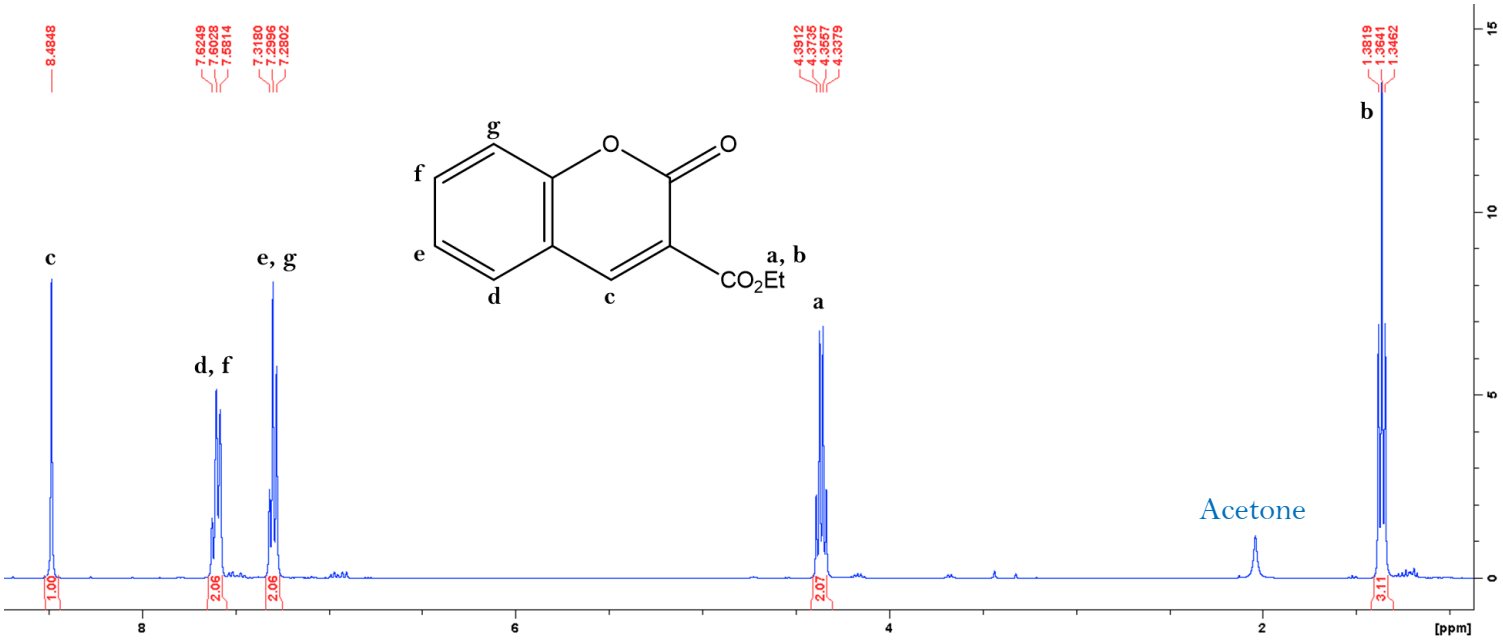

Figure 21: ^{1}H NMR spectra of 3-ester coumarin starting product **1** in $CDCl_3$.

Chapter 5

Table of Contents

List of Figures

List of Tables

List of Schemes

Chapter 5:
Application of coumarin-derived Schiff bases and azo-dyes towards ionic sensing strategies

Summary

Three novel coumarin derived Schiff bases and a single azo dye have been synthesized, characterized, and tested for their sensing abilities towards cations and anions. Sensors **D1-3** possessed the imine functionality, whilst sensor **D4** supported the azo-group. Sensors **D3** and **D4** displayed a strong preference towards Hg^{2+} in water and acetonitrile respectively, with sensor **D4** displaying a strong colorimetric response towards the metal by a rapid colour change from yellow to red. Competition studies displayed a high degree of selectivity of both sensors towards Hg^{2+} even in the presence of all competing cations. The detection limit (LOD) was determined to be 0.74 and 0.24 μM for **D3** and **D4** respectively, in their chosen solvents. The association constant (K_a) was determined by Benesi-Hildebrand analysis from the titration data. The association constants were determined to be 4.4 and 8.9 x 10^4 M^{-1} for **D3** and **D4** respectively. Both sensors displayed a stoichiometric binding ratio of 1:1 determined by Jobs plot analysis. Emission studies indicated the non-fluorescence of **D4** and the weak fluorescence of **D3** is due to C=N isomerization. The quantum yield (ϕ) was determined to be 0.012 for **D3**. The complexation site of each sensor with Hg^{2+} was elucidated via ^{1}H NMR, ^{13}C NMR, ^{15}N NMR, FT-IR, and Molecular Modelling studies. Complexation of **D3** with Hg^{2+} was shown to involve the lone electron pairs of both the imine-nitrogen and neighbouring phenol-oxygen in a stable pseudo-6-membered ring conformation; whilst complexation of **D4** towards Hg^{2+} involved the lone pairs of the coumarin- and neighbouring ester-carbonyl functionalities in a stable pseudo-6-membered ring conformation. Hydrogen potential studies (pH) of both sensors from pH of 2-14 indicated usability over a vast range of pH values. Reversibility studies with EDTA elucidated the partial reversibility of **D3** and the full reversibility of **D4** towards Hg^{2+}. This reversibility of **D4** permitted the construction of an IMPLICATION type logic gate and Molecular Keypad Lock as extended applications. Furthermore, **D4** was able to be implemented towards inexpensive on-site Hg^{2+} assay methods. Spike and recovery methods showed that both **D3** and **D4** were able to be used towards quantitative Hg^{2+} determination in environmental water samples. Molecular orbital

studies indicate the presence of and ICT, ESIPT, and ESICT mechanism upon Hg^{2+} complexation with **D3**; whilst **D4** exhibits strong ICT characteristics upon metal binding. Anionic screening studies showed the affinity of **D3** towards CN^- and **D4** towards PF_6^- in water and acetonitrile respectively. Competition studies indicated poor selectivity of both sensors towards their preferred analytes in their respective solvent systems. Binding site studies of **D3** with CN^- support a proton-transfer mechanism by nucleophilic attack of the CN^- nucleophile.

5.1 Results and Discussion

5.1.1 Synthesis and characterization of coumarin-derived imine and azo dye sensors D1-4

The synthesis of the four novel coumarin-derived imine and azo sensors **D1-4** is outlined in **Scheme 1**. The formation of derivatives **1**, **1a**, and **1b** has been shown previously in **Chapter 4**. The formation of diazonium derivative **1c** was synthesized according to well-known diazotization reactions of primary amines with a nitrating agent. The formation of the coumarin-azo derivative **D4** was achieved following general literature procedure.[1] The crude product (from TLC analysis) was purified further by column chromatography. The formation of coumarin-imine derivatives **D1-3** was achieved by refluxing the desired aldehydes with coumarin-amine derivative **1b** in ethanol. Imine-derivative **D1** precipitated directly from solution and was confirmed by ^{1}H NMR. This compound was able to be used without further purification. Derivatives **D2** and **D3** were filtered, monitored by TLC, and subsequently purified by column chromatography. General procedures for the formation of an imine group from an aldehyde are well documented in the literature.[2]

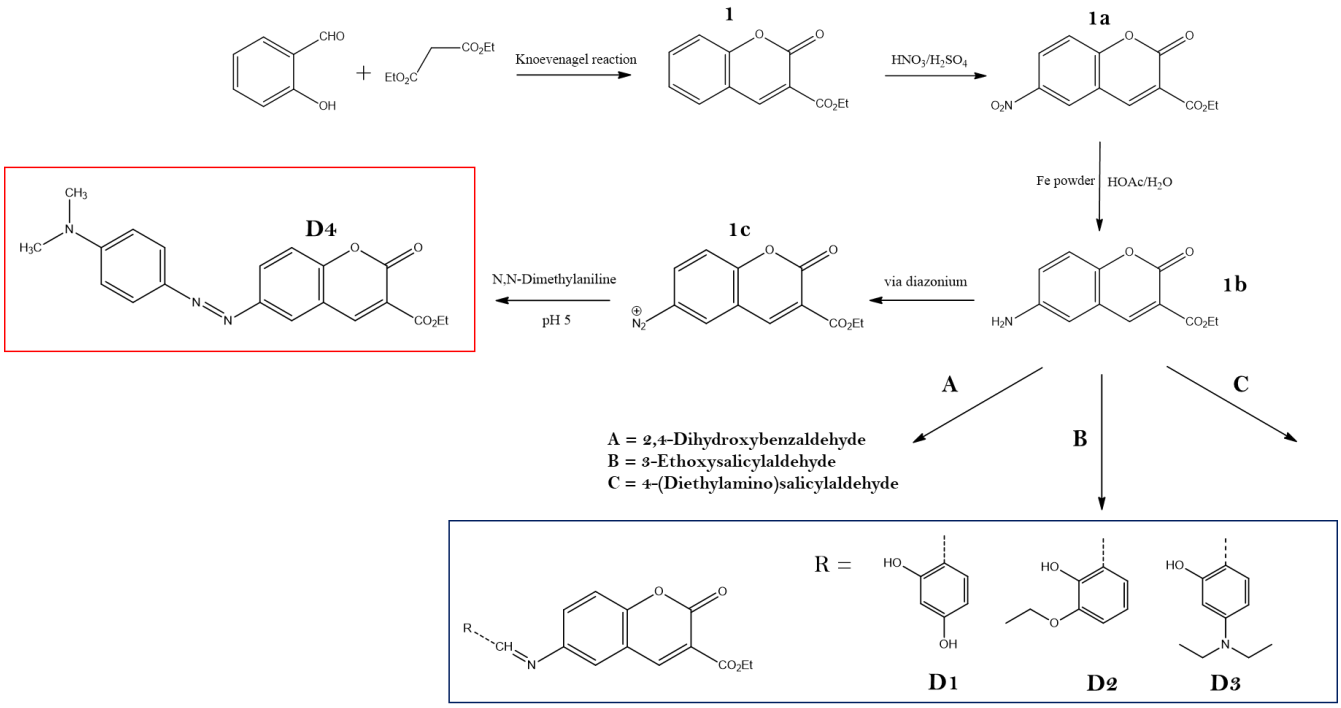

Scheme 1: Synthesis of coumarin-imine (**D1-3**) and coumarin-azo (**D1**) derivatives.

The ^{1}H NMR, ^{13}C NMR, and FT-IR spectra of coumarin-derivatives **1a** & **1b**, and XRD structure of coumarin-ester derivative **1**, were previously reported in **Chapter 4**. Diazotization derivative **1c** was formed in situ, and the success of the diazonium step was confirmed by the formation of desired coumarin-azo derivative **D4**. The ^{1}H NMR spectra of coumarin-imine & -azo derivatives **D1-4** are shown in **Figures 1-4** (for the ^{13}C NMR of derivatives **D1-4**, see **Appendix D Figures 1-4**).

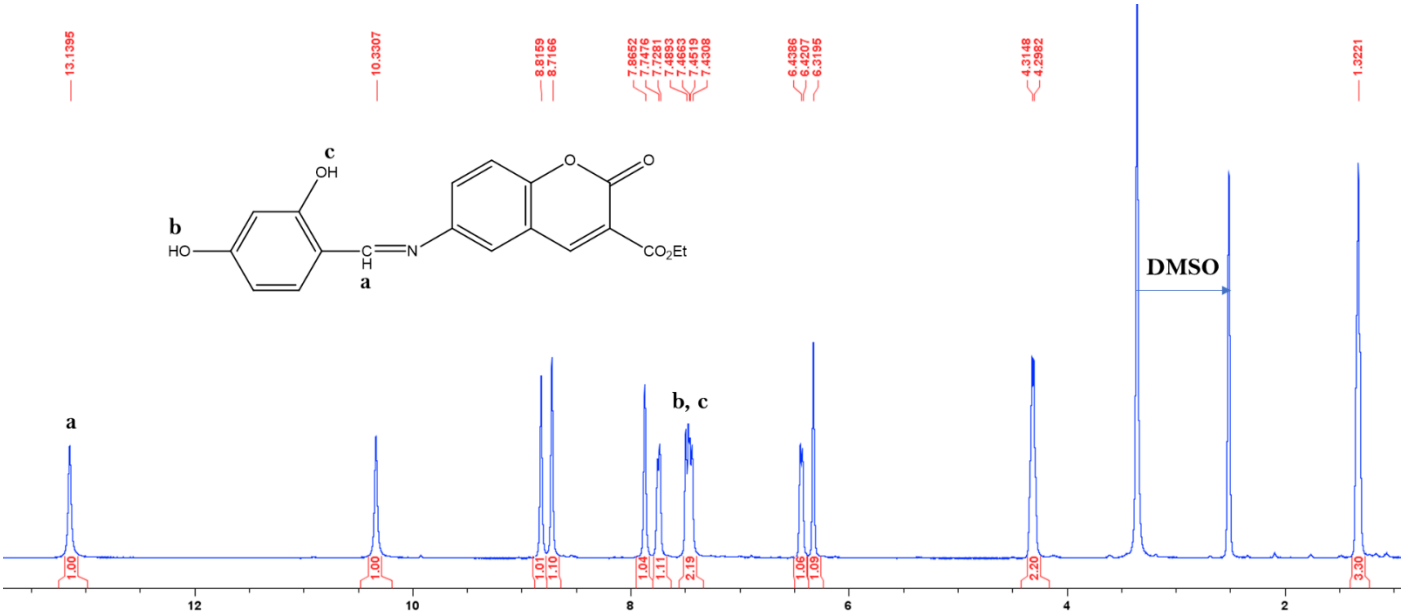

Figure 1: ^{1}H NMR of coumarin-imine derivative **D1** in d_6-DMSO.

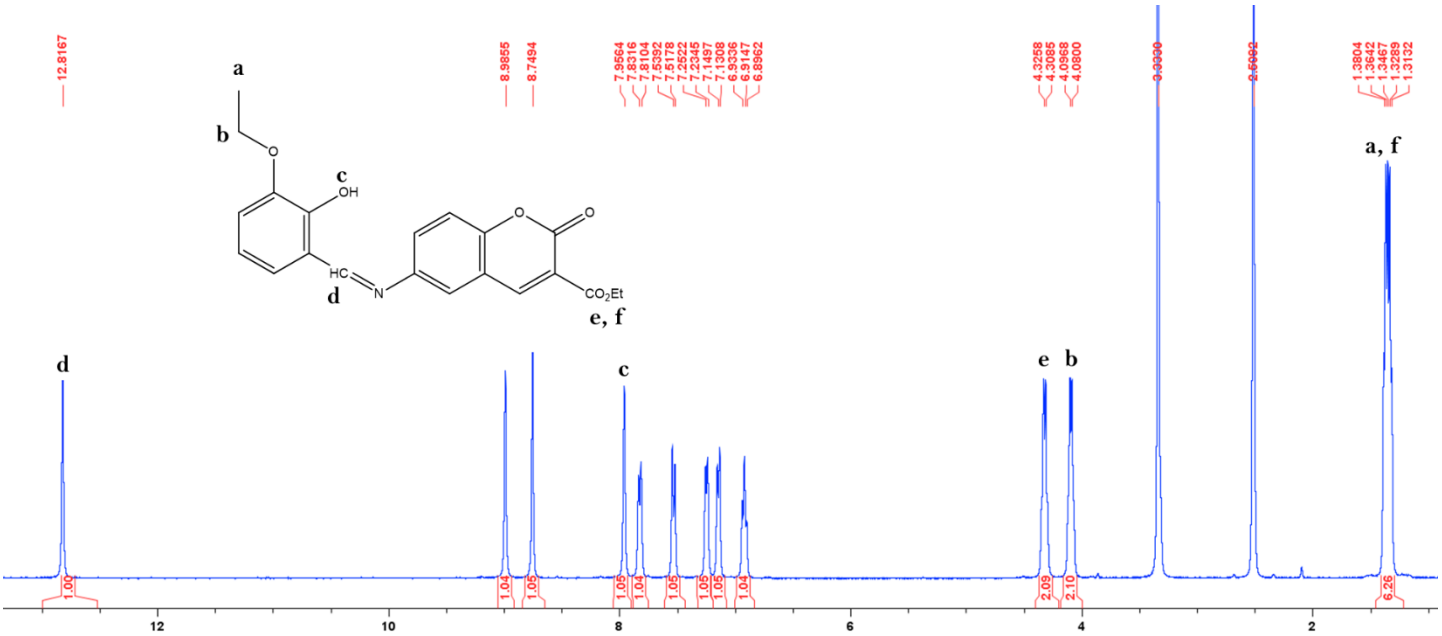

Figure 2: ^{1}H NMR of coumarin-imine derivative **D2** in d_6-DMSO.

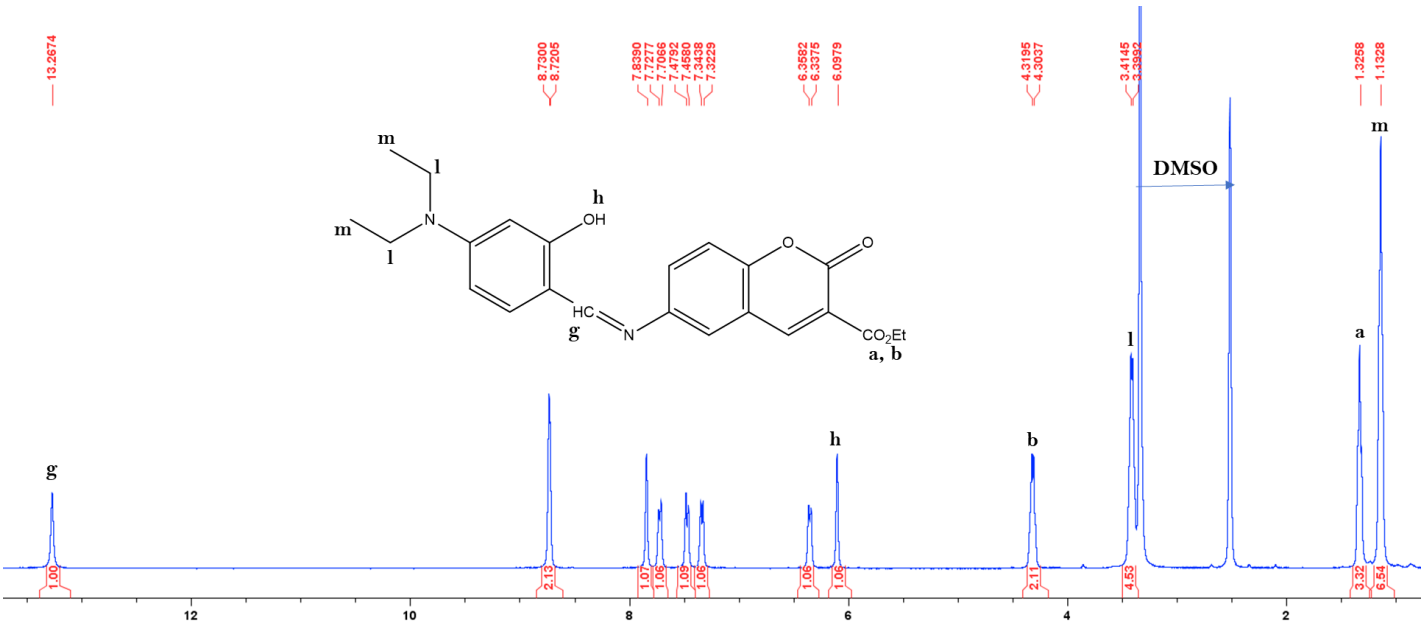

Figure 3: ^{1}H NMR of coumarin-imine derivative **D3** in d_6-DMSO.

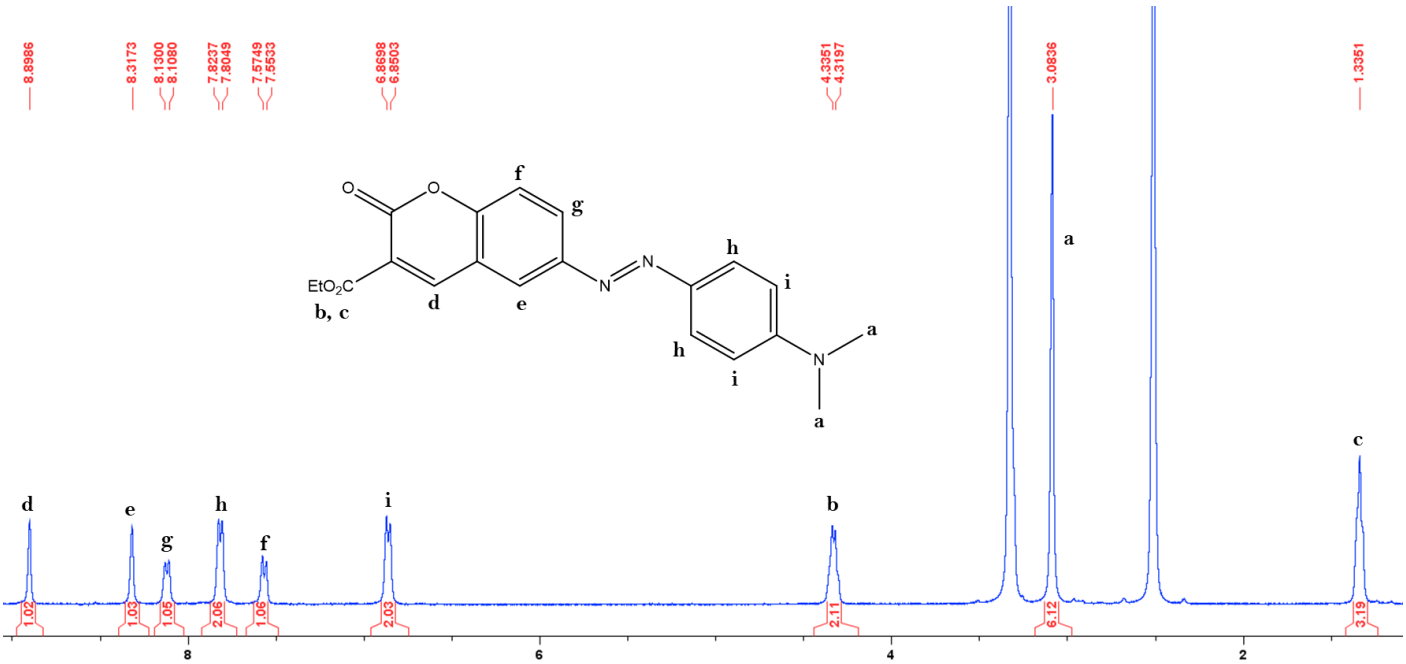

Figure 4: ^{1}H NMR of coumarin-azo derivative **D4** in d_6-DMSO.

The single-crystal XRD confirmed the desired formation of imine and azo sensor **D2-4**. Sensor **D1** did not form any crystals for analysis, however, the desired structure was confirmed by ^{1}H NMR, ^{13}C NMR and FT-IR spectral analysis. Notably, coumarin-azo derivative **D4** is capable of crystallizing in more than one type of space-group, suggesting its polymorphism or ability to crystallize into different crystalline forms. Both crystals were found to crystallize in a monoclinic crystal system, differing only by their space-groups. The single-crystal XRD structures of **D2-4** are shown in **Figure 5**.

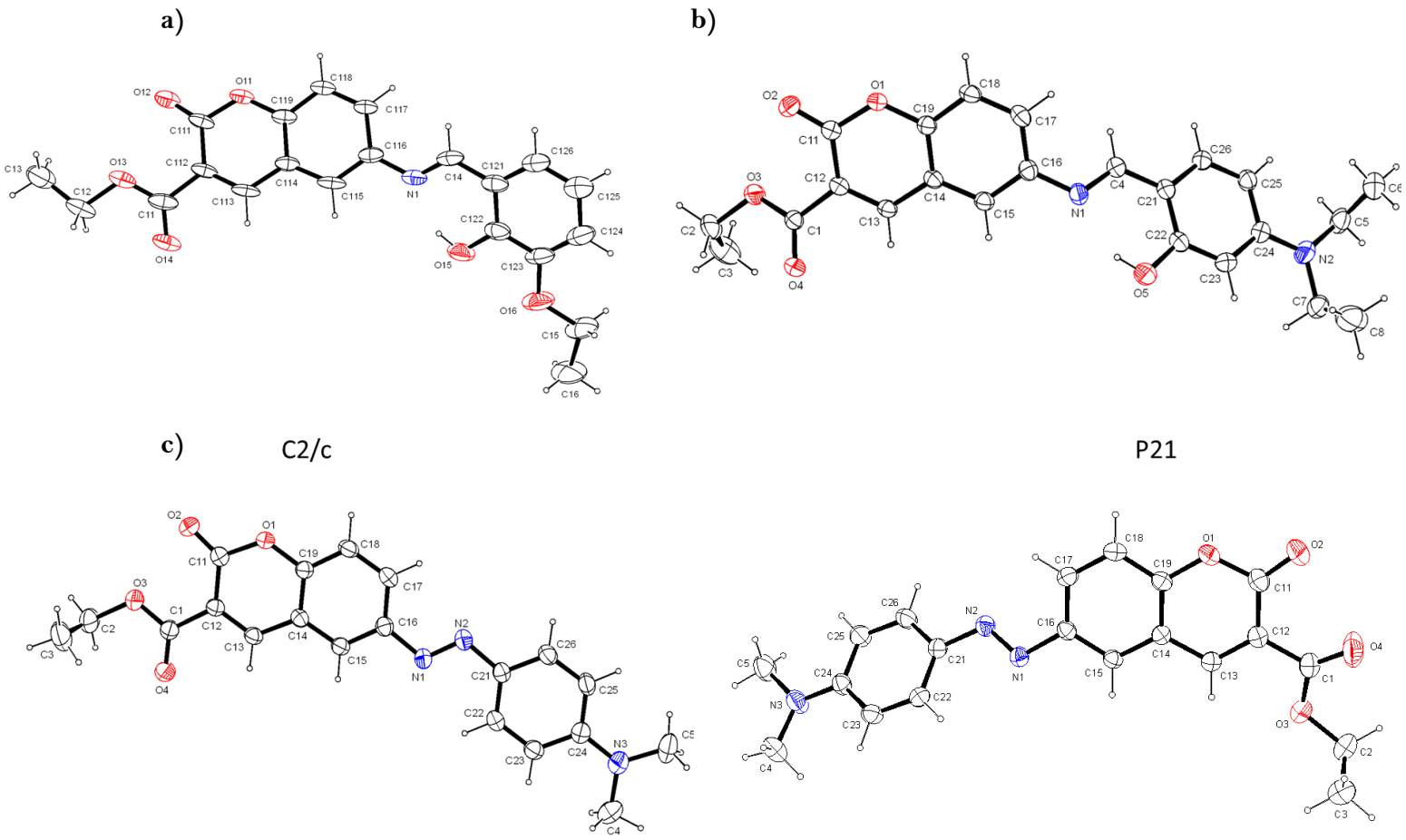

Figure 5: Single-crystal XRD results of coumarin-imine and -azo sensors (a) **D2**, (b) **D3**, and (c) **D4** with two different crystalline forms and corresponding space-groups.

The FT-IR spectra of sensors **D1-4** highlighted some interesting tautomeric and isomeric characteristics, in addition to substantiating the formation of the desired products. The FT-IR spectra of sensors **D1-4** are shown in **Figure 6**.

a)

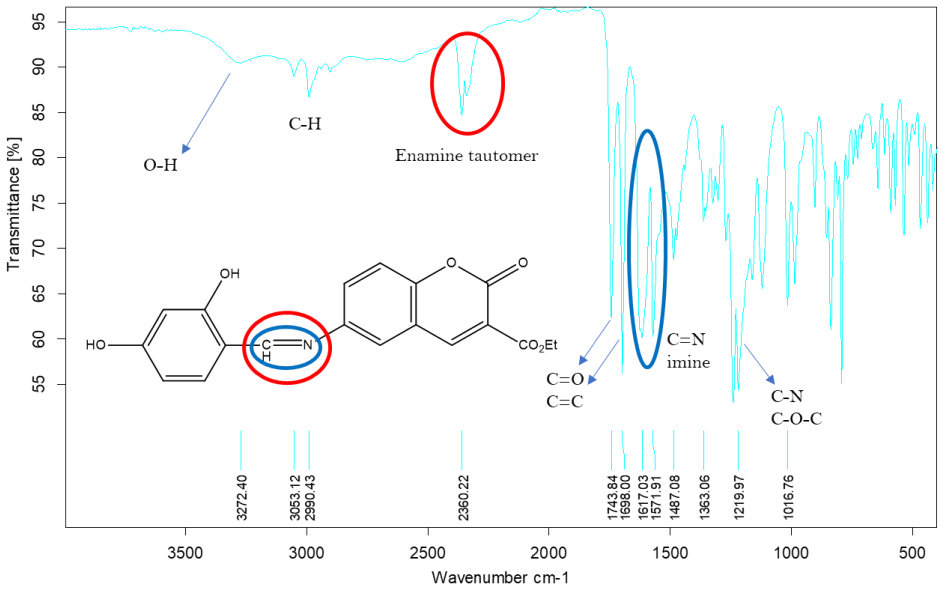

b)

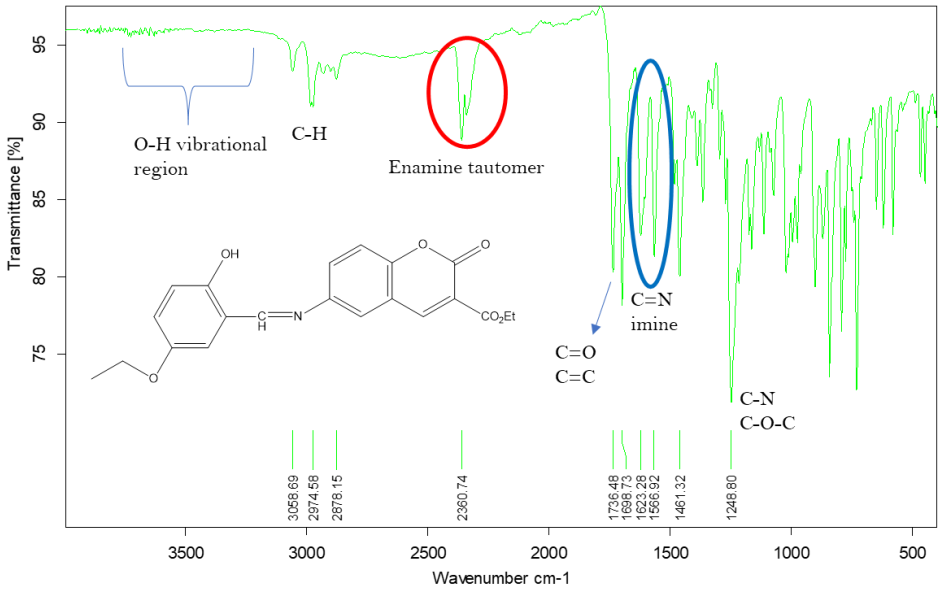

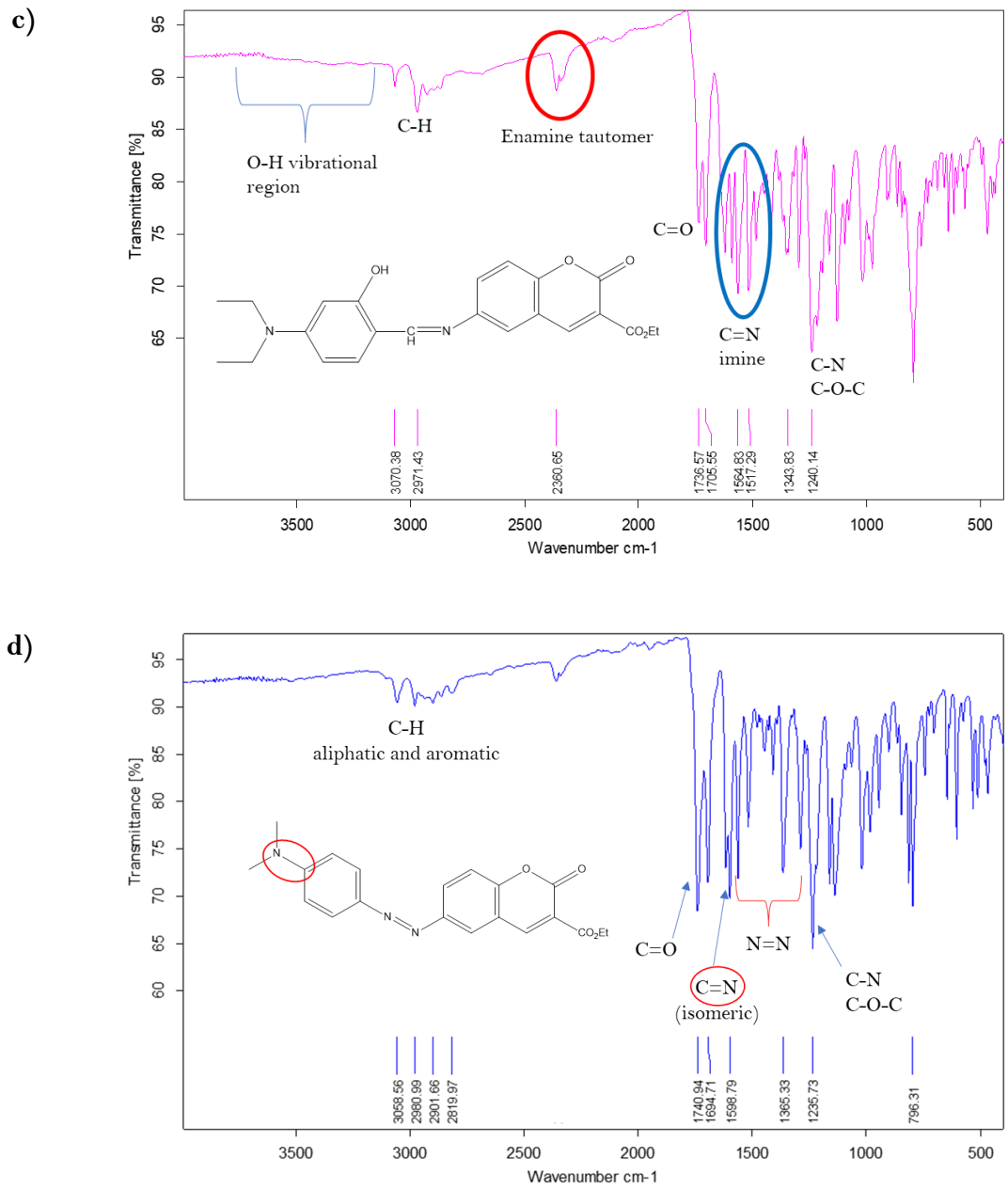

Figure 6: FT-IR spectra of coumarin-imine and coumarin-azo derivatives **D1-4** (a-d).

In the FT-IR spectra for compounds **D1-3**, a sharp peak at 2360 cm^{-1} is possibly indicative of an enamine tautomer present in equilibrium with the imine. This group could arise from intramolecular proton transfer, resulting in enol-imine and keto-enamine tautomerism, leading to two distinct tautomers present in solid form (**Figure 7**). From the ^{1}H NMR and ^{13}C NMR spectra of **D1-3**, only one form of the tautomer is stable in solution (d_6-DMSO). Additionally, the stability of the original enol-imine tautomer lends it towards being able to crystallize from solution upon solvent evaporation, which is why it was not present in the XRD crystal structures. The existence of OH---N and NH---O type hydrogen bond tautomers between enol-imine and keto-enamine forms serve as very important ligands.[3]

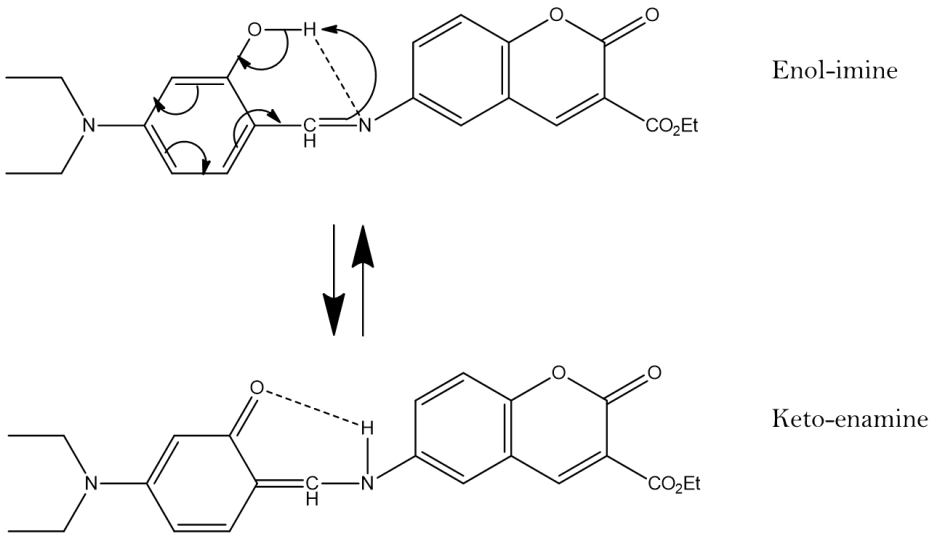

Figure 7: Possible tautomerism through proton transfer in coumarin-imine derivative **D3**.

The tautomerism present in imine derivatives **D1-3** leads to the formation of pseudo-6-membered ring conformations in both equilibrium structures through hydrogen bonding. Additionally, the most energetically stable conformer of **D3**, calculated by Molecular Modelling studies at PM3 calculation level, indicated this hydrogen bonding between the imine nitrogen and neighbouring hydroxy proton. This further substantiates why the enol-imine tautomer has greater stability and is the main compound present in both the NMR and XRD studies (**Figure 8**).

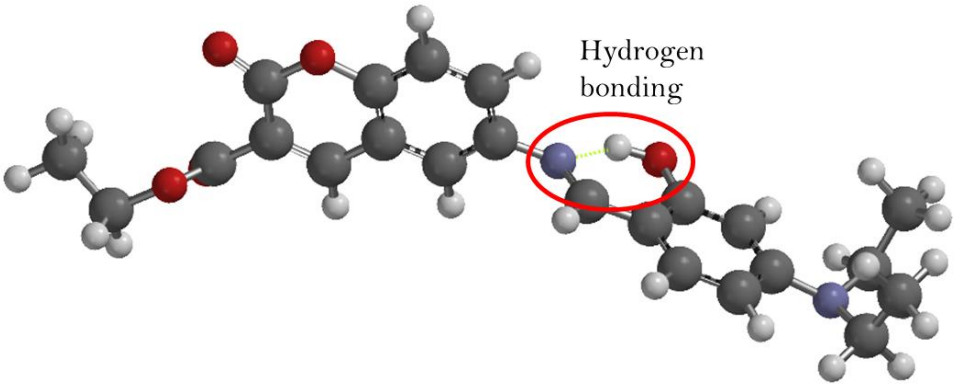

Figure 8: Most energetically stable conformer of **D3** calculated at PM3 molecular level.

In coumarin-imine derivatives **D1-3**, the imine C=N bond is observed between 1650-1500 cm^{-1}.[4–6] Notably, a strong absorbance band between 3500-3000 cm^{-1} characteristic of hydroxy functionality, is weakly visible if not entirely absent for all three coumarin-imine derivatives. From the XRD and ^1H NMR analysis, the presence of the OH group is undeniable. Therefore, it is possible that the hydrogen bonding between the imine-nitrogen and hydroxy-proton of the enol-imine tautomer prevents/reduces bond vibrations of the OH functionality. Tautomerism between the enol and keto tautomers may also serve to reduce the proportion of freely vibrating enol forms present in the solid state. In **D1** the para-hydroxy that is not involved in tautomerism is still partially visible, whilst the single tautomeric OH group in both **D2** and **D3** is entirely absent. For coumarin-azo derivative **D4**, the characteristic azo N=N functionality may be observed between 1600-1300 cm^{-1}.[7–9]

5.1.2 Absorbance and emission studies of coumarin-imine and -azo derivatives D1-4

The UV-Vis absorbance characteristics of derivatives **D1-4** were investigated in acetonitrile, water, methanol, THF, and DMF. Stock solutions of the sensors were prepared in methanol to a final concentration of 0.001 M. The UV-Vis comparison of **D1-4** in different solvent systems are shown in **Figure 9**.

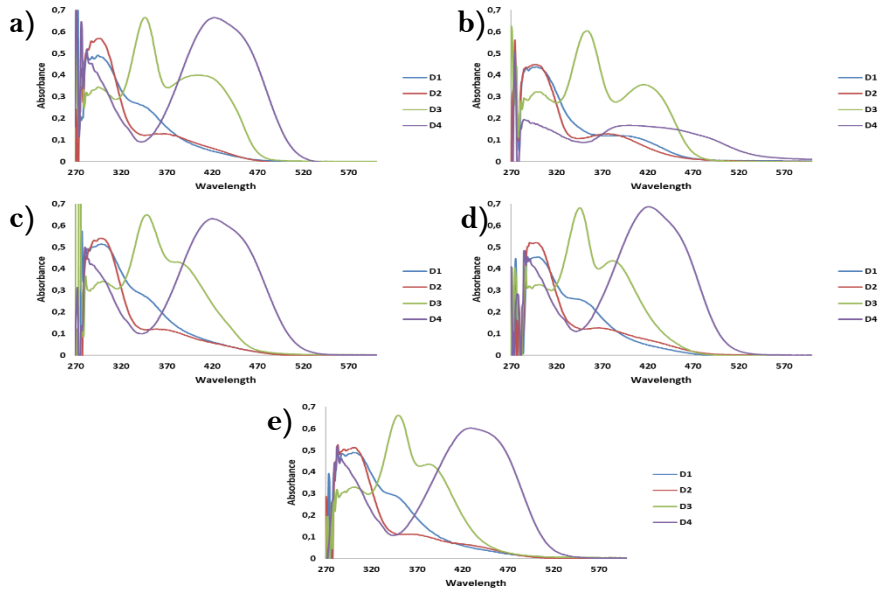

Figure 9: UV-Vis absorbance characteristics of coumarin-imine and azo derivatives D1-4 in a) acetonitrile, b) H_2O, c) methanol, d) THF, and e) DMF.

The excitation wavelengths remain consistent for **D1-4** with minor shifts in peak maxima in different solvents. Derivatives **D1** and **D2** show an excitation maximum of 300 nm in the selected solvent systems, with minor secondary/shoulder peaks visible at longer wavelengths. Derivative **D3** exhibits strong absorbance characteristics in all five solvent systems with the first band situated at 300 nm, the second between 345 and 355 nm and the third band/shoulder peak situated between 390 and 420 nm depending on the solvent. The first absorbance band is proposed to be due to the π-π* electronic transitions of the conjugated coumarin-imine species, whilst the second band is proposed to arise from the electronic transitions in the -N=CH- group, and the conjugation occurring between the coumarin rings and the imine group.[10,11] The weaker and broader third absorption band could possibly arises due to the intra-molecular hydrogen bond between the N atom in the imine group and the ortho-hydroxyl group on the adjacent phenyl ring, as the result of the optical excitation of the molecule. In this case, this band is defined as n-π* transition as it is involved in delocalization with lone-pair electrons.[12] Coumarin-azo derivative **D4** shows an excitation wavelength maxima between 420 and 430 nm depending on the solvent. This characteristic absorbance band in this wavelength region is indicative of π-π* and/or n-π* electronic transitions.[13] Azo-derivative **D4** displays good absorbance intensity in all organic solvents apart from water, where the absorbance intensity is comparatively diminished.

Clearly, the solvent system influences the absorbance characteristics (intensity and/or wavelength) of the coumarin-imine and coumarin-azo derivatives **D3** and **D4**. Solvent characteristics play a pertinent role in both the chemical and physical processes by regulating the photochemical/photophysical behaviour of molecules.[14,15] Specifically, the polarity of the solvent is the key factor that controls the thermodynamic and kinetic aspects of a chemical reaction.[16] The positions of the absorption/emission bands of the molecules may shift and/or the intensities of these bands may be reduced due to the interaction of molecules with solvents with differing polarities. This phenomena is popularly known as solvatochromism.[17] Generally, molecules whose excited and ground states differ greatly depending on the change of solvent polarity will experience this phenomena. Solvation differences may be attributed to the nature of chromophoric and auxochromic groups in the molecule. This interaction with the solvent can occur either through non-specific forces like electrostatic and polarization forces or specific interactions like hydrogen bonding and acceptor-donor interactions via electron pairs.[18] The preferential solvent model; the dipole moment ratio between the ground state and excited state; the enhancement of the basicity of the probe through the introduction of the substituent; and the stabilization of the ground or excited state are the primary reasons

for the solvatochromic phenomena.[19–21] Factors including the nature and position of the substitution; the temperature of the surrounding medium; and the nature of the solvent can induce/enhance/prevent solvatochromism, resulting in either the positive or negative response (increase or decrease in wavelength and intensity).[22]

Emission comparisons of **D3** and **D4** in acetonitrile, methanol, and water are shown in **Figure 10**. The various excitation wavelengths from the UV-Vis analysis of **D3** and **D4** in these respective solvents were used for emission studies.

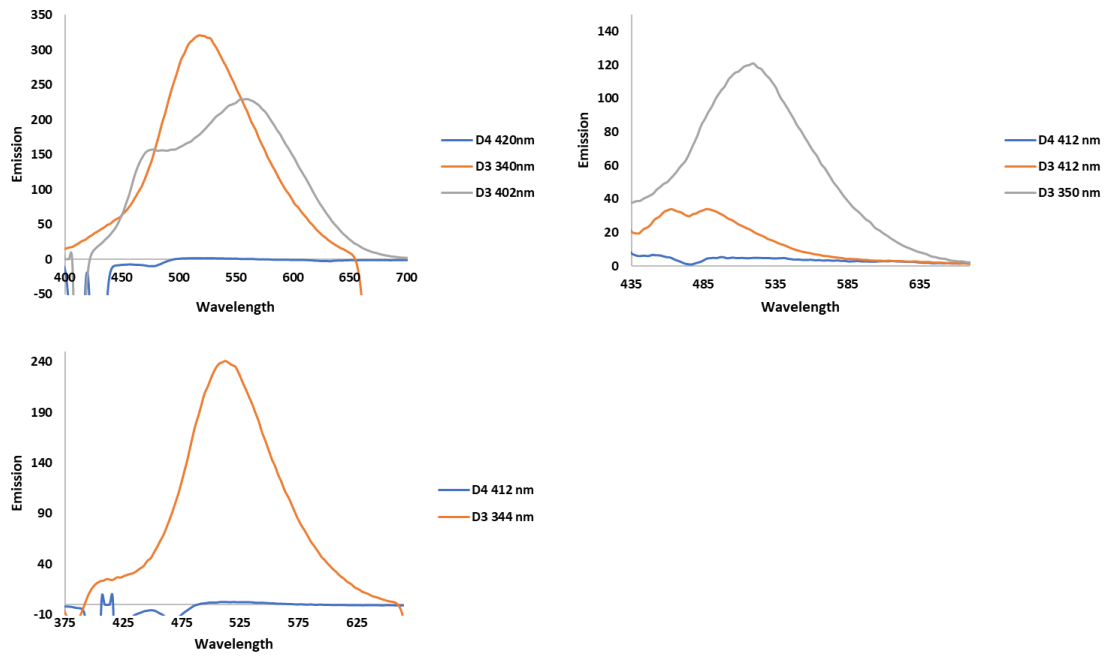

Figure 10: Emission studies of derivatives **D3** and **D4** at different excitation wavelengths in a) acetonitrile, b) water, and c) methanol.

In all three emission studies, coumarin-azo derivative **D4** exhibits weak to no fluorescence at the respective excitation wavelengths. It has been reported that compounds bearing the azo functionality exhibit low fluorescent properties.[23,24] For example, azobenzenes readily undergo photoisomerization in the photoexcited state, which is a reason for their non fluorescence. Photoisomerization accompanies the change in the direction of the lone pair of one nitrogen atom.[25,26] Coumarin-imine derivative **D3** shows weak fluorescence in all three solvent systems. This weak emission is plausibly due to C=N isomerization. This diminished emission intensity is as a result of a non-radiative emission pathway due to isomerization in

the excited state.[27–30] The fluorescent quantum yield (ϕ) of **D3** with anthracene as standard was determined to be 0.012 (see **Chapter 2 Equation 2**).

The effect of solvatochromism on derivative **D3** was further supported by a comparison of the solvent effects on the emission intensity of **D3** at 340 nm. As mentioned previously, the solvent polarity plays a key role in the kinetic and thermodynamic aspects of a chemical reaction. Notably, the emission intensity of **D3** decreases with increasing solvent polarity from acetonitrile<methanol<water (**Figure 11**).

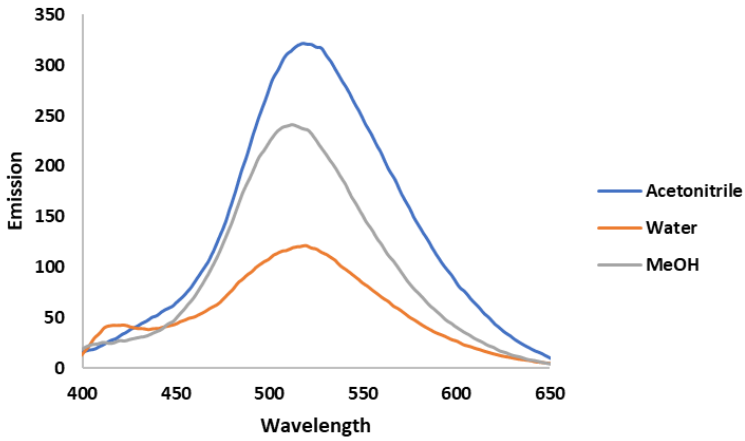

Figure 11: Emission comparison of equimolar amounts of D3 in acetonitrile, methanol, and water. Excitation of 340 nm.

Cationic sensing studies

5.1.3 Sensing response of coumarin-imine and azo derivatives D3 and D4 towards various metal cations in organic and aqueous media

Coumarin-imine and -azo derivatives **D3** and **D4** were chosen for further studies owing to their favourable absorbance properties compared to that of **D1** and **D2**. Screening studies were conducted in acetonitrile, methanol, and water, with the omission of DMF due to its environmentally unfavourable properties. The metals for analysis were prepared in water from their nitrate salts. These metals included Hg^{2+}, Ag^{+}, Fe^{3+}, Fe^{2+}, Pb^{2+}, Cd^{2+}, Cu^{2+}, Ba^{2+}, Zn^{2+}, Ca^{2+}, Co^{2+}, Cr^{2+}, Al^{3+}, K^{+}, Ni^{2+}, and Na^{+}. Owing to the colour changing capabilities of

the imine and azo functionalities upon metal coordination (chromophores), the colour of the compound in solution before and after metal addition was observed. Derivative **D3** displayed a strong affinity towards Hg^{2+} in water, characterized by a strong decrease of absorbance in the band associated with the imine C=N bond (425 nm). This foreshadows the possible involvement of the imine functionality towards Hg^{2+} complexation. Moreover, the colour of the solution changes from light yellow to clear upon Hg^{2+} addition. Derivative **D4** on the other hand exhibits a strong bathochromic shift upon Hg^{2+} addition in acetonitrile (**Figure 12**). Furthermore, a rapid and distinct colour change from yellow to red was observed upon metal coordination. Both derivatives have displayed a unique visible colour response towards Hg^{2+} in their respective solvent systems, highlighting their applications as colorimetric sensors for Hg^{2+} detection. The changes in solution colour upon Hg^{2+} complexation of **D3** and **D4** in different solvents is shown in **Figure 13** (for the screening studies of **D3** in acetonitrile and methanol and **D4** in water and methanol, see **Appendix D Figures 5-8**).

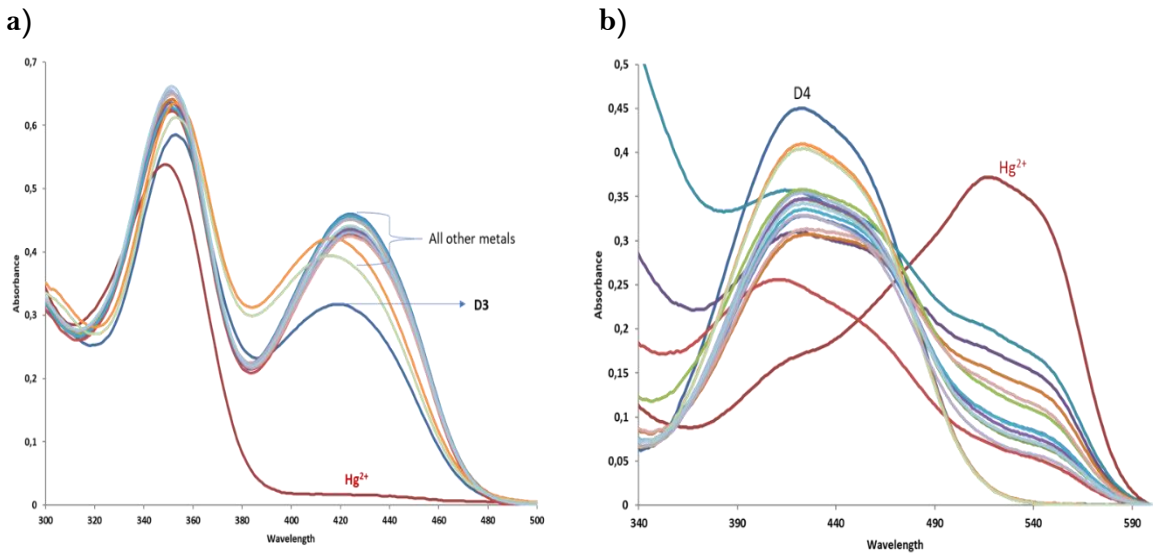

Figure 12: UV-Vis metal screening studies of a) **D3** in water and b) **D4** in acetonitrile.

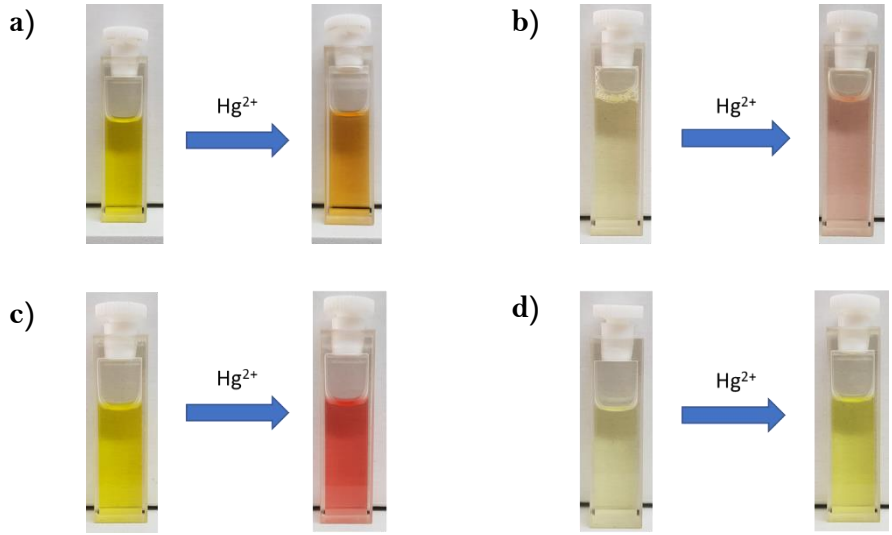

Figure 13: Visual "naked-eye" colour changes of sensor **D4** in a) methanol, b) water, and c) acetonitrile; and sensor **D3** in d) water upon Hg^{2+} addition.

5.1.4 Competition studies of D3 and D4 towards Hg^{2+}

The selectivity studies of **D3** and **D4** towards Hg^{2+} was conducted in water and acetonitrile respectively. The effects of the competing cations towards Hg^{2+} complexation with **D3** and **D4** is shown in **Figure 14**. Both sensors display appreciable selectivity towards Hg^{2+} in the presence of competing metal cations. Additionally, both sensors displayed selectivity towards Hg^{2+} when all metal cations were competing against Hg^{2+} in solution. For the competition studies of **D3** towards Hg^{2+} in MeOH; and **D4** towards Hg^{2+} in MeOH and water, see **Appendix D Figures 9-11**. Both sensors showed good selectivity towards Hg^{2+} in MeOH and water respectively; however, the selectivity towards Hg^{2+} in water and acetonitrile for **D3** and **D4** respectively was far superior.

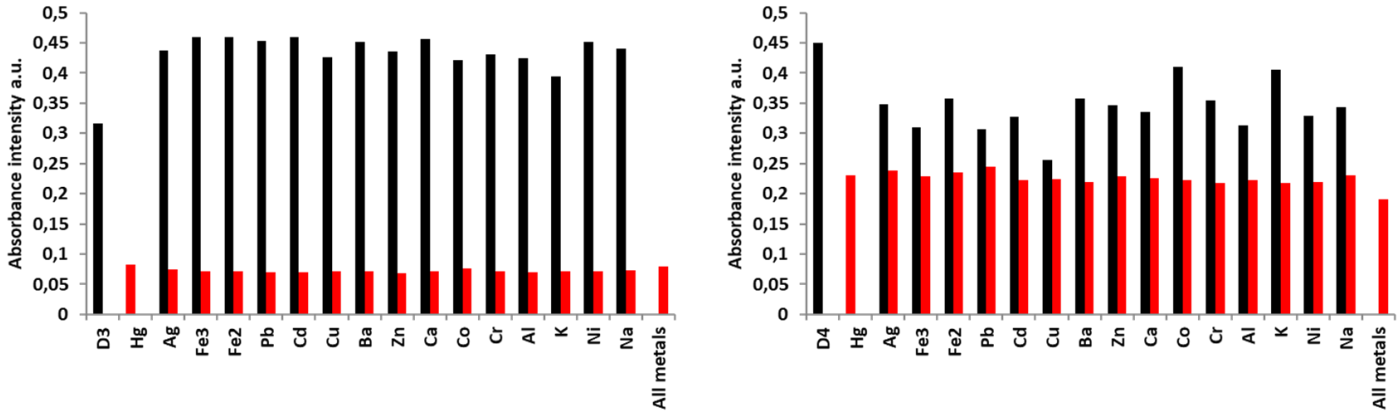

Figure 14: Selectivity studies of a) D3 and b) D4 towards Hg^{2+} in water and acetonitrile respectively.

Moreover, sensor **D4** displayed remarkable visual selectivity towards Hg^{2+} in the presence of competing cations. Furthermore, **D4** showed selectivity towards Hg^{2+} after competing cations had been initially added (in the absence of Hg^{2+}) to a solution of the sensor in acetonitrile (**Figure 15**).

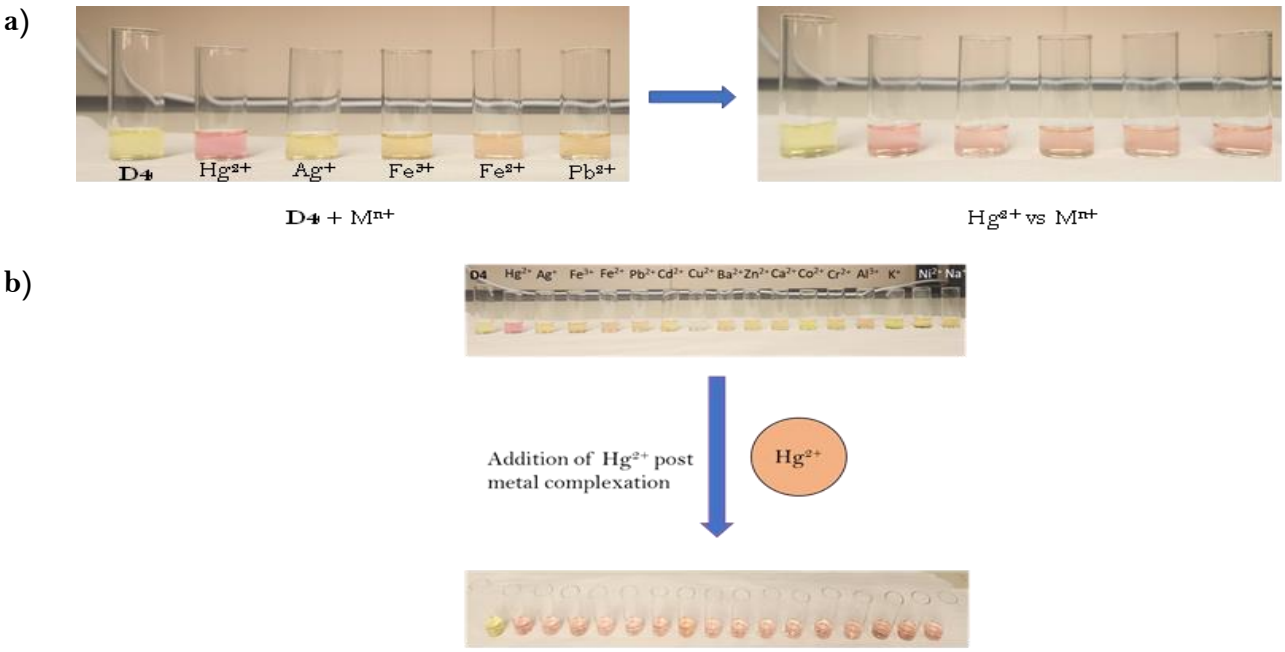

Figure 15: Visual selectivity of **D4** towards Hg^{2+} in acetonitrile in a) the presence of competing metal cations, and b) visual colour change upon Hg^{2+} addition post competing metal complexation with **D4**.

5.1.5 UV-VIS titration studies, detection limit, association constant, and binding stoichiometry for D3 with Hg^{2+} in water

The UV-Vis titration of **D3** with Hg^{2+} was conducted in water at room temperature. Equal aliquots of the Hg^{2+} solution was added to **D3** and the absorbance intensity monitored. Results indicate an increase in absorbance in the second absorbance band (A_{max} 350 nm) with a subsequent decrease in the absorbance value in the third absorbance band (A_{max} 420 nm) associated with the imine-hydroxy system. This led to the formation of a clear isosbestic point at 368 nm (**Figure 16**).

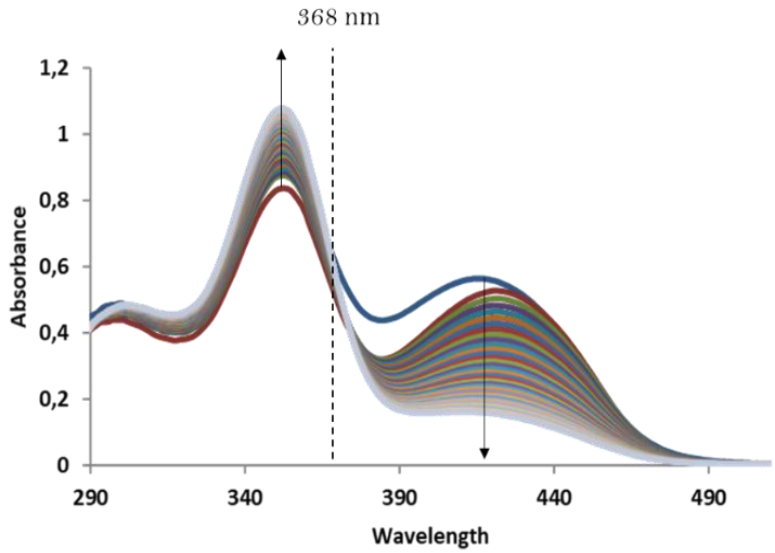

Figure 16: UV-Vis titration analysis of **D3** with Hg^{2+} in water. Titrations completed in triplicate.

As mentioned in **Chapter 2**, an isosbestic point indicates a clear transformation from the starting product to the sensor-metal complex in a chemically selective fashion.[31,32] This isosbestic point remains stable for the duration of the titration experiment and does not shift to higher or lower wavelengths. This is indicative of a reaction proceeding without the formation of an intermediate or multiple products.[33] The bathochromic shift in wavelength upon Hg^{2+} addition could arise due to a possible ICT mechanism, accounting for the observable colour change from clear to a brighter yellow. This shift was not as prominent as that observed between **D4** and Hg^{2+}, and the colour change less pronounced.

The detection limit of **D3** with Hg^{2+} was determined from the calibration of A_0/A vs $[Hg^{2+}]$ according to the equation LOD = $3\sigma/m$ where σ is the standard deviation of the regression curve and m is the gradient/slope of the graph itself. The detection limit was calculated at the lower $[Hg^{2+}]$ region of the graph where linearity is maintained. Deviation from linearity at higher concentrations of Hg^{2+} could arise due to limited sensor accessibility. The detection limit was calculated to be 7.37×10^{-7} M (0.74 μM). The calibration curve of **D3** with Hg^{2+} is shown in **Figure 17**.

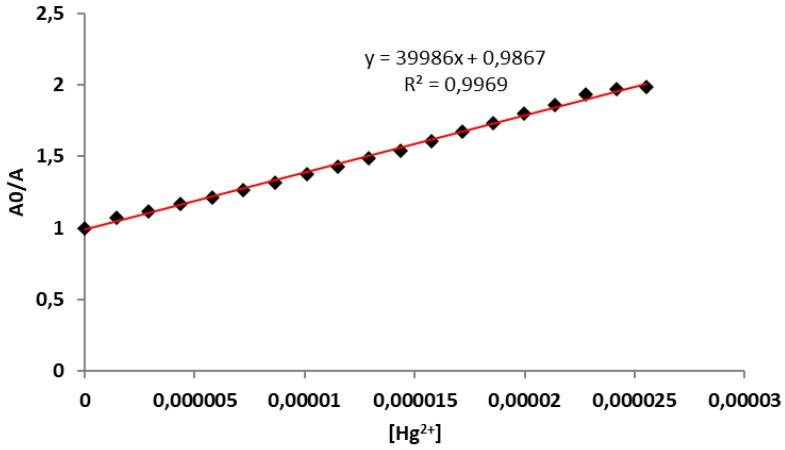

Figure 17: plot of A_0/A vs $[Hg^{2+}]$ for the titration of **D3** with Hg^{2+}.

The association constant (K_a) was determined using the titration data recorded and plotted according to the Benesi-Hildebrand equation as previously described in **Chapters 2-4**. The value of the association constant was calculated from the ratio of the intercept to the slope of the calibration curve. The association constant was determined to be 4.4×10^4 M^{-1}. Additionally, the linearity of the plot suggests a 1:1 binding ratio between **D3** and Hg^{2+}. This was later confirmed by Job's plot analysis. The Benesi-Hildebrand plot from **D3** and Hg^{2+} titration data is shown in **Figure 18**.

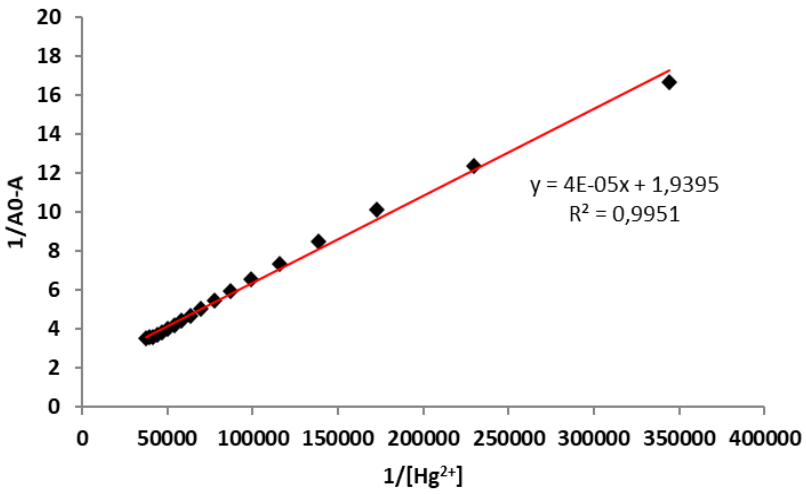

Figure 18: Benesi-Hildebrand plot of **D3** with Hg^{2+}.

The Job's plot analysis of **D3** with Hg^{2+} in water is shown in **Figure 19**. The binding stoichiometry between the sensor and metal was shown to occur in a 1:1 ratio. This value is determined at the intersection of the two plots where absorbance intensity is greatest.

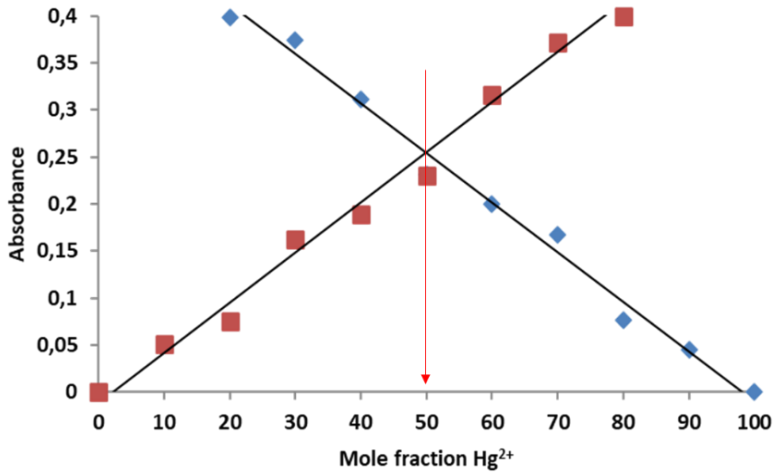

Figure 19: Job's plot of **D3** with Hg^{2+} in water.

5.1.6 UV-VIS titration studies, detection limit, and association constant for D4 with Hg^{2+} in acetonitrile

The UV-Vis titration of **D4** with Hg^{2+} was conducted in acetonitrile at room temperature. As illustrated in **Figure 20**, upon the incremental addition of Hg^{2+} to the solution of **D4**, a new absorption band appeared at 520 nm. Conversely, the absorption band at 422 nm subsequently decreased upon Hg^{2+} addition, forming a clear isosbestic point at 470 nm. This isosbestic point characterizes the appearance of the new sensor-metal complex as a single, stable coordination species.

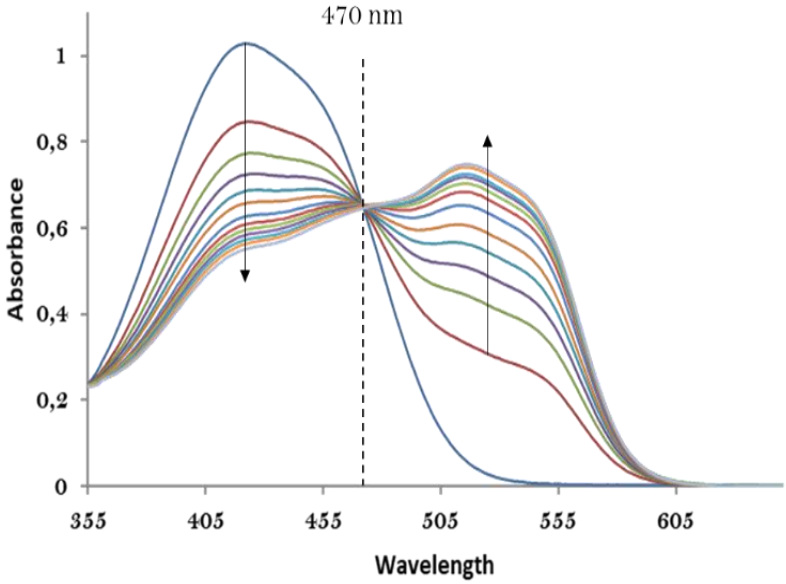

Figure 20: UV-Vis titration of **D4** with Hg^{2+} in acetonitrile. Titrations conducted in triplicate.

The detection limit of **D4** with Hg^{2+} was determined by the same method described for **D3** with Hg^{2+} and was found to be 2.4 x 10^{-7} M (0.24 μM). This detection limits for both **D3** and **D4** towards Hg^{2+} is lower than the accepted limit of mercury in drinking water as reported by the WHO and U.S. EPA.[34–36] This highlights these sensors possible applications towards environmental Hg^{2+} sensing and determination. The detection limit was calculated at lower analyte concentrations where linearity was maintained.

The association constant was determined by the same methods as described for **D3** with Hg^{2+}. The Benesi-Hildebrand plot of **D4** with Hg^{2+} is illustrated in **Figure 21**. The value of K_a was found to be 8.9 x 10^4 M^{-1}. As mentioned in previous chapters, the association constant is a measure of the strength of the sensor-analyte interaction. As the value for K_a for **D4** is double that of **D3** with Hg^{2+}, it could explain both the visible and spectroscopic differences observed in their complexation strategies. This stronger interaction between **D4** and Hg^{2+} could explain the observed bathochromic (red) shift in absorbance wavelength upon Hg^{2+} addition; and the more striking colour change from yellow to red than that of **D3** with Hg^{2+}.

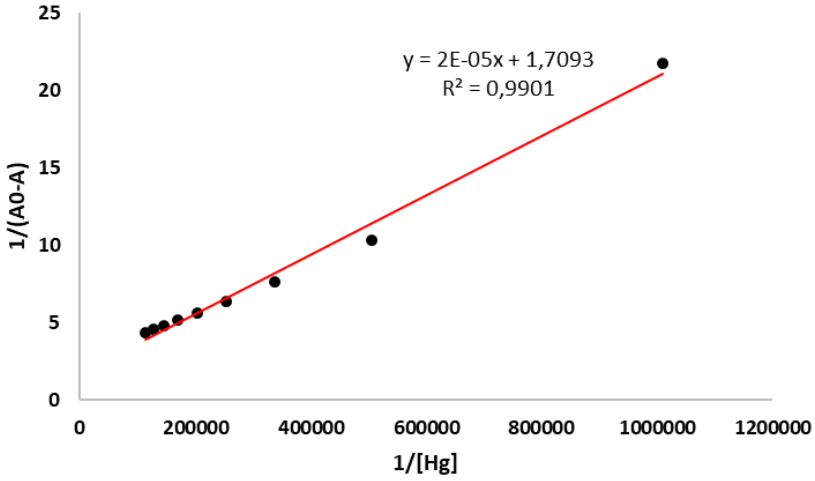

Figure 21: Benesi-Hildebrand plot of **D4** with Hg^{2+}.

The stoichiometric binding ratio as described by the Job's plot analysis of **D4** and Hg^{2+} is shown in **Figure 22**. Complexation is shown to occur in a 1:1 ratio which is complimented by the linearity of the Benesi-Hildebrand plot.

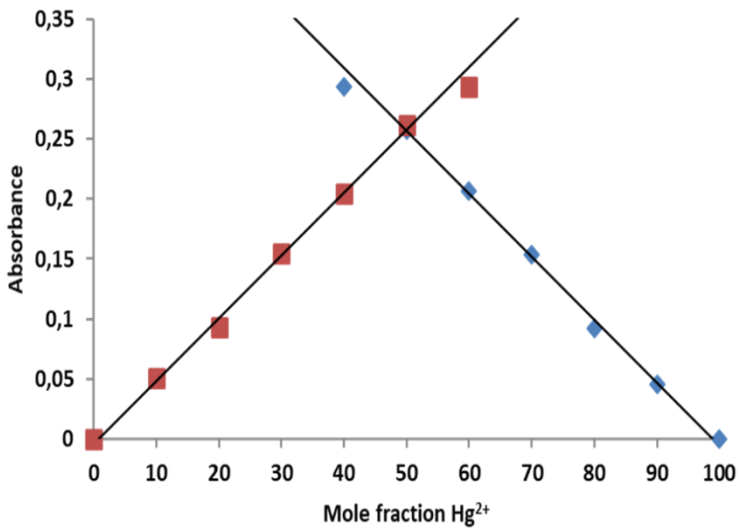

Figure 22: Job's plot of **D4** with Hg^{2+} in acetonitrile.

5.1.7 Reversibility studies of D3-Hg^{2+} and D4-Hg^{2+} complexation with EDTA

The reversibility of **D3** and **D4** towards Hg^{2+} complexation was investigated in the presence of hexadentate chelating ligand EDTA. The reversibility of **D3** and **D4** was investigated in water and acetonitrile respectively. In this study, both sensors were titrated with 60 µL of an Hg^{2+} solution and the absorbance response measured. Therefore, the resulted complex was titrated with an EDTA solution and the changes in absorbance monitored. The titration of **D3** and **D4** Hg^{2+} complexes with EDTA is shown in **Figure 23**.

a)

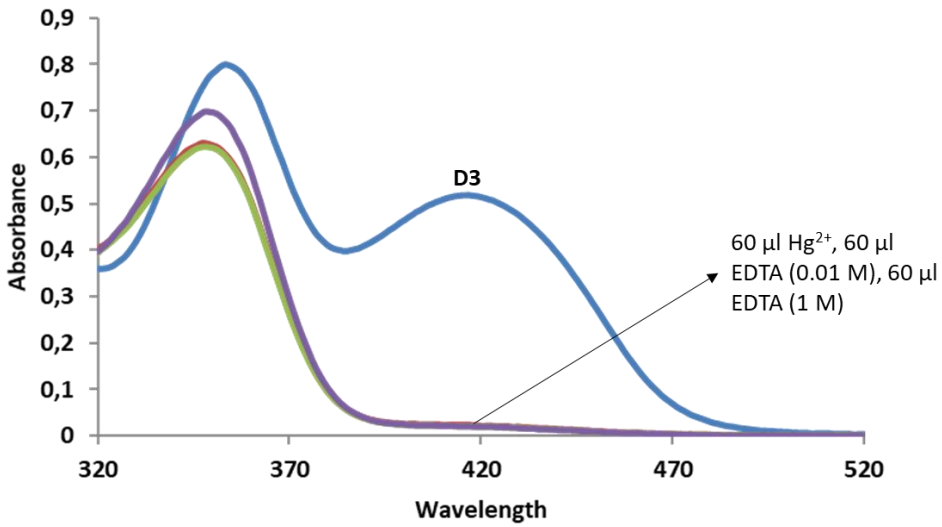

b)

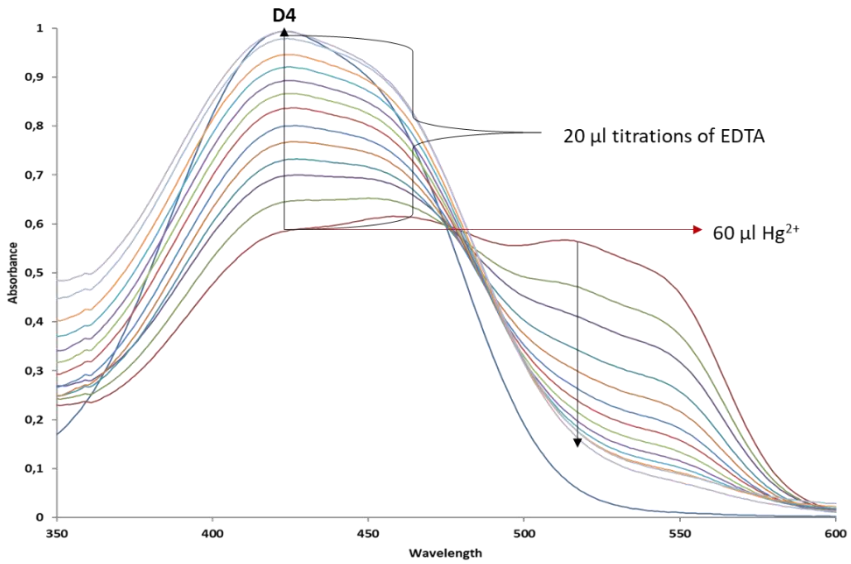

Figure 23: Reversibility studies of Hg^{2+} complexation with a) **D3** and b) **D4** with EDTA in water and acetonitrile respectively.

The reversibility towards Hg^{2+} is remarkably different for **D3** and **D4**. Sensor **D3** does not display any reversible complexation abilities in the presence of EDTA. Moreover, when a more concentrated aliquot of EDTA was added (1 M), the absorbance intensity failed to reach the original value of **D3** alone. Conversely, sensor **D4** displayed excellent reversibility towards Hg^{2+} complexation in the presence of EDTA. The absorbance intensity of **D4** was able to be restored by EDTA after Hg^{2+} complexation, hence 100% reversibility. Owing to this excellent reversible complexation behaviour of sensor **D4**, it was used towards the construction of a Molecular Logic Gate for extended sensor applications.

5.1.7.1 Construction of a Molecular Logic Gate and Keypad Lock based on the reversible nature of D4-Hg^{2+} complexation with EDTA

Processing input signals by logic gates is one of the focal points in information technology. In recent years, an expanding number of exploratory efforts have been invested to the development of molecular logic gates owing to their practicality.[37] Molecular logic gates are molecules able to execute logical responses by receiving one or more physical or chemical input signals and yielding a singular output. Such input and output responses may include chemical processes, such as ionic recognition and with output signals based on spectral response.[38] To determine whether **D4** had the capabilities as a molecular mimicking device, cyclic reversibility studies with Hg^{2+} and EDTA were conducted in acetonitrile. This study determines whether cycling between '1' and '0' states are possible for numerous analyte additions (cycles). This cyclic nature is imperative for effective logic gate construction. The cyclic reversibility of the sensor-metal complex with EDTA is shown in **Figure 24**.

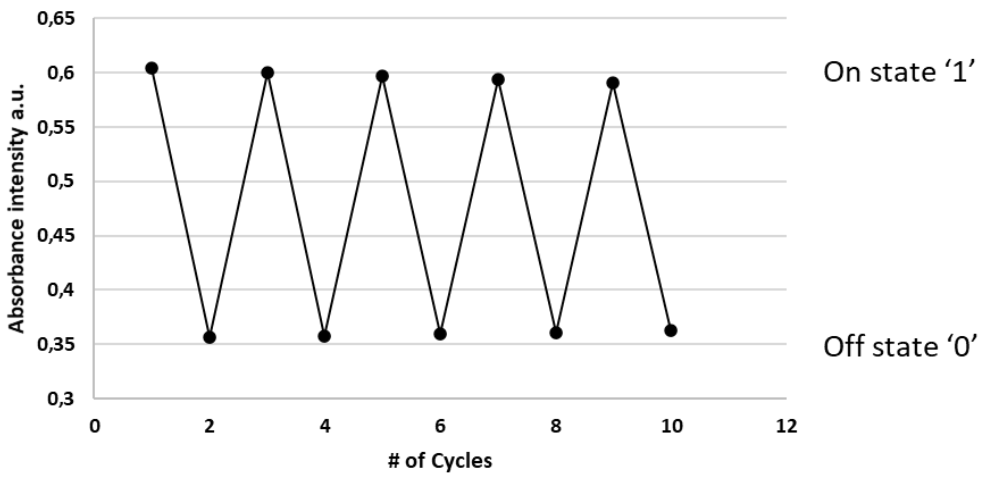

Figure 24: Cyclic reversibility of the absorbance intensity of **D4** upon Hg^{2+} (off state) and EDTA (on state) respectively.

The cyclic reversible nature of **D4** to Hg^{2+} upon sequential additions of EDTA illustrates the digital action of the sensor and thus it was applied towards a Boolean function molecular logic gate. The two chemical inputs, "input 1" (Hg^{2+}), and "input 2" (EDTA) were defined as binary '1' and '0' states representing their presence and absence, respectively. The appearance and disappearance of the absorbance peak at 422 nm was considered as "output" for the logic gate and assigned as binary states '1' and '0' respectively. **D4** exhibited a UV-Vis absorption peak at 422 nm thus the output is designated as '1'. After the addition of Hg^{2+} (input 1 = 1; input 2 = 0) the absorbance decreased to the final absorbance value (output=0) (see **Appendix D Figure 12**). However, upon the introduction of EDTA to the sensor-analyte complex, the absorbance increased to its initial intensity. Considering the other input combinations ((0,0), (0,1), and (1,1)), the output is equal to '1'. This established a clear "on-off-on" input/output spectral response of **D4** in the presence and absence of Hg^{2+} and EDTA which imitates the IMPLICATION type logic gate at the molecular level. In other words, the Boolean function provides and output of '1' in all situations, except for the case where one input is '1' (described here as Hg^{2+}). The proposed logic circuit together with the truth table is shown in **Figure 25**.

a)

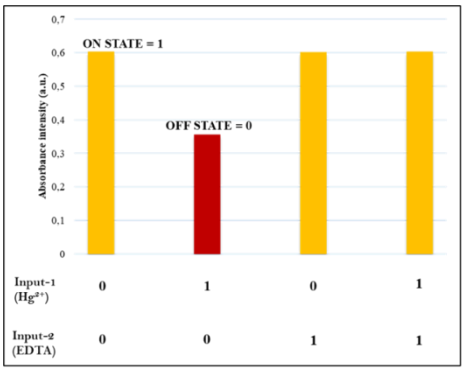

Input 1 (Hg^{2+})	Input 2 (EDTA)	Output (λ = 422 nm)
0	0	1
1	0	0
0	1	1
1	1	1

b)

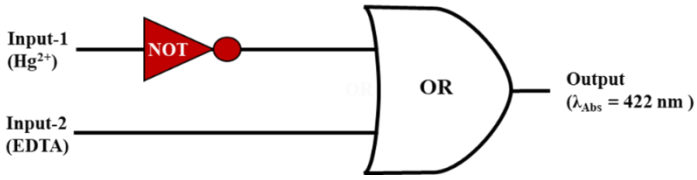

Figure 25: a) UV-Vis absorbance values of **D4** with four different binary inputs and corresponding truth table, b) circuit diagram for an IMPLICATION logic gate operation. Experiments conducted in acetonitrile.

The molecular or chemical computing keypad lock systems have been utilized as a modern strategy for information security and data-restriction applications.[39,40] Herein, the proposed molecular model was used to construct a sequence-dependent molecular keypad lock based on the appreciable selectivity and reversibility of **D4** with Hg^{2+} and EDTA. Herein, azo dye **D4**, Hg^{2+}, and EDTA are introduced as the three chemical inputs (labelled A, H, and E respectively). The six possible ordered input combinations are AHE, AEH, HAE, HEA, EAH, and EHA. The specific ordered combination of chemical compounds that can produce the same absorbance response at 422 nm of **D4** in the absence of Hg^{2+} is able to "unlock" the system, much like a combination lock. The combination 'AHE' produced the identical absorbance response compared to that of **D4** (A) alone, whereas contrasting output was unveiled for the remaining five combination inputs (**Figure 26**). Although other input signals attain an absorbance intensity close to that of **D4** alone, they do not achieve the correct "turn-on" absorbance response able to "unlock" the system. Additionally, this security could be made safer and more complex due to the solvatochromic nature of **D4** seen previously.

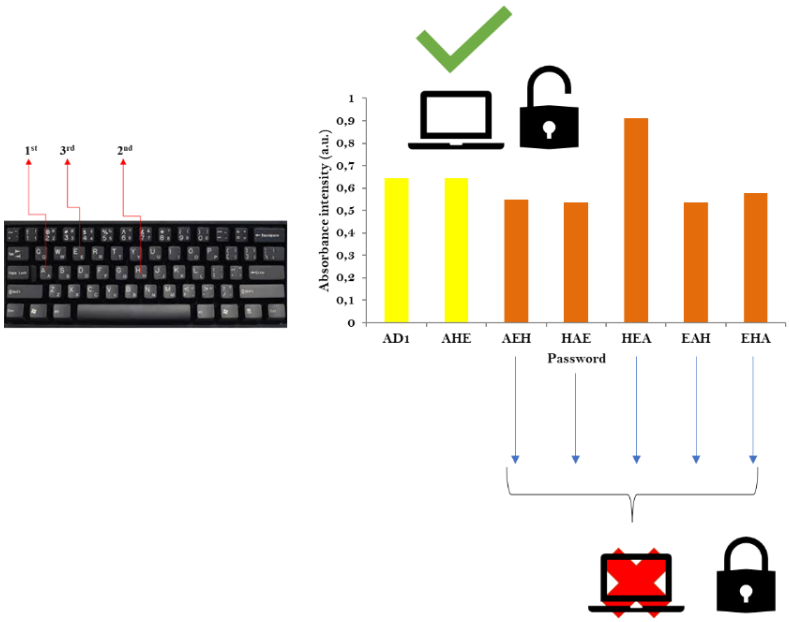

Figure 26: Absorbance output for **D4** corresponding to the six possible ordered input combinations at 422 nm. Experiments conducted in acetonitrile.

5.1.8 pH studies of D3 and D4

The effect of Hg^{2+} on the absorbance of **D3** and **D4** was observed at the original pH of the solution. To investigate the effect of pH towards sensor usability, equal aliquots of the Hg^{2+} solution was added to the sensor in different pH solutions and the absorbance intensity recorded. Solutions with pH of 2-14 were prepared in deionized water for analysis. For sensor **D3** absorbance was monitored between 320 and 500 nm where the second absorbance band related to the C=N group appears. The absorbance of sensor **D4** was recorded at 520 nm before and after Hg^{2+} addition. The effect of pH towards sensor absorbance response to Hg^{2+} is shown in **Figure 27**.

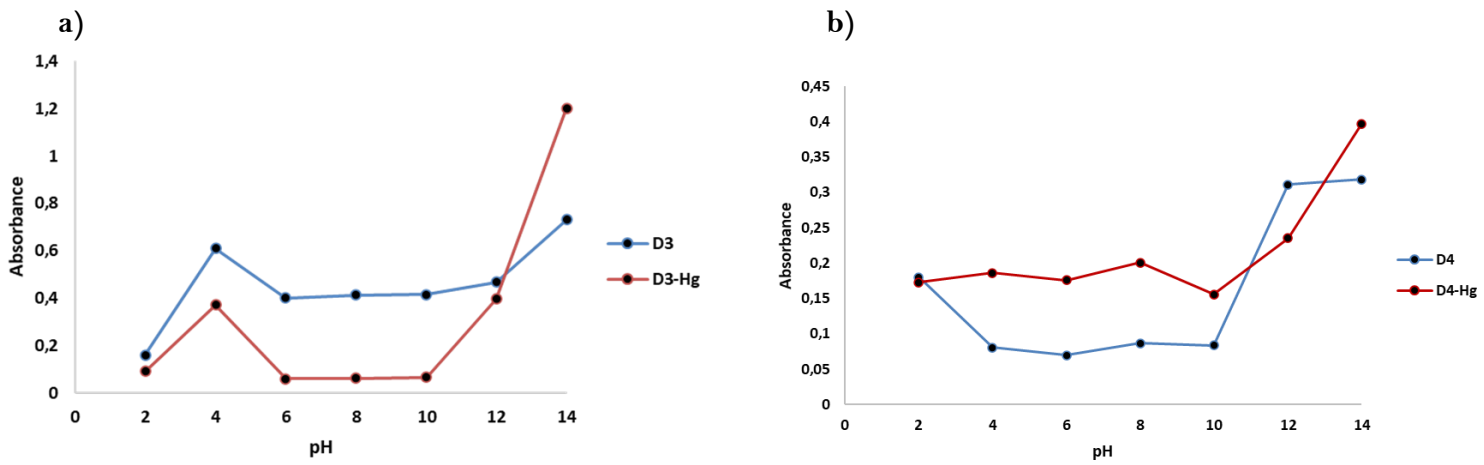

Figure 27: Effect of pH on the absorbance response of a) **D3** and b) **D4** upon the addition of Hg^{2+}.

Visibly, the absorbance response of **D3** towards Hg^{2+} in different pH solutions continues to display a decrease in absorbance upon metal addition as seen in the original pH of the solution. The pH of the water used for screening and titration analysis was recorded as 5.22. The absorbance response of **D3**-Hg^{2+} only appears to increase beyond that of **D3** at higher pH values. Conversely, the solvent medium and pH of the solution effects the absorbance response of **D4** upon the introduction of the Hg^{2+} cations. Acetonitrile is a polar aprotic solvent; therefore, the likelihood of free-floating protons is improbable and are unlikely to affect the sensing and absorbance response. Conversely, water is a polar protic solvent which could cause the sensing and binding discrepancies observed. Although the absorbance response is different in most solutions compared to that in acetonitrile, it does not imply that **D4** cannot be an effective sensor for Hg^{2+} in different pH solutions. To determine this, screening and competition studies would need to be evaluated individually in the different pH solutions. One can infer that the absorbance response of **D4** towards Hg^{2+} is pH dependent.

5.1.9 Determination of binding site between D3 and Hg^{2+}

Literature has reported the donor capabilities of the imine-nitrogen and neighbouring hydroxyl moieties towards transition metal complexation.[41–47] Recently, a coumarin-derived Schiff base for the detection of Hg^{2+} and Pb^{2+} cations in aqueous media has been reported.[48] Coordination occurred in a 2:1 sensor-metal binding ratio, with complexation occurring via the imine-nitrogen and hydroxyl lone electron pairs. Therefore, ^{1}H, ^{13}C & ^{15}N NMR studies

were conducted to investigate the possible involvement of these moieties towards metal complexation.

The ^{1}H NMR titration experiment of **D3** with aliquots of $Hg(NO_3)_2$ in d_6-DMSO is shown in **Figure 28**.The imine-proton signal (encircled in red) appears to become less resolved and shift in ppm value the more Hg^{2+} solution is added. The signal assigned to the hydroxy group (encircled in green) appears to decrease upon Hg^{2+} addition. Moreover, the disappearance of the hydroxy signal could occur due to proton-transfer during nucleophilic attack of the NO_3^- counterion with the proton attached to the imine functionality. This proton-transfer leads to the formation of an N-H group which is postulated to appear at 9.5 ppm (encircled in yellow).

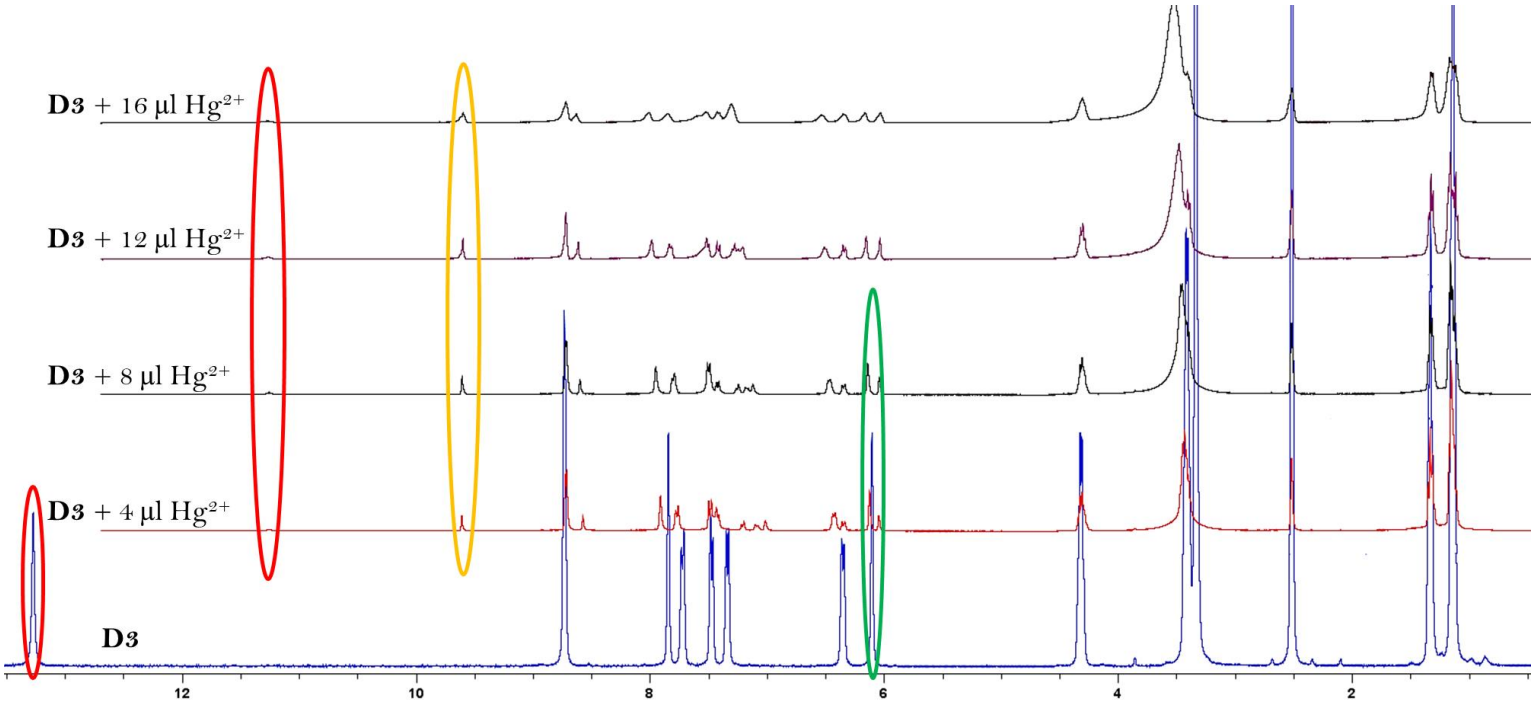

Figure 28: ^{1}H NMR titration of sensor **D3** with the Hg^{2+} solution in d_6-DMSO.

Furthermore, additional peaks in the region of the coumarin scaffold were observed upon the addition of the Hg^{2+} solution. This may indicate the formation of two different coordination species in solution (cationic and anionic); or the separation of the two proposed enantiomeric forms of **D3**.

The appearance of a new singlet at 9.6 ppm was postulated to arise due to a hydrogen transfer mechanism occurring around the azomethine group, likely forming a signal assigned to a N-H bond in this region. The upfield shift in ppm value of the imine-proton signal is postulated to be as a result of the increased electron density around the imine-carbon atom. The decrease

in peak resolution may not be indicative of proton abstraction, but rather due to perturbation of the surrounding electronic environment

The proposed possible proton-transfer mechanisms that involves NO_3^- complexation with the imine group is shown in **Scheme 2**. Literature has reported that Schiff bases supporting an *ortho* hydroxy group are most likely to undergo intramolecular hydrogen bonding and proton transfer.[12]

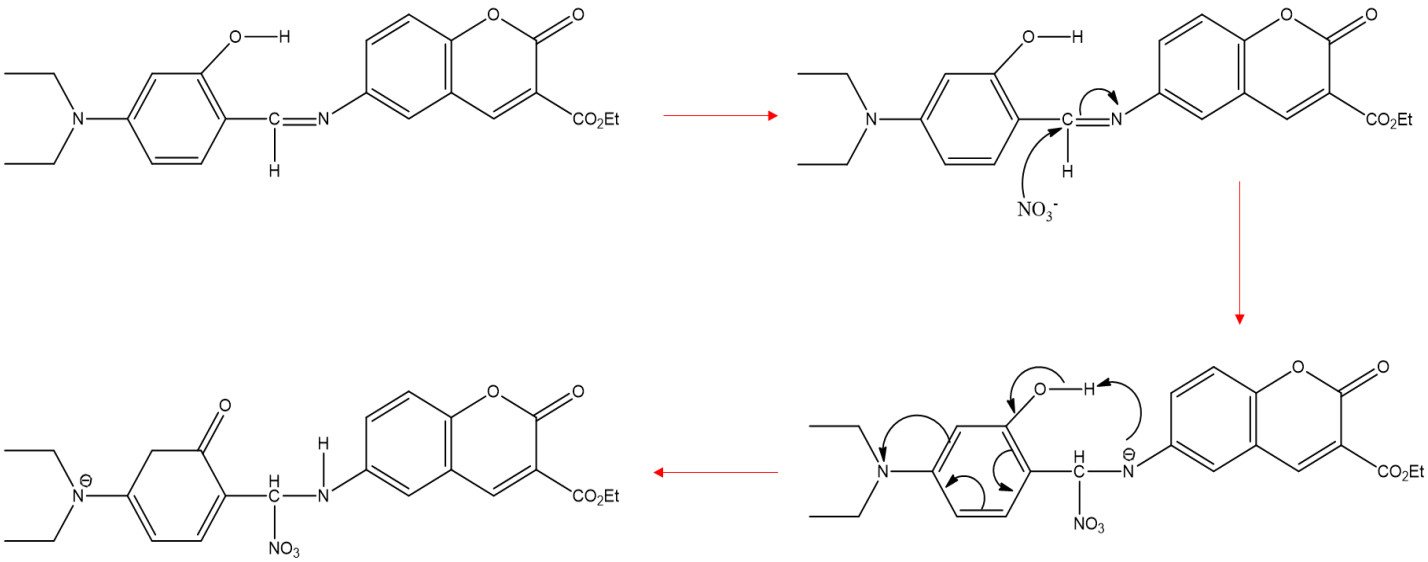

Scheme 2: Possible proton transfer involving neighbouring phenolic hydrogen atom with the imine-nitrogen during NO_3^- nucleophilic addition.

The ^{13}C NMR spectra of **D3** after the addition of 16 µL of $Hg(NO_3)_2$ in d_6-DMSO is shown in **Figure 29**. Unfortunately, the spectra could not serve to confirm the involvement of the hydroxyl group towards Hg^{2+} complexation. As mentioned previously, the solvent used (d_6-DMSO) exhibits different electronic and solvent properties than that of H_2O used in the UV-Vis selectivity and titration studies. Therefore, the effect of the solvent towards Hg^{2+} complexation could explain the discrepancies observed in the NMR titration studies. Notable was the deshielding of a single carbon signal from the region of 160 ppm to 190 ppm is proposed. As viewed in the titration spectra, new peaks at similar ppm values adjacent to the original peaks are present after the addition of 16 µL aliquot of the $Hg(NO_3)_2$ solution. The three peaks between 165-160 ppm (encircled in red) are assigned to the 3-substituted ester C=O, salicylaldehyde C-OH, and imine C-H carbon atoms respectively. This new deshielded

signal could arise from C-OH or C-H imine interaction with either the Hg^{2+} cation or NO_3^- counterion respectively.

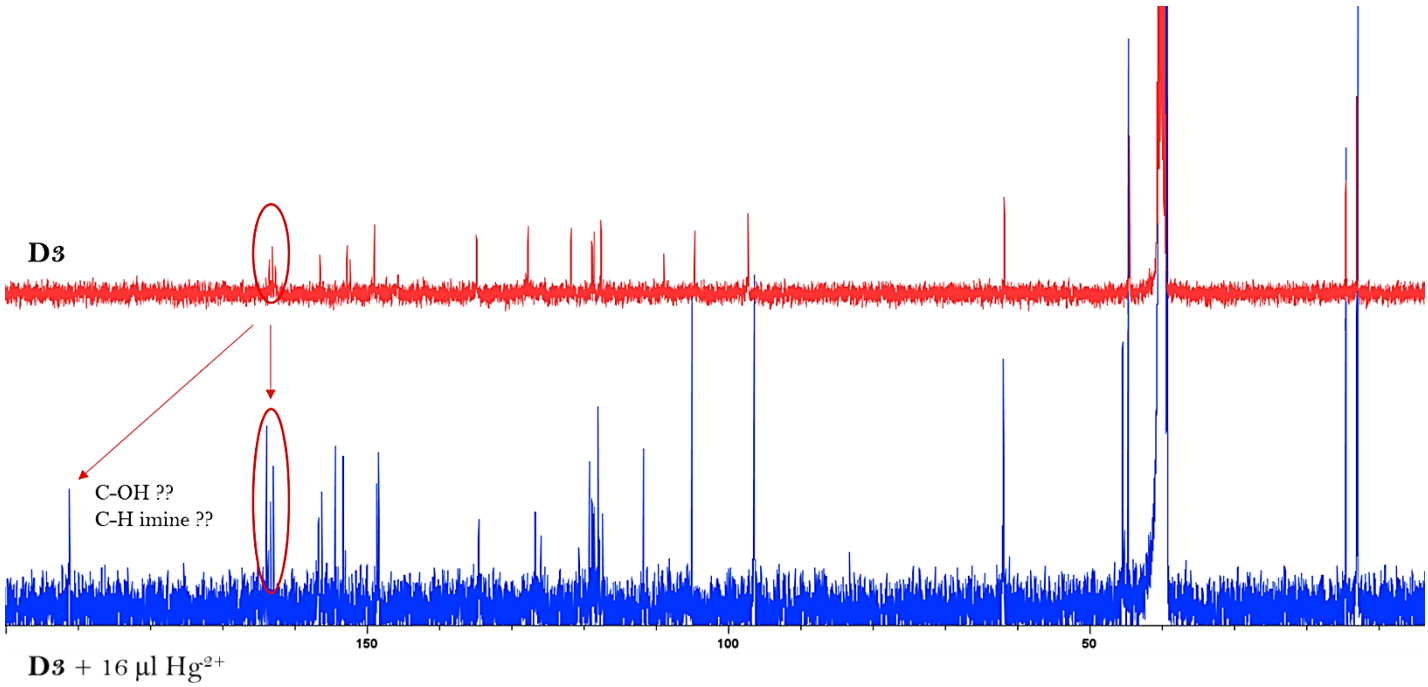

Figure 29: ^{13}C NMR titration experiment of **D3** after the addition of 16 µL $Hg(NO_3)_2$ solution in d_6-DMSO.

To determine whether the imine-nitrogen atom was involved in metal complexation, ^{15}N NMR titration experiments of **D3** with the Hg^{2+} solution in d_6-DMSO were conducted. Sensor **D3** supports two different nitrogen atoms, namely on the imine and substituted diethylamino group. A comparison of the ^{15}N NMR signals before and after Hg^{2+} addition is shown in **Figure 30**. Two signals are visible in the ^{15}N NMR spectrum of **D3**. The first signal is observed at 222 ppm and the second is observed at 330 ppm. After the addition of Hg^{2+}, the signal at 222 ppm is no longer observed or has appeared to shift upfield. This signal was attributed to the imine-nitrogen atom as it is believed to be involved in metal complexation. The second signal at 330 ppm shifted slightly downfield to 336 ppm. This signal was attributed to the diethylamino substituent as metal complexation is most unlikely to occur at this site. The signal attributed to the imine-nitrogen has either disappeared or shifted further upfield to 14 ppm. Whether the peak has disappeared or shifted, the involvement of the imine nitrogen towards metal complexation is highly plausible. Mercuric(II)acetate was used for titration experiments to prevent unwarranted nitrogen signals from mercuric nitrate.

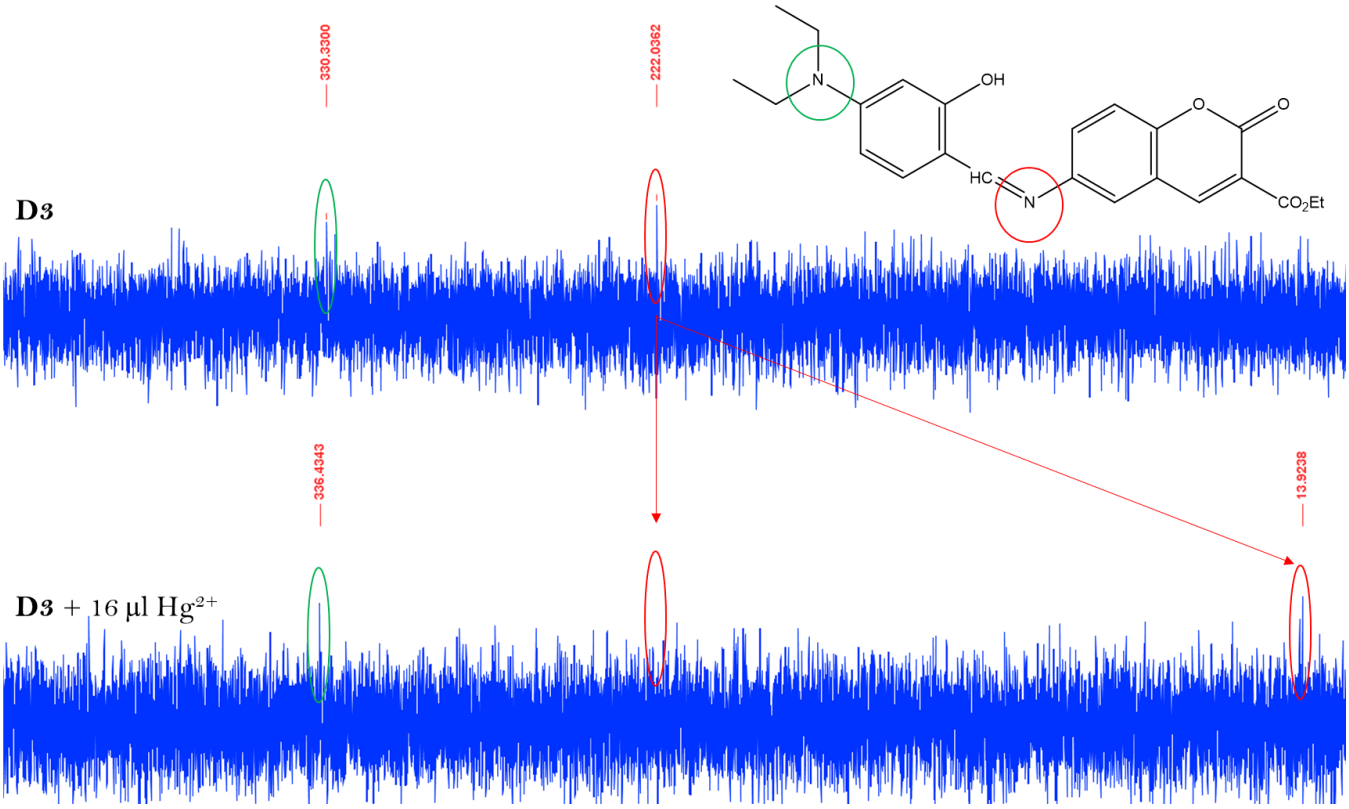

Figure 30: ^{15}N NMR spectral comparison of **D3** before and after Hg^{2+} addition in d_6-DMSO.

Finally, the FT-IR was able to confirm the involvement of the OH and imine group towards metal complexation. The FT-IR spectral overlay of **D3** and the **D3**-Hg^{2+} complex is shown in **Figure 31**. The **D3**-Hg^{2+} complex was prepared by dissolving mercuric acetate in ethanol:water (9:1) and adding it to a solution of **D3** in methanol. The resulting mixture was refluxed for 2hrs, after which a yellow solid precipitated from solution. This solid was filtered, washed with ether, dried, and used for FT-IR analysis. The spectra of the complex exhibited an enhancement of the OH vibrational signal in the range of 3500-3000 cm^{-1} which was previously absent. This could be due to the inhibition of the enol-imine/keto-enamine tautomerism during metal complexation with the hydroxy group. However, some tautomers may still be present in the solid complex, exhibited by the presence of the proposed enamine peak in the region between 2500-2000 cm^{-1}. Additionally, the signal related to the imine C=N vibration has shifted to a singular broader peak at 1527 cm^{-1}, characteristic of the interaction of this functionality with a metal cation.[49,50] The coordination of the imine-nitrogen with the central Hg^{2+} cation was confirmed by the broad, strong peak between 700-500 cm^{-1} which is characteristic of ν(M-N) vibrations and stretching.[51]

The enhancement of the phenolic ν(OH) may infer that the donation of the lone electron pair is involved towards metal coordination, and not the donation of bonding electrons through proton abstraction. Therefore, coordination to Hg^{2+} is expected to involve both the imine-nitrogen, and adjacent *ortho* hydroxy as supported by literature.[52]

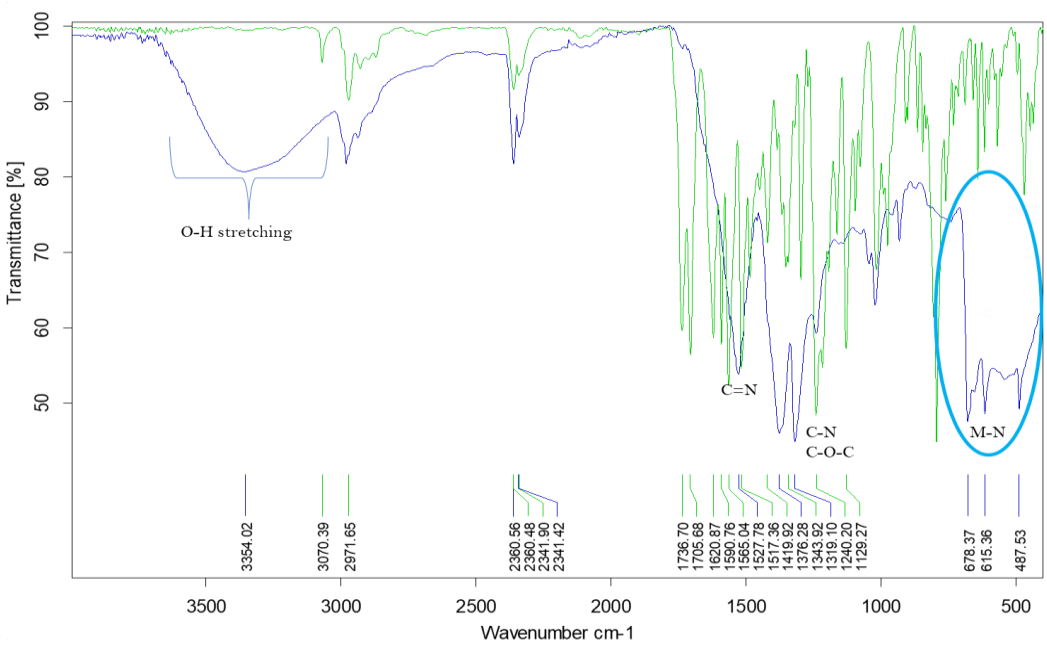

Figure 31: FT-IR comparison of **D3** (green) and **D3**-Hg^{2+} (blue).

Molecular modelling studies were able to resolve the proposed binding site between **D3** with Hg^{2+}. The binding with the NO_3^- counterion was not modelled as this complexation scenario is not important for this study. The proposed binding site between **D3** and Hg^{2+} is shown in **Figure 32**. Results indicate the coordination of the Hg^{2+} centre with both the imine-nitrogen and hydroxy-oxygen atom in a pseudo-6-membered ring conformation, supported and stabilized by water molecules and hydrogen bonding. This agrees well with the reported results from literature and resolves the discrepancies observed in both the ^{1}H and ^{13}C NMR titration analysis. Moreover, it supports the results from both the ^{15}N NMR titration analysis and FT-IR spectral comparison with respect to the proposed signal assignment and interaction of the imine-nitrogen and hydroxy group towards metal complexation.

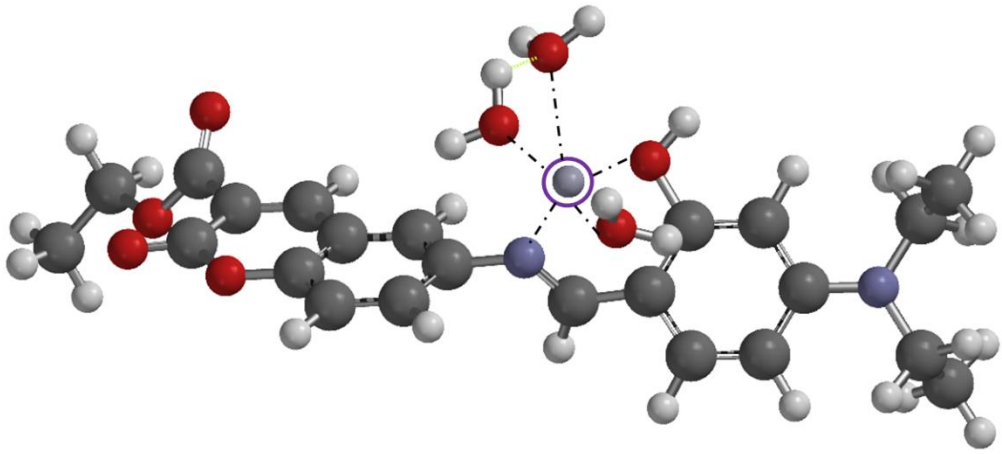

Figure 32: Molecular modelling studies of the interaction of **D3** with Hg^{2+} (circled in purple) at PM3 calculation level.

5.1.10 Determination of binding site between D4 and Hg^{2+}

Azo dyes play an important role in coordination chemistry as they can easily form complexes with most transition metals cations.[53] Dyes containing N and O donor atoms in close proximity to the N=N group afford multiple density and exceptional stability in complexes with d-block metals, stemming from the phenomenon of chelation in geometry.[54] Literature has reported many azo-metal complexes with coordination assisted by neighbouring donor groups forming stable multidentate chelates.[55,56] An example of such a system is shown in **Figure 33**.[57]

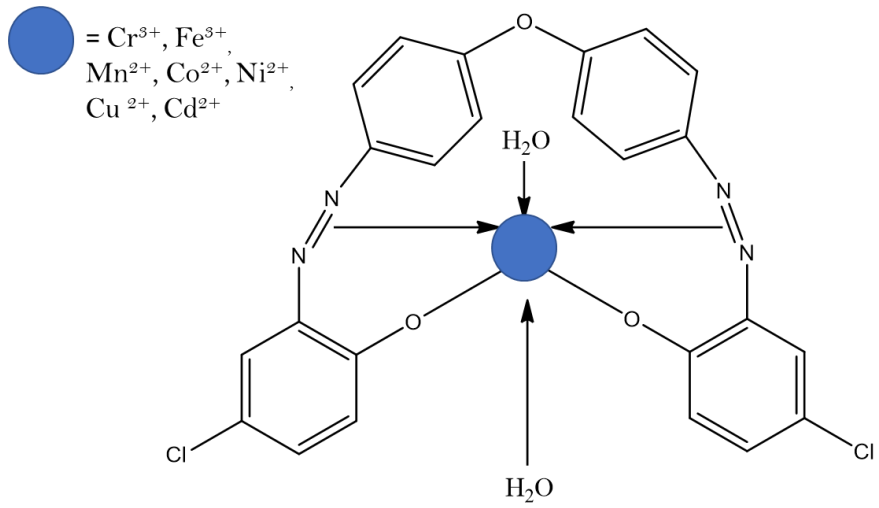

Figure 33: Structure of azo dye metal complexes with neighbouring donor groups.

The structure of coumarin-azo derivative **D4** does not support any neighbouring O or N donor groups to assist during the chelation process. Therefore, the observed colour change and spectral response upon Hg^{2+} addition could involve a different mode and site(s) of complexation as compared to literature findings. For this reason, ^{1}H, ^{13}C, and ^{15}N NMR together with FT-IR and molecular modelling studies were used to validate the correct binding site of Hg^{2+} with sensor **D4**.

^{1}H NMR titration studies of **D4** with $Hg(NO_3)_2$ were initially conducted in d_6-DMSO. From UV-Vis metal screening studies, azo dye **D4** exhibited different colour responses and metal affinities depending on the solvent systems. Therefore, different coordination results may be obtained depending on the solvent system used in titration analysis. For this reason, deuterated acetonitrile (CD_3CN) was used for titration analysis and compared to that of titration studies in d_6-DMSO. Acetonitrile gave the strongest visible and UV spectral response upon Hg^{2+} addition as compared to DMSO. The ^{1}H NMR titration studies of **D4** with Hg^{2+} in d_6-DMSO and CD_3CN are shown in **Figure 34** & **35** respectively.

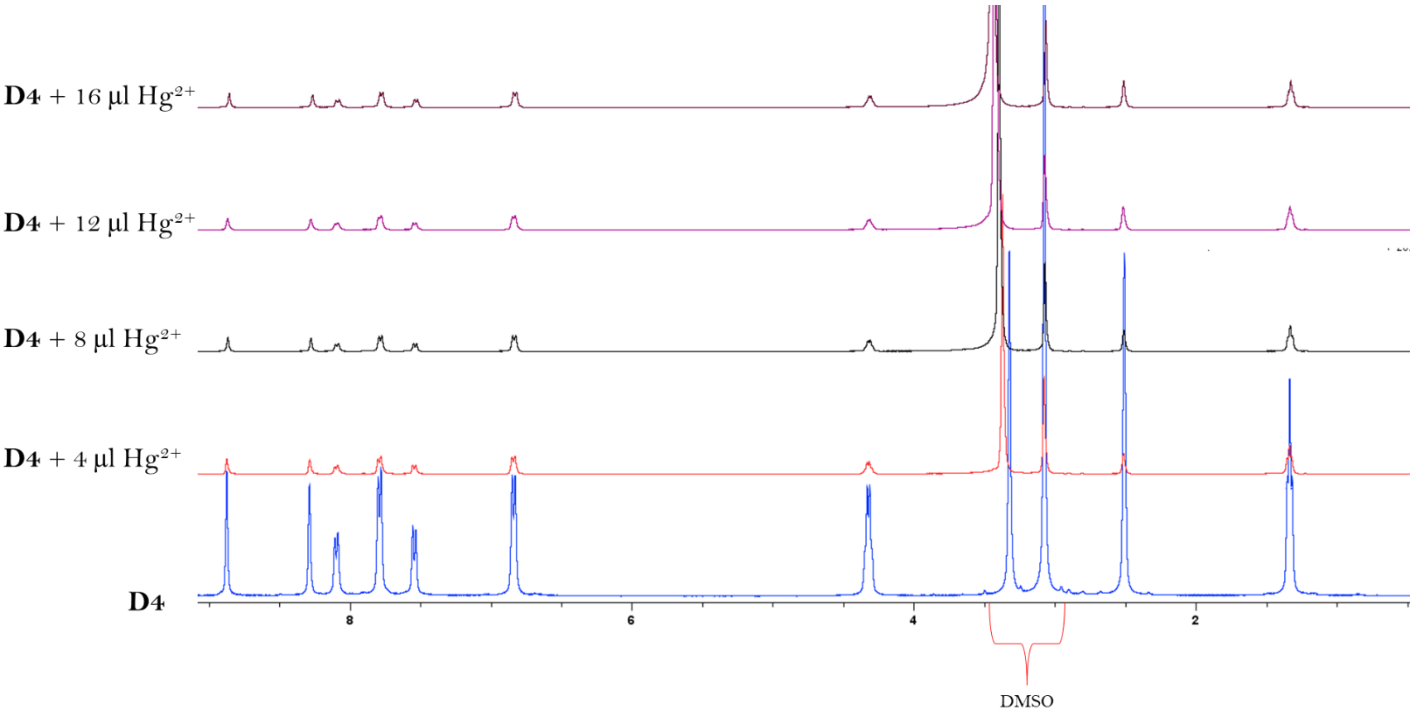

Figure 34: ^{1}H NMR titration of **D4** with $Hg(NO_3)_2$ in d_6-DMSO.

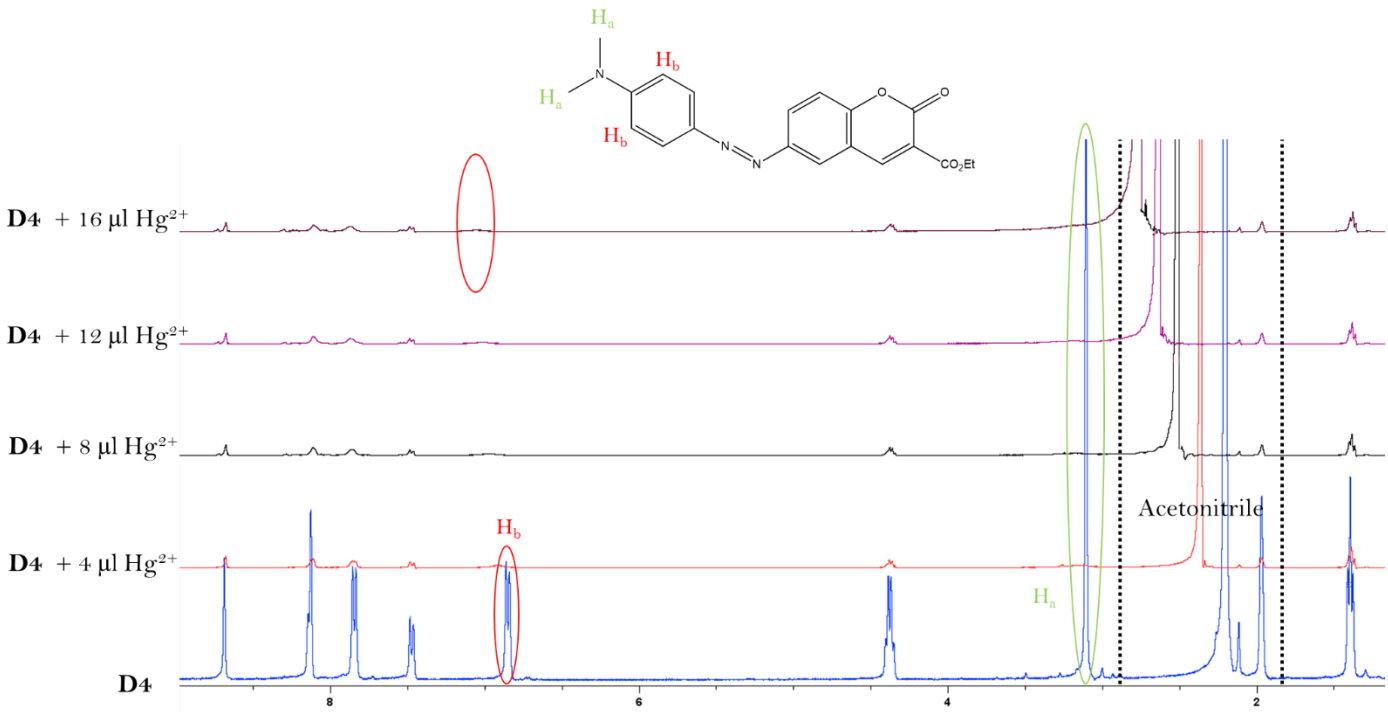

Figure 35: ^{1}H NMR titration of **D4** with $Hg(NO_3)_2$ in CD_3CN.

In the d_6-DMSO titration studies, additions of Hg^{2+} aliquots appeared to have no effect on any of the signal's ppm values in the proton spectrum. The peaks became less resolved and diminished in intensity as more Hg^{2+} was added. Conversely, titration studies conducted in CD_3CN displayed two unique proton responses upon Hg^{2+} addition. These signals were assigned to the protons residing on the substituted dimethylaniline derivative (labelled H_a and H_b). Upon Hg^{2+} addition, the peaks assigned to these protons become less resolved/disappear and display a minor shift compared to their original ppm value. Since metal complexation is not expected to occur at this site (see also Molecular orbital theory explanations), the effect of the NO_3^- counterion could be causing the observed effects to the dimethylaniline derivative.

Moreover, the titration analysis in both d_6-DMSO and CD_3CN resulted in different colour responses upon Hg^{2+} addition. This further supports the solvent dependency of analyte interaction. The changes in solution colour of **D4** before and after Hg^{2+} addition in d_6-DMSO and CD_3CN are shown in **Figure 36**. The d_6-DMSO experiment maintains the same orange colour before and after Hg^{2+} addition; whilst the solution colour changes from light orange to red in the CD_3CN titration experiment. This is the same colour change observed in the

UV-Vis screening and titration analysis previously reported. This leans towards the validity of the CD_3CN NMR titration experiments over that of d_6-DMSO.

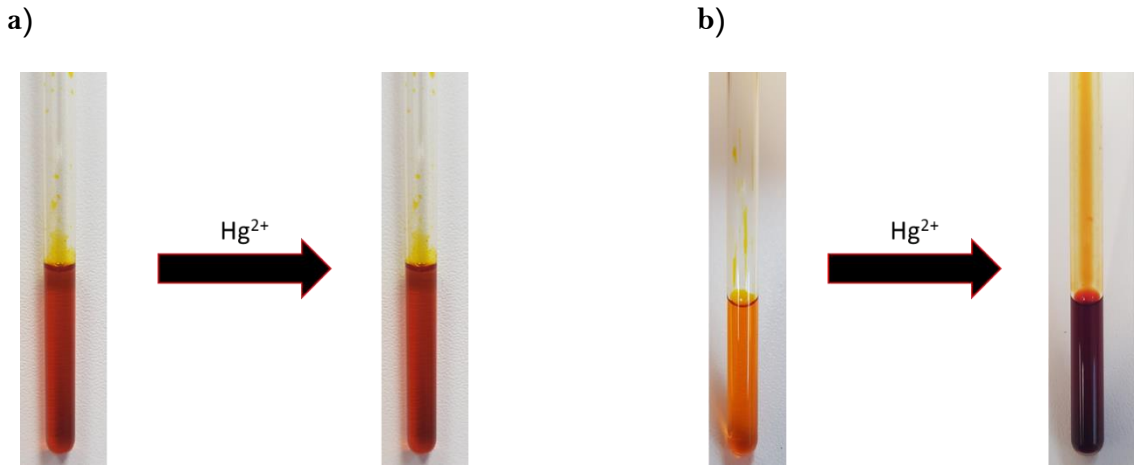

Figure 36: Colour response of **D4** upon Hg^{2+} addition in a) d_6-DMSO and b) CD_3CN.

The ^{13}C NMR titration experiments also showed different spectral responses in d_6-DMSO as compared to CD_3CN. The ^{13}C NMR titration experiments of **D4** with $Hg(NO_3)_2$ in d_6-DMSO is shown in **Figure 37**.

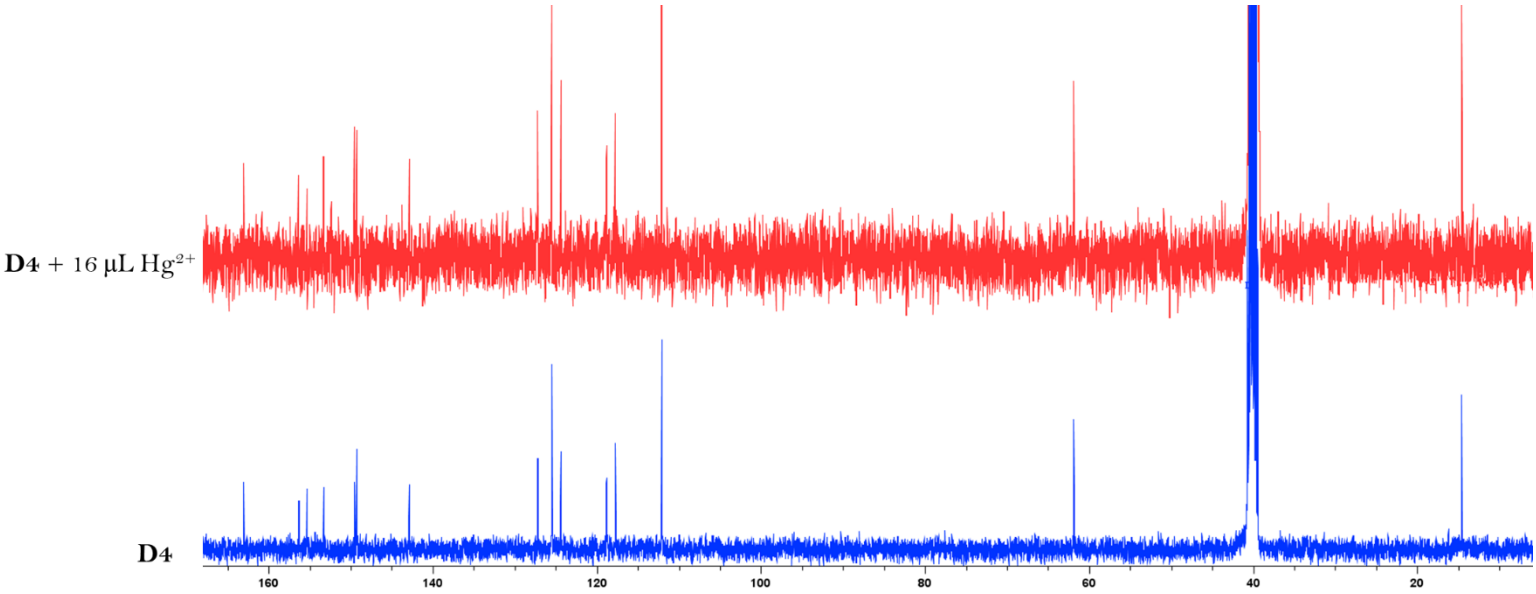

Figure 37: ^{13}C NMR titration study of **D4** with $Hg(NO_3)_2$ in d_6-DMSO.

Similar to the ^{1}H NMR titration experiments, the ^{13}C NMR titration experiments show different results with respect to the different solvent systems. Titration experiments in d_6-DMSO yielded no shift in any of the carbon signals after $Hg(NO_3)_2$ addition. These observations are also supported by the ^{1}H NMR titration experiments in this solvent.

Conversely, titration experiments of **D4** in CD_3CN show unique signal shifts after analyte introduction. To determine the postulated involvement of the azo functionality towards Hg^{2+} complexation; ^{15}N NMR experiments before and after analyte addition was conducted. Literature has reported the shift of the azo functionality to appear between 430-580 ppm.[58,59] Unfortunately, the ^{15}N NMR of **D4** displayed no signals in this range. This could be due to the low magnetogyric ratios of these atoms.[60] Therefore, a more in-depth analysis and possible binding site was proposed by ^{13}C NMR analysis.

The ^{13}C NMR titration analysis of **D4** with $Hg(NO_3)_2$ supports the complexation of Hg^{2+} with the substituted ester and coumarin carbonyl, and the nitrate counterion with the *N,N*-dimethylaniline substituent (**Figure 38**).

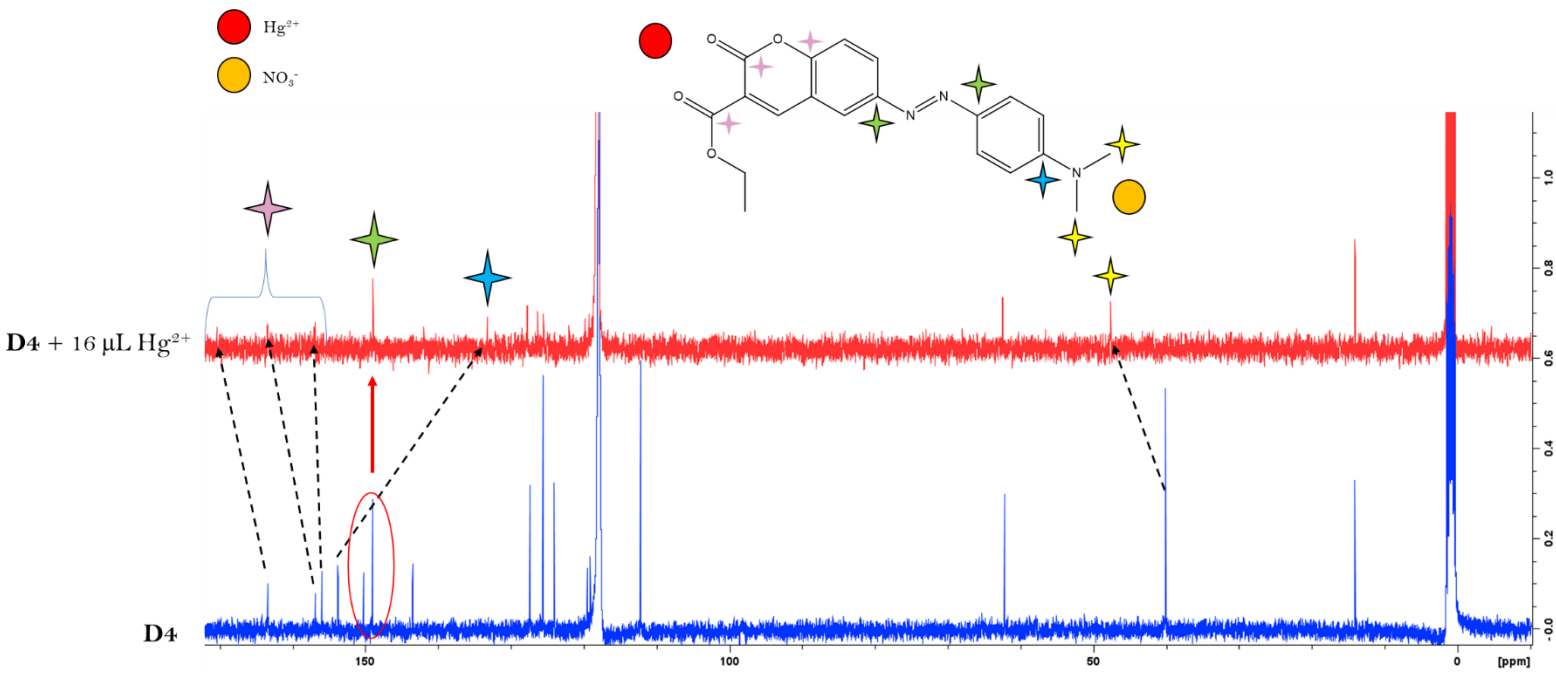

Figure 38: ^{13}C NMR titration analysis of **D4** with $Hg(NO_3)_2$ in CD_3CN.

Upon analyte addition, a minor shift in most of the peak signals was observed, however, four signals related to carbon atoms on the coumarin, and tertiary aniline derivatives displayed notable shifts. The signals relating to the aniline methyl groups in **D4** are observed as a single peak at 40 ppm. Upon proposed coordination with NO_3^-, a downfield shift of this signal to 48 ppm is observed. This deshielding of these respective methyl signals may be attributed to the hydrogen-bonding between the nitrate-oxygen and the methyl-proton atoms, thus withdrawing electron density from these carbon atoms. Conversely, the carbon signal related to the C-N bond observed at 154 ppm has experienced an upfield shift to 133 pm. This indicates a migration in electron density towards this carbon atom, facilitating this observed shielding. Electron density is postulated to be drawn away from the two neighbouring hydrogen atoms, resulting in the observable shift and decrease in intensity seen in the ^1H NMR titration experiments. The two signals for the azo C-N connectivity from the coumarin scaffold and substituted aniline derivative are observed at 150 and 148 ppm respectively. Upon complexation, both signals appear to merge into a singular peak at 149 ppm. If the complexation of Hg^{2+} occurred on the azo N=N bond, a greater shift in these respective signals would be expected. The proposed involvement of the carbonyl functionalities towards Hg^{2+} complexation was observed by the deshielding and subsequent shift in both peak values from 157 and 163 ppm to 163 and 174 ppm respectively. The comparatively small shift in ppm value suggests that coordination with Hg^{2+} is assisted by solvent and water molecules. The observed deshielding is indicative of the shift in electron density from the carbonyl oxygen atoms to the Hg^{2+} orbitals. It is postulated that the lone pair of electrons on the oxygen atoms are involved in coordination, resulting in a less noticeable shift than donation from the C=O π-bond.

FT-IR spectral analysis of the solid **D4**-Hg^{2+} complex strongly suggested the involvement of the carbonyl functionalities towards Hg^{2+} complexation, and the coordination of NO_3^- with the *N,N*-dimethylaniline substituent (**Figure 39**). Furthermore, the FT-IR showed evidence of a tautomeric form of **D4** by which the C-N connection of the dimethylaniline derivative can isomerize between a single- and double-bond via the lone electron pair on the nitrogen atom. As a result, the % transmittance of the signal pertaining to the C=N tautomer decreases drastically upon NO_3^- addition due to the involvement of the nitrogen lone pair towards coordination. In **D4**, the signals at 1740 and 1694 cm^{-1} are due to the C=O vibrations. The tautomeric C=N vibration of the dimethylaniline derivative is observed at 1599 cm^{-1}. The azo N=N stretching is assigned at 1355 cm^{-1} whilst the C-N vibrations of the azo nitrogen connectivity to the coumarin and aniline derivatives, and the C-N vibration from the aniline

derivative is registered at 1235 cm^{-1}. Upon complexation, the signals pertaining to the C=O and C=N functionalities showed a drastic reduction in % transmittance. The two new absorbance bands between 3000-3500 cm^{-1} and 1000-1500 cm^{-1} are suggested to arise due to the absorption of water, acetonitrile, and nitrate onto **D4**.[61] Additionally, the new signal observed at 522 cm^{-1} is indicative of metal-oxygen ν(M-O) interactions.[62,63]

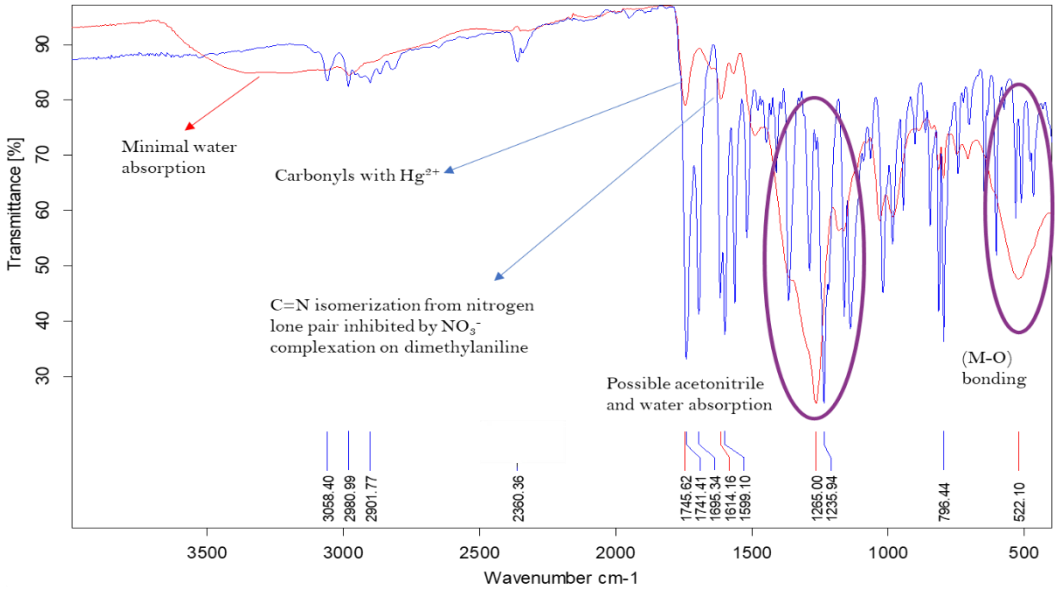

Figure 39: FT-IR spectral overlay of **D4** (blue) and the **D4**-Hg^{2+} metal complex (red).

Computational analysis confirmed the proposed binding site of Hg^{2+} and the NO_3^- counterion with **D4**. Calculations of the most preferred binding site agrees well with the conclusions determined by the NMR and FT-IR experiments. The most preferred binding site of both ions are shown in **Figure 40**. The most energetically preferred conformer of Hg^{2+} complexation involves the coumarin and ester carbonyl oxygen atoms; with complexation supported by nitrate and solvent molecules in a stable pseudo-6-membered ring conformation. This 6-membered ring coordination is not possible in a binding scenario involving the azo functionality alone, as no neighbouring donor groups are present to support complexation in a possible ring conformation. The binding of Hg^{2+} with these two carbonyl atoms is further presented in molecular orbital energy calculations and comparisons of **D4** with the **D4**-Hg^{2+} complex and the subsequent electronic transitions behind the spectral and visible coordination response. Moreover, the binding of NO_3^- with the dimethylaniline substituent was confirmed, accounting for the observable changes in the ^1H & ^{13}C NMR and FT-IR spectral analysis.

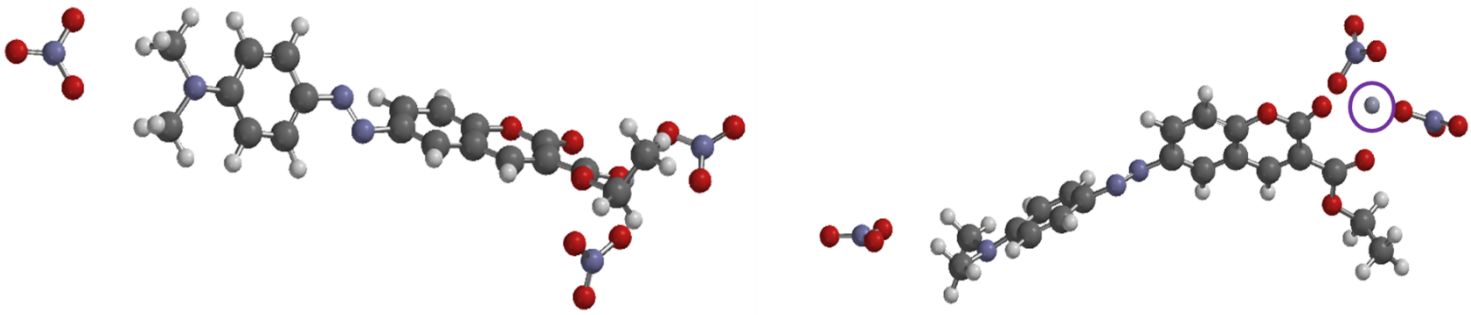

Figure 40: Computational calculations showing the optimized and most preferred binding site of Hg^{2+} and NO_3^- with **D4**. The Hg^{2+} cation is encircled in purple.

5.1.11 Molecular orbital energy diagrams of D3 and D4 and their respective Hg^{2+} metal complexes and related spectral responses

5.1.11.1 Studies with D3 and Hg^{2+}

Coumarin-imine sensor **D3** displays both absorbance and emission characteristics. The interaction with Hg^{2+} induces a minimal bathochromic shift in the absorbance spectrum, accompanied by a visible colour change from clear to a brighter yellow in water. The sensor was proposed to exhibit ICT characteristics due to the large extent of π-conjugation in the donor-π-acceptor (D-π-A) system. This arrangement is a poignant property for an effective ICT mechanism.[64] The molecular orbital energies and the position of the HOMO and LUMO of **D3** and the **D3**-Hg^{2+} complex is shown in **Figure 41**. Energies were calculated once the most stable conformer was determined, together with the complexation site of Hg^{2+} interaction. In **D3**, the HOMO resides around the substituted salicylaldehyde derivative; and the LUMO is observed around the coumarin scaffold. Therefore, electron density is shifted from the donor salicylaldehyde derivative towards the acceptor coumarin moiety through a conjugated system. The increase in electron density in the coumarin scaffold (fluorophore) may result in the observable fluorescent response, however, the effect of fluorescence is diminished owing to C=N isomerization discussed previously. In the **D3**-Hg^{2+} complex, the position of the LUMO now resides mostly around the imine functionality and neighbouring hydroxy group. In this way, the acceptor site of electron transfer has changed. This new

acceptor site of the **D3**-Hg^{2+} permits the observable colour change and bathochromic shift in wavelength upon metal complexation.

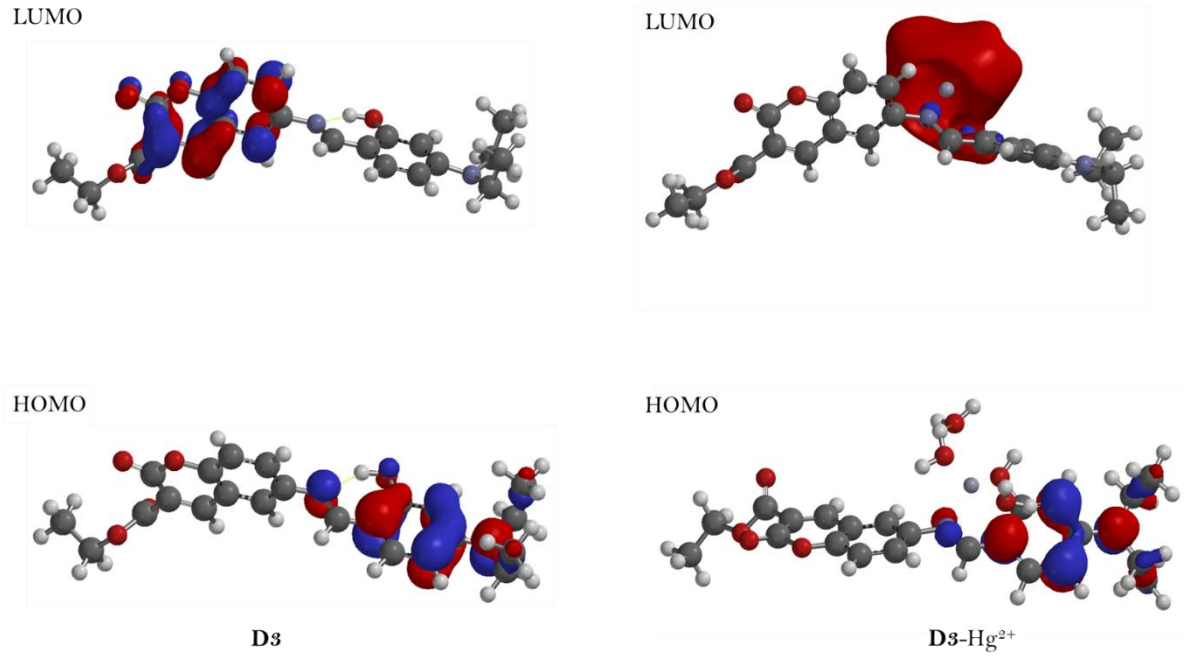

Figure 41: Molecular orbital arrangements of **D3** and the D3-Hg^{2+} complex.

It is proposed that the coordination between **D3** and Hg^{2+} could enhance the π-delocalization, thereby reducing the energy of the π-π* transitions accounting for the visible colour change and bathochromic shift.[65] This shift in absorbance wavelength is proposed to be due to analyte interaction with the acceptor unit in the D-π-A conjugated system. Upon complexation, the electron withdrawing character of the acceptor unit increases, leading to a bathochromic (red-shift) in the absorbance spectrum.[66–68] If complexation occurred on the salicylaldehyde substituent (donor site), a hypsochromic (blue-shift) in absorbance wavelength would occur. The bathochromic shift and colour change after Hg^{2+} introduction is not as prominent for **D3** as it is for **D4**. This could infer that the interaction of **D3** with Hg^{2+} is not as strong as that of **D4**. This was previously shown from the values of the association constants (K_a) determined from the Benesi-Hildebrand plots. The interaction of **D4** with Hg^{2+} is stronger than that of **D3**, which could account for the reason as to why the bathochromic shift was not as great, nor the colour change as intense upon Hg^{2+} complexation with **D3**.

In addition to the ICT mechanism occurring in this system, the possibility of a ESIPT (excited-state intramolecular proton transfer) could be occurring simultaneously. ESIPT is prominent in systems where the imine and phenolic functionalities are in close proximity, promoting proton transfer.[69]

This weak fluorescent signal of **D3** at the excitation wavelength could be attributed to ESIPT *via* the enol-imine/keto-enamine tautomerism. Intramolecular hydrogen bonding between phenolic OH and the neighbouring N atom of the imine leads to the ESIPT process.[70,71] In the excited state, the capacity of the hydrogen donor and acceptor sites increases and promotes the ESIPT phenomenon through keto-enol tautomerism. During the proton transfer in the excited state, the keto form is stabilized relative to its enol-form, consequently resulting in emission with significant Stokes shift.[72,73] Moreover, the presence of electron-donating substituent tunes the redistribution of electron density which interplays the ESIPT phenomenon together with the ESICT (excited-state intramolecular charge transfer). The imine nitrogen and phenolic oxygen atoms distribute the lone pair electrons to Hg^{2+} reduces the emission of the coumarin moiety through disruption of the conjugated system. In this way, the mechanism of ESIPT in the excited state is prohibited through the binding of Hg^{2+} with the N and O donor atoms, together with the π-cloud of the coumarin and neighbouring salicylaldehyde derivative.[48] The normalized absorbance and emission of **D3** is shown in **Figure 42**. The Stokes shift was calculated to be 165 nm. This large shift favours the proposed ESIPT mechanism. Additionally, no spectral overlap is observed, negating the possibility of a FRET mechanism as described in **Chapters 2-4**. The proposed mechanism of complexation of **D3** with Hg^{2+} is shown in **Figure 43**.

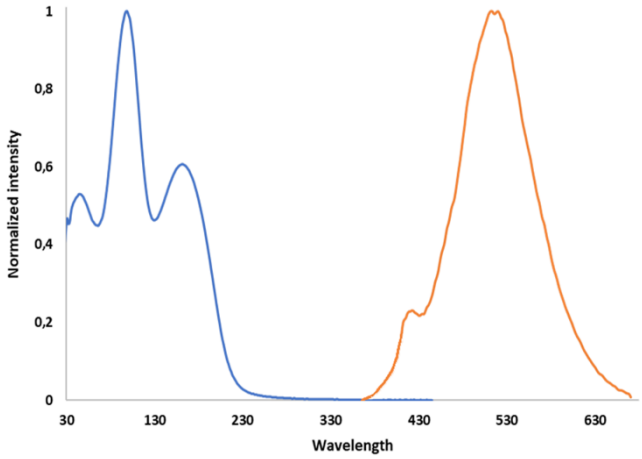

Figure 42: Normalized absorbance (blue) and emission (orange) spectra of coumarin-imine derivative **D3** in water.

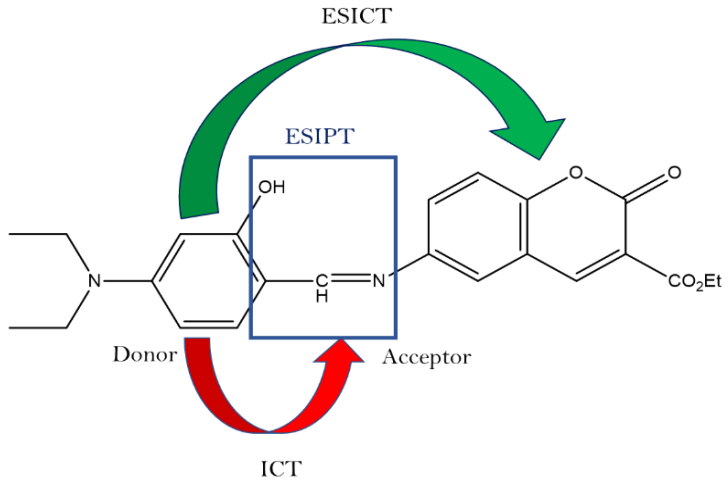

Figure 43: Possible mechanisms in **D3** and the **D3**-Hg^{2+} complex accounting for the observable UV and emission responses.

5.1.11.2 Studies with D4 and Hg^{2+}

Azo-derivative **D4** contains a strong push-pull π-conjugated electronic system with the coumarin moiety postulated as the acceptor (pull) species and the *N,N*-dimethylaniline derivative as the donor (push) species. In a similar fashion to that described for **D3**-Hg^{2+} complexation above, the D-π-A system together with the strong bathochromic shift and visible colour change leans towards an ICT mechanism.[74,75] This proposed mechanism for the **D4**-Hg^{2+} complexation scenario is shown in **Figure 44**.

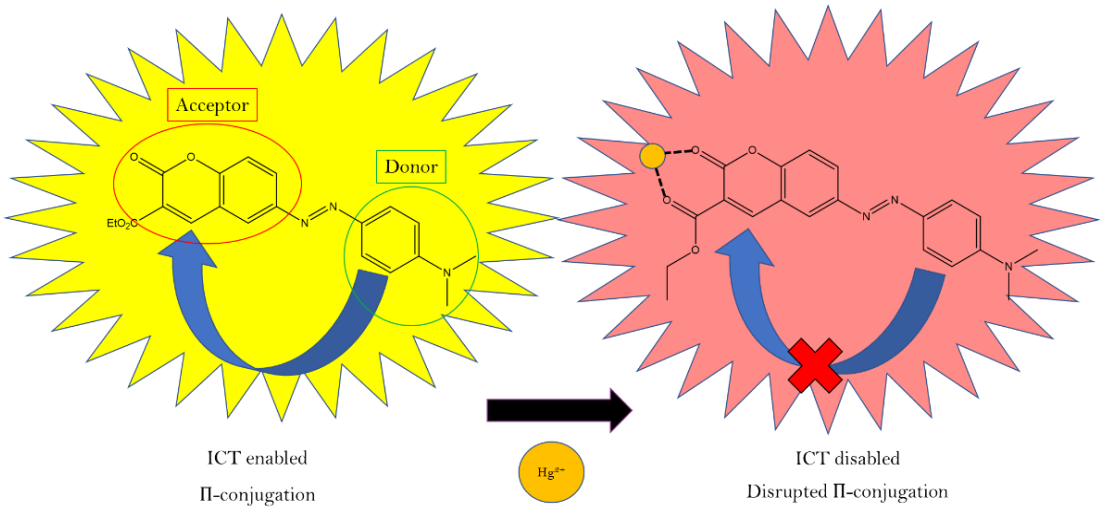

Figure 44: Proposed ICT mechanism of **D4**-Hg^{2+} complexation resulting in bathochromic shift from 422-520 nm and the observable colour change from yellow to red.

Moreover, the calculated HOMO and LUMO energies of **D4** and the **D4**-Hg^{2+} complex confirmed the spectral shift and resulting colour change. In an ICT mechanism, red-shift occurs when the energies of the HOMO and LUMO of the resulting sensor-analyte complex are lower in energy relative to that of free sensor. The HOMO and LUMO energy diagrams of **D4** and the **D4**-Hg^{2+} complex is shown in **Figure 45**. Evidently, the HOMO of **D4** resides on the substituted *N,N*-dimethylaniline and azo-group (donor unit) whilst the LUMO resides around the coumarin moiety and carbonyl of the 3-substituted ester functionality (acceptor unit). Therefore, the ICT from the *N,N*-dimethyl to the coumarin moiety is highly feasible. Upon complexation with the carbonyl groups of the coumarin and ester functionalities, an overall decrease in the orbital energies occurs, facilitating the strong spectral red-shift and rapid, naked-eye colour change upon Hg^{2+} complexation. Calculations were conducted once the most energetically preferred conformer of **D4** was confirmed.

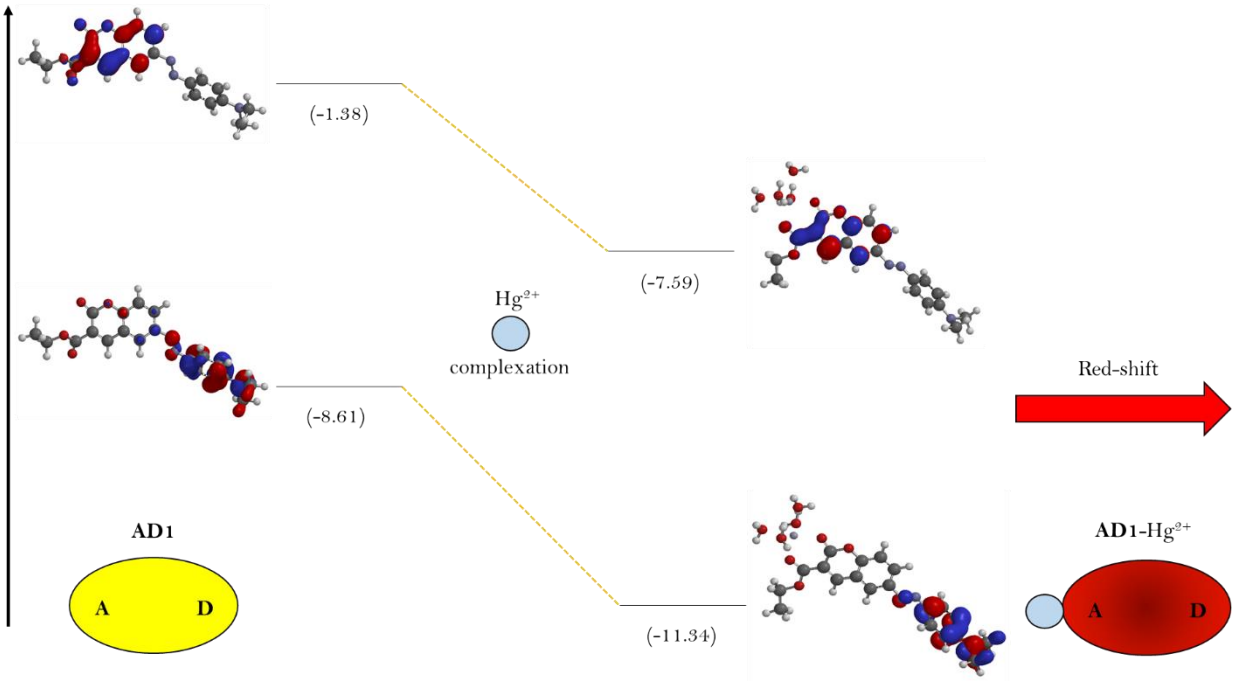

Figure 45: Calculated frontier orbital energy levels (eV) of the HOMO and LUMO of **D4** and the **D4**-Hg^{2+} complex.

5.1.12 Extended applications of D3 & D4 towards Hg^{2+} sensing strategies

Owing to the strong reversible nature of **D4** towards Hg^{2+} complexation with EDTA, a molecular logic gate and keypad lock was able to be constructed for extended applications outside of metal sensing strategies. Additionally, **D4** was able to be used for on-site assay studies as well as Hg^{2+} determination in environmental water sources. Although sensor **D3** did not display the same reversibility as **D4**, it was able to be used for Hg^{2+} determination in environmental water systems.

5.1.12.1 On-site assay studies of D4 with Hg^{2+}

Portable sensing methods for mercury detection and/or quantification warrants detection technologies that can be easily interpreted and manipulated by inexperienced personnel and general population. Given the many ways in which information can be related, optical readouts are among the easiest to interpret. Accordingly, detection based on a naked-eye colorimetric responses using inexpensive and disposable paper substrates are an attractive alternative to conventional analyte detection methods.[76] Cellulose, a large constituent of paper, contains numerous hydroxyl and carboxyl groups; thus, the surface of commonly used filter papers contains negatively charged adsorption sites. Therefore, they exhibit sorption potential for heavy metals.[77] However, there is a clear technological advantage of the laboratory equipment compared to on-site assay methods, however, equipment is usually heavy and non-portable. Therefore, techniques which are bound to the laboratory setting are at a disadvantage if to consider environmental monitoring and widespread on-line and on-site sensing.

To investigate the practical capabilities of **D4** towards on-site naked-eye Hg^{2+} determination, a cellulose paper-strip method was applied. To do this, strips of Whatman filter paper is exposed to a solution of **D4** (0.001 M) and then dried in air. A constant aliquot of different molar concentrations of Hg^{2+} (ranging from 3.7-37 μM) was added sequentially to individual test-strips. The prepared paper strips were orange in the absence of Hg^{2+}. Upon Hg^{2+} addition, visible naked-eye colour change from orange to pink was observed. The intensity of the colour increased as the concentration of the Hg^{2+} solution used increased. A visible colour change was observed from an Hg^{2+} concentration as low as 3.7 μM. Therefore, this solid- and

liquid-state sensing method offers simpler, cost-effective methods for naked-eye on-site detection of Hg^{2+} (**Figure 46**).

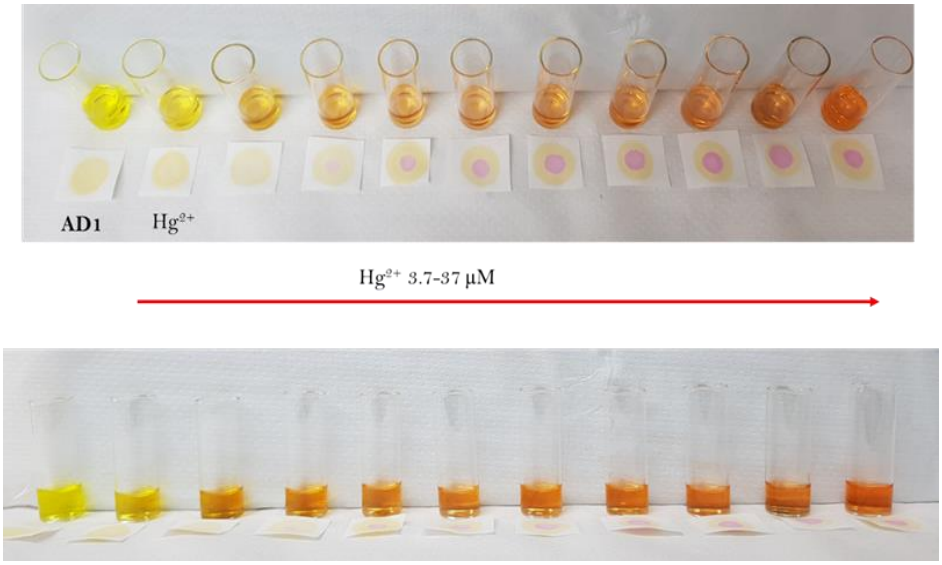

Figure 46: Photograph of the test strips and solutions of **D4** upon addition of increasing concentration of Hg^{2+}. Solutions in acetonitrile.

5.1.12.2 Quantitative determination of Hg^{2+} in real-world water samples

The practical applicability of sensors **D3** and **D4** were studied by collecting various water samples from different areas of the 'Swartkops' river system in the Eastern Cape Province of South Africa. Samples were collected from three different sites in the system, namely the upper (A), middle (B), and estuary (C) (**Figure 47**). The system is bordered by different residential suburbs, one of which is an informal settlement named Motherwell. Additionally, the river flows adjacent to numerous industrial sites and wastewater treatment works (WWTW's) located further upstream from where sampling was conducted. The introduction of competing cations, anions, and pollutants by anthropogenic and industrial activities into the water system has been investigated for many years. Poorly maintained WWTW's, polluted stormwater run-off and solid waste have all contributed to the deterioration in the water quality of the Swartkops river and estuary.

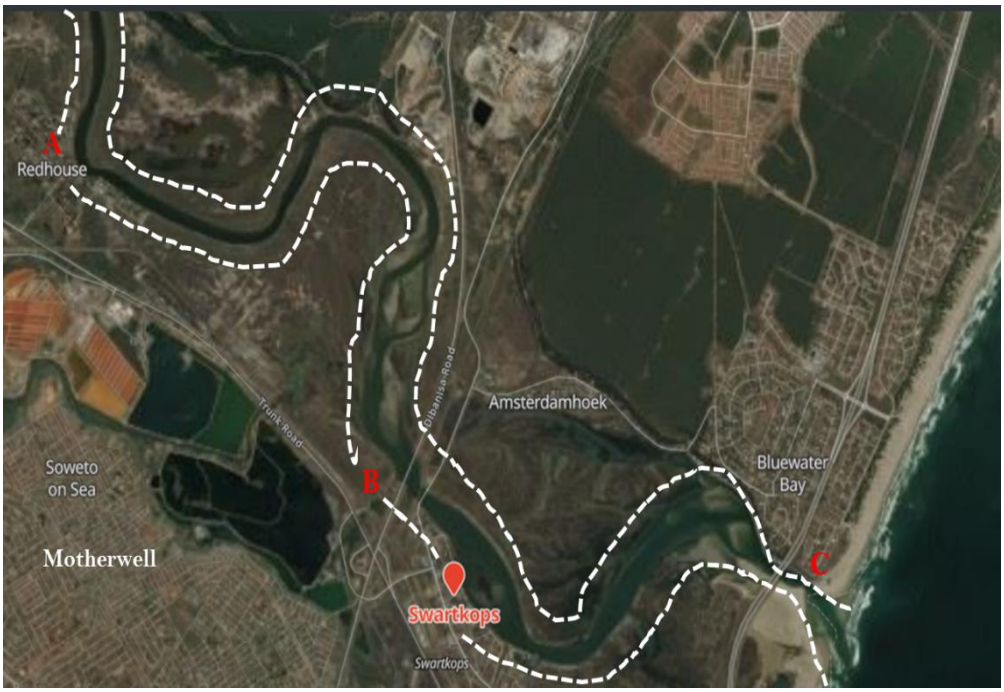

Figure 47: Sampling sites along the Swartkops river in the Eastern Cape, South Africa.

It has been reported that elevated levels of heavy metals in the sediment can be a good indication of anthropogenic activities. Studies have found concentrations of chromium, lead, zinc, titanium, manganese, strontium, copper, iron, and tin in the sediments of the Swartkops. Results indicated that the highest heavy metal concentrations (in both the river and mouth) were recorded where the runoff from the surrounding informal settlements and industrial sites entered the system.[78,79] The 'Motherwell Canal', which runs into the river, has been identified as a major source of nitrogen (particularly as NH_4^+). The river has also been found to contain phosphorus, with excessive inputs from the cumulative effect of three wastewater treatment plants upstream.[80]

Spike and recovery method was used to evaluate the concentration of Hg^{2+} in these three water samples. To conduct this experiment, a standard curve was calculated by spiking the solution of **D3** and **D4** with Hg^{2+} and measuring the resulting optical density. Absorbance values were determined in water and a 50:50 mixture (by volume) of CH_3CN:H_2O for **D3** and **D4** respectively. The suspended and insoluble particles were removed from the collected samples by means of a syringe-filter. To ensure a steady-state system, 50:50 (by volume) of the environmental water sample and acetonitrile was used for the recovery experiments with **D4**. Increasing concentrations of Hg^{2+} were added to the samples and the resulting absorbance intensity recorded. For each location (**A**, **B**, **C**) from which samples were collected, three duplicate spike and recover analyses were tested under analogous conditions. The real water sample analysis data for **D3** and **D4** is shown in **Table 1** and **Table 2** respectively.

The calculated recovery for the known amount of Hg^{2+} added was between 98-100% for both sensors. Results indicate that both sensors showed remarkable selectivity towards Hg^{2+} regardless of the presence of competing cations, anions, and soluble pollutants described above. Furthermore, the increase in salinity from upstream location '**A**' to mouth location '**C**' had little to no effect on the sensing capabilities and selectivity of both sensors towards Hg^{2+}. Henceforth, sensors **D3** and **D4** exhibit promising applications for mercury determination in real-world water samples.

Table 1: Detection of Hg^{2+} in real-world water samples with **D3**.

Sample	**Hg^{2+} spiked (μM)**	**Hg^{2+} recovered (μM) mean [(a)], ± SD[(b)]**	**% Recovery**
A (Upper)	**9.6**	9.548 ± 0.005	99.46
	19	18.987 ± 0.002	99.93
	28	27.997 ± 0.001	99.99
	37	36.904 ± 0.003	99.74
B (Middle)	**9.6**	9.586 ± 0.002	99.86
	19	18.882 ± 0.003	99.38
	28	27.986 ± 0.001	99.95
	37	36.878 ± 0.003	99.67
C (Estuary)	**9.6**	9.593 ± 0.005	99.93
	19	18.939 ± 0.002	99.68
	28	27.997 ± 0.001	99.99
	37	36.785 ± 0.002	99.42

[a] Mean of three measurements, [b] Standard deviation.

Table 2: Detection of Hg^{2+} in real-world water samples with **D4**.

Sample	Hg^{2+} spiked (μM)	Hg^{2+} recovered (μM) mean [a], ± SD[b]	% Recovery
A (Upper)	**0.95**	0.948 ± 0.005	99.84
	2.82	2.812 ± 0.002	99.71
	4.94	4.929 ± 0.003	99.79
	6.56	6.559 ± 0.003	99.99
B (Middle)	**0.95**	0.945 ± 0.006	99.53
	2.82	2.796 ± 0.006	99.17
	4.94	4.926 ± 0.003	99.71
	6.56	6.546 ± 0.002	99.79
C (Estuary)	**0.95**	0.940 ± 0.01	98.99
	2.82	2.818 ± 0.012	99.96
	4.94	4.938 ± 0.006	99.97
	6.56	6.491 ± 0.023	98.95

[a] Mean of three measurements, [b] Standard deviation.

Anionic sensing studies

5.1.13 UV-Vis screening studies of D3 and D4 towards various anions in organic and aqueous media

Owing to the selectivity and sensitivity that coumarin-imine and -azo compounds **D3** and **D4** displayed towards Hg^{2+} in their chosen solvent systems, these sensors were chosen for further analysis towards anionic sensing strategies in three solvent systems. The solvents used as the medium for screening studies included water, acetonitrile, and methanol. The anions chosen for the study included CN^-, SCN^-, SO_4^{2-}, NO_3^-, CH_3COO^-, I^-, Br^-, Cl^-, F^- and PF_6^-. These solutions were prepared in deionized water from their ammonium salts. Sensor **D3** showed a unique response towards CN^- in water; whilst **D4** displayed a singularly large enhancement in the absorbance intensity upon PF_6^- addition in acetonitrile. Both sensors displayed no unique response towards any of the anions in methanol. The screening studies of **D3** and **D4** in their respective solvents are illustrated in **Figure 48** (for the screening studies of **D3** in acetonitrile and methanol and **D4** in water and methanol, see **Appendix D Figures 13-16**).

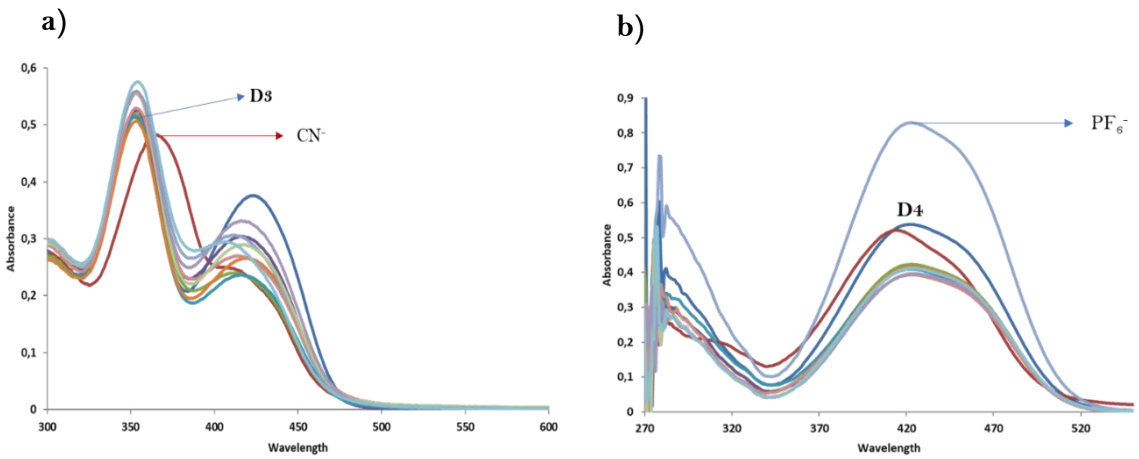

Figure 48: UV-Vis screening studies of a) **D3** and b) **D4** towards selected anions in water and acetonitrile respectively.

5.1.14 Competition studies of D3 and D4

Competition studies of **D3** with CN^- and **D4** with PF_6^- were conducted in water and acetonitrile respectively. As previously mentioned, **D3** displayed a unique response towards CN^- whilst **D4** exhibited an increase in absorbance intensity upon PF_6^- addition. The competition studies of **D3** and **D4** towards their respective anions in their solvent systems are shown in **Figure 49**.

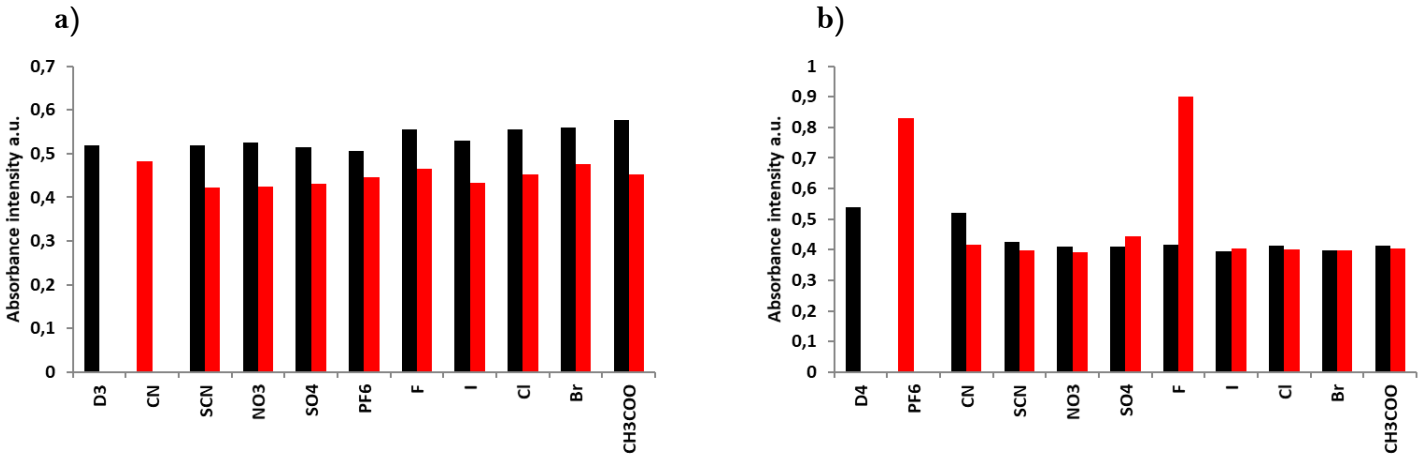

Figure 49: Competition studies of a) **D3** with CN^- and b) **D4** with PF_6^- in water and acetonitrile respectively.

Studies indicated that both sensors showed no affinity towards their preferred anions in the presence of competing analytes. Sensor **D4** only displayed selectivity towards PF_6^- in the presence of F^-. Evidently, the selectivity that both sensors exhibited towards Hg^{2+} cations is far superior to that shown towards anions.

5.1.15 Emission screening and competition studies of D3 towards various anions in water

As a result of the emission properties of **D3**, screening studies of this sensor towards a variety of anions was conducted in water to determine whether it displayed different affinities on the fluorescence spectrophotometer as compared to the UV-Vis. The screening studies of **D3** with the chosen analytes are shown in **Figure 50**. Sensor **D3** exhibited a large enhancing spectral response upon CN^- relative to the other analytes. The singularly "unique" response towards

CN^- was observed in both the absorbance and emission spectra. Competition studies of **D3** with CN^- were conducted owing to this large fluorescent enhancing response.

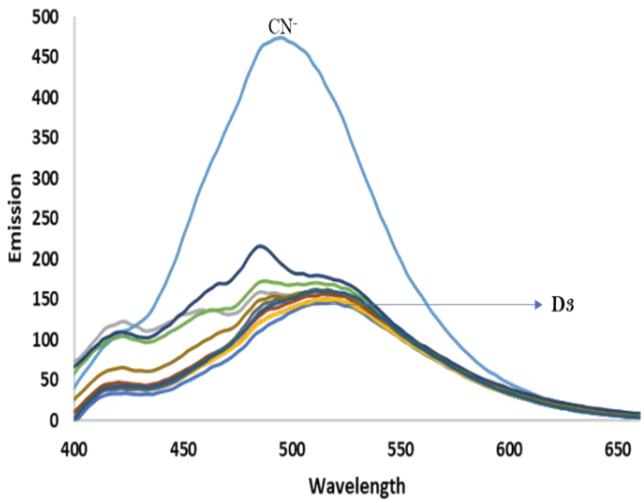

Figure 50: Fluorescent screening studies of D3 with selected anions in water. Excitation of 450 nm.

Selectivity studies of **D3** towards CN^- in the presence of competing anions was conducted in water (**Figure 51**). Sensor **D3** once again does not show the same level of selectivity towards CN^- as it showed towards Hg^{2+}. Moreover, the selectivity of **D3** towards CN^- did not change between the absorbance or emission studies. Owing to the poor selectivity both **D3** and **D4** displayed towards anionic species, further investigations were ceased.

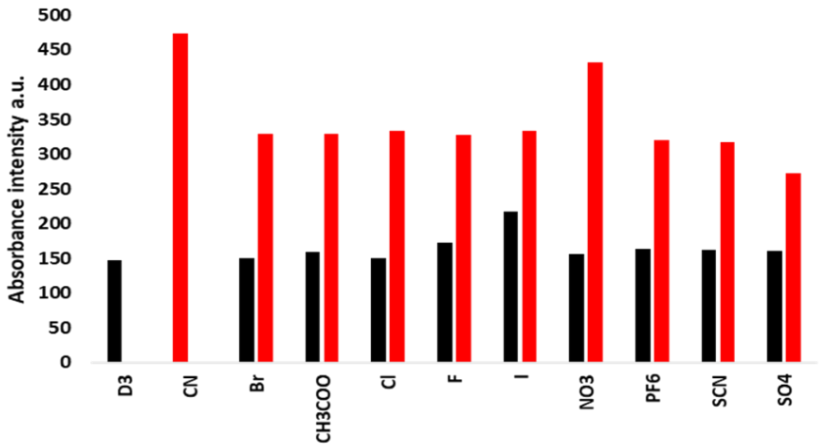

Figure 51: Competition studies of **D3** towards CN^- in the presence of competing anions in water. Excitation of 450 nm.

5.2 Conclusion

Herein, three coumarin-imine and a coumarin-azo based sensor(s) for the purpose of cationic and anionic recognition strategies in organic and aqueous media have been synthesized. Coumarin-imine based sensors **D1-3** were synthesized by a four-step procedure from the starting compound, whilst coumarin-azo derivative **D4** required an additional step. UV-Vis spectral analysis of all four sensors in a variety of solvents were investigated. Sensors **D3** and **D4** displayed the most desirable absorbance response in each solvent system. Both sensors were tested for their emission response in chosen solvent systems. Sensor **D4** displayed no fluorescent response in all chosen solvents; whilst **D3** showed a weak fluorescent response in water, attributed to C=N isomerization. The quantum yield (ϕ) of **D3** was determined to be 0.012. Progressing forward, both sensors were chosen for further cationic and anionic sensing strategies in their respective solvent systems. Coumarin-imine sensor **D3** displayed a strong UV spectral response towards Hg^{2+} in water with a visible colour change from clear to yellow; whilst coumarin-azo derivative **D4** also displayed a strong affinity towards Hg^{2+} characterized by a strong bathochromic shift in wavelength and a vivid colour change from yellow to red in acetonitrile. Competition studies of **D3** and **D4** with Hg^{2+} in their respective solvent systems yielded a high degree of selectivity towards Hg^{2+} in the presence of competing cations. Furthermore, both sensors showed good selectivity towards Hg^{2+} when all competing cations were present in solution. The detection limit of each sensor towards Hg^{2+} in their respective solvents was determined by UV-Vis titration analysis. The detection limits of **D3** and **D4** were calculated to be 0.74 and 0.24 μM respectively. The association constant (K_a) was determined by Benesi-Hildebrand analysis from the titration data. The association constants were determined to be 4.4 and 8.9 x 10^4 M^{-1} for **D3** and **D4** respectively. The linearity of the Benesi-Hildebrand plots suggested a 1:1 binding stoichiometry which was confirmed by Jobs plot analysis. Hydrogen potential studies (pH) of both sensors from pH of 2-14 indicated usability over a vast range. Reversibility studies of both sensors with hexadentate chelating agent EDTA was investigated. Sensor **D3** did not display adequate reversibility in the presence of EDTA; whilst **D4** exhibited complete reversibility denoted by a colour change from red to yellow. This complete reversibility of **D4** permitted the construction of an IMPLICATION type logic gate and the construction of a Molecular Keypad Lock system. Owing to the appreciable sensitivity and selectivity of **D3** and **D4** towards Hg^{2+}, both sensors were tested for their real-world water sampling strategies from a locally acquired water source. Spike and recovery methods were used for investigations.

Results indicate that both **D3** and **D4** can quantitatively detect Hg^{2+} in environmental water sources despite the presence of competing analytes and organic materials. Moreover, the vivid naked-eye interaction of Hg^{2+} permitted the construction of inexpensive on-site assay capabilities. The binding site of Hg^{2+} with **D3** and **D4** was investigated by ^{1}H, ^{13}C, ^{15}N NMR titration, and FT-IR spectral analysis of the free sensor and the sensor after the introduction of the metal cation. Results indicate that complexation of **D3** with Hg^{2+} occurs via a 6-membered ring conformation between the lone electron pairs of the imine nitrogen and neighbouring phenol functionality. Complexation between Hg^{2+} and **D4** was also found to occur via a stable 6-memebered ring conformation using the lone electron pairs from the coumarin carbonyl and neighbouring ester carbonyl functionalities. The complexation sites of both sensors with Hg^{2+} was confirmed by Molecular Modelling studies. The molecular orbital investigations of both sensors enabled the determination of the mechanism of the relative visible and emission spectral responses. Sensor **D4** exhibited ICT, ESIPT, and ESICT characteristics upon Hg^{2+} complexation; whilst **D4** exhibited strong ICT attributes. Anion screening studies with both sensors were investigated by UV-Vis in methanol, water, and acetonitrile. Sensor **D3** displayed a unique response towards CN^- in water; whilst **D3** exhibited a response towards PF_6^- in acetonitrile. Neither sensor displayed any affinity towards any anions in methanol. Competition studies of each sensor towards their chosen analyte was investigated. Results indicate very little selectivity towards the chosen analytes in the respective solvent systems. Owing to the emission properties of **D3**, screening and competition studies were conducted by fluorescent analysis. Results indicate an affinity towards CN^-, however, poor selectivity nullified further titration studies.

5.3 Experimental

5.3.1 Materials

Stock solutions of **D1-4** were prepared in methanol and diluted to a final concentration of 0.001 M. Deionized water was used to prepare the stock samples of the cations and anions. Cationic solutions were prepared from their nitrate salts (apart from Fe^{2+} which was prepared from its corresponding sulphate) whilst anionic solutions were prepared from their ammonium salts to a stock concentration of 0.01 and 0.1 M respectively.

Synthesis of coumarin derivatives 1, 1a, and 1b

The synthesis of coumarin derivatives **1**, **1a**, and **1b** was previously outlined in **Chapter 4 Experimental**.

Synthesis of coumarin-diazonium derivative 1c

To a cold aqueous solution of **1c** (4.3 mmol) in HCl (20 mL) and HOAc (5 mL), $NaNO_2$ (8.6 mmol) was added dropwise under continuous stirring for 2 hrs. This afforded the diazonium intermediate **1d** in situ.

Generalized synthesis of coumarin-imine derivatives D1-3

The generalized synthesis of coumarin-imine derivatives **D1-3** was carried out according to literature procedure.[81] Coumarin derivative **1b** (4.36 mmol) was added to a solution of the chosen aldehyde (4.36 mmol) in EtOH. The aldehydes chosen for synthesis included 2,4-dihydroxybenzaldehyde, 3-ethoxysalicylaldehyde, and 4-(diethylamino)salicylaldehyde to form coumarin-imine sensors **D1**, **D2**, and **D3** respectively. The solution was refluxed under stirring for 2 hrs. For sensor **D1**, the yellow solid precipitated from solution and was

monitored by NMR analysis. The compound was able to be used without further purification. After solvent removal under reduced pressure, **D2** and **D3** were precipitated by DCM and ether. The solids were monitored by NMR and TLC analysis and subsequently purified by column chromatography using an 80:20 hexane:ethyl acetate solution as eluent to afford pure products **D2** and **D3** as yellow solids. Sensors **D1-3** were synthesized in yields of 89%, 25%, and 23% respectively.

Sensor **D1**: ^{1}H NMR (400 MHz, d_6-DMSO) δ_H (ppm): 1.32 (s, 3H), 4.30 (d, 2H, *J* 6.64), 6.32 (s, 1H), 6.43 (d, 1H, *J* 7.16), 7.45 (m, 2H), 7.73 (d, 1H, *J* 7.8), 7.86 (s, 1H), 8.71(s, 1H), 8.81 (s, 1H), 10.33 (s, 1H), 13.14 (s, 1H). ^{13}C NMR (100 MHz, d_6-DMSO) δ_C (ppm): 14.51, 61.76, 102.86, 108,59, 112.49, 117.63, 118.59, 118.79, 122.22, 127.82, 134.90, 145.46, 148.82, 153.14, 156.37, 162.99, 163.21, 163.24, 163.74. IR ν_{max} (cm^{-1}): 3272 (OH), 3053-2900 (C-H), 2360 (HC-NH taut.), 1743 (C=O), 1617-1571 (HC=N), 1219 (C-O-C; C-N).

Sensor **D2**: ^{1}H NMR (400 MHz, d_6-DMSO) δ_H (ppm): 1.33 (m, 6H), 4.09 (d, 2H, *J* 6.72), 4.31 (d, 2H, *J* 6.92), 6.91 (t, 1H, *J* 7.48), 7.13 (d, 1H, *J* 7.56), 7.24 (d, 1H, *J* 7.08), 7.52 (d, 1H, *J* 8.56), 7.82 (d, 1H, *J* 8.48), 7.95 (s, 1H), 8.75 (s, 1H), 8.98 (s, 1H), 12.82 (s, 1H). ^{13}C NMR (100 MHz, d_6-DMSO) δ_C (ppm): 14.52, 15.23, 61.80, 64.65, 117.77, 118.74, 118.83, 119.30, 119.82, 122.68, 124.38, 128.03, 145.08, 147.52, 148.78, 151.09, 153.62, 156.33, 162.97, 164.70. IR ν_{max} (cm^{-1}): 3059-2878 (C-H), 2380 (HC-NH taut.), 1738 (C=O), 1623-1599 (HC=N), 1249 (C-O-C; C-N).

Sensor **D3**: ^{1}H NMR (400 MHz, d_6-DMSO) δ_H (ppm): 1.13 (s, 6H), 1.32 (s, 3H), 3.40 (d, 4H, *J* 6.12), 4.31 (d, 2H, *J* 6.32), 6.09 (s, 1H), 6.34 (d, 1H, *J* 8.28), 7.33 (d, 1H, *J* 8.36), 7.46 (d, 1H, *J* 8.48), 7.71 (d, 1H, *J* 8.44), 7.84 (s, 1H), 8.72 (d, 2H, combined signal), 13.27 (s, 1H). ^{13}C NMR (100 MHz, d_6-DMSO) δ_C (ppm): 13.00, 14.51, 44.42, 61.75, 97.27, 104.54, 108.97, 117.57, 118.54, 118.83, 121.72, 127.70, 134.75, 145.84, 148.89, 152.25, 152.71, 156.44, 162.76, 163.05, 163.43. IR ν_{max} (cm^{-1}): 3070-2971 (C-H), 2360 (HC-NH taut.), 1736-1705 (C=O), 1564-1517 (HC=N), 1240 (C-O-C; C-N).

Synthesis of coumarin-azo derivative D4

The reaction mixture containing diazonium derivative **1d** was added dropwise to a cold solution of *N,N*-Dimethylaniline (4.3 mmol) in 20 mL by volume EtOH:H_2O mixture and left

to stir at 0 °C for 2 hrs. The pH of the reaction mixture was adjusted using an ammonia solution to pH 5.5. A precipitate formed which was separated from the reaction by means of filtration. The crude product was monitored by TLC and subsequently purified by column chromatography using hexane:ethyl acetate 80:20 as eluent to afford the pure product **D4** as a bright orange solid (0.2108 g, 0.17 mmol, 32%). ^{1}H NMR (400 MHz, d_6-DMSO) δ_H (ppm): 1.33 (s, 3H), 3.08 (s, 6H), 4.32 (d, 2H, *J* 6.16), 6.86 (d, 2H, *J* 7.8), 7.56 (d, 1H, *J* 8.64), 7.81 (d, 2H, *J* 7.52), 8.12 (d, 1H, *J* 8.4), 8.31 (s, 1H), 8.89 (s, 1H). ^{13}C NMR (100 MHz, d_6-DMSO) δ_C (ppm): 14.53, 61.79, 112.02, 117.68, 118.72, 118.78, 124.32, 125.41, 127.14, 142.81, 149.19, 149.45, 153.21, 155.29, 16.24, 162.99. IR ν_{max} (cm^{-1}): 3059-2819 (C-H), 1740-1694 (C=O), 1599-1365 (N=N); 1235 (C-O).

5.4 References

(1) Alothman, A. A.; Albaqami, M. D.; Alshgari, R. A. Synthesis, Spectral Characterization, Quantum Chemical Calculations, Thermal Studies and Biological Screening of Nitrogen and Oxygen Donor Atoms Containing Azo-Dye Cu(II), Ni(II) and Co(II) Complexes. *J. Mol. Struct.* **2021**, *1223*, 128984. https://doi.org/10.1016/j.molstruc.2020.128984.

(2) Rafiee Samani, Z.; Mehranpour, A. Synthesis of New Allylidene Amino Phenol-Containing Schiff Bases and Metal Complex Formation Using Trimethinium Salts. *RSC Adv.* **2021**, *11* (35), 21695–21701. https://doi.org/10.1039/d1ra04214a.

(3) Nozha, S. G.; Morgan, S. M.; Ahmed, S. E. A.; El-Mogazy, M. A.; Diab, M. A.; El-Sonbati, A. Z.; Abou-Dobara, M. I. Polymer Complexes. LXXIV. Synthesis, Characterization and Antimicrobial Activity Studies of Polymer Complexes of Some Transition Metals with Bis-Bidentate Schiff Base. *J. Mol. Struct.* **2021**, *1227*, 129525. https://doi.org/10.1016/j.molstruc.2020.129525.

(4) Solmaz, A.; Ilter, Z.; Kaya, I. Synthesis, Characterization, Thermal Behavior, and Dielectric Properties of Methacrylate Polymers Containing Imine Bonding. *J. Electron. Mater.* **2021**, *50* (9), 5348–5358. https://doi.org/10.1007/s11664-021-09063-8.

(5) Celik, S.; Ozkok, F.; Ozel, A. E.; Cakir, E.; Akyuz, S. Synthesis, FT-IR and NMR Characterization, Antibacterial and Antioxidant Activities, and DNA Docking Analysis of a New Vanillin-Derived Imine Compound. *J. Mol. Struct.* **2021**, *1236*, 130288. https://doi.org/10.1016/j.molstruc.2021.130288.

(6) Mokhtari, N.; Khataei, M. M.; Dinari, M.; Hosseini Monjezi, B.; Yamini, Y. Imine-Based Covalent Triazine Framework: Synthesis, Characterization, and Evaluation Its Adsorption. *Mater. Lett.* **2020**, *263*, 127221. https://doi.org/10.1016/j.matlet.2019.127221.

(7) Abdullah, A. F.; Kadhim, M. M.; Naser, A. W. Novel Azo Compounds Syntheses from Sodium Saccharin Salt: Characterization and DFT Studies. *Mater. Today Proc.* **2021**. https://doi.org/10.1016/j.matpr.2021.04.522.

(8) Maroudas, A.; Pandis, P. K.; Chatzopoulou, A.; Davellas, L. R.; Sourkouni, G.; Argirusis, C. Synergetic Decolorization of Azo Dyes Using Ultrasounds,

Photocatalysis and Photo-Fenton Reaction. *Ultrason. Sonochem.* **2021**, *71*, 105367. https://doi.org/10.1016/j.ultsonch.2020.105367.

(9) Seyednoruziyan, B.; Zamanloo, M. R.; Esrafili, M. D.; Shamkhali, A. N.; Alizadeh, T.; Noruzi, S. Y-Shape Structured Azo Dyes with Self-Transforming Feature to Zwitterionic Form as Sensitizer for DSSC and DFT Investigation of Their Photophysical and Charge Transfer Properties. *Spectrochim. Acta - Part A Mol. Biomol. Spectrosc.* **2021**, *261*, 120062. https://doi.org/10.1016/j.saa.2021.120062.

(10) Vashisht, D.; Kaur, K.; Jukaria, R.; Vashisht, A.; Sharma, S.; Mehta, S. K. Colorimetric Chemosensor Based on Coumarin Skeleton for Selective Naked Eye Detection of Cobalt (II) Ion in near Aqueous Medium. *Sensors Actuators, B Chem.* **2019**, *280*, 219–226. https://doi.org/10.1016/j.snb.2018.10.020.

(11) Kaur, K.; Chaudhary, S.; Singh, S.; Mehta, S. K. An Azaindole-Hydrazine Imine Moiety as Sensitive Dual Cation Chemosensor Depending on Surface Plasmon Resonance and Emission Properties. *Sensors Actuators, B Chem.* **2016**, *222*, 397–406. https://doi.org/10.1016/j.snb.2015.07.072.

(12) Sıdır, İ.; Sarı, T.; Gülseven Sıdır, Y.; Berber, H. Synthesis, Solvatochromism and Dipole Moment in the Ground and Excited States of Substitute Phenol Derivative Fluorescent Schiff Base Compounds. *J. Mol. Liq.* **2021**, 16–26. https://doi.org/10.1016/j.molliq.2021.117075.

(13) B, M.; Bodke, Y. D.; R, S. kumar J.; N, L. T.; A, S. M. Novel Isoxazolone Based Azo Dyes: Synthesis, Characterization, Computational, Solvatochromic UV-Vis Absorption and Biological Studies. *J. Mol. Struct.* **2021**, *1244*, 130933. https://doi.org/10.1016/j.molstruc.2021.130933.

(14) Khadem Sadigh, M.; Zakerhamidi, M. S. Solvent Polarity Sensitive Characteristics of Various Tautomers of Azo Compounds: Linear and Nonlinear Optical Properties. *Spectrochim. Acta - Part A Mol. Biomol. Spectrosc.* **2020**, *239*, 118445. https://doi.org/10.1016/j.saa.2020.118445.

(15) Krawczyk, P.; Bratkowska, M.; Wybranowski, T.; Hołyńska-Iwan, I.; Cysewski, P.; Jędrzejewska, B. Experimental and Theoretical Insight into Spectroscopic Properties and Bioactivity of 4-(4-Formylbenzylidene)-2-Phenyloxazol-5(4H)-One Dye for Future Applications in Biochemistry. *J. Mol. Liq.* **2020**, *314*.

https://doi.org/10.1016/j.molliq.2020.113632.

(16) Sousa, R. R.; Silva, A. S. A.; Fernandez-Lafuente, R.; Ferreira-Leitão, V. S. Solvent-Free Esterifications Mediated by Immobilized Lipases: A Review from Thermodynamic and Kinetic Perspectives. *Catal. Sci. Technol.* **2021**, *11* (17), 5696–5711. https://doi.org/10.1039/d1cy00696g.

(17) de Melo, C. E. A.; Domínguez, M.; Rezende, M. C.; Machado, V. G. Solvatochromism of Dyes Inspired in Effenberger's Probe. *Dye. Pigment.* **2021**, *184* (May 2020). https://doi.org/10.1016/j.dyepig.2020.108757.

(18) Novák, M.; Foroutan-Nejad, C.; Marek, R. Solvent Effects on Ion-Receptor Interactions in the Presence of an External Electric Field. *Phys. Chem. Chem. Phys.* **2016**, *18* (44), 30754–30760. https://doi.org/10.1039/c6cp05781k.

(19) Li, X.; He, Y.; Xu, Y.; Zhang, X.; Zheng, M.; Zhao, H. 5-Nitrosalicylaldehyde in Aqueous Co-Solvent Mixtures of Methanol, Ethanol, Isopropanol and Acetonitrile: Solubility Determination, Solvent Effect and Preferential Solvation Analysis. *J. Chem. Thermodyn.* **2020**, *142*, 106014. https://doi.org/10.1016/j.jct.2019.106014.

(20) Upadhyay, A.; Kar, P. K.; Dash, S. A Spectrophotometric Study of Impact of Solvent, Substituent and Cross-Conjugation in Some 4-Aminoantipyrine Based Schiff Bases. *Spectrochim. Acta - Part A Mol. Biomol. Spectrosc.* **2020**, *233*, 118231. https://doi.org/10.1016/j.saa.2020.118231.

(21) Ray, A.; Sengupta, S.; Chattopadhyay, N. Concurrent Ground and Excited State Proton Transfer of (E)-2-((Napthalen-2-Ylimino)-Methyl)Phenol: Modulation in Micellar Media. *J. Photochem. Photobiol. A Chem.* **2019**, *371*, 433–443. https://doi.org/10.1016/j.jphotochem.2018.11.026.

(22) Panigrahi, S.; Biswal, S. P.; Misra, P. K. Disclosure of the Solvatochomism and the Reversal Switch in Some Tailor-Made Electron Push-Push Anils. *J. Mol. Liq.* **2021**, *329*, 115536. https://doi.org/10.1016/j.molliq.2021.115536.

(23) Tathe, A. B.; Sekar, N. Red Emitting Coumarin—Azo Dyes : Synthesis, Characterization, Linear and Non-Linear Optical Properties-Experimental and Computational Approach. *J. Fluoresc.* **2016**, *26* (4), 1279–1293. https://doi.org/10.1007/s10895-016-1815-2.

(24) Wang, C.; Zhang, S.; Huang, J.; Cui, L.; Hu, J.; Tan, S. Novel Designed Azo Substituted

Semi-Cyanine Fluorescent Probe for Cytochrome P450 Reductase Detection and Hypoxia Imaging in Cancer Cells. *RSC Adv.* **2019**, *9* (37), 21572–21577. https://doi.org/10.1039/c9ra02741f.

(25) Yoshino, J.; Kano, N.; Kawashima, T. Fluorescent Azobenzenes and Aromatic Aldimines Featuring an N-B Interaction. *Dalt. Trans.* **2013**, *42* (45), 15826–15834. https://doi.org/10.1039/c3dt51689j.

(26) Shao, J.; Lin, H.; Lin, H. A Novel Chromo- and Fluorogenic Dual Responding H2PO4- Receptor Based on an Azo Derivative. *Dye. Pigment.* **2009**, *80* (2), 259–263. https://doi.org/10.1016/j.dyepig.2008.07.012.

(27) Chen, S. Y.; Li, Z.; Li, K.; Yu, X. Q. Small Molecular Fluorescent Probes for the Detection of Lead, Cadmium and Mercury Ions. *Coord. Chem. Rev.* **2021**, *429*, 213691. https://doi.org/10.1016/j.ccr.2020.213691.

(28) Gupta, A.; Kumar, N. A Review of Mechanisms for Fluorescent "Turn-on" Probes to Detect Al^{3+} Ions. *RSC Adv.* **2016**, *6* (108), 106413–106434. https://doi.org/10.1039/c6ra23682k.

(29) Wei, T. B.; Zhang, P.; Shi, B. B.; Chen, P.; Lin, Q.; Liu, J.; Zhang, Y. M. A Highly Selective Chemosensor for Colorimetric Detection of Fe^{3+} and Fluorescence Turn-on Response of Zn^{2+}. *Dye. Pigment.* **2013**, *97* (2), 297–302. https://doi.org/10.1016/j.dyepig.2012.12.025.

(30) Bhatta, S. R.; Mondal, B.; Vijaykumar, G.; Thakur, A. ICT-Isomerization-Induced Turn-On Fluorescence Probe with a Large Emission Shift for Mercury Ion: Application in Combinational Molecular Logic. *Inorg. Chem.* **2017**, *56* (19), 11577–11590. https://doi.org/10.1021/acs.inorgchem.7b01304.

(31) Ludwanowski, S.; Hoenders, D.; Kalayci, K.; Frisch, H.; Barner-Kowollik, C.; Walther, A. Modular Functionalization and Hydrogel Formation: Via Red-Shifted and Self-Reporting [2+2] Cycloadditions. *Chem. Commun.* **2021**, *57* (6), 805–808. https://doi.org/10.1039/d0cc07429b.

(32) Dhamija, S.; De, A. K. Elucidating Contributions from Multiple Species during Photoconversion of Enhanced Green Fluorescent Protein (EGFP) under Ultraviolet Illumination. *Photochem. Photobiol.* **2021**, *222* (8). https://doi.org/10.1111/php.13409.

(33) Hemdan, Sokaina & Mansour, Asma & Ali, Fatma. (2019). Importance of isosbestic

point in spectroscopy: review. 62. 1-21.

(34) Ortone, V.; Matino, L.; Santoro, F.; Cinti, S. Merging Office/Filter Paper-Based Tools for Pre-Concentring and Detecting Heavy Metals in Drinking Water. *Chem. Commun.* **2021**, *57* (58), 7100–7103. https://doi.org/10.1039/d1cc02481g.

(35) Sharma, N.; Nigam, A.; Lobanov, D.; Gupta, A.; Novikov, A.; Kumar, M. Mercury (II) Ion Detection Using AgNWs-MoS2 Nanocomposite on GaN HEMT for IoT Enabled Smart Water Quality Analysis. *IEEE Internet Things J.* **2021**, *4662* (II), 1–8. https://doi.org/10.1109/JIOT.2021.3071382.

(36) Kan, C.; Wang, X.; Wu, L.; Shao, X.; Xing, H.; You, M.; Zhu, J. A Fluorescent Probe for Rapid Detection of Low Concentration Mercury Ions and Its Application in Biological Cells. *Anal. Methods* **2021**. https://doi.org/10.1039/d1ay01109j.

(37) Yang, L.; Li, M.; Ruan, S.; Xu, X.; Wang, Z.; Wang, S. Highly Efficient Coumarin-Derived Colorimetric Chemosensors for Sensitive Sensing of Fluoride Ions and Their Applications in Logic Circuits. *Spectrochim. Acta - Part A Mol. Biomol. Spectrosc.* **2021**, *255*. https://doi.org/10.1016/j.saa.2021.119718.

(38) Tripathy, M.; Subuddhi, U.; Patel, S. An Azo Dye Based D-π-A Chromogenic Probe for Selective Naked-Eye Detection of Hg^{2+} Ion: Application in Logic Gate Operation. *ChemistrySelect* **2020**, *5* (16), 4803–4815. https://doi.org/10.1002/slct.202000659.

(39) Bogireddy, N. K. R.; Barba, V.; Agarwal, V. Nitrogen-Doped Graphene Oxide Dots-Based "Turn-OFF" H_2O_2, Au(III), and "Turn-OFF-ON" Hg(II) Sensors as Logic Gates and Molecular Keypad Locks. *ACS Omega* **2019**, *4* (6), 10702–10713. https://doi.org/10.1021/acsomega.9b00858.

(40) Kumar, R.; Ravi, S.; Immanuel David, C.; Nandhakumar, R. A Photo-Induced Electron Transfer Based Reversible Fluorescent Chemosensor for Specific Detection of Mercury (II) Ions and Its Applications in Logic Gate, Keypad Lock and Real Samples. *Arab. J. Chem.* **2021**, *14* (1), 102911. https://doi.org/10.1016/j.arabjc.2020.11.017.

(41) Kabeer, H.; Hanif, S.; Arsalan, A.; Asmat, S.; Younus, H.; Shakir, M. Structural-Dependent N,O-Donor Imine-Appended Cu(II)/Zn(II) Complexes: Synthesis, Spectral, and in Vitro Pharmacological Assessment. *ACS Omega* **2020**, *5* (2), 1229–1245. https://doi.org/10.1021/acsomega.9b03762.

(42) Antić, A.; Bjelošević, D.; Brkić, K.; Cipurković, A.; Hasić, N.; Horozić, E.; Marić, S.;

Mujić, Z.; Pelemiš, K. Synthesis, Characterization and Bioactivity of Selected Metal Complexes with Imine Ligands. *Technol. Acta Sci. J. Chem. Technol.* **2020**, *13* (2), 39–42. https://doi.org/10.5281/zenodo.4540207.

(43) Joshi, N.; Gore, V.; Tekale, S.; Nawale, R.; Rajani, D.; Bembalkar, S. Synthesis and Biological Evaluation Study of New Bis-Imine Ligand and Metal Complexes. *Lett. Appl. NanoBioScience* **2020**, *10* (2), 2207–2214. https://doi.org/10.33263/lianbs102.22072214.

(44) M. Ibrahim, F.; M. Abdalhadi, S. Performance of Schiff Bases Metal Complexes and Their Ligand in Biological Activity: A Review. *Al-Nahrain J. Sci.* **2021**, *24* (1), 1–10. https://doi.org/10.22401/anjs.24.1.01.

(45) Siedzielnik, M.; Pantazis, D. A.; Bruniecki, J.; Kaniewska-Laskowska, K.; Dołęga, A. The Reactivity of the Imine Bond within Polynuclear Nickel(II) Complexes. *Crystals* **2021**, *11* (5), 1–15. https://doi.org/10.3390/cryst11050512.

(46) Asha, M. S.; Sangamesha, M. A.; Pinto, O.; Sandra, T. O.; Shaji, R. P. Synthesis and Characterization of Hetero Cyclic Imine and Its Metal Complexes for Anticorrosion Application. *Mater. Today Proc.* **2021**, *46*, 2436–2444. https://doi.org/10.1016/j.matpr.2021.01.356.

(47) Yildirim, S. Oksim-İmin Grubu İçeren. Metal Komplekslerinin Sentezi, Morfolojisi, Spektral Karakterizasyonu ve Termal Davranışları. *Erzincan Üniversitesi Fen Bilim. Enstitüsü Derg.* **2020**, *13* (3), 1263–1270. https://doi.org/10.18185/erzifbed.789893.

(48) Muthusamy, S.; Rajalakshmi, K.; Zhu, D.; Zhu, W.; Wang, S.; Lee, K. B.; Xu, H.; Zhao, L. Dual Detection of Mercury (II) and Lead (II) Ions Using a Facile Coumarin-Based Fluorescent Probe via Excited State Intramolecular Proton Transfer and Photo-Induced Electron Transfer Processes. *Sensors Actuators B Chem.* **2021**, *346* (August), 130534. https://doi.org/10.1016/j.snb.2021.130534.

(49) Kherrouba, A.; Bensegueni, R.; Guergouri, M.; Boulkedid, A. L.; Boutebdja, M.; Bencharif, M. Synthesis, Crystal Structures, Optical Properties, DFT and TD-DFT Studies of Ni (II) Complexes with Imine-Based Ligands. *J. Mol. Struct.* **2021**, *1247*, 131351. https://doi.org/10.1016/j.molstruc.2021.131351.

(50) Wang, L.; Qin, W.; Liu, W. A Sensitive Schiff-Base Fluorescent Indicator for the Detection of Zn^{2+}. *Inorg. Chem. Commun.* **2010**, *13* (10), 1122–1125.

https://doi.org/10.1016/j.inoche.2010.06.021.

(51) Asha, M. S.; Sangamesha, M. A.; Pinto, O.; Sandra, T. O.; Shaji, R. P. Synthesis and Characterization of Hetero Cyclic Imine and Its Metal Complexes for Anticorrosion Application. *Mater. Today Proc.* **2021**, *46*, 2436–2444. https://doi.org/10.1016/j.matpr.2021.01.356.

(52) Makki, S. Q.; Alhussein, N. M. A.; Tizkam, H. H.; Balakit, A. A. Highly Sensitive and Selective Colorimetric Sensor for Iron (II) Ion Detection Based on 4-Amino-Antipyrine Derivative. *AIP Conf. Proc.* **2020**, *2290*. https://doi.org/10.1063/5.0027459.

(53) El-Sonbati, A. Z.; Diab, M. A.; El-Bindary, A. A.; Nozha, S. G. Structural and Characterization of Novel Copper(II) Azodye Complexes. *Spectrochim. Acta - Part A Mol. Biomol. Spectrosc.* **2011**, *83* (1), 490–498. https://doi.org/10.1016/j.saa.2011.08.070.

(54) Pervaiz, M.; Sadiq, S.; Sadiq, A.; Younas, U.; Ashraf, A.; Saeed, Z.; Zuber, M.; Adnan, A. Azo-Schiff Base Derivatives of Transition Metal Complexes as Antimicrobial Agents. *Coord. Chem. Rev.* **2021**, *447*, 214128. https://doi.org/10.1016/j.ccr.2021.214128.

(55) Mahmoud, W. H.; Sayed, F. N.; Mohamed, G. G. Azo Dye with Nitrogen Donor Sets of Atoms and Its Metal Complexes: Synthesis, Characterization, DFT, Biological, Anticancer and Molecular Docking Studies. *Appl. Organomet. Chem.* **2018**, *32* (6), 1–19. https://doi.org/10.1002/aoc.4347.

(56) Turan, N.; Buldurun, K.; Adiguzel, R.; Aras, A.; Turkan, F.; Bursal, E. Investigation of Spectroscopic, Thermal, and Biological Properties of FeII, CoII, ZnII, and RuII Complexes Derived from Azo Dye Ligand. *J. Mol. Struct.* **2021**, *1244*. https://doi.org/10.1016/j.molstruc.2021.130989.

(57) Deghadi, R. G.; Mahmoud, W. H.; Mohamed, G. G. Metal Complexes of Tetradentate Azo-Dye Ligand Derived from 4,4′-Oxydianiline: Preparation, Structural Investigation, Biological Evaluation and MOE Studies. *Appl. Organomet. Chem.* **2020**, *34* (10), 1–20. https://doi.org/10.1002/aoc.5883.

(58) Marek, R.; Lycka, A.; Kolehmainen, E.; Sievanen, E.; Tousek, J. 15N NMR Spectroscopy in Structural Analysis: An Update (2001 - 2005). *Curr. Org. Chem.* **2007**, *11* (13), 1154–1205. https://doi.org/10.2174/138527207781662519.

(59) Thorn, K. A. ^{13}C and ^{15}N NMR Identification of Product Compound Classes from Aqueous and Solid Phase Photodegradation of 2,4,6-Trinitrotoluene; 2019; Vol. 14. https://doi.org/10.1371/journal.pone.0224112.

(60) Wiedemann, C.; Fushman, D.; Bordusa, F. ^{15}N NMR Studies Provide Insights into Physico-Chemical Properties of Room-Temperature Ionic Liquids. *Phys. Chem. Chem. Phys.* **2021**, *23* (21), 12395–12407. https://doi.org/10.1039/d1cp01492g.

(61) Algorithm, D.; Gan, F.; Wu, K.; Ma, F.; Du, C. In Situ Determination of Nitrate in Water Using Fourier Transform Mid-Infrared Attenuated Total Reflectance Spectroscopy Coupled With. **2020**, No. 2.

(62) Abass, B. F.; Musa, T. M. A.-D.; Aljibouri, M. N. Preparation and Spectroscopic Studies of Cadmium(II), Zinc(II),Mercury(II) and Vanadium(IV) Chelates Azo Ligand Derived from 4-Methyl-7-Hydroxycoumarin. *Indones. J. Chem.* **2021**, *21* (4), 912. https://doi.org/10.22146/ijc.63032.

(63) El-Wakiel, N. A.; Rizk, H. F.; Ibrahim, S. A. Synthesis and Characterization of Metal Complexes of Azo Dye Based on 5-Nitro-8-Hydroxyquinoline and Their Applications in Dyeing Polyester Fabrics. *Appl. Organomet. Chem.* **2017**, *31* (10), 1–10. https://doi.org/10.1002/aoc.3723.

(64) Seyednoruziyan, B.; Zamanloo, M. R.; Nasser Shamkhali, A.; Alizadeh, T.; Noruzi, S.; Aslani, S. Improving the Optoelectronic Efficiency of Novel Meta-Azo Dye-Sensitized TiO2 Semiconductor for DSSCs. *Spectrochim. Acta - Part A Mol. Biomol. Spectrosc.* **2021**, *247*, 119143. https://doi.org/10.1016/j.saa.2020.119143.

(65) Dhaka, G.; Jindal, G.; Kaur, R.; Rana, S.; Gupta, A.; Kaur, N. Multianalyte Azo Dye as an On-Site Assay Kit for Colorimetric Detection of Hg^{2+} ions and Electrochemical Sensing of Zn^{2+} Ions. *Spectrochim. Acta - Part A Mol. Biomol. Spectrosc.* **2020**, *229*, 117869. https://doi.org/10.1016/j.saa.2019.117869.

(66) Wan, J.; Zhang, X.; Zhang, K.; Su, Z. Biological Nanoscale Fluorescent Probes: From Structure and Performance to Bioimaging. *Rev. Anal. Chem.* **2020**, *39* (1), 209–221. https://doi.org/10.1515/revac-2020-0119.

(67) Chen, B.; Ni, S.; Sun, L.; Luo, X.; Zhang, Q.; Song, Y.; Zhong, Q.; Fang, Y.; Huang, C.; Chen, S.; Wu, W. Intramolecular Charge Transfer Tuning of Azo Dyes: Spectroscopic Characteristic and Third-Order Nonlinear Optical Properties. *Dye. Pigment.* **2018**, *158*,

474–481. https://doi.org/10.1016/j.dyepig.2018.05.063.

(68) Caricato, M.; Coluccini, C.; Vander Griend, D. A.; Forni, A.; Pasini, D. From Red to Blue Shift: Switching the Binding Affinity from the Acceptor to the Donor End by Increasing the π-Bridge in Push-Pull Chromophores with Coordinative Ends. *New J. Chem.* **2013**, *37* (9), 2792–2799. https://doi.org/10.1039/c3nj00466j.

(69) Tümay, S. O.; Şenocak, A.; Mermer, A. A "Turn-on" Small Molecule Fluorescent Sensor for the Determination of Al^{3+} Ion in Real Samples: Theoretical Calculations, and Photophysical and Electrochemical Properties . *New J. Chem.* **2021**, *45* (39), 18400–18411. https://doi.org/10.1039/d1nj03462f.

(70) Kumar, G.; Singh, I.; Goel, R.; Paul, K.; Luxami, V. Dual-Channel Ratiometric Recognition of Al^{3+} and F^{-} Ions through an ESIPT-ESICT Signalling Mechanism. *Spectrochim. Acta - Part A Mol. Biomol. Spectrosc.* **2021**, *247*, 119112. https://doi.org/10.1016/j.saa.2020.119112.

(71) Kanakala, M. B.; Yelamaggad, C. V. Exceptional Dual Fluorescent, Excited-State Intramolecular Proton-Transfer (ESIPT) Columnar Liquid Crystals Characterized by J-Stacking and Large Stokes Shifts. *J. Mol. Liq.* **2021**, *332*, 115879. https://doi.org/10.1016/j.molliq.2021.115879.

(72) Padalkar, V. S.; Seki, S. Excited-State Intramolecular Proton-Transfer (ESIPT)-Inspired Solid State Emitters. *Chem. Soc. Rev.* **2016**, *45* (1), 169–202. https://doi.org/10.1039/c5cs00543d.

(73) Zhu, T.; Hu, Y.; Chen, X.; Shao, H.; Chen, Z.; Zhang, H.; Liu, C. Novel Chromene-Derived Fluorescent Probe for Detection of Cyanides by Imine-Controlled ESIPT. *Dye. Pigment.* **2021**, *195*, 109693. https://doi.org/10.1016/j.dyepig.2021.109693.

(74) Özarslan, A.; Çakmaz, D.; Erol, F.; Şenöz, H.; Seferoğlu, N.; Barsella, A.; Seferoğlu, Z. Synthesis and Investigation of Photophysical, NLO and Thermal Properties of D-π-A-π-D Dyes. *J. Mol. Struct.* **2021**, *1229*. https://doi.org/10.1016/j.molstruc.2020.129583.

(75) Yadav, S. B.; Kothavale, S.; Sekar, N. Triphenylamine and N-Phenyl Carbazole-Based Coumarin Derivatives: Synthesis, Solvatochromism, Acidochromism, Linear and Nonlinear Optical Properties. *J. Photochem. Photobiol. A Chem.* **2019**, *382*, 111937. https://doi.org/10.1016/j.jphotochem.2019.111937.

(76) Ramesh, S.; Kumaresan, S. A Highly Selective Coumarin-Based Chemosensor for Naked-Eye Detection of Cyanide Anions via Nucleophilic Addition in Pure Aqueous Environment. *Microchem. J.* **2021**, *169*, 106584. https://doi.org/10.1016/j.microc.2021.106584.

(77) Ding, R.; Cheong, Y. H.; Ahamed, A.; Lisak, G. Heavy Metals Detection with Paper-Based Electrochemical Sensors. *Anal. Chem.* **2021**, *93* (4), 1880–1888. https://doi.org/10.1021/acs.analchem.0c04247.

(78) Binning, K.; Baird, D. Survey of Heavy Metals in the Sediments of the Swartkops River Estuary, Port Elizabeth South Africa. *Water SA* **2001**, *27* (4), 461–466. https://doi.org/10.4314/wsa.v27i4.4958.

(79) Gyedu-Ababio, T. K. Pollution Status of Two River Estuaries in the Eastern Cape, South Africa, Based on Benthic Meiofauna Analyses. *J. Water Resour. Prot.* **2011**, *03* (07), 473–486. https://doi.org/10.4236/jwarp.2011.37057.

(80) Adams, J. B.; Pretorius, L.; Snow, G. C. Deterioration in the Water Quality of an Urbanised Estuary with Recommendations for Improvement. *Water SA* **2019**, *45* (1), 86–96. https://doi.org/10.4314/wsa.v45i1.10.

(81) García-Beltrán, O.; Cassels, B. K.; Pérez, C.; Mena, N.; Núñez, M. T.; Martínez, N. P.; Pavez, P.; Aliaga, M. E. Coumarin-Based Fluorescent Probes for Dual Recognition of Copper(II) and Iron(III) Ions and Their Application in Bio-Imaging. *Sensors (Switzerland)* **2014**, *14* (1), 1358–1371. https://doi.org/10.3390/s140101358.

APPENDIX D

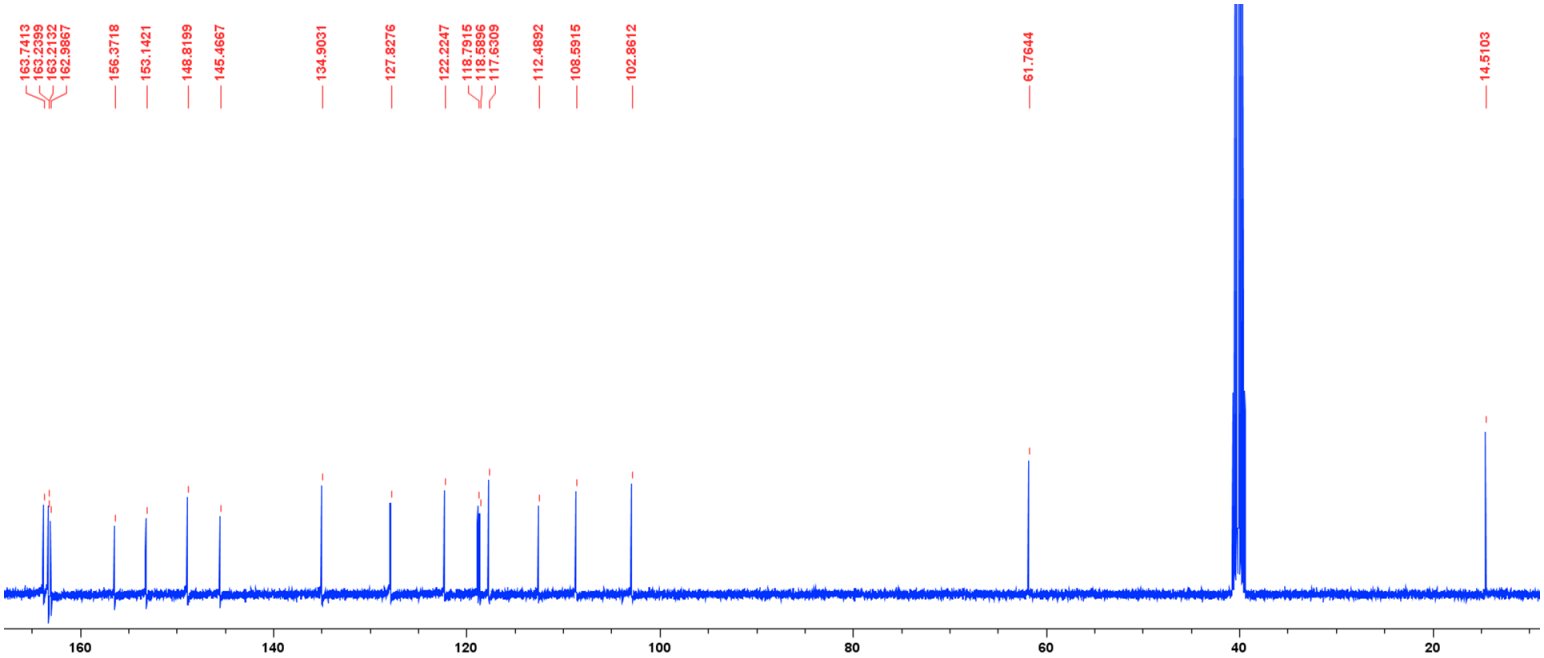

Figure 1: ^{13}C NMR spectra of coumarin-imine derivative **D1** in d_6-DMSO.

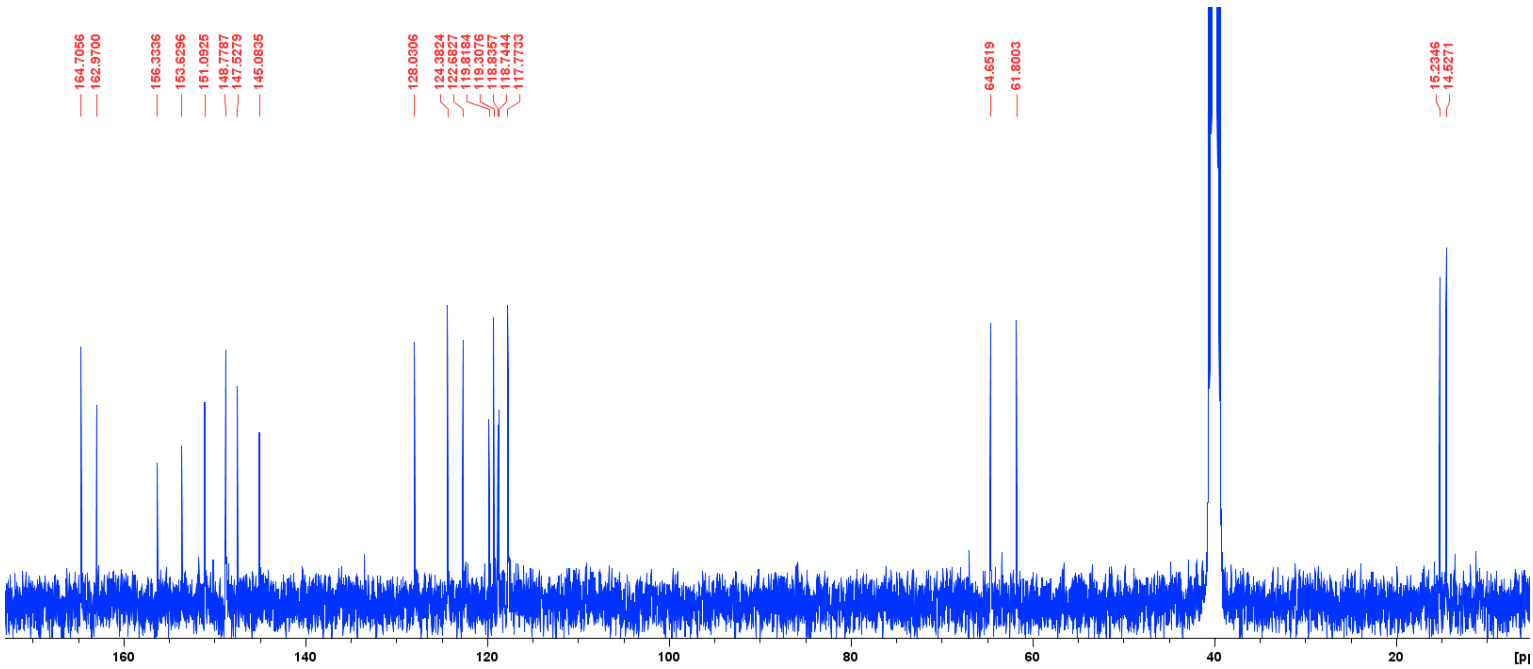

Figure 2: ^{13}C NMR spectra of coumarin-imine derivative **D2** in d_6-DMSO.

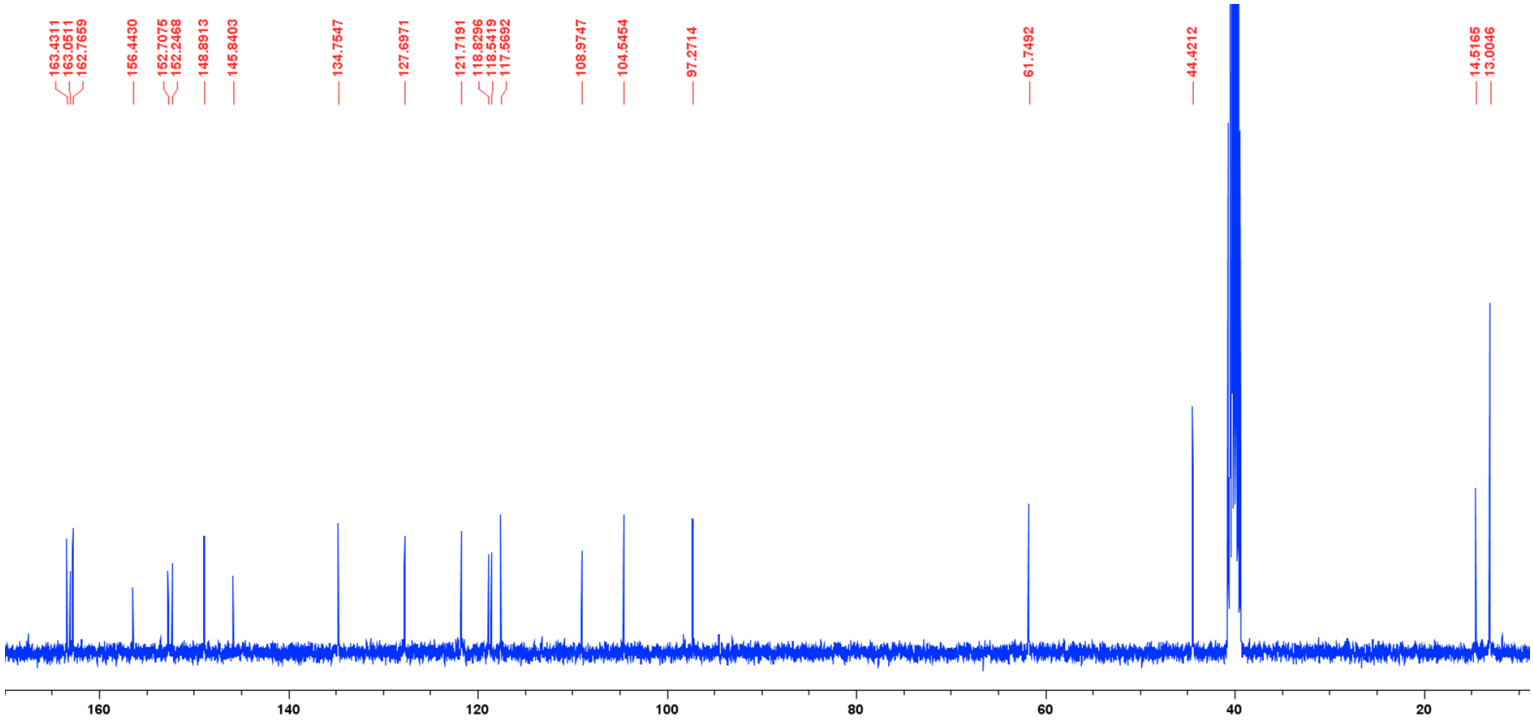

Figure 3: ^{13}C NMR spectra of coumarin-imine derivative **D3** in d_6-DMSO.

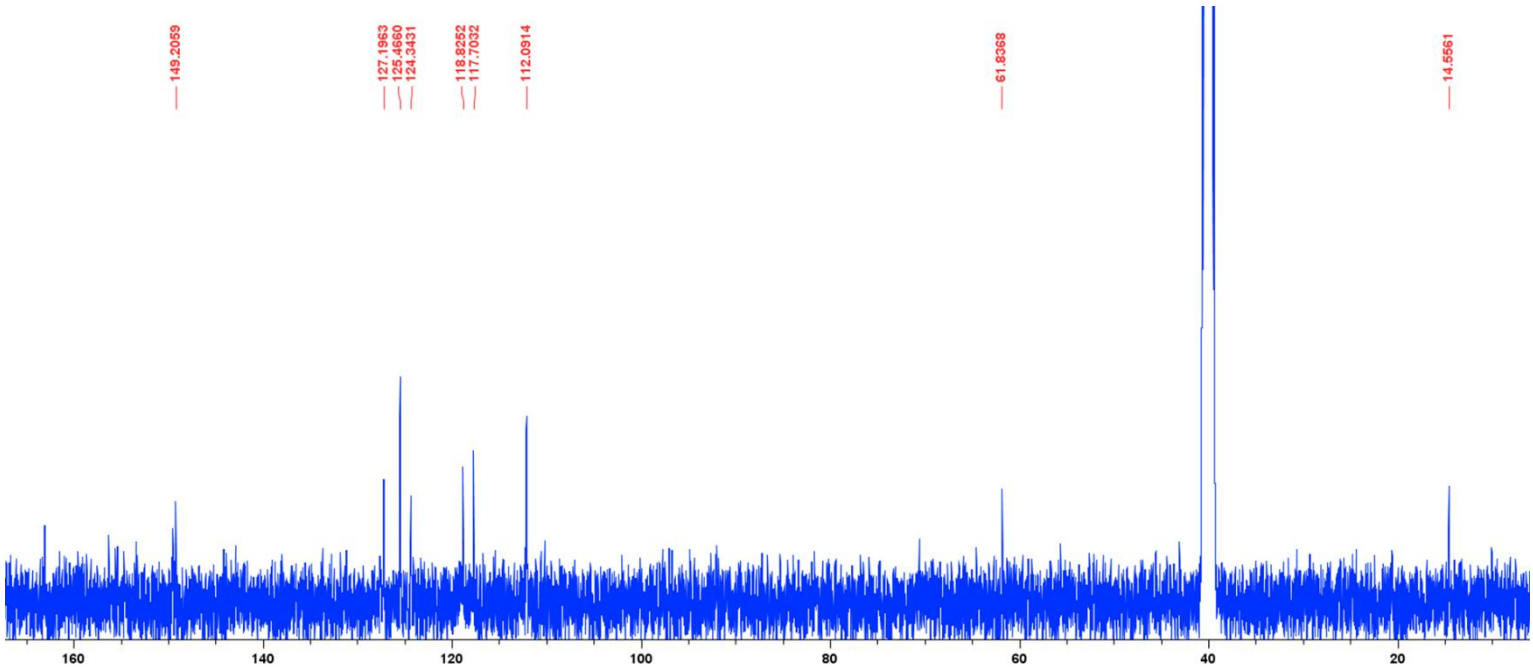

Figure 4: ^{13}C NMR spectra of coumarin-azo derivative **D4** in d_6-DMSO.

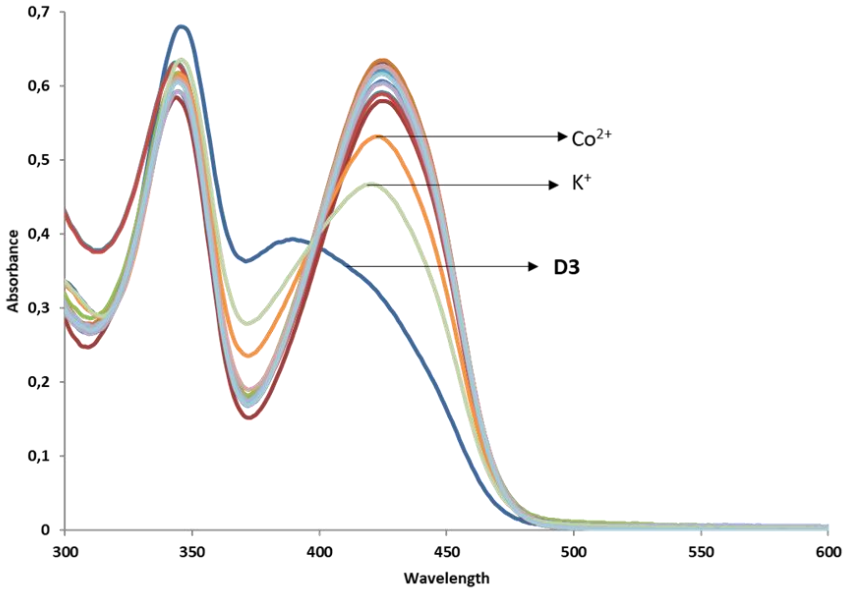

Figure 5: UV-Vis screening studies of **D3** with selected metal cations in acetonitrile.

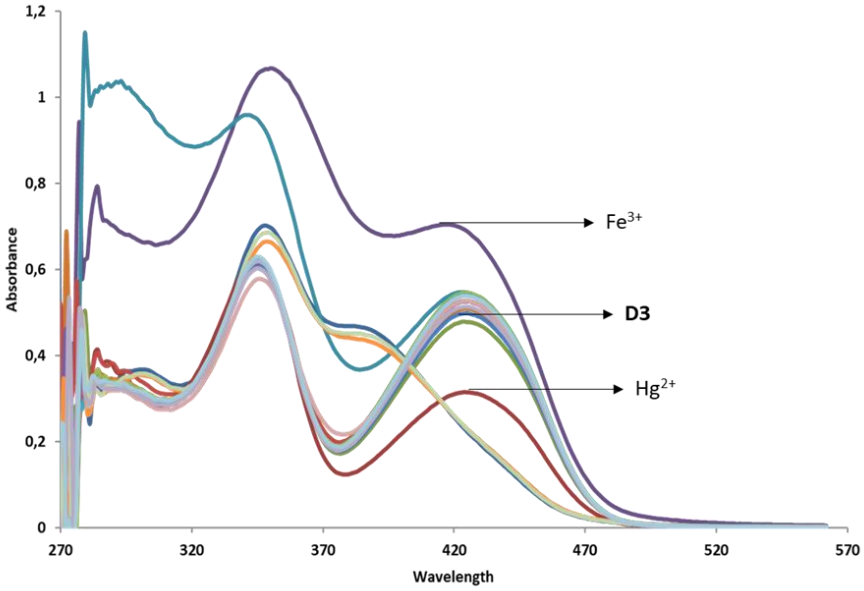

Figure 6: UV-Vis screening studies of **D3** with selected metal cations in MeOH.

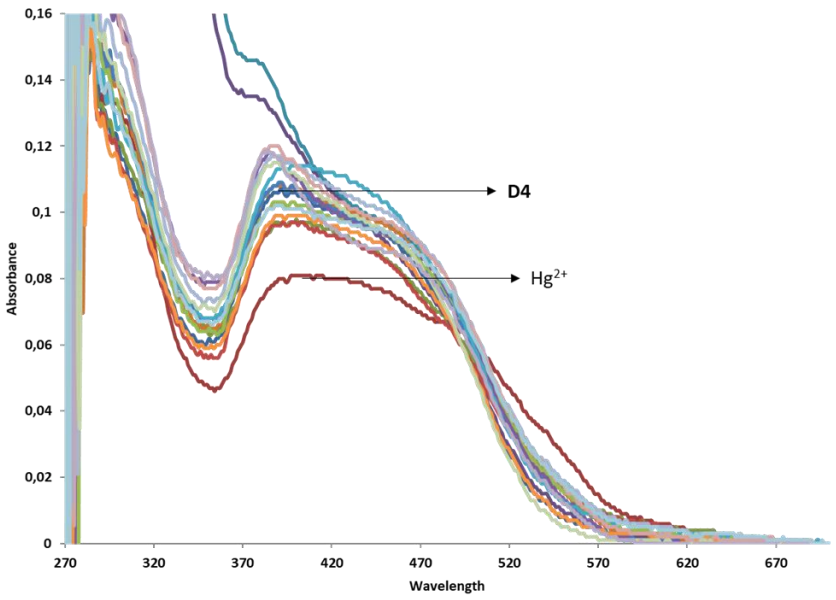

Figure 7: UV-Vis screening studies of **D4** with selected metal cations in water.

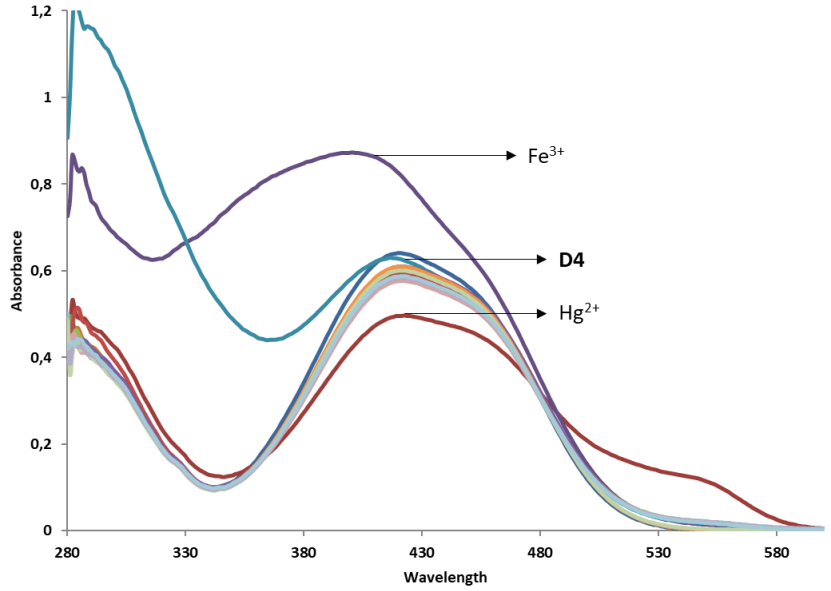

Figure 8: UV-Vis screening studies of **D4** with selected metal cations in MeOH.

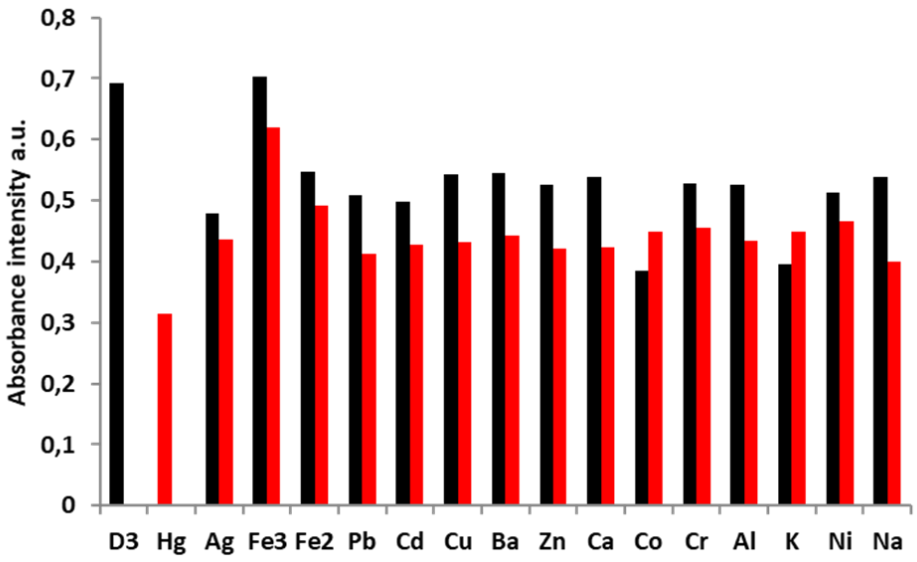

Figure 9: Selectivity studies of **D3** with Hg^{2+} in the presence of competing cations in MeOH.

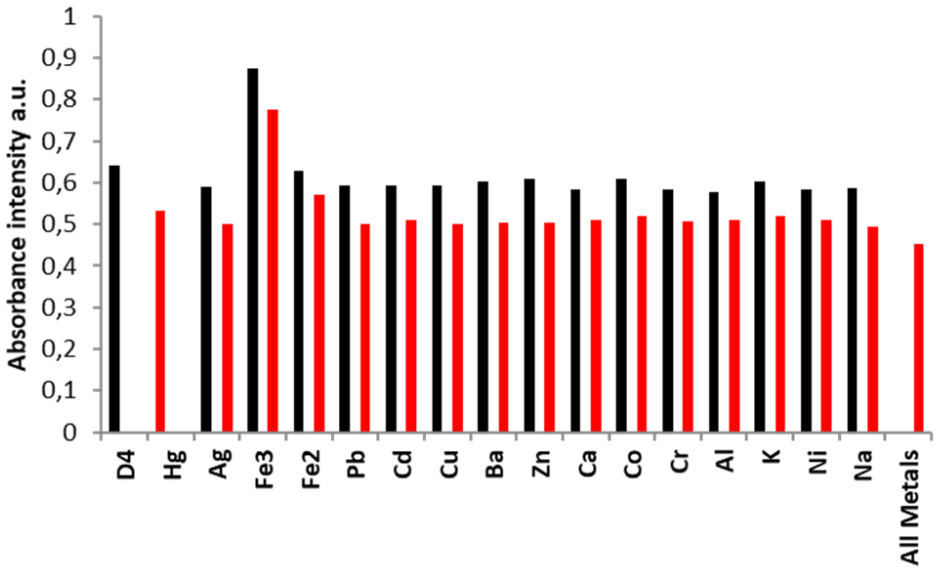

Figure 10: Selectivity studies of **D4** with Hg^{2+} in the presence of competing cations in MeOH.

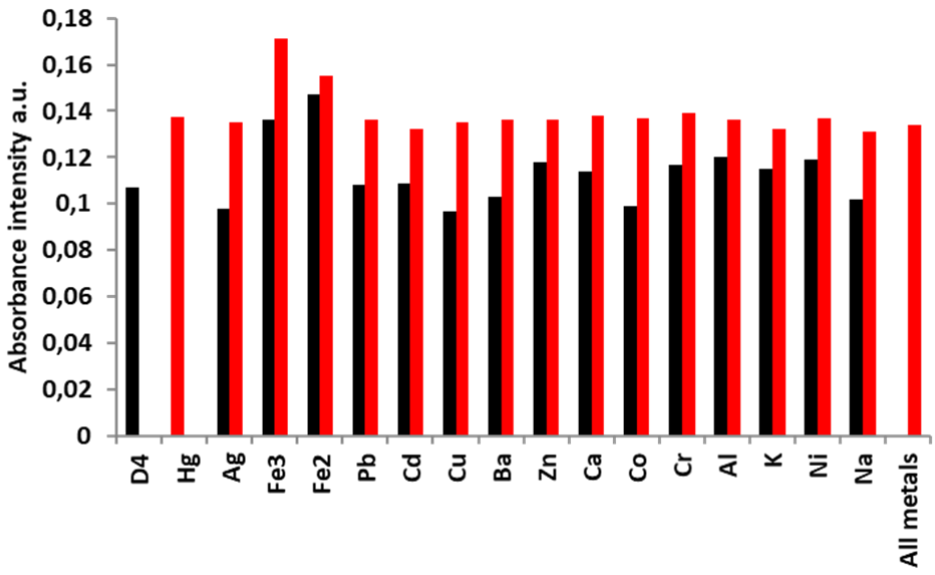

Figure 11: Selectivity studies of **D4** with Hg^{2+} in the presence of competing cation in water.

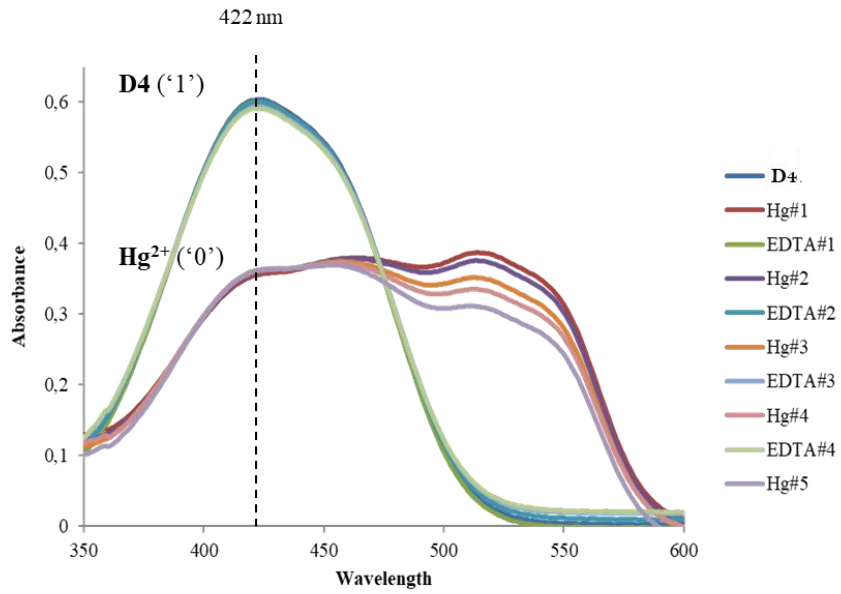

Figure 12: Cyclic titration of Hg^{2+} and EDTA with **D4** in acetonitrile.

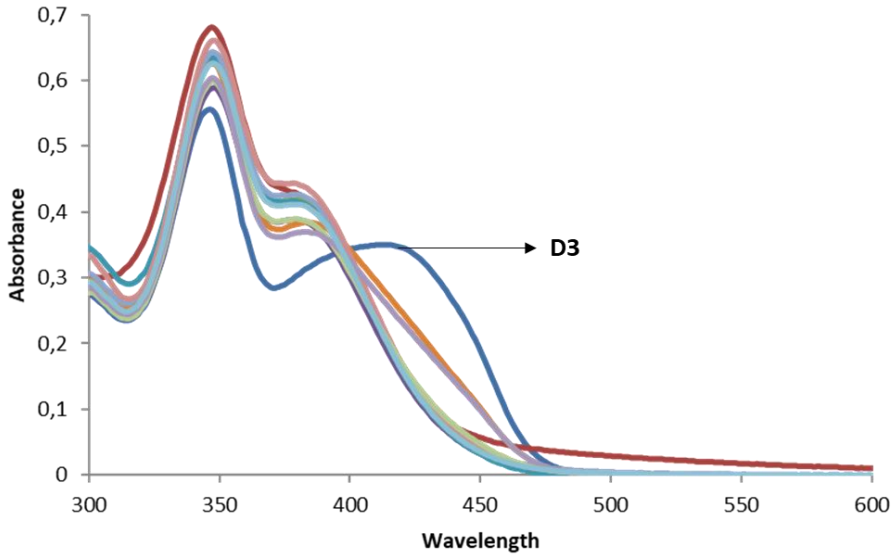

Figure 13: UV-Vis screening studies of **D3** with various anions in acetonitrile.

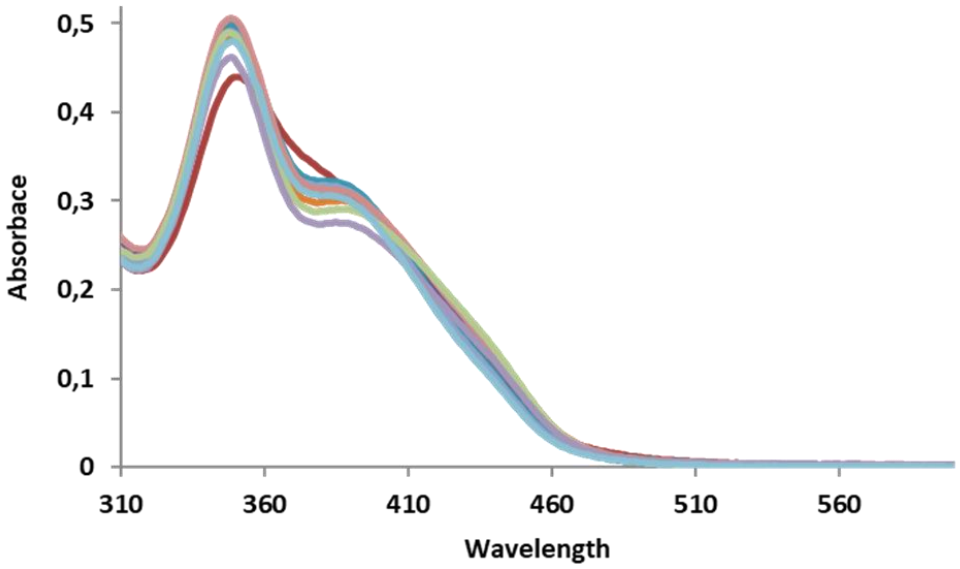

Figure 14: UV-Vis screening studies of **D3** with various anions in MeOH.

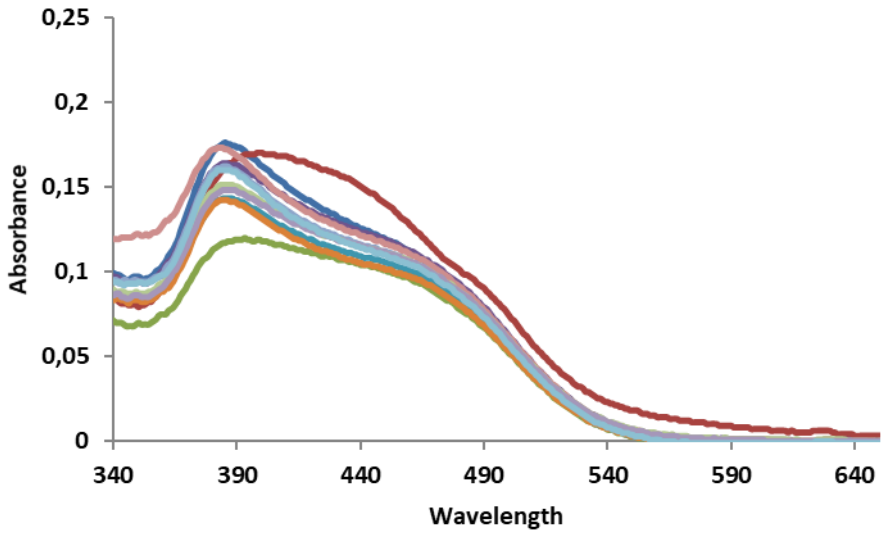

Figure 15: UV-Vis screening studies of **D4** with various anions in water.

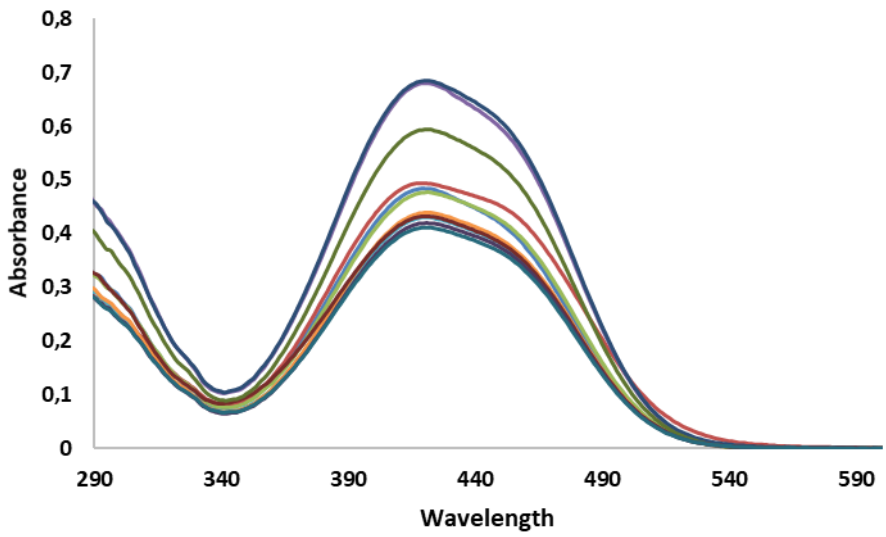

Figure 16: UV-Vis screening studies of **D4** with various anions in MeOH.

Chapter 6

Attempted synthesis of coumarin-derived polymeric sensors

The question as to whether small-molecule or polymeric based sensors display the most favourable sensing attributes has been continuously debated. In recent years, many small molecule-based sensors have exceeded the sensing capabilities of polymeric compounds and are being favoured owing to these excellent sensing properties, selectivity, and uncomplicated synthetic methods.

Attempts towards the synthesis of polymer-based sensors was done using the 7-subsituted coumarin derivatives as pendant groups (used in **Chapter 3**). The proposed methods for the synthesis **P1** are outlined in **Scheme 1**.

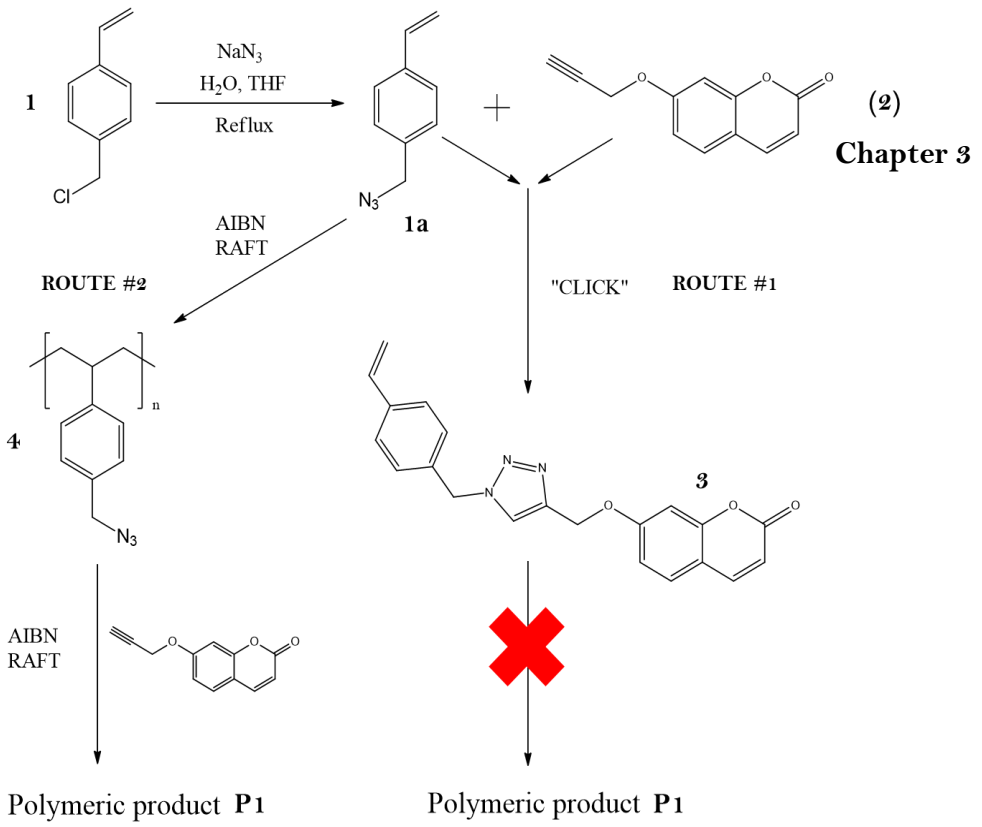

Scheme 1: Attempted synthesis of coumarin-derived polymer derivative **P1** by two different synthetic routes.

The reaction to form azo-vinyl derivative **1a** was carried out according to literature procedure.[1] The product was isolated as a yellow oil in good yield. The presence of the N_3 azide group was confirmed using FT-IR spectral analysis, and the desired product further supported by ^{1}H NMR studies. The FT-IR and ^{1}H NMR spectra of vinyl-azide derivative **1a** is shown in **Figures 1** & **2**.

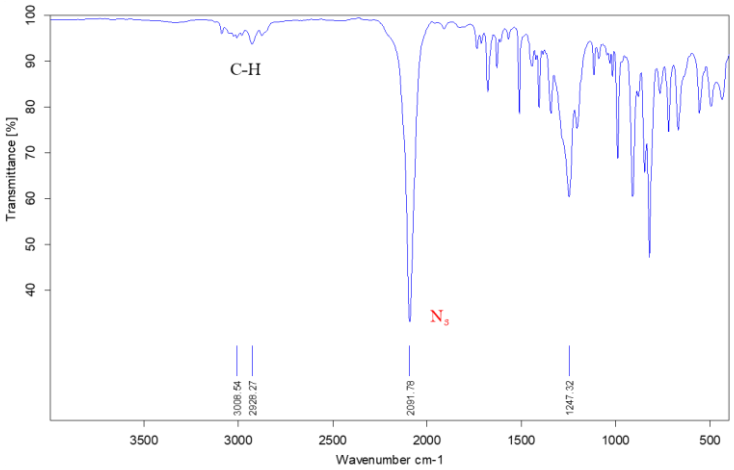

Figure 1: FT-IR of vinyl-azide derivative **1a**.

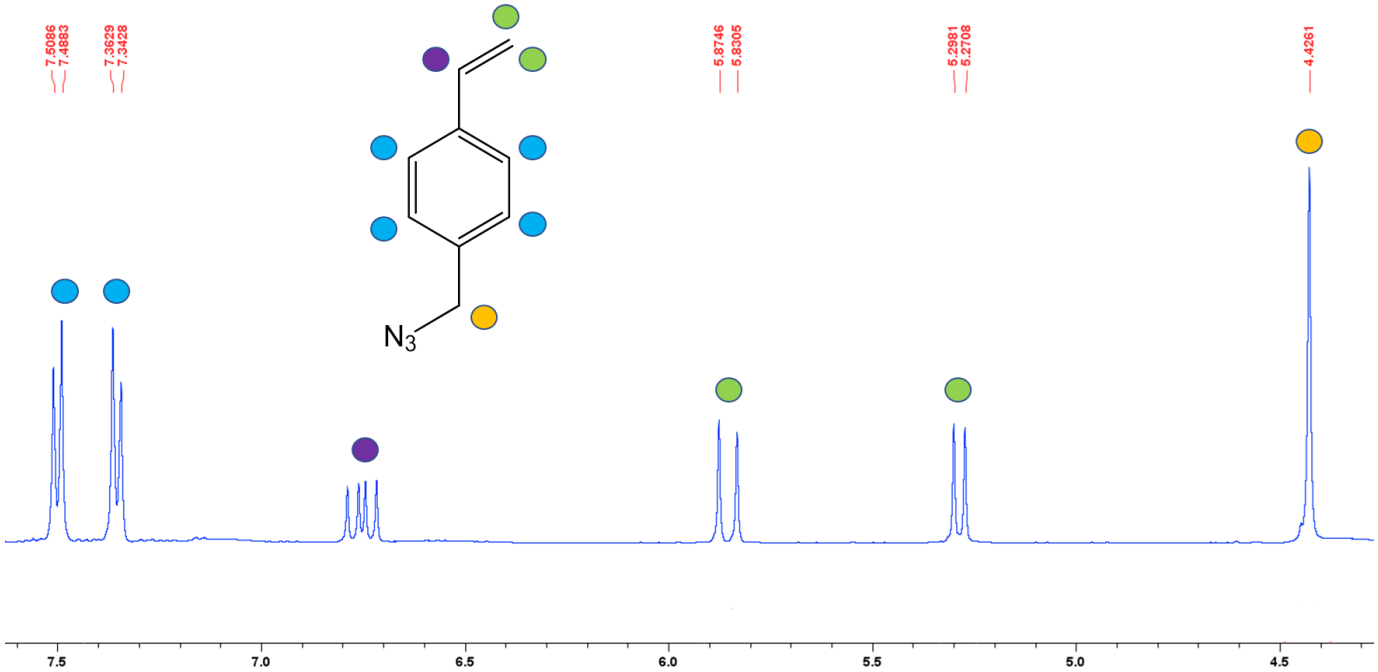

Figure 2: ^{1}H NMR spectra of vinyl-azide derivative **1a** in d_6-DMSO.

[1]. doi.org/10.1080/00304948.2011.594002

After the formation of **1a**, two different synthetic routes to form polymer **P1** were investigated. Route 1 involved the formation of a coumarin-vinyl monomer supporting a triazole moiety; and subsequent free-radical polymerization. Route 2 involved post-polymerization functionalization of the polymer backbone carrying an azide group by click reactions.

Route #1

Equal equivalence of **1a** and **2** were added under 'click' conditions in THF and left to stir at room temperature for 24 hrs. The product formation was monitored by TLC. The product was washed with water and extracted with ethyl acetate. The extracts were combined and dried over anhydrous Na_2SO_4. The solvent was removed under reduced pressure and precipitated from solution by DCM and ether to afford coumarin-vinyl derivative ***3*** as a white solid (52%). The structure was elucidated by ^{1}H NMR analysis and confirmed by single crystal X-ray analysis (**Figure 3** & **4**).

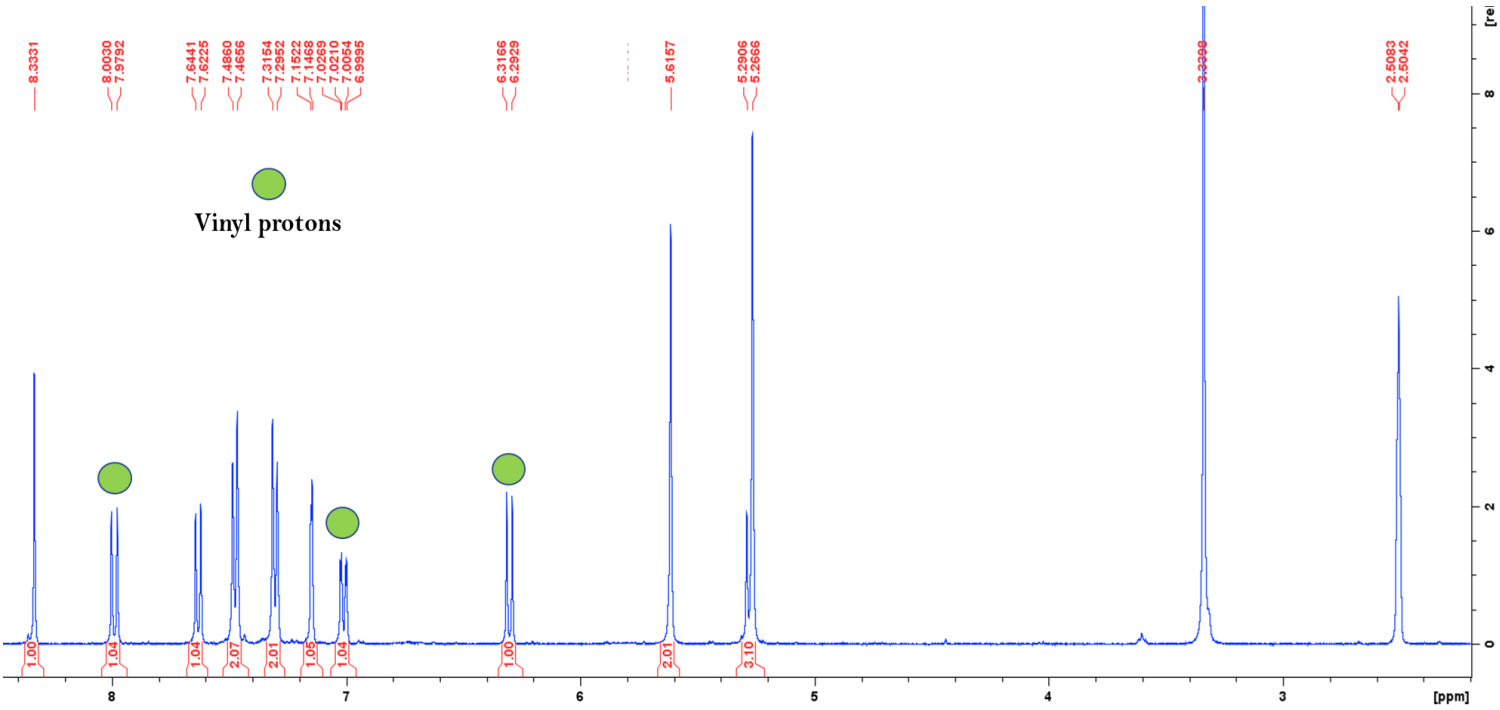

Figure 3: ^{1}H NMR of coumarin-vinyl monomer ***3*** in d_6-DMSO.

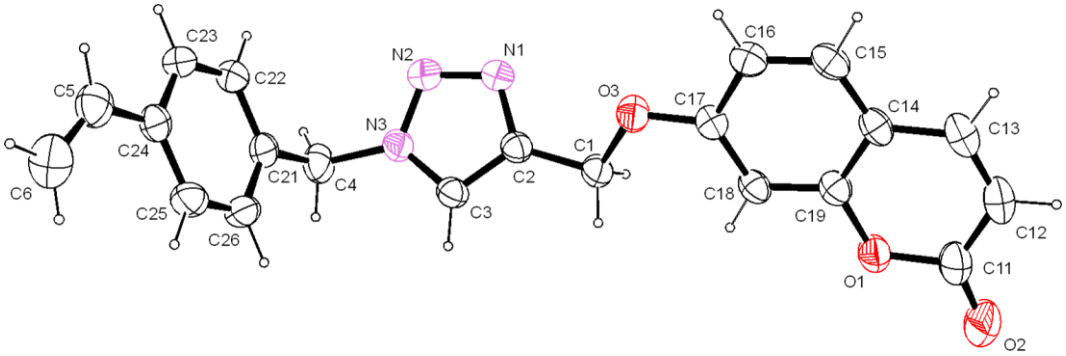

Figure 4: Single crystal X-ray structure of coumarin-vinyl derivative **3**.

Coumarin-vinyl derivative **3** was added to 0.1 equivalence of (AIBN) in a 25 mL Schlenk flask with minimal DMF. Five cycles of freeze-pump-thaw method were used to degas the system. After the system was degassed, the mixture was heated for 5 hrs and then left to stir for 72 hrs. The mixture was then precipitated in cold hexane to yield an off-white solid. The solid was filtered, recrystallized from DCM and ether, and characterized by ^{1}H NMR. Spectral analysis indicated that only the starting vinyl monomer **3** had precipitated from solution, therefore, the free-radical polymerization was not successful. This radical polymerization may have failed due to the size of the monomer and thus the resulting pendant groups. These large pendant groups could cause a great degree of steric hinderance on the polymer chain.

Route #2

This route involved the post-polymerization functionalization of a polymer backbone supporting an azide functionality (**4**) with the 7-propinyoxy coumarin derivative (**2**) under Cu(I) catalysed click conditions. For this purpose, vinyl-azide monomer **1a** was polymerized by free-radical reactions using 0.1 eq of AIBN in DMF. A freeze-pump-thaw method was used to degas the system. After degassing, the mixture was heated under argon and then left to stir for 72 hrs. The mixture was added dropwise into cold hexane, however, the polymeric product failed to precipitate from solution as confirmed by NMR analysis.

Experimental

Synthesis of vinyl-azide derivative 1a

4-vinylbenzyl chloride (6.55 mmol) was reacted with NaN_3 (6.55 mmol) in a THF-water solvent system and let reflux under stirring for 5 hrs. Thereafter, THF was removed under reduced pressure and the resulting solution extracted with 3 x 20 mL ethyl acetate. The extracts were combined, washed with water, and dried over anhydrous Na_2SO_4. Ethyl acetate was removed under reduced pressure to afford vinyl-azide derivative **1a** as a yellow oil (0.96 g; 6.04 mmol; 92 %). ^{1}H NMR (400 MHz, d_6-DMSO) δ_H (ppm): 4.43(s, 2H), 5.28(d, 1H, *J* 10.92), 5.85(d, 1H, *J* 17.64), 6.75(m, 1H), 7.35(d, 2H, *J* 8.04), 7.49(d, 2H, *J* 8.12). IR ν_{max} (cm^{-1}): 3008-2928 (C-H), 2019 (N_3).

Synthesis of coumarin-vinyl monomer 3

Vinyl-azide derivative **1a** (6.72 mmol) was added to a solution of **2** (6.72 mmol) in minimal THF under Cu(I) catalyzed click reaction conditions and left to stir at room temperature for 24 hrs. Thereafter, the solvent was removed under reduced pressure. The residue was dissolved in ethyl acetate and separated with water. The organic layer was dried over anhydrous Na_2SO_4 and the solvent removed under reduced pressure. The solid product was recrystallized from DCM and ether to yield coumarin-vinyl derivative ***3*** as a white solid (3.51 mmol, 1.26 g, 52 %). ^{1}H NMR (400 MHz, d_6-DMSO) δ_H (ppm): 5.26(s, 2H), 5.29(s, 1H), 5.61(s, 2H), 6.30(d, 1H, *J* 9.48), 7.01(m, 1H), 7.14(s, 1H), 7.30(d, 2H, *J* 8.08), 7.47(d, 2H, *J* 8.16), 7.62(d, 1H, *J* 8.64), 7.99(d, 1H, *J* 9.52), 8.33(s, 1H). ^{13}C NMR (100 MHz, d_6-DMSO) δ_C (ppm): 53.06, 62.12, 102.05, 113.05, 113.15, 113.39, 115.36, 125.45, 126.95, 128.78, 129.96, 135.93, 136.50, 137.51, 142.74, 144.74, 155.75, 160.71, 161.56.

Conclusion and Future work

Conclusion

Herein we report the synthesis and characterization of 14 novel coumarin-based sensors towards the fluorescent and colorimetric sensing of ionic species in organic and aqueous media. In **Chapters 2-4**, the majority of the coumarin-triazole based sensors displayed good affinity, selectivity, and sensitivity towards Fe^{3+}. Complexation was determined to occur in a 1:1 binding ratio, with complexation proposed to involve nitrogen atoms of the heterocyclic triazole moiety; and supported by neighbouring groups and solvent molecules. These complexation scenarios were supported by Molecular Modelling studies. Titration analysis indicated that the fluorescent quenching effect upon Fe^{3+} addition occurred via a PET "on-off" mechanism. Reversibility studies of the sensor-metal complexes with EDTA indicated partial reversibility. Anionic sensing studies displayed reasonable affinities towards CN^- and F^- characterized by a fluorescent quenching and enhancing response respectively. Quenching and enhancing was determined to occur via a PET "on-off" and "off-on" mechanism respectively. Poor selectivity and sensitivity of these sensors towards these chosen anions prevented further studies. In **Chapter 5** the chosen coumarin-imine and -azo derivatives displayed a high degree of selectivity and sensitivity towards Hg^{2+} in water and acetonitrile respectively. Furthermore, the coumarin-azo derivative displayed a visible colorimetric response from yellow to red upon Hg^{2+} addition. Complexation was determined to occur in a 1:1 sensing ratio for both derivatives with Hg^{2+}. UV-Vis Titration analysis indicated a dual ICT-ESIPT-ESICT mechanism for the imine derivative, whilst the azo derivative displayed a strong ICT response, characterized by a bathochromic shift in wavelength. Reversibility studies of the azo derivative described the total reversible nature of the complex; with applications extending towards the construction of a molecular logic gate and a molecular keypad lock system. Owing to the high degree of selectivity both sensors displayed towards Hg^{2+}, it was possible to quantitatively determine the concentrations of Hg^{2+} in real-world water samples. Owing to the unique colour change of the azo derivative upon Hg^{2+} addition, it was applied for inexpensive test strips towards on-site assay studies. Complexation studies described the involvement of the imine-nitrogen and neighbouring hydroxyl group towards Hg^{2+} complexation in the coumarin-imine sensor; whilst complexation in the azo derivative

was determined to involve the coumarin- and ester-carbonyl groups in a pseudo-6-membered ring conformation. These complexation scenarios were supported by molecular modelling studies. Anionic sensing studies displayed little to no specific affinity nor selectivity of these coumarin derivatives to any of the chosen anions, thus they were concluded as unsuitable for further titration analyses and experiments.

Future work

Chapters 2-4 described the synthesis, characterization, photophysical, and sensing properties of coumarin-triazole derivatives derived via 'click' reaction protocol. These fluorescent sensors showed an affinity towards Fe^{3+} with good selectivity and sensitivity. The binding of Fe^{3+} was characterized by a fluorescent quenching response suggested to occur via a static process. Anionic sensing studies showed affinity towards CN^-, PF_6^-, and F^-, however, poor selectivity and sensitivity towards these anions ceased further experiments. **Chapter 5** described the synthesis, characterization, and application of coumarin-imine and -azo derivatives towards UV-Vis and colorimetric cationic recognition strategies in organic and aqueous media. Both imine and azo sensors displayed good selectivity and sensitivity towards Hg^{2+}. The azo dye characterized the presence of Hg^{2+} by a vivid colour change from yellow to red. Both sensors were able to be used towards environmental water Hg^{2+} recognition strategies. Additionally, the azo dye was able to be used as a molecular logic gate, molecular security system, and on-site assay studies. **Chapter 6** describes the attempted synthesis of a coumarin-based polymeric sensor towards ionic sensing strategies in aqueous media. Some observations and ideas for future work will be briefly outlined:

1. **Why are all the fluorescent sensors responding strongly to Fe^{3+}?**

As seen in the screening studies, all the sensors showed chemical affinities to Fe^{3+} in a variety of organic and aqueous systems; characterized by a fluorescent quenching response. The question as to whether this is because of the coumarin scaffold alone, or the interaction between coumarin that is directly connected to a triazole moiety has yet to be determined.

2. **Sensors supporting the phenol-alkyne precursor exhibit greater selectivity and better photophysical properties compared to other alkyne derivatives.**

In all three chapters, derivatives supporting the phenol-alkyne precursor exhibit the most favourable sensing characteristics as compared to the other alkyne derivatives. The coumarin derivative supporting this functionality displayed advanced selectivity towards Fe^{3+}compared to the other alkyne precursors. The effect of this derivative towards sensing could be investigated

3. **Determination of the effect of dynamic quenching in the Stern-Volmer quenching model.**

As mentioned previously, the effect of dynamic quenching on the linear Stern-Volmer quenching model could not be determined due to equipment constraints. Dynamic quenching is determined by calculations involving fluorescent lifetimes. To calculate this, TCSPC (time-correlated single photon counting) is used.

4. **The role of coumarin-metal complexes in medicine and live-cell imaging.**

The efficacy of coumarin, its derivatives, and metal complexes towards anti-cancer treatments and other medicinal applications have been widely discussed in the literature. Future work could include toxicology studies of the coumarin derivatives and its metal complexes, determination of anti-cancer properties, and live-cell imaging recognition strategies.

5. **Dual colorimetric-fluorescent coumarin based sensors.**

The coupled favourable visible colorimetric response of the azo/imine functionality together with the sensitive fluorescent response of the triazole moiety could produce a dual sensor that can identify different cations based on their photophysical responses and binding strategies.